

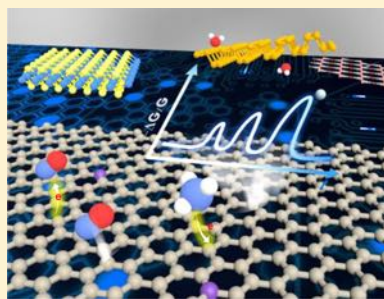
Electrically-Transduced Chemical Sensors Based on Two-Dimensional Nanomaterials

Zheng Meng[†] Robert M. Stoltz,[†] Lukasz Mendecki,[†] and Katherine A. Mirica^{*}

Department of Chemistry, Burke Laboratory, Dartmouth College, Hanover, New Hampshire 03755, United States

 Supporting Information

ABSTRACT: Electrically-transduced sensors, with their simplicity and compatibility with standard electronic technologies, produce signals that can be efficiently acquired, processed, stored, and analyzed. Two dimensional (2D) nanomaterials, including graphene, phosphorene (BP), transition metal dichalcogenides (TMDCs), and others, have proven to be attractive for the fabrication of high-performance electrically-transduced chemical sensors due to their remarkable electronic and physical properties originating from their 2D structure. This review highlights the advances in electrically-transduced chemical sensing that rely on 2D materials. The structural components of such sensors are described, and the underlying operating principles for different types of architectures are discussed. The structural features, electronic properties, and surface chemistry of 2D nanostructures that dictate their sensing performance are reviewed.



Key advances in the application of 2D materials, from both a historical and analytical perspective, are summarized for four different groups of analytes: gases, volatile compounds, ions, and biomolecules. The sensing performance is discussed in the context of the molecular design, structure–property relationships, and device fabrication technology. The outlook of challenges and opportunities for 2D nanomaterials for the future development of electrically-transduced sensors is also presented.

CONTENTS

1. Introduction	
1.1. Unique Features of Electrically-Transduced Detection	479
1.2. Role of Sensing Material in Electrically-Transduced Chemical Sensing	479
1.3. Unique Features of 2D Materials in Chemical Sensing	480
1.4. Scope and Organization of this Review	482
2. Electrically-Transduced Sensors	482
2.1. Components of Electrically-Transduced Chemical Sensors	
2.1.1. Sensing Materials and Their Variable Electronic Properties	483
2.1.2. Transducers	484
2.1.3. Data Processing	484
2.2. Sensing Mechanisms	485
2.2.1. Mechanisms of Analyte–Material Interactions	485
2.2.2. Mechanisms of Transduction	485
2.3. Performance Parameters	487
2.4. Electrically-Transduced Sensing Architectures	488
2.4.1. Chemiresistors	488
2.4.2. Chemical Diodes	489
2.4.3. Field-Effect Transistors	490
2.4.4. Chemical Capacitors	491
2.4.5. Electrochemical Sensors	492
3. Structure and Surface Chemistry of 2D Materials	494
3.1. Graphene and Graphene Oxides	494

3.2. Black Phosphorus	496
3.3. Transition Metal Dichalcogenides	496
3.4. Metal Oxides	497
3.5. Metal–Organic Frameworks	498
3.6. Other 2D Materials	500
4. Sensing Applications	501
4.1. Detection of Gases	501
4.1.1. Graphene and Graphene Oxides	501
4.1.2. Black Phosphorus	506
4.1.3. Transition Metal Dichalcogenides	507
4.1.4. Metal Oxides	509
4.1.5. Metal–Organic Frameworks	512
4.1.6. Other 2D Materials	513
4.2. Detection of Volatile Compounds	515
4.2.1. Graphene and Graphene Oxides	515
4.2.2. Black Phosphorus	523
4.2.3. Transition Metal Dichalcogenides	525
4.2.4. Metal Oxides	528
4.2.5. Metal–Organic Frameworks	529
4.2.6. Other 2D Materials	530
4.3. Detection of Ions	534
4.3.1. Graphene and Graphene Oxides	534
4.3.2. Black Phosphorus	537
4.3.3. Transition Metal Dichalcogenides	538
4.3.4. Other 2D Materials	539
4.4. Detection of Biomolecules	539

Special Issue: Chemical Sensors

Received: May 16, 2018

Published: January 3, 2019

4.4.1. Graphene and Graphene Oxides	542
4.4.2. Black Phosphorus	550
4.4.3. Transition Metal Dichalcogenides	551
4.4.4. Metal Oxides	554
4.4.5. Other 2D Materials	555
5. Conclusions and Perspectives	565
Associated Content	566
Supporting Information	566
Author Information	566
Corresponding Author	566
ORCID	566
Author Contributions	566
Author Contributions	566
Notes	566
Biographies	566
Acknowledgments	567
Abbreviations	567
References	569

1. INTRODUCTION

1.1. Unique Features of Electrically-Transduced Detection

The senses of smell, taste, sight, touch, and hearing are some of the most elegant and powerful mechanisms through which living systems interact with their surroundings.¹ Each sense has a specific function to help living systems collect chemical or physical information from the surrounding environment. Physical organs have developed sensing systems that leverage thermodynamics, Nernstian potentials, photochemical processes, and molecular recognition to interpret exterior perturbations into neuronal impulses. The remarkable success of natural sensing systems continues to inspire the development of new technologies. Building upon the principles of molecular recognition has propelled the development of analytical instrumentation that can probe physical parameters, such as temperature, pressure, or light intensity, and obtain chemical information about a sample.² The desire to create technologies that enhance the perception of the surrounding environment further drove the progress in the development of physical and chemical sensors.²

Since the second half of the 20th century, chemical sensors and biosensors have become an indispensable part of modern society with broad applications in industrial chemical production processes, pharmaceuticals, food products, environmental monitoring, security, industrial safety, healthcare, and indoor monitoring applications (Figure 1).^{3,4} Portable chemical sensors, that are easy to operate, economical, sensitive, and simple to construct, have become an effective tool in situations where the use of more precise analytical techniques and equipment is restricted by sample pretreatment requirements, the need for hazardous reagents, or access to qualified personnel.⁵ Portable chemical sensors can be broadly classified into gas, liquid, and solid particulate sensors, depending on the nature/phase of the targeted analytes.⁶ These groups of sensors can be further subdivided according to their underlying principles of signal transduction into either optical, electrochemical, thermometric, or gravimetric sensors.⁴ Of these, a class of electrically-transduced devices has gained a significant role in the sensing field owing to the simplicity, compatibility with wireless transmission, nonline-of-sight detection, possibility of continuous monitoring, portability, and compatibility with standard electronic equipment (Figure

2).^{7–15} These features have the potential to enable highly interconnected networks of physical, chemical, and biological sensors with the ability to link different realms of human experience with measurements of causality that are currently unavailable.¹⁶ In particular, wireless sensing networks can enhance spatial and temporal resolution of acquired information, and permit continuous monitoring at otherwise highly inaccessible locations.^{17,18} Realizing next-generation transformation in electronic-sensor science necessitates access to high quality conductive materials capable of converting physical and chemical stimuli into electronic signals, as well as development of methods of their integration into functional sensing devices.

1.2. Role of Sensing Material in Electrically-Transduced Chemical Sensing

A sensing device typically comprises two main components: the sensing material and the transducer.⁴ The sensing material is responsible for interacting with the stimuli, either in the form of a physical perturbation (e.g., temperature or pressure change) or a chemical entity, inducing a change in one or several of its properties, which are then transformed into readable signals by the transducer (Figure 3).^{28–30} Sensors that probe physical changes have been attained by synergistic breakthroughs in material development through the engineering of their physical properties and the refinement in the methods of integrating these materials into devices.^{31,32} Physical sensors, which have been widely used in various fields—such as in wearable consumer electronics, soft robotics, smart medical prosthetics and electronic skins, and real-time healthcare monitoring^{33,34}—function on a direct cause-effect relationship.³⁵ For example, the touch screen of a cellphone changes its capacitance upon contact with a finger due to¹⁶⁶ alterations in the dielectric characteristics of the screen, thus producing a measurable response to a touch stimulus.³⁶

In contrast to physical sensors, progress in electrically-transduced chemical sensing entails an additional level of complexity posed by the chemical interfaces between the material and the analyte (Figure 3).⁴ These interfaces play a key role in determining the sensitivity, selectivity, stability, and biocompatibility of chemical sensing devices.^{38–40} The role of the sensing material is twofold.²⁹ First, it must (be able to) interact covalently or noncovalently with the analyte on its surface. Second, it must respond to this interaction by changing its electrically related physical properties. The transduction mechanism can be a function of conductivity, work function, or electrical permittivity and can be transduced as a change in capacitance, resistance, or inductance.⁴¹ Using standard electronic components, generally including resistor,⁴² diode,⁴³ field-effect transistor,⁴⁴ capacitor,⁴⁵ and electrochemical sensor⁹ configuration, these transduction events can be measured as changes in the resistance/impedance, current, voltage/electrical potential, and capacitance, where magnitude, frequency, and phase of the signal can provide valuable information regarding the sensing event (Figure 3).⁴⁶ Therefore, the design of a sensing material must consider its ability to selectively interact with targeted analytes and consequently undergo a change in its electrical property.

Ideally, a sensing material should have a large exposed surface available for the material-analyte interaction, suitable active sites for effective and selective analyte binding, the ability to transduce the binding events into a detectable signal, as well as good mechanical and processing properties.



Figure 1. Chemical sensors are widely used in different aspects of human life. Adapted Illustration 78407701. Copyright Monicaodo - Dreamstime.com.

Advances in the development of modified carbon-based electrodes,^{47,48} boron-doped diamond,⁴⁹ coupled with the discoveries of conductive polymers,^{12,50} fullerenes,^{51,52} carbon nanotubes,^{53–56} and metallic and semiconductive nanoparticles,^{57–59} have led to extensive applications of these materials in electrically-transduced chemical sensing. These materials have their own distinct advantages and disadvantages in the context of chemical sensing.⁷ For example, conductive polymers are straightforward to synthesize and integrate into electrical devices and they exhibit high sensitivity to a broad range of analytes.¹¹ However, conductive polymers need to be doped to obtain sufficient electrical conductivity for chemical sensing applications.^{12,50,60} Metallic nanoparticles can achieve high sensitivity through feasible functionalization, however, they may be difficult to integrate into functional devices due to aggregation effects on the surface of a substrate.⁶¹ A good material candidate for electrically-transduced sensing should have a synergistic combination of its surface chemistry, desired electronical properties, as well as fabrication with control over dimensionality, flexibility, mechanical stability, and lattice matching with the device substrate. It should also possess the ability to respond to the recognition event by changing its electrical properties that could be further transformed into a readable signal.

1.3. Unique Features of 2D Materials in Chemical Sensing

Two-dimensional (2D) materials,^{70–73} with thicknesses ranging from few to tens of nanometers and lateral dimensions reaching up to many centimeters,^{74,75} possess remarkable physical and chemical properties with promising potential utility in electrically-transduced chemical sensing. Graphene (Gr),⁷⁶ a one-atom-thick sheet of carbon atoms with a 2D hexagonal crystal structure, has shown great promise for

applications in electronics, photonics, energy conversion and storage, medicine, and chemical/biological sensing due to its unique physical, chemical, electrical, optical, thermal, and mechanical properties.^{77–80} The diversity of 2D materials has grown appreciably to include phosphorene,^{67,81} hexagonal boron nitride (*h*-BN),^{82,83} transition metal dichalcogenides (TMDCs),^{84,85} layered metal oxides,^{86,87} 2D metal–organic frameworks (MOFs),^{88,89} covalent organic frameworks (COFs),^{90,91} and other 2D compounds.⁷³ These materials exhibit exceptional properties—large surface-to-volume ratio, rich surface chemistry, atomic-level thickness, exceptional electrical properties—that are distinct from their 3D bulk counterparts, which make them uniquely suited to detect and transduce chemical events. Table 1 compares the unique features of 2D materials with other materials of different dimensionality (0D, 1D, and 3D) in the context of potential utility in electrically-transduced sensing.

Compared with their 0D, 1D, and 3D analogs, the large surface-to-volume ratio of most 2D materials⁹² ensures tremendous surface area available for the material-analyte interactions, which are beneficial for realizing high sensitivity even at extremely low concentrations of the analyte. For example, the occupancy by highly reactive surface Sn and O atoms with low coordination numbers of five-atomic-layer-thick SnO₂ sheets (0.66 nm) is as high as 40%.⁹³ The rich surface chemistry is manifested by the presence of active sites that could effectively and selectively interact with targeted species.⁹⁴ The surface of the materials can also act as a molecular scaffold for the immobilization of additional recognition components (e.g., metallic nanoparticles, metal oxides, and enzymes), which can further improve the sensing performance of a device, including its sensitivity and

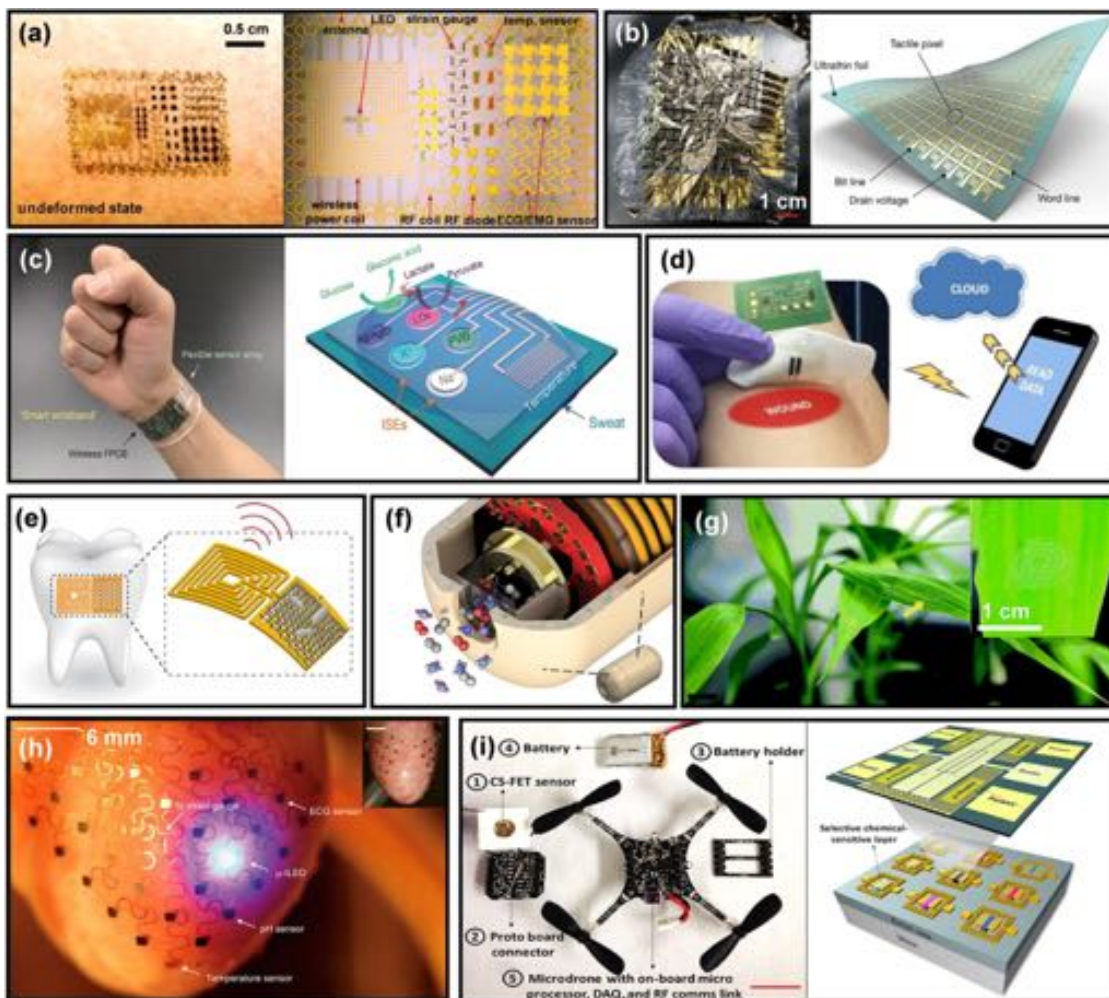


Figure 2. Electrically-transduced sensors can be used in a diverse range of applications and sensor architectures. (a) Multifunctional epidermal electronic system (EES) on compressed skin for the measurement of physiological activities (left). The physical EES integrates electrophysiological, temperature, strain sensors, and other electronic components (right).¹⁹ (b) Illustration of a thin large-area field-effect transistor (FET) based bolometer sensor with 12×12 tactile pixels (right). The devices are ultraflexible, are extremely lightweight (3 g m^{-2} , left), and can be crumpled like a sheet of paper (left).²⁰ Adapted with permission from ref 20. Copyright 2013 Springer Nature. (c) Photograph of a wearable flexible integrated sensing array (FISA) on a subject's wrist, integrating multiplexed sweat sensor array with a wireless (flexible printed circuit board) FPCB (left). Schematic of the sensor array (including glucose, lactate, sodium, potassium, and temperature sensors) for multiplexed perspiration analysis (right).²¹ Adapted with permission from ref 21. Copyright 2016 Springer Nature. (d) Bandage-based uric acid sensor for monitoring wound healing. Demonstrated wireless communication with a computer and smartphone.²² Adapted with permission from ref 22. Copyright 2015 Elsevier B.V. (e) Graphene-based wireless resistive sensor integrated on tooth enamel for bacteria monitoring.²³ Adapted with permission from ref 23. Copyright 2012 Springer Nature. (f) Ingestible electronic capsules capable of sensing gases in the gut.²⁴ Adapted with permission from ref 24. Copyright 2018 Springer Nature. (g) A graphene-based FET sensor transferred onto leaf for nerve gas simulant dimethyl methylphosphonate sensing.²⁵ Scale bar, 1 cm. Adapted with permission from ref 25. Copyright 2016 The Royal Society of Chemistry. (h) Images of a representative 3D multifunctional integumentary membrane integrated on a Langendorff-perfused rabbit heart. The white arrows highlight various function elements in this system. The electronics can cover both anterior and posterior surfaces of the heart (inset). Scale bars, 6 mm.²⁶ Adapted with permission from ref 26. Copyright 2014 Springer Nature. (i) A microdrone equipped with a CS-FET and data acquisition components for environmental pollution mapping and personal air-quality monitoring (left). Schematic illustration of a single-chip CS-FET array functionalized with different selective sensing layers (bottom, right) and optical microscope image of a single chemical-sensitive FET (CS-FET) functionalized with a Pd–Au sensing layer integrated with microheaters (top, right).²⁷ Adapted with permission from ref 27. Copyright 2017 Science/AAAS.

selectivity.^{95–97} For example, each P atom on the surface of phosphorene can potentially function as an active site for the chemical adsorption of a gaseous analyte.⁹⁸ Theoretical studies demonstrated that chemical doping of heteroatoms of phosphorene can tune its bandgap, and also enhance the strength and selectivity of the phosphorene-analyte interactions.^{99,100} 2D materials also exhibit a rich variety of electrical properties. Their conductivities encompass metals, semimetals, insulators, and semiconductors with direct and indirect bandgaps ranging from ultraviolet to infrared, and

throughout the visible spectrum (Figure 4).⁶² The fine structural and compositional tuning can also improve the electrical characteristics of 2D nanomaterials enabling efficient signal transduction as a result of molecular binding event.¹⁰¹

The charge transport in 2D materials is strongly confined in the 2D plane, leading to remarkable changes in their electronic properties upon analyte binding. In contrast to 1D nanostructures, 2D nanomaterials can offer good conformal and intimate electrical contact with metal electrodes due to their relatively large lateral sizes.¹⁰² The geometry of 2D

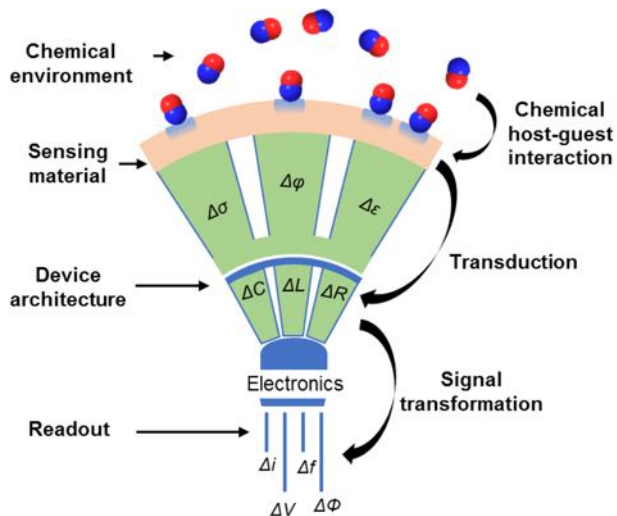


Figure 3. Logical structure of a chemical sensor.²⁹ Analytes interact with the sensing material changing some of its physical properties including conductivity (σ), work function (φ), and permittivity (ϵ). The transducer converts one of these physical quantities into the variation of its electric parameters (here, capacitance C , inductance L , and resistance R are mentioned).³⁷ The circuit to which the device is connected gives rise to the sensing signal. Electrical signals are current (I), voltage (V)/electrical potential (E), and capacitance with measurable changes in magnitude, frequency (f), and phase (Φ). Reproduced from ref 29. Copyright 2017 American Chemical Society.

materials also shows excellent compatibility with current thin film manufacturing techniques in the semiconductor industry, which can facilitate the coupling of 2D structure with traditional electronic materials, such as Si.¹⁰² 2D materials, such as graphene, also demonstrate other excellent physical properties, including a large Young's modulus (~1000 GPa), high strain limit (~25%), and good optical transparency (>90%).¹⁰³ Compared to conventional inorganic semiconductors that heavily rely on mechanical design to minimize intrinsic strain below 1% to prevent material breakage, the large modulus and strain limit of 2D materials reinforce their potential in fabricating sensing devices with good stability and flexibility.^{8,104}

1.4. Scope and Organization of this Review

This review provides a comprehensive discussion of the recent advancements in the fundamental and applied research on 2D nanomaterials in the context of electrically-transduced chemical sensing. We outline the components necessary for the fabrication of functional devices and the transduction principles underlying their operation. Subsequently, we discuss the device architectures of current and emerging electrically-transduced sensing platforms, and then highlight the fundamental detection principles governing their response. We describe the structural and compositional features of 2D nanostructures that determine their electrical properties, ultimately leading to applications in the development of sensors. We then highlight key advances in the application of 2D materials in electrically-transduced sensors, both from a historical and analytical perspectives with respect to four major groups of analytes: gases, volatile organic compounds (VOCs), ions, and biomolecules. We conclude by offering insights into the challenges and opportunities facing the development and application of 2D materials within electrically-transduced sensing platforms.

The increasing exploration of the electronic properties of 2D nanostructures has burgeoned into a new field within chemical sensing. Although excellent reviews on the broad subject of electronic transduction in chemical sensing using nanomaterials,⁷ the synthesis and structure of 2D materials,^{115,116} their physio-chemical properties,^{71,119} and their applications in energy, electrocatalysis, and electronics,^{102,120,121} are separately available, a comprehensive review focusing on the progress and challenges of 2D materials that act as electronic sensors and transducers does not exist. This review focuses on facilitating insights into the connection between the low dimensionality, surface chemistry, electronic properties, and the analytical response of electrically-transduced sensors based on 2D nanomaterials. The organization of this review is structured to introduce the readers to key components, sensing mechanisms, performance parameters, and device architectures of electrically-transduced sensors based on the 2D materials. Although certain aspects of these topics have been reviewed for a general class of nanomaterials,^{7,29,122} carbon nanotubes,⁵³ graphene,^{78,123–126} and metal oxide semiconductors,^{127–129} we offer a comprehensive overview based on the latest literature pertinent to the broad topic of 2D materials.

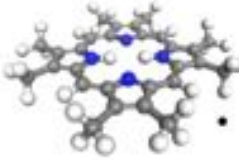
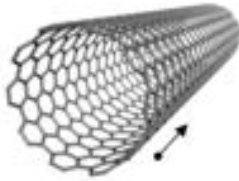
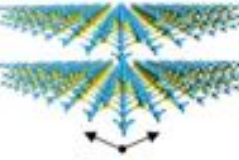
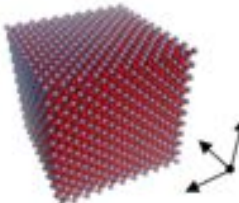
The organization of the review is intended not only to help the readers grasp and assess the latest advancements in the surface chemistry and structural characterization of 2D materials, but also to compare the important characteristics across the broad range of materials in this review. By organizing this review with a focus on four major classes of analytes promotes cross-cutting examination of how the structural features of 2D materials and the strategic modifications of their surface enable the sensitivity and selectivity of target-oriented electroanalysis.

2. ELECTRICALLY-TRANSDUCED SENSORS

2.1. Components of Electrically-Transduced Chemical Sensors

Chemical sensors consist of a chemical recognition element coupled with a transducing element that together can detect changes in the chemical environment and translate that information into a readable signal.⁴ In the recognition step, the sensing material identifies a chemical parameter—the identity and concentration of a gas, ion, or biomolecule—and undergoes a change in a physical parameter of the sensing material as a function of concentration of the sensed analytes. Electrically-transduced sensors rely on a few key physical parameters that can be altered in response to an analyte, including electrical conductivity (σ), work function (φ), and permittivity (ϵ ; Figure 3). The transducer then converts the change produced by the sensory material into a measurable electrical signal, including current (I), capacitance (C), resistance (R)/impedance (Z), voltage (V), or electrical potential (E).⁷ These electrical signals, or data, can undergo further processing, including amplification, filtering, analysis, or display to generate information about the identity of the analyte and its concentration.¹³⁰ Each of the components is responsible for a specific step in the sensing process that stems from initial molecular recognition between the analyte and the active 2D material and the readout signal for application. The specific choice of sensing material, transducer, and the method of integration into a device dictates the behavior and performance characteristics of sensing devices. In the following section we discuss the function of sensing materials, trans-

Table 1. Representative Structure of Materials from 0 to 3 Dimensions and the Comparison of Their Features in Context of Electrically-Transduced Sensing Materials

Dimension	Example	Advantage	Disadvantage
0D		<ul style="list-style-type: none"> Regio- and stereo-selective functionalization⁹⁶ Atomic control of structure–property relationship Large area-to-volume ratio Single-molecular electronic based sensing¹⁰⁵ Tunable size and shape^{106–108} 	<ul style="list-style-type: none"> Low conductivity Difficulty with device integration Limited stability of devices Potential toxicity¹⁰⁹
1D		<ul style="list-style-type: none"> High surface-to-volume ratio¹¹⁰ High aspect ratio Excellent stability High density of reactive sites Good thermal stability Compatible with device miniaturization^{111–112} 	<ul style="list-style-type: none"> Required chemical modification to enhance selectivity Difficulty in establishing reliable electrical contacts Difficult purification Limited structure and precision control^{53, 113}
2D		<ul style="list-style-type: none"> Wide tunability of conductivity Large surface-to-volume ratio Thickness dependent electronic properties Good optical transparency Excellent mechanical flexibility Good functionalization ability Potential for good processability Compatible with ultra-thin silicon channel technology^{73, 98, 113–114} 	<ul style="list-style-type: none"> Lack of mass production of materials with large area, high and uniform quality Lack of facile, effective, and reliable strategies for device integration Limited stability of some forms at ambient conditions^{73, 94}
3D		<ul style="list-style-type: none"> Strong analyte adsorption/binding Good mechanical strength Good thermal stability Easy to interface with solid-state devices Good designability to improve selectivity¹¹⁵ 	<ul style="list-style-type: none"> Low surface area (for non-porous materials) Difficulty with miniaturization¹¹⁶ Slow dynamics of analyte transport¹¹⁵

ducers, and data processors in the context of electrically-transduced sensing.

2.1.1. Sensing Materials and Their Variable Electronic Properties. The role of a sensing material is to interact with analytes and to respond to this interaction by changing its internal physical parameters.¹³¹ First, this process necessitates the presence of active sites capable of binding guest analytes. These active sites can be either inherently imbedded in the material during their synthesis, or deliberately incorporated via post-synthetic modifications.³ Integrated bottom-up approaches often provide more precise control over the spatial distribution of incorporated host–sites in the final structure of the 2D nanomaterials.^{132,133} However, these approaches may be difficult to realize as they require the compatibility of host–site chemistry with available material synthetic methods. Alternatively, the active sites necessary for host–guest interactions can be incorporated onto the surface of 2D material through post-synthetic modifications.^{134–136} This approach relies on the decoration of surfaces with covalent or non-covalent modifiers that act as host sites.^{97,137} Because the materials are synthesized prior to the chemical

modifications, a diverse range of methods are available for the incorporation of desired recognition elements. However, in certain situations, harsh experimental conditions may unfavorably alter the physical, chemical, and electronic properties of 2D materials.^{73,138,139} Typically, post-synthetic modification methods cannot offer the same level of organization of host sites in the 2D nanostructure as can be obtained by bottom-up methods.

Second, the interaction between analyte and sensing material must induce an observable change in the conductivity, work function, or permittivity of the material. Conductivity of a material (σ) is governed by the charge carrier mobility μ_i and charge carrier population n_i as given in eq 1.¹⁴⁰

$$\sigma = e(\mu_e n_e + \mu_h n_h) \quad (1)$$

where μ_e and μ_h are the mobility of electrons and holes, n_h and n_e are the electron and hole populations, and e is the fundamental charge. In 2D materials, both electrons in the conduction band or electron holes in the valence band may act as charge carriers.¹⁴¹ The mobility of these carriers is related to the drift velocity under the influence of an electric field.

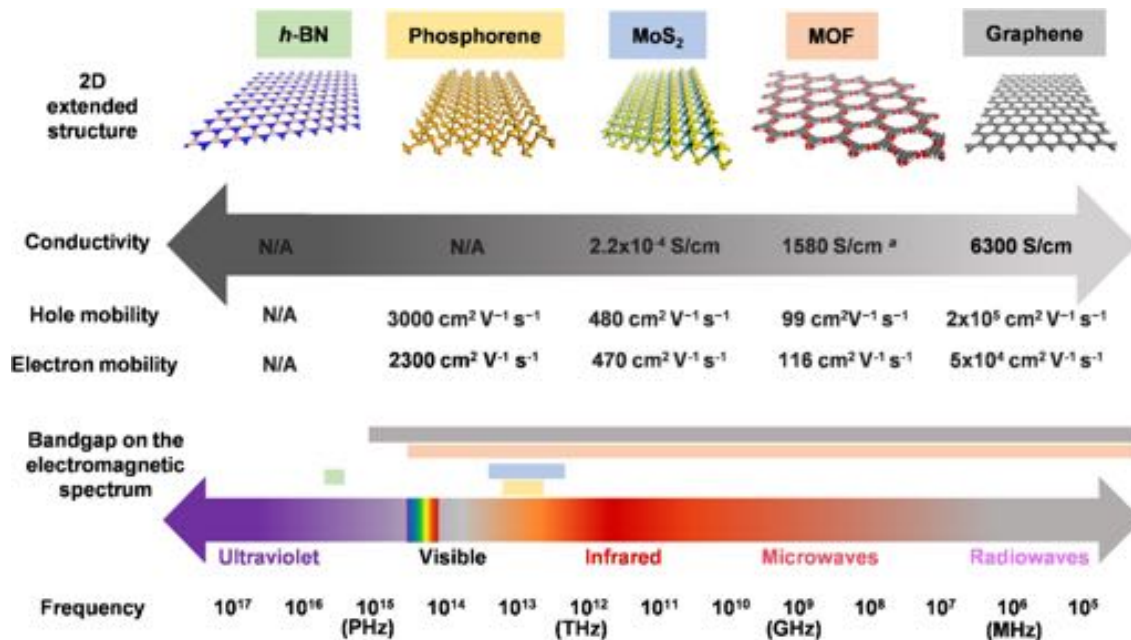


Figure 4. Atomically thin 2D materials span a wide range of chemical structures, conductivities, carrier mobilities, and bandgaps.⁶² Chemical structures of 2D materials have been discovered with a mixed elemental structure such as *h-BN*,⁶³ 2D-MOFs,⁶⁴ and *MoS₂*,⁶⁵ as well as well as pure elemental sheets such as black phosphorus^{66,67} and graphene.^{68,69} The electronic structure of 2D materials covers a wide range from insulating *h-BN* to the metallic conductivity of graphene. This wide range of properties exhibited by diverse 2D materials is the key to their success in sensing applications. ^aValue reported from material Cu-BHT, ref 64. N/A: no known reports of this value exist.

Changes in conductivity, according to eq 1, stem from the modifications in the mobility or population of charge carriers. The population of charge carriers n_i (n_e or n_h) is further related to the bandgap of the conductive material (E_g) by a constant (C) and temperature (T ; eq 2). Equation 2 shows that changes in temperature can alter conductivity of the 2D material by changing the population of electrons in the conduction band. This equation also demonstrates that increasing bandgap also reduces the population of carriers at a given temperature, leading to a decrease in overall conductivity. In the band theory of conductivity, the bandgap is the energetic difference between an electron in the conduction band (E_c) and in the valence band (E_v ; eq 3).¹⁴²

$$n_i = CT^{3/2} e^{-E_g/2k_B T} \quad (2)$$

$$E_g = E_c - E_v \quad (3)$$

The work function (W) of a material measures how much thermodynamic work is required to remove an electron from the Fermi level (E_F) to the vacuum level or directly outside the material surface (eq 4).¹⁴³

$$W = -e\varphi - E_F \quad (4)$$

The work function dependence on the electrostatic potential (φ) shows that W is dependent on the bias potential applied to the material. When the relationship is rewritten to consider externally applied potentials (V , eq 5), one can understand phenomena such as Schottky barriers and band-bending.¹⁴⁴

$$\varphi = V - \frac{W}{e} \quad (5)$$

The permittivity of a material is a measure of how easily electromagnetic radiation can travel through it. The permittivity of a material is directly related to the permittivity of a vacuum (ϵ_0), and the material property of relative static

permittivity (ϵ_r), which is a function of the electric susceptibility (χ ; eq 6).¹⁴⁵

$$\epsilon = \epsilon_r \epsilon_0 = (1 + \chi) \epsilon_0 \quad (6)$$

Together, perturbations to conductivity, electrostatic potential, and permittivity are responsible for the changes in electronic properties of a material. Analyte binding may influence one or all of these factors, which in turn will be translated by a transducer into a readable electrical signal.

2.1.2. Transducers. Transduction refers to converting the changes in physical properties of the sensing materials to a specific electrical signal.³ This signal conversion is realized by integrating the sensing materials into an electronic device. A material-analyte interaction may induce more than one physical property change (e.g., permittivity, work function, or conductivity) in the sensing material.¹⁴⁶ However, one of these alterations in physical parameters can be more prominent than others.⁴¹ For example, the adsorption of gaseous analytes on graphene can theoretically alter both conductivity and permittivity in the material, while sensing of these types of analytes is mostly realized by monitoring changes in current/resistance, as the associated capacitance changes (resulting from the permittivity change upon graphene-gas interaction) can be relatively small.^{147,148} Based on the electronic properties of different 2D materials and the nature of sensed analytes, 2D materials can be integrated into a diverse range of devices to transduce the chemical interaction into a readable electrical signal. These aspects will be discussed in section 2.4.

2.1.3. Data Processing. All readouts obtained from a sensing device must undergo signal processing and interpretation. Algorithmic processing of raw sensor data is a method of analyzing selectivity of a sensor without modifying device chemistry or architecture.¹⁴⁹ Methods such as principle component analysis (PCA) and linear discriminant analysis (LDA) can be applied to multiple devices to distinguish classes

of analytes.¹³⁰ PCA uses linear combinations of correlated parameters to describe the greatest amount of variation in a data set. Such methods of data processing in arrays have been applied in numerous examples to successfully distinguish broad patterns, such as functional group recognition.¹³⁰ As sensors become increasingly mobilized by miniaturization, important design criteria, like portability and cost of data processing units, must be taken into consideration. Different techniques for conditioning individual outputs from a multivariable sensor are also being explored with the goal of providing more reliable sensor performance.¹⁵⁰ The best practices in data analytics of dynamic and steady-state features should be shared proactively across different types of platforms and sensors. In recent years, technologies for integrating 2D materials into a new generation of highly integrated devices have begun to develop,¹⁰² making it possible to leverage the compact and powerful computing ability of smart terminals for sharing and analyzing data online.¹⁰⁴

2.2. Sensing Mechanisms

The underlying principles of most chemical sensors that enable their operation rely on two consecutive parts: molecular recognition and transduction of the recognition event.⁴ In the recognition step, an analyte molecule interacts with the active site or receptor molecule present in the structure of the sensing material. These interactions either change the chemical structure and composition of the sensory materials or the chemical environment around it, resulting in a characteristic alteration in one or more physical parameters. This change is then reported by means of an integrated transducer that generates the output signal.²⁹ These two principles behind the sensing mechanism of the electrically-transduced sensor, namely analyte–material interaction and the mechanism of transduction, are further discussed in the following sections.

2.2.1. Mechanisms of Analyte–Material Interactions.

The interaction between analyte and material is a prerequisite for the operation of any chemical sensor. We can distinguish two types of interactions between the chemical species and the sensory material: (i) non-covalent interactions between the analyte and the sensing material, including van der Waals forces, hydrogen bonding, coordination, and π – π interactions; and (ii) covalent bonding arising from the reactivity of a sensory material with the analyte. Non-covalent interactions may lead to a reversible or partially reversible response. Covalent bonding, which can provide high selectivity and sensitivity, often leads to an irreversible response. The specific type of interaction is determined by the chemical structure of analyte and sensing material, which together are the key factors that define sensitivity, selectivity, and reversibility of sensing devices. Different 2D materials possess distinct structural features, surface chemistries, and contain active sites for analyte–material interactions that are unique from each type of 2D material. For example, graphene has a large, electron-rich π -surface, which enables interactions with targeted analytes through van der Waals forces, charge transfer, and π – π interactions. Metal oxides contain chemically adsorbed oxygen molecules on their surface, which are responsible for the interaction with gaseous analytes through oxygen-involved chemical reactions.^{151,152} The potential active sites existing in each type of 2D material and the nature of the resulting interactions are summarized in Table 2.

Active sites with specific and strong binding affinities can be strategically introduced through the controlled incorporation

Table 2. Typical Analyte–Material Interaction in Electrically-Transduced Sensing Using 2D Materials

material	active sites	resulting interactions
graphene	sp ² orbital of carbon (large π system), defects ^{153,154}	π – π interaction, ^{155,156} van der Waals, ¹⁵³ charge transfer ¹⁵⁷
black phosphorus	p _z orbital of P atom ¹⁵⁸	charge transfer ^{98,159,160}
Xenes	unstable sp ² orbital, defects ¹⁶¹	charge transfer, ¹⁶² dispersive interaction, ¹⁶³ chemical reaction ¹⁶³
metals	zero-valent metal atom, ¹⁶⁴ pre-adsorbed oxygen species ¹⁶⁵	charge transfer, chemical reaction
TMDCs	p orbital of chalcogenide atoms, ^{166,167} defects ^{168,169}	charge transfer ¹⁷⁰
metal oxides	pre-adsorbed oxygen species ^{152,171,172}	redox reaction
2D MOFs	d orbital of metal node, ^{173–175} adsorbed water/oxygen	charge transfer, coordination, H-bond ¹⁷⁶
MXene	O, OH, and F on surface, ^{177,178}	van der Waals, H-bond, ¹⁷⁹ charge transfer
h-BN, g-CN	electron deficient π system, ¹⁸⁰ defects ¹⁸¹ , absorbed O ₂ ¹⁸²	π – π interaction, van der Waals, oxidation reaction

of defects, doping, and functionalization, which together can lead to improvements in the selectivity and sensitivity of sensing devices. For example, Al-doped Gr showed stronger response to CO than the pristine Gr due to the formation of Al–CO bonds.¹⁸³ In another example, the surface of MoS₂ functionalized with bio-recognition receptors can induce selectivity for targeted biomolecules.¹⁸⁴

2.2.2. Mechanisms of Transduction. In order to complete electrically-transduced sensing, the analyte–material interaction should induce change in one or several physical parameters including conductivity, work function, and/or permittivity, which are usually realized through the fundamental mechanisms listed below: modulation of doping level and Schottky barrier, as well as the formation of dipole and interfacial layer.

2.2.2.1. Modulation of the Doping Level. During the interaction of an analyte with the material, the distance between the target molecule and sensory material becomes close enough to allow for electron transfer between them.¹⁸⁵ Based on the relative energy levels of the material and analyte, the analyte can act either as an electron donor (n-type dopant) or acceptor (p-type dopant) resulting in augmentation or compensation of the doping charge density (Figure 5). This process is often described as a secondary doping of the sensing material. The primary doping (inherent doping) is carried out during the synthesis of the materials by incorporating doping ions or during the chemical or electrochemical preparation processes.¹⁸⁶ In some instances, the doping induced by a

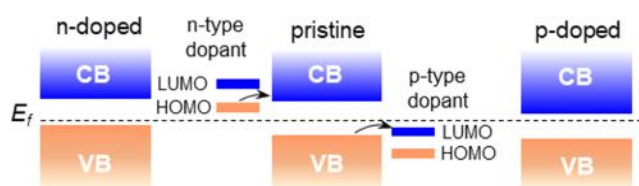


Figure 5. Scheme showing the n- and p-type doping of a semiconductor. The arrows denote the direction of electron transfer.¹⁸⁸

proximal analyte can drastically alter the inherent doping levels of the material. The primary doping effect of the material can be minimized or undergo complete deactivation due to analyte–dopant interactions. Modification of the doping density thus alters the density of states, in the barrier region, and consequently, the conductivity of the sensor. The conductance change of the device, through the modulation of doping level, is closely related to the sensing material surface occupancy of the analyte molecules. This mechanism is described by the site-binding hypothesis, where atoms on the surface of the sensing material can act as binding sites for molecular adsorption.^{80,187} The large specific surface area of most 2D materials, which is beneficial in obtaining a high-density surface occupancy, makes them very sensitive to these chemical environmental perturbations.

2.2.2.2. Modulation of Schottky Barrier (ϕ_b). Metal–semiconductor junctions are involved in many types of electronic devices. When a metal and a semiconductor are in contact, a potential barrier can arise due to the mismatch in their work functions (ϕ_M and ϕ_S , Figure 6a). This energy

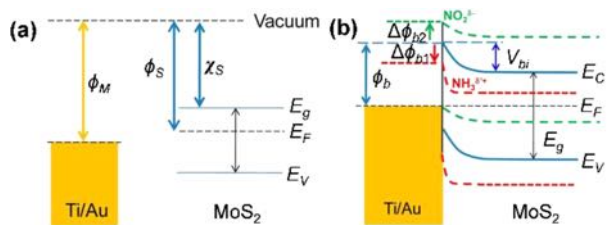


Figure 6. (a) Energy diagram of the Ti/Au and MoS₂ before contact. ϕ_M and ϕ_S are work functions of the metal and semiconductor, respectively, and χ_S is the electron affinity of the semiconductor. E_C , E_F , and E_V represent the energy level of conduction band and Valence band, and Fermi level, respectively. E_g is the band gap. (b) Band realignment and energy diagram of the Ti/Au and MoS₂ after contact and the formation of Schottky barrier. Blue, green, and red lines indicate the energy band of the pristine MoS₂ (solid blue), after exposure to NO₂ (dashed green), and after exposure to NH₃ (dashed red), respectively. V_{bi} is the built-in voltage.¹⁹¹ Reproduced from ref 191. Copyright 2014 American Chemical Society.

barrier can prevent efficient transport of charge carriers (electrons or holes) between the two adjacent materials. In this situation, only a small fraction of carriers have enough energy to overcome this barrier and cross through the metal–semiconductor junction. When a bias is applied to the junction, it can bend the barrier lower or higher from the semiconductor side, depending on the type of the semiconductor, but it does not change the barrier height from the metal side. This effect leads to the formation of a Schottky barrier (rectifying contact), in which the junction conducts charges for one bias polarity but not the other.^{189,190} Figure 6b depicts that a Schottky barrier is created upon the contact of n-type semiconductor MoS₂ with the electrode (Ti/Au). Almost all metal–semiconductor junctions will exhibit some rectifying behavior. The height of the Schottky barrier depends on the work function difference of the two materials in electrical contact.¹⁹¹

In sensing, the adsorption of analytes can cause a change in the doping level of the material, altering the Fermi level and work function, which successively modulates the barrier height at the metal–semiconductor junction. Donor and acceptor type analytes change the Schottky barrier height in the opposite

directions according to the specific location of the work function and primary doping type of the semiconductor. For instance, in a MoS₂/(Ti/Au) device, the exposure to NH₃ gas (n-type dopant) lowers the Schottky barrier height, while NO₂ (p-type dopant) leads to an increased energy barrier.¹⁹¹ In electrically-transduced devices, where Schottky barriers contribute significantly to the total charge transport, the modulation of barrier height will be an important factor for measurements of conductivity change. Under these conditions, the sensing device operates as a junction-controlled device.¹⁹² In an ohmic contact, where a metal–semiconductor junction conducts current in both directions without rectification, the modulation of Schottky barrier is typically negligible and does not significantly affect the conductance of the device.

2.2.2.3. Formation of Dipole and Interfacial Layer. The interactions of analytes with the material can cause two effects: (1) polarization or ionization of the analytes at the surface of the material (pinning or unpinning of the Fermi level), giving rise to a dipole layer that changes the interface state density;¹⁹³ (2) an excess of charge states at the metal electrode/material interface, formed in the presence of analytes, that modulates the Schottky barrier height. In the first situation, the analyte polarized/ionized layer redistributes the electrical charges in the depletion region and abates the degree of the band bending at the material/metal interface. The corresponding output signal, such as current, would be correlated to the quantity of the analyte that was adsorbed at the interface of the material. This sensing mechanism is evident in n-type metal oxide semiconductors for which oxygen molecules are usually adsorbed on the surface of the metal oxide in the presence of an oxygen-rich atmosphere. The adsorbed oxygen species accept electrons from the inside of the metal oxide film to form negatively charged ions, including O₂⁻, O⁻, and O²⁻. These negatively charged species build a space-charge region on the surface of the metal oxide, also known as a depletion layer (Figure 7a), which results in the formation of a potential

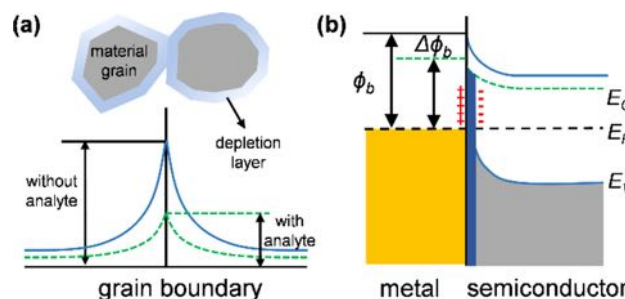


Figure 7. Band diagrams of a metal/semiconductor Schottky contact (a) without and (b) with formation of an interfacial layer after the analyte adsorption.^{152,186}

barrier for the electronic conduction between each grain boundary. When the sensor is exposed to reducing gases, like alcohols, the negatively charged oxygen species are consumed by the reaction with the analytes. During this process, the electrons previously trapped by the adsorbed oxygen species will be transferred back to the metal oxide film, leading to a decrease in the potential barrier height and thus an increase in conductivity.^{127,151,152} This effect becomes dominant when grain size within the material is close to the scale of the depth of the depletion layer.^{194,195}

When an analyte is adsorbed on the surface of the material, an equilibrium between the concentration of charge carriers at the material surface, and the metal electrode/material interface is reached resulting in the modulation of the device double layer. If exposure to the targeted analytes can alter the degree of the double layer formation, this effect would lead to the modification of the barrier height, and consequently in the current flowing across the metal/semiconductor interface. Analytes that cause the barrier height to increase will enhance the rectifying current–voltage behavior, while species that can reduce the energy barrier will improve the ohmic current–voltage behavior (Figure 7b).¹⁹² In addition, the interfacial layer should be capable of supporting the transport of electrons or holes through the interface. If the layer is considered as an electrical insulator, the transport of charge carriers must proceed through tunneling, which requires the thickness of the interfacial layer to be less than 50 Å.^{196,197}

2.3. Performance Parameters

Sensitivity of a sensor can be defined as the slope of the output characteristic curve or, more generally, the minimum perturbation of physical parameters that will create a detectable output change.^{4,198,199} In some sensors, the sensitivity is also defined as the input parameter change required to produce a standardized output signal. Site-binding hypothesis assumes that atoms on the surface of sensing materials can act as binding sites for analyte adsorption, and thus the conductance change of the device would be related to the surface occupancy of the analyte molecules on the sensing materials.¹⁸⁷ High sensitivity to analytes in electrically-transduced sensors based on 2D materials can be ascribed to large available surface area and large abundance of active sites on their surface for analyte–material interactions. Strategies for improving sensitivity can be further realized through introducing analyte-specific receptors that have high binding affinities to analytes, as discussed in more detail in section 4.

The limit of detection (LOD) is the smallest concentration of an analyte that can be reliably distinguished from its absence in a sample (blank) with a specified precision and reproducibility (99% confidence interval).^{199,200} A commonly used experimental method to determine LODs utilizes the exposure of a sensing device to known concentrations of the analyte of interest to generate a calibration curve.^{200,201} The detection limit can be obtained by comparing the sensor resolution by its sensitivity. Numerous analytical specifications depending on the techniques (e.g., the concentration at signal that is 3 times of noise level) have been used to ensure that the recorded analytical signal is indeed meaningful and distinguishable from the baseline. As the LOD is dictated by sensitivity and resolution of the sensor, it can be targeted through improving material–analyte interactions, available surface area, surface functionalization, and signal amplifications.²⁰² The high coverage of functional groups on 2D materials can allow effective and strong interactions with targeted analytes to afford high sensitivity; meanwhile, the intrinsic high conductivities found in this group of materials and the quality of interfaces lead to a low signal noise. This combination has already rendered 2D materials attractive in gas sensing development with low LODs.²⁰³

Selectivity describes the extent to which an analytical method can discriminate between analytes of interest in multicomponent mixtures, without interference from other components.^{198,204} In the current literature, selectivity can be

estimated directly from analytical measurements by comparing signal resolution between the obtained analytical signals or/and through means of statistical analysis (e.g., principle component analysis) or computational modeling. In addition, the reported selectivity values/coefficients should only be directly compared if the experimental conditions used for their determination were standardized to eliminate bias. Selectivity of analytical devices is usually induced by the presence of recognition elements capable of producing selective interactions with a targeted analyte. Depending on the sensor, selectivity can be further improved through manipulating experimental conditions such as temperature, pressure, or via use of alternative materials that can, for example, exclude interferents based on their size or affinity of binding. Specificity is the ability of an analytical technique to distinguish the targeted analyte from other compounds that are present within the analyzed sample and is often considered as the ultimate selectivity. Obtaining selectivity in complex mixtures of interferents is a primary goal of sensor research and a driving force in the exploration of new materials that may provide new selective host–guest surface chemistries.²⁰⁵

The diversity of surface chemistries of different types of 2D materials is well poised for targeted molecular design of selective interactions. For instance, black phosphorus can be oxidized to phosphorus oxides or phosphoric acid upon exposure to water molecules under oxygen, which has been applied to develop an efficient humidity sensor (section 4.2). The oxygen-rich surface of metal oxides makes them unusually sensitive toward reducing analytes (sections 4.1–4.2). Selectivity to targeted analytes can be achieved/modulated by either installing different functional groups on the surface of 2D materials using postsynthetic modifications or/and through incorporating molecular building blocks with high affinity to species of interest. For example, graphene functionalized with aptamer molecules can promote excellent selectivity to small biomolecules (e.g., dopamine) in the presence of interferents such as ascorbic acid or uric acid.²⁰⁶ Alternatively, the incorporation of different metallic nodes within a conductive MOF can lead to tunable selectivity to volatile organic compounds and small gaseous molecules (e.g., NH₃).¹⁷⁴

Response time is the time required to reach a stable output reading upon the exposure to analytes.²⁰⁷ Typically, it is the time at which the analytical signal reaches a certain percentage (e.g., 90–95%) of its final value, in response to a step change of the input.²⁰⁸ The response time is strongly dependent on the device architecture, recognition components, and analytical techniques used to generate the signal. The specific requirement for the response time is often dictated by the final application of the analytical device. For example, the response time required to monitor changes in physiological concentrations of analytes in human body is usually at ms scale.⁹ Recovery time is considered as the converse of the response time, and it is defined as the time required for the sensor signal to return to its initial value after a step concentration change from a certain value to zero. Reversibility is extent to which the signal is restored to its initial state prior to analyte exposure.^{209,210} Full recovery of the analytical device is paramount for practical applications of sensors for continuous sample monitoring. However, in the case of fabrication of one-measurement disposable devices, semi-reversible or irreversible interactions between the recognition element and the analyte may be utilized. Owing to high surface-to-volume ratio of 2D materials, the chemical perturbation on their surface is often

sufficient to cause a detectable change of the bulk property.^{114,211} The low-dimensionality of 2D materials also promotes rapid diffusion of analyte across the active surface sites, thus triggering a rapid change in electronic properties.²¹² Quick diffusion rates are also expected in porous 2D materials, for example, 2D MOFs, whose inherent channel-like structure can serve as the analyte diffusion pathway.¹¹⁵

Dynamic response range is defined as the concentration range that corresponds to the maximum usable readout (e.g., upper detection limits) and the minimum operable analytical signal (LOD) that can be measured by a sensing system.²⁰⁴ An ideal sensor would give responses that can be correlated to specific concentrations at a range wide enough to meet the sensing requirement. This range results in a meaningful and accurate output for the sensing system. All sensing systems are designed to perform over a specified range. Output signals that fall outside of the response range may cause large inaccuracies in recorded data, and possibly result in an irreversible damage to the sensing system. The response range of a sensing system is determined experimentally through repetitive measurements of the response of the sensor over the range of concentrations of targeted analyte. Linear response range of the sensing system refers to the part of the recorded calibration curve through which a fitted linear regression demonstrates either no or minimal deviation from linearity. The dynamic response range of sensors comprising 2D materials, as in the case of their low detection limits, is dependent on the material-analyte interactions, available surface area, and surface modifications. The role of incorporated nanostructures on the dynamic response range and low detection limits in the context of electrically-transduced sensing of gases, volatile organic compounds, ions, and biomolecules is further emphasized in section 4.

Drift is the slow, non-random change of analytical signal with time while the concentration of measured analyte remains constant.^{213,214} It can be caused by mechanical, thermal, or electrical instability, as well as contamination, rearrangement, or degradation of materials used for the fabrication of an analytical device. The contribution of drift to the analytical response may be minimized by frequent device recalibration, referencing, or through computational data processing. Signal drift can be overcome through careful device design in which the influence of external environment is reduced by application of protective coatings or encapsulating layers,⁵³ thermal or electrical pretreatment, or background drift subtraction techniques in relation to a reference standard.

Reproducibility is the ability of the analytical device to produce the same signal output after the experimental conditions have been altered.²⁰⁴ It can be quantified by measuring the variation in calibration data obtained for different devices, using the same test protocols and test equipment. Reproducibility should be reported together with specification of experimental conditions. In sensors comprising 2D materials, the device-to-device reproducibility is primarily dictated by the ability to synthesize the nanomaterial in a well-defined and controllable fashion, as well as its integration into a functional device. For instance, chemical vapor deposition was realized as a suitable method for large-scale manufacturing of graphene or MoS₂ with good control over the structure of synthesized materials (see also in section 3). Development of synthetic methods that permit deposition of the 2D nanostructures directly onto the sensing device can

promote and improve the signal reproducibility in analytical measurements.²¹⁵

Stability is the ability of a sensor to produce the same output signal when performing the same analytical measurement over a period of time.¹⁹⁹ This concept includes a retention of sensitivity, selectivity, response, and recovery time. It can be quantified by comparing the response produced by an aged device with a new device. Stability is particularly important for the fabrication of devices that are employed for continuous and prolonged monitoring of analytes, as in the case of environmental analysis. Ideally, the fabricated device should remain unchanged over the lifespan of the device. The lifetime of analytical devices based on 2D nanostructures is primarily dictated by the stability of the sensing material to the chemical environment, and to the external stimuli, such as applied potential, temperature, or mechanical/physical stress.²¹⁶

The requirements for specific parameters of the sensing system are primarily dictated by its final application. For instance, sensors used for continuous sample monitoring need to exhibit exceptional signal stability, minimal drift, and no degradation in the selectivity and sensitivity over prolonged period of time. Furthermore, systems used for in vivo clinical analysis should be able to respond to sensed analyte within the shortest time possible to ensure that the measured sample did not undergo degradation/contamination due to the presence of numerous biological processes. In this case, the stability of the analytical device can be compensated for by short response times to targeted analytes.

2.4. Electrically-Transduced Sensing Architectures

The architectures of electrically-transduced chemical sensors, with few exceptions, will fall into five categories: chemiresistor, chemical diode, field-effect transistor, chemical capacitor, and electrochemical sensor.⁷ In the following sections, the general configuration and operation mechanism of each type of architecture is discussed.

2.4.1. Chemiresistors. A chemiresistor consists of two electrodes connected with a chemiresistive material deposited onto an insulating support (Figure 8a).^{217,218} The sensing materials used for chemiresistor fabrication can be either semiconductive (e.g., metal oxides, TMDCs) or metallic (e.g., graphene). The resistance of a chemiresistive material can be altered by exposure to gaseous analytes. By measuring the change in resistance or current of the sensor device, the concentration of analytes can be measured.

The resistance of the device can be mainly divided into two components:

$$R = R_{\text{mat}} + R_{\text{contact}} \quad (7)$$

Here, the R , R_{mat} , and R_{contact} are the total resistance of the device, the resistance of the sensing material, and the sum of contact resistance originating from the metal electrode/sensing material junctions and junctions of the material grains, respectively. The response (S) of the sensor is given by eq 8:

$$S = \frac{\Delta R}{R_0} = \frac{R_{\text{analyte}} - R_0}{R_0} \times 100\% \quad (8)$$

or

$$S = \frac{\Delta I}{I_0} = \frac{I_{\text{analyte}} - I_0}{I_0} \times 100\% \quad (9)$$

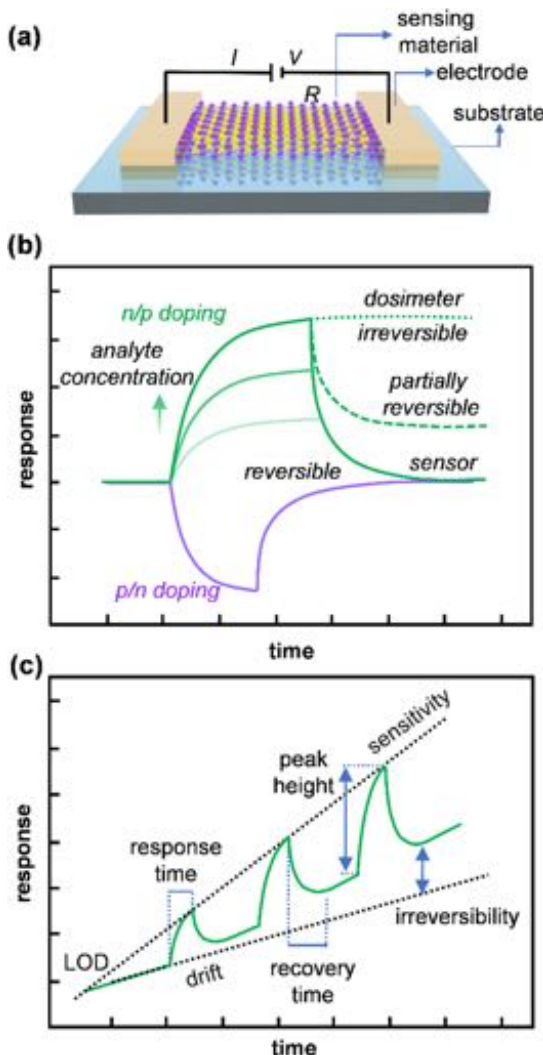


Figure 8. (a) Scheme diagram of a typical chemiresistor-based sensor made of metal chalcogenide. V is the voltage applied to the device, and I is the current flowing through the device. (b) A typical response curve of a sensor exposed to analyte with opposite type (green and purple line) of electronic character at different concentration. Depending on the reversibility of interaction between analyte and sensing material, the response of the sensor can be irreversible, partially or fully reversible. (c) Graphical representation of selected performance parameters in a device successively exposed to increasing concentrations of analyte.⁵³ Adapted with permission from ref 53. Copyright 2016 Wiley-VCH Verlag GmbH & Co. KGaA, Weinheim.

where I_0 and R_0 are the current and resistance of the circuit in the device under an applied voltage, V , and I_{analyte} and R_{analyte} are the current and resistance upon exposure to analyte, respectively.

The sensing process of chemiresistive devices is mainly dictated by three distinct mechanisms, including change of doping level, modulation of Schottky barrier, and modulation of junction distance, which can work independently or synergistically, to alter the resistance of the device.^{53,219} In the case of p-type semiconductors like reduced graphene oxide (rGO), the exposure to electron donating analytes (e.g., NH_3) results in electron transfer to the valence band of the rGO semiconductor, diminishing the concentration of holes, and subsequently causing a decrease in the conductance; conversely, electron withdrawing gases such as NO_2 , trigger

the electron transfer from the p-type semiconductor material to the analyte, increasing the hole concentration, and thus improving its conductance (Figure 8b).¹⁵⁷ The adsorption of analyte can alter the work function of the material layer, successively modifying the height of Schottky barrier of the material–electrode contact. In addition, the adsorption of the analytes at the junctions between crystallites or particles of the material can cause the grains of the chemiresistive material to separate from each other, which increases the hopping distance for charge transport, thus leading to an increase in the resistance.^{220,221} Figure 8c shows a representative sensing trace of a chemiresistive sensor upon three successive exposures to increasing analyte concentrations, that graphically represent the key features of the sensing performance, including sensitivity, LOD, response/recovery time, drift, and reversibility.

Chemiresistive sensors are one of the most widely applied device architectures for electronic sensing of gaseous analytes due to their simplicity, compatibility with conventional DC circuits, low cost, predictable electrical properties, and the ease of high precision measurement.^{217,218} Chemiresistive architectures are best employed in systems where rapid prototyping is necessary. The straightforward design and operation of this type of device makes them attractive starting platforms for investigating chemical sensitivity of new materials. The wide variety of techniques for incorporating sensing materials, and the macroscale features typically used, make this architecture highly suitable for initial testing when the morphology of materials has not been optimized, or to reduce device fabrication costs. In addition, chemiresistors typically exhibit good sensitivity, good reproducibility, and low power consumption.⁵⁴

2.4.2. Chemical Diodes. A diode is a two-terminal electronic component that exhibits low resistance to passing current in one direction, and high resistance in the opposite direction.²²² There are two types of diodes, p–n junction diodes and Schottky diodes. The p–n junction diode is formed by joining a p-type semiconductor with an n-type semiconductor, while the Schottky diode is composed of only one type of a semiconductor (p or n) material that is in contact with a metal or semimetal electrode (Figure 9a).²²³ Schottky barrier diode sensors are simple to fabricate, obviating the need for photolithography or high-temperature diffusion/oxidation steps.^{224,225}

The current–voltage (I – V) characteristic of the Schottky diode can be explained by a charge carrier transport mechanism,¹⁸⁶

$$I = I_S \left[\exp\left(\frac{eV}{kT}\right) - 1 \right] \quad (10)$$

where V is the forward bias voltage, k is the Boltzmann constant, and T is temperature. The reverse bias saturation current (or scale current) I_S is defined by eq 11.

$$I_S = eN_c \mu_e E_{\max} \exp\left(-\frac{\phi_b}{kT}\right) \quad (11)$$

In eq 11 ϕ_b is the Schottky barrier height for an ideal contact between a metal and a semiconductor, N_c is the effective density of states in the conduction band, μ_e is the electron mobility, and E_{\max} is the maximum field strength at the metal/semiconductor interface. The current density–voltage (J – V)

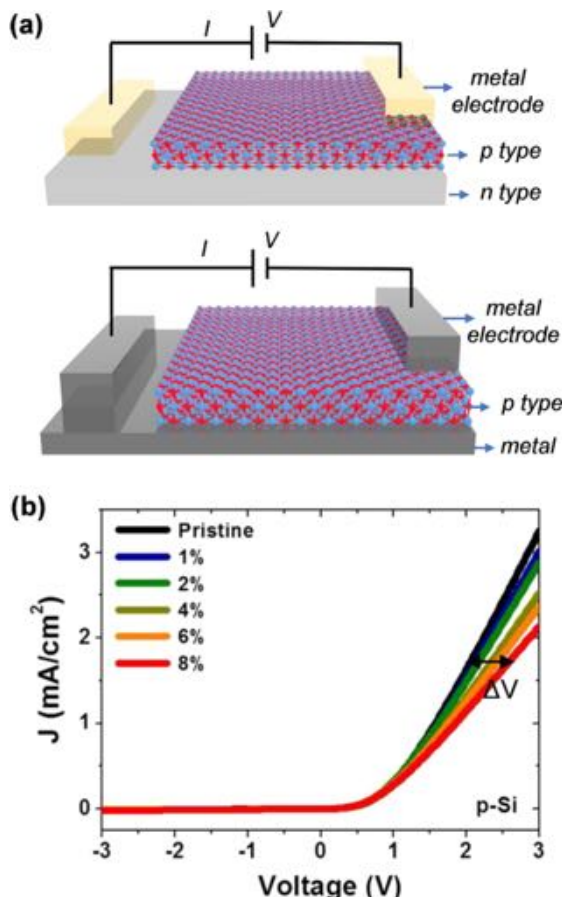


Figure 9. (a) Scheme diagram of a typical PN diode sensor (top) and a typical Schottky diode sensor (bottom); (b) Typical response curves of a Schottky diode–based sensor expressed by I – V curve upon exposure to analyte. ΔV indicates the gas or vapor induced voltage shift at constant current density.²²⁶ Reproduced from ref 226. Copyright 2013 American Chemical Society.

curve is also widely used to describe the characteristics of a diode, which follows a similar relationship as that of I – V curve.

A typical change in the J – V characteristic of a Schottky barrier diode due to analyte–material interactions is shown in Figure 9b. The sensitivity of diodes is represented by the analyte–induced voltage shift at a given diode current I (or current density J), ΔV , extracted from current–voltage characteristics and is defined by the following equation,

$$S = \frac{\Delta V}{V_0} = \frac{V_{\text{analyte}} - V_0}{V_0} \times 100\% \quad (12)$$

where V_{analyte} and V_0 are the applied voltages at a constant current density with and without the exposure to analyte, respectively. If the devices are operated at constant voltage, then the sensitivity can also be given by $\Delta I/I$.

The generation of signal in Schottky barrier diodes originates from the change of junction characteristics (i.e., I – V or J – V characteristics) by altering the Schottky barrier height, ϕ_b , or modifying the built-in voltage, V_{bi} .^{186,227} The response can be due to either the adsorption of species at the surface of a metal that affects the interfacial polarization by formation of a dipole layer or caused by the adsorption of analytes onto the semiconductor, which changes its work function and, hence, the contact potential or built-in voltage of the diode. The former is mostly encountered in Schottky

barrier diodes based on inorganic semiconductors, whereas the latter is related to diodes based on organic semiconductors.¹⁸⁶

Chemical diodes are effective sensors that are comparable in sensitivity and power consumption to chemiresistors. Device integration is more involved than chemiresistors since the connection between the semiconductive material and metal must be precisely controlled. Lithographic techniques are often used to ensure placement of 2D materials with respect to electrodes. A disadvantage of chemical diodes is that sensitivity is dependent on the applied voltage, and this requires that materials must be stable under bias voltages higher than those typically required by chemiresistors.^{226,227}

2.4.3. Field–Effect Transistors. Field–effect transistor (FET) is another type of device with high utility in chemical sensing.^{228,229} FET devices consist of source and drain electrodes, a semiconductive material channel, an insulating gate oxide, and a gate electrode (Figure 10).²³⁰ The current

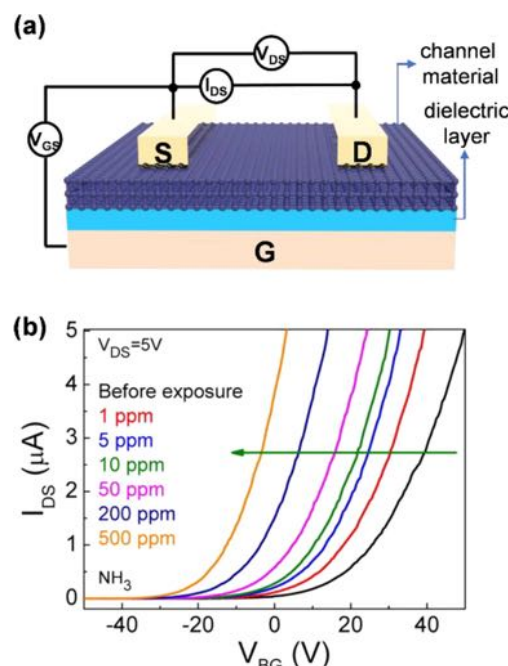


Figure 10. (a) Scheme diagram of a typical bottom-gated FET sensor made of metal oxides. (b) Typical response curves (I_{DS} – V_{g}) of a MoS₂ FET upon exposure to NH₃ with different concentrations.¹⁹¹ Reproduced from ref 191. Copyright 2014 American Chemical Society.

flows through the contact terminals via the channel (called the drain current, I_{DS}) that can be modulated by an electric field perpendicular to the semiconductor originating from a voltage (V_{GS}) applied to the gate electrode and the source. The electric field acts upon the number of mobile charge carriers in the semiconductor, and consequently, controls the current, I_{DS} . The conductivity of the channel is a function of the potential applied across the gate and source terminals. The drain current I_{DS} is given by

$$I_{\text{DS}} = \frac{C_i \mu W}{L} \left[(V_{\text{GS}} - V_{\text{th}}) - \frac{1}{2} V_{\text{DS}} \right] V_{\text{DS}} \quad (13)$$

where C_i is the capacitance of the gate insulator per unit area, μ is the charge carrier mobility in the channel, W/L is the width-to-length ratio of the channel, V_{GS} and V_{DS} are the applied gate–source and drain–source voltage, and V_{th} is the threshold

voltage defined as the (minimum) voltage required on the gate to create a layer of minority charge carriers under the insulating layer.²³¹ The curves are characterized by a linear region when $V_{DS} \ll (V_{GS} - V_{th})$ and a saturation region when $V_{DS} > (V_{GS} - V_{th})$. At low drain–source voltages the I_{DS} current follows Ohm's law and is proportional to V_{DS} at a fixed V_{GS} (linear regime).

In a FET-based chemical sensor, the channel is usually composed of a semiconducting material that is sensitive to analyte molecules.²²⁹ It operates by monitoring current change in the channel material before and after the adsorption of target analytes.²²⁹ Most FET sensors operate in the linear range of I_{DS} and act as resistive sensors. Their performance is governed by the intrinsic properties of the channel material, such as the work function, carrier mobility, and band gap, of which, band gap is the most important parameter in engineering sensor performance.²²⁹ Depending on the geometry of the devices, the type of a semiconductor (p-type vs n-type), the nature of the analyte (reducing vs oxidizing), the quality/morphology of the sensing materials, and physicochemical interactions, including hydrogen bonding, charge transfer, hydrophobic interactions, and dipole–dipole interactions, can contribute to the modulation of electrical conductivity in the 2D nanomaterial.^{228,232} The interactions between the analyte and semiconductor can induce a change in Fermi-level and thus alter the height of a Schottky barrier. These interactions can also involve a change in electronic coupling along the charge carrier transfer path in the semiconductor, which is attributed to morphological changes or interactions at grain boundaries.²³³ As a consequence, a change in conductance occurs upon exposure to a targeted analyte.

The response of the FET-based sensor can thus be expressed by $\Delta I_{DS}/I_{DS}$ at the given gate–source and drain–source voltage:

$$S = \frac{\Delta I_{DS}}{I_{DS}} = \frac{I_{DS}' - I_{DS}}{I_{DS}} \times 100\% \quad (14)$$

where I_{DS}' is the current upon exposure to analyte.

FET sensors have attracted considerable attention because of their potential for miniaturization in nanoscale, parallel sensing, high sensitivity, and ability to provide insight into the sensing mechanism. Additionally, they can be engineered to exhibit fast response and are easily integrated with electronic manufacturing processes. FET sensor platforms can work in both gas and liquid environments permitting detection of a wide range of analytes including gases, ions, and biomolecules.^{228,229} FET devices are commonly used to increase sensitivity compared with other device architectures because charge carrier mobility can be modulated by controlling gate voltage. FET devices can be fabricated with microscale or nanoscale features and present a useful means of providing strong device characterization (charge carrier mobility, conductivity, and major carrier species). However, the integration of materials into FET devices requires advanced techniques such as lithography and a high degree of control over material morphology. FET for solution-phase sensing has been limited primarily to measurements in nonphysiological or/and low-ionic strength solutions due to the charge screening effects (Debye screening length).^{234–236} The charge of targeted molecules in solution (e.g., DNA and proteins) is screened by dissolved solution electrolytes (cations and

anions). Current methods to overcome these limitations primarily rely on solution desalting (decrease in ionic-strength),²³⁷ incorporation of antibody receptors,²³⁸ and aptamers,²³⁹ which can minimize the distance between analytes and the FET surface and application of permeable polymer coatings that increase the effective Debye length immediately adjacent to the FET surface.²⁴⁰ A recent strategy relying on a conformational change of aptamer-based receptors integrated into FET devices has enabled a new approach to overcoming Debye length limitations in the context of solution-phase sensing of charged, neutral and zwitterionic small molecules (e.g., dopamine, serotonin, glucose, sphingosine-1-phosphate).¹¹³⁰ Adapting similar approaches using modified 2D materials may offer opportunities for new advances in chemical sensing.

2.4.4. Chemical Capacitors. A capacitor is a device that consists of two conducting electrodes separated by a non-conducting substance called a dielectric (Figure 11a). The

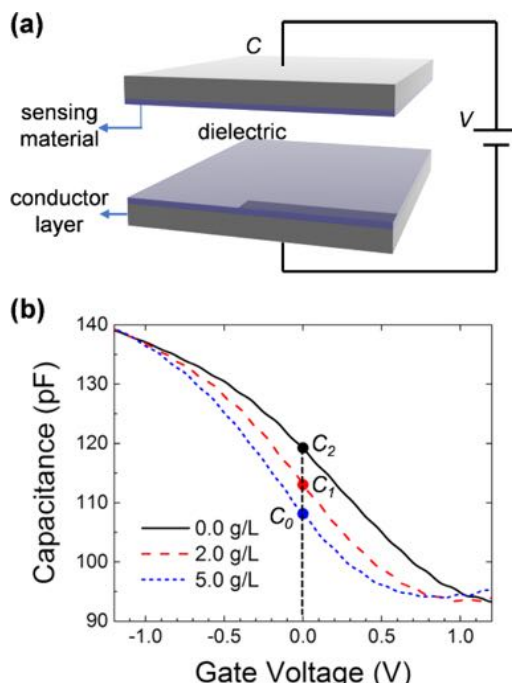


Figure 11. (a) Scheme diagram of a typical chemicapacitor-based sensor. (b) Response of a graphene-based chemicapacitor under different concentrations of glucose as expressed by the shift of the C–V curve toward negative gate voltages with increase in glucose concentration.²⁴³ Reproduced from ref 243. Copyright 2017 American Chemical Society.

dielectric may be either air, mica, ceramic, organic solvent, or other suitable insulating material. Electrical energy is stored as a build-up of charge on the opposing electrodes. In general, the capacitance value is determined by the dielectric material (ϵ_r), distance between the electrodes (d), and the area of each plate. The capacitance of a system can be expressed in terms of its geometry and dielectric constant as²⁴²

$$C = \epsilon_r \frac{\epsilon_0 A}{d} \quad (15)$$

where C is the capacitance in farads (F), ϵ_r is the relative static permittivity (dielectric constant) of the material between the plates, ϵ_0 represents the permittivity of free space ($8.854 \times$

10^{-12} F/m), A is the area of each plate, in square meters, and d corresponds to the separation distance (in meters) of the two plates.

Any adsorption or binding of analytes onto the dielectric layer will change the thickness (d) and/or dielectric behavior (ϵ_r), and consequently the capacitance of the system. The binding event between the sensing material and analyte further induces alterations in the electrical properties or dimensions of the material, resulting in a measurable analytical signal.²⁴⁴ For example, changes in the dielectric constant (ϵ_r) due to the interactions between an immobilized antibody and antigen on a surface of 2D material are frequently utilized in biomolecules sensing. Chemical capacitors based on the change of dielectric constant (ϵ_r) are not generally applied to gas sensing applications because the relative permittivity of most inorganic gases (except H₂O) are similar. Instead, changes in dielectric layer thickness (d) are more frequently found in gas sensing.¹⁴⁸ For humidity sensing, the change in the electrode area is also possible.²⁴⁵ Figure 11b shows the C–V characteristic of a capacitor-based sensor before and after interacting with an analyte. The sensitivity can be defined in terms of the change in capacitance ΔC at a fixed voltage V .²⁴³

$$S = \frac{\Delta C}{C_0} = \frac{C_{\text{analyte}} - C_0}{C_0} \times 100\% \quad (16)$$

It could also be defined as $\Delta V/V$ at a given C value. Often the sensitivity is simply given as is the change of the flat band potential (ΔV_{FB}), the bias needed to force the surface potential (ψ_s) of the semiconductor in the capacitor to zero.²⁴⁶

Capacitive-type sensors are characterized by low cost and simple device configuration that enables their miniaturization for sensing applications. Multiple capacitive sensors containing different recognition elements can be integrated onto a single-chip platform, to form a compact array of micro-sensors for targeting different molecules. Since chemical capacitor devices do not require static power consumption, they are suitable for use in energy-constrained applications, including wireless sensor networks and low power battery-operated technologies (as low as a few μW).²⁴⁷ The amplification of the capacitance signal can be readily performed by using oscillator circuits thus enabling sensitive detection of analytes.^{148,244} A wide scope of 2D materials can be used for electronic transduction of chemical sensing, because adsorption of chemical analytes can lead to a permittivity change. However, chemical capacitors are generally less selective than other sensing architectures. They are more often sensitive to humidity and swelling effects.

2.4.5. Electrochemical Sensors. Electrochemical sensors are one of the largest groups of chemical sensors. They are composed of integrated receptor-transducer devices capable of providing selective and quantitative analytical information regarding the investigated system (Figure 12a).¹⁰ Electrochemical sensing measurements typically generate a measurable response in the form of current, potential, charge accumulation, or impedance change of a medium between electrodes.⁹

2.4.5.1. Potentiometric Sensors. Potentiometric sensing devices measure the difference in electrical potential between the connecting leads of the working electrodes relative to the potential of a suitable reference electrode.²⁴⁸ Potentiometric measurements are carried out in a two-electrode galvanic cell under ideally zero current conditions.²⁴⁹ In this situation the measured potential is defined by the charge distribution of ions

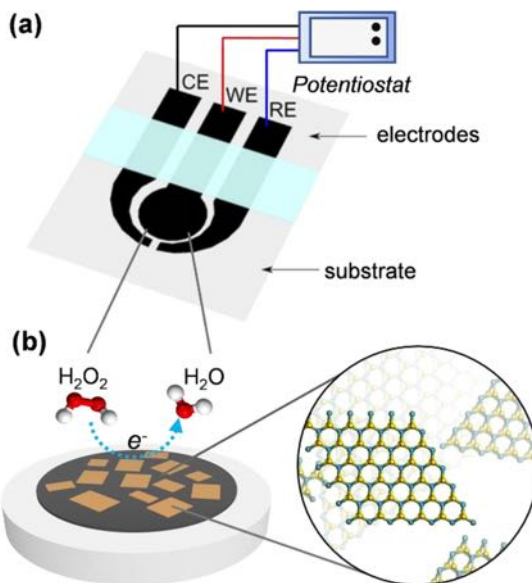


Figure 12. (a) Typical configuration of electrochemical sensor with counter, working, and reference electrodes connected to a potentiostat. CE, counter electrode, WE, working electrode, RE, reference electrode. (b) A working electrode that consists of a glassy carbon electrode functionalized with redox active MoS₂.²⁵⁰ Adapted from ref 250. Copyright 2013 American Chemical Society.

and electrons, at the solution/working electrode interface, as a function of ion activity in a measured sample.²⁴⁹ This relationship is defined by the Nernst equation indicating that, at room temperature, a 10-fold increase in the activity of measured ions is followed by an increase in the potential/electromotive force (EMF) of 59.2 mV/z_i.²⁰⁴

$$E_{\text{PB}} = E_i^0 + \frac{RT}{z_i F} \ln \frac{a_i(\text{aq})}{a_i(\text{org})} \quad (17)$$

E_{PB} is the electrical potential developed between the working and reference electrode, E_i^0 is a cell potential under standard conditions (273.15 K and 100 kPa), and $a_i(\text{aq})$ and $a_i(\text{org})$ are the activities of primary ions in the aqueous and organic phase, respectively. z_i is the ionic charge of the ion i and F , R , and T are the Faraday constant, the universal gas constant, and the absolute temperature, respectively.²⁰⁴

In direct potentiometry, the measured phase boundary potential is ideally a function of the activity of only one specific analyte ion due to the charge separation at the water/water immiscible interface, allowing selective detection of targeted analytes even in the presence of ionic interferents.²⁴⁸ Therefore, selectivity of ion selective electrode (ISE) is directly related to the equilibrium constant of the exchange reaction of targeted and interfering ions between the organic and aqueous phases.²⁵¹ Many modern potentiometric sensors rely on the presence of either ionically conductive mono- or polycrystalline solids (e.g., lanthanum trifluoride) or ion-selective membranes (ISM), whose nature/composition dictates the sensing properties of the electrodes. Typically, an ISM is composed of an ionophore (ion ligand), lipophilic salt (ion exchanger), polymer, and plasticizer, which together form the matrix of the membrane.²⁵² These polymeric membranes have proven to be suitable for numerous sensing applications because their electrochemical response and sensing properties (e.g., selectivity and sensitivity) can be relatively easily

modulated by using different components during the ISE fabrication.²⁵²

Since the input signal in potentiometric measurements refers to the activity of a target ion, while the output is an electrical potential, the effective conversion of the charge carriers from ions to electrons is needed. This signal conversion can be achieved using transducers.²⁵³ To achieve stable electrode potential, it is required to obtain sufficiently fast and reversible ion-to-electron transduction across the ionically active polymeric ion-selective membrane and the electrochemically active transducer, and the electrical contact, without any contribution from side reactions.²⁵⁴ In conventional liquid contact ISEs, usually AgCl coated Ag wire serves as inner reference electrode submerged in the internal electrolyte containing fixed concentration of Cl⁻ ions. In this situation, the ion-to-electron transduction proceeds through the reversible redox reaction between AgCl(s) + e⁻ ⇌ Ag(s) + Cl⁻(aq), which provides stable interfacial potential between the AgCl/Ag electrode and the inner filling solution.²⁵²

Advancements in the development of potentiometric ion-selective sensors led to the elimination of internal filling solution giving rise to solid-contact ISEs, which are more durable and easier to miniaturize than their conventional counterparts.²⁵⁴ Although first reports of solid contact ISEs emerged in early 1970s with the invention of the coated-wire electrodes (CWE), the poor potential stability of the resulting CWEs due to the blocked interface between ISM and electrical conductor strongly inhibited their further analytical applications.²⁵⁴ Solid-contact electrodes with enhanced potential stability have been produced by using numerous electroactive materials with both mixed electronic and ionic conductivities that can work as ion-to-electron transducers when sandwiched in between the ISM and underlying conductor.²⁵³ Among these materials, electroactive conductive polymers (e.g., poly(3,4-ethylenedioxythiophene)-poly(styrenesulfonate) (PEDOT-PSS), poly(3-octyl)thiophene or polyaniline (PANI)),^{255,256} carbon materials,^{257–260} and 2D nanomaterials including graphene^{261–263} were recognized as one of the most promising ion-to-electron transducers for solid-contact ISEs.

Potentiometric sensing has three beneficial characteristics that allow these types of sensors to perform well for chemical detection. First, potentiometric sensors use only two electrodes, allowing simplified device design. Second, analysis happens at thermodynamic equilibrium, meaning observation of the system may be performed without applying a potential that may motivate chemical reactions to occur. Third, potentiometry is able to detect chemical species without redox processes occurring, meaning redox-inert species are possible analytes. Main limitations of ion-selective electrodes include the interferences from other ions present in a solution, at high concentrations the effect of ionic strength is more pronounced causing deviations in the recorded activity, and need for frequent sensor recalibration due to potential drift.

2.4.5.2. Voltammetric Sensors and Amperometric Sensors. Voltammetry and amperometry are the most utilized transducing methods in the development of electrochemical sensing platforms due to their overall simplicity, low-cost instrumentation, and significant sensitivity to targeted analytes.^{9,10,264–266} In both methods, the applied potential is a driving force for electron transfer reactions, which produce a measurable change in current.²⁶⁷ Since the magnitude of measured current is proportional to the number of oxidized/reduced molecules in the solution, it is possible to monitor

relative concentrations of molecules at physiological timelines.²⁶⁷ Voltammetric and amperometric measurements typically utilize a three-electrode set-up comprising working electrode, counter electrode, and reference electrode.²⁰⁴ The zero or “reference” potential is set by the presence of the reference electrode. The third electrode is the counter electrode, which acts as an electron source/sink.²⁶⁸ In the development of sensing devices, the surface of a working electrode (e.g., Au, Pt, or GCE) is most commonly functionalized with an electroactive layer to induce selectivity to targeted analytes as shown in Figure 12b.^{9,10,269,270} Electrodes modified with redox active polymers, ionic liquids, carbons, metals, and 2D nanomaterials are only a small representation of available modifications that led to the development of excellent sensing platforms for applications spanning across many disciplines and industries.^{8,11,266,271–275}

In amperometry, the electrode is held at a fixed potential and the current is monitored over time.²⁷⁶ Current magnitude is then related to the concentration of the analyte present.²⁷⁷ Amperometric sensors typically have response times, dynamic ranges, and sensitivities similar to potentiometric sensors.^{278,279} The main limitation of amperometry is that it is difficult to confirm the identity of detected molecules solely by the shape of recorded current.^{9,280}

In cyclic voltammetry (CV), the applied potential at the working electrode is ramped linearly with time and the current flowing between the working electrode and an auxiliary electrode is measured.²⁶⁷ When the CV scan, in either cathodic or anodic direction, reaches the set potential, the potential ramp is reversed to bring the potential of the working electrode back to its initial value.²⁸¹ This potential inversion can occur multiple times during a single experiment, until a desired number of electrochemical cycles is obtained. Because many biologically important molecules undergo redox transformations at different potentials, a cyclic voltammogram can be used as a fingerprint technique to identify the presence of targeted analytes.^{10,266,270,278} Besides cyclic voltammetry, numerous other voltammetric techniques have been employed in electrochemical detection to further enhance the sensitivity of sensing platforms in the context of quantitative analysis.^{8–11,14,59,264–266,270,272–275,278,279,282} Typically, pulse voltammetry techniques such as differential pulse voltammetry (DPV), square-wave voltammetry (SWV), and normal pulse voltammetry (NPV) are encompassed within this category.^{10,266,283} Recent review articles have focused on specific applications or methods for voltammetric sensors.^{8–10,13,121,273}

Voltammetry and amperometry-based sensors access a regime of chemical sensing that provides exceptional selectivity and sensitivity. The advantage of voltammetry is that a positive or negative bias can be applied to assess the redox profile of a solution. Specific redox couples can be observed to give information about the reversibility of reactions, the nature of the species present, and how they interact with 2D surfaces. Amperometry has many of the same benefits of voltammetry, and like voltammetry, can only detect redox active species. Amperometry can be performed with stirring or other disturbances with no ill effect on sensing performance. This is beneficial to mobile applications of these sensors, such as wearable sensors or installations for environmental monitoring.

2.4.5.3. Impedance Sensors. Electrochemical impedance spectroscopy (EIS) is a non-destructive steady-state technique capable of probing the relaxation phenomena over a wide range of frequencies typically spanning from 10⁶ to 10⁻⁴ Hz.²⁸⁴

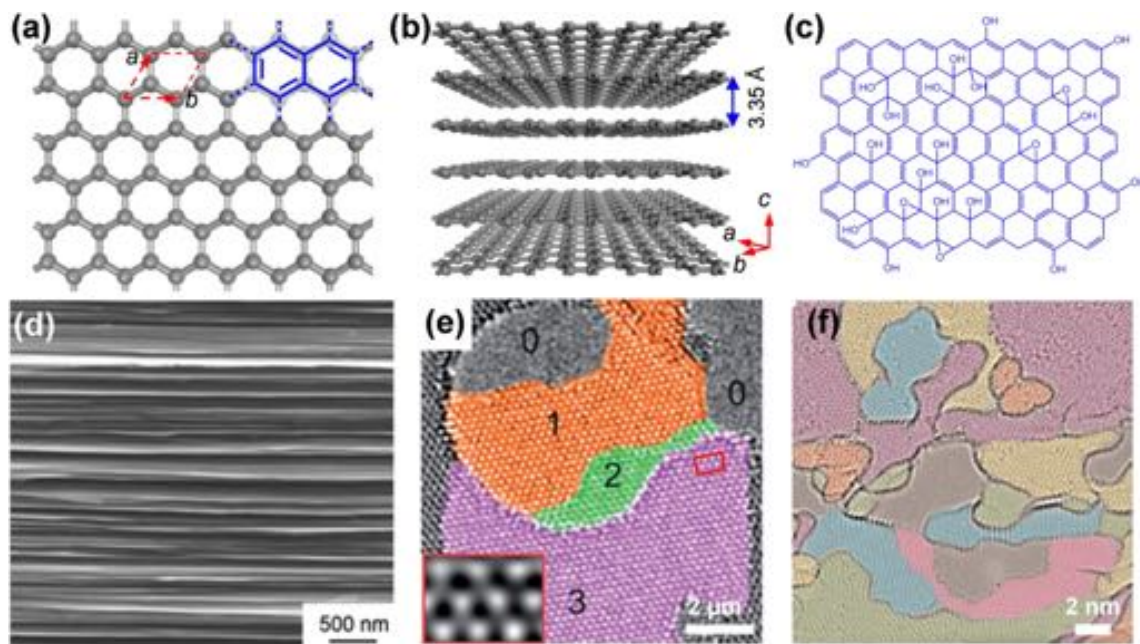


Figure 13. (a) Ideal structure of a sheet of graphene that consist of atomic-scale hexagonal lattice made of carbon atoms. (b) Structure of graphene layers. (c) Chemical structure of graphene oxide based on the Lerf–Klinowski model.³⁰⁵ Epoxy and hydroxyl groups functionalize the surface. (d) SEM images of highly ordered pyrolytic graphite consisting of many layers of graphene.³⁰⁶ Reproduced with permission from ref 306. Copyright 2013 Elsevier Ltd. (e) HRTEM image of a region containing 0, 1, 2, and 3 layers of graphene. Scale bar, 2 μm .³⁰⁷ Reproduced with permission from ref 307. Copyright 2010 IOP Publishing Ltd. (f) Overlaid color representation of few-layer graphene oxide at 700 °C imaged with an in situ TEM heating holder. Scale bar, 2 nm.³⁰⁸ Adapted from ref 308. Copyright 2016 American Chemical Society.

Similarly to voltammetric/amperometric techniques, EIS predominantly utilizes a three-electrode configuration for electroanalytical measurements in solutions. During the EIS experiments, a small AC perturbation signal (2–10 mV) is imposed to the electrochemical cell, and the resulting current is measured.²⁸⁵ The current response to the AC potential is a sine function with the same frequency, but with different amplitude and phase.²⁸⁶ The in-phase current response determines the real component (resistive) of the impedance, while the out-of-phase current response determines the imaginary component (capacitive).²⁸⁷ The magnitude of the recorded phase shift depends on the nature of the electrolyte, diffusion process, electrode kinetics, and chemical reactions that may take place in the electrochemical cell.²⁶⁷

In general, impedance data can be represented using either Cartesian or polar coordinates. The plot of real part of the impedance $\text{Re}Z(j\omega)$ (x axis) versus the imaginary part of the impedance $\text{Im}Z(j\omega)$ (y axis) is typically referred as a Nyquist plot. A Bode plot is a log–log plot of the magnitude $|Z(j\omega)|$ and phase (ϕ) of the impedance $Z(j\omega)$ as a function of the frequency of a sinusoidal excitation (ω or $f = \omega/2\pi$).²⁸⁶ Since the Nyquist plot combines gain (magnitude) and phase into one plot in the complex plane, the information regarding frequency is thus unavailable and needs to be extracted from the Bode plot.²⁶⁷ EIS results are most often fitted, through modeling, into equivalent circuits made up of resistors, capacitors, or inductors, which can be used to describe most of the electrochemical systems.²⁸⁷ Impedance methods are thus capable of characterizing physicochemical processes of widely differing time constants, such as sampling the electron transfer at high frequency and mass transfer at low frequencies.²⁸⁸ Since EIS is particularly sensitive to changes caused by either surface or bulk phenomena, its prominence as

an analytical tool for electrochemical research and sensor applications have been on a rise.^{289–296}

In the context of 2D materials, EIS is a powerful technique for investigating the properties and phenomena at different stages of development and integration of materials into targeted applications. Interfacial phenomena important for sensing, energy storage, and electronic applications can be characterized.²⁹⁷ For example, EIS can offer information about double layer capacitance of materials in solution. EIS can be used to help characterize the conductive junction between electrode and 2D material. Finally, chemical processes enabled by 2D materials that are essential to sensing and catalysis, such as rate constants and diffusion coefficients, can be characterized using EIS techniques.²⁹⁸

3. STRUCTURE AND SURFACE CHEMISTRY OF 2D MATERIALS

3.1. Graphene and Graphene Oxides

Graphene is a single layer of sp^2 -hybridized carbon atoms covalently bound together in a honeycomb lattice (Figure 13a).⁷⁷ It is the basic building block of other carbon-based allotropes, such as graphite, carbon nanotubes (CNTs), and fullerenes.²⁹⁹ The distance between two neighboring carbon atoms in a single sheet of graphene is about 1.42 Å. Individual layers are held together by the van der Waals interactions to form graphite (Figure 13d,e), in which the distance between the adjacent layers is about 3.35 Å (Figure 13b). The first successful isolation of graphene—obtained by exfoliation of graphite—was reported in 2004 by Geim and Novoselov.⁷⁶ Since then, it has become one of the most published topics for material scientists due to its extraordinary thermal, optical, electrical, mechanical, and physicochemical properties arising from its two-dimensional crystal structure.⁷³ Graphene displays

an extremely high carrier mobility of $2 \times 10^5 \text{ cm}^2 \text{ V}^{-1} \text{ s}^{-1}$ and high carrier density of 1012 cm^{-2} at room temperature, which corresponds to a resistivity of $10^{-6} \Omega$.^{300,301} Its bandgap and conductivity are dependent on the number of layers in the stack, and approach those of graphite with increasing number of layers.³⁰² Graphene exhibits a large theoretical specific surface area of $2630 \text{ m}^2 \text{ g}^{-1}$, which is twice as high as that of single-walled CNTs.³⁰³ It also has remarkable mechanical properties, and it is considered as one of the strongest materials available, with an intrinsic tensile strength of 130.5 GPa and a Young's modulus of 1 TPa .³⁰⁴

Well-established methods to produce graphene include micromechanical cleaving,⁷⁶ solution-phase exfoliation from graphite,^{309,310} chemical vapor deposition (CVD),^{311–314} and organic synthesis-based methods.^{315,316} Micromechanical cleaving technique, also known as the "Scotch tape" or peel-off method, tends to produce graphene with the best quality and the least amount of structural and compositional defects.³¹⁷ However, this method offers only limited control over the number of mechanically peeled-off layers, and it is not suitable for mass manufacturing of graphene. CVD relies on the epitaxial growth of graphene layers on the surface of other single-crystal substrate (e.g., SiC, Ni, and Cu) under high temperatures ($>600^\circ\text{C}$) in the presence of hydrocarbon vapors as a source of carbon.³²³ CVD is suitable for producing macroscale areas/quantities of graphene, which then can be readily transferred onto desired surfaces after the dissolution of the single-crystal supporting substrate. However, the uniform growth of single-layer graphene sheet, using CVD methods, remains challenging and requires further development.^{75,117} Solution-phase exfoliation usually involves the oxidation of graphite under strongly acidic conditions (e.g., Brodie,³¹⁸ Staudenmaier,³¹⁹ and Hummer's methods³²⁰) and leads to the formation of graphene oxide (GO), which has many oxygen-containing functional groups on the surface, such as carboxyls, epoxides, and hydroxyls (Figure 13c).^{73,321,322} GO retains a layered structure (Figure 13f), but in contrast to graphene, it is an electrical insulator due to the existence of a large proportion of sp^3 C–C bonds. To regain the structural features of graphene that define its unique electrical properties, GO can be reduced either by thermal, electrical or chemical treatments.³²² The resulting product—reduced graphene oxide (rGO)—contains a significant amount of C–O bonds. This method allows the low-cost and high-volume production of rGO; however, it results in the incorporation of structural and compositional defects with limited control over their spatial distribution.

The high electrical conductivity of graphene, together with its large specific surface area, high mechanical strength, and potential for mass production, makes it an excellent platform for applications in chemical sensing.^{78,123,125,232,272,324,325} First, graphene exhibits remarkably high carrier mobility and high carrier density at room temperature.²⁹⁹ These outstanding electronic properties make graphene a good candidate for the fabrication of high-performance electrically-transduced analytical devices.^{102,317} Second, the surface of graphene can interact with a broad range of analytes through van der Waals force, electron transfer, or covalent bonding.^{77,326} These interactions can result in the perturbation of electronic properties of graphene, usually reflected in a conductivity change.²⁶⁴ Theoretical studies indicate that the adsorption of different gas molecules on graphene can also modulate electrical conductivity through changes in doping states.^{327–330}

Electron density within graphene-based materials can be localized around its edges and structural defects giving rise to much faster electron transfer rates than encountered on its basal plane, thus demonstrating a versatile nature of graphene as electrocatalyst for electrically-transduced sensing applications.³³¹ Third, graphene possesses high surface-to-volume ratio, meaning that every carbon atom in graphene is a surface atom, providing the greatest possible surface area per unit volume. Therefore, the charge transport through graphene is highly sensitive to its chemical environment.^{80,125} Fourth, graphene has inherently low electrical noise due to the high quality of its crystal lattice, making it capable of screening charge fluctuation compared to one-dimensional counterparts (e.g., CNTs).^{76,332,333} Only one electron change in the local carrier concentration in graphene can lead to a step-like alterations in its resistance resulting in single-molecule sensitivity.¹⁵⁷ Fifth, graphene offers outstanding mechanical strength and flexibility, which are compatible with electronic-devices that have the form of flexible, stretchable, or even conformal features.^{124,324,334} These extraordinary properties enable graphene to be considered as a promising material for wearable electronics.¹²⁴

Because the surface of graphene plays a crucial role in intermolecular interactions, tuning the surface chemistry of graphene materials is the most primary and direct approach to adjust its sensing properties. To provide enhanced specificity and strength of the interactions, the surface of graphene can be modified through various covalent and noncovalent methods.^{97,335} Molecular level tuning of graphene surfaces through either post-synthetic incorporation of functional groups or dopants, as well as by achieving a high level of control over the structural and compositional defects may enhance its sensing properties for the fabrication of functional devices. Theoretical and experimental studies on graphene-based gas sensors revealed that the presence of defects and dopants increases sensitivity of devices compared to pristine graphene.^{336–339} Introducing electron-withdrawing groups (e.g., epoxide and carboxylic groups) generates holes in the valence band of rGO, and consequently improves the response toward reducing molecules. Conversely, surface modifications with functional groups containing lone-pair electrons (e.g., ethylenediamine or sulfonate) can improve the response toward oxidizing molecules.

The sensing properties of graphene materials, such as sensitivity and selectivity, can be further improved by creating graphene hybrid materials with other functional nanostructures, including metal^{340,341} and metal oxide nanoparticles,^{342–344} organic receptors,³⁴⁵ conducting polymers,³⁴⁶ proteins, or nucleic acids.²⁷² The optimized performance arises from the synergistic effects of different components.^{78,123,125,264,283,334,347} For example, modification with conductive polymers can enhance carrier scattering of graphene, leading to the formation of an adsorbent layer providing additional electrochemical or acid–base interactions with a range of molecules,³⁴⁸ while modifications with enzymes can induce selectivity to biomolecules.³⁴⁹ A holistic understanding of the surface chemistry and modified surface species, lattice defects, electronic properties, and how each attribute can be tailored, should be considered when applying graphene to chemical sensing applications.

3.2. Black Phosphorus

The most stable allotrope of phosphorus—black phosphorus (BP)—was first synthesized by Bridgman in 1914 by subjecting white phosphorus to high temperature (200 °C) and pressure (1.2 GP).³⁵⁰ A century later, Ye group⁶⁷ and Zhang group³⁵¹ used mechanical exfoliation to isolate single and few atomic layers of 2D PB-phosphorene, respectively. The resulting 2D material exhibits unique properties, such as hinge-like structure, structural anisotropy, quasi-one-dimensional excitonic nature, and layer dependent band gap features that often contrast those found in other 2D materials.^{67,351,352} 2D BP exists as a single-elemental layered crystalline material composed of sp^3 hybridized phosphorus atoms, arranged in a layered orthorhombic crystal structure with the *Cmca* space group.³⁵³ It forms a honeycomb lattice structure with notable non-planarity in the shape of structural ridges, with lattice constants of $a = 3.31$, $b = 10.50$, and $c = 4.38 \text{ \AA}$.³⁵⁴ BP also displays a puckered conformation along the armchair direction, with a bilayer structure being dominant along the zigzag direction (Figure 14a). Stacks of 2D layered BP are held

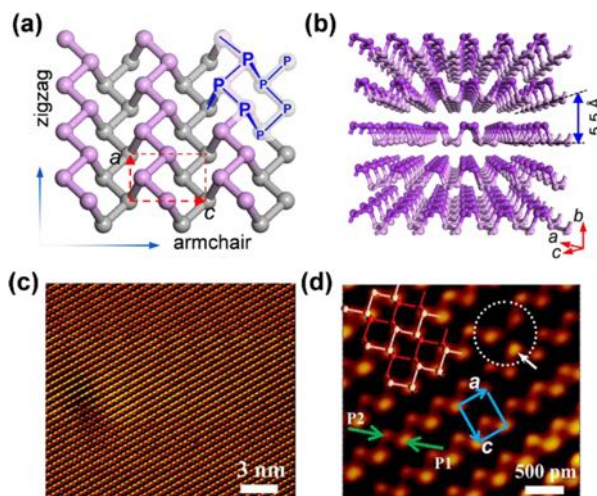


Figure 14. (a) Schematic diagram and chemical structure of single-layer phosphorene. (b) Few layers of phosphorene stacked by van der Waals force. (c) Large-scale STM image of BP surface with atomic resolution. (d) Close-up STM image showing that only the upper atoms of the topmost puckered layer can be seen with no reconstructions. The unit cell is indicated by blue dashed lines and a vacancy is marked by a green dashed circle. There is a contrast between the two rows in the same zigzag chain, indicated by red arrows and labeled as P1 and P2, respectively.³⁵⁵ Adapted from ref 355. Copyright 2009 American Chemical Society.

together by interlayer van der Waals interactions with the distance of 5.5 Å between the adjacent layers (Figure 14b,c). In each phosphorene layer, P atoms display triangular pyramidal structure due to the presence of three covalently bonded phosphorus atoms with one lone pair of electrons; defects may exist in the single layer due to the loss of the P atoms (Figure 14d).³⁵⁵

In addition to the tunable direct bandgap of BP, which can be modulated by increasing the layer multiplicity, from 1.51 eV for a monolayer to 0.59 eV for a five-layer system,³⁵⁶ BP also possesses the drain current modulation up to 10^5 and carrier mobility up to $1000 \text{ cm}^2 \text{ V}^{-1} \text{ s}^{-1}$.³⁵¹ Recent theoretical studies showed that the band gap of BP can be further engineered by controlling the direction of the edges (e.g., zigzag or armchair),

as well as controlling the functional groups at the edges.³⁵⁷ For example, Tran et al. demonstrated that the magnitude of the band gap for BP nanoribbons is dependent on the width of the nanoribbons due to quantum confinement effect.³⁵⁸ Peng et al. further demonstrated that the armchair P-nanoribbons exhibited semi-conductive behavior for all investigated edge functionalized groups (H, F, Cl, OH, O, S, and Se), while the zigzag nanoribbons displayed either semiconductive or metallic behavior, depending on their edge chemical groups.³⁵⁹

The increasing use of BP in electrically-transduced sensing technologies arises from the combination of its unique electronic properties (e.g., small intrinsic band gap and anisotropic electrical conductance) and unique surface chemistry.¹⁵⁹ In particular, BP possesses high chemical adsorption energy, as well as large abundance of available adsorption sites for analyte interactions as a result of its puckered surface structure.^{98,159} Charge transfer between analyte and BP, and consequently sensitivity, can be further improved by introducing structural ripples into the surface of BP.³⁶⁰ In addition, large surface-to-volume ratio of BP could be utilized as a scaffold for the immobilization of known molecular receptors to induce selectivity to targeted analytes.^{361–363} The introduction of dopants is another approach to improve ability of BP to sense analytes.³⁶⁴ BP also exhibits faster heterogeneous electron transfer rates at the edge plane sites than on its basal plane, in similar fashion to that of graphene. Thus, with the future improvements in control over the orientation of fabricated layers, BP may find large utility in sensing applications.³⁵³ However, the biggest challenge in the application of BP for sensing technologies lies in its limited stability to light and oxygen, and the possibility of formation of phosphoric acid species in the presence of moisture.^{159,365} Known strategies to improve stability of BP to degradation under ambient conditions rely on the incorporation of protective coatings,³⁶⁵ nanomaterials,³⁶⁶ or ionic liquids.³⁶⁷

3.3. Transition Metal Dichalcogenides

Transition metal dichalcogenides (TMDCs) are a family of inorganic materials with a chemical formula of MX_2 , where M is a hexavalent transition metal ion and X is a divalent chalcogen (S, Se, and Te).^{84,368} A subset of TMDCs (mainly those based on group 4–7 transition metals) crystallize as layered structures, in which the monolayers stack together through the van der Waals forces. In MoS_2 , each monolayer contains three rows of atoms, a layer of metal atoms sandwiched between the top layer and bottom layer of the chalcogenide atoms. Each layer has a covalently bound $\text{X}-\text{M}-\text{X}$ unit with 6-coordinate metal sites adapting either trigonal prismatic (D_{3h}) symmetry or trigonal antiprismatic (D_{3d}) symmetry (Figure 15a,b).⁸⁴ The solution-suspended monolayers of MoS_2 were first prepared through lithium intercalation in 1986.³⁶⁹ This accomplishment was followed up on in 2010 with a report characterizing free-standing monolayers of this material.³⁷⁰

In contrast to graphene, TMDCs can display a wide range of polymorphs and polytypes.^{371,372} For example, MoS_2 has four different crystal structures, 2H, 1T, 1T', and 3R, depending on the coordination modes between the Mo and S atoms and/or stacking orders between layers.³⁷³ Conductivity of bulk TMDCs ranges from insulators (HfS_2), to semiconductors (MoS_2 and WS_2), semimetals (WTe_2 and TiSe_2), and metals (NbS_2 and TaS_2).³⁷⁴ The electronic properties of TMDCs layered structures differ significantly from the bulk properties

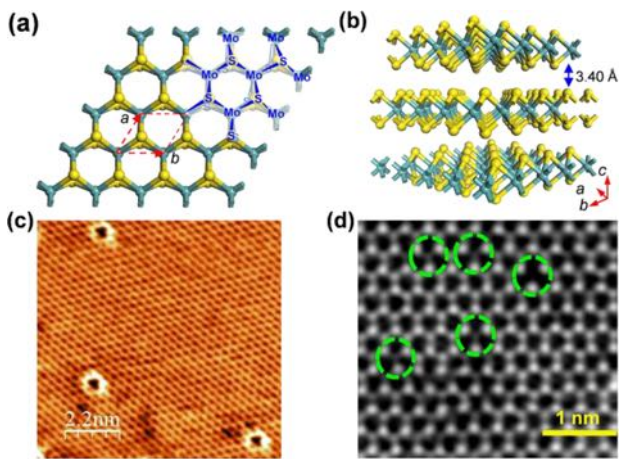


Figure 15. (a) Schematic diagram of single layer of MoS₂. (b) Three-dimensional representation of the structure of MoS₂. (c) STM images of single-layer MoS₂ with triangular and circular shaped point defects.³⁸⁴ Reproduced with permission from ref 384. Copyright 2016 Nature Publishing Group. (d) Atomic resolved STEM-ADF images to reveal the distribution of different point defects.³⁸⁵ Reproduced with permission from ref 385. Copyright 2015 Nature Publishing Group.

due to confinement effects, as well as the scission of interlayer coupling.^{368,375,376} Exfoliation of bulk TMDCs disrupts the s-p_z orbital interactions between adjacent layers and causes the band gap to widen.³⁶⁸

Synthesis of single and few layer TMDCs can be accomplished through top-down methods including mechanical or liquid-phase exfoliation of bulk layered crystals,^{377–380} or through bottom-up methods such as CVD.^{381–383} Currently, mechanical exfoliation provides the highest quality monolayer samples at the cost of low synthetic yield. However, inherent atomic scale defects are still found in MoS₂ single layers made by mechanical exfoliation (Figure 15c,d).^{384,385} CVD methods are more suitable for large-scale manufacturing of TMDCs than exfoliation techniques. The uniform growth of single-layer TMDCs remains a challenge.⁸⁴

When TMDC is exfoliated into a 2D thin sheet, both the basal planes and the prismatic edges are exposed, presenting distinct structural and electrical features.⁷³ The surface chemistry of the basal plane of TMDCs is dominated by chalcogenide lone pairs, which are projected perpendicularly to the TMDC basal surface;^{73,138,386} on the prismatic edges, either metal or chalcogenide atoms can be present, depending on the growth environment.³²¹ Once the lateral size is decreased, the presence of low-coordination step-edges, kinks, and corner atoms dominate the overall observed chemistry of the TMDC materials.³⁸⁷ For example, the location and amount of S vacancies at the edges of MoS₂ nanosheets can critically influence their stability and catalytic activity.³⁸⁸ Theoretical calculations show that MoS₂ with S vacancies exhibits excellent adsorption ability for several nonpolar gases, while perfect MoS₂ sheets show little or no adsorption.³⁸⁷ S vacancies in MoS₂ are most favorably formed either at the edge or the corners of the nanosheet layer, whose specific location/distribution is further dictated by the size of the 2D sheet. Therefore, it is important to control the specific shape (e.g., hexagonal platelets, plate-like crystallites, and trigonal sheets) of TMDC nanosheets both in the context of their morphology and dimensionality.^{389,390} For small-sized

MoS₂ nanosheets, the shape of the material can be engineered by the edge-plane functionalization, as the equilibrium shape geometry is highly sensitive to the energetics of the edge atoms. Both metal-terminated and sulfur-terminated examples of TMDCs fabricated using this experimental approach have been demonstrated. This level of molecular control allows great tunability in the reactivity and electronic properties of 2D TMDC nanosheets for applications in sensing technologies. Post-transition metal dichalcogenides (pTMDCs), like SnS₂, exhibit many of the similar properties to TMDCs due to their isostructural nature.^{391–393}

TMDCs encompass diverse morphological and compositional structures.³⁸⁶ Numerous metals and chalcogens have been used as components in 2D sheets from bottom-up synthetic methods.⁷³ TMDCs can be found as insulators, semiconductors, or metallic conductors,^{368,386} allowing them to be incorporated into a broad range of analytical devices in which charge transport can be easily modulated by surface adsorbents. Despite compositional control over physical parameters such as conductivity, a wide range of synthetic options for producing TMDCs must be optimized.³⁸⁷ There is also a significant challenge in obtaining TMDCs with specific layer multiplicity and tailored edge functionality.³⁸⁷ Both aspects play a large role in the sensitivity toward various analytes.³⁹⁴ Yet, the numerous benefits of TMDCs such as high thermal and chemical stability coupled with large abundance of metal host-guest sites render these materials as promising candidates for gas detectors and future gas sensing applications.

3.4. Metal Oxides

Metal oxides are compounds formed from metal and oxygen in the form of oxide ion, which constitute one of the most diverse classes of solids, exhibiting a variety of structures and properties.^{86,395,396} 2D metal oxides can be divided into two groups: 2D layered metal oxides, e.g., MoO₃, TaO₃, and WO₃, and 2D non-layered metal oxides (e.g., ZnO, CuO, and SnO₂ in their nanosheet or nanofilm forms), depending on the presence/absence of van der Waals layered structure in the bulk.^{86,102,121} As shown in Figure 16a,b, orthorhombic MoO₃

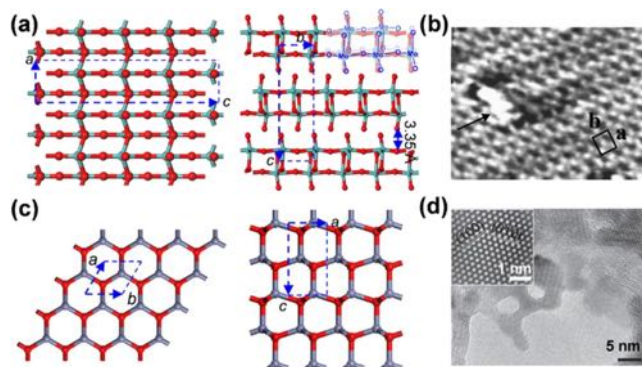


Figure 16. (a) Layered crystal structure of MoO₃. (b) High resolution STM image showing a rectangular unit cell with $a = 0.50$ nm and $b = 0.57$ nm $\pm 10\%$, obtained at 300 K. Defects are indicated by arrows.⁴⁰² Reproduced with permission from ref 402. Copyright 2004 AIP Publishing. (c) Structure of ZnO which is intrinsically nonlayered. (d) TEM images of ultrathin 2D ZnO nanosheets. The inset is high resolution TEM images of the crystal lattice structure of the nanosheets.³⁹⁹ Reproduced with permission from ref 399. Copyright 2014 Nature Publishing Group.

(space group $Pcmn$, $a = 3.963 \text{ \AA}$, $b = 3.696 \text{ \AA}$, $c = 13.855 \text{ \AA}$) possesses layered crystal phase of molybdenum trioxide, in which dual layer planar crystals of distorted MoO_6 octahedra are held together in the vertical direction by weak van der Waals forces.⁸⁷ These weak interactions between layers are favorable for exfoliation by either liquid or gas phase techniques to obtain nanosheets.^{397,398} The basal surfaces of layered metal oxides are terminated by oxygen atoms leading to high chemical stability under air and water. 2D metal oxides without the intrinsically layered structures, like nanosheets of ZnO as shown in Figure 16c, are not readily synthesized by top-down approaches because such materials contain strong chemical bonds between different crystal layers. Instead, ultrathin sheets with atomic thickness (Figure 16d) can be obtained via morphological transformations,³⁹⁹ self-assembly from its corresponding oligomers with the assistance of surfactants,³⁹⁹ and salt-template methods.⁴⁰⁰ Different metal oxides give rise to distinct electronic properties, and their conductivity can range from metallic to wide-gap insulating.³⁹⁵ Additionally, the conductivity of specific metal oxides can be further tuned by varying the crystal size, morphology, dopant, contact geometry, and operation temperature.^{73,401}

The oxygen ions and the ionic character of metal–oxygen bond are the two key factors that determine the surface properties of the metal oxides.⁴⁰³ The unique character of the oxygen ion dominates the surface properties of 2D metal oxides in the context of chemical sensing including molecular adsorption, charge transfer, and catalytic performance.^{404–406} The high polarizability of O^{2-} enables 2D metal oxides to exhibit large, nonlinear, and non-uniform distributions of charges within their lattices, leading to electrostatic screening zone (1–100 nm in thickness) that generates exceptional local surface and interfacial properties.⁴⁰³ For this reason, the specific energy states near or on the surface of 2D metal oxides can induce significant Columbic interactions with adjacent ions. Therefore, if surfaces of two metal oxides are brought in contact with one another, a built-in interface potential will arise, shifting the Fermi levels of the surface planes.⁴⁰⁷ Due to the strongly ionic character of transition metal oxides, the surfaces of 2D metal oxides can become electronically activated.⁴⁰⁸ The surface of a metal oxide can be treated as ordered arrays of Lewis acid–base centers, which enable adsorption of various small molecules on its surface. For example, oxygen is usually chemisorbed on the surface of 2D metal oxide, at room temperature, in the form of negatively charged species.⁴⁰⁹

Metal oxides have been widely used in chemical sensors due to their semiconductive properties.⁸⁶ These materials become more conductive at elevated temperatures ($T > 250 \text{ }^\circ\text{C}$) as atmospheric oxygen increases hole-carrier concentration by binding to oxygen vacancies on the metal oxide surface.^{110,127} Synthetically, metal oxides are one of the least expensive, most readily produced materials that can exist on a 2D scale.^{114,410,411} They are robust to oxidizing and reducing conditions, elevated temperatures, and humid analyte mixtures.¹²⁸ However, the application of metal oxides toward mobile and miniaturized sensing platforms requires elevated operating temperatures, which consume large amounts of power, relative to sensors that can be operated at room temperatures.^{412,413} The 2D subfamily of metal oxides have recently shown great promise in overcoming the drawbacks of high temperature operation, enabling room temperature sensing of gaseous analytes.^{114,127}

3.5. Metal–Organic Frameworks

First developed in the 1990s,^{414,1131–1133} metal–organic frameworks (MOFs) are crystalline and porous hybrid materials formed via molecular self-assembly of inorganic metallic nodes with ditopic or polytopic organic ligands (e.g., carboxylate, hydroxyl, thiol, and amino) to form bulk crystals.⁴¹⁴ MOFs can adopt various forms of crystal structures in different space groups depending on the type of metals and linkers used for their synthesis, resulting in 1D, 3D, as well as in 2D layered structures.⁴¹⁵ Two experimental approaches have been developed for the fabrication of 2D sheets of MOFs, the top-down and bottom-up methods. Top-down techniques rely on the exfoliation (e.g., through sonication) of layered bulk MOFs, which is sufficient to break down the weak interactions between adjacent stacks (van der Waals forces or hydrogen bonding).¹¹⁵ In the case of solvothermal bottom-up synthesis, the growth of 2D MOF proceeds parallel to the basal plane, while vertical growth is restricted. Although, MOFs serving as molecular-scale cages/scaffolds for the integration/immobilization of electrical components have been widely reported,^{115,416,417} the limited electrical conductivity of the vast majority of MOFs renders them often unusable for the development of electrically-transduced sensors. Section 4 thus focuses on inherently conductive 2D MOFs and their application in electronic devices for chemical sensing.

Conductive 2D MOFs have been synthesized from redox-active planar aromatic ligands with ortho-disubstituted heterodonor atoms (O, S, or NH) coordinated to late transition metal ions that display square planar coordination environment. Taking Ni_3HITP_2 as an example, its hexagonal pores with a diameter of approximately 2 nm are formed through the coordination between the hexaaminotriphenylene ligand and Ni^{2+} node in a 2D extended sheet, which are further held together by non-covalent interactions with a interlayer distance of $\sim 3.3 \text{ \AA}$ (Figure 17a,c).⁴²⁹ The charge neutrality of the framework can be preserved by the redox activity of the organic linker, which can adopt multiple oxidation states to

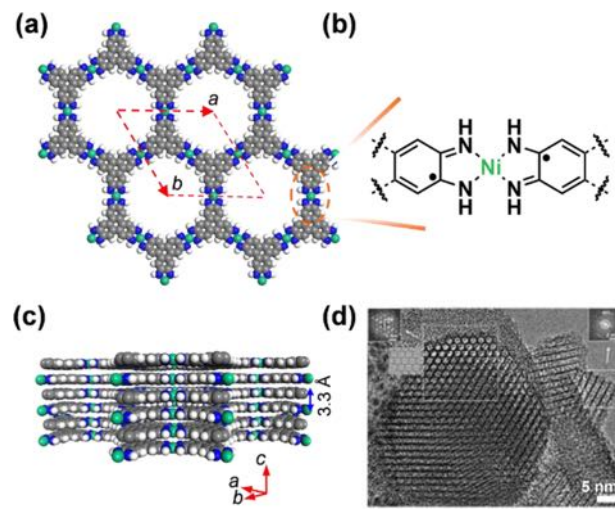


Figure 17. (a) Schematic diagram of single layer of MOF Ni_3HITP_2 . (b) Chemical details of the metal complex that constitute the hexagonal pore. (c) Side view of the MOF layers.⁴²⁹ (d) High magnification TEM image of MOF Ni-CAT-1; the inset images are the fast Fourier transform (FFT) analysis of the corresponding areas indicated by arrows.⁴²² Reproduced from ref 422. Copyright 2012 American Chemical Society.

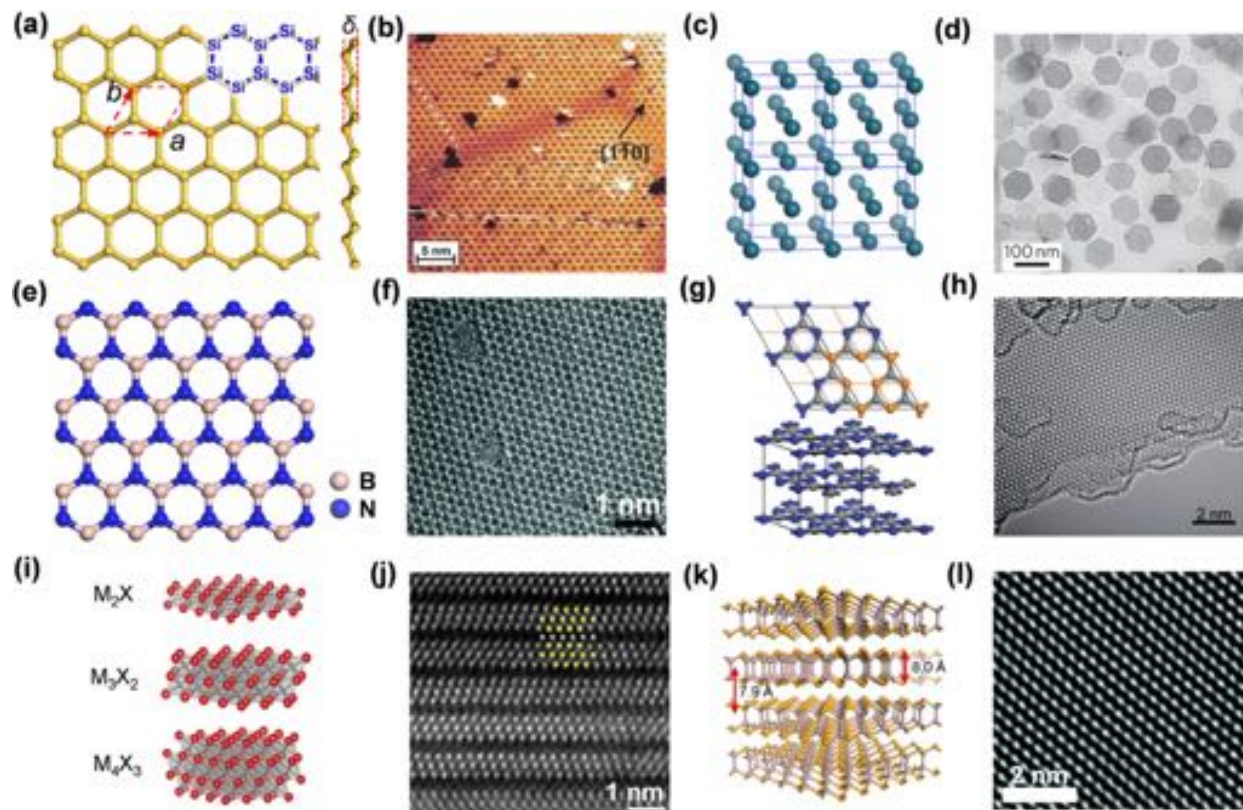


Figure 18. (a) Front and side view of schematic diagram of single layer of silicene. (b) Filled-states STM image of the 2D Si layer on Ag (111) showing the honeycomb-like structure.^{431,450} Reproduced with permission from ref 411. Copyright 2012 American Physical Society. (c) Crystal structure of palladium. (d) TEM images of palladium nanosheets.⁴³⁸ Reproduced with permission from ref 438. Copyright 2011 Nature Publishing Group. (e) Flat structure diagram of *h*-BN. (f) TEM image of *h*-BN showing triangular holes defects.^{451,452} Reproduced with permission from ref 452. Copyright 2015 The Royal Society of Chemistry. (g) Crystallographic unit cell and AB stacking arrangement of triazine-based graphitic carbon nitride (TGCN) layers. Carbon and nitrogen atoms are represented as gray and blue spheres, respectively. A hexagonal grid of half-cell size with nitrogen atoms at its nodes has been overlaid as guide for the eye in orange. (h) High-resolution TEM image of mechanically cleaved layers of TGCN.^{453,454} Reproduced with permission from ref 454. Copyright 2014 Wiley-VCH Verlag GmbH & Co. KGaA, Weinheim. (i) MXene sheets consist of 3, 5, or 7 atomic layers for M_2X , M_3X_2 , and M_4X_3 , respectively.^{177,455} (j) HR STEM image of $Mo_2TiC_2T_x$.⁴⁵⁵ Reproduced from ref 455. Copyright 2015 American Chemical Society. (k) Crystal structure and (l) high resolution TEM images of few-layer GaSe.⁴⁵⁶ Reproduced with permission from ref 456. Copyright 2016 The Royal Society of Chemistry.

ensure the charge balance with the metal centers.^{88,419} For instance, in the structure of Ni_3HITP_2 the ligand adopts a tris-semiquinone form that leaves an unpaired radical on the ligand (Figure 17b).^{426,429} Depending on the metal ion or linker, 2D MOFs can display different packing modes, including slipped parallel, eclipsed stacking, and staggered modes.^{89,419} The mode of stacking may potentially influence charge mobility across the 2D stacks.⁸⁸ The band gap of 2D conductive MOFs can be strategically engineered by careful selection of structural motifs (metal centers and organic ligands) which dictate the efficiency of through-bond or through-space charge transport in the MOF.^{88,89,419–421} This structural tunability allowed the development of 2D MOFs with electrical conductivities ranging from 10^{-6} to 2500 S cm^{-1} at room temperature.^{88,89,419–421}

Besides their porous scaffolds, ordered structure, and tunable conductivity, 2D conductive MOFs have versatile and unique surface chemistry.^{88,89,176} The metal centers on their 2D surface can adapt either octahedral or square planar coordination, featuring equatorial coordination with the organic likers and two axial ligands.^{89,422} The axial ligand can be absent in the pristine MOFs or may be possible to remove through activation procedures, which will result in the presence

of open coordination sites on the MOF surface, available for molecular interaction.⁴²³ Theoretical and experimental calculations showed that gas molecules, e.g., CO, NO, and NH₃, can be chemically adsorbed on the surface of the 2D MOF nanosheet through binding at the open metal centers.^{173,424} Experimental results based on MOFs containing ligand centered radicals also demonstrated that molecular adsorption of analytes onto the MOFs can proceed through the ligand-adsorbent radical recombination.^{425,426} The existence of potential defects, edges (Figure 17d), and the permanently trapped adsorbents, however, can complicate the chemical environment of the MOF surface. Improved understanding of the surface chemistry of conductive MOFs is critically important to the continued advancement of this class of materials in chemical sensing.

In summary, the majority of reported MOFs are topological insulators.^{427–429} Introducing planar and fully conjugated ligands have given rise to MOFs that are semiconductive or conductive in nature.^{88,89} These MOFs combine typical MOF multifunctionality, such as porosity, high surface area, and tunability, with nontraditional MOF characteristics of conductivity and charge transport.^{88,89,419} The coalescence of

these properties may provide enhanced responses in chemical sensing.⁴²¹

3.6. Other 2D Materials

With the rapid development of 2D materials for sensing applications, other 2D materials, including Xenes, 2D metals, carbon nitride, boron nitride, MXenes, and layered Group III–IV semiconductors, also show great potential in electrically transduced sensing.^{94,113,114,146,229}

Xenes refer to a mono-elemental class of 2D crystals of group IVA elements, including silicene, germanene, and stanene.^{430–432} In their most stable form, 2D Xenes based on Si, Ge, or Sn atoms, adopt a buckled hexagonal honeycomb structure (Figure 18a,b). The bond length in silicene ($\sim 2.28 \text{ \AA}$) is much longer than in graphene ($\sim 1.42 \text{ \AA}$) preventing the Si atoms from forming strong π bonds. The buckling of the Si atoms brings them closer together to enable a stronger overlap of their p_z orbitals, resulting in a mixed sp^2 – sp^3 hybridization, which further stabilizes their hexagonal arrangement. Xenes have higher reactivity compared to graphene, which can be beneficial in terms of functionalization, but it causes fast degradation and oxidation under ambient atmosphere, complicating the establishment of scalable routes for device integration.⁴³² Their electronic structure ranges from insulators, through semiconductors with tunable gaps, to semi-metallic, depending on the substrate, chemical functionalization, and strain. Theoretical calculations show that the band gaps of Xene monolayers can be tuned effectively by the adsorbed molecules.^{162,163,433,434} Depending on different types of molecules, the material–analyte interactions can be varied from weak van der Waals to strong charge transfer interactions. Vacancy defects and doping pristine silicene with either B or N atoms, can lead to enhanced binding energy, as well as charge transfer, and subsequently significant improvements in sensitivity.^{161,163}

Metals are a class of materials that play an important role in the fundamental studies of sensing and industrial applications.^{435,436} In the crystal lattice of a metal, atoms are closely positioned to neighboring ones (for example, Pd shown in Figure 18c) in one of three most common arrangements, including body-centered cubic, face-centered cubic, and hexagonal close-packed.^{437–440} Ultrathin 2D metal nanostructures normally exhibit the same crystal structures as their corresponding bulk materials.^{437–440} However, as the thickness of the metal layer decreases, the contribution of the electrons close to the surface to the total conductivity of the material increases, and the charge mobility and scattering then depends on the surface interactions. Similar to graphene and its inorganic analogues, metal nanoplates and nanosheets have also shown some unique sensing properties compared to nanostructures with other shapes, such as nanoparticles, nanorods, and nanowires.^{438,440,441} Thin metal sheets (Figure 18d) can be prepared via bottom-up methods from metal salts or small metal nanoparticles. Top-down approaches, such as electron beam nanolithography, nanoimprint lithography, and hole-mask colloidal lithography, have also been developed.⁴³⁶ On the surface of some metals (e.g., iron, zinc, and copper), a layer of metal oxides can be formed due to the presence of atmospheric oxygen.¹⁶⁵ Other metals, like palladium, platinum and gold, though they do not react with oxygen, they can have special reactivity toward some molecules. For example, palladium and platinum can catalytically dissociate hydrogen,⁴⁴² while gold has strong affinity toward thiol compounds

through the formation of Au–S bond.⁴⁴³ Due to the close packing of metal atoms, ultrathin metallic structures with a plethora of unsaturated atoms are difficult to stabilize and their synthesis remains challenging.^{444–446}

Hexagonal boron nitride (*h*-BN), commonly known as “white graphene”, has a similar periodic structure in plane to graphene, but exhibits different stacking order (Figure 18e,f).⁴⁴⁷ The adjacent layers, with a distance at 3.30 to 3.33 \AA , are held together by van der Waals force to form a bulk crystal. *h*-BN is an electrical insulator with a band gap of 5.2 eV and high thermal conductivity ($\sim 2000 \text{ W m}^{-1} \text{ K}^{-1}$ obtained by theoretical calculations and $380 \text{ W m}^{-1} \text{ K}^{-1}$ experimentally determined), excellent dielectric properties, and high-temperature抗氧化 resistance.^{63,447–449} *h*-BN nanosheets exhibit lower surface areas than their other 2D counterparts,⁴⁴⁸ but the doped or defective *h*-BN nanosheets can show response to several gaseous molecules as suggested by theoretical calculations.

Graphitic carbon nitride (*g*-C₃N₄) is another analogue of graphite with a layered van der Waals structure, where each layer is formed through the sp^2 hybridization of carbon and nitrogen atoms.⁴⁵⁷ There are two different structural models that account for the geometry and stoichiometry of *g*-C₃N₄, which are based on triazine⁴⁵⁴ and heptazine units, respectively (Figure 18g,h).⁴⁵⁸ The semiconducting bandgaps of *g*-C₃N₄ are around 2.5–2.8 eV, which lead to poor electronic conductivity. Due to the incomplete condensation during the synthesis, *g*-C₃N₄ contains a small amount of hydrogen in the form of primary and/or secondary amine groups on the terminating edges. The presence of terminal hydrogen together with high electron affinity of nitrogen to many analytes results in rich surface properties of *g*-C₃N₄, including basic surface functionalities, electron-rich character, and H-bonding motifs.⁴⁵⁹ The structural features of *g*-C₃N₄ nanosheets, such as the homogeneous dispersion of carbon and nitrogen elements in each nanosheet, thermal stability, and tunable bandgap may lead to enhanced performance in chemical sensing applications.

MXenes are a class of 2D transition metal carbides (Figure 18i,j) generated by selectively etching a certain element from M_{n+1}AX_n phases where M represents an early transition metal, A is related to a main group (mostly group III A and IV A) element, X is C and/or N, and n = 1, 2, or 3.⁴⁶⁰ O, F, and OH functional groups are generally found on the surfaces of exfoliated MXenes, which are introduced during the chemical etching process.^{177,178} The choice of synthetic method has a great influence on the ratio of these groups on the surface of synthesized MXene. Monolayers of MXene are predicted to be metallic, with a high electron density near the Fermi level.^{178,461,462} Density functional theory (DFT) calculations showed that the type and concentration of these surface terminations largely affect the properties of MXenes, through which analytical performance of MXenes can be tailored in compliance with various applications.^{462–464} The metallic and tunable conductivity, as well as the high abundance of functional groups on the outer surface, makes MXene a new generation of promising materials for sensing applications.

The III–VI layered semiconductors are a class of metal chalcogenides with a general formula of MX (M = Ga, In; X = S, Se, and Te).^{465,466} In the bulk material, each of the layers can be recognized as a double Ga or In layer intercalated in two layers of chalcogen to form the structure X–M–M–X as shown in Figure 18k,l. Different layers are held together by van

der Waals interactions at an interlayer distance of ~8 Å. The atomically thin films of III–VI layered semiconductors have limited stability under ambient atmosphere, and the chalcogen atoms on its surface can react with oxygen and water in the air.^{467–470} Theoretical calculations have revealed that the lone pair states of Se were located at the top of the valence band of InSe, close to the Fermi energy level, which indicates the ability of InSe to interact with external molecules.⁴⁷¹ The lone-pair on the chalcogen atom could be harnessed for surface functionalization via Lewis acid–base chemistry, which could improve their versatility and widen their applicability in electronics and sensing.⁴⁷²

2D materials share a general morphological structure that exhibits strong in-plane bonding to form 2D sheets, and weak interlayer van der Waals forces that lead to stacked layers of 2D sheets.^{70,73,321} This structural anisotropy allows isolation of robust atomically thin sheets by exfoliation of stacked layers.⁴⁷³ The trend of strong in-plane bonding often gives rise to the anisotropic charge transport of 2D materials that favors in-plane rather than through-stack transport.⁴⁷⁴ In systems with isolated 2D atomically thin materials, this confines charge transport to directions parallel to the free surface.⁴⁷⁴ This free surface is the location of host sites that allows host–guest interactions with the surrounding environment.⁹⁴ The proximity of charge transport to the host–guest sites, forced by the 2D nature of the material, can lead to large changes in electronic properties instigated by small changes in the chemical environment.⁵³ These morphological similarities across many classes of 2D materials are beneficial to their function in chemical sensing. In addition to a beneficial morphological trend, broad chemical diversity has been achieved in 2D systems, stemming from diverse element utilization and expansion of synthetic methods.⁷³ Such diversity has provided a great deal of tunability of exposed host–guest sites that can be adjusted to favor or discriminate against specific analyte–material interactions.^{114,146} The future focus on sensing with these 2D materials will be concerned with controlling both the morphology and surface chemistry of 2D materials.

4. SENSING APPLICATIONS

Many families of 2D materials have been applied to sensing across a wide range of analytes.^{73,138,321,475} This review classifies analytes into four main categories: gases, volatile compounds, aqueous ions, and aqueous biomolecules. Because each category offers unique challenges and requires unique strategies to resolve them, these four categories are addressed separately. To provide the most suitable comparisons, each family of sensing material is reviewed separately under each category of analyte. We have demarcated 2D materials into six subfamilies: graphene and graphene oxides, black phosphorus, transition metal and post-transition metal dichalcogenides, metal oxides, metal–organic frameworks, and other 2D materials (e.g., MXenes, hexagonal boron nitride, metals, and graphitic carbon nitride).

4.1. Detection of Gases

Carbonous (CO and CO₂), sulfurous (H₂S and SO_x), and nitrogenous (NH₃, NO, N₂O, N₂O₄, etc.) gases originate from a wide range of anthropogenic and natural sources. All of these chemicals are gases at standard temperature and pressure and are targets for chemical sensing as their local concentrations carry implications for human health and safety, industrial

process monitoring, as well as emissions control and air quality management.^{56,476,477} Many of these gases are byproducts of industrial processes, others are important feedstocks for world economies, and some play a vital role in physiological signaling. For example, suboptimal combustion of fossil fuels can lead to exhaust gases that carry hazardous compounds in addition to CO₂. A few examples of these are CO, which is produced from hypothermic combustion,⁴⁷⁸ NO and NO_x which are produced during hyperthermic combustion,⁴⁷⁹ and H₂S and SO_x compounds, which are byproducts of combustion of sulfur-containing fuels.⁴⁸⁰ Other gases are important precursors for commodity, fine, or specialty chemicals. For example, NH₃ mostly produced by the reduction of N₂ by H₂, the nitrogen-fixing Haber–Bosch process, is an important feedstock for fertilizers and is the backbone of the world's agricultural infrastructure.⁴⁸¹ Monitoring NH₃ production, as well as down-stream utilization, requires solutions that allow ubiquitous monitoring such as robust, inexpensive, miniaturized sensors with strong analytical characteristics.⁴⁸¹

Beyond their well-known role in industrial chemistry and hazardous presence in other aspects of life, CO, H₂S, and NO, so-called gasotransmitters, are known to have biological importance as endogenously produced signaling molecules that are important modulators of various cellular processes.⁴⁸² Furthermore, these biologically-produced species have recently been explored as therapeutic vectors to treat ischemia related reperfusion injury, carcinomas, and neurodegenerative diseases, yet are highly toxic at elevated concentrations from external sources. Monitoring these gases for biomedical purposes requires a unique set of sensor design criteria, where cost, size, and reusability are still determinants of a successful sensing platform. Sensors that can monitor *in vivo* processes are of great interest as well.⁴⁸³

Detection of gaseous compounds, such as small reactive gases (SRG) is the most straightforward subsect of chemical sensing. The concentration of analyte streams can be accurately dialed from sub-ppb to 100% concentrations using mass-flow controllers and inert gas streams. Additionally, powerful reducing gases such as NH₃, or oxidizing gases such as NO₂, circumscribe the family of SRGs that easily induce observable electronic changes in many conductive materials. However, less reactive species such as H₂, CO₂, and C₂H₄ gases require more specialized materials or material hybrids to provide robust detection. As such, many fundamental studies of chemical sensing using novel materials are demonstrated by the detection of SRGs. This testing ground for potential materials offered the first demonstration of the gas-sensing capabilities of graphene, BP, MOFs, TMDCs, and more.

As the need for industrial, environmental, and human health and safety related sensors increases, the demand for easily produced, robust, inexpensive, and highly integrable devices and design strategies is expected to foster continued research in the field of gas sensing using 2D materials.^{484,485} The following section highlights state-of-the-art theory and practice of gas sensing in the regime of electronic transduction using 2D materials.

4.1.1. Graphene and Graphene Oxides. *4.1.1.1. NH₃ and N_xO_y* Novoselov and co-workers demonstrated the first application of atomically thin graphene in sensing of gaseous analytes.¹⁵⁷ Graphene monolayers (area ~10 μm²) were prepared by micromechanical cleavage of HOPG. The isolated graphene sheets were transferred to the surface of SiO₂, and e-beam lithography was then used to fabricate a Hall-bar device

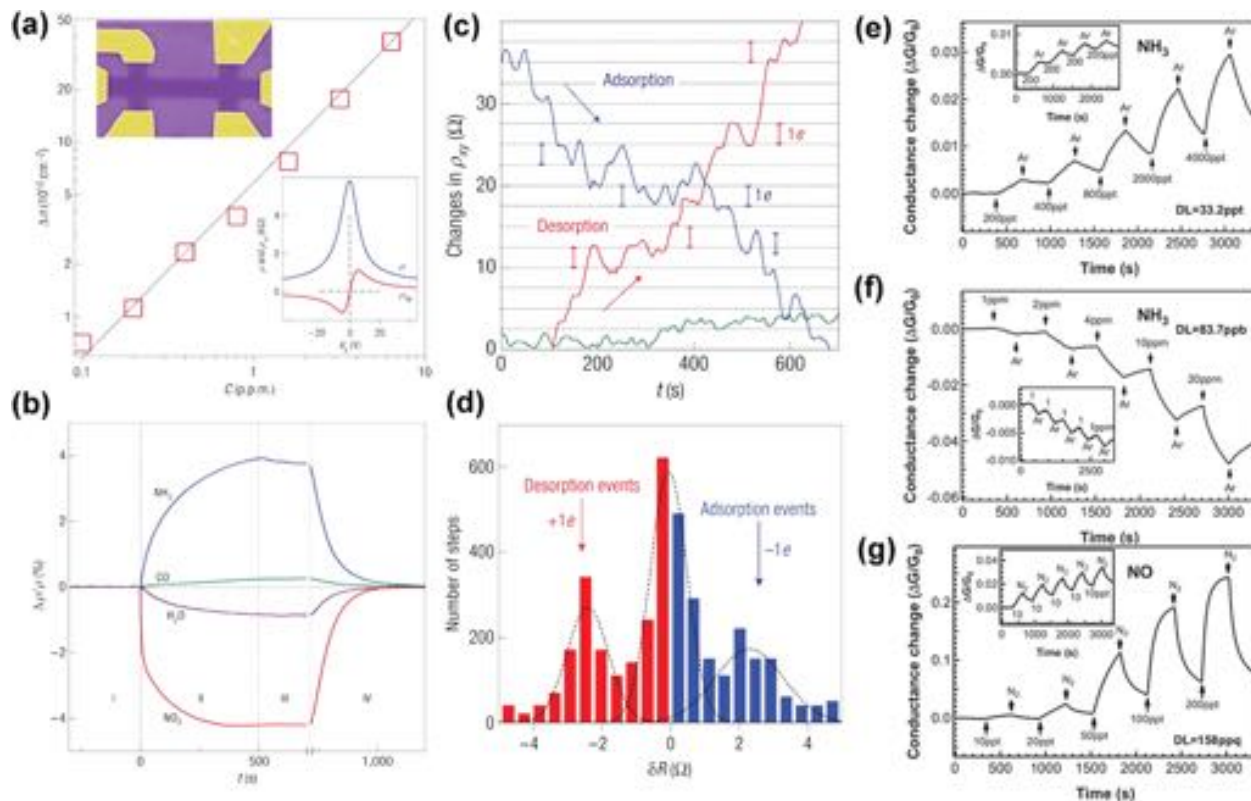


Figure 19. (a) Concentration, Δn , of chemically induced charge carriers in single-layer graphene exposed to different concentrations, C , of NO_2 . Upper inset: Scanning electron micrograph of this device (in false colors matching those seen in visible optics). The scale of the micrograph is given by the width of the Hall bar, which is $1\ \mu\text{m}$. Lower inset: Characterization of the graphene device by using the electric-field effect. (b) Changes in resistivity, ρ , at zero B caused by graphene's exposure to various gases diluted in concentration to 1 ppm. The positive (negative) sign of changes is chosen here to indicate electron (hole) doping. Region I: the device is in vacuum before its exposure; II: exposure to a diluted chemical; III: evacuation of the experimental set-up; and IV: annealing at $150\ ^\circ\text{C}$.¹⁵⁷ (c) Examples of changes in Hall resistivity observed near the neutrality point ($|n| < 10^{11}\ \text{cm}^{-2}$) during adsorption of strongly diluted NO_2 (blue curve) and its desorption in vacuum at $50\ ^\circ\text{C}$ (red curve). (d) Changes in ρ_{xy} larger than $0.5\ \Omega$ and quicker than 10 s were recorded as individual steps.¹⁵⁷ Reproduced with permission from ref 157. Copyright 2001 Springer Nature. (e) Response to NH_3 under *in situ* UV light illumination. The inset shows the reproducibility of sensor response at 200 ppt of NH_3 exposure. The detection limit is estimated at 33.2 ppt. (f) Response to NH_3 without UV light illumination, where the detection limit is estimated to be 83.7 ppb. (g) Relative change of conductance ($\Delta G/G_0$) versus time recorded with NO exposures ranging from 10 to 200 ppt. The inset shows the reproducibility of sensor response at 10 ppt of NO exposure. The detection limit is estimated at 158 ppq.⁴⁹⁰ Reproduced from 490, with the permission of AIP Publishing.

with evaporated Au as electrodes (Figure 19a). This device allowed the authors to investigate the electronic properties of graphene as it was perturbed by the adsorption of NH_3 , NO_2 , H_2O , and CO gases. The charge carrier concentration in graphene increased linearly with increasing concentration of NO_2 gas. This device was able to detect 1 ppm of NH_3 and NO_2 in an inert atmosphere, which was comparable with the most sensitive gas sensors. The authors also observed reverse electronic responses upon exposure to electron donating (e.g., NH_3) vs electron withdrawing gases (e.g., NO_2 ; Figure 19b). Annealing the device at $150\ ^\circ\text{C}$ removed the doping effects of the gases. When a high driving current was used to suppress the Johnson noise, step-like changes in resistivity were observed during the long-term exposure to dilute NO_2 gas (1 ppm), originating from single-molecule adsorption/desorption events and subsequent charge transfer between the gas and graphene (Figure 19c,d), indicating that the Gr-based sensor could detect even single NO_2 molecules. Four characteristics of graphene help explain its excellent sensing performance.¹⁵⁷ First, graphene is strictly two-dimensional with its whole volume exposed to surface adsorbates, which maximizes the possibility of their interaction with the 2D

material. Second, graphene possess metallic conductivity, thus has very low Johnson noise. Third, graphene exhibits low levels of excess ($1/f$) noise due to its high crystallinity. Fourth, graphene can be integrated into diverse device architectures with ohmic contact that have low resistance.

Since the first application of graphene in sensing, graphene-based materials have become extensively utilized in the development of gas sensors, prompting both theoretical and experimental investigation into the working principles of graphene-based devices. Wehling et al. used calculations based on local density approximation (LDA) and gradient-corrected exchange correlation (GGA) method to show that open shell NO_2 is a more effective electron acceptors than the closed-shell N_2O_4 system.⁴⁸⁶ Additional first-principles studies conducted by Leenaerts et al. examined the interaction of NO_2 and NH_3 with pristine graphene surfaces.⁴⁸⁷ Two primary mechanisms for charge transfer between small molecules and the graphene surfaces were proposed based on their work. The first mechanism, applicable to all molecules, operates through orbital hybridization and results in a small charge transfer, as in the case of physisorption. The second mechanism depends on the position of the HOMO and LUMO of the molecule with

respect to the Dirac point of graphene and is only applicable to open shell molecules leading to large charge transfer between adsorbed molecules and graphene.⁴⁸⁷

Sensing ultralow concentration of analyte is important in environmental monitoring, control of chemical and agricultural processes, space missions, and medical applications.^{488,489} Chen and co-workers demonstrated that pristine graphene can detect gas molecules at extremely low concentrations with detection limits for NO estimated to be as low as 158 parts per quadrillion (ppq) at room temperature.⁴⁹⁰ This response was approximately 300% better than the sensitivity of CNT-based gas sensors tested under the same experimental conditions. This unprecedented sensitivity was achieved by continuous in situ cleaning of the sensing material with ultraviolet light, which probably involved a photo induced molecular desorption mechanism.⁴⁹¹ The ultra-sensitivity of pristine graphene was further confirmed by the ppt to ppb level detection of other common gas species, including NO₂, NH₃, N₂O, O₂, SO₂, CO₂, and H₂O (Figure 19e–g).⁴⁹⁰

Koley and co-workers fabricated reverse-biased graphene/Si heterojunction capable of detecting NO₂ and NH₃ at 200 ppb and 10 ppm concentrations, respectively.⁴⁹² The alteration of Schottky-barrier height due to molecular adsorption of gaseous analytes on graphene surface led to the exponential change in the junction current, thus resulting in ultrahigh sensitivity. The developed sensing devices at ambient conditions were approximately 13 times and 3 times more sensitive to NO₂ and NH₃ gases than analogous graphene-based amperometric devices. The reverse bias operation also led to significant reduction in the operating power of the sensor (~500 times) for the same magnitude of applied voltage. In addition, the reverse bias operation permitted modulation of the work function of graphene, and consequently Schottky-barrier height, enabling wide tunability of the sensor performance characteristics (sensitivity and response time).⁴⁹²

The presence of defects and intentional doping can significantly influence the properties and gas sensitivity of intrinsic graphene. Using first-principles calculations, Zhang et al. explored the role of dopants (B, P) and defects in graphene on the interaction of the material with NH₃, NO, NO₂, and CO gases.³³⁶ The authors demonstrated that the interactions of gaseous molecules with pristine graphene are substantially weaker than of the defective or doped graphene. These findings suggested that the sensing performance of pristine graphene could be deliberately improved either by doping or by the incorporation of defects. Defective graphene was able to enhance interactions with NO and NO₂ gases, but did not alter the response of the device to NH₃. Furthermore, the degree of doping by a specific analyte was not affected by the location of binding to the graphene surface, but instead was highly dependent on the geometry and orientation of the host-guest interaction.³³⁶ This computational study also suggested that the doping ability of NH₃ toward pristine graphene was very limited, which was inconsistent with the high sensitivity of graphene to NH₃ demonstrated by Novoselov and co-workers.¹⁵⁷

To examine the impact of the defects of graphene made from conventional nanolithography procedure on the sensor characteristics, Johnson and co-workers experimentally compared the sensing performance of FET devices fabricated through mechanically exfoliated graphene followed by a standard electron beam lithography (EBL) procedure before or after undergoing a high temperature cleaning process.⁴⁹³

The authors showed that standard EBL processing leads to a formation of ~1 nm thick layer on the surface of graphene, which can affect the charge transport properties of this 2D material. The thermally cleaned devices contained roughly 1/3 of the concentration of doped carriers and exhibited four times higher carrier mobility. However, the cleaned devices produced a much weaker electrical response to gases such as NH₃. It was found that the contaminant layer enhanced carrier scattering and acted as an absorbent for preconcentration of analyte molecules at the graphene surface, thereby enhancing the sensor response.⁴⁹³

Before 2009, the development of graphene-based sensors was limited by laborious preparation of single-layer graphene through either mechanical exfoliation or EBL processes, which are typically low yielding and time-consuming. These issues were gradually resolved between 2007–2009 when novel methods for the preparation of reduced graphene oxide (rGO) were developed. The chemical reduction of GO, for example using Hummer's method, proved to be most suitable for nanoelectronics fabrication at low-cost with increased yield.^{494–497} However, the use of harsh chemical treatment (e.g., strong acids) may result in the formation of structural and compositional defects in the final structure of the material, which may influence the gas sensing properties of the resulting device. Recently, GO and rGO have been demonstrated as promising materials for gas sensing applications due to their versatile chemical, physical, and electronic properties, such as large surface-to-volume ratio, the presence of oxygen functional groups or defects, and high feasibility for surface functionalization.^{498–500}

Fowler et al. reported on the development of chemical sensors based on rGO synthesized via Hummer's method.⁴⁹⁸ The dispersions of rGO were spin-coated onto interdigitated electrode arrays to create single-layer films for detection of NO₂ and NH₃. Furthermore, a micro hot plate sensor substrate was employed to increase the recovery speed of the device, however at the expense of diminished sensitivity to NO₂.⁴⁹⁸ Guha and co-workers used chemically reduced GO to sense ammonia at room temperature.⁵⁰¹ The sensing layer was synthesized directly onto a ceramic substrate with pre-patterned platinum electrodes. The resulting sensors exhibited 5.5% change in response to NH₃ at 200 ppm and 23% change at 2800 ppm of NH₃, as well as good recovery time without the application of heat. In addition, the sensor was exposed to different vapors and found to be selective toward NH₃.⁵⁰¹ Manohar and co-workers developed a flexible sensor based on rGO, chemically reduced by vitamin C, for reversible detection of NO₂ and Cl₂ gases at room temperature, with ppb sensitivity.⁵⁰² Chen and co-workers utilized porous rGO, synthesized from one-pot hydrothermal treatment, for room temperature sensing of NO₂.⁵⁰³ High porosity of rGO provided not only sufficient active sites for gas adsorption, but also supplied channels for gas diffusion. The resulting sensor exhibited an enhanced performance to NO₂ gas with ppb detection limits. These results demonstrated that the structural modification of rGO by perforation was a promising approach for improving the sensing performance of graphene-based devices.

Recently, laser irradiation has attracted increasing attention as an alternative approach for the direct reduction and patterning of GO films due to its rapid material processing speed, large scan area, nanometer spatial resolution, and single-step capability.^{504,505} Kaner et al. reported on the development

of gas sensors fabricated directly through laser-induced reduction and patterning of rGO, on various flexible substrates.⁵⁰⁶ By varying laser intensity, the conductivity of the synthesized rGO could be precisely tuned over 5 orders of magnitude, which has proven difficult to achieve through chemical reduction methods.^{495–497} The resulting rGO-based sensors exhibited high sensitivity and reversible response to NO₂, demonstrating the feasibility of this fabrication approach for gas sensor development.

Through chemical modifications of rGO, functional groups or atoms can be introduced into the material to further tailor the surface properties of rGO, which may lead to enhancements in sensing performance. For example, Shi and co-workers fabricated chemiresistive gas sensors based on chemically modified graphene materials including sulfonated rGO (rGO-S) or ethylenediamine-modified rGO (rGO-EDA).⁵⁰⁷ The resulting devices exhibited high sensitivity to NO₂ with low detection limits of 0.07 and 3.6 ppm for rGO-S and rGO-EDA sensor materials respectively.⁵⁰⁷ The rGO-S and rGO-EDA sensing devices also showed 4–16 times stronger responses to NO₂ than the non-functionalized rGO-based gas sensors. The complete sensor recovery was observed upon the delivery of N₂ gas to the device without the need for UV, or IR irradiation, or thermal assistance. These results indicated that chemical modification of rGO is an effective approach for improving its gas-sensing performance through the incorporation of the high energy adsorption sites for analyte interactions. However, chemical modifications can alter the electronic properties of the 2D material, which may permanently increase the resistivity and noise of graphene oxide-based devices, thus diminishing the sensitivity of the fabricated sensors.⁵⁰⁸ Therefore, the structure-property relationship should be comprehensively balanced in the material design step.

Functionalization of graphene-based materials with metal nanoparticles, metal oxides, and polymers has led to the formation of unique hybrid nanostructures with exciting properties arising from synergistic effect between the incorporated components. Liu and coworkers developed highly sensitive NO sensors by decorating reduced graphene oxide with Pd nanosheets and incorporating the hybrid material (rGO-Pd) into a FET device.⁵⁰⁹ The FET sensors responded to NO gas in the concentration range of 2 to 420 ppb at room temperature. CVD-grown graphene contacts of rGO-Pd improved the stability and sensitivity of the devices due to the work function matching between graphene and rGO. Improved gas-sensing performance can be further realized by combining chemical modification approaches with metal nanoparticle decoration.⁶⁶⁷ Huang et al. reported on a flexible NO₂ sensor composed of the sulfonated rGO (rGO-S) decorated with Ag nanoparticles (rGO-S-Ag), which was printed onto a polyimide (PI) substrate by a gravure printing technique. Surface functionalization of rGO with –SO₃H groups and Ag NPs resulted in high sensitivity of the fabricated chemiresistive device to NO₂ (74.6% for 50 ppm), at room temperature.⁶⁶⁷ In addition, the sensor demonstrated fast response and recovery times of 12 and 20 s, respectively.⁶⁶⁷

Surface functionalization of graphene or rGO with metal oxides has proven to be another effective method for achieving high-performance detection of gases. Sow and co-workers immobilized Cu₂O nanowires on rGO sheets, and investigated their ability to detect NO₂.⁵¹¹ The response of rGO-Cu₂O hybrid material was 67.8% for 2 ppm of NO₂, much higher

than that of rGO (22.5%) or Cu₂O nanowires (44.5%) alone. The LOD recorded for the composite material was 64 ppb compared with 81 ppb and 82 ppm for unmodified rGO or Cu₂O, respectively. The composite material displayed a significantly enhanced sensing performance to NO₂ at concentrations higher than 1.2 ppm. Blending of Cu₂O with rGO can eliminate the need for an oxygen activation layer, which is usually required in metal-oxide based sensing.¹⁵² Recently, Yang et al. reported on the synthesis of In₂O₃ cubes uniformly embedded into rGO networks for detection of NO₂.⁵¹² The gas sensors based on In₂O₃-rGO composite exhibited a significant response to NO₂ at room temperature with a LOD of <1 ppm and excellent selectivity against interfering gases. The effective electronic interaction between n-type In₂O₃ cubes and p-type rGO facilitates the gas molecule detection via the resistance change of the hybrid architectures.⁵¹² Meanwhile, the existence of Gr sheets in the hybrid composite improves the electrical conductivity and provide high surface areas of In₂O₃ at room temperature.⁵¹² This synergistic effect enhanced sensing performance of the nanocomposites comprising uniformly distributed In₂O₃ cubes and rGO sheets. Similar strategy toward the improvements in the sensitivity for the detection of NH₃ and NO₂ have also been demonstrated by integrating WO₃,⁵¹³ Fe₂O₃,⁵¹⁴ SnO,^{515–518} and ZnO⁵¹⁹ graphene-based composites into functional sensing devices.

Composite systems formed by coating graphene materials with polymers, including PANI, polypyrrole (PPy), and poly(3,4-ethylenedioxythiophene) (PEDOT) have also been shown as effective strategies to further enhance the sensing performance of graphene-based sensors.^{520–525} For example, conjugated polymer PANI demonstrates sensitivity toward many analytes due to possible transformations between different forms of PANI; however, it has limited chemical stability.⁵²⁶ PANI can interact with rGO sheets through π–π interactions,⁵²⁷ which is helpful to improve the stability of the PANI. In addition, the electron transfer may occur between PANI and rGO sheets and consequently improve the sensing performance (e.g., sensitivity and reversibility) of the resultant material.⁵²⁸ Hybrid devices utilizing rGO-PANI exhibited much better response to NH₃ than the devices constructed from individual PANI nanofibers or rGO material (3.4 and 10.4 times, respectively, at 50 ppm of NH₃).⁵²⁰

4.1.1.2. H₂. Hydrogen gas sensors are of increasing relevance, in connection with the development and more extensive use of hydrogen gas as a fuel gas or chemical reactant in energy applications, automotive industries, and aerospace.⁵²⁹ Since hydrogen gas is odorless, colorless, and highly flammable, the development of early warning systems for H₂ monitoring together with the implementation of appropriate safety protocols is essential. The low adsorption energy of H₂ is reflected by a weak interaction between this gas molecule and graphene resulting in its challenging detections even under high concentrations.⁵³⁰ The incorporation of defects and dopants is an effective strategy to enhance the ability of graphene to interact with H₂. Ural and co-workers reported on the H₂ detection with a functionalized graphene substrate.⁵³¹ The sensing material was a hybrid of multilayer graphene nanoribbons and Pd nanoparticles (Figure 20a) mounted on a micromachined porous substrate. A response of –55% was reported for H₂ at 40 ppm. The improvement in sensitivity to H₂ was attributed to the presence of metallic NP that can form metal–hydride bonds, as in the case of Pd and Pt. (Figure

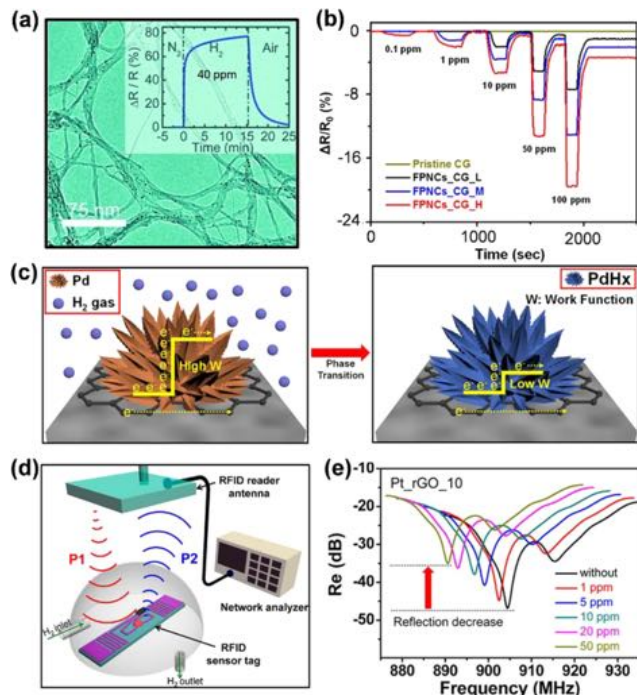


Figure 20. (a) Pd-functionalized multilayer graphene and its response to 40 ppm of H_2 .⁵³¹ Reproduced with permission from ref 531. Copyright 2010, John Wiley and Sons. (b) Normalized resistance changes of palladium decorated graphene at room temperature upon sequential exposure to H_2 gas of increasing concentrations (0.1 to 100 ppm). (c) Scheme of hydrogen gas sensing mechanism of palladium decorated graphene.⁵³² Reproduced with permission from ref 532. Copyright 2018 Springer Nature. (d) Schematic diagram of the ultrahigh frequency-RFID wireless sensor system for H_2 sensing which is composed of a RFID sensor tag and RFID-antenna-connected network analyzer. (e) Change in the reflectance of rGO-Pt-based wireless sensors as a function of the hydrogen gas concentration for a 2 min exposure.⁵³⁴ Reproduced from ref 534. Copyright 2015 American Chemical Society.

20b).⁵³¹ A similar experimental approach was utilized by Jang and co-workers, who integrated Pd-decorated graphene into the chemiresistive device architecture for the detection of H_2 .⁵³² The fabricated sensor could detect H_2 gas at concentrations as low as 0.1 ppm. Hydrogen molecules could react with Pd to produce PdH_x , which decreased the work function of the hybrid material, and consequently resulted in the decrease of the resistance (Figure 20c). Hong et al. also fabricated a highly sensitive H_2 sensor using a polymer-coated Pd nanoparticle-Gr hybrid. The resulting device exhibited high selectivity to H_2 over CH_4 , CO , and NO_2 gases.⁵³³

Based on these developments, Jang and co-workers fabricated wireless H_2 sensors by using rGO-Pt composite materials.⁵³⁴ The sensor system was composed of a radio frequency identification (RFID) reader and rGO-Pt sensing material immobilized on the RFID sensor tag that included the dipole tag antenna, sensing area, and IC chip (Figure 20d). The network analyzer emitted an interrogation signal at a power threshold of P1 to activate the sensor tag, which was then reflected back to the RFID-reader antenna at a power level of P2 based on its radar cross section. The rGO-Pt based RFID sensor tag exhibited a high sensitivity to hydrogen gas at unprecedentedly low concentration of 1 ppm.⁵³⁴ The increasing resistance of tag antenna upon exposure to H_2 led to impedance mismatching between the antenna and the IC

chip. Then, the RFID sensor tag decreased the radar cross section resulting in a diminished reflection (Figure 20e).

Besides doping with metal NP,⁵³⁵ surface functionalization of graphene materials with metal oxides and polymers that are able to respond to H_2 has also proven to be effective in enhancing the sensitivity of graphene to H_2 . This strategy of detecting H_2 gas has been reported with metal oxides including SnO_2 ⁵³⁶ and ZnO ⁵³⁷ decorated on graphene. For example, Al-Mashat et al. using Gr-PANI nanocomposite for H_2 sensing, demonstrated a sensitivity of 16.57% toward 1% of H_2 , which was considerably larger than of the sensors based on either graphene sheets or PANI nanofibers alone.⁵³⁸ Maeng and co-workers demonstrated that fully organic PEDOT-PSS heterojunctions, modified with graphene, could be used to detect H_2 at 100 ppm.⁵³⁹

4.1.1.3. CO and CO_2 . CO is a colorless, odorless, and tasteless gas with high toxicity to humans and animals. Therefore, it is important to develop reliable sensing platforms that would enable continuous monitoring of CO in both industrial and home-based applications. The initial report by Novoselov and co-workers showed that graphene produced a significantly weaker response to CO than to more reactive gases such as NH_3 or NO_2 .¹⁵⁷ First-principles calculation performed by Ao et al. demonstrated that the incorporation of defects and dopants can enhance the reactivity of graphene toward CO .¹⁸³ Majumdar and co-workers synthesized rGO and used it for chemiresistive detection of CO .⁵⁴⁰ The resulting sensor produced a 33% $\Delta R/R_0$ change in response to 10 ppm of CO at room temperature with minimal response to interferences such as CH_4 , H_2 , or NH_3 . CO detection by a three-component hybrid system was also achieved by Kim and co-workers.⁵⁴¹ The application of rGO/ SnO_2 /Au hybrid materials enabled the detection of CO at 2 ppm levels with 20.3% change in response. A sub-ppm-level CO gas sensor with a wide detection range of 0.25 to 1000 ppm, based on CuO -decorated graphene hybrid nanocomposite, was recently reported by Zhang et al.⁵⁴² The superior sensing performance for the presented sensor was ascribed to the hierarchical porous nanostructure and the heterojunction formed at the CuO -graphene interfaces.

One of the earliest reports of CO_2 sensing with pristine graphene was demonstrated by Cheng and co-workers in 2011, who were able to detect CO_2 at concentrations as low as 10 ppm.⁵⁴³ The resulting graphene sensor showed significant change in conductance when exposed to 10–100 ppm of CO_2 in air with a response time of less than 10 s. Due to the weak nature of interactions between CO_2 and graphene, the device response was rapid and reproducible. Nemade and Waghuley using few-layered graphene-based chemiresistive devices could detect CO_2 at 3 ppm concentrations, with the response time of 11 s. The improved sensitivity to CO_2 was attributed to the presence of defect sites in graphene materials that could interact with CO_2 gas molecules.⁵⁴⁴ The highest sensitivity to CO_2 was achieved by Chen et al. through an *in-situ* cleaning of graphene using UV light. The resulting sensor could detect CO_2 at concentrations as low as 136 ppt.⁴⁹⁰ Composites including Gr- Y_2O_3 quantum dots (QDs), Gr-Sb₂O₃, and Gr-Al₂O₃ were also successfully used for CO_2 sensing at room temperature.^{545–547}

4.1.1.4. H_2S and SO_2 . Hydrogen sulfide (H_2S) and sulfur dioxide (SO_2) are atmospheric pollutants and the main contributors to acid rain. Both gases are toxic to humans and ecosystems. Detection of H_2S and SO_2 with graphene materials

has been widely explored by first-principles methods.^{548–553} These investigations showed that SO_2 and H_2S adsorb only weakly on pristine graphene, yet various modifications, including doping with defects and additives, can improve sensitivity to these gases. In recent years, several sensors based on graphene materials have been developed for the detection of H_2S and SO_2 . Shen et al. fabricated a FET sensor using chemically edge-tailored GO nanosheet-based materials that could selectively detect SO_2 gas at room temperature in ambient air.⁵⁵⁴ The fabricated GO sensor showed good sensing performance including a wide range of sensitivities, fast response, and recovery times. The high sensitivity to SO_2 was attributed to the presence of holes induced by the protonation and isomerization of edge-tailored GO nanosheets upon exposure to the acidic sulfurous gases. In addition, the GO-based sensing devices exhibited limited response to a series of organic vapors (e.g., tetrahydrofuran, formaldehyde, or benzene) confirming its high selectivity for SO_2 gas. Ruoff and co-workers found that increasing the temperature can not only speed up the response and recovery of the graphene-based FET sensor for SO_2 , but can also improve its sensitivity.⁵⁵⁵ Zhang et al. fabricated layer-by-layer self-assembled TiO_2 /graphene film device and used it for the detection of SO_2 gas at room temperature.¹¹³⁶ The resulting sensor exhibited ppb-level detection, rapid response and recovery (71–73 s and 95–128 s, respectively), good reversibility, selectivity, and repeatability for SO_2 gas sensing.

Sensing of H_2S has mainly been realized by using composite materials where graphene or graphene oxide was modified with metal oxides in the form of nanorods/nanocrystals,^{556–558} nanofibers, nanosheets,^{343,344,559,560} or polymers,^{561,562} because metal oxides usually show strong chemisorption of toxic H_2S gas at room temperature.^{563,564} For example, Zhou et al. fabricated a rGO/ Cu_2O nanocomposite-based sensor, which demonstrated the detection limit of 5 ppb at room temperature.⁵⁵⁶ The observed high sensitivity to H_2S was due to the high surface activity for adsorption of H_2S gas molecules onto the surface of Cu_2O and the high electron transfer efficiency in the conducting network.⁵⁵⁶ Jiang et al. reported on the ultrafast responses to H_2S of 500 μs , as well as a fast recovery time of less than 30 s.⁵⁵⁹ The authors used magnetic fields with different orientations to control the fabrication progress of the Gr- Fe_2O_3 nanosheets. The experimental results illustrated that structural orientation of nanosheets played an essential role in maximizing efficiency of the device. Another strategy to fabricate sensitive H_2S sensor was demonstrated by Fattah and Khatami, who used mechanically exfoliated graphene as a sensing layer in the Schottky heterojunction device configuration (Gr/n-Si).⁵⁶⁵ The authors observed increase in sensitivity from 71% to 435% as the concentration of H_2S was varied from 10 to 1000 ppm with the response time of approximately 20 s at 100 °C.

4.1.1.5. O_2 . Oxygen is a reactive species that composes more than 20% of air. It is an important analytical target in a variety of areas including industrial safety, combustion process monitoring, as well as environmental and biomedical fields.⁵⁶⁶ Detection of oxygen by monolayer graphene in gas flow has been achieved by Hung and co-workers in 2011.⁵⁶⁷ The CVD-grown monolayer graphene device, exhibited a p-type doping response to O_2 at 1.25 vol % concentrations. Zhang et al. also observed that the sensitivity of fabricated sensors to O_2 could be further improved (LOD of 134 ppm) by illumination with UV light.⁵⁶⁸ These results are comparable with earlier reports

of a Gr- TiO_2 hybrid O_2 sensor by Wang et al.⁵⁶⁹ A carbon nitride/rGO hybrid system developed by Star and co-workers was capable of detecting oxygen in the 300–100 000 ppm concentration range.⁵⁷⁰

A wide variety of graphene and graphene-oxide sheets have been constructed that had increased functionality imbued by metal nanoparticles and metal-oxide nanoparticles. The growing set of methodologies for modifying graphene to provide more selective and sensitive hybrid materials will promote the fabrication of novel sensing technologies. The reports of flexible sensors based on graphene materials integrated onto the cotton or paper substrates opened the doors for low cost sensing and the development of wearable, wireless sensors.¹²⁴ Future work in the field of graphene-based sensors will continue to look toward new methods of integrating graphene and graphene hybrid materials in ways that allow for facile integration into specific applications.^{125,324}

4.1.2. Black Phosphorus. Phosphorene was initially predicted to be a superior gas sensing material over graphene and MoS_2 by a first-principles study carried out by Chen's group in 2014.⁹⁸ Their work predicted optimal adsorption positions of gas molecules on a monolayer of phosphorene. They also showed that high charge transfer is the driving mechanism behind strong adsorption of analytes on the surface of BP. The first experimental reports utilizing BP as an active element in gas sensing were demonstrated in two independent publications in 2015. Zhou and co-workers integrated chemically synthesized BP into FET devices to detect NO_2 down to 5 ppb in an argon environment (Figure 21a,b).¹⁵⁹ The authors observed a systematic increase in conductance with changing concentrations of NO_2 , which was indicative of hole doping charge transfer and was consistent with the p-type semiconductor electronic structure of BP (Figure 21c,d). The change in conductance fitted well within the Langmuir

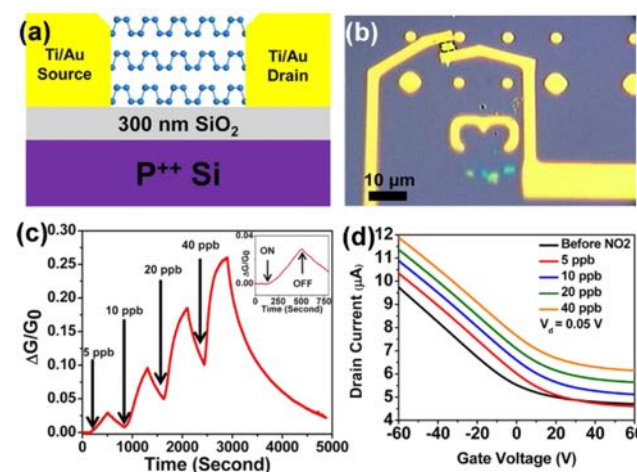


Figure 21. (a) Scheme of a multilayer BP FET. (b) An optical image of the multilayer BP flake between two Ti/Au electrodes used in this study. The BP flake is bordered by a dashed black line to guide the eye. (c) Relative conductance change ($\Delta G/G_0$) vs time (seconds) for a multilayer BP sensor showing a sensitivity to NO_2 concentrations (5–40 ppb). The inset shows an enlarged image of a 5 ppb NO_2 exposure response with identification of points in time where the NO_2 gas is switched on and off. (d) I_d - V_g curves of multilayer BP FET under different concentrations of NO_2 showing a clear upshift in the curves as the concentrations increase.¹⁵⁹ Reproduced from ref 159. Copyright 2015 American Chemical Society.

isotherm, confirming that molecular adsorption of NO_2 through active site binding, and that the charge transfer was the principal sensing mechanisms governing the response of the fabricated sensing devices.¹⁵⁹

In the same year, Cui et al. incorporated 2D layers of BP into the FET devices by using the “Scotch tape” mechanical exfoliation method (Figure 22a,b) and utilized the resulting

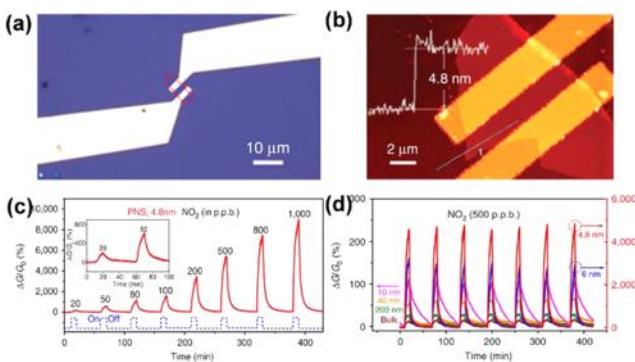


Figure 22. (a) Optical microscopy and (b) AFM images of the BP sensor device showing that the BP nanosheet electrically bridges the gold electrodes. (c) Dynamic response curves of relative conductance change versus time for NO_2 concentrations ranging from 20 to 1000 ppb (balanced in dry air) for BP nanosheet (thickness 4.8 nm). A drain-source voltage of 0.6 V was applied to the device. The dashed line demonstrates the “on/off” of NO_2 gas. The sensitivity here is defined as the differential response between $D_G/G_0 = 0$ in the air environment at the first cycle and the D_G/G_0 at the end of gas “off” for each concentration. (b) Thickness-dependent multi-cycle responses of the BP nanosheet sensor to 500 ppb. NO_2 .¹⁵⁸ Reproduced from ref 158. Copyright 2015 American Chemical Society.

device for the sensitive detection of NO_2 at a wide concentration range of 20–1000 ppb (Figure 22c).¹⁵⁸ The authors reported on the thickness dependent sensitivity of BP layers to targeted analyte, with an optimal thickness of 4.8 nm (Figure 22d).¹⁵⁸ DFT calculations showed that the change in sensitivity with respect to thickness was dictated by the band gap for thinner sheets (<10 nm) and by the change in the effective thickness on gas adsorption for thicker sheets (>10 nm). The authors also demonstrated that BP exhibited a significantly higher response to NO_2 over analytes such as CO, H_2 , and H_2S , suggesting that layered BP could be potentially used for the fabrication of selective gas sensors. Donarelli et al. expanded on device integration technology by fabricating chemiresistive devices through drop-casting chemically exfoliated BP sheets onto a Si_3N_4 substrate, pre-patterned with Pt comb-type interdigitated electrodes.¹⁶⁰ The resulting analytical devices displayed a p-type response to NO_2 and NH_3 , with LODs of 7 ppb and 1 ppm at room temperature, respectively, with minimal interference from CO or CO_2 . The authors suggested that the high edge-plane content as a function of BP morphology enhanced the sensitivity of this 2D material to targeted gaseous molecules.¹⁶⁰

Further improvements in sensing properties of BP to gaseous analytes were realized by means of surface functionalization through the incorporation of metal nanoparticles on the surface of BP. For example, Jung and co-workers enabled chemiresistive sensing of H_2 , which typically cannot be achieved using pristine BP, by incorporating either Au or Pt nanoparticles directly onto the surface of BP.⁵⁷¹ The fabricated devices based on BP-Pt NP could sense H_2 at a

concentration as low as 5 ppm at room temperature without significant degradation in the response over the 30 day testing period. The enhanced stability of BP to ambient conditions (oxygen and humidity) was attributed to the increase in effective blockage of the lone pair of electrons on the surface of BP by the NPs. Interestingly, the authors also observed that, through the incorporation of Au NP onto the 2D BP, the work function of this 2D material can be further modulated by the transfer of electrons from the Au, thus causing a change in response from p-type to n-type in the presence of oxidizing gases. This approach demonstrated a great potential for developing tunable BP-based gas sensors. Using first-principles calculations, Lei et al. also explored the effect of metal doping on the sensitivity of BP to CO.⁵⁷² The authors reported that the presence of incorporated Li, Na, K, Ca, Sr, Ba, and La-metals improved the adsorption energy of CO on the surface of BP. This effect was attributed to enhanced coupling between carbon monoxide and tested metals, indicating that these systems can be potentially employed in electrically-transduced gas sensing of CO.

BP-based materials have been increasingly used in the development of gas sensing technologies due to their intriguing electrical properties, such as tunable band gap, large electronic anisotropy, and high surface area. Although, BP possesses many attractive features for sensor development, its limited stability to oxygen and water remains the biggest challenge for practical applications. This issue can be partially addressed through the incorporation of nanoparticles, or by using protective coatings that would inhibit outside environmental influence.^{367,573} In addition, novel scalable and cost-effective chemical strategies that allow fabrication of BP with precisely controlled structure and composition need to be developed for further progress toward practical applications in gas sensing.^{574–576}

4.1.3. Transition Metal Dichalcogenides. 2D transition metal dichalcogenides have attracted attention in chemical gas sensing applications for their outstanding properties, including tunable band gap,^{577,578} large surface-to-volume ratio, and possibility of operating at room temperature, following the popularity of graphene and other carbon-based materials.⁵⁷⁹

4.1.3.1. NH_3 and N_xO_y . Zhang and co-workers demonstrated the first application of MoS_2 in gas sensing by integrating thin layers of mechanically exfoliated MoS_2 into a FET device.⁵⁸⁰ The resulting devices exhibited n-type doping behavior upon the exposure to NO with a detection limit of 0.8 ppm (Figure 23a,b). The authors also observed that single-layered MoS_2 produced a faster response (5 s) to NO than multilayer (2–4 layers) MoS_2 ; however, its analytical signal was largely unstable. Interestingly, the signal stability of the fabricated FET devices was improved by increasing the number of MoS_2 layers. Thickness-dependency of MoS_2 layers on the sensitivity to NO_2 was further investigated by Late et al.¹⁰¹ They demonstrated that 5-layer MoS_2 exhibited improved gas-sensing performances as compared to 2-layer MoS_2 for detection of NO_2 (100 ppm) and NH_3 (100 ppm; Figure 23c,d). First-principles calculations showed that the charge transfer mechanism and contact resistance between the MoS_2 layer and electrodes dictates the response of MoS_2 -based FET devices. A very slight increase in the adsorption with the increase in the number of MoS_2 layers was also found, which may explain the very small increase in sensitivity for five layers as compared to two layers.

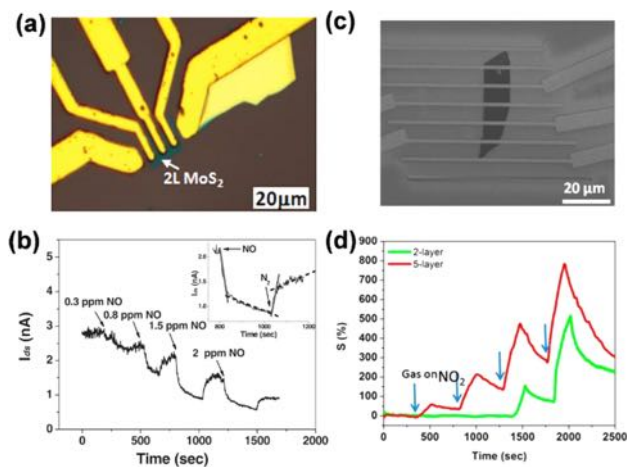


Figure 23. (a) Optical microscope image of an FET device based on the 2L MoS₂ film. (b) Real-time current response after exposure of the 2L MoS₂ FET to NO with increasing concentrations. Inset: A typical adsorption and desorption process of NO on the 2L MoS₂ FET.⁵⁸⁰ Reproduced with permission from ref 580. Copyright 2011 John Wiley and Sons. (c) SEM image of two-layer MoS₂ transistor device. (d) Comparative two- and five-layer MoS₂ cyclic sensing performances with NO₂ (for 100, 200, 500, and 1000 ppm).¹⁰¹ Reproduced from ref 101. Copyright 2013 American Chemical Society.

Duesburg and co-workers employed chemical vapor deposition to integrate MoS₂ layers directly onto interdigitated gold electrodes and used this device for the detection of ammonia gas.⁶⁵² The resulting device displayed high sensitivity to NH₃ at 300 ppb concentration with a theoretical LOD of 51 ppb. MoS₂ was also demonstrated to exhibit excellent sensing characteristics for O₂ detection.⁶⁵² Kim et al. reported a chemiresistive device with a broad linear response range to O₂ concentrations (1–100%) at 300 °C using liquid-exfoliated MoS₂ with a high abundance of edge sites.⁵⁸¹ First-principles calculations showed that the density of states in liquid-exfoliated MoS₂ was localized along the edges of the material resulting in the large presence of active sites for O₂ adsorption, thus being responsible for high sensitivity of the MoS₂-based device.

Numerous other chalcogenides including MoSe₂, MoTe₂, WS₂, and SnS₂ have demonstrated great potential in the development of functional devices for gas sensing applications. Bougouma and co-workers integrated a single layer of MoSe₂, obtained through mechanical exfoliation from bulk crystal, into a FET device for sensing of gaseous NH₃.⁵⁸² The authors reported on detection limits of 50 ppm for NH₃ with the response time of 2.5 min and recovery time of 9 min.⁵⁸² The sensing mechanism of the MoSe₂-based FET was proposed to occur through charge transfer between the adsorbed gas molecules and the 2D nanomaterial. Tuning the electrical

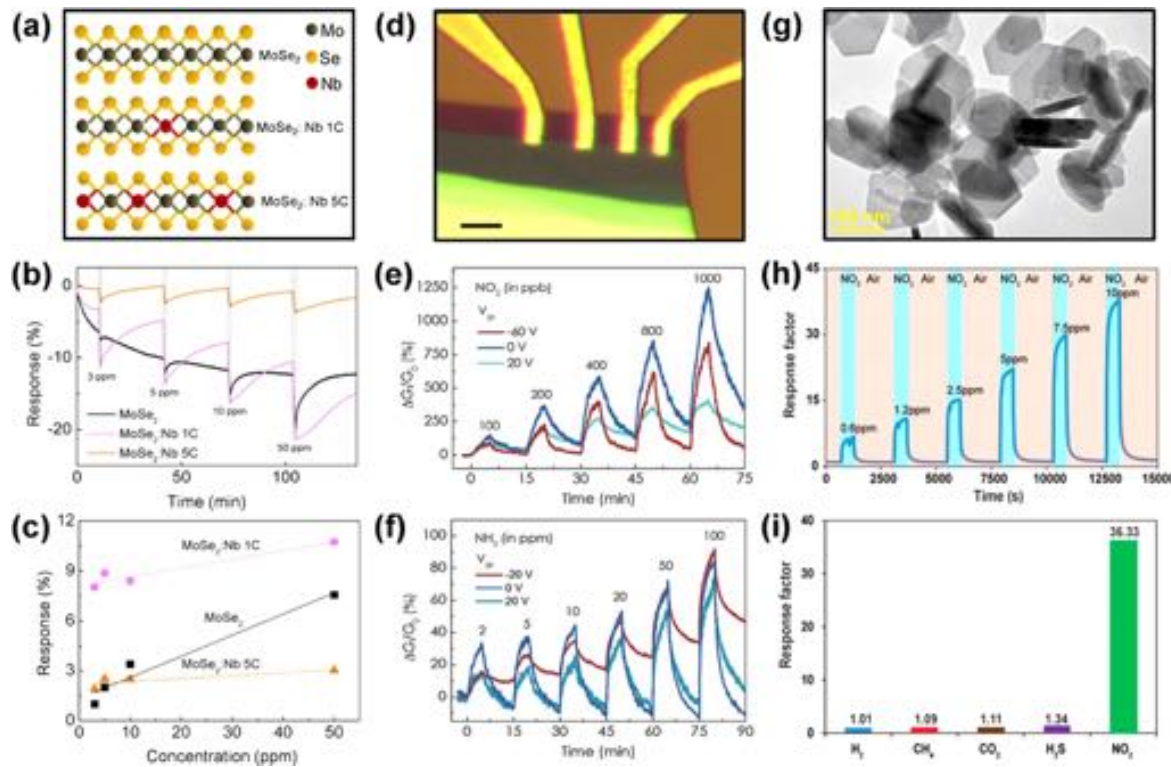


Figure 24. (a) Schematic atomic structures of MoSe₂ (top), MoSe₂:Nb 1C (middle), and MoSe₂:Nb 5C (bottom). (b) Transient gas response of the MoSe₂, MoSe₂:Nb 1C, and MoSe₂:Nb 5C devices at NO₂ concentrations ranging from 3 to 50 ppm. (c) Comparison of gas responses of the three devices as a function of the NO₂ gas concentration.⁵⁸⁴ Reproduced from ref 584. Copyright 2017 American Chemical Society. (d) Optical microscope image of the MoTe₂ FET on top of SiO₂/Si substrate with Ti/Au electrodes. Scale bar is 5 μ m. (e) Real-time conductance change of p-type MoTe₂ FET sensor upon exposure to different concentrations of NO₂ under different gate biases. (f) Real-time conductance change of n-type MoTe₂ FET sensor to different concentrations of NH₃ under different gate biases.⁵⁸⁷ Reproduced with permission from ref 587. Copyright 2016 IOP Publishing Ltd. (g) TEM image of 2D SnS₂ flakes. (h) Dynamic sensing performance of 2D SnS₂ flakes toward NO₂ gas at concentrations ranging from 0.6 to 10 ppm under the operation temperature of 120 °C. (i) Measured cross-talk of 2D SnS₂ flakes toward H₂ (1%), CH₄ (10%), CO₂ (10%), H₂S (56 ppm), and NO₂ (10 ppm).³⁹¹ Reproduced from ref 391. Copyright 2015 American Chemical Society.

properties of TMDCs through doping has been shown to be an effective strategy to increase sensitivity to gaseous analytes.⁵⁸³ Recently, Choi et al. investigated the effect of Nb doping of MoSe₂ on its gas sensing performance,⁵⁸⁴ in which Nb concentration could be precisely controlled by varying the number of Nb₂O₅ deposition cycles in the plasma enhanced atomic layer deposition process (Figure 24a). Addition of Nb along the grain boundaries can mediate a large number of dangling bonds and vacancies which are more vulnerable to the oxidation. Thus, by doping 2D layered MoSe₂ with Nb, a stable gas response as well as a long-term stability can be achieved.⁵⁸⁵ However, high Nb doping concentration deteriorated the response to NO₂ which might be attributed to a considerable increase in the number of metallic NbSe₂ regions that did not respond to gas molecules (Figure 24b,c).⁵⁸⁶ At relatively low Nb dopant concentrations, MoSe₂ showed enhanced device durability, as well as improved response to NO₂, attributed to both its small grains and stabilized grain boundaries.⁵⁸⁴ Higher molecular weight MoTe₂ materials have been also shown to exhibit high sensitivity to gaseous analytes. Zhang and co-workers fabricated FET devices by using MoTe₂ (Figure 24d). The device could detect NO₂ and NH₃ at concentrations of 100–1000 ppb and 2 ppm, respectively (Figure 24e,f).⁵⁸⁷ They found that the recovery kinetics after each sensing cycle can be effectively modulated by biasing the sensor at different gate voltages and can achieve more than 90% recovery within 10 min at room temperature under the optimum biasing potential.⁵⁸⁷

O'Brien et al. utilized plasma assisted synthesis to deposit nanolayers of WS₂ onto interdigitated electrodes for the detection of NH₃.⁵⁸⁸ They observed high sensitivity to NH₃ with the LOD of 1.4 ppm in N₂ at room temperature. Zhang and co-workers further explored the gas sensing properties of WS₂ to NH₃ using a chemiresistive electrode configuration.⁴⁷⁰ The resulting device displayed a p-type response to ammonia in the concentration range of 1–10 ppm with minimal interference from ethanol, methanol, formaldehyde, benzene, and acetone. This sensor also showed increased response at higher humidity levels due to sulfide ion-assisted hydroxylation process of adsorbed water molecules, and the oxidation of the solvated ammonia with adsorbed oxygen ions at the surface of the 2D WS₂. Ko et al. explored the utility of WS₂ in chemiresistive sensing of NO₂ and acetone.⁵⁸⁹ The pristine WS₂-based device exhibited high sensitivity to acetone, while minimal analytical response coupled with partial recovery was observed for 500 ppm of NO₂. Interestingly, incorporation of Ag NWs onto the surface of WS₂ resulted in a 12-fold improvement in sensitivity (667%) and recovery (>90%) to NO₂ due to the catalytic and n-type doping effect of Ag NWs.⁵⁸⁹

TMDCs, like MoS₂ and MoSe₂, showed good selectivity to NO₂, but suffered from slow recovery kinetics.¹⁰¹ Compared to TMDCs, SnS₂ has a larger electronegativity, potentially enhancing gas adsorption sites.⁵⁹⁰ Moreover, the electronic band structure of SnS₂ has relatively stronger temperature dependency. This feature can possibly enable the optimization of sensing response and be used for enhancing recovery kinetics at moderately elevated temperatures.⁵⁹¹ Ou et al. explored the sensing of NO₂ by incorporating 2D SnS₂ nanoflakes into chemiresistive device.³⁹¹ The planar 2D SnS₂ flake, synthesized via a facile wet chemical route (Figure 24g), both provided large active surface area and also facilitated gas accommodation into the van der Waals spacing due to small

SnS₂ interlayer binding energy. The hybrid sensor displayed good sensitivity to NO₂ at concentrations ranging from 0.6 to 10 ppm at 120 °C with a LOD of 30 ppb (Figure 24h). An excellent NO₂ selectivity was observed with respect to H₂, CH₄, CO₂, and H₂S (Figure 24i), which is uncommon for NO₂ gas sensors operating based on the charge-transfer mechanism. This unique selectivity was ascribed to the strong physical affinity of paramagnetic NO₂ gas molecules toward SnS₂ surfaces, as well as the relatively favorable position between the Fermi level of SnS₂ and partially occupied molecular orbitals of NO₂. This gas sensor also showed excellent recovery to the baseline in contrast to other 2D TMDCs, such as 2D MoS₂.^{580,101}

Although excellent sensing properties using 2D TMDCs in the context of chemical gas sensing have been realized, there are still numerous challenges that need to be addressed prior to their practical implementation in sensing technologies. First, novel synthetic approaches need to be developed to allow for controlled large-scale production of TMDCs.⁵⁷⁹ Second, the long-term stability of these 2D materials is often compromised by surface oxidation and moisture absorption.⁵⁹² This issue may be addressed by forming hybrid composite materials, e.g., through the incorporation of nanoparticles, or by using protective coatings that block the 2D material from ambient conditions.⁵⁷⁷ Third, the partial recovery of 2D TMDC-based gas sensors after exposure to certain analytes may pose challenges for practical applications. Thermally induced recovery may assist with answering this problem, but this process would compromise one of the biggest advantages of TMDC-based gas sensors, the ability to operate at room temperature. Therefore, new strategies that would ensure full system recovery during the analytical measurements are required to harness the full potential of 2D metal chalcogenides in sensing applications.

4.1.4. Metal Oxides. Metal oxide (MO) gas sensors constitute a well-established class of analytical devices that have revolutionized gas sensing applications since the 1960s.²¹⁸ Traditional materials, such as thick films or particles of SnO₂, ZnO, TiO₂, WO₃, In₂O₃, Fe₂O₃, or MoO₃, have shown excellent sensitivity for gas sensing at elevated temperatures.²¹⁸ Many commercial systems rely on MOs technologies to provide inexpensive reliable sensing of gaseous compounds.⁵⁹³ MOs materials operate at high temperatures because of the high activation energy required for the reaction between the surface-adsorbed oxygen and analyte.¹⁵² Room temperature sensing can be achieved through the strategic control over the structure and surface chemistry of MOs at the nanoscale.⁴¹³ Surface functionalization approaches with nanowires, nanotubes, and nanoparticles are effective methods for improving the sensing performance of MOs, not only with respect to working temperature, but also to enhance sensitivity and response time.¹²⁷

4.1.4.1. NO₂. The sensing of NO₂ has been realized by using various 2D MOs, including ZnO, NiO, and WO₃. Among these, ZnO, in the form of either nanosheet, nanowall, or nanoflake, has been mostly applied for gas detection due to its high sensitivity, stability, and low cost.⁵⁹⁴ In 2011, Chen et al. reported NO₂ detection using ZnO polygonal nanoflakes (thickness of 40–80 nm) synthesized by microwave hydrothermal method.⁵⁹⁵ The resulting ZnO sensor, with an optimal operating temperature of 175 °C, exhibited excellent selectivity to NO₂ at 0.5 ppm concentrations over other nine gaseous interferents fixed at 80 ppm. Because intrinsic defects of ZnO,

including oxygen vacancy and zinc interstitial sites, are involved in the mechanism of gas sensing, the gas sensing properties of ZnO nanoflakes were found to be independent of particle size, but greatly relied on the crystal defect structure in the material. In situ diffuse reflectance infrared Fourier transform spectroscopy technique indicated that nitrate and nitrite anions were the main adsorbed species on the surface of ZnO.⁵⁹⁵

The application of ZnO in the form of nanosheet or nanowall with smaller thickness than that of nanoflake can usually exhibit superior sensing performance, e.g., higher sensitivity, faster response/recovery, and lower operation temperature. Yu et al. showed the ability of ZnO nanowalls, deposited on an ITO glass substrate, to sense NO₂ in the concentration range of 1–50 ppm.⁵⁹⁶ The ZnO nanowalls with average thickness of ~20 nm exhibited good response toward 50 ppm of NO₂ ($S = 30$) at the operating temperature of 220 °C, together with fast response and recovery times of 30 and 48 s, respectively.⁵⁹⁶ Further study showed that ZnO annealing can significantly improve its sensing performance.⁵⁹⁷ The ZnO nanowalls annealed at 450 °C could be used for room-temperature detection of NO₂ with fast response and recovery time (23 and 11 s, respectively). The enhanced performance may be due to the presence of significant porosity and oxygen vacancies introduced into the nanowalls during annealing. Xiao et al. synthesized ZnO nanosheets with an average thickness of 20 nm and (100) exposed facets.⁵⁹⁸ The ZnO nanosheets could detect NO₂ in a range of 1–400 ppm at 180 °C. This ZnO nanosheet-based sensor showed fast response/recovery times (3 and 12 s to 10 ppm of NO₂, respectively) and excellent selectivity over 8 other interfering gases. The abundant oxygen vacancies on the (100) exposed surfaces were considered as the active sites for NO₂ adsorption, which were responsible for the high response. Au-decorated ZnO nanosheets⁵⁹⁹ and ZnO-polymer composites⁶⁰⁰ were also used for NO₂ sensing, giving rise to enhanced sensitivity compared to non-modified ZnO.

The aggregation of conventional nanosheet can lower its specific surface area and the number of activation sites.⁶⁰¹ The utilization of mesoporous metal oxide nanosheets not only reduces the synthesis expense, but also expands their potential applications in gas sensing. Hoa et al. reported on a facile synthesis of NiO sheets with large degree of mesoporosity from the hydrothermal treatment of NiCl₂ with NH₄OH followed by calcination at 300 °C (Figure 25a).⁶⁰² Sensors using the calcined NiO materials were able to detect NO₂ at 1 ppm with a response change of 13% (Figure 25b,c).⁶⁰² The fabricated sensor was selective to NO₂ over CO (0% response to 20 ppm of CO). The sensing mechanism was hypothesized to arise from the injection of holes into the p-type semiconductive NiO material as electronegative NO₂ reacts with the surface conduction band. The exposure to NO₂ reduced the resistance of the material, which is consistent with the proposed mechanism of sensing and material properties. In this study, gas sensing was performed at 250 °C, which is a lower temperature than typical MOs operating temperatures but is still far from room temperature. The operating temperature of NiO based NO₂ sensors was lowered by the construction of NiO/WO₃ heterogeneous nanoparticles. NiO is a p-type semiconductor, while WO₃ is an n-type semiconductor. Bao et al. combined the p- and n-type character of the NiO and WO₃, respectively, by synthesizing sheet-like heterogeneous nanoparticles from the thermal

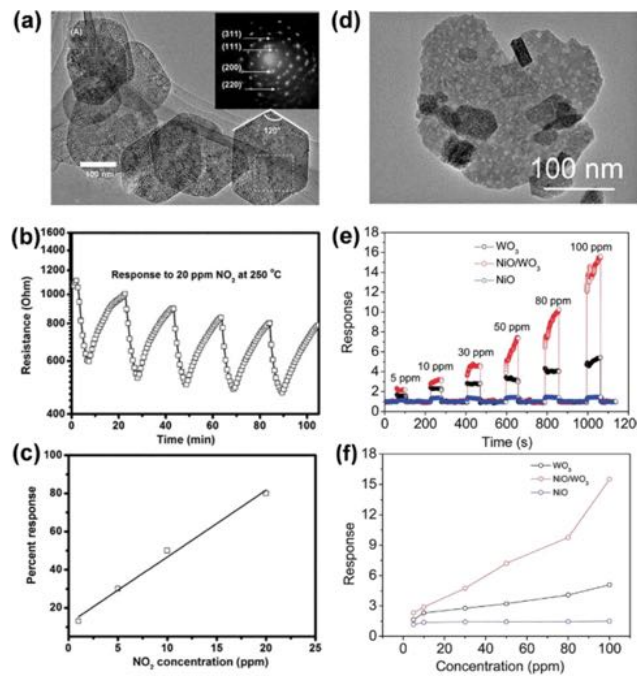


Figure 25. (a) TEM image of mesoporous NiO nanosheets that have irregular hexagonal shapes with average sizes of 250 nm. (b) The change in sensor resistance upon five-cycle exposure to 20 ppm of NO₂. (c) Sensor response as a function of NO₂ concentration.⁶⁰² Reproduced with permission from ref 602. Copyright 2011 John Wiley and Sons. (d) TEM image of NiO/WO₃ composites. (e) Sensing response of hybrid material NiO/WO₃ (red trace) and starting materials WO₃ (black trace) and NiO (blue trace) to NO₂ from 5 to 100 ppm. (f) Sensor response for all three materials as a function of concentration.⁶⁰³ Reproduced with permission from ref 603. Copyright 2014 Royal Society of Chemistry.

annealing on Ni(OH)₂ sheets and H₂WO₃ sheets (Figure 25d).⁶⁰³ The resulting materials showed an enhanced sensing response to NO₂ over WO₃ or NiO in their pristine states (Figure 25e,f). The materials were able to sense a range of toxic gaseous analytes at 30 ppm at room temperature. The authors observed that the fabricated device responded more strongly to NO₂ than to other analytes, suggesting that this composite material could be used for a selective detection of NO₂. Overall, the device exhibited p-type sensing behavior, probably due to the high molar ratio of NiO:WO₃ (2.7:1).⁶⁰³

4.1.4.2. NH₃. Liu and co-workers demonstrated that porous ZnO, prepared by annealing ZnS(ethylenediamine)_{0.5} precursor, can be used for indoor detection of NH₃.⁶⁰⁴ The authors reported on high sensitivity to the targeted gas in the concentration range of 50–500 ppm, at 250 °C and 30% RH with excellent retention of sensitivity after 3 months of operation.⁶⁰⁴ Nguyen et al. integrated ZnO-WO₃ nanocomposite, synthesized from hydrothermal treatment, into gas sensing devices for the detection of NH₃.⁶⁰⁵ The fabricated device exhibited n-type response to varying concentrations of NH₃ in the 25 ppm to 300 ppm range at operating temperature of 300 °C with good selectivity over ethanol and liquid petroleum gas. The high sensitivity to NH₃ gas was attributed to the large exposed surface area of ZnO-WO₃ material and the existence of the hetero-junctions between the WO₃ and ZnO in the composite.

Yang and co-workers further enhanced sensitivity to NH₃ by incorporating ZnO-PPy hybrid material into chemiresistor

device architecture.⁶⁰⁶ This nanocomposite showed high sensitivity to NH₃ with relative resistance change of ~20% toward 0.5 ppm of the gas analyte, wide response range of 0.5–200 ppm, and high selectivity over 9 other gaseous interferents (e.g., methanol, acetone, ether, hexane, tetrahydrofuran, ethanol, propylamine, butylamine, and diethylamine). The formation of p/n junction between p-type PPy and n-type ZnO was suggested to be responsible for the improved sensing performance to NH₃ of the fabricated device.⁶⁰⁶ Sensitive detection of NH₃ could be also achieved by using NiO-based materials. For example, Wang et al. used hydrothermal synthesis coupled with high temperature oxidation method to fabricate porous NiO films composed of small particles with diameters ranging from 8 to 30 nm.⁶⁰⁷ The resulting gas sensor exhibited 18% conductance change to 30 ppm of NH₃ with response time of 27 s and high selectivity toward ammonia over other organic gases, such as chloroform, dichloromethane, ethyl acetate, formaldehyde, heptane, iso-propanol, and toluene at room temperature. Zhang and co-workers integrated NiO-TiO₂ composite into a chemiresistive gas sensing device, which could detect ammonia in 10 to 100 ppm concentration range at room temperature under UV illumination.⁶⁰⁸ The prepared sensor also showed minimal response to VOCs including ethanol, methanol, formaldehyde, and acetone. High selectivity to ammonia was attributed to the formation of the p-n heterojunction, which led to the cancelation of the opposite responses of n-type TiO₂ and p-type NiO materials to tested reducing gases.

4.1.4.3. H₂S. Detection of H₂S has been accomplished with a number of MOs systems and traditional thick-films of bulk materials. Recent advancements using nanoscale materials, have led to significant improvement in sensing performance of gas sensors for H₂S detection. In 2010, Zhang and co-workers used CuO nanosheets to detect H₂S in the concentration range of 2 ppb to 1.2 ppm.⁶⁰⁹ The nanosheets were synthesized via a facile surfactant-free method. The response and recovery times were 6 and 9 s, respectively, at an operating temperature of 240 °C.⁶⁰⁹ Li and co-workers also integrated sheets of CuO with thickness of 62.5 nm, prepared using a facile hydrothermal synthesis, into H₂S gas sensing devices.⁶¹⁰ The resulting sensors responded to H₂S in the concentration range of 10 ppb to 60 ppm at room temperature and demonstrated high selectivity to targeted analyte at 0.2 ppm over SO₂, NO, NO₂, H₂, CO, ethanol, and NH₃ gases at 40 ppm.⁶¹⁰ In addition, CuO nanosheets exhibited good long-term stability with only <5% deviation in response after testing the sensor performance for 1 month at 200 ppb of H₂S. The high sensitivity of CuO-based sensor to H₂S was attributed to the large abundance of nanopores in the nanosheet of the 2D material, which favored adsorption and desorption of the gas on its surface. Huo and co-workers further improved the sensitivity to H₂S by using hierarchically structured, porous nanowall NiO arrays grown by hydrothermal reaction and subsequent calcination onto ceramic tubes with pre-patterned Au electrodes.⁶¹¹ The authors could detect H₂S in the range of 1 ppb to 100 ppm at 92 °C with high selectivity over triethylamine, formaldehyde, chlorobenzene, acetone, ethanol, carbon monoxide, and ammonia. The excellent sensing performance of the fabricated gas sensors was attributed to the porous structure of the NiO material with a large specific exposed surface area, which promotes adsorption/desorption of H₂S gas molecules onto/from its surface, as well as improves electron transfer.

WO₃ in the form of nanosheets, formed by solvothermal synthesis, was recently utilized for the detection of H₂S by Gardner and co-workers.⁶¹² The response of the fabricated device to H₂S was measured from 100 ppb to 5 ppm with normalized responses of 1.4% and 3.9%, respectively. The same sensor also displayed high cross reactivity with humidity (25% RH) at 350 °C.⁶¹² MoO₃ nanobelts were used to sense H₂S by depositing a mat of fibers described as “nanopaper” across interdigitated electrodes (Figure 26a). The resulting device

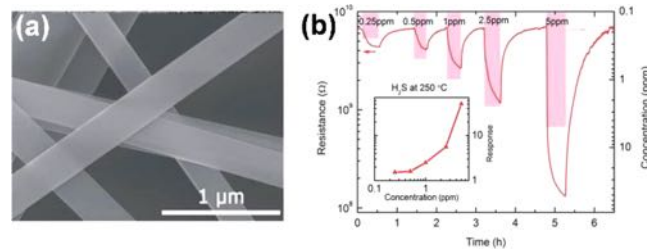


Figure 26. (a) SEM images of the MoO₃-nanopaper. (b) Response-recovery curves of the MoO₃-nanopaper sensor to different H₂S concentrations at 250 °C. The insets show the response of the sensor to various gas concentrations.⁶¹³ Reproduced with permission from ref 613. Copyright 2017 Royal Society of Chemistry.

was used to detect 250 ppb H₂S at an operating temperature of 250 °C (Figure 26b).⁶¹³ Hu et al. reported on ultra-fast detection time at sub-ppm concentrations of H₂S by integrating MO₃-WO₃ composite, synthesized by stirring WO₃ nanosheets with definite amounts of ammonium heptamolybdate tetrahydrate in H₂O followed by calcination at 500 °C, into a gas sensor. The resulting chemiresistor was capable of detecting 20 ppb H₂S with a response time of 2 s and a recovery time of 5 s at 250 °C.⁶¹⁴ The excellent gas sensing performance of the MO₃-WO₃ samples might be ascribed to the heterojunction structure in which a thicker electron depletion layer forms at the interface between MoO₃ and WO₃, resulting in larger resistance change compared to the pure WO₃.

4.1.4.4. Other Gases. 2D metal oxides have also been applied in the sensing of other gaseous analytes, such as CO, H₂, CH₄, and more, most of which are reducing gases. Lee and co-workers reported on the highly sensitive and fast responding CO sensor fabricated from a sheet-like SnO₂.⁶¹⁵ The response of 2D SnO₂ nanosheets to 10 ppm of CO was 2.34, with a response time of 6 s, which is significantly improved over the SnO₂ bulk powder (1.57 and 88 s, respectively). The realization of both high sensitivity and fast response was explained in terms of rapid gas diffusion over the entire sensing surface and the very thin structure of SnO₂ nanosheets. Jones and Maffei's experimentally tested a mathematical model of the reactions on the surface of a ZnO nanosheet-based CO sensor.⁶¹⁶ The sheets, with thicknesses of 20–100 nm, were exploited to investigate the response to different CO concentrations ranging from 50 to 200 ppm at different operating temperatures (393 to 484 °C). The measured responses of this system were well described by the theoretical model, where the CO reacts only with the surface oxygen species via an Eley–Rideal mechanism.⁶¹⁶ Nanostructures with the high surface area and surface accessibility can improve the gas-sensing properties. Zeng et al. prepared a sensor based on hierarchically porous ZnO nanosheet thin films, vertically grown on a silicon substrate,

which could sense CO in the range of 5 ppm to 500 ppm with excellent sensitivity ($S = 11.2$ at 100 ppm of CO) and short response/recovery times (25 and 36 s, respectively) at 300 °C.⁶¹⁷ The same device also exhibited good selectivity against typical interfering gases such as SO₂, NO₂, NH₃, H₂, and VOCs.⁶¹⁷ The less agglomerated and porous network of the ZnO structure, in addition to providing a high surface area, favored rapid access to the surface and effective diffusion of CO molecules.⁶¹⁷ Chang et al. investigated the CO sensing performance of ZnO nanowalls with (001) exposed crystal planes, vertically grown on a glass substrate, which could detect CO in a range 100 to 5000 ppm with a response of 0.3 s to 100 ppm of CO at 300 °C.⁶¹⁸

Chen et al. investigated the H₂ and CH₄ sensing performance of ZnO-based gas sensor consisting of interconnected ZnO nanowalls of 1.3 μm in length and approximately 60 nm in thickness, grown along the *c* axis.^{619,620} The resulting sensor showed good response to 100–3000 ppm of both gases at 300 °C, but higher sensitivity was observed for methane. The good sensitivity and short response/recovery times were attributed to the presence of ZnO nanowalls with large surface-to-volume ratio that favored the effective and fast adsorption/desorption of gas molecules. H₂ sensing was also realized by 2D layered MoO₃ by Alsaif et al.⁶²¹ and Gu and co-workers.⁶²² Notably, [001]-oriented α-MoO₃ nanoribbons exhibited a room-temperature response to H₂ with high sensitivity at concentrations as low as 500 ppb and good selectivity against CO, ethanol, and acetone. The impressive analytical performance of these devices was attributed to the 2D flake-like structure of MoO₃.^{621,622}

The development of thin MOs materials allows the fabrication of sensors capable of detecting a range of toxic gaseous compounds. Although somewhat limited by the necessity of operating at high temperatures, MOs sensors display excellent response/recovery times, robustness over time in terms of sensor reversibility, and the ease of synthesis. Further advancements in the field of MOs sensors will be focused on: the development of materials with low operating temperature, diversifying the range of applicable analytes, the exploration of the properties imbued by nanostructured confinement, and the ability of those properties to enhance sensing behaviors of these materials.

4.1.5. Metal–Organic Frameworks. Benefiting from a set of unique properties, such as large surface-to-volume ratio, synthetic accessibility through bottom-up strategies, tunable band gap, and large electrical modularity that enables integration of highly tailored host–guest interactions into the porous scaffold, 2D conductive MOFs hold remarkable promise in gas sensing applications.^{88,89,421} The first demonstration of chemical gas detection using 2D conductive MOFs was reported by Dincă and co-workers in 2015.⁴¹⁸ The authors used a drop-casting method to integrate the Cu₃HITP₂ MOF within a chemiresistive device architecture to achieve the detection of NH₃ gas at sub-ppm concentrations (0.5 ppm) at room temperature (Figure 27a,b). Sensing performance of the resulting devices was also unaltered in the presence of high levels of humidity (<60%; Figure 27c). Interestingly, under the same experimental conditions, the isostructural Ni₃HITP₂ MOF did not produce a measurable response during the exposure to NH₃, indicating metal-induced selectivity in chemiresistive sensing with MOF-based devices.⁴¹⁸

Our group developed a unique approach that merged synthesis and device integration of MOFs into a one-step

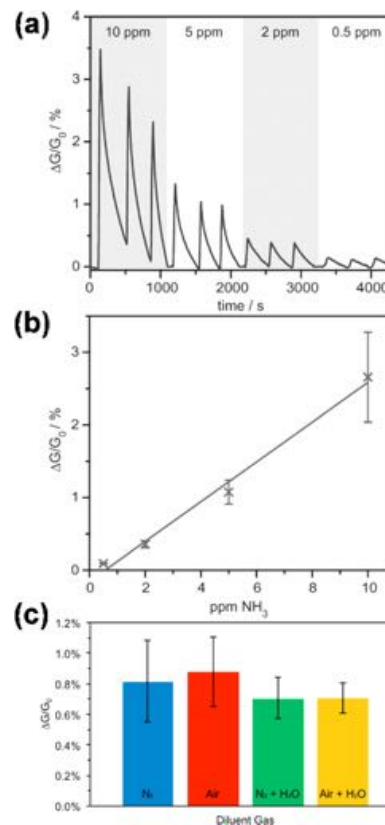


Figure 27. (a) Relative responses of a Cu₃HITP₂ device to 0.5, 2, 5, and 10 ppm ammonia diluted with nitrogen gas. (b) Device response as a function of ammonia concentration. (c) Comparison of responses of Cu₃HITP₂ devices to a 5 ppm ammonia under various oxygen and relative humidity levels.⁴¹⁸ Reproduced with permission from ref 418. Copyright 2015 John Wiley and Sons.

process.⁶²³ Using solvothermal synthesis, we integrated 2D conductive M₃HHTP₂ MOFs (M = Ni and Cu) into polymeric device platforms with pre-patterned graphitic electrodes (Figure 28a).⁶²³ The fabricated devices were capable of detecting and discriminating between NH₃, NO, and H₂S gases at ppm concentrations (10–80 ppm; Figure 28b). Our group also fabricated flexible NO and H₂S gas sensors through the direct solution self-assembly of Ni₃HHTP₂ and Ni₃HITP₂ MOFs on cotton-based substrates (Figure 28c).⁶²⁴ The resulting sensors were simultaneously capable of detecting and filtering NO and H₂S with sub-ppm limits of detection (NO = 0.16 ppm and for H₂S = 0.23 ppm; Figure 28d). The chemiresistive response was largely unaltered by the presence of humidity (18% RH) and was fully recoverable by washing the devices in water. Another contribution by our group has also involved the fabrication of chemiresistive sensing arrays comprising of M₃HHTP₂ MOFs/graphite blends (M = Fe, Co, Cu, and Ni) by mechanical abrasion using a compressed MOF powder.¹⁷⁶ The formation of graphite/MOF composites was required to establish good electrical contact within the fabricated chemiresistive devices and enabled direct integration of only moderately conductive MOFs that were otherwise difficult to integrate into electrically-transduced sensors. The fabricated gas sensing devices could detect and differentiate between NH₃, NO, and H₂S at 80 ppm.

A significant advancement in gas sensing using 2D conductive MOFs was recently demonstrated by Xu and co-workers.¹⁷³ The authors utilized layer-by-layer liquid-phase

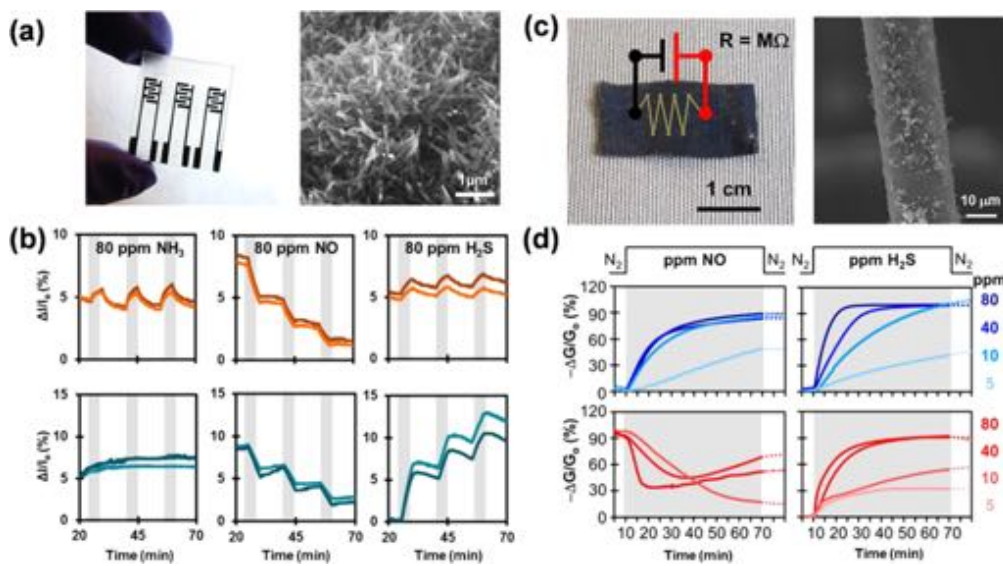


Figure 28. (a) Photograph showing the process of drawing electrodes on a shrinkable polymeric film with a commercial HB pencil (left). SEM images of MOF films incorporated into devices (right). (b) Representative sensing traces (3×80 ppm) for Cu_3HHTP_2 (upper row) and Ni_3HHTP_2 (lower row).⁶²³ Reproduced from ref 623. Copyright 2016 American Chemical Society. (c) Conductive SOFT devices: textiles coated with nanoporous MOF (left). SEM image of MOF coating on fibers (right). (d) Representative response for Ni_3HHTP_2 (blue) and Ni_3HHTP_2 (red) SOFT-sensors when exposed to (from left to right) NO or H_2S .⁶²⁴ Reproduced from ref 624. Copyright 2017 American Chemical Society.

epitaxial growth method to install epitaxially-oriented thin-films of Cu_3HHTP_2 MOF into the chemiresistive devices.¹⁷³ The resulting sensors exhibited detection limits of 0.5 ppm to NH_3 gas and minimal interference from 10 other reducing gases (benzene, H_2 , toluene, acetone, ethanol, methanol, methane, n-hexane, CO, and ethylbenzene). In addition, the response and recovery time was up to 54% faster than observed for bulk powder counterparts.¹⁷³ This observation was attributed to enhanced contact of gaseous analytes with the active sites in the MOF with minimal diffusion barriers.¹⁷³

Recently, Rubio-Giménez et al. combined experimental data with computational modeling to describe a possible origin for the underlying mechanism of chemiresistive response for NH_3 in ultrathin films (~ 30 nm) of Cu_3HHTP_2 .¹⁷⁵ The results indicate that the chemiresistive response of this family of conductive MOFs is linked to the direct interaction of gas molecules with the Cu(II) inorganic linker. This interaction was proposed to result in slight distortions of the internal structure of the layer or changes in the coordination geometry of the metal node, subsequently leading the modifications of the band gap of the material. These demonstrations are consistent with previous reports,^{173,174,418} which suggest a possible relationship between the nature of the metal nodes and the coordination ability of the analytes with the intensity and selectivity of the “turn-on” response.

Despite many improvements and great promise in the applications of 2D conductive MOFs in gas sensing technologies, many challenges need to be addressed prior to their practical implementation in sensing. First, the host–guest interactions between 2D MOFs and targeted analytes are not yet well understood¹⁷⁵ and require more rigorous computational modeling and experimental investigation. Second, the preparation of ultrathin 2D MOF nanostructures with desired structural characteristics in a highly controllable manner remains a key challenge. Third, the influence of structural and compositional defects on electronic properties of MOFs must be studied to fully understand the nature of host–guest

interactions that dictate the sensing performance of MOF-based devices. Fourth, the stability of 2D conductive MOFs in ambient conditions has not been fully investigated and remains a critical issue for the practical use in sensing applications. Improvements in stability and robustness of 2D MOFs may be realized through strategic modifications of the bond strength of metal–ligand structural units. Nonetheless, the potential of 2D conductive MOFs in gas sensing lies in the vast modularity of the building blocks that enable the incorporation of host–guest interactions directly into the basal plane of the 2D material.

4.1.6. Other 2D Materials. MXenes have only recently been explored as a novel class of 2D materials with remarkable possibilities for compositional variations and property tuning in the development of gas sensing technologies. Lee et al. integrated the 2D $\text{Ti}_3\text{C}_2\text{T}_x$ (T_x represents functional group, which can be O^{2-} , OH^- , or F^-) sheets synthesized through the removal of Al atoms from Ti_3AlC_2 onto flexible polyimide platforms to fabricate gas sensing devices.²⁰³ The $\text{Ti}_3\text{C}_2\text{T}_x$ -based sensor, operating at room temperature, exhibited a p-type sensing behavior to gaseous analytes (ammonia, ethanol, methanol, and acetone) with the highest sensitivity observed for NH_3 at 100 ppm concentrations. The high sensing performance of the fabricated device was attributed to the effective adsorption of NH_3 onto the surface of the $\text{Ti}_3\text{C}_2\text{T}_x$ facilitated by the analyte interactions with surface functional groups and defects.²⁰³ Jung and co-workers through chemiresistive gas sensing measurements further confirmed high sensitivity of $\text{Ti}_3\text{C}_2\text{T}_x$ MXene to NH_3 .⁶²⁵ The authors reported on the high selectivity of the fabricated sensor to hydrogen bonding gases such as NH_3 , ethanol, or acetone with minimal interference from acidic gases (e.g., SO_2 , NO_2 , or CO_2). The same sensor could detect NH_3 in a wide range of concentrations from 50 to 1000 ppb with the LOD of 0.13 ppb at room temperature. Noise power spectral density measurements and density functional calculations showed that the metallic conductivity of the core channels in the

$Ti_3C_2T_x$ together with the strong adsorption energy of the surface functional groups and defects, are responsible for the good sensing properties of the fabricated sensors. Recently, plane wave-based DFT calculations explored the selectivity and reactivity of M_2C MXenes ($M = Ti, V, Nb, Mo$) and their oxygen-functionalized counterparts (M_2CO_2) to 11 gaseous analytes including H_2 , H_2O , H_2S , NH_3 , CO , CO_2 , SO_2 , NO , NO_2 , NH_3 , and N_2 .³³³ The authors observed that the selectivity of MXenes to gases such as NO or NH_3 was improved upon oxygen surface functionalization.

An ever-expanding range of 2D conductive materials continues to be explored by ab initio calculations for their ability to selectively interact with gaseous analytes in sensing applications. Prominent examples include 2D borophene,⁶²⁶ GaN,⁶²⁷ and C_2N .⁶²⁸ Experimental demonstration of C-rich nitrides as gas sensors were first reported in 2014 by Wang et al.⁶²⁹ The $g\text{-}C_3N_4$ prepared by a two-step thermal treatment of glucose and urea exhibited porous structure and high abundance of pyridine N atoms with good binding affinity for NO_2 . The fabricated $g\text{-}C_3N_4$ chemiresistive sensor was able to sense NO_2 at 140 ppb under ambient conditions (65% RH). The sensitivity of $g\text{-}C_3N_4$ to NO_2 was further enhanced (LOD of 60 ppb) by the surface functionalization with Au nanoparticles.⁶³⁰ The improvement in sensing performance after doping with AuNP was attributed to the increased interface area for gas absorption, as well as the formation of Schottky-type junctions, whose potential barrier may be modulated by analyte-material interactions. The synthesis of $g\text{-}C_3N_4$ composites is another strategy to enhance sensing performance of gas sensing devices.⁶³¹ For example, Long and co-workers fabricated an impedance semiconductor gas sensor based on Pt-ZnO- $g\text{-}C_3N_4$ hybrid materials for detection of NO_2 with sub-ppm sensitivity (LOD of 0.072 ppm).⁶³² This good sensing response to NO_2 was attributed to the synergistic effects between the 2D materials, ZnO and Pt, which together improved the separation of electron-hole pairs in the material leading to enhanced charge transport properties.

Using surface functionalization of $g\text{-}C_3N_4$ with Pd NPs, Raghu et al. were able to detect H_2 at 4% levels (99.8% sensitivity) with the response time of 88 s at 30 °C.⁶³³ $h\text{-}BN$ based materials have been also recently utilized in electrically-transduced detection of gaseous analytes including CH_4 , NH_3 , and NO_2 .^{634,635} For example, Sajjad and Feng demonstrated that atomically thin nanosheets of $h\text{-}BN$ synthesized using CO_2 -pulsed laser deposition methods were capable of reversible detection of CH_4 gas at operating temperature of 175 °C.⁶³⁴ Wang and co-workers tested the gas-sensing properties of the ultra-thin $h\text{-}BN$ nanosheets toward NH_3 and found that the fabricated gas sensors showed a fast response and excellent repeatability to ethanol at optimal operating temperature of 300 °C.⁶³⁵

Ayari et al. fabricated AlGaN/GaN gas sensors on the 2D nanolayer of $h\text{-}BN$. The existence of $h\text{-}BN$ layer allowed the transfer of the devices to a flexible and heat insulating acrylic tape,⁶³⁶ which resulted in a modification of relevant device properties, leading to a doubling of the sensitivity to 100 ppm of NO_2 gas at 30 °C and an average response time of 5 min, 6 times faster than before transfer. Besides using single 2D materials, different types of 2D materials can be stacked together and held by van der Waals forces, creating an artificial van der Waals hetero-structure despite lattice mismatches. The van der Waals hetero-structures have an abrupt transition between the two materials and a sharp gradient of carrier

concentration across the interface. Furthermore, owing to their nanoscale thickness, the carrier concentration and band alignment inside the hetero-structure can be very effectively modulated by electrical means, which provides possibilities for a large array of novel devices and applications.^{637,638}

Jiao and co-workers synthesized a fiber-like rGO-MoS₂ composite, where graphene provides a substrate for nucleation of MoS₂.⁶³⁹ Compared to traditional film or sheet-type devices, the fiber form of devices is more advantageous for their lower weight, flexibility, and compactness in practical applications.⁶⁴⁰

In the composite, MoS₂ nanosheets can be anchored onto the surface of graphene through both physical adsorption and electron transfer by hydrothermal method. The obtained composite fiber devices showed an excellent sensitivity and selectivity to NO_2 and NH_3 than the individual components under different light illumination. The LOD of rGO-MoS₂ (3:1) to NO_2 was 53 ppb, which was comparable with or lower than the high-performance NO_2 sensors based on the rGO-Cu₂O NWs conjugates (64 ppb).⁵⁰⁷ Recently, Zhou et al. prepared rGO/MoS₂ composite films for NO_2 sensing at low temperature with a LOD as low as 5.6 ppb.⁶⁴¹ The experimental results revealed a significant improvement in response (~200% enhancement) for rGO/MoS₂ composite film, as compared to pure rGO, together with a high selectivity over NH_3 , H_2S , CO , and HCHO.

The similarity in 2D structures, as well as the complementary properties between $g\text{-}C_3N_4$ and graphene, can result a synergetic effect in sensing performance when the two components are composited as a gas sensor material. A $g\text{-}C_3N_4\text{-Gr}$ nanocomposite prepared by Zheng et al. was demonstrated to be a promising sensing material for detecting NO_2 gas at room temperature, which exhibited better recovery as well as two-times faster response compared to pure graphene sensor.⁶³¹

Zhang and co-workers demonstrated a BP/MoSe₂ van der Waals hetero-junction chemical sensor with excellent sensing performance for NO_2 detection.⁶⁴² The hetero-junction was created by stacking multi-layered BP on top of the MoSe₂ flake (Figure 29a,b). The response of the hetero-junction for NO_2 was 4.4 and 46 times higher than those of the MoSe₂ and BP FETs at 200 ppb concentration, respectively. The device also exhibited ultra-low detection limit of 10 ppb for NO_2 , which was 6 times and 20 times lower than the MoSe₂ and BP FET sensors built on the same chip, respectively (Figure 29c-f). The modulation of barrier height in MoSe₂, which is induced by the modulation of both the total built-in potential and the ratio between majority carrier concentrations of both materials, was believed to be responsible for the enhanced sensitivity. This novel configuration provides a new platform for a variety of sensing applications.

Despite the rapid progress, the sensing application of MXenes, $g\text{-}C_3N_4$, or $h\text{-}BN$ nanostructures is only at the beginning and faces ample challenges. The fabrication of uniform 2D films with controlled structure and composition, at industrially relevant scale, remains a big challenge.¹¹⁴ Novel synthetic approaches, that are ideally compatible with current sensor manufacturing technologies are needed to fully harness the potential of these 2D materials in gas sensing applications.¹¹⁷ The gas sensing performance of MXenes, $g\text{-}C_3N_4$, or $h\text{-}BN$ -based materials was also demonstrated to be strongly dependent on their surface chemistry (e.g., presence of compositional and structural defects). Therefore, the role of defects on the sensing parameters of these 2D materials needs

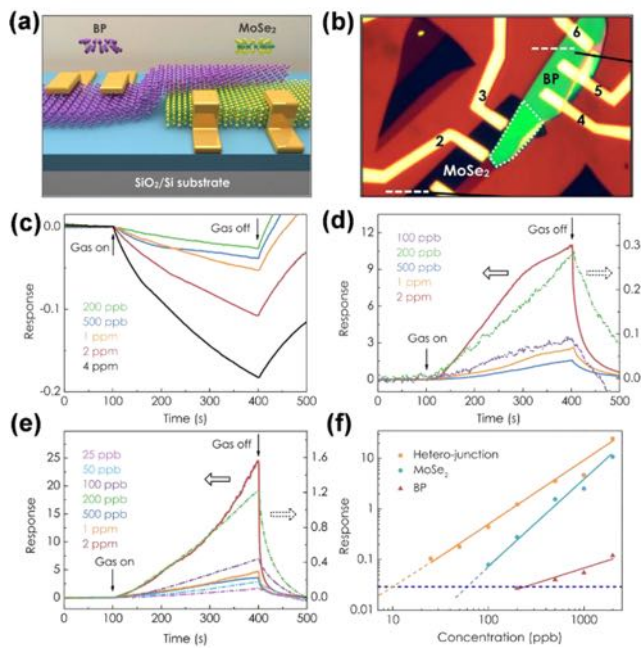


Figure 29. (a) Schematic illustration of the BP/MoSe₂ heterojunction device. (b) Optical microscope image of the device. Real-time response of BP FET (c), MoSe₂ FET (d) and hetero-junction (e) sensors to different concentrations of NO₂. (f) Response of all three sensors as a function of gas concentration in logarithm scale.⁶⁴² Reproduced with permission from ref 642. Copyright 2016 IOP Publishing Ltd.

to be further investigated, which will ideally lead to improvements in sensitivity and selectivity through careful ligand functionalization or defect engineering. In addition, the landscape for creating nanocomposite materials is rich in potential, with numerous possibilities to benefit from the unique chemical, electrical, and physical properties of each component and yet to be explored for gas sensing applications. Most of the reported gas sensors based on MXenes, *g*-C₃N₄, or *h*-BN have been investigated in proof-of-concept studies, and only few sensors have been utilized for sample detection in complex environments. It is, therefore, critical to construct robust sensing interfaces with low nonspecific adsorption to satisfy the requirements for sensitive and selective determination of analytes in practical applications.

4.2. Detection of Volatile Compounds

Volatile compounds include organic and inorganic compounds that are easily vaporized but exist as solids or liquids under standard temperature and pressure. Volatile inorganic compounds mainly include water, volatile acids, halogen streams and mercury streams. Among these, humidity sensing is especially important. Because humidity has a great influence on people's lives including physiological activities, climate, building constructions, storage facilities for medicines and foods, electronic devices, chemical refineries, corrosion, and degradation of instruments.⁶⁶⁸ Humidity sensors with high sensitivity, selectivity, repeatability, long-term stability under ambient conditions, corrosion resistance to pollutants, and low cost of manufacturing are in great demand.

Detection and monitoring the concentration of volatile organic compounds (VOCs) is important in environmental protection, chemical process control, and personal safety.⁶⁶⁹ VOCs are composed of a variety of chemicals, examples

including gasoline, alcohols, formaldehyde, aromatic solvents such as benzene, toluene and xylene, styrene, and perchloroethylene. Long-term exposure to VOCs can cause damage to the liver, kidneys, and central nervous system.⁶⁷⁰ Short-term exposure can cause eye and respiratory tract irritation, headaches, dizziness, visual disorders, fatigue, loss of coordination, allergic skin reactions, nausea, and memory impairment.⁶⁷⁰ VOCs also constitute an important fraction of gaseous pollutants over urbanized areas, which originate from exhaust gases, evaporation of petroleum products and utilization of organic solvents. The World Health Organization (WHO) recognized VOCs as the most important pollutants of indoor air.⁶⁷¹ For these reasons, the concentrations of VOCs both indoors and outdoors are strictly regulated. Taking formaldehyde as an example, which is one of the VOCs widely used in household materials, the WHO has set a 30 min exposure limit of 0.08 ppm, and the U.S. National Institute for Occupational Safety and Health (NIOSH) has established a maximum long-term exposure limit of 0.016 ppm (TWA).⁶⁷² This section highlights the sensing of volatile compounds using different types of sensory materials.

4.2.1. Graphene and Graphene Oxides. **4.2.1.1. Humidity.** At relatively low concentration, the adsorption of water molecules can break the sublattice and symmetry of graphene and successively widen its band gap.⁶⁷³ The functional groups on graphene and graphene oxide, like defects, hydroxyl, and carbonyl groups, can interact with water, causing a conductance change.^{674,675} These water molecules usually act as an electron donor, leading to an increase in the resistance of p-type graphene material. Water molecules can also induce the ionization of the oxygen-containing groups (for example, -OH and -COOH) in GO bulk material to generate a concentration gradient of protons. This gradient facilitates the diffusion of protons through the material to deliver a voltage and current in the external circuit.⁶⁷⁶ In addition, graphene oxide has high permeability to water molecules, which can lead to sensing devices with fast response time.⁶⁷⁷ Together with their flexibility and suitability for large-scale manufacturing, graphene-based materials have emerged as key elements for fabricating humidity sensors.

Borini et al. developed a chemiresistive humidity sensor by using GO as the active material.⁶⁷⁸ Ultra-thin (15–25 nm) GO films were deposited by either drop-casting or spray coating on silver screen-printed interdigitated electrodes on a polyethylene naphthalate (PEN) substrate (Figure 30a). The effect of water molecules on the electrical properties of GO films was investigated by impedance measurements. The response and recovery times were less than 100 ms (Figure 30b). The sensing performance of the GO sensor was comparable to the commercial sensors (Figure 30c) and allowed to observe the change of moisture content in breath (Figure 30d).

Sun and co-workers fabricated a microscale capacitive humidity sensor by using graphene oxide films as sensing material.⁶⁷⁹ Compared with conventional capacitive humidity sensors with sensitivities ranging from 43% to 2900%,^{680–684} this GO-based sensor exhibited sensitivity of up to 37 800%, which was more than 10 times higher than that of the best sensor among conventional sensing devices at 15%–95% relative humidity. This humidity sensor also showed a faster response time and recovery time (10.5 and 41.0 s, respectively), which are less than 25% and 50% of those observed for conventional devices. To overcome mechanical stability issues of the fabricated sensors, including swelling of

Table 3. Summary of Sensing Performances for Gases by 2D Materials^a

analyte	material	architecture	LOD	experimental range	sensing environment	ref
Cl ₂	rGO	chemiresistor: Au/rGO/Au	N/A	6–75 ppm	air, r.t.	502
Cl ₂	rGO–PET	chemiresistor: rGO/rGO–PET/rGO	6 ppm	6–75 ppm	air, r.t.	502
CO	Gr	chemiresistor: Au–Ti/Gr/Au–Ti	N/A	1 ppm	He	157
CO	rGO	chemiresistor: Au/rGO/Au	10 ppm	10–30 ppm	r.t.	540
CO	rGO–SnO ₂ –Au	N/A	2 ppm	2–5 ppm	400 °C	541
CO ₂	Gr	chemiresistor: Au–Ti/Gr/Au–Ti	136 ppt	200 ppt	N ₂ , r.t.	490
CO ₂	Gr	chemiresistor: Ag/Gr/Ag	3 ppm	3–50 ppm	air, 320 to 470 K	544
CO ₂	Gr	chemiresistor: Cr/Gr/Au	10 ppm	10–100 ppm	air	543
H ₂	BP–Pt NPs	microelectrode/BP–Pt NPs	10 ppm	10–10 000 ppm	N ₂ , r.t.	571
H ₂	Gr–Pd NPs	chemiresistor: Ti/Gr/Pd NPs/Au	40 ppm	40–8000 ppm	N ₂ , r.t.	531
H ₂	Gr–Pd NPs	chemiresistor: Ag/Gr/Pd NPs/Ag	20 ppm	20–1000 ppm	N ₂ , r.t.	643
H ₂	Gr–Pd NPs	chemiresistor: Au/Gr/Pd NPs/Au	0.1 ppm	0.1–100 ppm	air _D	532
H ₂	Gr–Pd NTs	chemiresistor: Au/Gr–Pd NTs/Au	10 ppm	10–10 000 ppm	air, r.t.	644
H ₂	Gr–p–H ₂ O ₃ P–calix[8]arene–Pt NPs	chemiresistor: IDE/Gr–p–H ₂ O ₃ P–calix[8]arene–Pt NPs/IDE	0.2 vol %	0.1–10 vol %	N ₂ , r.t.	645
H ₂	Gr–PMMA–Pd NPs	chemiresistor: Ti–Au/Gr–PMMA–Pd NPs/Ti–Au	250 ppm	0.025–2 vol %	N ₂ , r.t.	533
H ₂	Gr–Pt NPs–MWCNT	chemiresistor: Cu/Gr–Pt NPs–MWCNT/Cu	4 vol %	4 vol %	air, r.t.	646
H ₂	Gr–Pt–SiC	chemiresistor: Ti–Au/Gr–Pt–SiC/Ti–Au	50 ppm	50 ppm to 20 vol %	N ₂ , r.t.	647
H ₂	Gr–Pt–SiC	chemiresistor: Ti–Au/Gr–Pt–SiC/Ti–Au	1 vol %	1 vol %	N ₂ , 27–175 °C	341
H ₂	Gr–SnO ₂ NPs	FET: Si/SiO ₂ /Gr–SnO ₂ NPs/Cr/Au	1 ppm	1–100 ppm	50 °C	648
H ₂	MoS ₂ –M (M = Ag, Pd, Pt, Sc, Y)	FET: Si/SiO ₂ /MoS ₂ –M/Ni–Au/Ni–Au	<3 ppm	N/A	air, r.t.	583
H ₂	rGO–PEDOT–PSS	chemiresistor: W/GO–PEDOT–PSS/W	100 ppm	30–180 ppm	100 °C	539
H ₂ S	Cu ₃ HHTP ₂ , Ni ₃ HHTP ₂	chemiresistor: Gr/Cu ₃ HHTP ₂ (Ni ₃ HHTP ₂)/Gr	N/A	2.5–80 ppm	N ₂ , r.t.	623
H ₂ S	CuO	chemiresistor: Al ₂ O ₃ /Au/CuO/Au	2 ppb	2 ppb–1.2 ppm	dry air, 240 °C	609
H ₂ S	Gr–PSS–PANI	chemiresistor	1 ppm	1–50 ppm	air _D , r.t.	561
H ₂ S	M ₃ HHTP ₂ –Gr (M = Fe, Co, Ni, or Cu)	chemiresistor: Ag/M ₃ HHTP ₂ –Gr/Ag	35 ppm	5–80 ppm	N ₂ , r.t.	176
H ₂ S	MoO ₃	FET: Si/SiO ₂ /Pt/MoO ₃ /Pt	250 ppb	0.25–5 ppm	air, 250 °C	613
H ₂ S	Ni ₃ HHTP ₂ , Ni ₃ HHTP ₂	chemiresistor: Au/Ni ₃ HHTP ₂ (Ni ₃ HHTP ₂) on cotton/Au	0.52 ppm	5–80 ppm	N ₂ and 18% RH, r.t.	624
H ₂ S	rGO–Cu ₂ O	chemiresistor: Au/rGO–Cu ₂ O/Au	5 ppb	5–100 ppb	N ₂ , r.t.	556
H ₂ S	rGO–SnO ₂ NW	chemiresistor: Au/rGO–SnO ₂ NW/Al ₂ O ₃ /Au	1 ppm	1–5 ppm	95% RH, 200 °C	560
H ₂ S	WO ₃	chemiresistor: Au/WO ₃ /Au	0.1 ppm	0.1–5 ppm	air, 350 °C	612
H ₂ S	WO ₃ –MoO ₃	chemiresistor: Ni–Cr/WO ₃ –MoO ₃ /Ni–Cr	20 ppb	50 ppb to 10 ppm	air, 250 °C	614
N ₂ O	Gr	chemiresistor: Au–Ti/Gr/Au–Ti	103 ppt	200 ppt	N ₂ , r.t.	490
NH ₃	BP	chemiresistor: Pt/BP/Pt	10 ppm	10–300 ppm	N ₂ , r.t.	160
NH ₃	Cu ₃ HHTP ₂	chemiresistor: Au/Cu ₃ HHTP ₂ /Au	0.5 ppm	1–100 ppm	air _D , r.t.	173
NH ₃	Cu ₃ HHTP ₂ and Ni ₃ HHTP ₂	chemiresistive: Gr/Cu ₃ HHTP ₂ (Ni ₃ HHTP ₂)/Gr	N/A	2.5–80 ppm	N ₂ , r.t.	623
NH ₃	Cu ₃ HIIP ₂	chemiresistor: Au/Cu ₃ HIIP ₂ /Au	0.5 ppm	0.5–10 ppm	N ₂ and air 60% RH, r.t.	418
NH ₃	Gr	chemiresistor: Au–Ti/Gr/Au–Ti	N/A	1 ppm	He	157
NH ₃	Gr	chemiresistor: Au–Ti/Gr/Au–Ti	33.2 ppt	200 ppt	N ₂ , r.t.	490
NH ₃	Gr	chemiresistor: Au–Cr/Gr/Au–Cr	1000 ppm	1000 ppm	N ₂ , r.t.	493
NH ₃	Gr	FET: Si/SiO ₂ /Gr/Ti–Au/Ti–Au	160 ppb	5–100 ppm	air _D , r.t.	649
NH ₃	Gr	FET: Si/SiO ₂ /Mica/Gr/Au–Ti/Au–Ti	N/A	10–500 ppm	air, r.t.	650
NH ₃	Gr–MoS ₂	chemiresistor: Au–Ti/Gr–MoS ₂ /Au–Ti	N/A	5–100 ppm	N ₂ , 100 °C	651
NH ₃	M ₃ HHTP ₂ –Gr (M = Fe, Co, Ni, or Cu)	chemiresistor: Ag/M ₃ HHTP ₂ –Gr/Ag	19 ppm	5–1200	N ₂ , r.t.	176
NH ₃	MoS ₂	FET: Si/SiO ₂ /Ni–Au/MoS ₂ /Ni–Au	0.3 ppm	0.3–30 ppm	N ₂ , r.t.	652
NH ₃	MoS ₂	FET: Si/SiO ₂ /MoS ₂ /Ti–Au/Ti–Au	1 ppm	1500 ppm	air, r.t.	191
NH ₃	MoS ₂	FET: Si/SiO ₂ /MoS ₂ /Ti–Au/Ti–Au	N/A	100–1000 ppm	N ₂ , r.t.	101
NH ₃	MoSe ₂	chemiresistor: Ti–Au/MoSe ₂ /Au	50 ppm	50–1000 ppm	Ar, r.t.	582
NH ₃	MoTe ₂	FET: Si/Si–O ₂ /Ti–Au/MoTe ₂ /Ti–Au	1 ppm	2–100 ppm	N ₂ , r.t.	587
NH ₃	rGO	chemiresistor: Au/rGO/Au	5 ppm	5 ppm	N ₂ , r.t. 21–149 °C	498
NH ₃	rGO	chemiresistor: Cr–Au/rGO–PANI/Cr–Au	20 ppm	20–50 ppm	air, 25 °C	653
NH ₃	rGO	chemiresistor: Cr–Au/rGO/Cr–Au	1 ppb	1 ppb to 50 ppm	air, r.t.	654
NH ₃	rGO–Cu ₂ O	chemiresistor: Au/rGO–Cu ₂ O/Au	100 ppm	100–500 ppm	air, r.t.	655
NH ₃	rGO–P3HT	FET: Si/SiO ₂ /rGO–P3HT/Ti–Au/Ti–Au	N/A	10–50 ppm	air, r.t.	656
NH ₃	rGO–Py	chemiresistor: Au/rGO–Py/Au	5 ppb	5 ppb to 100 ppm	air, r.t.	657
NH ₃	SnS ₂ –SnO ₂	chemiresistor: Au/SnS ₂ –SnO ₂ /Au	10 ppm	10–500 ppm	air _D , r.t.	658

Table 3. continued

analyte	material	architecture	LOD	experimental range	sensing environment	ref
NH ₃	Ti ₃ C ₂ T _x	chemiresistor: Au/Ti ₃ C ₂ T _x /Au	0.13 ppb	100–1000 ppb	N ₂ , r.t.	625
NH ₃	WS ₂	chemiresistor: Au/WS ₂ /Au	1 ppm	1–10 ppm	air, r.t.	470
NO	Cu ₃ HHTP ₂ and Ni ₃ HHTP ₃	chemiresistor: Gr/Cu ₃ HHTP ₂ (Ni ₃ HHTP ₂)/Gr	N/A	2.5–80 ppm	N ₂ , r.t.	623
NO	Gr	chemiresistor: Au–Ti/Gr/Au–Ti	158 ppq	10 ppt	N ₂ , r.t.	490
NO	M ₃ HHTP ₂ –Gr (M = Fe, Co, Ni, or Cu)	chemiresistor: Ag/M ₃ HHTP ₂ –Gr/Ag	17 ppm	5–80 ppm	N ₂ , r.t.	176
NO	MoS ₂	FET: Si/SiO ₂ /MoS ₂ /Ti–Au/Ti–Au	0.8 ppm	0.3 to 2 ppm	N ₂ , r.t.	580
NO	Ni ₃ HHTP ₂ and Ni ₃ HHTP ₂	chemiresistor: Au/Ni ₃ HHTP ₂ (Ni ₃ HHTP ₂) on fabrics/Au	0.16, 1.4 ppm	5–80 ppm	N ₂ and 18% RH, r.t.	624
NO ₂	BP	FET: Si/SiO ₂ /BP/Au/Au	20 ppb	20–1000 ppb	air, r.t.	158
NO ₂	BP	FET: Si/SiO ₂ /Ti–Au/BP/Ti–Au	5 ppb	5–40 ppb	Ar, r.t.	159
NO ₂	BP	chemiresistor: Pt/BP/Pt	20 ppb	20–1000 ppb	N ₂ , r.t.	160
NO ₂	BP–MoSe ₂	PN Diode: Ti–Au/BP–MoSe ₂ /Ti–Au	10 ppb	25 ppb to 2 ppm	r.t.	642
NO ₂	BP–Pt NPs	FET: Au–Ti/BP–Pt NPs/Au–Ti	1 ppm	1–50 ppm	N ₂ , r.t.	571
NO ₂	g-C ₃ N ₄	chemiresistor: Ti–Au/g-C ₃ N ₄ /Ti–Au	140 ppb	1–40 ppm	air 25% RH, r.t.	629
NO ₂	GO	chemiresistor: Au/GO/Au	1.3 ppb	0.2–200 ppm	r.t.	659
NO ₂	Gr	chemiresistor: Au–Ti/Gr/Au–Ti	N/A	1 ppm	He	157
NO ₂	Gr	chemiresistor: Au–Ti/Gr/Au–Ti	2.06 ppt	40 ppt	N ₂ , r.t.	490
NO ₂	Gr	FET: Si/SiO ₂ /Gr/Ti–Au/Ti–Au	15 ppb	1–10 ppm	air _D , r.t.	649
NO ₂	Gr–MoS ₂	chemiresistor: Au–Ti/Gr–MoS ₂ /Au–Ti	1.2 ppm	5–100 ppm	N ₂ , 100 °C	651
NO ₂	Gr–NiO	chemiresistor: Ni–Au/Gr–NiO/Ni–Au	N/A	1–15 ppm	N/A	660
NO ₂	Gr–PETP	chemiresistor: Au/Gr–PETP/Au	200 ppm	N/A	air	661
NO ₂	Gr–WO ₃	chemiresistor	1 ppm	1–20 ppm	air, r.t. and 200–300 °C	662
NO ₂	MoS ₂	FET: Si/SiO ₂ /MoS ₂ /Ti–Au/Ti–Au	20 ppb	20–400 ppb	air, r.t.	191
NO ₂	MoS ₂	FET: Si/SiO ₂ /MoS ₂ /Ti–Au/Ti–Au	100 ppm	100–1000 ppm	N ₂ , r.t.	101
NO ₂	MoS ₂ –Pt NPs	FET: Si/SiO ₂ /MoS ₂ –Pt/rGO/rGO	2 ppb	0.5–5 ppm	N ₂	663
NO ₂	MoS ₂ –rGO	FET: Si/SiO ₂ /MoS ₂ –rGO/Ti–Au/Ti–Au	5.7 ppb	0.12–8 ppm	air, 60 °C	641
NO ₂	MoS ₂ –SnO ₂	chemiresistor: Si/SiO ₂ /MoS ₂ –SnO ₂ /Au/Au	0.5 ppm	0.5–10 ppm	air, r.t.	664
NO ₂	MoSe ₂ –Nb	chemiresistor: Cr–Au/MoSe–Nb/Cr–Au	3 ppm	3–50 ppm	150 °C	584
NO ₂	MoTe ₂	FET: Si/SiO ₂ /Ti–Au/MoTe ₂ /Ti–Au	12 ppb	100–1000 ppb	N ₂ , r.t.	587
NO ₂	NiO	chemiresistor: Ni–Au/NiO/Ni–Au	1 ppm	1–20 ppm	air, 250 °C	660
NO ₂	NiO–WO ₃	chemiresistor: Au/NiO–WO ₃ /Au	5 ppm	5–100 ppm	air, r.t.	603
NO ₂	rGO	chemiresistor: Cr–Au/rGO/Cr–Au	1 ppm	1–20 ppm	53 ± 3% RH, 23.0 ± 1.5 °C	665
NO ₂	rGO–Fe ₂ O ₃	chemiresistor: Au/rGO–Fe ₂ O ₃ /Au	0.18 ppm	0.18–90 ppm	air, r.t.	666
NO ₂	rGO–PET	chemiresistor: rGO/rGO–PET/rGO	0.5 ppm	0.5–10 ppm	air, r.t.	502
NO ₂	rGO–S–Ag	chemiresistor: Ag/rGO–S–Ag/Ag	0.5 ppm	0.5–50 ppm	air, 30% RH, 25 °C	510
NO ₂	rGO–ZnO	chemiresistor: Au/rGO–ZnO/Au	5 ppm	1–25 ppm	air, 25% RH, r.t.	519
NO ₂	SnS ₂	chemiresistor: Pt/SnS ₂ /Pt	0.6 ppm	0.6–10 ppm	120 °C	391
NO ₂	WS ₂ –Ag NW	chemiresistor: Cr–Au/WS ₂ –Ag NW/Cr–Au	1 ppm	25–500 ppm	air, 100 °C	589
NO ₂	ZnO	chemiresistor: Au/ZnO/Au	50 ppb	0.05–10 ppm	air, 180 °C	595
O ₂	Gr	chemiresistor: Au–Ti/Gr/Au–Ti	38.8 ppt	200 ppt	N ₂ , r.t.	490
O ₂	Gr	chemiresistor	1.25%	1.25–4.7 vol %	N ₂ , r.t.	567
O ₂	Gr–g-C ₃ N ₄	chemiresistor: Au/Gr–g-C ₃ N ₄ /Au	300 ppm	300–100 000 ppm	N ₂ , r.t.	570
O ₂	Gr–TiO ₂	chemiresistor: Au/Gr–TiO ₂ /Au	134 ppm	134 ppm to 100 vol %	N ₂ , r.t.	568
O ₂	MoS ₂	chemiresistor: Ti–Pt/MoS ₂ /Ti–Pt	1 vol %	1–100 vol %	N ₂ , 300 °C	581
SO ₂	GO	chemiresistor: Au/GO/Au	5 ppm	5–1100 ppm	air, r.t.	554
SO ₂	Gr	chemiresistor: Au–Ti/Gr/Au–Ti	67.4 ppt	200 ppt	N ₂ , r.t.	490
SO ₂	Gr	FET: Si/SiO ₂ /GO/Au/Au	50 ppm	50 ppm	40–100 °C	555

^aNote: chemiresistor is described in a way of electrode/conductive material/electrode. FET is described in a way of gate electrode/insulator/channel material/source electrode/drain electrode. Diode is described in a way of electrode/semiconductor/electrode. N/A, not available. Air_D, dry air and r.t., room temperature.

the material upon exposure to humidity, the graphene oxide layer was covalently anchored to the substrate, which improved the long-term stability of the device.⁶⁸⁵

To fabricate flexible humidity sensor, Zhang et al. deposited rGO on polyimide substrate and poly(diallylimethylammonium chloride) (PDPA) nanocomposite (Figure 31a).⁶⁸⁶ The sensor worked within 11–97% RH range at room temperature and

showed good repeatability when used for five exposure/recovery cycles at 43%, 75%, and 97% RH (Figure 31b,c). The authors also reported on a response time of 108–147 s and recovery time of 94–133 s during analytical measurements. Two-beam-laser interference was used for the simultaneous reduction, patterning, and nanostructuring of graphene oxide on flexible polyethylene terephthalate substrates for the

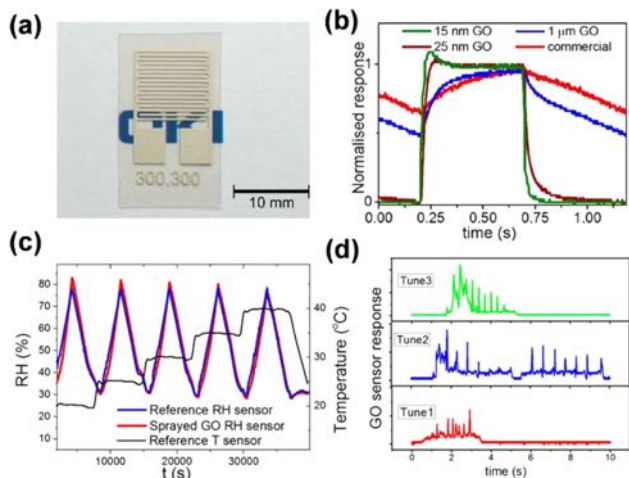


Figure 30. (a) Photograph of a sprayed GO sensing element. Due to the transparency of the ultrathin GO film, only the printed Ag electrodes on top of the PEN substrate are visible. (b) Normalized response of a 15 nm thick GO sensor to a modulated humid air flow at 10 Hz. (c) Sensing performance of a 15 nm thick GO sensor (red line) compared to the response of a commercial high precision RH sensor (blue line). (d) Responses of an ultrathin GO sensor to 3 different tunes whistled by three different users.⁶⁷⁸ Reproduced from ref 678. Copyright 2013 American Chemical Society.

development of high performance humidity sensing devices.⁶⁸⁷ Ma and Tsukruk demonstrated a flexible GO-silk-based chemiresistive sensor, which showed a fast response time of 3 s, high sensitivity to humidity in the 20–97% RH range, and good stability to thousands of folding-unfolding cycles and chemical solvents.⁶⁸⁸ Knopf and co-workers printed graphene interdigitated capacitive (IDC) sensors on the flexible polyimide substrates.⁶⁸⁹ As the total capacitance of the IDC sensor is determined by multiplying each unit cell capacitance,

interdigitated configuration can increase the effective capacitance of the structure and the effective active area of the sensor. The printed sensors were used to measure water content of ethanol solution, which demonstrated the fabrication methodology for creating chemical sensors on thin membranes by using conductive aqueous graphene ink.⁶⁸⁹ Layer-by-layer inkjet printing technique was also used to print the polymer particles and graphene oxide to fabricate humidity sensors.⁶⁹⁰ Deen et al. recently demonstrated a wireless humidity sensor based on the quantum capacitance effect in graphene.⁶⁹¹ The sensor consisted of a metal oxide/graphene variable capacitor (varactor) coupled to an inductor, to create a resonant oscillator circuit. The resonant frequency was found to shift in proportion to water vapor concentration for relative humidity (RH) values ranging from 1% to 97% with a linear frequency shift of 5.7 ± 0.3 kHz/%RH.

Understanding the interactions of ambient molecules with graphene and adjacent dielectrics is of fundamental importance for a range of graphene-based sensors, particularly for sensors where such interactions could influence the analytical operation of the device.^{692–694} Using a metal–oxide/graphene varactor structure, Koester and coworkers showed that graphene can be used to capacitively sense the intercalation of water between graphene and HfO₂ and that this process was reversible on a time scale of minutes.⁶⁹⁵ Molecular dynamics simulations indicated that a likely mechanism for the intercalation involved adsorption and lateral diffusion of water molecules beneath the graphene. Shehzad et al. designed multimode environment sensors by fabricating a graphene-based metal–semiconductor field-effect transistor.⁶⁹⁶ This FET device was composed of graphene as the channel material in the horizontal direction, and the graphene contact with silicon in the vertical direction to form a graphene/silicon Schottky junction (Figure 31d).⁶⁹⁶ The device was sensitive toward humidity under both forward and reverse biases and

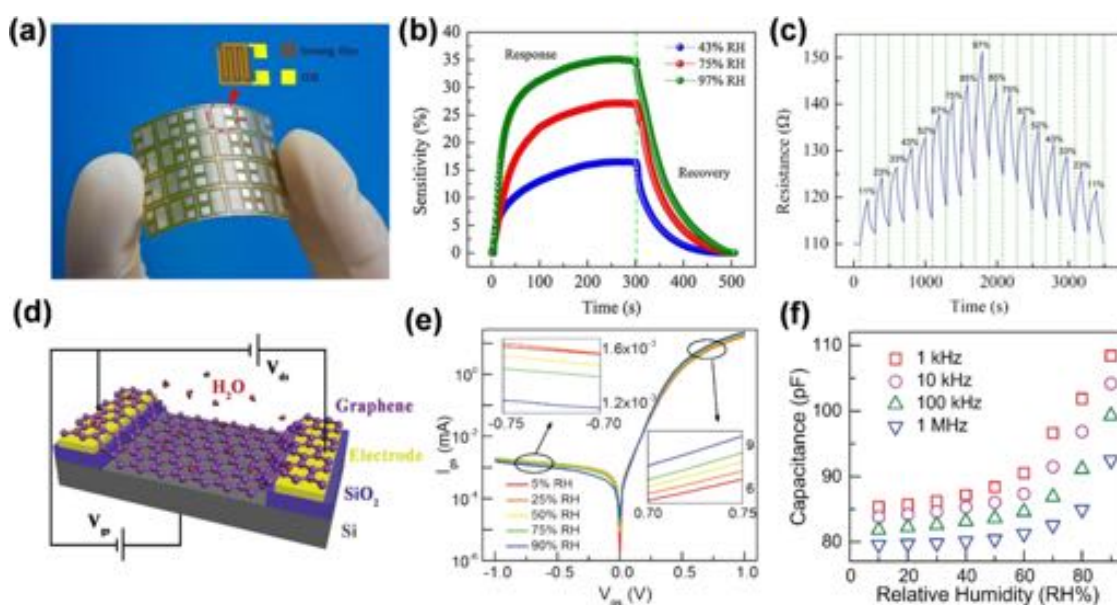


Figure 31. (a) Optical image of a 4 × 6 sensors array on a flexible PI substrate. (b) Response and recovery curves of the PDPA/RGO film sensor to a relative humidity pulse at 0% 43%, and 97% RH, respectively. (c) Resistance measurement of the PDPA/RGO film sensor under switching RH.⁶⁸⁶ Reproduced with permission from ref 686. Copyright 2014 Elsevier B.V. (d) Schematic of the multimode humidity sensor with source-drain voltage V_{ds} and gate voltage V_{gs} control. (e) I – V curves under various humidity conditions. (f) Capacitance change under different humidity.⁶⁹⁶ Reproduced with permission from ref 696. Copyright John Wiley and Sons.

operated in resistive, as well as capacitive modes (Figure 31e,f). Sensitivity of these devices reached to 17%, 45%, 26%, and 32% per relative humidity (%RH) for reverse biased, forward biased, resistive, and capacitive modes, respectively. Lemme and co-workers performed humidity sensing using a change in the electrical resistance of single-layer graphene, deposited on top of a SiO₂ layer on a Si wafer through chemical vapor deposition.⁶⁹⁷ The measured response and recovery times of the graphene humidity sensors were on the order of several hundred milliseconds from 1% to 96% RH. Density functional theory simulations showed that the interactions between the electrostatic dipole moment of the water and the impurity bands in the SiO₂ substrate led to electrostatic doping of the graphene layer.

Besides unmodified graphene-based sensor, humidity sensors based on functionalized graphene and graphene oxides are also routinely utilized, which usually exhibit improved performance over the non-functionalized graphene sensors. Aziza et al. showed that the sensing performance of graphene-based FET humidity sensor could be largely improved through polymer functionalization (Figure 32a).³⁶⁴ After the chemically

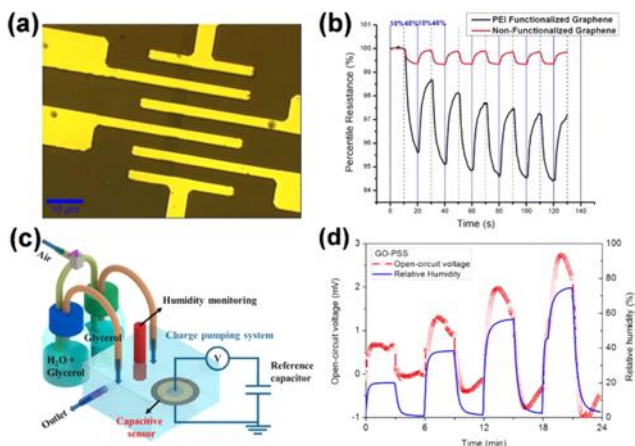


Figure 32. (a) Optical image of FET fabricated on silicon oxide/p⁺-doped silicon substrate; the channel width and length are both equal to 4 μm . (b) Humidity responses (RH: 10%–40%) at room temperature for non-functionalized (red) and functionalized (black) graphene.³⁶⁴ Reproduced with permission from ref 364. Copyright John Wiley and Sons. (c) Schematic diagram of the RH controlled-environment chamber and charge pumping system. (d) Performance evaluation of the self-powered humidity sensor. Voltage outputs of GO-PSS sensors were investigated over the RH range, 0–80%.⁶⁹⁸ Reproduced from ref 698. Copyright 2014 American Chemical Society.

vapor deposited graphene was functionalized with amine rich polymer, the electron transfer from amine groups in the polymer to graphene was enhanced. The functionalized sensor showed 4% resistance change for a variation of RH from 10% to 40%, which is about 10 times higher than the non-functionalized graphene (Figure 32b). Kang and co-workers reported a self-powered humidity sensor based on graphene oxide (GO) and poly(styrenesulfonate) (PSS)-intercalated composite films, which were used as humidity-responsive dielectrics (Figure 32c).⁶⁹⁸ The fabricated sensors were equipped with the charge pumping system to produce a voltage output in a response to humidity. The GO-PSS sensor showed enhanced sensing responses compared to the GO

sensor, providing ~5.6 times higher voltage output and three times faster responses in humidity sensing (Figure 32d).

Polypyrrole is a conducting polymer with good environmental stability, but itself has limited sensitivity for humidity.²⁷⁵ Lin et al. showed that a graphene–polypyrrole composite containing only 10% graphene could sense humidity within a range between 12% and 90% with high sensitivity ($S = 138$). The response and recovery times were approximately 15 and 20 s, respectively.⁶⁹⁹ Gr-PPy composites showed better humidity sensing properties than either pure graphene or PPy because of the formation of the irregular coverage of PPy by graphene that could result in different conduction mechanism under low or high humidity.⁶⁹⁹ Su et al. developed flexible impedance-type humidity sensors using GO and AuNPs by self-assembly and the sol–gel technique. The AuNPs-GO-hydrolyzed 3-mercaptopropyltrimethoxysilane (MPTMOS) sol–gel film with 9.0 wt % added GO exhibited optimal flexibility, sensitivity, linearity, and long-term stability.⁸¹⁸ Su et al. also developed impedance-type humidity sensors from diamine-functionalized GO films coated on alumina or plastic substrates.⁷⁰⁰

4.2.1.2. Hydrogen Cyanide. Hydrogen cyanide (HCN) is widely used in various manufacturing processes including electroplating or precious metal extraction; however, it is highly toxic to humans. Therefore, it is necessary to develop portable sensing devices capable of detecting trace amounts of HCN in the surrounding environment.⁷⁰¹ Robinson et al. fabricated molecular sensors based on rGO thin film networks. These devices were capable of detecting 10 s exposure to HCN at the concentration of 70 ppb.⁷⁰² Graphene quantum dots (GQDs) are atomically thick, conductive nanosheets of sp² hybridized carbons and can be considered as the nanometer-sized fragments of graphene with abundant edge groups (e.g., carboxyl and hydroxyl group).^{703,704} Alizadeh et al. developed a chemiresistive HCN sensor by using GQDs with average lateral size of 18 nm.⁷⁰⁵ The detection limit of the sensor was estimated at 0.6 ppm (S/N) with the response range of 1 to 100 ppm. The sensing was reversible with a response time of 1.5 min, which was faster than the response of many metal oxide and polymeric film-based sensors.^{706–709}

4.2.1.3. Alcohols. Alcohols, including methanol and ethanol, are valuable materials as solvents and fuels.⁷¹⁰ Monitoring the concentration of alcohols is also important for air quality inspection, diagnosis of disease, and detection of alcohol consumption.^{711,712} Manohar and co-workers described a flexible and lightweight chemiresistor made of a thin film of overlapped and reduced graphene oxide.⁵⁰² Inkjet techniques were used to print the surfactant-supported dispersions of rGO powder onto flexible plastic surfaces. The sensor could not only reversibly and selectively detect chemically reactive vapors such as NO₂ and Cl₂ but also showed good response to alcohols (CH₃OH and C₂H₅OH). Chen et al. investigated the fabrication of back-gated graphene FET arrays on micro-channels.⁷¹³ The I_{DS} of the FET immediately changed by 17% upon the exposure to ethanol vapor, and the device showed full recovery immediately after the ethanol was pumped out. This work provided a convenient way of constructing back-gated graphene FETs for sensing applications.

Park and co-workers reported on the fabrication of an ethanol gas sensor with an oleylamine-modified graphene oxide (OA-GO)-poly(9,9-diethyl-fluorene-co-bithiophene) (F8T2) composite as an active layer.⁷¹⁴ This sensor showed 6 times better sensitivity toward ethanol than that of a comparable

device with the F8T2-only active layer due to the presence of polar functional groups of OA-GO that could undergo stronger interactions with analytes. Zhu and co-workers developed the strategy for anchoring α -Fe₂O₃-nanoparticles on graphene and used it as ethanol sensor material.⁷¹⁵ The α -Fe₂O₃-graphene composite exhibited better sensing performance to ethanol in comparison with pure α -Fe₂O₃ counterpart, which was due to the enhancement in the specific surface area, with the addition of only 2% of graphene. Liu et al. reported on the technique to selectively sense H₂O and methanol, using a single graphene FET device by measuring real-time conductance as a function of gate voltage.⁷¹⁶ By analyzing the conductance versus gate voltage of the graphene-based device, the long-range scattering limited carrier mobility and the Dirac Point voltage could be derived and then utilized for selective gas sensing in real time.

4.2.1.4. Formaldehyde. Formaldehyde (HCHO) is one of the most harmful gases among indoor air pollutants. It has been proven to be a human carcinogen and an allergen and can cause dermatitis, respiratory irritation, asthma, and pulmonary edema.^{672,717} Alizadeh and Soltani used graphene/poly-(methylmethacrylate) blends as a sensitive and selective materials for the detection of formaldehyde vapor.⁷¹⁸ The use of the polymer-graphene composite led to an enhanced physical durability of the sensor and decreased the interfering effect of humidity on the sensor performance. The graphene/polymer ratio was found to be an important parameter in defining the dominant sensing mechanism and sensor performance. The response of the optimized sensor showed a good linear relationship within 0.05 to 5.0 ppm concentration range with the LODs of 10 ppb. Lee and co-workers developed a new class of chemical sensors for formaldehyde determination at ppb levels.⁷¹⁹ This diode-based sensor consisted of a composite layer of reduced graphene oxide with epitaxially oriented zinc oxide nanorods together with a Schottky contact material of Al_{0.27}GaN_{0.73}(~25 nm)/GaN. The Schottky diode exhibited high sensitivity (0.875 ppm) with the LOD down to 120 ppb and fast response time (~2 min) at room temperature.

4.2.1.5. Acetone. Acetone is known as a biomarker for diabetes, and exhaled breath of diabetes patients contains more than 1.8 ppm of acetone.⁷⁰⁴ Selective real-time detection of acetone at sub-ppm concentration thus can be a promising non-invasive diagnostic tool to identify at-risk populations.^{720–722} Kim and co-workers reported on acetone sensor fabricated by sensitizing electrospun SnO₂ nanofibers with reduced graphene oxide (rGO) nanosheets.⁵⁶⁰ The LODs of this sensor were as low as 100 ppb for acetone with good selectivity over other gases (Figure 33a,b), such as ethanol, toluene, CO, and NH₃. However, a high operating temperature of 350 °C was needed. GO/Co₃O₄ sensors could achieve a detection limit of 120 ppb at 300 °C in a highly humid atmosphere (90% RH) similar with the humidity in human breath.⁷²³ To decrease the working temperature, Liu et al. investigated the gas-sensing properties of composite, grapheme-mixed ZnFe₂O₄ for acetone vapor detection.⁷²⁴ Experimental results revealed that the mixing of graphene with ZnFe₂O₄ could lower the operating temperature to 275 °C. Staii and co-workers quantitatively analyzed the chemical gating effects in rGO-based chemical sensors.⁷²⁵ The authors combined the electronic transport/Kelvin probe microscopy measurements to directly image the surface potential and local charge distribution of rGO before and after chemical doping. This approach enabled quantification of the amount of charge

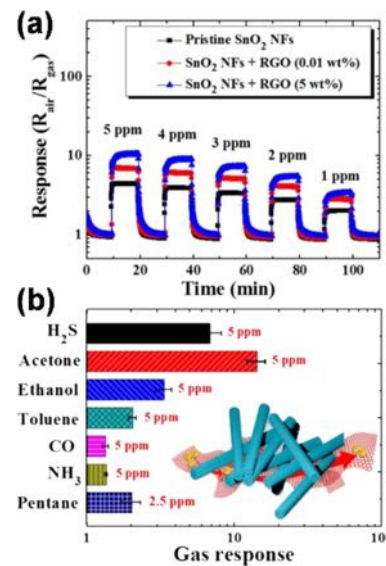


Figure 33. (a) Response of pristine SnO₂ NFs and rGO NS-SnO₂ NF composite sensors upon cyclic exposure to residual acetone concentrations between 1 and 5 ppm in humid air at an operation temperature of 350 °C. (b) rGO NS (5 wt %)-SnO₂ NF toward acetone at 350 °C with respect to the interfering gases of ethanol, toluene, carbon monoxide, ammonia, and pentane.⁵⁶⁰ Reproduced from ref 560. Copyright 2014 American Chemical Society.

transferred to rGO during the exposure to electron-acceptor (acetone) and electron-donor (ammonia) analytes.⁷²⁵ This method can be potentially applied to explore other two-dimensional chemical sensors where the sensing mechanism is based on the charge transfer between the analyte and the sensory materials.

4.2.1.6. Aromatics. Graphene-based sensors have proven to be highly sensitive to gaseous analytes; however, their limited ability to distinguish between different molecular species remains a major problem for practical applications. Detection of weakly interacting organic molecules is still challenging. To understand the influence of weak non-covalent molecular interactions on the electronic structure of graphene and the charge transfer mechanism, Cervenka et al. used a CVD method to grow a single layer of graphene in the bottom-gated FET device (Figure 34a).²³⁰ The gate dependence of I_{SD} showed a clear change upon adsorption of the melamine molecules onto the graphene FET, with the Dirac point shifting to the higher gate voltage with deposition of melamine, corresponding to electron removal (p-type doping; Figure 34b). Deposition of triazine on graphene-based FETs has resulted in a similar behavior as observed during the exposure to melamine. Molecules containing polar functional groups adsorbed on graphene exhibited different coverage behavior to nonpolar molecules. These results indicated that, particularly for molecules possessing strong dipoles, depolarization plays a significant role in charge transfer mechanisms even at submonolayer coverage.²³⁰

Myers et al. reported on the detection of a series of aromatic VOCs, including benzene, toluene, ethylbenzene, and xylenes, in water at low ppm concentration levels, by using functionalized graphene incorporated into a microelectrode chemiresistor platform.⁷²⁶ The use of microelectrodes resulted in a small double layer capacitance that impeded the charge transfer through the solution and allowed the resistance of the graphene film to be measured preferentially. Both the non-

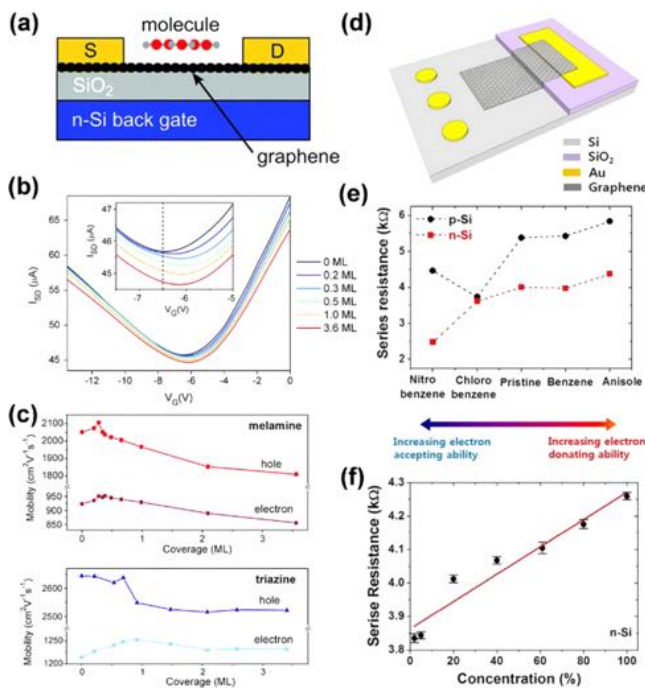


Figure 34. (a) Schematic illustration of the cross-section through a graphene FET with adsorbed molecules on the surface. (b) Gate voltage dependent source-drain current (I_{SD}) spectra of a graphene FET at a constant source voltage ($V_{SD} = 50$ mV) as a function of increasing melamine coverage. The inset shows a positive shift of the conductivity minimum (the Dirac point) upon adsorption of melamine, corresponding to p-type doping. (c) Graphene charge carrier mobility as a function of increasing melamine (top) and triazine (bottom) coverage.²³⁰ Reproduced with permission from ref 230. Copyright 2015 The Royal Society of Chemistry. (d) Graphical presentation of a graphene diode sensor. (e) Variation of the series resistance for n-Si and p-Si GDS's upon exposure to liquid aromatic molecules. (f) R_s of the n-Si GDS as a function of the concentration of anisole in benzene.²²⁶ Reproduced from ref 226. Copyright 2013 American Chemical Society.

aromatic molecule (cyclohexane) and aromatic compounds (e.g., toluene) had very distinct charge transfer ability, but they showed comparable analytical response. Thus, the occurrence of response was due to film swelling rather than doping through the direct interaction of the gaseous molecules with the graphene basal plane.⁷²⁶

Duesberg and co-workers developed graphene diode sensors (GDS) composed of monolayer graphene laterally in contact with the n- and p-type silicon substrates, consequently allowing exposure to liquids and gases from above (Figure 34d).²²⁶ The resulting sensor displayed good sensitivity toward aromatic electron donor and acceptor substances, such as anisole, benzene, chlorobenzene, and nitrobenzene. Pristine graphene in ambient conditions displayed a p-type response upon the exposure to aromatic molecules, due to the presence of adsorbed moisture or oxygen, resulting in an increase in the resistance of the material for the electron donor gases and the decrease for electron acceptors, independently of the substrate type (Figure 34e). This resistance change can be used to determine the concentration of electron donor or acceptor in neutral solvent (Figure 34f).²²⁶ The resistance also increased linearly with increasing anisole concentration. The recorded data fitted into an equivalent circuit model showed that the adsorption of various analytes caused a variation of the

Schottky barrier height and consequently in the conductivity of graphene.⁷²⁷

4.2.1.7. DMMP. Dimethyl methylphosphonate (DMMP) is a simulant of the nerve agent sarin (2-(fluoro-methyl-phosphoryl)oxypropane), which is one of the most toxic warfare agents.⁷²⁸ Alizadeh and Soltani designed a sensor array for the discrimination of DMMP vapor from triethylamine, tetrahydrofuran, acetonitrile, and alcohols rGO,⁷²⁹ obtained by the reduction of graphene oxide with hydrazine hydrate or sodium borohydride. This sensor was capable of interacting with DMMP vapor in the chemiresistor configuration. The reducing agents had a significant effect on the DMMP sensitivity, in which rGO prepared by hydrazine hydrate and sodium borohydride showed best ability to discriminate DMMP than rGO prepared by other reductants. Hu and co-workers also used rGO, prepared through the reduction of GO from *p*-phenylenediamine (PPD) for DMMP sensing. PPD reduced rGO exhibited much better (5.7 times with the concentration of DMMP at 30 ppm) response to DMMP than that of rGO reduced with hydrazine.⁷³⁰ Na et al. developed a wireless sensing system for DMMP detection by using the integrated arrays of field-effect transistors and sensors comprising graphene channels and silver nanowire electrodes⁷³¹. These devices were highly flexible and could be readily transferred onto both planar and non-planar substrates, including paper, clothes, fingernails, and human skin. The printed wireless sensing antenna responded to the gases by detecting the change in sensor resistance.

Defects in graphene, like grain boundaries, ripples, wrinkles, and point defects, are important factors that dictate the sensing characteristics of the device.^{493,732} Sensing with a defect-free graphene may thus provide better understanding of the mechanistic nature of interactions between the targeted gas analytes and the 2D materials, as well as deepen the understanding on the role of defects on sensing performance. Salehi-Khojin and co-workers explored the mechanisms of gas detection (DMMP and 1,2-dichlorobenzene) in pristine graphene-based chemical FETs and showed that only a small change in the conductivity of the fabricated pristine graphene-based chemFETs was observed upon the exposure to gaseous analytes, indicating that graphene was not intrinsically sensitive to the adsorbed gas molecules.⁶⁹² The sensitivity of pristine graphene chemFETs was enhanced by the presence of external defects in the insulating substrate, which could modulate the electronic properties of graphene.⁶⁹²

4.2.1.8. Other VOCs. Nagareddy et al. studied chemiresistive sensing of graphene oxide synthesized by plasma processing for polar vapors, including ethylene glycol, hydrogen peroxide, dimethyl acetamide, *N*-methyl-2-pyrrolidone, and acetic anhydride. Compared with the non-functionalized graphene, this GO sensor showed a significant increase in response rate and a one order of magnitude improvement in the recovery rate.⁷³³ This example illustrated the role of oxygen functionalization on the sensor response, whose presence not only improved the selectivity of the sensor but also greatly reduced the response and recovery times.^{702,734} The analytical performance showed a strong dependence on the analyte properties, in which the sensor resistance increased upon the exposure to polar protic analytes and decreased in the presence of polar aprotic vapors. The molecular dipole moment of analytes, arising from the presence of attached functional groups and their asymmetrical molecular arrangement,

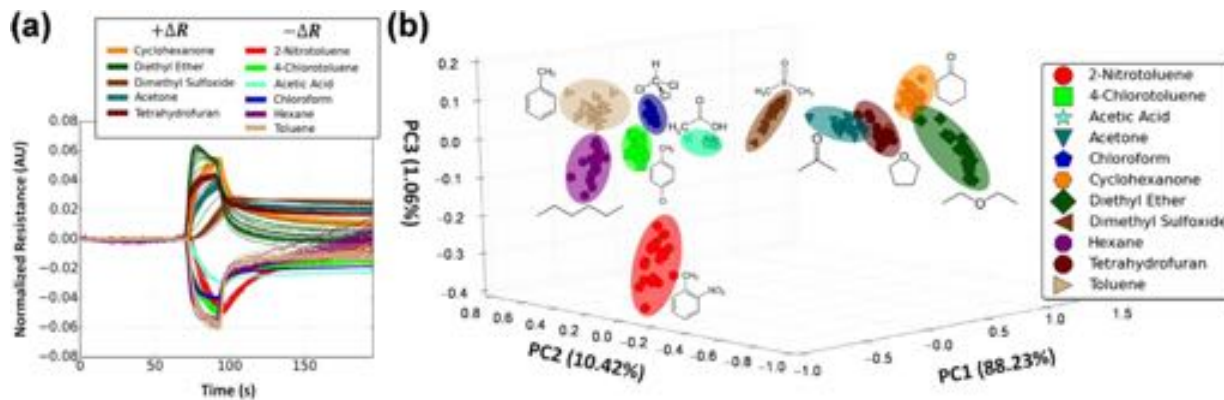


Figure 35. (a) Normalized sensor response to a chemically diverse set of compounds and (b) corresponding PCA transform.⁷³⁶ Reproduced from ref 736. Copyright 2016 American Chemical Society.

determines the adsorption ability of analyte on the surface of materials.⁷³⁵ The magnitude of the change in the sensor response was found to be linearly proportional to the dipole moment of the analyte.⁷³⁵

Li and co-workers fabricated chemical vapor sensors based on unmodified graphene and characterized their sensing properties through the exposure to headspace vapors containing a variety of solvents and related compounds (Figure 35a).⁷³⁶ The resulting sensor exhibited excellent discrimination power toward a variety of chemical compounds including cyclohexanone, diethyl ether, and dimethyl sulfoxide. Principle component analysis (PCA) was performed to explore the extent of grouping and separation between compounds and chemical classes. The combination of PCA and prediction accuracies further confirmed the discrimination capability of an unmodified graphene chemical vapor sensor (Figure 35b). These sensors exhibited desirable characteristics for practical applications, such as room temperature operation, rapid response and recovery, reversibility, and reproducibility; however, the magnitude of response for most of the gases was rather low due to lack of available binding sites in the unmodified graphene.

Fattah et al. fabricated a graphene/silicon heterojunction Schottky diode sensor for detection of different chemical vapors, including chloroform, phenol, and methanol, using EIS.⁷³⁷ The adsorbed molecules changed the local carrier concentration in graphene, which led to the changes in impedance response. Highly sensitive and selective impedance responses when graphene layer was in contact with different vapors were observed. The impedance responses to vapors were triggered by using phenol solutions of different concentrations. The resulting device exhibited a linear response for phenol within the range of 0.001 to 1 M with a high reproducibility (RSD 4.4%). Taromi and co-workers demonstrated a highly efficient chemiresistive sensor based on the nanocomposite fabricated from PEDOT-PSS and ultra-large graphene oxide.⁷³⁸ This sensor was able to sense several VOCs, including methanol, ethanol, acetone, toluene, water, chlorobenzene, and propanol at room temperature. The incorporation of GO in PEDOT-PSS led to considerable enhancement of sensing performance for VOCs, due to the improvements in the direct charge transfer, increase of the specific surface area, and $\pi-\pi$ interaction in the sensing film. The sensitivity, response, and recovery times of the gas sensor with 0.04 wt % of GO were 11.3%, 3.2 s, and 16 s, respectively, at methanol vapor concentrations as low as 35 ppm. Teradal et

al. developed a capacitive vapor sensor based on phenyl group functionalized porous graphene oxide, with large open pores and high surface area, to enhance molecular interactions with the vapor analytes.⁷³⁹ The data indicated that porous GO was responsible for the excellent sensing properties of this capacitive detector including low detection thresholds, recyclability, short response and recovery times, and applicability for the detection of diverse target molecules, including humidity, ethanol, phenol, toluene, and cyclohexane.

Kulkarni et al. reported on a fundamentally different sensing mechanism, based on molecular dipole detection, enabled by a pioneering graphene nanoelectronic heterodyne sensor.⁷⁴⁰ The device, different from other nanoelectronic sensing technologies, used graphene FET as a high-frequency (>100 kHz) mixer, with surface-adsorbed molecules as an oscillating gate. The oscillating molecular dipole (excited by AC-driving voltage) induced a conductance modulation on the graphene channel; this conductance fluctuation was frequency-mixed with the AC excitation, thus generating a heterodyne mixing current (Figure 36a,b). Importantly, by using higher frequencies, the slow sensing response, which usually hinders conventional nanoelectronic sensors, could be overcome when the AC field switching outpaced the slow dynamics of interface states. This prototype graphene sensor could achieve simultaneous rapid (down to 0.1 s) and sensitive (down to 1 ppb) detection of a wide range of VOCs (Figure 36c,d), demonstrating orders of magnitude improvement in both response time and sensitivity over state-of-the-art nanoelectronic sensors.

Johnson and co-workers fabricated chemical vapor sensor based on graphene field effect transistors functionalized with single-stranded DNA.⁷⁴¹ Single-stranded DNA was chosen as the functionalization layer due to its affinity to a wide range of target molecules, while $\pi-\pi$ stacking interaction with graphene ensured minimal degradation of device performance. DNA-decorated graphene sensor arrays showed analyte- and DNA sequence-dependent responses down to ppb concentrations. DNA/GFET sensors were able to differentiate among chemically similar analytes, including a series of carboxylic acids, and structural isomers of carboxylic acids and pinene.⁷⁴¹

Gautam and Jayatissa used CVD to grow graphene surface as a sensing channel for the detection of organic vapors (ethanol, acetic acid, and acetone) at concentrations lower than 200 ppm, at room temperature.⁷⁴² They showed that the response of the sensor could be further enhanced by functionalizing its surface with catalytic metals such as platinum (Pt), palladium

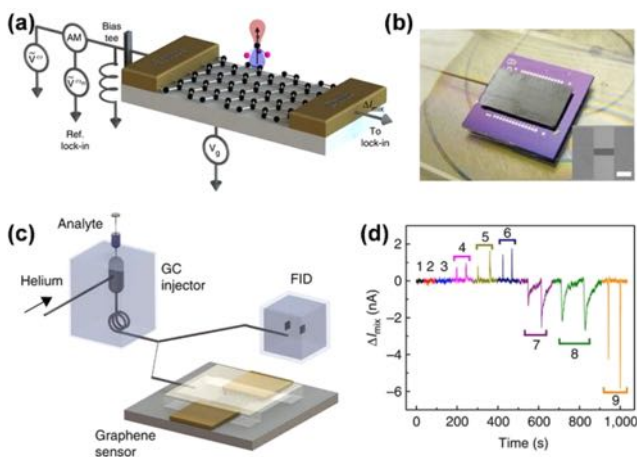


Figure 36. Rapid and high-sensitivity graphene nanoelectronic heterodyne sensor. (a) Schematic showing a graphene transistor configured as a high-frequency mixer for heterodyne vapor sensing and an illustration of a chloroform molecule on top of a graphene channel. (b) Optical image of the graphene sensor capped with a silicon flow channel and a GC guard column inserted at one end. (c) Experimental setup showing a GC injector connected to the graphene sensor and a FID through a GC separation column and a Y-split. (d) Mixing current response of a graphene heterodyne sensor to injections of various masses of (1) pentane, (2) hexane, (3) benzene, (4) chlorobenzene, (5) dichloromethane, (6) chloroform, (7) DMF, (8) DMMP, and (9) acetone.⁷⁴⁰ Reproduced with permission from ref 740. Copyright 2014 Springer Nature.

(Pd), aluminum (Al), and gold (Au). Waghuley et al. investigated chemiresistive sensing of liquid petroleum gas (LPG), at room temperature, by using few-layer graphene.⁵⁴⁶ The chemiresistor exhibited good sensing response (0.92 for 100 ppm), short response and recovery time (5 and 18 s, respectively), LOD of 4 ppm, and excellent stability for LPG at room temperature. Further study showed that the composite of graphene and 20 wt % CeO₂ quantum dots can improve the sensing response for 100 ppm LPG to 1.3.⁷⁴³ The enhanced response of graphene-CeO₂ quantum dots may be due to the catalytic oxidation reaction of the LPG happening at the surface of CeO₂.⁷⁴⁴ Sevilla and co-workers prepared graphene-nylon-6 nanocomposite that could be used in chemiresistor architecture for gas sensing of triethylamine vapor.^{745,746} The detection limit was as low as 0.39 mg L⁻¹ within a working concentration range of 23–230 mg L⁻¹.⁷⁴⁶

Graphene-based vapor sensors have attracted much attention due to their variety of structures, unique sensing performance, room-temperature working conditions, and tremendous application prospects. There are still several challenges associated with Gr-based vapor sensors need to be addressed before their broader and more practical application. First, to improve the selectivity, more functionalization methods need to be explored to provide graphene materials with specific analyte-binding property and long-term stability.^{347,475} Second, although drop casting, spin coating, and inkjet printing have been employed to deposit sensing materials on electrodes, development of technologies capable of low-cost and scalable production of sensing devices with high batch-to-batch reproducibility is still needed.¹²⁵ Third, standardized integration methods need to be explored to develop sensors with wearable and wireless features that have promising utility in healthcare, robotics, artificial intelligence, military, remote explorations.¹²⁴

4.2.2. Black Phosphorus. 4.2.2.1. *Humidity.* Black phosphorus can adsorb ambient moisture and form a layer of liquid as a result of its hydrophilicity.^{573,747} Due to the autoionization process of water molecules (formation of mobile H⁺ ions), the adsorbed moisture layer on the surface of BP can be ionically conductive. Additionally, previous studies have demonstrated that the BP can be oxidized to phosphorus oxides or phosphoric acid on exposure to water molecules and oxygen,⁷⁴⁸ which will further ionically dissolve in the moist media, thus enhancing the concentration of H⁺ ions on the surface. Both autoionization of water and ionic solvation of the phosphorus oxoacids, in the adsorbed hydration layer, provide a substantial number of mobile ions for the electric transport through BP.⁵⁷⁶ Although black phosphorus atomic layers undergo chemical degradation in humid air, in more robust configurations, such as films, composites, and embedded structures, BP can be potentially used as sensory materials for humidity. Salehi-Khojin and co-workers found that the films of BP nanoflakes exhibited excellent sensitivity and selectivity for humidity detection with quick recovery characteristics (Figure 37a).⁷⁴⁹ The drain

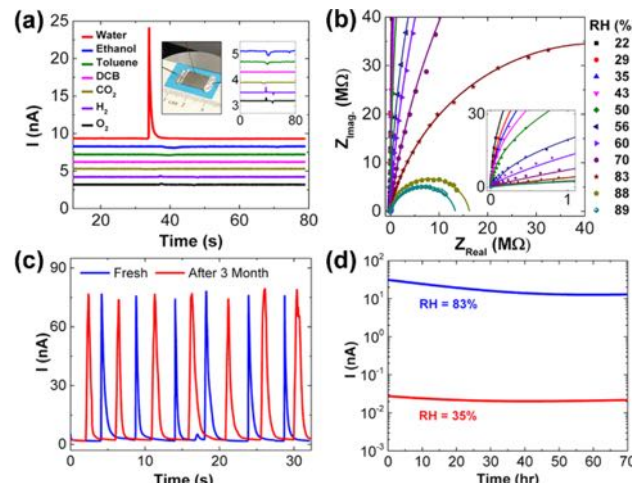


Figure 37. (a) Response of the stacked BP NFs to different analytes. The inset (right) magnifies the same curves. (b) The results obtained from a typical BP film sensor at different RH at 25 °C in a frequency range from ~300 Hz to 10 MHz. (c) Sensing response of the liquid exfoliated sensor upon exposure to multiple injections of water vapor immediately after preparation (blue) and after 3 months exposure to ambient conditions (red), without any noticeable change in its sensitivity. The responses are drawn with offset for clarity. (d) Drift of the sensor in prolonged exposure to 35% and 83% RH at 25 °C.⁷⁴⁹ Reproduced from ref 749. Copyright 2015 American Chemical Society.

current of the BP FET sensor increased by ~4 orders of magnitude as the relative humidity (RH) was varied from 10% to 85%. The impedance spectroscopy and electrical characterizations suggested that the sensing mechanism of the BP film sensors was based on modulation in the leakage ionic current (Figure 37b).⁷⁴⁹ Despite the ambient instability of atomically thin BP flakes, the BP films in this study revealed highly stable sensing characteristics after prolonged exposure (months) to humid environments (Figure 37c,d).⁷⁴⁹

Erando et al. synthesized few atomic layer thick nanosheets of black phosphorus using an electrochemical exfoliation method.⁷⁵⁰ The BP nanosheet thick film was integrated into

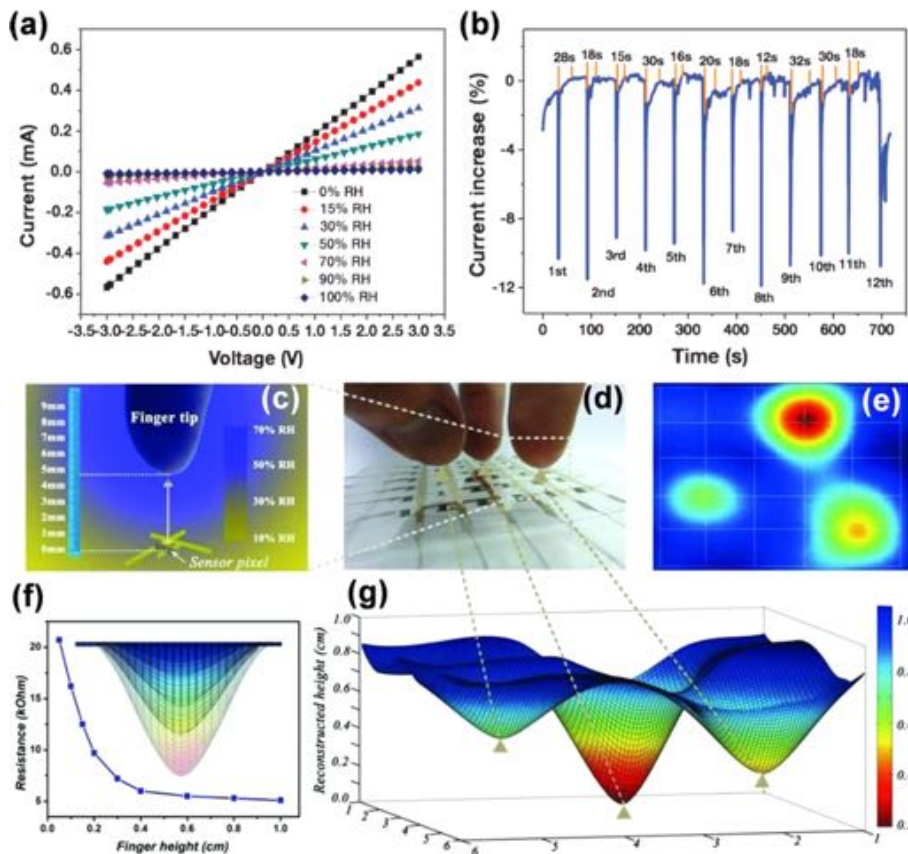


Figure 38. (a) I - V behavior of VS₂ measured under different RH values, showing an obvious slope decreasing with the increasing of RH. (b) The cycling behavior and recovery time under fast pulse moisture stimuli by rapidly turning on/off the fast-flowing humid gas (10% RH), revealing the high-speed responsiveness of the as-fabricated moisture detector. (c) The schematics of RH distribution on the near surface of a fingertip. (d) The digital photograph of the relative positions of three fingertips above the 6 × 6 matrix. (e) Top-viewed 2D signal intensity distribution measured from the sensor matrix by an electronic analyzer. (f) Height-resolved resistance diagram on the near surface of a fingertip measured by the as-established humidity sensor. Inset is the colored illustration of the surface humidity gradient of the finger. (g) Side-viewed 3D mapping of the relative positions of the applied three fingertips, showing successful 3D positioning function.⁷⁵⁶ Reproduced with permission from ref 756. Copyright 2012 John Wiley and Sons.

FET devices and used for the detection of humidity levels.⁷⁵⁰ The authors showed that the few layer (3–15 layer) thick film of BP nanosheets exhibited creditable sensitivity ($S = 521\%$) and fast recovery time of 26 s during exposure to humidity. Compared with bulk black phosphorus sample, whose resistance is on the order of a few hundred ohms, the resistance of nanosheets film under humid environments (11%–97% RH) of 13–81 k Ω attributed to the randomly stacked nanosheets. The large channel resistance is an advantage for the sensing of humidity, because the ionic conduction through the adsorbed water layer can be measurable; while it is not the case in bulk black phosphorus crystal because of the high conductance and instability at high current.⁷⁴⁹ Erande et al. also investigated the sensing properties of the FET devices fabricated from liquid exfoliated black phosphorus nanosheets. These devices showed an improved response and recovery time (255 and 10 s, respectively).⁷⁵¹

The lack of ambient stability makes incorporation of BP into practical devices very challenging as it demands for an inert operating environment. To produce air-stable BP sensors, Miao et al. explored the humidity sensing properties of BP field-effect transistors fully encapsulated by a 6 nm thick Al₂O₃ layer deposited by atomic layer deposition.⁷⁵² The encapsulated BP sensors exhibited superior ambient stability with no noticeable degradation in sensing response after being stored

in air for more than a week. Compared with the bare BP devices, the encapsulated sensors offered enhanced long-term stability, however, with a trade off in reduced (~50%) sensitivity.⁷⁵²

In order to analyze the deterioration of BP under ambient conditions, Walia et al. studied the individual effects of key environmental factors, such as temperature, light, and humidity on the performance of BP-based sensors.⁷⁵³ Few-layer BP was employed as a recoverable humidity sensor with detection levels down to 10% RH within a broad dynamic range of 10–90% RH at 30 °C. The detection range could be further extended with both more optimal device design and observed BP deposition techniques to achieve a sensitive layer with full coverage. It was shown that humidity itself does not lead to material degradation. Hence, by isolating BP from light, its lifetime can be prolonged even in the presence of O₂.

4.2.2.2. Methanol. The detection of methanol is of very high importance because of its human toxicity. In industrial settings, the inhalation of high concentrations of methanol vapor and the absorption of methanol through the skin are as effective as oral uptake in causing toxic effects.⁷⁵⁴ Pumera and co-workers developed a methanol sensing device based on an interdigitated gold electrode modified with layered black phosphorus using electrochemical impedance spectroscopy as the transduction method.⁷⁵⁵ The resulting device was highly

sensitive and selective to methanol over toluene, acetone, chloroform, dichloromethane, ethanol, and more, due to the higher dielectric constant of methanol over than other small molecules tested. The impedance phase depended linearly on the methanol concentration between 380 and 1900 ppm. The detection limit was 28 ppm, which is below the approved exposure limit of 200 ppm.

Although these studies have revealed the great potential of using BP as the vapor sensor to realize selective and sensitive detection, most of the applications are limited to the sensing of humidity and alcohols, probably because of the special reactivity of BP with these classes of analytes. It would be worthwhile to explore the utilization of BP for sensing of other volatiles, as the adsorption abilities of BP for a wide range of gaseous molecules have been theoretically and experimentally identified.^{98,159} More work, regarding the control of the directional alignment of nanosheets on the substrate, overcoming the environmental instability, as well as the control the chemical functionalization of the BP surface, needs to be addressed in the future.

4.2.3. Transition Metal Dichalcogenides. **4.2.3.1. Humidity.** Feng et al. used vanadium disulfide (VS_2) nanosheets with a quasi-two-dimensional electronic structure as the moisture responsive material.⁷⁵⁶ The electric conductivity of this oriented film was highly sensitive to environmental humidity, which showed a resistance change of almost 2 orders of magnitude in the range of 0% to 100% of RH (Figure 38a,b). Based on these results, a flexible and touchless positioning interface that could map the spatial distribution of moisture was developed (Figure 38c–e). This concept utilized VS_2 ultrathin nanosheets as the sole functional material, through which not only the 2D position of an applied humid pointer, like finger tips, could be localized but also the relative height information could be detected as the third dimensionality (Figure 38f,g). The moisture sensing positioning interface provided new avenues for real-time humidity mapping matrix or non-contact control interfaces for advanced human machine interactive systems.

Yang and co-workers reported on the fabrication of humidity sensor by using few-layer molybdenum disulfide (MoS_2), synthesized by ultrasound-assisted liquid method.⁷⁵⁷ The thin film sensors were exposed to relative humidity ranging from 0 to 60%. The sensors showed excellent sensitivity with very quick response (~9 s) and recovery (~17 s) speed to water vapor, which was partially attributed to the intrinsic hydrophobic property of MoS_2 that accelerated the desorption process of water molecules from the surface.⁷⁵⁸ The sensors showed a size-dependent performance, where the nanosheets with smaller size exhibited a better response toward humidity due to the increased surface area and larger abundance of exposed edge sites. Pawbake et al. reported on a one-step synthesis method of a wafer-scale, highly crystalline tungsten disulfide (WS_2) nanoparticle thin film by using a modified hot wire chemical vapor deposition (HW-CVD) technique.⁷⁵⁹ The WS_2 nanoparticle thin film-based device showed good response to humidity with excellent long-term stability.⁷⁵⁹ The resistance of the films decreased with the increasing RH. The maximum sensitivity of 469% along with the response time of ~12 s and recovery time of ~13 s was observed for this WS_2 thin film humidity sensor device.

Guo et al. fabricated a large-area WS_2 film through sulfurization of a tungsten film and assessed its humidity sensing performance in both the natural flat and high

mechanically flexible states (bending curvature down to 5 mm).⁷⁶⁰ The conductivity of as-synthesized WS_2 increased over a wide relative humidity range (0% to 90%) with fast response and recovery times (5–6 s). A transparent, flexible, and stretchable resistive type humidity sensor was subsequently fabricated by using graphene as electrodes and thin polydimethylsiloxane (PDMS) as a substrate (Figure 39a). The

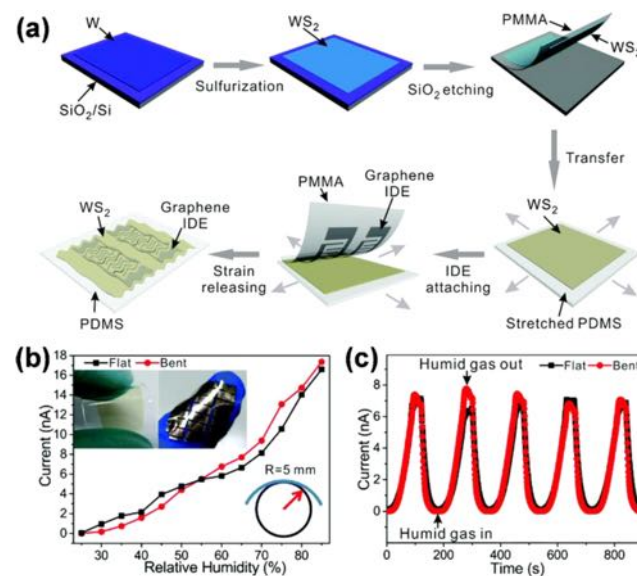


Figure 39. (a) Schematic of the device fabrication process. (b) Current response of the flexible sensor working in flat and bent states, respectively. (c) Dynamic response of the flexible humidity sensor in flat and bent states with the RH level periodically increasing and decreasing.⁷⁶⁰ Reproduced with permission from ref 760. Copyright 2017 The Royal Society of Chemistry.

resulting device, even when laminated onto the skin, retained stable water moisture sensing behavior in the undeformed relaxed state, as well as under compressive and tensile loadings (Figure 39b,c).⁷⁶⁰ Its high sensing performance enabled real-time monitoring of human breath.

4.2.3.2. Hg Vapor. Mercury is extremely toxic to aquatic life and humans due to its persistent and bioaccumulative properties. Elemental Hg, as one of the main forms of Hg, has a long lifetime and high migration ability, and it is difficult to detect because of its low melting point and high equilibrium vapor pressure, raising more concerns.⁷⁶¹ The permissible exposure limit of mercury vapor for an 8-h time-weighted average in the workplace set by Occupational Safety and Health Administration of U.S.A. is 0.1 mg/m^3 .⁷⁶² Wang et al. demonstrated a new room temperature elemental mercury sensor based on MoS_2 –polyaniline nanocomposite.⁷⁶³ The sensor exhibited fast response and recovery time, good selectivity, and long-term stability to a wide range of Hg vapor concentrations, spanning from 0.55 to 452.51 mg m^{-3} .

4.2.3.3. Triethylamine. Perkins and co-workers fabricated a resistor device by depositing single monolayer MoS_2 on SiO_2/Si wafer for the sensing of chemical vapors (Figure 40a).¹⁶⁶ As shown in Figure 40b, electrical contacts were deposited on the MoS_2 flake by using electron beam lithography, followed by electron beam evaporation of Au and Ti/Au. The device provided sensitive transduction of transient surface physisorption events to the conductance of the monolayer MoS_2 and exhibited highly selective reactivity to a range of analytes. Its

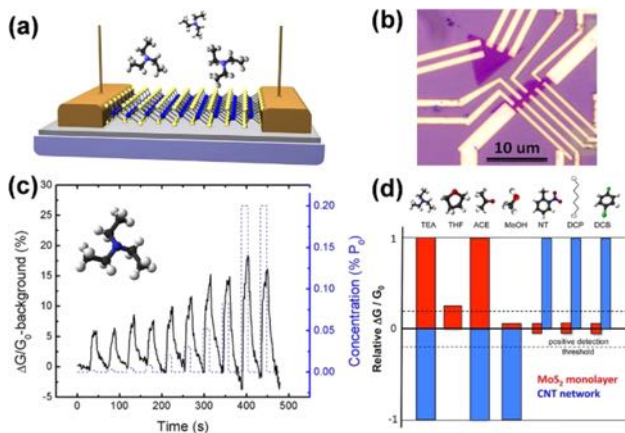


Figure 40. (a) Schematic and image of the MoS₂ monolayer sensor. A single monolayer of MoS₂ is supported on an SiO₂/Si substrate and contacted with Au contact pads. (b) An optical image of the processed devices showing the monolayer MoS₂ flakes electrically contacted by multiple Au leads. (c) Change in conductivity of the monolayer MoS₂ sensor channel upon exposure to TEA. (d) Histogram of MoS₂ and CNT-network sensor responses to various analytes.¹⁶⁶ Reproduced from ref 166. Copyright 2013 American Chemical Society.

conductance increased rapidly upon the exposure to triethylamine (Figure 40c) and was unaffected by the exposure to many other analytes or gases, including dichlorobenzene, dichloropentane, nitromethane, nitrotoluene, and water vapor. The sensor showed selective response to electron donors and limited response to electron acceptors (Figure 40d), which was consistent with the weak n-type character of MoS₂. The monolayer MoS₂-based sensing device also exhibited a much higher selectivity to triethylamine than carbon nanotubes-based sensors, which showed cross sensitivity with acetonitrile, methanol, and nitrobenzene vapors.

Friedman et al. fabricated MoS₂ FET sensors on a SiO₂ substrate and measured their responses to a variety of gaseous analytes.⁷⁶⁴ They found that the resulting sensing device produced the largest response to triethylamine, while the exposure to electron acceptors produced no change in the analytical signal.⁷⁶⁴ Mo 3d_{yz} orbitals and S 2p orbitals were identified as sites that were potentially free to interact with the environment on the surface of MoS₂.⁷⁶⁵ After the MoS₂ layer was deposited onto thermally grown SiO₂ substrate, the charge on the Mo 3d_{yz} orbital was compensated by the negative charge on SiO₂. This fabrication method subsequently resulted in the positively charged S 2p orbital as the only active sites available for gas/surface interactions.⁷⁶⁶ Thus, the MoS₂ sheet interacted strongly with donor-like analytes. The MoS₂ sensors provided comparable sensitivity and much higher selectivity toward triethylamine than other low-dimensional sensors, such as carbon nanotube and graphene chemical sensors.⁷⁶⁴

4.2.3.4. Ethanol. Wang and co-workers prepared composite electrodes consisting of SnO₂ nanoparticles dispersed on the surface of MoS₂ nanosheets by low temperature hydrothermal method.⁷⁶⁷ The combination of large surface area of MoS₂ nanosheets and the superior gas-sensing performance provided by ultra-small SnO₂ nanoparticles resulted in high response and good selectivity to ethanol gas by the SnO₂–MoS₂ composite sensor.⁷⁶⁷ Li and co-workers studied the sensing performance of FET sensors fabricated from the multilayer WS₂ nanoflakes to physically adsorbed ethanol.⁷⁶⁸ The study

showed that the charge transfer occurred between the multilayer WS₂ and adsorbed gas molecules, which influenced the photoelectrical properties of the devices. Ethanol molecules acted as “n-dopants” thus significantly enhancing the photoresponsivity, and external quantum efficiency, demonstrating that the multilayer WS₂ has great potential for applications in gas sensors.

Dwivedi et al. reported on a highly selective ethanol sensor based on MoS₂-functionalized porous silicon (PSi).⁷⁶⁹ Interdigitated electrodes (IDEs) were used to record resistive measurements from MoS₂/PSi sensors in the presence of VOCs and moisture at room temperature. Due to formation of p–n junction between MoS₂ and PSi, a substantial enhancement in sensitivity and selectivity for ethanol vapor was observed, with the LOD of 1 ppm.⁷⁶⁹ Compared with the single-layer MoS₂ on crystalline silicon, the ethanol sensitivity increased by a factor of 5 when MoS₂/PSi was used as a sensing material. As the devices composed of a MoS₂ thin film or PSi alone were not very sensitive to ethanol, the formation of the p–n heterojunction by PSi and MoS₂ may explain the higher sensitivity of MoS₂/PSi. The modulation of the resistance of interfaces played a more important role in affecting the sensor’s response than that of the bulk MoS₂.

4.2.3.5. Acetone. Ko et al. demonstrated that large-area WS₂ nanosheets (1, 2, and 4 layers, Figure 41a) exhibited a

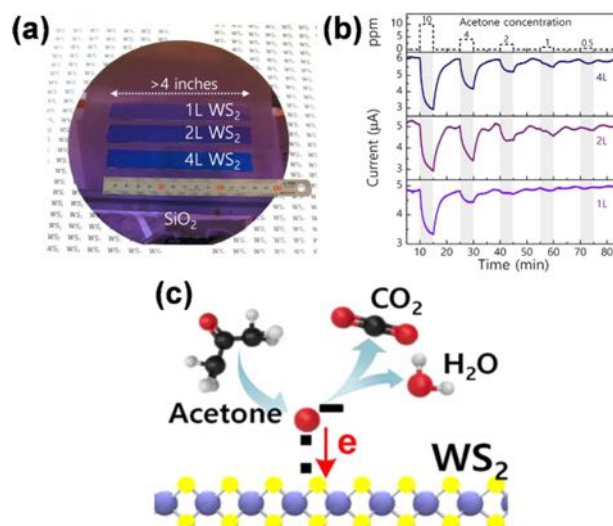


Figure 41. (a) Photograph of the synthesized large-area 1L, 2L, and 4L WS₂ nanosheets on an 8 in. SiO₂ wafer. The WS₂ nanosheets are uniform over a 4 in. length. (b) Gas-sensing results for the pristine WS₂ gas sensors consisting of 1L, 2L, and 4L WS₂ nanosheets upon acetone exposure (0.5, 1, 2, 4, and 10 ppm). (c) Schematic illustration of the gas-sensing mechanism. Upon acetone gas exposure, the adsorbed oxygen species interact with the acetone molecules, and volatile species such as CO₂ and H₂O are generated. The electrons are returned to WS₂.⁵⁸⁹ Reproduced from ref 589. Copyright 2016 American Chemical Society.

significant response to acetone.⁵⁸⁹ The schematic images in Figure 41c summarize the gas-sensing mechanism. When the pristine WS₂ sensor was exposed to acetone vapor, volatile molecules (CO₂ and H₂O) were formed via reaction between acetone and oxygen species adsorbed on the WS₂ surface. The oxygen species, such as O²⁻ and O⁻, were adsorbed during the air-purging step with dry air. Then, the captured electrons were released to the WS₂, resulting in the electron-hole

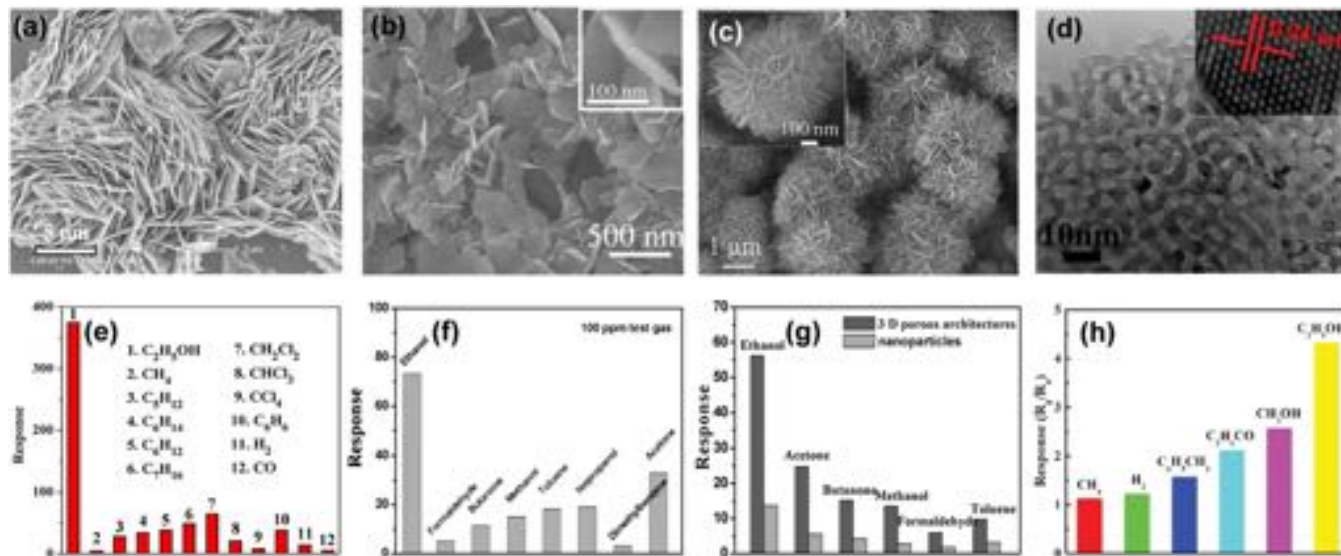


Figure 42. SEM image of (a) the ZnO nanosheet,⁷⁷⁹ (b) SnO₂ nanosheet,⁷⁸² (c) porous hierarchical nanosheets of SnO₂,⁷⁸⁴ and (d) TEM image of NiO nanosheets showing the porous nature.⁷⁹⁰ (e) The cross-response of the sensor to ethanol and other 11 interfering gases at 400 °C.⁷⁷⁹ Reproduced with permission from ref 779. Copyright 2012 Elsevier B.V. (f) Responses of the sensor using SnO₂ nanosheets to 100 ppm various test gases at 250 °C.⁷⁸² Reproduced with permission from ref 782. Copyright 2011 Elsevier B.V. (g) Responses of sensors based on porous SnO₂ architectures to various gases.⁷⁸⁴ Reproduced with permission from ref 784. Copyright 2011 The Royal Society of Chemistry. (h) The cross-response of the sensor to ethanol, methanol, acetone, toluene, hydrogen, and methane at a concentration of 500 ppm.⁷⁹⁰ Reproduced with permission from ref 790. Copyright 2013 The Royal Society of Chemistry.

compensation or recombination, and eventually diminishment in the hole concentration, which predominantly affected the current flow on the WS₂ surface. This reduced hole concentration caused a decrease in the current, as shown in Figure 41b.

4.2.3.6. Other VOCs. Balandin and co-workers demonstrated the selective VOC sensing using MoS₂ bilayer FET devices. The FETs were fabricated through the exfoliation from bulk MoS₂ crystals and its deposition onto Si/SiO₂ substrates.⁷⁷⁰ During the exposure to ethanol, acetonitrile, toluene, chloroform, and methanol vapors, the FET showed higher and quicker response to methanol and ethanol than to other probed analytes. The magnitude of the change for the source-drain current was strongly dependent on the polarity of the analyte.⁷⁷¹

Jung and co-workers reported on a high-performance chemiresistor with a tunable sensor response and high sensitivity for representative VOC groups by using thiolated ligand mercaptoundecanoic acid (MUA) functionalized molybdenum disulfide (MoS₂).⁷⁷² Pristine and MUA-conjugated MoS₂ sensing channels exhibited distinctly different responses toward VOCs. These MoS₂ sensors showed high sensitivity to representative VOCs, down to the concentrations of 1 ppm. Incorporation of noble metals, such as Au, Pt, or Pd, can be another effective way of doping 2D materials, as these elements have a high resistance to environmental corrosion and oxidation, which can further improve the stability of the doped semiconducting 2D materials under ambient conditions.^{583,773} Additionally, the catalytic properties of these metals can be further exploited to realize chemical and electrical sensitization of the semiconducting materials.^{773–775} TMDCs are known to non-specifically adsorb a diverse range of VOCs such as hydrocarbons, ketones, and alcohols, showing only a single response behavior upon adsorption of the target gases.⁷⁷² Jung and co-workers found that the sensing performance could be significantly enhanced and tuned

(from “turn on” to “turn off” type response or inversely) by the functionalization of MoS₂ with Au nanoparticles.⁷⁷⁴ Au nanoparticles caused n-doping effect and facilitated electron transfer from Au to MoS₂. Controlling the n-doping effect enabled the tuning of the response of hydrocarbon-based VOCs and oxygen-functionalized compounds. This controllable tuning of the VOC-sensing performance by MoS₂ can be used in early detection technologies, using multichannel sensing systems that have different responses and recognition patterns for target analytes. Umar et al. demonstrated the use of SnS₂ nanoflakes as efficient electron mediators for the fabrication of nitroaniline chemiresistive sensor.⁷⁷⁶ High-sensitivity of $\sim 505.8 \pm 0.02 \text{ mA cm}^{-2} \text{ mol L}^{-1}$ and experimental detection limit of $\sim 15 \times 10^{-6} \text{ mol L}^{-1}$ in a response time of $\sim 10.0 \text{ s}$ with LDR in the range of 15.6×10^{-6} to $0.5 \times 10^{-3} \text{ mol L}^{-1}$ were observed.

TMDCs are very promising candidates for the fabrication of high-performance vapor sensors operated in diverse environments, considering the wide diversity of the TMDCs family and their versatile and tunable properties. There have been extensive applications of TMDCs, especially in gas and vapor sensing. However, there is still significant room for improving the performance of sensing devices with respect to their selectivity, recovery, and large-scale fabrication. It would be beneficial to understand the details of the specific properties of nanostructured TMDCs and the change of the electronic properties upon the interaction with analytes, as the sensing mechanisms of devices based on TMDCs have not been completely explained. Theoretical calculations can be used to identify the appropriate modification of these materials, which would shed insights into material design with optimized performance. The density of active sites in TMDCs can also be improved for selective and effective analyte binding, which can be hopefully realized through the morphological control and post-synthetic modification. The vast number of possibilities in terms of designing and fabricating different members of

TMDCs and integrating them in functional devices to achieve tailored properties for specific applications will still require substantial experimental and theoretical efforts.

4.2.4. Metal Oxides. As demonstrated in previous sections, oxygen ions can be chemically adsorbed on the surface of metal oxides in air to form O_2^- , O^- , and O^{2-} , which withdraw electronic density from the metal oxide surface. When the sensor is exposed to a reducing gas, e.g., ethanol, a reaction occurs between adsorbed oxygen species and the reducing molecules, resulting in a change in the conductance of the sensor.^{151,152}

4.2.4.1. Alcohols. Jing and Zhan fabricated a chemiresistor-based gas sensor by using porous ZnO nanoplates synthesized through a simple microwave process after annealing the plate-like precursor hydrozincite at 400 °C.⁷⁷⁷ The sensor exhibited a strong response to ethanol at relatively high operating temperatures from 250 to 450 °C. The response and recovery times were 32 and 17 s for 100 ppm ethanol, respectively. The results suggested that porous ZnO nanoplates possessed multifunctional properties and thus showed promise in ethanol detection applications.

Zhang et al. investigated ethanol sensing using Au-functionalized ZnO nanoplates.⁷⁷⁸ They demonstrated that the Au/ZnO nanoplate sensors had faster response and recovery as well as enhanced response compared to the pristine ZnO sensor. At 300 °C, the response time of Au/ZnO to 5 ppm ethanol was 13 s, while the response time of ZnO was 135 s. The improved sensor performance was attributed to the unique chemical properties of Au nanoparticles and the electronic metal–support interactions. Zhu and co-workers also built a gas sensors based on the ZnO nanosheets, which exhibited high sensitivity; fast response and recovery time (7 and 19 s at 200 ppm); good selectivity over a series of alkanes, haloalkenes, and aromatics; and appreciable long-term stability (up to 2 months) to 0.01–1000 ppm ethanol at 400 °C (Figure 42a, 42e).⁷⁷⁹ Extremely low concentrations of ethanol (down to 10 ppb) could be readily detected using the same sensor configuration ($S = 3.05 \pm 0.21$). The excellent ethanol-sensing performance of ZnO was mainly attributed to its hierarchical structure with a large specific surface area, abundant mesopores, high crystallinity, the plane-contact between sheets, three-dimensional network architecture, and characteristically small thickness. These hierarchical structures made of sheets, at nanometer thicknesses, allowed rapid gas diffusion, which could consequently give fast sensing response. Chemiresistive sensors made from the flower-like hierarchical structures of ZnO nanosheet also showed shorter response and recovery times than those made with ZnO powder.⁷⁸⁰

Chen and co-workers synthesized multi-layer SnO₂ nanoplates by annealing single-layer SnO nanoplates under O₂ at 700 °C. The resulting thicknesses of the multi-layer SnO₂ ranged from 35 to 80 nm for 3–4 layers. They used the multi-layer SnO₂ nanoplates to fabricate a chemiresistive device capable of detecting 50 ppm ethanol at 350 °C. The observed sensitivity was more than double that of a single-layer SnO₂ nanoplates.⁷⁸¹ The increased sensitivity of the multi-layer nanoplates was attributed to their high surface/volume ratio. Sun used SnO₂ nanosheets synthesized by hydrothermal process, with a thickness of 10 nm, for ethanol sensing (Figure 42b).⁷⁸² At the operating temperature of 250 °C, the sensor showed higher response to ethanol than to the other seven tested VOCs at a concentration of 100 ppm (Figure 42f) and exhibited good linear concentration-dependence in the range

of 20–90 ppm. Zhang and co-workers fabricated an ethanol sensor, using SnO₂ nanosheets synthesized via a hydrothermal method, capable of operating at a low temperature of 165 °C within a wide concentration range of 1–1000 ppm.⁷⁸³ Porous annealed SnO₂ hierarchical nanosheets were also used by Sun et al., which exhibited better ethanol sensing properties compared with the sensor based on conventionally prepared SnO₂ nanoparticles (Figure 42c,g).⁷⁸⁴ Zhang's group also confirmed the high sensitivity of SnO₂ nanosheets to 100 ppm ethanol ($S = 39.6$ at 300 °C), which was approximately 3.6 and 6.1 times higher than that of the nanospheres-like and the nanoparticles, respectively.⁷⁸⁵ The findings from other reports utilizing hierarchical structure consisting of SnO₂ nanosheets indicated that enhanced gas sensing performance for the hierarchical SnO₂ nanosheets toward ethanol may be mainly attributed to the confined effect provided by numerous nano- or micro-interactions regions that provided adequate room for gas–sensing reactions.^{786–789}

Porous NiO nanosheets synthesized by a chemical bath deposition method showed a response to ethanol in a range of 5–500 ppm at a low temperature of 200 °C (Figure 42d,h).⁷⁹⁰ The enhanced gas-sensing performance toward ethanol could be explained in association with the ultrathin nanosheets that are close to Debye length scale.^{790,791} Jia et al. used CuO nanosheets made by mild hydrothermal synthesis for ethanol sensing. The authors demonstrated that the CuO nanosheets, with a thickness of 20–25 nm, had a stable response to ethanol.⁷⁹² Microspheres composed of the nanosheets responded to 100 ppm of ethanol in 13.7 s at a working temperature of 150 °C.⁶⁹⁹

2D nanosheets assembled from Co₃O₄ microspheres had been used for ethanol sensing, demonstrating a strong response of 8.3 and the response time of 16 s toward 100 ppm ethanol gas at 180 °C.⁷⁹³ Chen and co-workers used two-dimensional WO₃ nanoplates as an active element to fabricate chemiresistive devices for alcohols sensing.⁷⁹⁴ They showed that WO₃ nanoplate-based sensors were highly sensitive to alcohols (e.g., methanol, ethanol, isopropanol, and butanol) at moderate operating temperatures (260–360 °C). A response of 70 was realized for ethanol at 200 ppm. The response and recovery times of the WO₃ nanoplate sensors were less than 15 s for all tested alcohols. Liu and co-workers compared the ethanol sensing performance between bulk and 2D nanosheets of MoO₃ using chemiresistive device architecture.⁷⁹⁵ 2D-MoO₃ nanosheets provided a significantly enhanced chemical sensor performance compared with bulk MoO₃, including the increased response from 7 to 33 by using 2D-MoO₃ nanosheet. This superior performance was attributed to the 2D structure with increased surface area and high abundance of reactive sites. TiO₂ nanosheets with exposed [001] high-energy facets were also developed as gas sensing materials.⁷⁹⁶ The sensors displayed a regular n-type response to alcohols with high sensitivity at temperatures above 250 °C but exhibited an abnormal p-type sensing behavior over a wide temperature range spanning from room temperature to 120 °C. The unusual p-type sensing response, unprecedented for the n-type TiO₂ nanomaterials, was attributed to the proton transfer between alcohol molecules and adsorbed water molecules on the surface of TiO₂ nanosheets.

4.2.4.2. Formaldehyde. Liu et al. fabricated novel single-crystalline ZnO nanosheets with porous structure by annealing ZnS(en)_{0.5} (en = ethylenediamine) complex precursor.⁶⁰⁴ The as-prepared ZnO nanosheets were used for the fabrication of

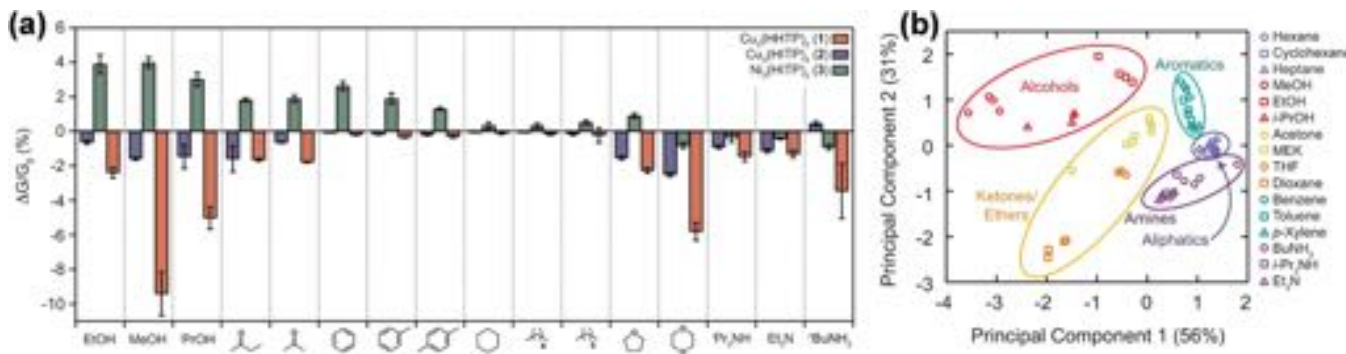


Figure 43. (a) Sensing responses of the MOF array to representative examples from different categories of VOCs, where $\Delta G/G_0$ is the relative response (change in conductance) upon a 30 s exposure to 200 ppm of the VOC vapor. (b) Principal component analysis of the MOF sensor array's responses to VOCs.¹⁷⁴ Reproduced from ref 174. Copyright 2015 American Chemical Society.

gas sensors for indoor air contaminant monitoring. The sensors not only exhibited highly sensitive performance, but also possessed significant long-term stability in sensing formaldehyde. These ZnO nanostructures could be promising for applications in electronic devices for environmental testing.

Guo et al. synthesized ultra-thin hexagonal ZnO nanosheets with a thickness of 17 nm by simple hydrothermal method.⁷⁹⁷ The ultrathin nanosheets exhibited excellent gas sensing properties to formaldehyde at optimal temperature of 350 °C at the concentration of 50 ppm. Zhang and co-workers used porous NiO sheets, obtained from β -Ni(OH)₂ ultrathin nanosheets, for formaldehyde sensing.⁷⁹⁸ The chemiresistive sensors, operating at 240 °C, showed good selectivity toward formaldehyde over other interferents including alkanes, humidity, and hydrogen, as well as a large detection range of 1–1000 ppm. The sensors fabricated from ultrathin SnO₂ nanosheets showed very fast response and recovery (1 and 6 s, respectively) toward 100 ppm of formaldehyde, good repeatability, and selectivity at a relatively low working temperature. The high sensitivity of this device was related to the ultrathin nanosheet morphology of SnO₂ that provided a large specific surface area and direct conduction pathways for analyte interactions.

4.2.4.3. Acetone. Ultrathin porous Co₃O₄ nanosheets have been also used for acetone sensing.⁷⁹⁹ The sensor showed a excellent response to acetone at low operating temperature of 150 °C. The response to 100 ppm acetone reached 11.4 with good reproducibility. The detection limit of the Co₃O₄ nanosheet sensor was lower than 1.8 ppm, which can be relevant for the diagnosis of diabetes.

4.2.4.4. Others. Su and co-workers reported on the detection of volatile and toxic gases including ethanol, ethyl acetate, acetone, xylene, and toluene, using 2D sheet-like CuO nanostructures obtained from the microwave-assisted synthesis.⁸⁰⁰ Porous ZnO nanoplate-based sensors exhibited high response to chlorobenzene at relatively low operating temperatures, from 150 to 250 °C.⁷⁷⁷ 2D SnO₂ nanosheets showed high sensitivity to 200 ppm of ethylene glycol with fast response/recovery (65 s/72 s) and a wide linear dynamic range from 5 to 1000 ppm.⁸⁰¹

Although metal oxides have been widely used in gas sensing because of their advantages, including low cost, easy production, compact size, and simple measuring electronics,^{410,411} the challenge for developing high performance metal oxide sensors still remains. First, many metal oxide sensors demonstrated high signal and low noise levels only at

high temperatures due to the high activation energy of the adsorbed oxygen mediated reaction, which is a critical limitation for the development of low-power devices. Second, although much of the current research is aimed at the investigations of the effects of morphology and crystal size on the sensing behavior, exploration of the crystal plane-dependent properties may be valuable,⁸⁰² because high energy crystal facets easily absorb oxygen species, which are primarily involved in the sensing mechanism of metal oxides toward different gases.^{594,598}

4.2.5. Metal–Organic Frameworks. Dincă and co-workers developed a cross-reactive sensor array through the use of 2D MOFs capable of discriminating several classes of volatile organic compounds (VOCs) containing different functional groups, including alcohols, ketones, ethers, aromatics, amines, and aliphatics.¹⁷⁴ Three structurally related MOFs—Ni₃HITP₂, Cu₃HITP₂, and Cu₃HHTP₂—were used to fabricate chemiresistive sensors by drop-casting the dispersion of each MOF onto interdigitated gold electrodes. The chemiresistive responses of the devices toward various VOC vapors at 200 ppm concentration levels are shown in Figure 43a. Polar VOCs produced higher response, while the exposure to aliphatic hydrocarbons showed no appreciable signal. These observations may be related to the reductive or oxidative nature of tested analytes and their varied affinities for the surface of 2D conductive MOFs.^{418,427,623,803} Both “turn-on” and “turn-off” type responses were observed for a single analyte when a different MOF was used, which was proposed to be related to the different semiconductor characteristic of the material.¹⁷⁴ Using statistical analysis method, PCA, it was shown that the chemiresistive responses could be used to distinguish between five categories of VOCs with >90% accuracy (Figure 43b). Recently, Behrens and co-workers prepared thin and homogeneous films by spray-coating water-based dispersions of Cu₃HHTP₂ MOF on glass and on polymer substrates.⁸⁰⁴ In the films, the nanoplatelets of the MOF were oriented parallel to the substrate with intimate contact. This fabrication method led to a high electrical conductivity combined with an easily accessible pore system. The coatings deposited with Cu₃HHTP₂ plates showed excellent response to methanol vapor.⁸⁰⁴

The mechanisms of VOCs sensing with 2D MOFs are still under investigation, but the preliminary results,^{174,418,427,623,803} reported to date, suggest that MOF-based chemiresistors are promising platforms in the field of sensing.⁴²¹ Rational tuning of chemical and electronic structure of the MOF may lead to

the development of improved sensor materials with excellent sensitivity and selectivity. Conductive MOFs hold the promise for engineering both its surface chemistry and electronic property through a bottom-up strategy and thus provide an exciting and powerful platform for the development of new sensing technologies.^{89,416,421}

4.2.6. Other 2D Materials. $g\text{-C}_3\text{N}_4$ planes consist of highly ordered triazine units linked through planar tertiary amino groups, which contain many coordination sites called “nitrogen pots” where the nitrogen lone-pair electrons can interact with the metal ions. The weak van der Waals layered structure of $g\text{-C}_3\text{N}_4$ is beneficial for the formation of intercalation compounds with improved physicochemical properties. These properties of $g\text{-C}_3\text{N}_4$ would create new opportunities for the development of intercalated $g\text{-C}_3\text{N}_4$ nanosheets in sensing devices. Mesoporous $g\text{-C}_3\text{N}_4$ decorated with Ag NPs was incorporated into impedance-based device by Tomer et al. for sensitive detection of humidity in the 11–98% RH range with the response time of 3 s and recovery time of 1.4 s at room temperature.⁸⁰⁵ The presence of Ag NPs improved the sensing response by 4 \times compared with nonfunctionalized mesoporous $g\text{-C}_3\text{N}_4$. These impressive features originated from not only the planar morphology of $g\text{-C}_3\text{N}_4$, but also unique physical affinity and favorable electronic band positions of Ag that facilitated water adsorption and charge transport.⁸⁰⁶ Using a similar strategy, Dong and co-workers fabricated a humidity sensor composed of $g\text{-C}_3\text{N}_4$ with intercalated LiCl guest molecules.⁸⁰⁷ The resulting devices exhibited ultra-fast response and recovery times of 0.9 and 1.4 s, respectively, to changing concentrations of humidity (11–95% RH). The improved sensing response was ascribed to an increase in the concentration of protons in 2D $g\text{-C}_3\text{N}_4$ as a function of enhanced H_2O adsorption onto the surface of LiCl decorated 2D nanostructures. Choi and co-workers explored the potential of a *h*-BN and poly(ethylene oxide) composite in humidity monitoring through impedance-based sensing. The resulting device produced response to humidity in the 0% to 90% RH range with response time of 2.7 s and minimal interference from O_2 , N_2 , and CH_4 .⁸⁰⁸

Chemical sensors have been historically fabricated on solid substrates such as silicon wafers and indium tin oxide-coated glass, which are not directly amenable for integration into wearable electronics without further development. The commercially available metal oxide sensors usually operate at relatively high temperature (over 100 °C), which significantly limits their application in wearable technologies.^{809,810} It is thus essential to explore new materials capable of operating at room temperature and that can be integrated onto flexible substrates. To obtain high sensitivity in resistive sensor mode, the sensory materials should be able to provide low electrical noise and strong analytical signal. MXenes, such as $\text{Ti}_3\text{C}_2(\text{OH})_2$, not only possess metallic conductivity,⁴⁶² but also have abundant functional groups at the outer surface (Figure 44a).⁸¹¹ This combination renders them highly attractive for chemical sensor development with a high signal-to-noise ratio, as the high coverage of functional groups allows effective and strong interactions with targeted analytes; meanwhile, the high metallic conductivity intrinsically leads to a low signal noise. Kim and co-workers demonstrated, for the first time, the room temperature gas sensing of ethanol, methanol, acetone, and ammonia using $\text{Ti}_3\text{C}_2\text{T}_x$ devices.²⁰³ The $\text{Ti}_3\text{C}_2\text{T}_x$ sensors successfully detected ethanol, methanol, and acetone vapors at room temperature showing a p-type

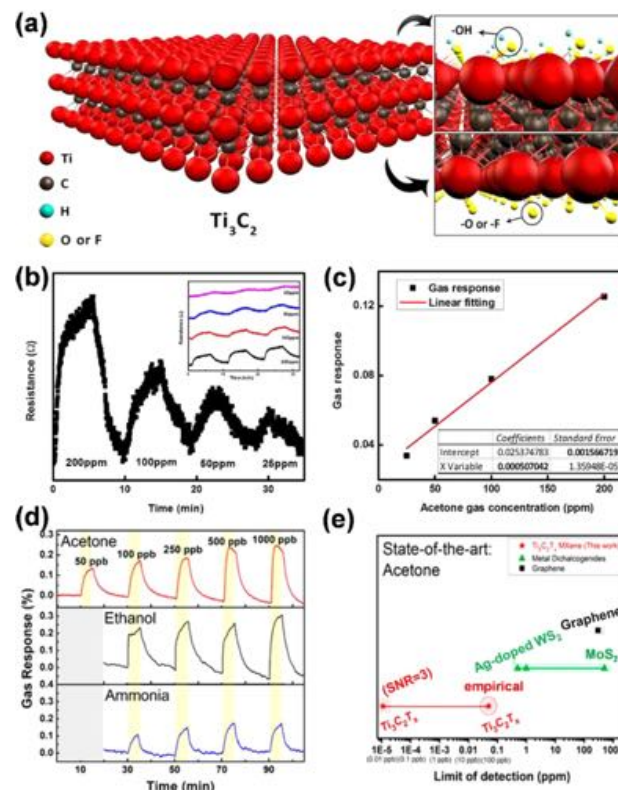


Figure 44. (a) Schematic representation of $\text{Ti}_3\text{C}_2\text{T}_x$ structure and different functional groups on the surface of $\text{Ti}_3\text{C}_2\text{T}_x$ nanosheets. (b) Combined resistance profile of a $\text{Ti}_3\text{C}_2\text{T}_x$ sensor as a function of the acetone concentration.²⁰³ Reproduced from ref 203. Copyright 2017 American Chemical Society. (c) Relationship between gas response and acetone concentration.²⁰³ Reproduced from ref 203. Copyright 2017 American Chemical Society. (d) Resistance variation versus time upon exposure to acetone (top), ethanol (middle), and ammonia (bottom) in 50–1000 ppb. (e) State-of-the-art diagram of the LOD for room temperature sensors based on 2D materials to detect acetone, showing $\text{Ti}_3\text{C}_2\text{T}_x$ MXene has the smallest LOD.⁶²⁵ Reproduced from ref 625. Copyright 2018 American Chemical Society.

response (Figure 44b,c). The theoretical limit of detection for acetone was calculated at 9.27 ppm, demonstrating good performance compared to other sensors based on 2D materials, including graphene and MoS₂.^{166,812} The proposed sensing mechanism involved the interactions between the majority charge carriers of $\text{Ti}_3\text{C}_2\text{T}_x$ and VOCs. This study opened new directions for the potential applications of this $\text{Ti}_3\text{C}_2\text{T}_x$ for VOC-sensing applications.

The detection of VOCs at the ppb level is critical for the early diagnosis of diseases.^{813,814} Kim et al. further experimentally demonstrated that MXenes could act as metallic channels in chemiresistive devices with ultrahigh sensitivity for acetone, ethanol, and ammonia (Figure 44d). $\text{Ti}_3\text{C}_2\text{T}_x$ MXene sensors exhibited a very low limit of detection of 50 ppb for acetone with SNR of 25.6 at room temperature (Figure 44e). Also, the low magnitude of noise resulted in a signal-to-noise ratio of 2 orders of magnitude higher than that of other 2D materials. DFT calculations showed that $\text{Ti}_3\text{C}_2(\text{OH})_2$ displayed strong binding energy, which was more than twice that of other 2D materials, like MoS₂, graphene, and BP. These outstanding gas adsorption properties of the hydroxyl groups of $\text{Ti}_3\text{C}_2\text{T}_x$ may largely contribute to the high sensitivity of this material. This result provided insight

Table 4. Summary of Sensing Performances for Volatile Compounds by 2D Materials^a

analyte	material	architecture	LOD	experimental range	sensing environment	ref
2-butanone	M ₃ HXTP ₂ (Cu ₃ HHTP ₂ , Cu ₃ HITP ₂ , Ni ₃ HITP ₂)	chemiresistor: Au/M ₃ HXTP ₂ /Au	N/A	200 ppm	N ₂ , r.t.	174
acetaldehyde	MoS ₂ -Au	chemiresistor: Au/MoS ₂ /Au/Au	N/A	1000 ppm	N ₂	774
acetic acid	Gr-Au NPs or Pt NPs	chemiresistor: Au/G-AuNPs or Pt NPs/Au	50 ppm	50–200 ppm	air _d , r.t.	742
acetone	Co ₃ O ₄	chemiresistor: Ag-Pd/Co ₃ O ₄ /Ag-Pd	1.8 ppm	1–100 ppm	air, 150 °C	799
acetone	GO-Co ₃ O ₄ NFs-Ir NPs	chemiresistor: Au/GO-Co ₃ O ₄ NFs-Ir NPs/Al/Au	120 ppb	1–5 ppm	air, 90% RH, 300 °C	723
acetone	Gr	FET: Si/thermal oxide/Gr/Ti-Au/Ti-Au	N/A	N/A	air, r.t.	740
acetone	Gr-ZnFe ₂ O ₄	chemiresistor	N/A	1–1000 ppm	180 °C	724
acetone	M ₃ HXTP ₂ (Cu ₃ HHTP ₂ , Cu ₃ HITP ₂ , Ni ₃ HITP ₂)	chemiresistor: Au/M ₃ HXTP ₂ /Au	N/A	200 ppm	N ₂ , r.t.	174
acetone	MoS ₂	chemiresistor: Ti-Au/MoS ₂ /Ti-Au	500 ppm	50–5000 ppm	N ₂ , r.t.	166
acetone	MoS ₂ -mercaptoundecanoic acid	chemiresistor: Au-Cr/MoS ₂ -mercaptoundecanoic acid/Au-Cr	<1 ppm	1–1000 ppm	N ₂ , 25 °C	772
acetone	MoS ₂ -Au	chemiresistor: Au/MoS ₂ -Au/Au	N/A	1000 ppm	N ₂	774
acetone	rGO	FET: Si/SiO ₂ /rGO/Au/Au	N/A	200 ppm	air, r.t.	725
acetone	rGO-SnO ₂	chemiresistor: Au/rGO-SnO ₂ /Au	100 ppb	1–5 ppm	air, 85–95% RH, 350 °C	560
acetone	SnO ₂ -Eu	chemiresistor: Au-Ti/SnO ₂ -Eu/Au-Ti	131 ppb	5–100 ppm	30–70% RH, 210 °C	815
acetone	Ti ₃ C ₂ T _x	chemiresistor: Pt/Ti ₃ C ₂ T _x /Pt	9.27 ppm	25–200 ppm	air, r.t.	203
acetone	Ti ₃ C ₂ T _x	chemiresistor: Au/Ti ₃ C ₂ T _x /Au	0.011 ppb	50–1000 ppb	N ₂ , 25 °C	625
acetone	WS ₂ -Ag	chemiresistor: Cr-Au/WS ₂ -Ag/Cr-Au	25 ppm	0.5–10 ppm	air _d , 100 °C	589
acetonitrile	MoS ₂	FET: Si/SiO ₂ /MoS ₂ /Au/Au	N/A	N/A	N/A	771
benzene	Gr-ODA	chemiresistor: Au/Gr-ODA/Au	10 ppm	5–100 ppm	1 vol % ethanol	726
benzene	M ₃ HXTP ₂ (Cu ₃ HHTP ₂ , Cu ₃ HITP ₂ , Ni ₃ HITP ₂)	chemiresistor: Au/M ₃ HXTP ₂ /Au	N/A	200 ppm	N ₂ , r.t.	174
chlorobenzene	Gr	FET: Si/thermal oxide/Gr/Ti-Au/Ti-Au	N/A	N/A	air, r.t.	740
chlorobenzene	ZnO	chemiresistor: Pt/ZnO/Pt	N/A	100–250 ppm	air, 200 °C	777
chloroform	GO-PPr	chemiresistor: Pt/GO-PPr/Pt	400 ppm	400–1000 ppm	N ₂ , r.t.	816
chloroform	Gr	PN diode: Au-Cr/Gr-Si/Au-Cr	N/A	N/A	r.t.	737
chloroform	MoS ₂	FET: Si/SiO ₂ /MoS ₂ /Au/Au	N/A	N/A	N/A	771
chloroform	Gr	FET: Si/thermal oxide/Gr/Ti-Au/Ti-Au	N/A	N/A	air, r.t.	740
cyclohexane	Gr-ODA	chemiresistor: Au/Gr-ODA/Au	5 ppm	5–100 ppm	1 vol % ethanol	726
dichloromethane	Gr	FET: Si/thermal oxide/Gr/Ti-Au/Ti-Au	N/A	N/A	air, r.t.	740
DMA	GO	chemiresistor: Ti-Au/Gr/Ti-Au	N/A	N/A	N/A	733
DNT	rGO	chemiresistor: Ti-Au/rGO/Ti-Au	0.1 ppb	N/A	N ₂	702
DMMP	Gr	chemiresistor: Ag/Gr/Ag	N/A	5–15 ppm	N/A	731
DMMP	Gr	FET: Si/SiO ₂ /Gr/Au/Au	N/A	N/A	N/A	692
DMMP	Gr	FET: Si/thermal oxide/Gr/Ti-Au/Ti-Au	0.64 ppb	N/A	air, r.t.	740
DMMP	rGO	chemiresistor: Pt/rGO/Pt	N/A	10–60 ppm	N ₂ , 25 °C	729
DMMP	rGO	chemiresistor: Cr-Au/rGO/Cr-Au	N/A	5–80 ppm	air _d , 25 °C	730
DMMP	rGO	chemiresistor: Ti-Au/rGO/Ti-Au	5 ppb	N/A	N ₂	702
ethanol	Co ₃ O ₄	chemiresistor: Pt/Co ₃ O ₄ /Pt	N/A	5–500 ppm	air, 180 °C	793
ethanol	CuO	chemiresistor: Au/CuO/Au	N/A	10–1000 ppm	air, 260 °C	800
ethanol	Gr-AuNPs or Pt NPs	chemiresistor: Au/G-Au NPs or Pt NPs/Au	50 ppm	50–200 ppm	air _d , r.t.	742
ethanol	GO-OA-F8T2	FET: Si/SiO ₂ /GO-OA-F8T2/Au/Au	N/A	N/A	r.t.	714
ethanol	GO-phenyl	capacitor: Au/GO-phenyl/Au	N/A	70–1000 ppm	r.t.	739
ethanol	Gr	FET: Si/SiO ₂ /Gr/Pt/Pt	N/A	N/A	N/A	713
ethanol	Gr-Fe ₂ O ₃	chemiresistor: Pt/Gr-Fe ₂ O ₃ /Pt	N/A	1–1000 ppm	280 °C	715
ethanol	M ₃ HXTP ₂ (Cu ₃ HHTP ₂ , Cu ₃ HITP ₂ , Ni ₃ HITP ₂)	chemiresistor: Au/M ₃ HXTP ₂ /Au	N/A	200 ppm	N ₂ , r.t.	174
ethanol	MoO ₃	chemiresistor: Ag-Pd/MoO ₃ /Ag-Pd	N/A	10–500 ppm	air, 300 °C	795

Table 4. continued

analyte	material	architecture	LOD	experimental range	sensing environment	ref
ethanol	MoS ₂	FET: Si–SiO ₂ /Oxide/MoS ₂ /Au/Au	N/A	N/A	N/A	771
ethanol	MoS ₂	chemiresistor: Cr–Au/MoS ₂ –Si/ Cr–Au	1 ppm	5–40 ppm	r.t.	769
ethanol	MoS ₂	FET: Si/SiO ₂ / MoS ₂ /metal/matal	N/A	N/A	r.t.	770
ethanol	MoS ₂ – mercaptoundecanoic acid	chemiresistor: Au–Cr/MoS ₂ – mercaptoundecanoic acid/Au–Cr	<10 ppm	1–1000 ppm	N ₂ , 25 °C	772
ethanol	MoS ₂ –SnO ₂	chemiresistor: Au/MoS ₂ –SnO ₂ /Au	N/A	50–1000 ppm	air, 280 °C	767
ethanol	NiO	chemiresistor	N/A	5–500 ppm	air, 200 °C	790
ethanol	NiO	chemiresistor: Au/NiO/Au	N/A	100–700 ppm	air, 300 °C	791
ethanol	rGO	FET: Si/SiO ₂ /rGO/Ti–Pt/Ti–Pt	N/A	N/A	N/A	713
ethanol	SnO ₂	chemiresistor: Au/SnO ₂ /Au	N/A	1.5–50 ppm	air, 350 °C	781
ethanol	SnO ₂	chemiresistor: Au/SnO ₂ /Au	N/A	20–90 ppm	air, 250 °C	782
ethanol	SnO ₂	chemiresistor: Au/SnO ₂ /Au	N/A	1–1000 ppm	air, 165 °C	783
ethanol	SnO ₂	chemiresistor: Au/SnO ₂ /Au	N/A	100 ppm	air, 300 °C	784
ethanol	SnO ₂	chemiresistor: Au/SnO ₂ /Au	N/A	5–200 ppm	air, 300 °C	786
ethanol	SnO ₂	chemiresistor	N/A	10–100 ppm	air, 250 °C	787
ethanol	SnO ₂	chemiresistor: Au/SnO ₂ /Au	1.37 ppm	50–300 ppm	air, 250 °C	788
ethanol	SnO ₂	chemiresistor: Au/SnO ₂ /Au	<5 ppm	5–500 ppm	N/A	789
ethanol	SnS ₂	chemiresistor: Cu/SnS ₂ /Cu	N/A	N/A	r.t.	393
ethanol	Ti ₃ C ₂ T _x	chemiresistor: Pt/Ti ₃ C ₂ T _x /Pt	N/A	100 ppm	air, r.t.	203
ethanol	Ti ₃ C ₂ T _x	chemiresistor: Au/Ti ₃ C ₂ T _x /Au	<1 ppb	100–100 ppb	N ₂ , 25 °C	625
ethanol	TiO ₂	chemiresistor: Ag–Pd/TiO ₂ /Ag–Pd	N/A	200–6000 ppm	air, r.t./310 °C	796
ethanol	WO ₃	chemiresistor: Pt/WO ₃ /Pt	N/A	10–300 ppm	air, 300 °C	794
ethanol	WS ₂	FET: Si/SiO ₂ / WS ₂ /Au/Au	N/A	N/A	r.t.	768
ethanol	ZnO	chemiresistor: Pt/ZnO/Pt	N/A	100–250 ppm	air, 380 °C	777
ethanol	ZnO	chemiresistor	10 ppb	0.01–1000 ppm	air, 400 °C	779
ethanol	ZnO–Au	chemiresistor: Pt/ZnO–Au/Pt	N/A	50–800 ppm	air, 300 °C	778
ethyl acetate	CuO	chemiresistor: Au/CuO/Au	N/A	10–1000 ppm	air, 260 °C	800
ethylbenzene	Gr–ODA	chemiresistor: Au/Gr–ODA/Au	3 ppm	5–100 ppm	1 vol % ethanol	726
ethylene glycol	SnO ₂	chemiresistor: Au/SnO ₂ /Au	1.3758 ppm	5–1000 ppm	air _D , 220 °C	801
formaldehyde	Gr–PMMA	chemiresistor: Pt/Gr–PMMA/Pt	10 ppb	0.05–5.0 ppm	N ₂ , r.t.	718
formaldehyde	NiO	chemiresistor: Au/NiO/Au	100 ppb	1–1000 ppm	air, 240 °C	798
formaldehyde	rGO–ZnO	diode: Au–Ti/rGO–ZnO/Au–Ti	0.875 ppm	120 ppb to 1 ppm	air _D , r.t.	719
formaldehyde	ZnO	chemiresistor: Au/ZnO/Au	N/A	50–500 ppm	air _D , 250 °C	604
formaldehyde	ZnO	chemiresistor: Au/ZnO/Au	N/A	50 ppm	air, 350 °C	797
H ₂ O	BP	FET: Si/SiO ₂ /BP/Au/Au	21% RH	21–83% RH	Ar	752
H ₂ O	BP	chemiresistor: Au/BP/Au	N/A	10–85% RH	air, 25 °C	749
H ₂ O	BP	FET: Si/SiO ₂ /Gr–DNA/Ti–Au/ Ti–Au	N/A	11–97%	25 °C	750
H ₂ O	BP	FET: glass/ITO/BP/Ti–Au/Ti–Au	N/A	11–97%	r.t.	751
H ₂ O	BP QDs	chemiresistor: Al/BP/Al	N/A	15–90% RH	air, 21 °C	817
H ₂ O	GO	chemiresistor: Ag/GO/Ag	30% RH	30–80% RH	air, 10–40 °C	678
H ₂ O	GO	capacitor: electrode/GO/electrode	N/A	15–95% RH	25 °C	679
H ₂ O	GO	chemiresistor: Au/GO/Au	N/A	30–90% RH	air, 25 °C	685
H ₂ O	GO	chemiresistor: Au/GO/Au	N/A	11–95% RH	r.t.	687
H ₂ O	GO–PSS	capacitor: Ag/GO–PSS/Ag	N/A	0–80% RH	air	698
H ₂ O	GO–EA or HA	chemiresistor: Au/GO–EA/Au	N/A	20–90%	air, r.t.	700
H ₂ O	GO–phenyl	capacitor: Au/GO–phenyl/Au	<6%	6–97% RH	r.t.	739
H ₂ O	Gr	capacitor: Gr/analyte/Gr	N/A	0–25 w/w% in ethanol	ethanol	689
H ₂ O	Gr	varactor: Si/SiO ₂ /Gr/Ti–Pd–Au/ Ti–Pd–Au	N/A	1–97% RH	air, 23 °C	691
H ₂ O	Gr	varactor: Si/SiO ₂ /Gr/metal/metal	N/A	20–90% RH	air, r.t.	695
H ₂ O	Gr	FET: Si/SiO ₂ /Gr/metal/metal	N/A	5–90% RH	r.t.	696
H ₂ O	Gr	chemiresistor: Ti–Au/Gr/Ti–Au	N/A	1–96% RH	air, r.t.	697
H ₂ O	Gr–PEI	FET: Si/SiO ₂ /Gr–PEI/Au–Ti/ Au–Ti	N/A	10–60% RH	r.t.	364
H ₂ O	GO–Au NPs–MPTMOS	chemiresistor: Au/GO–AuNPs– MPTMOS/Au	N/A	20–90% RH	air, r.t.	818
H ₂ O	Gr–PPy	chemiresistor: Au/Gr–PPy/Au	N/A	12–90% RH	air, r.t.	699
H ₂ O	MoS ₂	chemiresistor: Pt/MoS ₂ /Pt	N/A	0–60% RH	N/A	757
H ₂ O	rGO–PEDOT	chemiresistor	N/A	0–98% RH	air, r.t.	690

Table 4. continued

analyte	material	architecture	LOD	experimental range	sensing environment	ref
H ₂ O	rGO–PDPA	chemiresistor: Cu–Ni/rGO–PDPA/Cu–Ni	N/A	11–97% RH	air, r.t.,	686
H ₂ O	SnS ₂	chemiresistor: Cu/SnS ₂ /Cu	N/A	11–97% RH	r.t.	393
H ₂ O	VS ₂	chemiresistor: Au/VS ₂ /Au	N/A	0–100% RH	25 °C	756
H ₂ O	WS ₂	FET: Si/SiO ₂ / WS ₂ /Ag/Ag	N/A	11.3–97% RH	r.t.	759
H ₂ O	WS ₂	chemiresistor: Gr/WS ₂ /Gr	N/A	0–90% RH	N ₂ , r.t.	760
HCN	Gr QDs	chemiresistor: Pt/Gr QDs/Pt	0.6 ppm	1–100 ppm	air, 25 °C	705
HCN	rGO	chemiresistor: Ti–Au/rGO/Ti–Au	70 ppb	N/A	N ₂	702
hexane	GO–PPr	chemiresistor: Pt/GO–PPr/Pt	<200 ppm	200–900 ppm	N ₂ , RT	816
hexanoic acid	Gr–DNA	FET: Si/SiO ₂ /Gr–DNA/Au–Ti–Pd/Au–Ti–Pd	N/A	3–63 ppm	air, 33% RH	741
Hg	MoS ₂ –PANI	chemiresistor: Pt/MoS ₂ –PANI/Pt	N/A	0.55–452.51 mg m ⁻³	r.t.	763
humidity	MoS ₂	FET: Si/SiO ₂ /MoS ₂ /Ti–Au/Ti–Au	N/A	4–84% RH	N ₂ , r.t.	101
isopropanol	M ₃ HXTP ₂ (Cu ₃ HHTP ₂ , Cu ₃ HITP ₂ , Ni ₃ HITP ₂)	chemiresistor: Au/M ₃ HXTP ₂ /Au	N/A	200 ppm	N ₂ , r.t.	174
isopropyl alcohol	SnS ₂	chemiresistor: Cu/SnS ₂ /Cu	N/A	N/A	r.t.	393
liquid petroleum gas	Gr	chemiresistor: Ag/Gr/Ag	4 ppm	N/A	air, r.t.	544
melamine	Gr	FET: Si/SiO ₂ /rGO/Au/Au	N/A	N/A	175 °C	230
methanol	BP	chemiresistor: Au/BP/Au	28 ppm	380–1900 ppm	r.t.	755
methanol	GO–PEDOT–PSS	chemiresistor: Au/GO–PEDOT–PSS/Au	N/A	35–1000 ppm	r.t.	738
methanol	Gr	FET: Si/SiO ₂ /Gr–Au/Cr–Au	N/A	N/A	r.t.	716
methanol	Gr	PN diode: Au–Cr/Gr–Si/Au–Cr	N/A	N/A	r.t.	737
methanol	M ₃ HXTP ₂ (Cu ₃ HHTP ₂ , Cu ₃ HITP ₂ , Ni ₃ HITP ₂)	chemiresistor: Au/M ₃ HXTP ₂ /Au	N/A	200 ppm	N ₂ , r.t.	174
methanol	MoS ₂	FET: Si/SiO ₂ /MoS ₂ /Au/Au	N/A	N/A	N/A	771
methanol	SnS ₂	chemiresistor: Cu/SnS ₂ /Cu	N/A	N/A	r.t.	393
methanol	Ti ₃ C ₂ T _x	chemiresistor: Pt Ti ₃ C ₂ T _x /Pt	N/A	100 ppm	air, r.t.	203
<i>m</i> -xylene	Gr–ODA	chemiresistor: Au/Gr–ODA/Au	3 ppm	5–100 ppm	1 vol % ethanol	726
DMF	Gr	FET: Si/thermal oxide/Gr/Ti–Au/Ti–Au	N/A	N/A	air, r.t.	740
<i>n</i> -butylamine	M ₃ HXTP ₂ (Cu ₃ HHTP ₂ , Cu ₃ HITP ₂ , Ni ₃ HITP ₂)	chemiresistor: Au/M ₃ HXTP ₂ /Au	N/A	200 ppm	N ₂ , r.t.	174
<i>n</i> -hexane	MoS ₂ –mercaptoundecanoic acid	chemiresistor: Au–Cr/MoS ₂ –mercaptoundecanoic acid/Au–Cr	<1 ppm	1–1000 ppm	N ₂ , 25 °C	772
nitroaniline	SnS ₂	LSV: SnS ₂ /GCE	15 × 10 ⁻⁶ mol/L	15.6 × 10 ⁻⁶ to 0.5 × 10 ⁻³ mol/L	N/A	776
NMP	GO	chemiresistor: Ti–Au/Gr/Ti–Au	N/A	N/A	N/A	733
octanoic acid	Gr–DNA	FET: Si/SiO ₂ /Gr–DNA/Au–Ti–Pd/Au–Ti–Pd	1 ppm	N/A	air, 33% RH	741
<i>o</i> -xylene	Gr–ODA	chemiresistor: Au/Gr–ODA/Au	3 ppm	5–100 ppm	1 vol % ethanol	726
phenol	GO–phenyl	capacitor: Au/GO–phenyl/Au	N/A	70–1000 ppm	r.t.	739
phenol	Gr	PN diode: Au–Cr/Gr–Si/Au–Cr	N/A	1 mM to 1 M	r.t.	737
propanal	MoS ₂ –mercaptoundecanoic acid	chemiresistor: Au–Cr/MoS ₂ –mercaptoundecanoic acid/Au–Cr	1 ppm	1–1000 ppm	N ₂ , 25 °C	772
propanal	Ti ₃ C ₂ T _x	chemiresistor: Au/Ti ₃ C ₂ T _x /Au	<1 ppb	N/A	N ₂ , 25 °C	625
propionic acid	Gr–DNA	FET: Si/SiO ₂ /Gr–DNA/Au–Ti–Pd/Au–Ti–Pd	N/A	50–1000 ppm	air, 33%RH	741
<i>p</i> -xylene	Gr–ODA	chemiresistor: Au/Gr–ODA/Au	3 ppm	5–100 ppm	1 vol % ethanol	726
<i>p</i> -xylene	M ₃ HXTP ₂ (Cu ₃ HHTP ₂ , Cu ₃ HITP ₂ , Ni ₃ HITP ₂)	chemiresistor: Au/M ₃ HXTP ₂ /Au	N/A	200 ppm	N ₂ , r.t.	174
tetrahydrofuran	M ₃ HXTP ₂ (Cu ₃ HHTP ₂ , Cu ₃ HITP ₂ , Ni ₃ HITP ₂)	chemiresistor: Au/M ₃ HXTP ₂ /Au	N/A	200 ppm	N ₂ , r.t.	174
tetrahydrofuran	M ₃ HXTP ₂ (Cu ₃ HHTP ₂ , Cu ₃ HITP ₂ , Ni ₃ HITP ₂)	chemiresistor: Au/M ₃ HXTP ₂ /Au	N/A	200 ppm	N ₂ , r.t.	174
toluene	GO–PPr	chemiresistor: Pt/GO–PPr/Pt	24 ppm	24–500 ppm	N ₂ , r.t.	816
toluene	Gr–ODA	chemiresistor: Au/Gr–ODA/Au	5 ppm	5–100 ppm	1 vol % ethanol	726
toluene	M ₃ HXTP ₂ (Cu ₃ HHTP ₂ , Cu ₃ HITP ₂ , Ni ₃ HITP ₂)	chemiresistor: Au/M ₃ HXTP ₂ /Au	N/A	200 ppm	N ₂ , r.t.	174
toluene	MoS ₂	FET: Si–SiO ₂ /Oxide/MoS ₂ /Au/Au	N/A	N/A	N/A	771
toluene	MoS ₂ –mercaptoundecanoic acid	chemiresistor: Au–Cr/MoS ₂ –mercaptoundecanoic acid/Au–Cr	<10 ppm	1–1000 ppm	N ₂ , 25 °C	772
triazine	Gr	FET: Si/SiO ₂ /rGO/Ti–Au/Ti–Au	N/A	N/A	140 °C	230
triethylamine	MoS ₂	chemiresistor: Ti–Au/MoS ₂ /Ti–Au	10 ppb	50–5000 ppm	N ₂ , r.t.	166

Table 4. continued

analyte	material	architecture	LOD	experimental range	sensing environment	ref
triethylamine	MoS ₂	chemiresistor: Ti–Au/MoS ₂ /Ti–Au	10 ppb	1–100 ppm	N ₂ , r.t.	166
triethylamine	MoS ₂	FET: Si/SiO ₂ / MoS ₂ /Ag/Ag	N/A	N/A	r.t.	764
triethylamine	rGO-nylon-6	chemiresistor: Au/rGO-nylon-6/Au	0.39 mg/L	23–230 mg/L	50% RH, r.t.	745

^aNote: chemiresistor configuration is described in a way of electrode/conductive material/electrode. FET is described in a way of gate electrode/insulator/channel material/source electrode/drain electrode. Diode is described in a way of electrode/semiconductor/electrode. N/A, not available. Air_D, dry air and r.t., room temperature.

into utilizing highly functionalized metallic sensing channels for the development of sensing technologies.

Although the use of MXenes for volatile sensing is at a very early stage, MXenes are exhibiting its great potential in this area with unique chemical and physical properties being recently realized.^{177,811} As the surface of MXenes is covered with functional groups, selectivity toward certain analytes may be further controlled by surface functionalization or defect engineering. It is noteworthy that only one type of MXenes is currently studied for volatile sensing,⁶²⁵ and a large family of other MXenes can be potentially employed as highly sensitive sensors. Nevertheless, the elegant combination of the abundant surface chemistry and their metallic conductivity, which are critically needed in the electrically-transduced devices, will ideally result in more applications of MXenes in sensing of volatile molecules in the future.^{203,625}

4.3. Detection of Ions

In recent years, there has been an increasing ecological and public health concern associated with environmental contamination of global natural resources. In particular, the discharge of metallic contaminants from industrial processes, most typically in the form of heavy metal ions, led to extensive contamination of drinking water and agricultural products.⁸¹⁹ Therefore, there is a big commercial demand to manufacture rapid, sensitive, and simple analytical platforms for the detection and monitoring of metallic contaminants in water and soil.⁸²⁰ In addition, ionic electrolytes are essential for various bodily functions such as cell functioning and cell signaling. Their imbalance can result in a number of life threatening conditions including cardiac arrest, neurological disorders, or kidney failure. It is, thus, important to develop portable point-of-care diagnostic devices that can provide real-time information about electrolyte concentrations in biological samples.⁸²¹ 2D materials have been identified as a new class of materials that can be used to construct sensitive detection platforms for sensing ionic analytes based on various electrochemical techniques.⁸²¹

4.3.1. Graphene and Graphene Oxides. *4.3.1.1. Heavy Metals.* Graphene and graphene oxide electrodes are capable of providing sensitive electrode interfaces due to the large surface area, fast electron transfer and mass transport rates.^{821,822} Graphene-based electrochemical sensors, for the analysis of heavy metals have achieved excellent analytical performance, surpassing those obtained either by using carbon nanotubes or metal nanoparticles.^{823–825}

A series of graphene nanocomposite modified electrodes have been used for Pb²⁺ and Cd²⁺ detection. Zhu et al. reported on the simultaneous detection of Pb²⁺ and Cd²⁺ ions in spring water samples using square wave anodic stripping voltammetry (SWASV) at a gold nanoparticle-cysteine graphene functionalized bismuth film electrode.⁸²⁶ They observed linear concentration dependence in the range

between 0.50 and 40 $\mu\text{g L}^{-1}$ with the LODs of 0.10 $\mu\text{g L}^{-1}$ for Cd²⁺ and 0.05 $\mu\text{g L}^{-1}$ for Pb²⁺ ions and high selectivity to target analytes against eight other cationic species. The improvement in stripping peaks of Pb²⁺ and Cd²⁺ resulted from the enlarged activated surface area and good electrical conductivity of the Au–Gr scaffold together with high affinity of cysteine to metal cations. A liquid-gated field-effect transistor chemical vapor grown graphene film as the conducting channel could detect Pb²⁺ at concentrations as low as 0.1 pM.⁸²⁷ To induce high sensitivity and selectivity to Pb²⁺ ions, the surface of graphene was decorated with AuNP, which served as the anchoring sites for covalent attachment of thiolated DNAzyme molecules. The fabricated devices responded to changing concentration of Pb²⁺ in a dose-dependent manner, where the Dirac point shifted to a more positive voltage at higher concentrations of Pb²⁺ ions.⁸²⁷ Park and co-workers further improved sensitivity to Pb²⁺ and Cd²⁺ ions by micropatterning rGO onto Si/SiO₂ wafers using lithography followed by electrodeposition of bismuth to form rGO–Bi nanocomposite electrodes.⁸²⁸ The fabricated microsensor, using SWASV, responded linearly from 1.0 to 120.0 $\mu\text{g L}^{-1}$ for both metal, with LODs of 0.4 and 1.0 $\mu\text{g L}^{-1}$ for Pb²⁺ and Cd²⁺, respectively. The improved performance was due to the efficient electrocatalytic activity of GO, which facilitated the electron transfer kinetics at the electrode surface. Li et al. fabricated Nafion-graphene electrodes for the detection of Pb²⁺ and Cd²⁺ using differential pulse anodic stripping voltammetry (DPASV).⁸²⁹ The LODs for both analytes were estimated to be at 0.02 $\mu\text{g L}^{-1}$. The practical application of this sensing platform was further verified in the water sample analysis. The authors indicated that the strong adsorptive capability and high specific surface area of graphene together with cationic exchange capacity of Nafion was responsible for the enhanced selectivity to metal detection.

Willemse et al. also used a graphene–Nafion modified glassy carbon electrode (GCE) with an in situ plated mercury film on the surface as electrochemical sensing platform for Zn²⁺, Cd²⁺, Pb²⁺, and Cu²⁺.⁸³⁰ SWASV selectively differentiated between Zn²⁺, Cd²⁺, and Pb²⁺, ions at sub-micromolar concentrations—0.07, 0.13, and 0.14 $\mu\text{g L}^{-1}$, respectively. However, Cu²⁺ analysis was performed independently due to intermetallic interference that exists between Cu²⁺ and Zn²⁺. Another multi-ion sensor was developed by Gode et al., who functionalized reduced graphene oxide with 1-ethyl-3-(3-dimethylaminopropyl)carbodiimide (EDC) calixarene and used it for simultaneous determination of Fe³⁺, Cd²⁺, and Pb²⁺.⁸³¹ SWV showed linear concentration dependence to all tested analytes in the 1.0×10^{-10} to 1.0×10^{-8} M range using the CA–rGO/GCE electrodes. The LODs for the metal ions determination were found to be at 2.0×10^{-11} M and were attributed to good selectivity of calixarene ionophore to target metals. The same sensors also demonstrated good analyte recovery for practical analysis of pharmaceutical formulations.

Pyrene-modified gold electrodes were also used as anchors for immobilization of free rGO sheets through $\pi-\pi$ stacking interactions.⁸³¹ The resulting sensing devices were capable of detecting Cu²⁺ at concentrations as low as 1.5 nM and Pb²⁺ at 0.4 nM levels with good reusability and repeatability. Using similar strategy, Teoh and co-workers covalently attached rGO sheets onto the surface of L-cysteine modified gold electrodes.⁸³² The attached rGO sheets provided the extended heterogeneous sites for the adsorption of metal ions, through the oxygenated sites, allowing detection of Pb²⁺ at 25 ppb levels. Alternatively, gold electrodes modified with 4-phenyl as scaffold for the attachment to GO demonstrated 1–2 orders improvements in detection limits for Pb²⁺ ions compared with the 4-aminophenyl modified analogue.⁸³³

Despite high sensitivity of Gr-Nafion modified electrodes to heavy metal ions, the typically employed preparation methods of the nanocomposite films, through mixing of reagents, were recently criticized.^{834,835} Drop-casting of Gr-Nafion films may lead to the formation of graphene aggregates, and consequently restacking of graphene sheets to form graphite due to van der Waals and $\pi-\pi$ stacking interactions between individual sheets of graphene. The proposed strategies to minimize the extent of aggregation of graphene were focused on the incorporation of metallic nanoparticles onto the surface of graphene. For example, Zhang and co-workers developed a nanocomposite electrode consisting of rGO functionalized with poly(vinylpyrrolidone), chitosan, and gold nanoparticles for the Hg²⁺ detection in river waters.⁸³⁶ The resulting sensor could detect Hg²⁺ at 0.6 ppt with 5 min accumulation time using SWASV. Selectivity studies confirmed the insensitivity to six ionic interferents. Wei et al. fabricated SnO₂/reduced GO nanocomposite modified GCE, for simultaneous determination of Cd²⁺, Pb²⁺, Cu²⁺, and Hg²⁺ ions in drinking waters.⁸³⁷ The LODs of this sensing platform, determined through SWASV, were 1.0×10^{-10} , 1.8×10^{-10} , 2.3×10^{-10} , and 2.8×10^{-10} M for Cd²⁺, Pb²⁺, Cu²⁺, and Hg²⁺, respectively. The analytes responded linearly within 0.3–1.2 μ M concentration range (Figure 45). Further improvements in sensitivity to Hg²⁺ could be realized through the incorporation of rGO-polyfuran (PF) nanohybrids into FET devices.⁸³⁸ The resulting sensors

demonstrated rapid response (<1 s), high sensitivity (10 pM) Hg²⁺ sensor, and excellent selectivity against Zn²⁺, Ce²⁺, Na⁺, Ni²⁺, Pb²⁺, Cu²⁺, Co²⁺, and Li⁺ ions. The high sensitivity and selectivity to Hg²⁺ was attributed to the enhanced surface area provided by the rGO-PF nanohybrid and the presence of PF nanotubes that could act as molecular probes for the detection of Hg²⁺.⁸³⁸

More recently, Zhang et al. developed a sensitive platform for Hg²⁺ detection based on the thymine–mercury(II)–thymine (T-Hg²⁺-T) interactions with chemically reduced GO employed as a transducer.⁸³⁹ They observed that the redox current of ferrocene labeled nucleic acid immobilized on the surface of graphene (ssDNA) was significantly amplified by the presence of graphene during DPV measurements. Upon the addition of Hg²⁺, the ferrocene-labeled thymine-rich DNA probe hybridized with target probe to form double stranded DNA (ds-DNA) via the Hg²⁺ mediated coordination of T-Hg²⁺-T base pairs. Because of the weak affinity of graphene to ds-DNA, the ferrocene complex was drawn away from the electrode surface consequently reducing the magnitude of recorded current. This sensor, under optimal experimental conditions, could sense Hg²⁺ ions at 5 pM with high specificity.

Noncovalent modification of an electrochemically reduced GO (ERGO)-based diode with N-[1-(1-pyrenyl-sulfonamido)-heptyl]-gluconamide (PG) used as the modifier allowed ultrasensitive detection of Hg²⁺ ions at 0.1 nM concentrations.⁸⁴⁰ The resulting sensor also demonstrated high selectivity to mercury over other ionic interferents including K⁺, Na⁺, Cu²⁺, Zn²⁺, Fe³⁺, and Cd²⁺. Sensitive detection of Hg²⁺ could be also realized using monolayer GO sheets functionalized with a single-stranded DNA aptamer assembled onto interdigitated electrodes in chemiresistor configuration.⁸⁴¹ High binding affinity of the DNA aptamer to mercury ions permitted detection of Hg²⁺ at 0.5 nM concentrations with high selectivity against Na⁺, K⁺, Li⁺, Cd²⁺, Ni²⁺, Zn²⁺, Co²⁺, Mg²⁺, Cu²⁺, Pb²⁺, Ag⁺, Ca²⁺, and Fe³⁺ ionic interferents. Another strategy to detect Hg²⁺ was demonstrated by Zhang et al., who functionalized surface of exfoliated graphene with a self-assembled monolayer of 1-octadecanethiol in FET device architecture.⁸⁴² The resulting sensor successfully detected Hg²⁺ ions at 10 ppm concentrations. The high sensitivity to mercury was attributed to the presence of thiol groups in 1-octadecanethiol monolayer. Baykara and co-workers further demonstrated that chemically vapor grown graphene functionalized with 1-octadecanethiol could detect both mercury and lead ions at 10 ppm concentrations.⁸⁴³ The authors proposed that the electrostatic gating effect was responsible for the sensing behavior of the fabricated sensing devices. Interestingly, the same devices modified with a self-assembled monolayer of 1-dodecanethiol instead of 1-octadecanethiol demonstrated p-type character, before and/or after exposure to heavy Hg²⁺ and Pb²⁺. This effect was attributed to the high degree of p-doping in the 1-dodecanethiol/Gr based FET, which caused the Dirac point to be located beyond the applicable gate voltage range.⁸⁴³

Graphene and graphene oxide based sensors have also been employed for the detection of noble metals, toxic elements, and nuclear waste.^{264,821} For instance, Wang and co-workers reported on the rGO-cysteic acid composite films for the detection of Ag⁺ in natural waters with nanomolar detection limits (1 nM).⁸⁴⁴ In addition, electrodes modified with graphene, bismuth, mercury, or AlOOH nanocomposites have been demonstrated as promising platforms for heavy

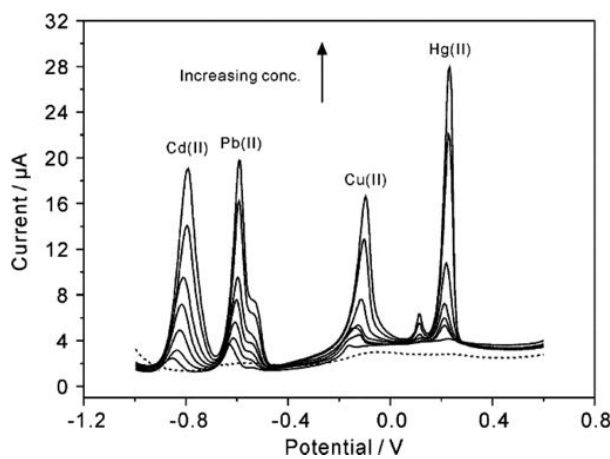


Figure 45. SWASV response of the SnO₂/reduced graphene oxide nanocomposite modified GCE for the simultaneous analysis of Cd²⁺, Pb²⁺, Cu²⁺, and Hg²⁺ over a concentration range of 0–1.2 μ M for each metal ions. From bottom to top, 0, 0.3, 0.4, 0.5, 0.6, 0.7, 0.9, and 1.2 μ M.⁸³⁷ Reproduced from ref 837. Copyright 2011 American Chemical Society.

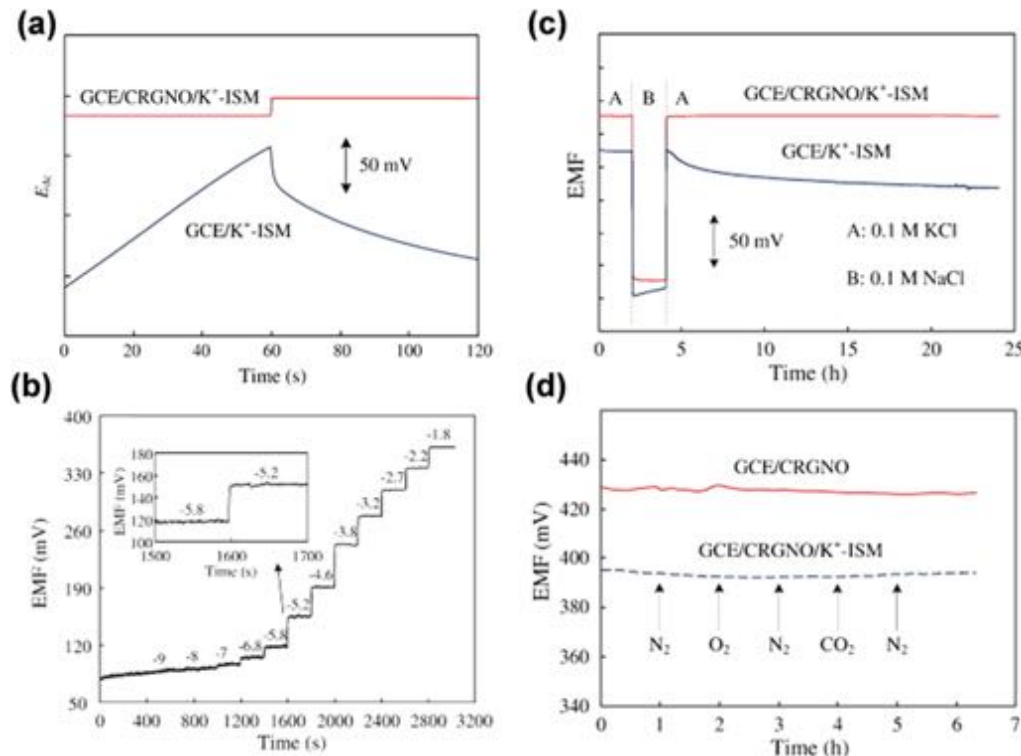


Figure 46. (a) Chronopotentiograms for GCE/K⁺-ISM and GCE/rGO/K⁺-ISM recorded in 0.1 M KCl solution. The applied current is +1 nA for 60 s and -1 nA for 60 s. (b) EMF measurements recorded for increasing the concentration of K⁺ in the solution, inset: expansion of the selected range. (c) Water layer test for the GCE/K⁺-ISM and GCE/rGO/K⁺-ISM; the measurements were switched between 0.1 M KCl and 0.1 M NaCl. (d) Sensitivity to O₂ and CO₂ in 0.1 M KCl solution for the GCE/rGO (solid line) and GCE/rGO/K⁺-ISM (dashed line).^{261,852} Reproduced with permission from refs 261 and 852. Copyright 2011 Elsevier B.V.

metal determination due to their strong complexing affinity for metals.^{845–847} Silwana et al., through the incorporation of Sb nanoparticles onto the surface of rGO, and by using dimethylglyoxime as a chelating agent, were able to simultaneously sense Pd²⁺, Pt²⁺, and Rh³⁺ cations.⁸⁴⁸ Under optimal conditions differential pulse cathodic stripping voltammetry could detect Pd²⁺, Pt²⁺, and Rh³⁺ at 0.45, 0.49, and 0.49 pg L⁻¹ concentrations, respectively. The developed electrochemical sensor also exhibited good precision with a relative standard deviation of 4.2, 2.55, and 2.67% with 92–117% recoveries for environmental samples containing Pd²⁺, Pt²⁺, and Rh³⁺, respectively.

Another notable example was demonstrated by Ziolkowski et al., who employed carboxylated graphene to sense uranyl ions in aqueous solutions using SWV.⁸⁴⁹ The enhanced selectivity to uranyl anions was ascribed to the high affinity of COO⁻ for UO₂²⁺ species through hydrogen bonding. These findings are consistent with the results of DFT calculations performed by Wu et al.⁸⁵⁰ The fabricated sensor platform showed linear response within the range of 5.0 × 10⁻⁸ to 5.0 × 10⁻⁶ mol L⁻¹ and significant selectivity toward UO₂²⁺ ions over seven other ionic interferents. Kumar et al. reported on the functionalization of GO with L-leucine and Nafion for selective detection of arsenic.⁸⁵¹ The GO-Au-Leucine-Nafion modified electrodes detected arsenic at 0.5 ppm levels in drinking water with minimal interference from common ionic contaminants such as Zn²⁺, Pb²⁺, and Hg²⁺. High selectivity of the resulting sensors was provided by the biorecognition element-L-leucine, while GO ensured good carrier mobility and increased electron transfer rates.

4.3.1.2. Electrolytes. Graphene-based electrodes were also used as solid ion-to-electron transducers in ion-selective electrodes (ISEs). Ying et al. and Niu et al. reported on the first application of graphene and graphene oxide as transducer layer in ISEs.^{261,852} The authors formed K⁺-ISEs through drop-casting graphene/GO onto GCE and covering the electrodes with K⁺-selective membrane (Figure 46a,b). The fabricated sensors exhibited high interfacial double layer capacitance of approximately 80 μF and potential drift as low as 12.6 ± 1.1 μV h⁻¹. In addition, the drop-cast layer of graphene/GO suppressed the formation of water layer at the electrode/ion-selective membrane interface, thus further minimizing potential drifts (Figure 46c). The same electrodes were also relatively insensitive to O₂, light, and redox interferences, showing promising advantages of 2D carbons over conductive polymers in ISEs (Figure 46d).²⁴⁷ Rius and co-workers found that 1500 nm layer of rGO drop-cast on GCE improved signal-to-noise ratio of fabricated Ca²⁺-ISEs, with potential drift of only 10 μV/h recorded during potentiometric measurements.²⁶³ They also demonstrated that mechanism of ion-to-electron transduction proceeds through the formation of double layer in which one side carries charge in the form of ions (ion selective membrane), while the other side is formed by electrical charge, e.g., electrons or holes in the 2D material. He et al. recently demonstrated an in situ fabrication of K⁺-ISEs, on a Si/SiO₂ wafer, which used inkjet printing technique for efficient integration of graphene as transducer and electronic conductor in potentiometric sensors.²⁶²

Another approach to achieve high sensitivity to electrolytes can be realized through the development of ion-sensitive field effect transistors (ISFET).^{853,854} However, the practical utility

of Si-based ISFET is often limited by the migration of ions (e.g., H^+ and OH^-) into the oxide and their accumulation at the SiO_2/Si interface. These effects cause alteration in the threshold voltage of the FET devices leading to the degradation of the device with repeated usage. Graphene's impermeability to ions opens a wide range of exciting opportunities in the development of ISFETs.^{854–858} Chemical vapor deposited graphene sandwiched with valinomycin based membrane coating in ISFET configuration was capable of detecting K^+ ions at 1 μM concentrations in the 1 μM to 20 mM range.⁸⁵⁹ The same sensor demonstrated high selectivity to K^+ with respect to common biological interferents Na^+ and Ca^{2+} with retention of performance over two-months testing period.

Mao et al. fabricated a FET device using rGO nanosheets as the sensing channel and ferritin as the specific detection probe for orthophosphate ions.⁸⁶⁰ This sensor could detect orthophosphate ions with detection limit of 26 nM, and good selectivity in the presence of Cl^- , SO_4^{2-} , and CO_3^{2-} . Chen and co-workers showed that the FET devices composed of rGO functionalized with calmodulin (Ca^{2+} binding protein) can detect calcium at 0.1–1 μM levels.⁸⁶¹ The binding of Ca^{2+} onto rGO can be attributed to the field-effect modulation of rGO-FETs introduced by the positively charged ions. The same device demonstrated good selectivity to Ca^{2+} against other interfering ions including Na^+ and K^+ . Sensitive detection of Na^+ was realized through integrating mechanically exfoliated graphene into the FET device configuration.⁸⁶² The fabricated device was capable of detecting Na^+ ions in solutions over a wide range of concentrations from 1.0 nM to 1.0 mM. Exposure to Na^+ modulated electrical potential of graphene channels, leading to shifts toward a negative direction of the transfer curves of the device with increasing Na^+ concentration. This effect was attributed to the accumulation of Na^+ on the graphene channel.⁸⁶² Recently, a Hall-effect ion sensor based on guanine-rich DNA immobilized on the surface of graphene was used for sensitive detection of K^+ .⁸⁶³ The resulting devices responded linearly in the 1 nM to 10 μM concentration range with high selectivity against other alkali cations, including Na^+ , Mg^{2+} , Ca^{2+} , Fe^{3+} , Zn^{2+} , NH_4^+ , and Mn^{2+} ions. High affinity of the developed sensor to K^+ was attributed to the presence of the guanine-rich DNA.

Despite many improvements and large promise in the application of graphene-based materials as either a transducer, molecular scaffold or recognition element in electrochemical sensing of ions, there are several challenges that require to be addressed. First, the impact of the structural and compositional defects and chemical functionalization of graphene on the electrical properties and the sensing performances of the fabricated analytical devices needs further investigation. Therefore, novel chemical strategies are required to tailor the physiochemical properties of graphene and consequently to induce the desired sensing characteristics for targeted applications. Second, interfacing graphene-based materials with other components (e.g., electrodes and substrates) within functional sensing devices will remain an important aspect to achieve flexible, miniaturized, and fully integrated electrochemical ion sensors. Third, scalable and cost-effective manufacturing strategies with high degree of control over the structure and properties of graphene-based materials need to be developed for such systems to be employed for practical sensing applications. Regardless of these challenges, graphene

holds a great promise as an active component for applications in ionic detection.

4.3.2. Black Phosphorus. Layered BP exhibits high carrier mobility^{864,865} ($1000 \text{ cm}^2 \text{ V}^{-1} \text{ s}^{-1}$) and larger current on/off ratio in field–effect transistors^{866,867} (1×10^3 to 1×10^5) and comparable or even stronger molecule adsorption abilities than those of graphene and MoS_2 .⁹⁸ These properties, together with its extremely large surface-to-volume ratio, make BP a promising nanomaterial for ion sensing. Cao and co-workers integrated BP into FET device through mechanical exfoliation by the Scotch tape-based method.¹⁹⁸ The resulting device was used for label-free trace detection of Hg^{2+} with LODs of 0.01 ppb and response time under 3 s. The sensing mechanism of BP was attributed to the carrier density variation due to surface charge gating effect. Li et al. also fabricated a FET device in which mechanically exfoliated BP was integrated between two Ti/Pd electrodes (Figure 47a) and subsequently covered with

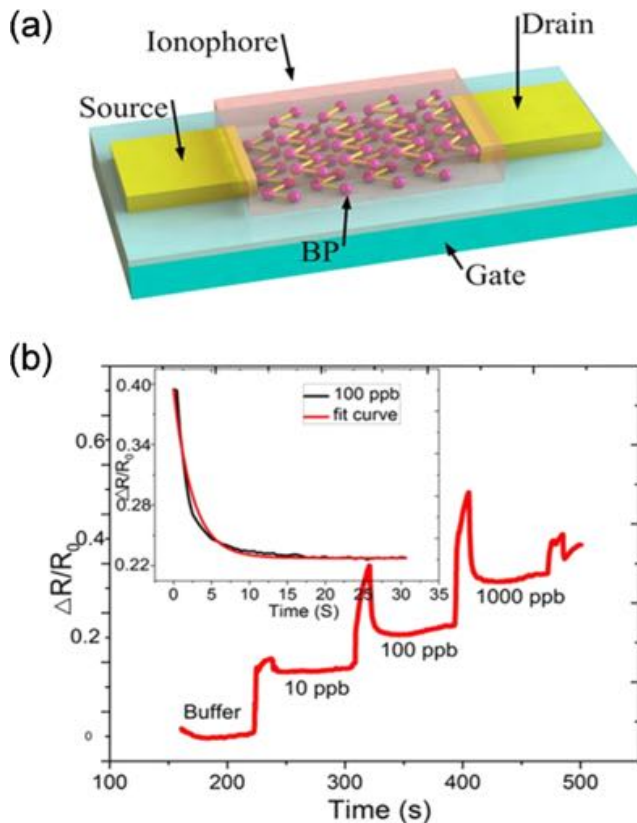


Figure 47. (a) Schematic view of a BP sensor in which the BP flake is covered with ionophore film. (b) Relative resistance change ($\Delta R/R_0$) of BP versus time ($V_{GS} = 0 \text{ V}$) under the different concentrations of Pb^{2+} . The curve fit in the inset demonstrates the time constant, τ , is 5 s.⁸⁶⁸ Reproduced from ref 868. Copyright 2015 American Chemical Society.

ion-selective membranes.⁸⁶⁸ The BP sensors were then employed for multiplexed detection of environmental pollutants, including As^{3+} , Pb^{2+} , Cd^{2+} , and Hg^{2+} with sub-ppm sensitivity to Pb^{2+} ions (Figure 47b). In each situation, the ion selective membrane was used as selective barrier that allowed diffusion of only targeted species toward the surface of BP and thus modulated the hole density and conductance of BP. Recently, a few layer BP film has been used as an ion-to-electron transducer in ISEs. The authors observed that the

presence of BP diminished the charge transfer resistance across the ion-selective membrane/BP/solid contact interfaces and led to increased signal stability of Ca^{2+} -ISEs.⁸⁶⁹ Recently, BP functionalized with ionophore was used to develop flexible sensor array for multiplex detection of Hg^{2+} , Cd^{2+} , Pb^{2+} , and Na^+ .⁸⁷⁰ The resulting device demonstrated high sensitivity to Hg^{2+} with LODs estimated at 1 $\mu\text{g/L}$ and short response time, demonstrating excellent mechanical flexibility (strain limits of 1%) and stability (bending 500 times). Small strain variation from 0.33% to 0.16% led to 175% improvement in sensitivity due to Schottky barrier modulation. The authors also demonstrated the capability of detecting Cd^{2+} ions in tap water samples and Na^+ in human sweat.

As shown above, BP-based materials represent a conceptually new class of 2D nanostructures with great potential utility in the development of ion sensing technologies. Without a doubt, the full potential of BP based ion sensors is far from being reached. Currently, the exploration of BP-based ion sensing devices is largely hindered by limited stability of BP to aerobic and aqueous environment that ultimately lead to material degradation. Therefore, considerable efforts must be devoted to improving stability of BP either through the use of protective coatings/inert masks that directly reduce the impact of outside environment or by altering its surface chemistry using novel synthetic approaches. Because of its tunable bandgap and anisotropic electronic properties, many challenges remain in finding new synthetic routes that offer a good degree of control over the size, composition, thickness, and number of incorporated defects. Finally, further experimental and computational mechanistic investigation of the structure–property relationship of BP is required to gain more understanding about the role of this material in ion sensing, which ideally will guide the design of future sensing technologies.

4.3.3. Transition Metal Dichalcogenides. Inspired by the use of graphene as recognition elements and transducers in electrochemical sensors,^{321,821} 2D TMDCs have been extensively employed in the development of sensing devices due to their good conductivity, large surface area, fast electron transfer kinetics, high signal/noise ratio, and, more importantly, their feasibility for forming composites.⁸⁷¹ Zhou et al. fabricated MoS_2 -Au nanoparticle-DNA functionalized on the surface of Si/SiO₂ FET device for determination of Hg^{2+} (Figure 48a).⁸⁷² In this configuration, the MoS_2 film served as the conducting channel with the dispersed Au nanoparticles acting as molecular anchors for the immobilization of Hg^{2+} specific DNA probes. The analytical measurements were enabled by monitoring the change of the source-drain current as a function of Hg^{2+} concentration in the p-type MoS_2 channel (Figure 48b). The developed biosensor displayed LODs of 0.1 nM and good selectivity to other ionic interferents. Jiang and co-workers integrated thin layers of MoS_2 into the FET device and used it as an electrochemical sensor for the determination of Hg^{2+} ions in solutions (Figure 48c,d).⁸⁷³ They observed that Hg^{2+} can readily coordinate with the sulfur sites on the surface of MoS_2 , producing a p-type doping effect and consequently modulating the electron transport in the 2D layer. The resulting sensors exhibited low detection limits (30 pM) and good specificity to Hg^{2+} in the presence of 15 ionic interferents demonstrating potential utility of the sensors for mercury determination (Figure 48e). Silver/halloysite nanotube/molybdenum disulfide modified carbon paste electrodes were recently realized as amperometric

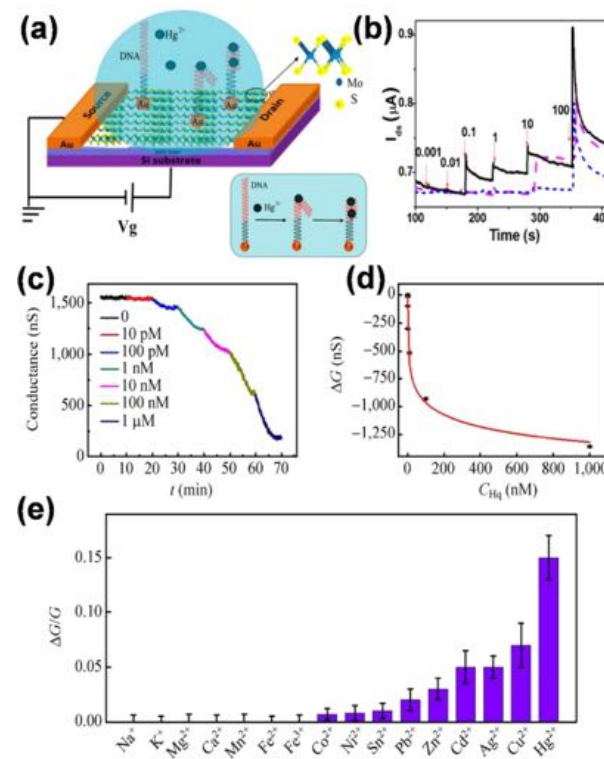


Figure 48. (a) FET sensor platform based on the hybrid structure. The formation of T-(Hg^{2+})-T chelates, through reactions between Hg^{2+} and the thymidine of the DNA molecules on the Au NPs, leading to (b) the change in the MoS_2 electrical conductivity as a sensor signal.⁸⁷² Reproduced from ref 872. Copyright 2016 American Chemical Society. (c) Real-time electrical readout of Hg^{2+} ion signal by MoS_2 sensor. Real-time electrical measurement at different concentrations of Hg^{2+} ions. (d) Calibration curve: conductance change versus Hg^{2+} ion concentration. (e) The red line is the fitted curve on a natural log scale. Selectivity of the MoS_2 mercury(II) sensor.⁸⁷³ Reproduced with permission from ref 873. Copyright 2015 Springer Nature.

sensors for nitrite detection.⁸⁷⁴ The resulting devices could detect NO_2^- in the 2 to 425 μM concentration range with detection limits of 0.7 μM and high selectivity against NaCl , CuSO_4 , KClO_4 , K_2CO_3 , $\text{Al}(\text{NO}_3)_3$, CH_3COONa , KIO_3 , urea, ascorbic acid, and glucose. The same ion-sensor retained 95.5% of its initial current response after the 3 week testing period with 96.5–99.6% recoveries in nitrite determination in tap water samples.

The application of TMDCs materials in the electrochemical sensing of ions have recently gained rapid momentum, due to their intriguing physical, chemical, and electronic properties. Nonetheless, this application area is still within its early stages, and, therefore, faces many challenges. From the materials standpoint, scalable and controlled synthesis of 2D TMDCs with predictable and desired structures remains difficult to achieve using available synthetic methods. Therefore, novel synthetic approaches are needed to fabricate uniform 2D TMDCs materials with consistent properties. In addition, further research focused on the chemical functionalization of TMDC structures to induce selectivity toward targeted analytes should be pursued, thus potentially opening wide the window for further implementation of these materials in ion sensing applications.

4.3.4. Other 2D Materials. The promising properties of 2D metal oxide nanostructures such as high electrochemical stability and large adsorption capacity to ions have shown great promise in the development of electrochemical sensing platforms.⁸⁷⁵ For example, glassy carbon electrodes modified with porous Co_3O_4 microsheet/Nafion composites were capable of sensing Pb^{2+} in the $0.05\text{--}0.275 \mu\text{M}$ concentrations with sensitivity of $71.57 \mu\text{A } \mu\text{M}^{-1}$ and detection limit of $0.018 \mu\text{M}$.⁸⁷⁶ High sensitivity of the fabricated sensor was attributed to the presence of a nanochannel in the structure of Co_3O_4 that are readily accessible for the diffusion of Pb^{2+} ions providing large available surface area for metal crystal growth. In a recent study, further improvements in analytical performance for the determination of Pb^{2+} ions in water were achieved through electrodeposition of Co_3O_4 nanosheets directly onto the indium tin oxide (ITO) electrodes.⁸⁷⁷ The resulting electrodes, using DPASV, were capable of detecting Pb^{2+} in $1\text{--}100 \mu\text{g L}^{-1}$ concentration range with the LOD of $0.52 \mu\text{g L}^{-1}$ and high selectivity against Ca^{2+} , Mg^{2+} , Fe^{2+} , Zn^{2+} , and Mn^{2+} ionic interferences. Lin and co-workers used ultrathin two-dimensional TiO_2 nanosheets doped with fluorine, in layered electrode architecture (TiO_2/GCE) for the detection of Pb^{2+} ions.⁸⁷⁸ The fabricated electrodes exhibited $53.63 \mu\text{A}/\mu\text{M}$ sensitivity toward Pb^{2+} ions in the concentration range of $0.2\text{--}1.4 \mu\text{M}$, the LOD of 7nM , and high selectivity over Al^{3+} , Mg^{2+} , Na^+ , NH_4^+ , K^+ , Ca^{2+} , Cl^- , PO_4^{3-} , SO_4^{2-} , and NO_3^- interferents. Theoretical calculations revealed that fluorine doping could enhance the adsorption energy of Pb^{2+} on the TiO_2 nanosheets and increase the ion loading capacity. In addition, the authors observed that F doping further facilitated the electron transfer to the electrode, which led to improvements in sensitivity for Pb^{2+} determination.⁸⁷⁸

Metal–organic frameworks have emerged as a unique class of multifunctional materials in electrochemical sensors due to their large surface area, tunable bandgap, and compositional and structural diversity accessible through bottom-up self-assembly. Conductive 2D MOFs (Ni_3HHTP_2 , Cu_3HHTP_2 , and Co_3HHTP_2) drop-cast onto the GCE and covered with a layer of polymeric ion-selective membranes were successfully utilized as ion-to-electron transducers in potentiometric detection of K^+ and NO_3^- ions (Figure 49).⁸⁷⁹ The resulting devices demonstrated excellent signal stability of $14.6 \mu\text{V s}^{-1}$ under polarizing conditions of 1nA , low long-term drift ($11.1 \mu\text{V s}^{-1}$), and high sensitivity to K^+ and NO_3^- with the detection limits of $6.31 \pm 0.01 \times 10^{-7}$ and $5.01 \pm 0.01 \times 10^{-7} \text{ M}$, respectively. The excellent analytical performance of fabricated sensors was attributed to large double-layer capacitance ($204.1 \mu\text{F}$) in MOF-coated electrodes. The authors proposed that ion-to-electron transduction proceeds through the formation of electrical double layer in the case of Ni_3HHTP_2 and Co_3HHTP_2 MOFs with an additional contribution from redox doping/undoping in Cu_3HHTP_2 MOFs.

The emerging properties of 2D nanomaterials such as large surface area, tunable conductivity, low-dimensionality, and synthetic accessibility carry great promise in the development of the next generation of electrochemical sensing devices for ion determination.^{73,321} In particular, a high degree of synthetic modularity in MOFs enables incorporation of functional groups or ion chelators that can impart high selectivity toward targeted ionic species.⁸⁹ Interfacing these materials with polymeric membranes, ion-receptors, electrodes, and flexible substrates will become crucial to fabricate portable,

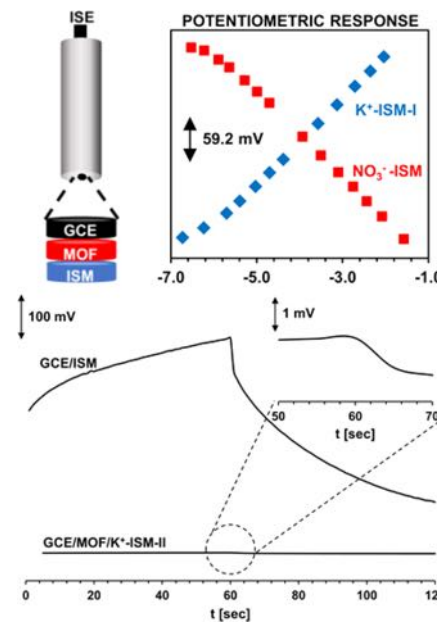


Figure 49. Schematic representation of layered electrode architecture used for potentiometric measurements.⁸⁷⁹ In this configuration, a thin film of 2D MOF was drop-casted directly on the top of a glassy carbon electrode (GCE) and then covered with an ion-selective membrane (ISM) to enable potentiometric ion sensing. Potentiometric response of GCE/ Ni_3HHTP_2 MOF/ISM devices to K^+ (blue diamonds) and NO_3^- (red squares) ions. Chronopotentiograms obtained during the analysis of K^+ -ISM-II based ISEs under polarizing conditions. (top) K^+ -ISM-II applied directly onto a GCE contact without the MOF as undelaying conductive layer; (bottom) GCE/ Ni_3HHTP_2 MOF/ K^+ -ISM-II electrode. Inset demonstrates a close-up of response obtained for the GCE/ Ni_3HHTP_2 MOF/ K^+ -ISM-II. Experimental conditions: applied current $+1 \text{nA}$ for 60s followed by -1nA for 60s in 0.1 M KCl .⁸⁷⁹ Reproduced from ref 879. Copyright 2018 American Chemical Society.

miniaturized, robust, and selective electrochemical ion sensors. To date, only a handful of metal oxides and 2D conductive MOFs have been explored in ion sensing applications indicating large potential for their applications as active components in ion sensing devices. The unique combination of structural tunability together with high electrical conductance, which are critically needed in the electrically-transduced devices, will ideally lead to more applications of these materials in sensing of ionic species in the future.

4.4. Detection of Biomolecules

The use of 2D materials in the context of electrochemical sensors has been widely reported due to their inherent properties, which include enhanced mass transport, large accessible surface area, high sensitivity, and excellent signal-to-noise ratio.³²¹ 2D nanomaterials can be used either as molecular carriers for loading signal labels or directly as recognition elements for sensitive and selective detection of biologically relevant molecules including vitamins, metabolites, neurotransmitters, biomarkers, and others.^{773,121,282,321,880–882} The application of 2D nanostructures can also improve heterogeneous electron transfer rates if integrated as functional materials on electrode surfaces. More recently, 2D nanomaterials have been utilized to increase the sensitivity of the electrochemical sensors to target molecules. The following subsections describe the analytical strategies employed to form electrochemical sensing platforms based on 2D materials. The

Table 5. Summary of Sensing Performances for Ions by 2D Materials^a

specific analyte	material	architecture	readout/method	LOD	experimental range	sensing environment	notes	ref	
Ag ⁺	rGO–CsA	rGO–CsA/GCE	DPASV	1.0 × 10 ⁻⁹	1.0 × 10 ⁻⁸ to 2.0 × 10 ⁻⁴ M	HNO ₃ (0.01 M)	Cd ²⁺ , Cu ²⁺ , Zn ²⁺ , Ni ²⁺ , Cr ⁶⁺ , Pb ²⁺ , Hg ²⁺ , Fe ³⁺	844	
As ³⁺	GO–LEU–Nafion	GO–LEU–Nafion/Au	CV	6.7 × 10 ⁻⁶ M	6.7 × 10 ⁻⁵ to 6.7 × 10 ⁻⁴ M	CB (0.1 M, pH 5.0)/river water	Zn ²⁺ , Pb ²⁺ , Hg ²⁺ , Cd ²⁺	851	
Ca ²⁺	BP	BP/Ca ²⁺ –ISM/GCE	E	4.0 × 10 ⁻⁷ M	1.0 × 10 ⁻¹ to 1.0 × 10 ⁻⁶ M	DI/wine samples	H ⁺ , Na ⁺ , K ⁺ , Mg ²⁺	869	
Ca ²⁺	rGO–calmodulin	FET: H ₂ O/SiO ₂ /rGO–calmodulin/Ag/Ag	I	1 nM	1–28 nM	lake water, DI water	Mg ²⁺	861	
Ca ²⁺	rGO/Ca ²⁺ –ISM	rGO/Ca ²⁺ –ISM/GCE	E	6.3 × 10 ⁻⁷ M	3.2 × 10 ⁻³ to 1.0 × 10 ⁻⁵ M	DI	Ba ²⁺ , Na ⁺ , Li ⁺ , Mg ²⁺ , K ⁺	263	
Cd ²⁺	Gr–Bi	Gr–Bi/CPE	SWASV	0.07 μg L ⁻¹	0.10–50.0 μg L ⁻¹	HCl (0.05 M)/tap and seawater	Pb ²⁺	845	
Cd ²⁺	Gr–Cys–AuNP	Gr–Cys–AuNP/GCE	SWASV	0.10 μg L ⁻¹	0.50–40 μg L ⁻¹	ABS (0.1 M, pH 4.5, Bi ³⁺)/river water	Co ²⁺ , Fe ³⁺ , Ni ²⁺ , Cr ³⁺ , Zn ²⁺ , Cu ²⁺ , In ³⁺ , Sn ²⁺	826	
Cd ²⁺	Gr–Nafion	Gr–Nafion/Hg	SWASV	0.08 μg L ⁻¹	1.0–7.0 μg L ⁻¹	ABS (0.1 M, pH 4.5)/wetland water	Pb ²⁺ , Cu ²⁺ , Zn ²⁺	830	
Cd ²⁺	Gr–Nafion–Bi	Gr–Nafion–Bi/GCE	DPASV	30 μg L ⁻¹	0.5–50 μg L ⁻¹	ABS (0.1 M, pH 4.5)/lake water	Triton X, SDS, CTAB	829	
Cd ²⁺	rGO–AlOOH	rGO–AlOOH/GCE	SWASV	3.52 × 10 ⁻¹¹ M	0.2–0.8 μM	ABS (0.1 M, pH 6.0)/real water	K ⁺ , Ca ²⁺ , Na ⁺ , Mg ²⁺ , Al ³⁺ , Cu ²⁺ , Hg ²⁺ , Zn ²⁺ , Cl ⁻ , NO ₃ ⁻ , SO ₄ ²⁻ , PO ₄ ³⁻	847	
Cd ²⁺	rGO–Bi	rGO–Bi/Au	SWASV	1.0 μg L ⁻¹	1.0–120.0 μg L ⁻¹	ABS (0.1 M, pH 4.5)/drinking water	Pb ²⁺	828	
Cd ²⁺	rGO–SnO ₂	rGO–SnO ₂ /GCE	SWASV	1.0 × 10 ⁻¹⁰ M	0.3–1.2 μM	ABS (0.1 M, pH 5.0)/drinking water	Pb ²⁺ , Cu ²⁺ , Hg ²⁺	837	
Cu ²⁺	GO-L-cystene	GO-L-cystene/Au	SWASV	1.2 ppb	1.2–200 ppb	ABS (pH 7)	N/A	832	
Cu ²⁺	GO–Ph	GO–Ph/Au	OSWV	1.7 × 10 ⁻⁹ M	1.7–100 × 10 ⁻⁹ M	ABS (pH 7)	Zn ²⁺ , Fe ³⁺ , Cd ²⁺ , Cr ⁶⁺ , Cu ²⁺ , Hg ²⁺	833	
Cu ²⁺	Gr–Nafion	Gr–Nafion/Hg	SWASV	0.13 μg L ⁻¹	20.0–190.0 μg L ⁻¹	ABS (0.1 M, pH 4.5)/wetland water	Pb ²⁺ , Cd ²⁺ , Zn ²⁺	830	
Cu ²⁺	rGO–pyrene	rGO–pyrene/Au	OSWV	1.5 × 10 ⁻⁹ M	1.5–20 × 10 ⁻⁹ M	ABS (pH 7)	Cd ²⁺ , Co ²⁺ , Ni ²⁺ , Zn ²⁺ , Ca ²⁺ , Mg ²⁺	831	
Cu ²⁺	rGO–SnO ₂	rGO–SnO ₂ /GCE	SWASV	2.3 × 10 ⁻¹⁰ M	0.3–1.2 μM	ABS (0.1 M, pH 5.0)/tap water	Pb ²⁺ , Hg ²⁺ , Cd ²⁺	837	
Hg ²⁺	BP	FET: HfO ₂ /PET/BP–ISM/Ti–Au/Ti–Au	I	1 μg/L	0.03–100 mg/L	CD ²⁺ , Pb ²⁺ , Na ⁺ , K ⁺ (array)	CD ²⁺ , Pb ²⁺ , Na ⁺ , K ⁺ (array)	870	
Hg ²⁺	Gr–SAM	FET: Si/SiO ₂ /G-SAM/ Au–Cr/Au–Cr	I	10 ppm	N.R.	N.R.	N.R.	842	
Hg ²⁺	Gr–SAM	FET: Si/SiO ₂ /Gr-SAM/ Au–Cr/Au–Cr	I	10 ppm	N.R.	DI water	DI water	843	
Hg ²⁺	Gr–AuNP–CT	Gr–AuNP–CT/GCE	SWASV	8.0 × 10 ⁻¹² M	4.0 × 10 ⁻¹¹ to 2.5 × 10 ⁻¹⁰ M _f	HCl (1 M)/river water	CD ²⁺ , Cu ²⁺ , Zn ³⁺ , Co ²⁺ , Fe ³⁺ , I ⁻	836	
Hg ²⁺	Gr–DNA	Gr–DNA/GCE	DPV	5 pM	5.0 × 10 ⁻¹⁰ to 3.0 × 10 ⁻⁷ M	25 pM to 10 μM	Tris–HCl (0.05 M, pH 7.4)/river water	Na ⁺ , K ⁺ , Ba ²⁺ , Mg ²⁺ , Mn ²⁺ , Pb ²⁺ , Hg ²⁺ , Co ²⁺ , Ni ²⁺ , Fe ²⁺ , Fe ³⁺ , Al ³⁺ , Mo, Mn, As, Cr, Cd, Cu, V, Ag ⁺	839
Hg ²⁺	MoS ₂	FET: Si/SiO ₂ /MoS ₂ /Ni–Au/Ni–Au	I	30 pM	0.0–1.0 μM	DI	K ⁺ , Ca ²⁺ , Na ⁺ , Mg ²⁺ , Mn ²⁺ , Cd ²⁺ , Hg ²⁺ , Ag ⁺ , Cd ²⁺ , Zn ²⁺ , Pb ²⁺ , Sn ²⁺ , Fe ²⁺ , Fe ³⁺ , Ni ²⁺ , Co ²⁺ , As ³⁺ , Cd ²⁺ , Cd ³⁺ , Cu ²⁺ , Fe ³⁺ , Cu ²⁺ , Fe ³⁺ , Pb ²⁺ , Na ⁺ , Pb ²⁺ , Zn ²⁺	873	
Hg ²⁺	MoS ₂ –DNA–AuNP	FET: Si/SiO ₂ /MoS ₂ –DNA–AuNP/Au/Au	I	0.1 nM	0.1–10 nM	DI	As ³⁺ , Cd ²⁺ , Cd ³⁺ , Cu ²⁺ , Fe ³⁺ , Mg ²⁺ , Na ⁺ , Pb ²⁺ , Zn ²⁺	872	
Hg ²⁺	rGO–SnO ₂	rGO–SnO ₂ /GCE	SWASV	2.8 × 10 ⁻¹⁰ M	0.3–1.2 μM	ABS (0.1 M, pH 5.0)/lake water	Pb ²⁺ , Cu ²⁺ , Cd ²⁺	837	
Hg ²⁺	rGO–metallothionein	FET: H ₂ O/SiO ₂ /rGO–metallothionein/Ag/Ag	I	1 nM	1–28 nM	DI water, DI water	Na ⁺ , K ⁺ , Li ⁺ , Cd ²⁺ , Zn ²⁺ , Co ²⁺ , Mg ²⁺ , Cu ²⁺ , Pb ²⁺ , Ag ⁺ , Cd ²⁺ , Mn ²⁺ , Fe ³⁺	841	
Hg ²⁺	rGO–DNA	Au/rGO–DNA/Au	I	5 × 10 ⁻⁹	5 × 10 ⁻⁹ to 1.02 × 10 ⁻⁶ M	river water/DI water	Na ⁺ , K ⁺ , Li ⁺ , Cd ²⁺ , Zn ²⁺ , Co ²⁺ , Mg ²⁺ , Cu ²⁺ , Pb ²⁺ , Ag ⁺ , Cd ²⁺ , Mn ²⁺ , Fe ³⁺	861	

Table 5. continued

specific analyte	material	architecture	readout/ method	LOD	experimental range	sensing environment	notes	ref
Hg ²⁺	rGO-PF	FET: PBS/SiO ₂ /rGO-PF/Au-Cr	I	1 × 10 ⁻¹³ M	1 × 10 ⁻¹³ to 1 × 10 ⁻⁹ M	PBS (pH 7.4)	Zn ²⁺ , Ge ²⁺ , Na ⁺ , Ni ²⁺ , Pb ²⁺ , Cu ²⁺ , Co ²⁺ , Li ⁺	838
Hg ²⁺	rGO-pyrene-glucose	Au/rGO-pyrene-glucose/Au	I	1 × 10 ⁻¹⁰	1–40 × 10 ⁻¹⁰	DI water	Cd ²⁺ , Zn ²⁺ , K ⁺ , Na ⁺ , Cu ²⁺ , Fe ³⁺	840
Hg ²⁺	GO-Ph	GO-Ph/Au	OSWV	1.7 × 10 ⁻⁹ M	1.7–150 × 10 ⁻⁹ M	ABS (pH 7)	Zn ²⁺ , Fe ³⁺ , Cd ²⁺ , Cr ⁶⁺ , Cu ²⁺ , Hg ²⁺	833
Hg ²⁺	GO-L-cystene	GO-L-cystene/Au	SWASV	0.8 ppb	0.8–10 ppb	ABS (pH 7)	N/A	832
K ⁺	Gr	FET: Si/SiO ₂ /Gr-K ⁺ : ISM/Ti-Ni/Ti-Ni	I	1 μM	1 μM to 20 mM	Tris-HCl (pH 7.4)	Na ⁺ , Ca ²⁺	839
K ⁺	Gr	Gr/K ⁺ -ISM/GCE	E	1.0 × 10 ⁻⁵ M	1.0 × 10 ⁻¹ to 3.2 × 10 ⁻⁵ M	DI	Ca ²⁺ , Na ⁺ , Li ⁺ , Mg ²⁺ , NH ₄ ⁺	852
K ⁺	Gr	Gr/K ⁺ -ISM/Gr	E	7.0 × 10 ⁻⁶ M	1.0 × 10 ⁻¹ to 1.0 × 10 ⁻⁵ M	DI	Ca ²⁺ , Na ⁺ , Mg ²⁺	262
K ⁺	Gr-DNA	Hall-device: Si/SiO ₂ /G-DNA/rGO	Hall-effect	1 nM	1 nM to 10 μM	TE buffer (pH 8)	Na ⁺	863
K ⁺	rGO	rGO/K ⁺ -ISM/GCE	E	6.3 × 10 ⁻⁷ M	1.0 × 10 ⁻¹ to 1.6 × 10 ⁻⁶ M	DI	Ca ²⁺ , Na ⁺ , Li ⁺ , Mg ²⁺	261
K ⁺	Ni ₃ HHTP ₂	ISM/Ni ₃ HHTP ₂ /GCE	E	6.76 ± 0.03 × 10 ⁻⁶ M	10 ⁻⁷ –5 × 10 ⁻¹ M	DI	Na ⁺ , NH ⁴⁺ , Ca ²⁺	879
HPO ₄ ²⁻	rGO-ferritin	FET: Si/SiO ₂ /rGO-ferritin/Au/Au	I	5 nM	5 nM to 10 μM	DI water (pH 7.5–8.9)	Cl ⁻ , SO ₄ ²⁻ , CO ₃ ²⁻	860
Na ⁺	Gr	FET: Si/SiO ₂ /G/Ni-Au/Ni-Au	I	1 nM	1 nM to 1 mM	Tris-HCl	N.R.	862
Pb ²⁺	BP	FET: Si/SiO ₂ /BP-Hg ²⁺ -ISM/Ti-Pd/Ti-Pd	I	0.48 × 10 ⁻⁸ M	4.8 × 10 ⁻⁸ to 4.8 × 10 ⁻⁴ M	ABS (0.1 M, pH 4.6)	Hg ²⁺ , Cd ²⁺ , AsO ₂ ⁻	868
Pb ²⁺	GO-L-cystene	GO-L-cystene/Au	SWASV	0.4 ppb	0.4–20 ppb	ABS (pH 7)	Zn ²⁺ , Fe ³⁺ , Cd ²⁺ , Cr ⁶⁺ , Cu ²⁺ , Hg ²⁺	832
Pb ²⁺	GO-Ph	GO-Ph/Au	OSWV	3 × 10 ⁻¹⁰ M	3–500 × 10 ⁻¹⁰ M	ABS (pH 7)	Zn ²⁺ , Fe ³⁺ , Cd ²⁺ , Cr ⁶⁺ , Cu ²⁺ , Hg ²⁺	833
Pb ²⁺	Gr-Bi	Gr-Bi/CPE	SWASV	0.04 μg L ⁻¹	0.10–50.0 μg L ⁻¹	HCl (0.05 M)/tap and seawater	Cd ²⁺	845
Pb ²⁺	Gr-Cys-AuNP	Gr-Cys-AuNP/GCE	SWASV	0.05 μg L ⁻¹	0.50–40 μg L ⁻¹	ABS (0.1 M, pH 4.5, Br ³⁺)/river water	Co ²⁺ , Fe ³⁺ , Ni ²⁺ , Cr ³⁺ , Zn ²⁺ , Cu ²⁺ , In ³⁺ , Sn ²⁺	826
Pb ²⁺	Gr-DNA-AuNP	FET: HEPEs/SiO ₂ /Gr-DNA-AuNP/Ag/Ag	I	2 × 10 ⁻¹¹	1 × 10 ⁻⁷	HEPEs buffer	Cu ²⁺ , Ca ²⁺ , Cd ²⁺ , Mg ²⁺ , Ni ²⁺ , Zn ²⁺	827
Pb ²⁺	Gr-Nafion	Gr-Nafion/Hg	SWASV	0.07 μg L ⁻¹	1.0–7.0 μg L ⁻¹	ABS (0.1 M, pH 4.5)/wetland water	Cd ²⁺ , Cu ²⁺ , Zn ²⁺	830
Pb ²⁺	Gr-Nafion-Bi	Gr-Nafion-Bi/GCE	DPASV	1.5 μg L ⁻¹	0.5–50 μg L ⁻¹	ABS (0.1 M, pH 4.5)/lake water	Triton X, SDS, CTAB	829
Pb ²⁺	Gr-SAM	FET: Si/SiO ₂ /Gr-SAM/Au-Cr	I	10 ppm	N.R.	DI water.	Hg ²⁺	843
Pb ²⁺	rGO-pyrene	rGO-pyrene/Au	OSWV	1.5 × 10 ⁻⁹	1.5–20 × 10 ⁻⁹	ABS (pH 7)	Cd ²⁺ , Co ²⁺ , Ni ²⁺ , Zn ²⁺ , Ca ²⁺ , Mg ²⁺	831
Pb ²⁺	rGO-AlOOH	rGO-AlOOH/GCE	SWASV	9.32 × 10 ⁻¹¹ M	0.2–0.8 μM	ABS (0.1 M, pH 6.0)/real water	K ⁺ , Ca ²⁺ , Na ⁺ , Mg ²⁺ , Al ³⁺ , Cd ²⁺ , Hg ²⁺ , Zn ²⁺ , Cl ⁻	847
Pb ²⁺	rGO-Bi	rGO-Bi/Au	SWASV	0.4 μg L ⁻¹	1.0–120.0 μg L ⁻¹	ABS (0.1 M, pH 4.5)/drinking water	PO ₄ ³⁻	828
Pb ²⁺	rGO-PPy	rGO-PPy/GCE	SWASV	4 PM	5 nM–60 nM	HCl/KCl (0.1 M, Hg ²⁺ , 1 μM)	Cd ²⁺ , Mg ²⁺ , Cd ²⁺ , Zn ²⁺ , As ³⁺	846
Pb ²⁺	rGO-SnO ₂	rGO/SnO ₂ /GCE	SWASV	1.8 × 10 ⁻¹⁰ M	0.3–1.2 μM	ABS (0.1 M, pH 5.0)	Cu ²⁺ , Hg ²⁺ , Cd ²⁺	837
Pd ²⁺	rGO-SbNP	rGO-SbNP/GCE	DPCSV	0.45 pg L ⁻¹	40–400 pg L ⁻¹	ABS (0.2 M, pH 5.2)/dust samples	Fe ²⁺ , Ni ²⁺ , Co ²⁺ , Na ⁺ , Cu ²⁺ , SO ₄ ²⁻ , PO ₄ ³⁻	848
Pd ²⁺	Co ₃ O ₄	Co ₃ O ₄ -nafion/GCE	SWASV	0.018 μM	0.05–0.275 μM	0.1 M acetate buffer (NaAc–HAc, pH 5.0)	N/A	883

specific analyte	material	architecture	readout/method	LOD	experimental range	sensing environment	notes
Pd ²⁺	Co ₃ O ₄	Co ₃ O ₄ /ITO	DPASV	0.52 $\mu\text{g L}^{-1}$	1–100 $\mu\text{g L}^{-1}$	0.1 M NaAc–HAc buffer, 400 $\mu\text{g L}^{-1}$ bismuth, pH 5.0	ref 877
Pd ²⁺	TiO ₂	TiO ₂ /GCE	SWASV	7 nM	0.2–1.4 μM	0.1 M NaAc–HAc solution, pH 5.0	ref 878
Pt ²⁺	rGO–SbNP	rGO–SbNP/GCE	DPCSV	0.49 pg L ⁻¹	0–260 pg L ⁻¹	ABS (0.2 M, pH 5.2)/dust samples	ref 848
Rh ³⁺	rGO–SbNP	rGO–SbNP/GCE	DPCSV	0.49 pg L ⁻¹	40–400 pg L ⁻¹	ABS (0.2 M, pH 5.2)/dust samples	ref 848
UO ₂ ²⁺	Gr–COOH	Gr–COOH/GCE	SQW	5.0 \times 10 ⁻⁸ M	5.0 \times 10 ⁻⁸ to 5.0 \times 10 ⁻⁶ M	Tris–HCl (0.05 M, pH 5.0)	ref 849
Zn ²⁺	Gr–Nafion	Gr–Nafion/Hg	SWASV	0.07 $\mu\text{g L}^{-1}$	1.0–7.0 $\mu\text{g L}^{-1}$	ABS (0.1 M, pH 4.5) /wetland water	ref 830
NO ₂ ⁻	MoS ₂ –halloysite-NT ₂ Ag	Pt/CPE/MoS ₂ –halloysite-NT ₂ Ag	I	0.7 μM	2–425 μM	0.1 M PBS (pH 4)	ref 874
NO ₃ ⁻	Ni ₃ HHTP ₂	ISM/Ni ₃ HHTP ₂ /GCE	E	$5.01 \pm 0.01 \times 10^{-7}$ M	10^{-7} – 5×10^{-1} M	DI	N/A

^aFET components are described in the following order: gate electrode/insulator/channel material/source electrode/drain electrode.

analytical performance was assessed through various analytical parameters such as sensitivity (detection limits), dynamic range of response, selectivity to interferences, and reproducibility, which are commonly used for validation of novel sensing platforms.

4.4.1. Graphene and Graphene Oxides. A great body of literature has been already dedicated to the application of graphene and graphene oxide in the development of electrochemical sensors for the analysis of biologically relevant molecules due to its unique properties such as high surface area, high electrical conductivity, excellent electrochemical stability in aqueous media, and strong mechanical strength.^{80,126,272,282,283,321,821,883} Graphene can interact with targeted analytes through π – π stacking, charge transfer interactions, and high electrostatic force. The electrochemical properties of graphene in sensing applications, however, are strongly dependent on the ratio of its basal and edge plane content. Typically, graphene containing a low proportion of edge plane sites exhibits slow heterogeneous electron transfer rates and consequently poor electrochemical responses toward various analytes.⁸²¹ Graphene can also serve as a molecular scaffold for immobilizing the desired functional groups to target biomolecular analytes, consequently leading to enhancements in the selectivity of biosensors (Figure 50). These

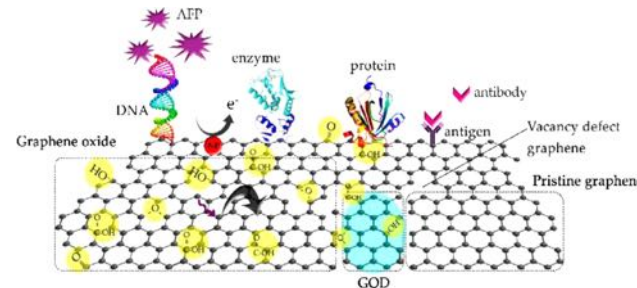


Figure 50. Schematic illustration of the graphene-based materials that can be immobilized with biomolecules as the receptor.²⁸² Reproduced with permission from ref 282. Copyright 2017 MDPI (Basel, Switzerland).

sensors have been applied for detecting clinically-relevant analytes, such as glucose, cholesterol, H₂O₂, dopamine (DA), ascorbic acid (AA), uric acid (UA), β -nicotinamide adenine dinucleotide (NAD⁺/NADH), carcinoembryonic antigen (CEA), α -fetoprotein, thrombin, and prostate specific antigen (PSA).⁸⁸¹

4.4.1.1. Glucose. Owing to the increasing number of people diagnosed with diabetes every year, the demand for constructing point-of-care portable glucose sensing platforms have also risen.²⁷³ Glucose-selective electrochemical biosensors are most often formed by the immobilization of glucose-specific enzymes such as glucose oxidase (GOD), which can function as either a mediator or recognition element during the sensing process.²⁷³ The two redox-active centers in GOD are wrapped by the protein layer, which inhibits the electron transfer between each redox center and the electrode surface. In this situation, Gr can be employed as an electrical conductor, which promotes enzyme activity and facilitates electron transfer between the electrode substrate and GOD redox-active centers, thus allowing detection of glucose. Kang and co-workers employed this experimental approach to fabricate rGO-chitosan-GOD modified GCE for sensitive detection of glucose.⁸⁸⁴ The resulting biosensors responded

Table 5. continued

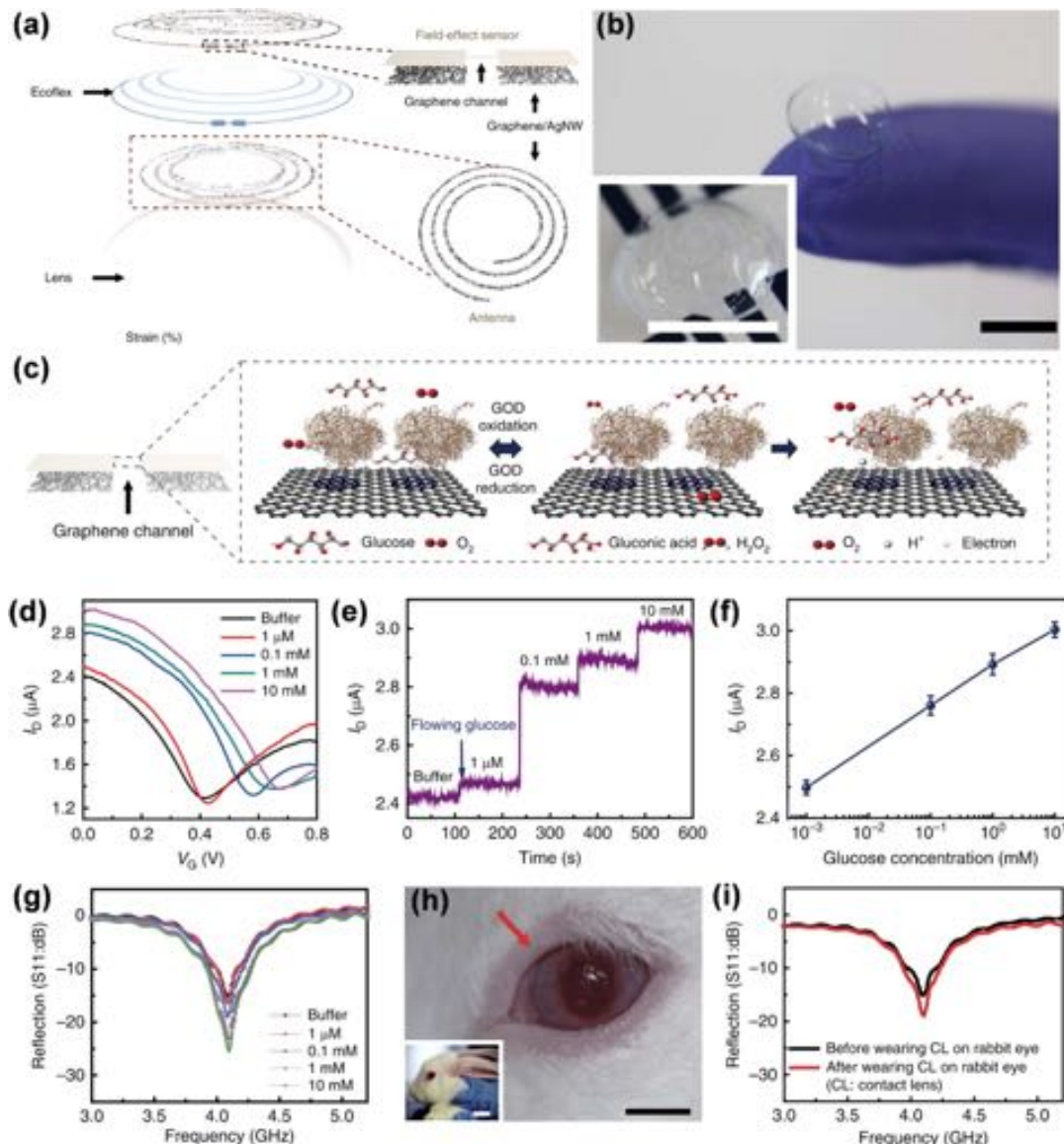


Figure 51. (a) Schematic of the wearable contact lens sensor, integrating the glucose sensor and intraocular pressure sensor. (b) Photograph of the contact lens sensor. Scale bar, 1 cm. (Inset: close-up image of the antenna on the contact lens. Scale bar, 1 cm.). (c) Schematic illustration and principle of glucose detection with the GOD-pyrene functionalized graphene. (d) Transfer (I_D - V_G) characteristics of the sensor at varied concentrations of glucose ($V_D = 0.1$ V). (e) Real-time continuous monitoring of glucose concentrations ($V_G = 0$ V). (f) The calibration curve generated by averaging current values and the glucose concentration from 1 to 10 mM. Each data point indicates the mean value for 10 samples, and error bars represent standard deviation. (g) Wireless monitoring of glucose concentrations from 1 to 10 mM. (h) Photographs of wireless sensor integrated onto the eyes of a live rabbit. Black and white scale bars, 1 and 5 cm, respectively. (i) Wireless sensing curves of glucose concentration before and after wearing contact lens on an eye of live rabbit.⁸⁹⁴ Reproduced with permission from ref 894. Copyright 2017 Springer Nature.

linearly in the 0.08–12 mM concentration range with the detection limit of 0.02 mM and an electron transfer rate constant of $2.83 \pm 0.18 \text{ s}^{-1}$. The enhanced performance of fabricated biosensors was ascribed to a large surface-to-volume ratio and high conductivity of graphene, together with good biocompatibility of chitosan, which enhanced the enzyme absorption, and promoted direct electron transfer between redox enzymes and the surface of electrodes.

Wang et al. used nitrogen-doped rGO-chitosan-GOD/GCE hybrid electrode for glucose biosensing with concentrations as low as 0.01 mM, in the presence of UA and AA interferents.⁸⁸⁵ Cai et al., by directly immobilizing GOD onto the surface of GO, could detect glucose at concentrations as low as 0.01 mM

through bio-electrocatalytic reduction of oxygen.¹¹³⁷ They observed that the native structure and bioactivity of GOD was retained after the successive immobilization on GO. This biosensor also underwent effective direct electron transfer reaction with an apparent rate constant of 2.68 s^{-1} . A Gr-polypyrrole (PPy)-GOD composite was used by Li and co-workers for glucose determination (LOD of $3 \mu\text{M}$).⁸⁸⁶ The PPy conductive polymer provided excellent conductivity, biocompatibility, and enhanced surface-to-volume ratio for Gr-GOD immobilization. Another glucose sensitive polymer-graphene composite was prepared by Zeng et al. through layer-by-layer deposition of alternating layers of Gr sheets modified with pyrene-grafted poly(acrylic acid) (PAA) and poly-

(ethylenimine) (PEI).⁸⁸⁷ The modified electrodes were then used for selective detection of glucose and maltose through the immobilization of multienzyme system (GOD and glucoamylase) on the surface of Gr nanocomposite. Both sensors exhibited good sensitivity to maltose and glucose with LOD of 1.37 and 0.168 mM, respectively. Expanding on this approach, Shan et al. immobilized polyvinylpyrrolidone (PVP)-protected graphene-polyethylenimine-functionalized ionic liquid nanocomposites onto GCE for glucose determination.⁸⁸⁸ This biosensor responded linearly to glucose in the range of 2 to 14 mM.

Further improvements in sensitivity to glucose were focused on the enhancements of the electron transfer rates through incorporation of nanomaterials such as Au,⁸⁸⁹ Pd,⁸⁹⁰ Ag,⁸⁹² and Pt.⁸⁹³ For example, Chen et al. used GOD-Au-Gr biosensor to determine blood sugar concentrations in human serum.⁸⁸⁹ The detection limit for glucose was found at 8.9 μ M, and the linear range of blood sugar concentration was found at 43.6–261.6 μ M. Wu et al. lowered the detection limits of glucose down to 0.6 μ M through electrochemical deposition of Pt nanoparticles onto rGO.⁸⁹³ Recently, Park and co-workers integrated a wireless FET device consisting of graphene-Ag NW composite as source and drain electrodes (Figure 51a,b), graphene with immobilized GOD as an active sensing channel layer, Cr/Au as interconnects, and SU8 as a passivation layer, onto a soft contact lens, and used it for the *in vivo* detection of glucose in tears (Figure 51c).⁸⁹⁴ The resulting sensing device could selectively respond to glucose in the presence of 50 μ M of AA, 10 mM of lactate, and 10 mM of UA with the detection limit of 1 μ M (Figure 51d–f). This wireless sensor also allowed glucose monitoring in the rabbit tear fluid (Figure 51g–i), exhibiting good stability to repeated eye-blinking and demonstrating its potential for the design of new generation technologies for personalized medicine.⁸⁹⁴

Despite high selectivity and sensitivity of enzyme-based biosensors their practical application is often limited by the lack of long-time stability of enzymes.⁸⁹⁵ A possible solution to this problem is through the development of non-enzymatic glucose sensors that can directly oxidize glucose in the measured sample. The majority of non-enzymatic glucose biosensor relies on the presence of metal catalysts (metal hybrids, alloys, metal oxides, and metal complexes) that can facilitate the electron transfer between glucose and electrode surface.²⁷³ However, these nanocomposites are often not suitable for direct glucose detection due to their poor electrical conductivity and limited mechanical and chemical stability. The presence of graphene in non-enzymatic glucose sensors improves electrical conductance and surface–volume ratio for the incorporation of guest molecules, thus improving electrocatalytic effect for glucose oxidation.⁸²¹ Graphene-based sensors doped with transition metals, such as CuO and CuS,^{896–898} PtNi,⁸⁹⁹ NiO,⁹⁰⁰ Co₃O₄,⁹⁰¹ and noble metals,^{902,903} were successfully employed for the enzyme-free detection of glucose. For instance, Yang and co-workers used rGO/CuS nanocomposites modified GCE to detect glucose in human urine and blood serum samples.⁸⁹⁸ This non-enzymatic platform exhibited good catalytic activity toward glucose oxidation over a wide linear range (1–2000 μ M), with LOD of 0.19 μ M. Dong et al. integrated cobalt oxide (Co₃O₄) nanowires onto the graphene foam via the hydrothermal procedure.⁹⁰¹ The resulting bio-platform could sense glucose amperometrically at concentrations as low as 25 nM. Recently, palladium nanoflower decorated CVD graphene/Nafion/⁹⁰⁴

glucose oxidase nanocomposite in a FET device was shown to detect glucose at 1 nM concentrations with excellent selectivity against uric and ascorbic acid.⁹⁰⁴ The high sensitivity to glucose was ascribed to the pointed morphology of Pd nanoflowers, which provided more active sites for analyte interactions.

4.4.1.2. Dopamine, Ascorbic Acid, and Uric Acid. Dopamine (DA) is an important neurotransmitter, which plays a vital role in proper functioning of the central nervous system (CNS), cardiovascular system, and hormonal systems.⁹⁰⁵ Abnormal levels of dopamine are often associated with schizophrenia, attention deficit hyperactivity disorder, restless legs syndrome (RLS), and Parkinson's disease.⁹⁰⁵ DA detection is typically challenged by its very low physiological concentration ranging from 0.01–1 μ M and interference from much more abundant biomolecules such as ascorbic acid (AA) and uric acid (UA).⁹⁰⁶ In addition, the redox oxidation potentials of DA, UA, and AA can be difficult to distinguish in complex media. Therefore, novel electrocatalytic systems are needed to ensure adequate sensitivity and selectivity. High density of edge sites in graphene together with its excellent electronic conductivity led to the development of numerous graphene-based sensors for the detection of these molecules.⁹⁰⁷ To demonstrate this approach, Shang et al. integrated multilayer graphene nanoflakes films (Figure 52a,b) onto the

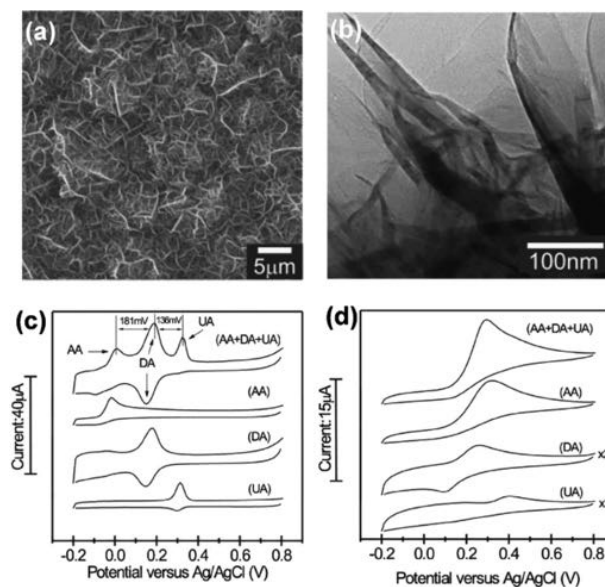


Figure 52. (a) SEM and (b) TEM images of MGNFs. (c and d) CV profiles of the MGNF and bare GCE electrodes, respectively, in the solution of 50 mM, pH 7.0 PBS with 1 mM AA, 0.1 mM DA, and 0.1 mM UA.⁹⁰⁸ Reproduced with permission from ref 908. Copyright 2008 John Wiley and Sons.

Si substrate through microwave plasma enhanced chemical vapor deposition for simultaneous determination of AA, DA, and UA.⁹⁰⁸ The edge plane defects in graphene facilitated the electrochemical transfer rates for oxidation of the three biomolecules allowing sensitive detection of DA with LODs of 0.17 μ M in the presence of 1 mM AA and 0.1 mM UA (Figure 52c,d). Another example of incorporating graphene to sense DA has been shown by Wang et al.⁹⁰⁹ The authors fabricated rGO-chitosan nanocomposite electrodes, which responded selectively to DA over linear response range of 5–200 μ M in the large excess of AA and UA (500 μ M). The

high selectivity of graphene to DA over AA was attributed to $\pi-\pi$ interactions between phenyl ring of DA and two-dimensional planar hexagonal carbon structure of graphene.

Hou et al. fabricated a sensitive bio-platform made of Nafion and *N*-(trimethoxysilylpropyl) ethylenediamine triacetic acid (EDTA) incorporated into rGO to detect dopamine with a LOD of $0.01\ \mu\text{M}$. The EDTA groups, combined with ionic sulfuric groups of Nafion, could preconcentrate the DA from solution, while the EDTA-rGO promoted electron transfer between dopamine and electrode. The oxygen rich rGO further inhibited the diffusion of AA and thus provided enhanced selectivity and sensitivity.⁹¹⁰ To further lower the LODs of DA, Tan et al. employed modified graphene sheets with β -cyclodextrin (β -CD) drop-cast on GCE. The adsorbed β -CD prevented the formation of graphene aggregates and ensured good accessibility of active sites in graphene for electron transfer.⁹¹¹ One of the most sensitive electrochemical sensors for DA detection was developed by Liu et al. through using a rGO-polyvinylpyrrolidone (PVP) polymer nanocomposite as a sensing layer. This biosensor displayed a wide linear response range of 5×10^{-10} to $1.13 \times 10^{-3}\ \text{M}$ to DA with a detection limit of $0.2\ \text{nM}$ in $1\ \text{mM}$ AA.⁹¹² Numerous other examples of electrodes modified with graphene and sulfonyl groups,⁹¹³ Fe_3O_4 ,⁹¹⁴ Pd nanoparticles,⁹¹⁵ or Al/Zn hydroxides⁹¹⁶ were reported for selective determination of dopamine. Interestingly, electrodes constructed of polydopamine (PDA)-rGO-SnO₂ layer coated on Au were able to detect dopamine at $5\ \text{nM}$ concentrations.⁹¹⁷ The outstanding sensitivity of this bio-platform was ascribed to (i) superior electronic conductivity of graphene sheets; (ii) Au and PDA prevented aggregation of graphene sheets and thus enhanced conductivity of the composite; (iii) SnO₂ improved ability of analytes to be adsorbed and transferred to the electrode surface. Aptamer functionalized rGO/Nile blue/AuNP complex-modified glassy carbon electrode was capable of detecting DA in $10\ \text{nM}$ to $0.2\ \text{mM}$ range with the LOD of $1\ \text{nM}$.⁹¹⁸ The resulting sensor also demonstrated good selectivity for DA in the presence of AA, UA, epinephrine, norepinephrine, and glucose. In real biological samples, this nanocomposite modified electrode could detect DA, with high detection recoveries of $97.0\text{--}104.0\%$.

Although AA and UA are widely recognized as bio-interferents during electrochemical sensing of dopamine, there is an on-going demand to develop reliable sensing bio-platforms for their determination due to their large biological importance.⁹¹⁹ Brownson et al. demonstrated that with increasing basal plane contribution in graphene modified electrodes, the heterogeneous electron transfer rate is significantly diminished resulting in poor kinetics for oxidation of biomolecules such as AA.⁹²⁰ Correspondingly, fast heterogeneous electron transfer can be achieved in the electrodes with an increased edge plane content. Keeley et al. used liquid phase exfoliation to fabricate a sensing platform for AA detection using graphene nanosheets immobilized on pyrolyzed photoresist film (PPF) electrodes. Effective response to AA was found in the range 0.4 to $6.0\ \text{mM}$ with a $0.12\ \text{mM}$ detection limit.⁹²¹ Shi and co-workers used graphene functionalized with positively charge gold nanoparticles to sense UA in the range of 2.0×10^{-6} to $6.2 \times 10^{-5}\ \text{mol L}^{-1}$ with the LOD of $2 \times 10^{-7}\ \text{mol L}^{-1}$.⁹²²

4.4.1.3. Cholesterol. Cholesterol and its esters are essential membrane constituents widely found in biological systems, which serve a unique purpose of modulating membrane

fluidity, elasticity, and permeability. The undesired accumulation of cholesterol and its esters may lead to critical health problems, including heart diseases, cerebral thrombosis, or atherosclerosis.⁹²³ Therefore, there is a continuous need for new point-of-care diagnostics to measure lipid panels, including total cholesterol. De and co-workers utilized β -CD modified Gr as a non-enzymatic platform for the electrochemical detection of cholesterol using methylene blue (MB) as a redox indicator.⁹²⁴ They observed that MB can form inclusion complexes with β -CD-Gr, which in the presence of cholesterol, undergo a displacement reaction releasing MB back into the solution. This process can be directly monitored with DPV permitting cholesterol detection at concentrations as low as $1\ \mu\text{M}$. Cao et al. used TiO₂-Gr-Pt-Pd nanocomposite modified electrodes to improve surface/volume ratio for immobilization of cholesterol oxidase (ChOx).⁹²⁵ The developed bio-platforms exhibited a wide linear range of responses to cholesterol in the concentrations spanning from 5.0×10^{-8} to $5.9 \times 10^{-4}\ \text{M}$, with the LODs of $0.017\ \mu\text{M}$ and response time under $7\ \text{s}$. The authors also demonstrated that cholesterol can be detected in food products such as eggs, meat, margarine, and fish oil. More recently, Galdino et al. prepared ionic liquid (1-(3-aminopropyl)-1H-imidazol-3-ium bromide) GO-Au-ChOx composite modified electrodes for cholesterol sensing.¹¹³⁸ Raj et al. successfully loaded cholesterol esterase and ChOx enzymes on the rGO-Pt modified electrodes.⁹²⁶ Pt nanoparticles catalyzed the electrochemical oxidation of hydrogen peroxide and the enzymes enhanced hydrolysis of cholesterol. The authors used then amperometry for the detection of cholesterol and its esters with a LOD of $0.2\ \mu\text{M}$.

4.4.1.4. NADH. The detection of dihydronicotinamide adenine dinucleotide (NADH) has received considerable attention, owing to its very important role as a cofactor in many naturally occurring enzymatic reactions, including the conversion of important substrates such as alcohol, lactate, and glucose.⁹²⁷ Govindhan et al. reported on non-enzymatic β -NADH biosensor based on rGO decorated with Au nanoparticles on GCE. The sensor exhibited a high sensitivity of $0.916\ \mu\text{A}/\mu\text{M cm}^2$ and wide linear range of $50\ \text{nM}$ to $500\ \mu\text{M}$ with detection limits of $1.13\ \text{nM}$.⁹²⁸ The interferences from glutathione, glucose, ascorbic acid, and quanine were negligible. The improved electrocatalytic activity to NADH oxidation of the rGO-Au/GCE nanocomposite was facilitated by the highly dispersed Au nanoparticles on the surface of rGO through the formation of a 3D electronic conductive network. This sensor could also detect NADH in human urine. Tabrizi and Zand prepared rGO through a hydrothermal process using NADH as a reducing agent.⁹²⁹ Amperometric measurements indicated that the rGO-modified GCE electrode exhibited good electrocatalytic activity toward the oxidation of NADH at the potential of $+0.35\ \text{V}$ yielding LOD of $0.6\ \mu\text{M}$. Li and co-workers utilized cycling voltammetry to electrodeposit ERGO-polythiophene (PTH) composite layer directly onto GCE and used it for the fabrication of NADH amperometric biosensor. The ERGO-PTH modified electrodes displayed LODs of $0.1\ \mu\text{M}$ over the $0.01\text{--}3.9\ \text{mM}$ concentration range.⁹³⁰ Sensitivity to NADH was further increased by Li et al., who used gold disk electrode coated with Gr-Au NPs-DNA tetrahedron, as scaffold for graphene immobilization, to form an amperometric biosensor. DNA-Au scaffold kept Gr fragments in a vertical position instead of lying down on the surface of electrode, which offered more opportunities for graphene fragments to

adsorb and react with NADH molecules due to larger density of edge-plane sites. The resulting platform could detect NADH at concentrations as low as 1 fM.⁹³¹

4.4.1.5. Hydrogen Peroxide. Hydrogen peroxide, aside from being an enzymatic end-product of many biological processes, is also an essential mediator in food, pharmaceutical, clinical, industrial, and environmental analysis.⁹³² Xu and co-workers fabricated a H₂O₂ sensor using rGO-chitosan nanocomposites as scaffolds for the immobilization of hemoglobin (Hb) molecules.⁹³³ The resulting bio-platform showed LODs of 0.51 μM. The enhanced electrocatalytic effect was attributed to the large available surface area of the rGO-chitosan matrix for Hb loading, allowing this enzyme to retain its native structure during electrochemical transformations. The electron transfer between the composite film and the electroactive center of Hb was further facilitated by the presence of rGO. The percolating 3D network of rGOs also provided multiplexed paths to rapidly conduct away the charges.

The integration of enzymes can improve the sensing performance. Lu et al. improved sensitivity to H₂O₂ through immobilization of horseradish peroxidase (HRP), a heme-containing enzyme, onto the surface of graphene.⁹³⁴ Graphene sheets, prepared through exfoliation by the tetrasodium 1,3,6,8-pyrenetetrasulfonic acid, enhanced the capacity to effectively anchor the HRP enzymes and to mediate the charge transfer. The resulting biosensors could sense H₂O₂ at lowest concentrations of 0.106 μM in the range of 0.63 μM to 16.8 μM. A different approach to immobilize HRP onto the surface of electrode was demonstrated by Zeng et al. The authors reported on a hierarchical nanostructure formed by layer-by-layer assembly of HRP enzyme together with the sodium dodecyl benzenesulfonate (SDBS) surfactant functionalized rGO as a sensitive platform for the detection of H₂O₂. Large capacity of rGO films for enzyme incorporation resulted in LODs of 0.1 μM for H₂O₂ detection.⁹³⁵ Zhou et al. decorated rGO with Au nanoparticles and microperoxidase-11 enzyme for the amperometric detection of H₂O₂ with a linear range from 2.5 to 135 μM.⁹³⁶ Wang and co-workers extended the linear response range (1 μM to 500 mM) and lowered LODs to 80 nM by using one-step microwave-assisted thermal reduction to fabricate Pt nanoparticle-rGO composite electrodes.⁹³⁷ The high performance of the fabricated bio-platform was ascribed to the high-density of uniformly distributed Pt nanoparticles on the rGO surface, which resulted in rapid charge transfer between metal nanoparticles and rGO.⁹³⁷

Using Prussian blue immobilized on the surface of rGO, Cao et al. improved the LODs for H₂O₂ detection to 45 nM.⁹³⁸ One of the most sensitive biosensor, to H₂O₂, was developed by Sun and co-workers. They assembled atomically thick Pt-Ni nanowires on the surface of rGO through ultrasonic self-assembly method to improve the electrocatalytic effect to H₂O₂ catalysis.⁹³⁹ This enzyme-free biosensor exhibited wide linear range of response to H₂O₂ spanning from 1 nM to 5.3 mM with the detection limits as low as 0.3 nM. Such electrode modifications enabled the detection of trace amounts of H₂O₂ released from Raw 264.7 cells.⁹³⁹ Through using rGO doped with manganese ferrite (MnFe₂O₄) nanoparticles, Rani et al. developed a non-enzymatic amperometric sensor for H₂O₂ determination. They reported on LODs of 0.35 μM and sensitivity of 1180 μA mM⁻¹ cm⁻² for H₂O₂ oxidation.⁹⁴⁰

4.4.1.6. Other Small-Molecule Bioanalytes. Other notable examples of graphene modified electrodes for biosensing of small molecules also include the detection of food additives,

psychoactive substances, or pesticides. For instance, Long and co-workers used graphene nanosheets decorated with cobalt-nickel bimetallic nanoparticles for the detection of octylphenol. The resulting platform was used to quantify the amount of target analyte at picomolar concentrations in plastic bottles, metal bottles, and food packaging bags.⁹⁴¹ Oliveira et al. developed a bi-enzymatic biosensor based on graphene and gold nanoparticles for the detection of common pesticides—carbamates. This sensor detected carbamates in citrus fruit samples (orange, lemon, and tangerine) without significant interferences from ascorbic acid, citric acid, and glucose.⁹⁴² For a comparative investigation on the determination of caffeine in coffee, energy drinks, and tea, the research group lead by Khoo et al. utilized several chemically modified graphene-based materials including graphite oxide (GPO), GO, and electrochemically reduced graphene oxide (ERGO). They concluded that ERGO exhibited the best response characteristics based on sensitivity, linearity, and reproducibility of the response because of the lowest content of oxygen functionalities.⁹⁴³

4.4.1.7. Nucleic Acid. Gene sequence data alone may be of limited clinical use unless it is directly correlated to sickness relevance. In order to screen significant populations for specific nucleotide sequences of their genomes, as well as to monitor gene expression, novel technologies are required.⁹⁴⁴

Two experimental approaches are typically employed for the electrochemical (voltammetric and amperometric) detection of nucleic acids: (i) direct detection of DNA bases and polynucleotides or (ii) via introducing DNA specific electroactive labels. Huang et al. electrochemically differentiated between adenine and guanine nucleobases at concentrations as low as 50 nM and 25 nM using GCE electrodes modified with Gr-COOH.⁹⁴⁵ The observed sensitivity was attributed to the presence of negatively charged graphene-COOH composite that facilitated adsorption of positively charged guanine and adenine onto the electrode surface and consequently enhanced the magnitude of the measured signal. Dong and co-workers employed GO modified GCE for simultaneous detection of all four DNA bases in both ssDNA and dsDNA without the need of a pre-hydrolysis step.⁹⁴⁶ GO nanosheets immobilized on disposable graphite electrodes were used by Muti et al. as a label free platform for nucleic acid determination in Hepatitis Virus B sequence.⁹⁴⁶ The modification of the electrode with a GO layer increased surface coverage by providing enhanced adsorption of nucleic acids onto the electrode, giving rise to higher sensitivity. Different experimental approach was demonstrated by Yin et al. in which rGO-chitosan electrodes were doped with Fe₃O₄ particles for sensitive determination of guanosine.⁹⁴⁷ The oxidation peak current, measured with DPV, was proportional to guanosine concentration in the range of 2.0×10^{-6} to 3.5×10^{-4} M with a LOD of 7.5×10^{-7} M. The authors indicated that the presence of metal-oxide nanoparticles diminished the electron transfer resistance. Du et al. constructed a DNA sensor based on ERGO decorated with Au nanoparticles through direct electrochemical deposition methods.⁹⁴⁸ They observed that the presence of gold nanoparticles was essential to differentiate the DPV signals of T from that of A within a single-base alteration. Gao et al. utilized composite films of PPy/Gr for the quantitative detection of adenine and guanine. PPy/GR electrodes enhanced the adsorption of the electropositive adenine and guanine through strong π–π interactions and electrostatic adsorption on negatively charged surface of the electrode. This biosensor demonstrated linear response in the 0.06–100 and

0.04–100 μM ranges and LODs of 0.02 and 0.01 μM , for adenine and guanine, respectively.⁹⁴⁹

Taking the advantage of its abundant electrochemically active edge sites, Ambrosi and Pumera fabricated GCE covered with stacked graphene nanofibers, which was able to distinguish four nucleobases with a sensitivity up to four fold larger than reported for CNTs electrodes.⁹⁵⁰ They employed this sensing platform for direct label-free detection of A(H1N1) human influenza strands. High sensitivity of stacked graphene nanofibers over CNTs could be due to large density of edge sites of individual graphene sheets in comparison to significant contribution of side walls in CNTs. Lim et al. utilized anodized epitaxial graphene modified electrodes to separate anodic peaks of all four nucleic acid bases with great selectivity in double stranded and single stranded nucleic acids (Figure 53a–d).⁹⁵¹ Impressive results were demonstrated by

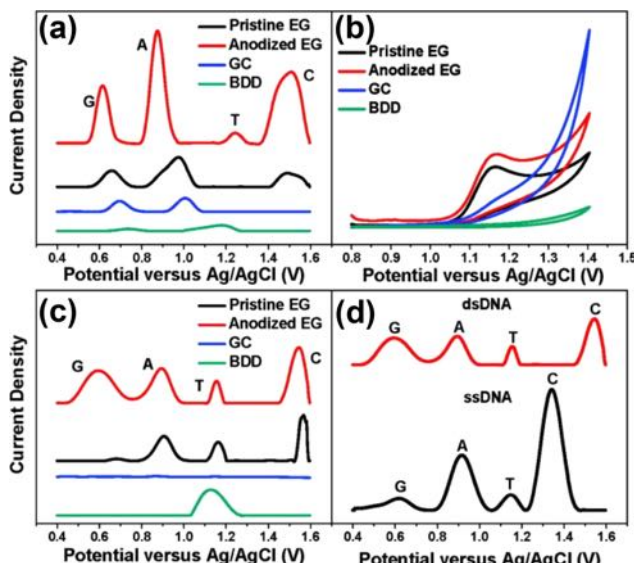


Figure 53. DPV profiles for pristine EG, anodized EG, GC, and BDD electrodes in (a) 30 μM equimolar mixture of G, A, T, and C, (b) 1.0 mM thymine, (c) 30 $\mu\text{g mL}^{-1}$ dsDNA, (c) anodized EG in 30 $\mu\text{g mL}^{-1}$ dsDNA and 30 $\mu\text{g mL}^{-1}$ ssDNA. Supporting electrolyte: 10 mM KCl/10 mM PBS solution at pH 7.⁹⁵¹ Reproduced from ref 951. Copyright 2010 American Chemical Society.

Akhavan et al., who used electrophoretic deposition to fabricate graphene oxide nanowalls, with a preferred vertical orientation, deposited on a graphite electrode for ultra-sensitive determination of DNA nucleotides (A, G, C, and T).⁹⁵² The resulting bio-sensors could successfully detect dsDNA oligonucleotides at concentrations as low as 9.4 zM. This extremely high sensitivity was ascribed to the high density of active edge sites in the 2D material.

Another strategy for nucleic acid detection involves a single-stranded probe sequence immobilized onto the electrode surface (recognition layer), where the base-pairing interactions can enable high affinity of the probe for target DNA sequences. To demonstrate the feasibility of this approach, Chu et al. formed a graphene-MoS₂ composite with immobilized DNA and used it as a label-free DNA sensing platform.⁹⁵³ This bio-platform could detect DNA at concentrations reaching 1.0×10^{-17} M within the 1.0×10^{-16} to 1.0×10^{-13} M range.⁹⁵³ Pham and co-workers developed an immunosensor for microRNA (miR-141 and miR-29b-1, which are known as

prostate and lung cancer biomarkers, respectively) determination based on screen printed electrodes modified with rGO and CNTs. This sensor detected miRNA with a limit of detection as low as 10 fM.⁹⁵⁴ Tran et al. fabricated a label-free electrochemical sensor for the determination of miRNAs using a GO conducting polymer modified electrode. This platform demonstrated high selectivity, with current increases upon hybridization from 1 fM to 1 nM of target miRNA, with LODs of 8 fM.⁹⁵⁵ Liu et al. used a graphene-gold nanoparticle composite as a scaffold for the immobilization of the DNA probes. They employed a sandwich-type detection strategy to bind target DNA strands and secondary HRP-labeled oligonucleotides.⁹⁵⁶ Through amperometric and CV measurements, the authors observed good linear relationship between the current signal and the logarithmic function of complementary DNA concentration in a range of 50–5000 fM with the LOD of 3.4 fM.

Lin and co-workers fabricated a DNA sensor based on the Gr-Au composite with 1,10-phenanthroline cobalt ($[\text{Co}(\text{phen})_2(\text{Cl})(\text{H}_2\text{O})]^+$) complex used as an electroactive indicator.⁹⁵⁷ The resulting sensor detected target DNA from *Escherichia coli* (*E. coli*) in a linear range from 2.50×10^{-11} to 1.25×10^{-9} M and LOD of 8.33×10^{-12} M. Bonnani et al. used GO nanoplatelets as an electroactive label for the discrimination of the single-base mutation in the DNA sequence related to Alzheimer's disease.⁹⁵⁸ They observed that the GO nanoplatelets exhibited different affinity for binding single- and double-stranded DNA, thus allowing selective differentiation among complementary, noncomplementary, and one-mismatch DNA sequences. In a recent study, Ping et al. developed a sensitive DNA FET biosensor with a scalable and reproducible (>90% yield) fabrication process.⁹⁵⁹ They used CVD-grown graphene monolayers (on the Si substrate) as scaffold for the immobilization of probe molecules, such as ssDNA to impart selectivity to target DNA strands. The resulting sensing device exhibited LOD of 1 fM for 60-mer DNA oligonucleotides in aqueous solutions. Dong et al. also fabricated a DNA selective sensor by incorporating probe-labeled gold nanoparticles (ssDNA-AuNP) onto electrochemically reduced graphene oxide modified electrodes with thiol group tagged (GT) DNA strand ($d(\text{GT})_{29}\text{SH}$) coupled with horseradish peroxidase (HRP) functionalized carbon sphere (CNS) used as tracer molecules.⁹⁶⁰ The authors observed high sensitivity to DNA with the LOD down to 5 aM and a linear response range spanning 5 orders of magnitude (from 1.0×10^{-17} to 1.0×10^{-13} M). This biosensor exhibited high selectivity differentiating single-base mismatched and three-base mismatched sequences of DNA. A DNA label-free electrochemical biosensor has been developed by Benvidi et al. for BRCA1 mutation detection based on Au nanoparticles-rGO/GCE functionalized with ssDNA BRCA1 5382 insC probe.⁹⁶¹ The rGO-Au nanocomposite enhanced the sensitivity of this sensor through increasing the number of immobilized active sites. This label-free electrochemical biosensor showed LODs of 1.0×10^{-20} M for target DNA and two linear response ranges spanning over 13 orders of magnitude in concentration, and effectively distinguished between the complementary and non-complementary sequences.⁹⁶¹

4.4.1.8. Proteins. Electrochemical protein biosensors typically rely on the presence of specific analyte recognition centers that are immobilized on the surface of electrode: (1) antibodies, which can selectively recognize and bind specific

target antigens, and (2) aptamers, which are small peptides or oligonucleotides that exhibit conformations and structures suitable for binding target biomolecules.²⁶⁵ Roy and co-workers used GO as scaffold for anti-IgG immobilization to detect rabbit IgG antibodies over the concentration range of 3.3–683 nM with the LODs of 0.67 nM. The developed impedimetric sensor exhibited high selectivity toward rabbit IgG antibody as compared to the non-complementary myoglobin.⁸⁸³ Zhang et al. developed a sandwich-type double-signal immunosensor for the detection of human IgG based on PDA-rGO-AuNPs and Ag/C nanocomposite acting as a signal label (Figure 54a,b).⁹⁶² The fabricated immuno-

concentrations. In addition, this biosensor was successfully employed for the determination of AFP in serum samples. Wei et al. further enhanced the sensitivity to AFP by incorporating anti-AFP on Gr and thionine (Thi) modified GCE through π - π interaction followed by covalent cross-linking of AFP antibodies with Thi.⁹⁶⁵ The AFP interactions with the electrode diminished electron-transfer and mass-transfer of Thi resulting in reduced read-out. This immunosensor detected AFP at levels down to 5.77 pg mL⁻¹. In recent studies, the immobilization of anti-carcinoembryonic antigen (CEA) on the surface of graphene in the FET device architecture enabled label-free detection of this cancer biomarker (CEA) at 0.5 pM concentrations, far exceeding that of the clinical diagnostics cutoff value.⁹⁶⁶ The fabricated device demonstrated excellent selectivity against neuron specific enolase (NSE) and cytokeratin-19-fragment (CYFRA21-1) interferents. The authors confirmed that the immobilized antibody (anti-CEA) exhibited high binding affinity to CEA (dissociation constant of 6.35×10^{-11} M), thus allowing selective detection of the targeted protein.

A sandwich-type immunoassay system using horseradish peroxidase modified GO nanosheets was developed by Tang and co-workers, who used it for the impedimetric detection of carcinoembryonic antigens.⁹⁶⁷ The dynamic concentration range of this biosensors ranged from 1.0 pg mL⁻¹ to 80 ng mL⁻¹ with LOD of 0.64 pg mL⁻¹.⁹⁶⁷ Yang et al. utilized nitrogen-doped graphene functionalized with Au nanoparticles as immunosensor for matrixmetalloproteinase-2 (MMP-2) determination.⁹⁶⁸ Notably, the design of the immunosensor also involved a polydopamine-functionalized graphene oxide hybrid conjugated to the horseradish peroxidase-secondary antibodies by covalent bonds as a multi-labeled and biocompatible probe to amplify the electrochemical response. This resulting biosensor successfully detected MMP-2 in human serum with LODs as low as 0.11 pg mL⁻¹. Chen and co-workers detected cell apoptosis through monitoring the caspase-3 triggered signal-on strategy with GO-assisted amplification. As the target protein, caspase-3 can be detected in a range of 0.1–100 pg mL⁻¹. A low detection limit of 0.06 pg mL⁻¹ was obtained, which is 103–105 times more sensitive compared to other reports.⁹⁶⁹ Antiapolipoprotein B 100 functionalized electrodes consisting of a mesoporous few layer rGO and NiO nanocomposites were used by Ali et al. for highly sensitive detection of low density lipoprotein molecules (LOD: 0.07 mg dL⁻¹).⁹⁷⁰ Recently, Ates et al. functionalized glassy carbon electrode with rGO-Pt NPs-Nafion nanocomposite to detect renin inhibitor-alistiren in human blood plasma at nanomolar concentrations (LODs of 8.2 nM).⁹⁷¹ Er et al., using the same device architecture, quantified the content of α_1 -AR antagonist silodosin in blood plasma.⁹⁷² The resulting bio-platform exhibited linear calibration curve in the range of 1.8–290.0 nM with the LODs of 0.55 nM. The group led by Pumera developed a selective thrombin biosensor through the modification of a disposable electrical printed carbon electrodes with the thrombin aptamer utilizing GO as the molecular label.⁹⁷³ The binding event between thrombin and the immobilized aptamer facilitates the partial release of the aptamer from the surface of the electrode, resulting in uncovered underlying surfaces available for charge transfer between GO and the electrode. The measured signal then corresponds to voltammetric reduction of the inherent oxygen groups from GO. Chemical vapor deposited graphene functionalized with DNA aptamer in FET biosensor enabled

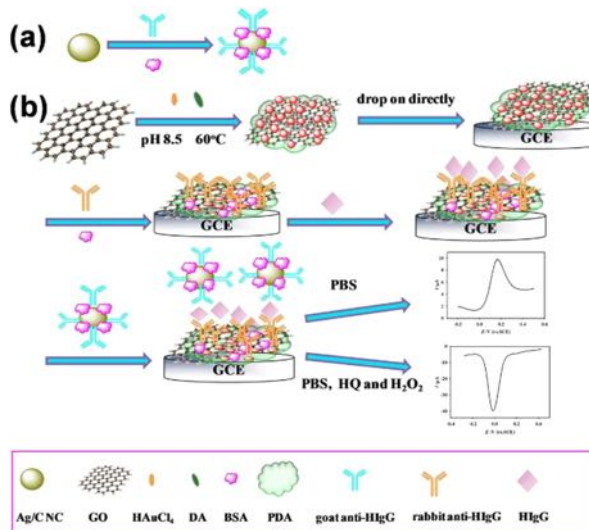


Figure 54. Fabrication processes for the electrochemical immunosensor.⁹⁶² (a) Preparation of the Ag/C nanocomposite by functionalization with bovine serum albumin (BSA) and goat anti-HLgG. (b) Preparation of GO-based sensing composite mounted on a GCE.⁹⁶² Reproduced with permission from ref 962. Copyright 2015 Elsevier B.V.

sensor responded to human IgG within the concentration ranges of 0.1–100 and 0.01–100 ng mL⁻¹ with the LODs of 0.001 ng mL⁻¹ in the absence and presence of H₂O₂ and hydroquinone.

Su et al. developed a sensitive immunosensor for the determination of alpha-fetoprotein (AFP) by means of immobilization of horseradish peroxidase-anti-AFP conjugates onto the Au functionalized graphene.⁹⁶³ The AFP antibody-antigen partially inhibited the active center of HRP and thus decreased the catalytic reduction of H₂O₂ by HRP. Meanwhile, the redox-active TH 55 together with HRP mediated the electron transfer from H₂O₂ to the electrode surface. This experimental approach allowed determination of AFP at concentrations as low as 0.7 ng mL⁻¹. The same immunoassay was also evaluated in clinical human serum analysis, correctly identifying samples containing AFP in accordance with the results from commercial clinical devices. Yang et al. used rGO-Au NP-PEDOT-PB composite film as a label-free AFP selective electrochemical immunosensor.⁹⁶⁴ Electrochemical measurements revealed good stability to prolonged voltammetric cycling with performance retention up to 89.45% after 100 consecutive measurements. The composite electrode demonstrated high specific capacity for capture of the AFP antibody, lowering detection limits down to 3.3 pg mL⁻¹

sensitive detection of thrombin at concentrations as low as 30 nM.⁹⁷⁴ The presence of DNA aptamer effectively reduced the distance between analytes and the FET surface, thus minimizing charge screening effects. Label-free biosensing of prostate specific antigen (PSA) in high ionic-strength solutions has been realized using polyethylene glycol (PEG) graphene nanocomposite in FET device.²⁴⁰ Incorporation of permeable PEG resulted in the increase in Debye screening length adjacent to the surface of FET device, enabling real-time measurements of PSA in the 1–1000 nM concentration range at physiological conditions.

The advantages of graphene-based nanomaterials that arise from their unique physio-chemical properties have already contributed to the development of ultrasensitive and selective biosensing technologies.^{80,264,821} Current advances in this field by the fabrication of hybrid materials by combining graphene and its derivatives with other known electrocatalytic compounds, such as metal nanoparticles or ionic liquids.^{272,340} The synergistic effect between the electrical characteristics of graphene and the incorporated constituents has allowed the fabrication of electrochemical biosensors with significantly improved analytical performance and eased integration into the sensing platforms. In particular, the incorporation of novel recognition elements with excellent recognition ability to targeted analytes as in the case of molecularly imprinted polymers (MIPs), on the surface of graphene, may further lead to enhancements in analytical performance. Since the electroanalytical performance of graphene is strongly dictated by the presence of structural defects, edges, and functional groups on its surface, novel synthetic methods with large degree of compositional control need to be developed to further increase its applicability in biosensing. Therefore, graphene analogs such as GO and rGO, with large abundance of surface functional groups, are more extensively employed in biosensing applications, due to their remarkable properties such as good water dispersibility and biocompatibility, large surface area, facile surface modification, and low manufacturing cost.

4.4.1.9. Cellular Detection. The detection of circulating tumor cells in a patient is crucial for early diagnosis of cancer, highly precise cancer therapy, and monitoring therapeutic outcomes in real time.⁸⁹⁵ To endow graphene with biosensing capabilities for cellular detection, it is often required to functionalize its surface with recognition elements that can interact with targeted analytes through specific interactions and sometimes also participate in signal transduction events.²⁷²

Feng et al. performed label-free detection of cancer cells with overexpressed nucleolin on plasma membrane, such as breast cancer cells and human cervical carcinoma cells, using graphene functionalized with AS1411 as electrochemical aptasensor.⁹⁷⁵ The developed electrochemical aptasensor distinguished between cancer and normal cells at concentrations as low as 1000 cells. The authors used a GO layer modified with 3,4,9,10-perylene tetracarboxylic acid (PTCA) to prevent aggregation of GO sheets on surface of the electrode and subsequently to covalently attach the NH₂-modified nucleolin aptamers with oligonucleotides antibodies acting as the recognition element. The binding interactions of the aptamer with cancer cells enhanced the electron transfer resistance for electron transfer of [Fe(CN)₆]^{3−/4−} complexes. Yang et al. developed a cytosensor using a carboxymethyl chitosan-modified graphene electrode functionalized with folic acid (FA). Folate receptors overexpressed on the membrane of

the tumor cells have a known affinity to FA. These sensors demonstrated LOD of 500 cells mL^{−1}.⁹⁷⁶

Besides small-molecule modified graphene demonstrated above, complex platforms that incorporate enzyme, aptamer, nanoparticles or their combinations have also been applied in cellular detection. Wu et al. functionalized graphene with laccase (Lac) and 2,2-azino-bis(3-ethylbenzothiazoline-6-sulfonic acid) (ABTS) for biocatalytic reduction of oxygen.⁹⁷⁷ ABTS and laccase were integrated on the surface of graphene through the π-π and electrostatic interactions of these components. This bio-platform could sense extracellular oxygen, released from human erythrocytes cells, at concentrations as low as 10 μM. Guo et al. monitored triggered cellular release of H₂O₂ from human cells by growing the cells on the surface of layered graphene-artificial peroxidase-protein modified electrodes.⁹⁷⁸ Graphene was used as a scaffold with good dimensional compatibility for human cell growth and substantial electrical conductivity for electrical detection. Selectivity to H₂O₂ together with enhanced cell adhesion and growth capability was ensured by incorporating artificial peroxidase (AP) and extracellular matrix protein onto the surface of graphene. The authors showed that through the stimulation of phorbol-12-myristate-13-acetate (PMA, 5 μg mL^{−1}), hydrogen peroxide was released from a single MCF-7 cell over 25 s, quantifying the number of extracellularly released H₂O₂ as 10¹¹ molecules per cell.

A prostate metastatic cancer cells (Du-145) specific cytosensor was fabricated by Yadegari et al. through using anti-CD166 monoclonal antibody-modified gold electrode as a capture and recognition element together with Gr-Au nanoparticle-HRP-conjugated trastuzumab antibody hybrid nanostructure as a nanoprobe for accurate recognition of target cells and efficient amplification of enzymatic signals.⁹⁷⁹ The developed biosensor demonstrated high sensitivity and selectivity toward Du-145 cancer cells with LOD of 20 cells mL^{−1} and an extended linear range from 10² to 10⁶ cells mL^{−1}. He and co-workers combined together negatively charged GO with poly-L-lysine to improve capacity for leukemia K562 cancer cells adhesion.⁹⁸⁰ This cytosensor responded linearly from 10² to 10⁷ cells mL^{−1}, with the detection limit of 30 cells mL^{−1}. Akhavan et al. further enhanced sensitivity to leukemia cells (LOD of 0.02 cell mL^{−1}) through electrophoretic deposition of chemically exfoliated graphene oxide sheets on graphite rods, which led to the formation of Mg²⁺-charged graphene composites.⁹⁸¹

Simultaneous detection of both acute myeloid leukemia and acute lymphocytic leukemia was realized by Wang and co-workers using dual aptamer-functionalized, multilayered graphene-Au nanoparticle electrodes (Figure 55a–e).⁹⁸² This biosensor displayed LOD of ~350 cells per mL and a wide linear response range of 5 × 10² to 1 × 10⁷ cells mL^{−1} for both HL-60 and CEM cells, with minimal cross-reactivity and interference from non-targeting cells, such as non-leukemia cancer cells, K562 (a chronic leukemia cell line), and normal red blood cells (Figure 55f,g). Free-standing graphene paper electrodes doped with Au nanoparticles allowed sensitive detection of *E. coli* O157:H7.⁹⁸³ This biosensor showed good analytical response to the foodborne bacterium in the concentration range spanning from 1.5 × 10² to 1.5 × 10⁷ cfu mL^{−1}, and the device exhibited a low detection limit of 1.5 × 10² cfu mL^{−1}. Khoshfetrat et al. immobilized the thiolated sgc8c aptamer onto Au-coated magnetic Fe₃O₄ nanoparticles with nitrogen-doped graphene nanosheets serving as platform

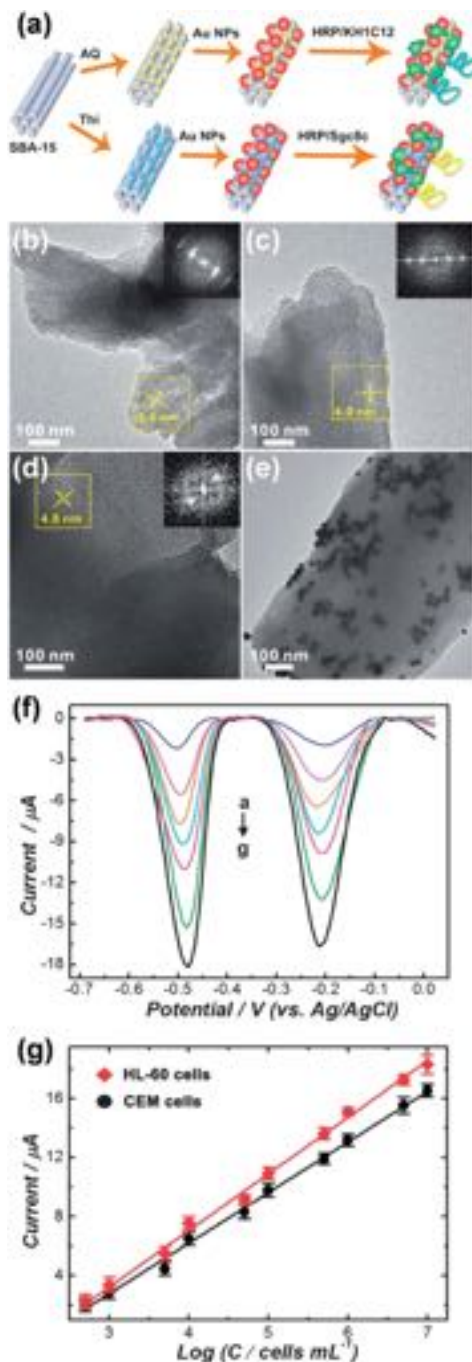


Figure 55. (a) Schemes illustrating the LBL assembly processes for the fabrication of SBA-15 redox-tags-Au NP-HRP-aptamer hybrid electrochemical nanoprobe. The relative sizes of the SBA-15, redox tags, Au NPs, HRP, and aptamers are not to scale. TEM images of SBA-15 (b) before redox tag loading and after loading of (c) Thi and (d) AQ. The insets show the Fourier transform patterns obtained from the selected regions in the TEM images. (e) TEM image of SBA-15 loaded with Thi and decorated with Au NPs. (f) DPV responses at different HL-60 and CEM cell concentrations (from curves a–g: 5×10^2 , 5×10^3 , 1×10^4 , 5×10^4 , 1×10^5 , 1×10^6 , and 1×10^7 cells mL^{-1} of HL-60 and CEM cells, respectively). (g) Calibration curves for HL-60 and CEM cells in PBS, pH 6.5, containing $1 \text{ mM H}_2\text{O}_2$.⁹⁸² Reproduced with permission from ref 982. Copyright 2013 The Royal Society of Chemistry.

for amplifying the read-out signal.⁹⁸⁴ Ethidium bromide could intercalate into the stem of the aptamer hairpin, providing the

DPV signal for the quantification of the leukemia cancer cells from 10 to 1×10^6 cell mL^{-1} .

4.4.2. Black Phosphorus. 2D black phosphorus is considered as an alternative material for the development of electrochemical biosensors due to its inherent bulk conductivity,⁹⁸⁵ electrocatalytic properties, and biocompatibility.⁹⁸⁶ Sofer et al. demonstrated large anisotropy in the electrochemical properties of black phosphorus with edge-plane sites exhibiting faster rates of electron transfer to inner and outer sphere redox probes as compared to basal plane sites.⁹⁸⁷ They also showed that the edge-plane monocrystal electrodes of BP exhibited over 1 order of magnitude higher sensitivity to dopamine and ascorbic acid oxidation than BP electrodes with basal sites. Yan et al. utilized BP to develop a non-enzymatic hydrogen peroxide sensor through drop-casting small aliquots of BP directly onto the GCE. The resulting sensors exhibited good sensitivity to H_2O_2 with LODs of $0.1 \mu\text{M}$.⁹⁸⁸ The same authors observed that BP on the electrode can be oxidized at higher concentrations of H_2O_2 , irreversibly diminishing the sensing properties of the sensor.

Black phosphorus functionalized with poly-L-lysine and a myoglobin-specific (Mb) aptamer on screen printed electrodes was used as a label-free electrochemical platform for myoglobin detection by Kumar et al. (Figure 56a).³⁶¹ CV measurements demonstrated 0.524 pg mL^{-1} sensitivity to myoglobin through oxidation of $\text{Fe}^{2+}/\text{Fe}^{3+}$ from Mb-heme group in human serum. Mayorga-Martinez et al. synthesized BP nanoparticles through electrochemical exfoliation and used them directly as labels for the detection of rabbit immunoglobulin G (IgG).³⁶² The functionalized BP-IgG nanoparticles were subsequently conjugated with anti-rabbit IgG-magnetic beads and together transferred onto screen printed electrodes. Upon the exposure to strong acid, the BP-IgG nanoparticles detached from the surface of the electrode, and consequently the BP nanoparticles could be detected via electrocatalytic reduction of H^+ by the impact of BP particles with the electrode. The frequency of the impacts was directly related to the concentration of rabbit IgG, allowing its determination at 0.98 ng mL^{-1} levels (Figure 56b). A different experimental approach was undertaken by Chen et al., who fabricated a FET device from few-layer BP nanosheets to detect IgG via anti-IgG linked to gold nanoparticles functionalized BP sheets (Figure 56c).³⁶³ The authors observed that IgG molecules induced a negative gate potential on the BP nanosheet, consequently increasing the drain-source current due to the p-type semiconducting nature of BP, thus permitting human IgG detection at 10 ng mL^{-1} levels. Recently, poly-L-lysine-black phosphorus (pLL-BP) hybrid was used as scaffold for the immobilization of hemoglobin to construct a sensitive H_2O_2 biosensor.⁹⁸⁹ The Hb-pLL-BP based enzymatic electrochemical device showed high catalytic activity toward the reduction of oxygen and hydrogen peroxide with linear concentration dependence in the 10 – $700 \mu\text{M}$ range of H_2O_2 and high selectivity against ascorbic and uric acid.

Although 2D black phosphorus has received increasing attention in the field of electroanalytical chemistry, still much remains to be done in discovering the unique properties of this exciting material. The primary limitation of using BP in biosensing applications is its lack of long-term stability induced by the surface oxidation and moisture adsorption. A possible approach to address this issue is to use a protective layer (e.g., metal oxide or polymer) that separates BP from the ambient environment, and thus improves its stability in sensing applications. In addition, the presence of structural defects in

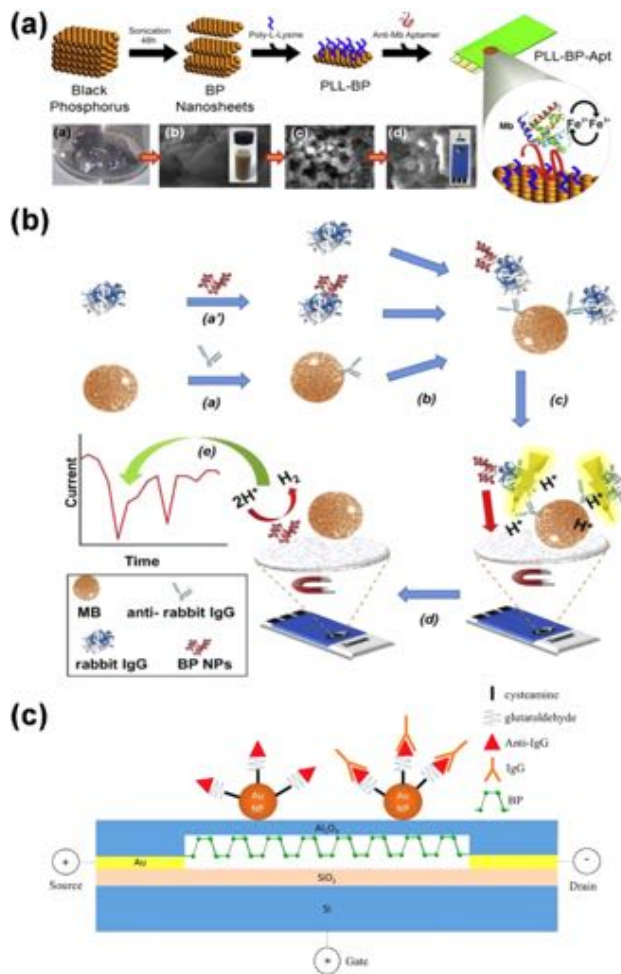


Figure 56. (a) Electrochemical myoglobin sensors.³⁶¹ Reproduced from ref 361. Copyright 2016 American Chemical Society. (b) 2D nanosheets of black phosphorus as labels for magneto immunoassay for rabbit IgG determination.³⁶² Reproduced from ref 362. Copyright 2016 American Chemical Society. (c) FET transistors based biosensors based on black phosphorus.³⁶³ Reproduced with permission from ref 363. Copyright 2017 Elsevier B.V.

the form of kinks or folds strongly influence the kinetics of electron transfer in biosensing applications. Therefore, the rational synthetic and experimental approaches leading to high degree of control over the structure and composition of BP together with detailed studies for understanding the underlying mechanism of BP in electrochemical sensing of bio-analytes are required for its broad implementation in practical applications.

4.4.3. Transition Metal Dichalcogenides. The increasing demand for developing highly sensitive, selective, low power, reliable, and portable sensing devices has stimulated active research on implementing novel 2D nanomaterials, after the great success of graphene. The high surface-to-volume ratio in 2D TMDCs offers potential for the detection of large amounts of target analytes per unit area as well as rapid response and recovery with low power consumptions. 2D TMDs nanosheets also hold a great promise as novel nanomaterial for biomedical applications as they can be readily synthesized on a large scale and can be directly dispersed in aqueous solution without the aid of surfactants.^{90,991}

4.4.3.1. Small Biomolecules, Hydrogen Peroxide, and Proteins. Sarkar et al. integrated 2D MoS₂ monolayers onto an oxidized silicon substrate with a streptavidin-functionalized

dielectric layer for selective detection of biotin at concentrations as low as 100 fM (Figure 57a–d).¹⁸⁴ The authors

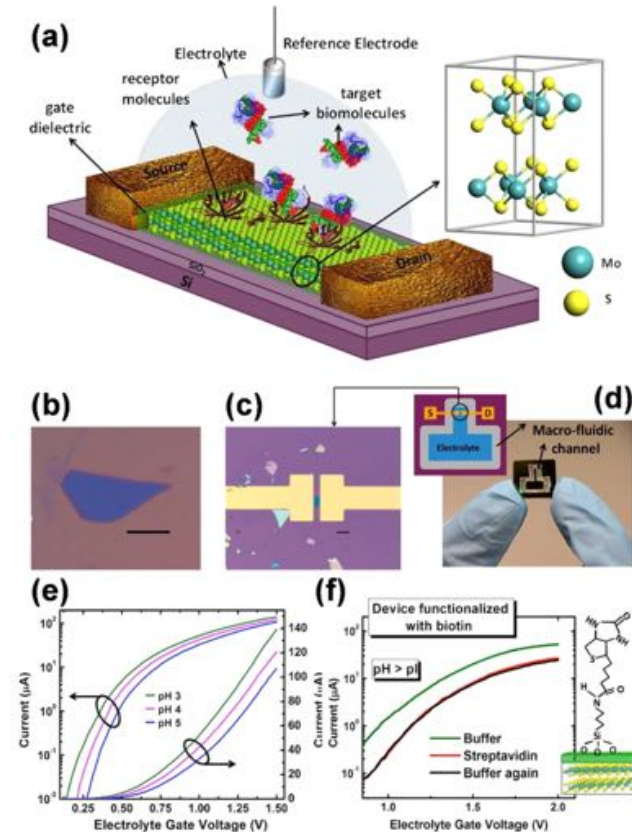


Figure 57. (a) Schematic diagram of MoS₂-based FET biosensor. For biosensing, the dielectric layer, covering the MoS₂ channel, is functionalized with receptors for specifically capturing the target biomolecules. The charged biomolecules, after being captured, induce a gating effect, modulating the device current. An electrolyte gate is in the form of a reference electrode (Ag/AgCl) is used for applying bias to the electrolyte.¹⁸⁴ (b) Optical image of a MoS₂ flake on 270 nm SiO₂ grown on degenerately doped Si substrate. Scale bar, 10 μ m. (c) Optical image of the MoS₂ FET biosensor device showing the extended electrodes made of Ti/Au. Scale bar, 10 μ m. (d) Image and schematic diagram (inset figure) of the chip with the biosensor device and macrofluidic channel for containing the electrolyte. (e) Linear region for a pH change of 4–5 of the electrolyte solution derived from the $I_d - V_g$ curves. (f) A device functionalized with biotin was first measured in pure buffer (0.01 PBS), as shown by the green curve. Addition of streptavidin solution (10 μ M in 0.01 PBS) leads to decrease in current (red curve) due to the negative charge of the protein, as the pH of the solution is more than the pI of streptavidin. The device is then measured again in pure buffer, leading to no significant change (black curve).¹⁸⁴ Reproduced from ref 184. Copyright 2014 American Chemical Society.

observed that current signal can be modulated via the gating effect due to biotin interactions in the FET device, indicating that this signal transduction mechanism can be further utilized for the determination of other biomolecules including proteins and nucleic acids (Figure 57e,f).¹⁸⁴

Extending the applicability of TMDCs in electrochemical sensor development, Lee and co-workers fabricated a dielectric layer-free MoS₂-based FET biosensor through incorporating anti-prostate specific antigen (anti-PSA) antibody on the surface of MoS₂ layer.⁹⁹² The hydrophobic nature of the MoS₂

improved physical adsorption between the anti-PSA antibodies and the electrode surface. The authors observed that the selective binding of negatively charged PSA (pH 7.8) to the immobilized antibodies modulated the off-state current, allowing sensitive detection at concentrations down to 1 pg mL^{-1} .⁹⁹² Employing a similar approach, Wang et al. also fabricated a label-free multilayer MoS₂-based FET for the sensitive determination of PSA. The drain current alteration in the FET device caused by the antibody-PSA interactions enabled real-time monitoring of cancer marker protein with good sensitivity (LOD of 375 fM), as well as high selectivity by showing no response to bovine serum albumin (BSA; ⁹⁹³ Figure 58a–c).

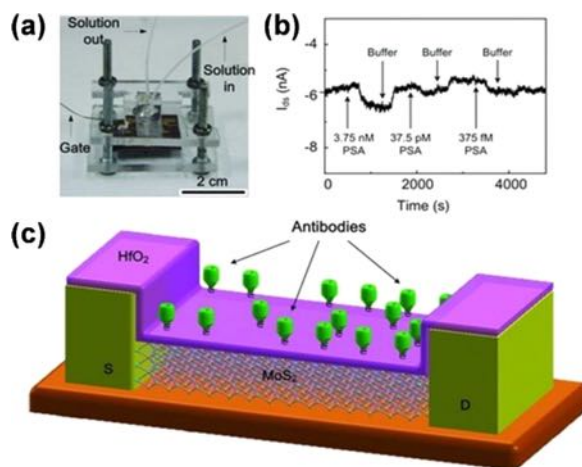


Figure 58. (a) Schematic of the biosensor configuration. (b) Conductance vs time data recorded during alternate delivery of PSA and pure buffer solutions; the PSA concentrations were 3.75 nM, 37.5 pM, and 375 fM, respectively. Dashed lines are the local baselines, and the length of the lines with arrows are the ΔI_{ds} (i.e., I_{ds} change in response to the presence of PSA). The buffer solutions used in all measurements were 100 μM phosphate buffer solutions. (c) Schematic of the biofunctionalization layers on the device surface (S: source, D: drain).⁹⁹³ Reproduced with permission from ref 993. Copyright 2014 John Wiley and Sons.

Using the same device architecture, Nam et al. functionalized the surface of MoS₂ with anti-human- α antibody receptors for detecting TNF- α molecules.⁹⁹⁴ The resulting insulating-layer-coated and insulating-layer-free MoS₂ FET biosensors exhibited V_T (threshold voltage) and g_m (ON-state transconductance) modulated responses upon the antigen–antibody interactions, respectively. The observed difference in bio-response was attributed to the effect of insulating layer thickness on the potential disorder in the MoS₂ FET channels. The same research group further lowered the LOD to 60 fM for the detection of TNF- α molecules by utilizing MoS₂ electrodes functionalized with anti-human TNF- α antibody.⁹⁹⁵ Interestingly, the developed sensors, operating in the subthreshold transport regime exhibited even higher current sensitivities in contrast with sensors working in the linear regime. This high operation subthreshold-regime sensitivity may be utilized to further lower the LOD for TNF determination.

Antibodies and nucleic acid aptamers have been progressively identified as potential molecular recognition elements for the construction of biosensors capable of detecting various biomolecular targets. Huang et al. developed

label-free electrochemical biosensor for 17b-estradiol determination through the immobilization of the selective aptamer on the surface of WS₂ nanosheets decorated with Au nanoparticles on GCE.⁹⁹⁶ The resulting biosensor responded linearly to 17b-estradiol in the 1.0×10^{-11} to 5.0×10^{-9} M concentration range with the LOD of 2.0×10^{-12} M and could be used for determination of biomolecule in serum and water samples. Huang et al. fabricated a bio-platform for immunoglobulin E (IgE) determination based on Au nanoparticle and aptamer functionalized WS₂-graphene nanocomposites.⁹⁹⁷ The synergistic effect between WS₂, graphene, and Au resulted in significant signal amplification, allowing determination of IgE at concentrations as low as 0.12 pM. Huang et al. constructed an electrochemical sensor for the determination of bisphenol A (BPA) based on MoS₂-chitosan-Au nanoparticle composite modified electrodes.⁹⁹⁸ A linear correlation between the oxidation peak current and BPA concentration was observed in the concentration range spanning from 0.05 to 100 μM with the LOD of 5.0×10^{-9} M. CEA selective immunosensor was recently fabricated by Wang et al., in which MoS₂-Au was used as the solid support for the immobilization of CEA primary antibody, Ag nanoparticles, GOD, and CEA secondary antibody.⁹⁹⁹ The fabricated immunosensor allowed detection of CEA in the range of 1 pg mL^{-1} to 50 ng mL^{-1} with the LODs of 0.27 pg mL^{-1} in human serum albumin samples. In addition, this immunoassay exhibited minimum degree of cross-reactivity with other biomolecules including human chorionic gonadotropin (HCG), α -fetoprotein (AFP), cancer antigen 125 (CA125), and PSA. Jing et al. used a sandwich-type electrochemical assay for sensitive detection of thrombin by using palladium nanoparticles decorated on poly-(diallyldimethylammonium chloride)-graphene-MoS₂ surface, which was further functionalized by hemin/G-quadruplex, GOD, and toluidine blue (Tb) serving as redox probes.¹⁰⁰⁰ The incorporated GOD catalyzed the oxidation of glucose to gluconolactone, which was linked with the reduction of the dissolved oxygen to H₂O₂. Both processes were then catalyzed by PdNPs and hemin/G-quadruplex species acting as hydrogen peroxide (HRP)-mimicking enzymes. This approach resulted in significant electrochemical signal amplification, allowing the determination of thrombin at 0.062 pM concentrations.

Pumera and co-workers incorporated several 2D TMDCs including WS₂, WSe₂, MoS₂, and MoSe₂ into the second-generation glucose biosensors through drop-casting each material onto the GCE, followed by immobilization of GOD and glutaraldehyde (GTA) on the electrode surface.¹⁰⁰¹ WS₂ and WSe₂ exhibited smaller peak-to-peak separation and faster electron transfer rates than electrodes based on other studied TMDCs. The enhanced performance of WX₂ (X = S, Se) modified electrodes was attributed to the presence of metallic 1T phase, which promoted the signal transduction in the developed sensor. The resulting sensors could detect glucose at concentrations as low as 52 μM . Wang and co-workers achieved comparable sensitivity to glucose (2.8 μM) by functionalizing the surface of MoS₂ with gold nanoparticles and used it as a large capacity scaffold for GOD adsorption.¹⁰⁰² A non-enzymatic glucose sensor based on the MoS₂ decorated with Cu nanoparticles covered with Nafion binder was developed by Huang et al.¹⁰⁰³ This device exhibited good response ($1055 \mu\text{A mM}^{-1} \text{cm}^{-2}$ sensitivity) to glucose in the concentration range of 0.2–4 mM with high selectivity over DA, UA, and AA.

2D TMDCs have also been demonstrated to exhibit appealing properties for the detection of small biological molecules including neurotransmitters, metabolites, or vitamins.³⁹⁴ Narayanan et al. utilized solvent assisted chemical exfoliation to prepare atomically thin sheets of MoS₂ and used those materials for the determination of DA in the presence of AA.¹⁰⁰⁴ They reported on the presence of surface negative charges in MoS₂, which eliminated the interference of negatively charged AA, at physiological pH, thus allowing differentiation between AA and DA. A different experimental approach to improve selectivity to DA was adopted by Wu et al., who prepared electrochemically reduced MoS₂ nanosheets on the 3-aminopropyltriethoxysilane modified GCE through irreversible voltammetric cycling of the film in 0.5 M NaCl under N₂ atmosphere.¹⁰⁰⁵ The formed electrode could differentiate between AA, UA, and DA with the strongest signal observed for DA. The high sensitivity to DA was explained by the presence of negative charges on the surface of rMoS₂ (after electrochemical reduction), which repelled the anionic forms of AA and UA but induced attractive interactions with the cationic form of DA.

Sarkar et al. employed template-free solvothermal method to prepare vanadium sulfide (VS₂)-Nafion modified GCE for a non-enzymatic electrochemical detection of H₂O₂.¹⁰⁰⁶ The resulting sensor responded to H₂O₂ in a broad concentration range of 0.5 μM to 3.0 mM, with the LOD of 0.224 μM. Wang et al. further improved sensitivity to H₂O₂ through the incorporation of hydroquinone, as redox mediator, on the surface of MoS₂.¹⁰⁰⁷ This sensor responded linearly in the concentration range of 1.0 × 10⁻⁶ to 9.5 × 10⁻⁴ M with the detection limit of 2.6 × 10⁻⁷ M, as demonstrated through DPV measurements. Another experimental strategy for sensitive H₂O₂ sensing was shown by Ni and co-workers.¹⁰⁰⁸ The authors used horseradish peroxidase immobilized onto the surface of MoS₂-graphene nanocomposite, detected H₂O₂ with sensitivity of 679.7 μA mM⁻¹ cm⁻² and LOD of 49 nM. In addition, the analytical response was not hindered by the presence of 1 mM interferents such as AA, lysine (Lys), DA, and cysteine (Cys). Yoon et al. performed electrochemical biosensing of H₂O₂ using myoglobin and MoS₂ nanoparticles encapsulated within GO.¹⁰⁰⁹ The sensor could detect H₂O₂ at 20 nM concentrations and exhibited good selectivity over AA, NaNO₂, and NaHCO₃ interferents. The encapsulation of MoS₂ nanoparticles in GO significantly enhanced the available surface area for myoglobin (Mb) immobilization, consequently improving the measured analytical signal. More recently, the group led by Zhu used GCE modified with MoS₂ nanoparticles for real-time trace amount monitoring of H₂O₂ (LODs 2.5 nM) released from Raw 264.7 cells.²⁵⁰ The authors attributed good electrocatalytic activity of the developed biosensor, for reduction of H₂O₂, to large fraction of exposed edge sites and a high surface area of formed nanoparticles.

4.4.3.2. Nucleic Acids. 2D TMDCs were also employed to construct an electrochemical biosensor for nucleic acids. Loo and co-workers developed a sensitive DNA sensor based on the disposable electrical printed carbon chip electrodes functionalized with probe DNA molecules by physical adsorption.¹⁰¹⁰ MoS₂ nanoflakes were then used as an electroactive label, with the oxidation peak exploited as the analytical signal. The mechanism of detection was based on the different affinity of MoS₂ toward ssDNA and dsDNA. The same research group also investigated the influence of different transition metals (Mo and W) and chalcogens (S and Se) on

the interactions between hairpin (Hp) and transition metal dichalcogenides.¹⁰¹¹ Se, and Mo, TMDCs materials displayed strong interactions with Hp DNA in contrast to WS₂ and WSe₂ TMDCs, respectively. Interestingly, upon chemical exfoliation, the difference in the degree of interactions between the immobilized Hp and each TMDCs became less significant.

Yang et al. electropolymerized xanthurenic acid (XA) directly onto the surface of MoS₂ and used it for direct sensing of guanine and adenine at nanomolar concentrations (LOD of 2.7 × 10⁻⁸ and 3.2 × 10⁻⁸ M for adenine and guanine, respectively).¹⁰¹² The negatively charged surface of the MoS₂-poly(XA) facilitated the adsorption of positively charged nucleotides on its surface, giving rise to enhanced electrocatalytic effect.¹⁰¹² Wang et al. exfoliated MoS₂ sheets through sonication in 1-butyl-3-methylimidazolium hexafluorophosphate ionic liquid and thionin to form MoS₂-thionin composites.¹⁰¹³ The resulting composite film was used as selective biosensor for the detection of dsDNA (0.09 ng mL⁻¹ to 1.9 ng mL⁻¹) through intercalation and electrostatic interactions of thionin with DNA. Lee et al. further improved the sensitivity to DNA by immobilization of ssDNA probe molecule onto the surface of MoS₂ in FET device.¹⁰¹⁴ The resulting sensor responded to targeted ssDNA with high sensitivity of 17 mV dec⁻¹, wide dynamic range of spanning over 6 orders of magnitude, and LOD of 10 fM. The hybridization of target ssDNA with probe molecule in the sensing channel of the biosensor led to the negative shift of the threshold voltage and an increase in the drain current. This observation was ascribed to electrostatic gating effects induced by the detachment of negatively charged probe DNA molecules from the MoS₂ electrode surface after hybridization.

To further improve adsorption capacity for the loading of probe DNA molecules, Jiao and co-workers electrodeposited free-standing ZnO directly on the surface of MoS₂ scaffold and consequently used the nanocomposite for the detection of DNA.¹⁰¹⁵ The authors reported on high sensitivity of the developed biosensor to DNA with LODs down to 6.6 × 10⁻¹⁶ M concentrations. The good adsorption of probe DNA to MoS₂ surface was attributed to strong electrostatic interactions between positively charged ZnO and negatively charged DNA. Yang et al. lowered the detection limits to DNA through the fabrication of MoS₂-PANI-DNA nanocomposite modified carbon paste electrode.¹⁰¹⁶ MoS₂ was prepared through a liquid exfoliation of bulk MoS₂, while the polyaniline-MoS₂ composite was prepared by oxidative polymerization of aniline monomer (ANI) directly on the surface of the MoS₂ film. The prepared nanocomposite served as a scaffold for the immobilization of probe DNA. This biosensor exhibited dynamic detection range for the complementary CaMV3SS gene sequence in the concentration range spanning from 1.0 × 10⁻¹⁵ to 1.0 × 10⁻⁶ M and the detection limit of 2.0 × 10⁻¹⁶ M. Comparable sensitivity was obtained by Huang et al., who functionalized the surface of WS₂-graphene composite with gold nanoparticles and chitosan and used it as a support for the immobilization of probe DNA molecules.¹⁰¹⁷ The resulting sensor could detect the target DNA at 2.3 fM concentration. Liu and co-workers further lowered the detection limit down to 0.79 fM by incorporating MoS₂-multiwall-carbon nanotubes-Au-GOD onto the surface of GCE. The same sensor could also differentiate between the three-base mismatched DNA and one-base mismatched DNA demonstrating high selectivity for nucleic acid detection.

One of the most sensitive sensors 2D TMDCs based for the label-free determination of DNA was fabricated by Jiao and co-workers by using ultrasonic exfoliation method to produce a thin-layer of MoS₂.¹⁰¹⁸ The thin MoS₂ layers were then used as scaffolds for the immobilization of probe ssDNA molecule, via the van der Waals interactions, between the basal plane of MoS₂ and nucleobases of ssDNA. Upon the hybridization with target ssDNA, the formed dsDNA detached from the MoS₂ surface causing a diminishment in the peak current of methylene blue. The response of this biosensor was linear within the DNA concentration range of 1.0×10^{-10} to $1.0 \times 10^{-4} \mu\text{M}$, exhibiting a detection limit of 0.019 fM.¹⁰¹⁸ Recently, phosphorodiamidate morpholino oligos (PMO) DNA functionalized MoS₂ in FET biosensor was used for label-free detection of DNA in serum samples.¹⁰¹⁹ The high affinity of PMO to bind DNA enabled the detection of target analyte at 6 fM concentrations, which is lower than that of the previously reported MoS₂ FET DNA biosensor based on DNA–DNA hybridization. The resulting MoS₂-based FET sensor demonstrated high sequence selectivity capable of discriminating between the complementary DNA from one-base mismatched DNA, three-base mismatched DNA, and noncomplementary DNA.¹⁰¹⁹

Beyond the DNA analysis, 2D TMDCs-based electrodes showed great potential for real-sample RNA and ATP monitoring. For example, Zhu et al. fabricated a label free micro-RNA-21 sensor using MoS₂-Au-thionine composites as transducer and recognition element.¹⁰²⁰ They observed that the formation of the DNA–RNA complex on the surface of the electrode hindered the electron transfer of thionine. This sensing platform responded linearly in the 1.0 pM to 10.0 nM concentration range with LOD of 0.26 pM and could detect micro-RNA-21 in human serum samples. Su et al. immobilized both thrombin and adenosine triphosphate (ATP) specific aptamers on the surface of MoS₂ modified with Au nanoparticles through Au–S bond formation.¹⁰²¹ This aptasensor could simultaneously detect ATP and thrombin at concentrations as low as 0.74 nM for ATP and 0.0012 nM for thrombin with high selectivity to target molecules over cytidine triphosphate, uridine triphosphate, and guanosine triphosphate, L-lysine, bovine serum albumin, Hb, and L-histidine.¹⁰²¹ The observed signal enhancement was due to the synergistic effect between the immobilized aptamer and the surface of MoS₂-Au modified electrode. The same group also developed a label-free immunosensor based on Au-thionine-MoS₂ composites for carcinoembryonic antigen (CEA) detection.¹⁰²² Under optimal experimental conditions, this bio-platform showed LOD as low as 0.52 pg mL⁻¹ and a wide linear response range spanning from 1 pg mL⁻¹ to 10 ng mL⁻¹.¹⁰²²

Despite the increasing number of successful demonstrations of 2D TMDCs in biosensing, the fundamental issue lies in the limited understanding of the influence of the structural and compositional defects, as well as lateral dimensions/thickness on their sensing properties. In particular, the presence of defects, kinks, and edges contributes to the formation of localized metallic or semi-conductive regions, which, similarly to graphene, demonstrate varying catalytic effect for biomolecule sensing.^{871,1023} Therefore, novel synthetic methods, with a large degree of structural control, are required to induce desired sensing properties for the engineering of biosensors. The formation of novel hybrid materials through incorporating other electroactive components, such as metal oxides, metals, graphene, or conductive polymers may be also of interest for

the design of new generation of biosensors. Besides the improvement in the manufacturing of high quality TMDCs, in large area, for biosensor applications, their production at the industrial-scale is still challenging. Nonetheless, the use of 2D TMDCs is an exciting development, and will provide unique opportunities for biosensing applications.

4.4.4. Metal Oxides. 2D metal oxides have recently become recognized as either sensing elements or immobilization scaffolds for the fabrication of biosensors due to their excellent electrical properties arising from the electron confinement effect, high surface-to-volume ratio, high surface reactivity, and catalytic activity along with strong adsorption ability for analytes. Impedimetric sensor was developed by Sticker et al., who employed atomic layer deposition to fabricate 15 nm thick coatings of ZrO₂, sandwiched between two Au electrodes, on the PDMS biochip.¹⁰²⁴ The developed sensor was then applied for label-free analysis of human lung adenocarcinoma epithelial cell cultures (H441) and human dermal fibroblast cells (NHDF). Vabbina and co-workers immobilized anti-cortisol antibody (Anti-Cab) onto the surface of 2D ZnO modified Au electrodes and used it as label-free cortisol specific immunosensor.⁹⁰⁵ The analytical response of these sensors was not affected by the presence of biological interferents in the sample such as PSA, NSE, EGFR, and BSA, and the sensor was suitable for cortisol detection at concentrations as low as 1 pM. The improved catalytic performance was attributed to the presence of large area in polarized (0001) plane in CuO and high surface charge density that could promote higher loadings of the Anti-Cab antibody on the surface. Tan et al. fabricated a nanocomposite film composed of TiO₂-CH- α -1-fetoprotein antibody and applied it for the amperometric detection of AFP in real serum samples. The resulting immunosensor responded to AFP within the concentration range of 1.0 to 160.0 ng/mL and LODs of 0.1 ng mL⁻¹. A nanostructured ZnO film with a wide bandgap (3.37 eV) and a large excitation binding energy (60 eV), prepared using sol–gel process, has been used for the immobilization of ChOx (IEP 4.7) to sense cholesterol with a wide linear range (5.0–400 mg dL⁻¹), low K_m (0.98 mg dL⁻¹), and high sensitivity (59 nA mg⁻¹ dL cm⁻²).¹⁰²⁵ The same research group synthesized ZnO films through radio-frequency magnetron sputtering at 50 mTorr and also utilized it as a scaffold for ChOx. The fabricated ChOx-ZnO-Au electrode demonstrated high sensitivity and linear responses to cholesterol in the range of 0.65–10.34 mM and K_m values as low as 2.1 mM. In later study, Ansari et al. immobilized rabbit-immunoglobulin antibodies (r-IgGs) together with BSA onto the surface of ZnO for the determination of ochratoxin-A.¹⁰²⁶ The resulting impedimetric sensor showed high sensitivity ($189 \Omega \text{nM dm}^{-3} \text{cm}^{-2}$) to ochratoxin-A in the concentration range of 0.006–0.01 nM dm⁻³ and LODs of 0.006 nM dm⁻³. Malhotra and co-workers electrochemically deposited ZrO₂ film onto gold electrode and used it as scaffold for the immobilization of 21-mer ssDNA probe, specific to *Mycobacterium tuberculosis*. The resulting biosensors exhibited LODs of 65 ng mL⁻¹ with a response time of less than 60 s.¹⁰²⁷ Solanki et al. also fabricated nanolayers of ZrO₂, through a sol–gel method, for the immobilization of 17-base ssDNA, identified from the 16s rRNA coding region of *Escherichia coli*. This biosensor demonstrated high selectivity and sensitivity toward hybridization detection of complementary DNA in the range of 10^{-6} to 10^6 pM.¹⁰²⁸

FETs based on metal oxides have attracted much attention in biosensing research and related applications due to their high sensitivity and specificity for rapid analyte detection.¹⁰²⁹ For example, Balendhran and co-workers incorporated 2D MoO₃ layers, prepared through liquid phase exfoliation, into a FET device for BSA determination with 250 µg mL⁻¹ sensitivity.¹⁰³⁰ The exposure of the prepared biosensor induced protein immobilization onto the surface of MoO₃ nanosheets. The negatively charged BSA induced a negative potential on the surface of the sensing layer further resulting in the reduction of the channel conductance. Another strategy to impart selectivity to targeted analytes was demonstrated by Lahav and co-workers, who imprinted (R/S)-2-methylferrocene carboxylic acids, (R/S)-2-phenylbutanoic acid, and (R/S)-2-propanoic acid onto a TiO₂ thin film on the gate surface of ISFET devices.¹⁰³¹ The imprinted sites demonstrated high chiroselectivity and chiospecificity only toward the imprinted target enantiomers. Pogorelova and co-workers fabricated an ISFET device utilizing a molecularly imprinted polymeric membrane containing specific recognition sites for benzyl-phosphonic acids and thiophenols through the polymerization of titanium(IV) butoxide in the presence of a titanium(IV) phosphonate complexes.¹⁰³² The imprinted TiO₂ films exhibited good sensitivity to different mercaptants and phosphonic acid derivatives in the concentration range of 1 × 10⁻⁶ to 5 × 10⁻⁴ M.

Mishra et al. employed fluorene-doped tin oxide (FTO)-coated conducting glass substrate modified with NiO for a non-enzymatic label-free glucose determination.¹⁰³³ The biosensor showed good selectivity to glucose over folic acid, AA, and UA, high-specific sensitivity of 3.9 µA µM cm⁻², LOD of 1 µM, and a response time of less than 1 s. High sensitivity of the NiO coated electrodes to glucose can be attributed to the oxidation of glucose molecules immobilized within larger surface area of the NiO film, catalyzed by the presence of Ni³⁺ sites created by electrochemical cycling. Yang and co-workers observed that the thin layers of CuO-Nafion nanocomposite, deposited on GCE, significantly enhanced sensitivity for non-enzymatic oxidation of glucose.¹⁰³⁴ The authors reported on the LOD of 50 nM, response time under 2 s, and linear response range spanning from 0.1 to 4.0 mM. The proposed mechanism for the oxidation of glucose on CuO film relied on the deprotonation and isomerization of glucose to its enediol form. This process was then followed by adsorption of glucose onto the electrode surface and subsequent oxidation by Cu^{II} and Cu^{III}.¹⁰³⁴

Xu et al. fabricated a H₂O₂ biosensor based on ZnO-Au nanoparticles-Nafion-HRP modified GCE.¹⁰³⁵ The observed catalytic current increased linearly with the H₂O₂ concentration in a range of 1.5 × 10⁻⁵ to 1.1 × 10⁻³ M, with the LOD of 9.0 × 10⁻⁶ M. Jia et al. further improved sensitivity to H₂O₂ by attaching vertically aligned Co₃O₄ nanowalls, synthesized by directly heating Co foil under ambient conditions, to the surface of GCE using silver paint.¹⁰³⁶ The Co₃O₄ modified electrodes showed good sensitivity to H₂O₂ oxidation (1671 µA mM⁻¹cm⁻²) and the detection limit of 2.8 µM. The improved electrocatalytic performance of Co₃O₄/GCE was due to an increased electron transfer rate between H₂O₂ and Co₃O₄ nanowalls and enhanced accessibility of many nano-scale transport channels in the composite film. Li and co-workers used benzyltrimethylammonium hydroxide (BTMAH) ionic liquid mediated autoclave reaction to synthesize 2D CuO nanoplates.¹⁰³⁷ The authors suggested

that the benzyltrimethylammonium cation preferentially adsorbs onto the (001) planes subsequently blocking the further growth along the [001] direction. This effect led to the growth along the (001) planes giving rise to a well-defined 2D nanostructure. The resulting CuO modified electrodes exhibited good electroactivity for the amperometric detection of H₂O₂. Li et al. fabricated 30 nM thick nanosheets of CuO directly onto the surface of Cu foil and applied this device for the amperometric sensing of H₂O₂.¹⁰³⁸

While 2D metal oxides have experienced rapid adoption in the field of biosensing, much remains to be done in exploring the unique features of these exciting materials. Focusing on understanding the nature of biomolecule–transducer interactions using these 2D materials in biosensing applications is also of growing interest. Formation of innovative 2D metal oxide composite materials, such as inorganic-organic and metal-semiconductor hybrids is also being explored as the new approach to harness their multifunctional properties, resulting from the combination of both nanostructures. For instance, the Schottky barrier formed at the interface between metal oxide and metal nanoparticles can significantly alter the electron transport properties in the material, and thus it may be utilized to enhance charge transfer between redox active enzymes and transducers, consequently improving the performance of bioanalytical devices. Furthermore, surface embedment/immobilization of bioactive molecules with desired bioanalytical properties for facilitating material–analyte interactions, as well as improving the charge transfer (e.g., enzymes, MIPs, and proteins) should be regarded as a promising strategy for the development of amplified biosensing technologies. Novel synthetic strategies that offer accurate control over the size, morphology, and nanostructure of 2D metal oxides may facilitate their incorporation into integrated bioanalytical devices, as well as provide a favorable environment for achieving the oriented immobilization of desired biomolecules on their surface, which can lead to signal amplification. Altogether, still much more should be done for the incorporation of 2D and layered metal oxides for future technological advances.

4.4.5. Other 2D Materials. Boron nitride, consisting of strong sigma bonds and weak van der Waals layered structure, is a material with high thermal conductivity and mechanical stability.⁴⁴⁷ 2D *h*-BN has already been utilized as an electrocatalyst in applications such as the oxygen reduction reaction (ORR)¹⁰³⁹ and in metal-free solar energy conversion.¹⁰⁴⁰ This electrocatalytic performance might be beneficial for the development of electrochemical sensors. Khan et al. demonstrated that GCE, boron-doped diamond (BDD), and screen-printed graphitic electrodes (SPEs) modified with *h*-BN exhibited electrocatalytic effect to DA oxidation (Figure S9a,b).¹⁰⁴¹ The electrochemical performance was largely dependent on the mass loading of the *h*-BN, and the nature of the underlying electrode. In particular, *h*-BN drop-cast layer was readily delaminated from the smooth electrode surface as observed for GCE, resulting in higher overpotential required for DA oxidation and decreased peak current. The resulting electrodes exhibited detection limits of 0.65 µM to DA in the presence of UA. Nonetheless, the simultaneous detection of DA and AA was not possible due to poor peak-to-peak resolution between these molecules. The same research group observed that through exfoliation of *h*-BN in surfactant solution the electrochemical performance of the *h*-BN modified SPE to DA oxidation was dominated by the

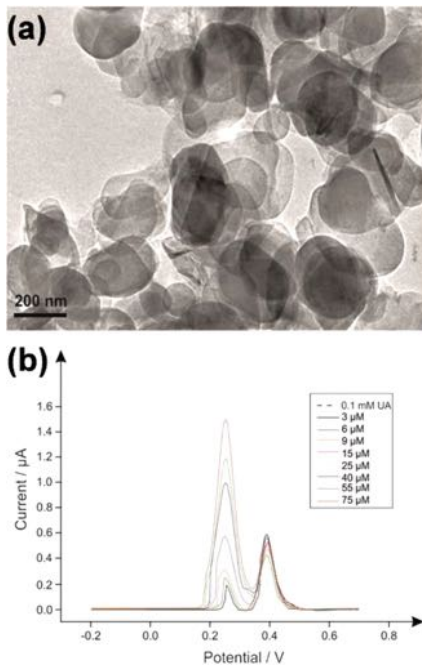


Figure 59. (a) TEM images of 2D-hBN nanosheets. (b) DPVs recorded by adding aliquots of DA at concentrations in the range of 3–75 μM (in 0.1 mM UA in pH 5.0 acetate buffer) utilizing an h-BN modified SPEs.¹⁰⁴¹ Reproduced from ref 1041. Copyright 2016 American Chemical Society.

presence of incorporated surfactant, e.g., sodium cholate. Such modifications led to diminishment of LOD to 1.57 μM versus pristine *h*-BN.¹⁰⁴² Li et al. prepared hexagonal *h*-BN flakes through low temperature combustion synthesis, carbothermal reduction, and nitridation methods.¹⁰⁴³ The synthesized *h*-BN material was largely amorphous and possessed layered structure with high density defects and active surface groups.

This sensor could simultaneously differentiate between AA, DA and UA within 30–1000, 0.5–150, and 1–300 μM concentration ranges, with detection limits of 3.77, 0.02, and 0.15 μM for AA, DA, and UA, respectively. The enhancement in the electroanalytical response was attributed to high specific surface area together with high density of defects in the *h*-BN.¹⁰⁴³ An amperometric sensor for the detection of indole-3-acetic acid (IAA) using hemin-boron nitride (hemin/BN) nanocomposite modified electrodes was developed by Liu et al.¹⁰⁴⁴ The hemin-BN nanocomposites were synthesized using a facile hydrothermal method. The sensor responded linearly to changing concentrations of IAA from 0.5 μM to 0.08 mM with a detection limit of 0.1 μM . Seckin and co-workers using polyimide-boron nitride (PI-BN) nanocomposite modified Pt electrodes prepared a DA biosensor. The resulting device exhibited LOD of $4 \times 10^{-8} \text{ M}$ to DA oxidation with good selectivity to UA, AA, lactose, urea, and sucrose.¹⁰⁴⁵ Non-enzymatic glucose sensor has been developed by Ranganathan et al. through the use of *h*-BN nanosheets-Cu-BTC MOF composite. Electrochemical measurements demonstrated a sensitivity of $18.1 \mu\text{A} \mu\text{M}^{-1} \text{ cm}^{-2}$, linear response range of 10–900 μM , and LOD of 5.5 μM to glucose. In addition, the biosensor exhibited satisfactory selectivity over dopamine, AA, UA, urea, and nitrate.¹⁰⁴⁶ Two-dimensional *h*-BN functionalized with graphene quantum dots and molecularly imprinted polymer (MIP) deposited on glassy carbon electrode was capable of detecting serotonin (5-HT) in the 1.0×10^{-12} to $1.0 \times 10^{-8} \text{ M}$ concentration range with LOD of $2.0 \times 10^{-13} \text{ M}$.¹⁰⁴⁷ The resulting electrodes exhibited high selectivity to serotonin over dopamine, tryptophan, and norepinephrine, and were suitable for direct quantification of this neurotransmitter in urine samples due to high binding affinity of MIP to 5-HT.

MXenes have attracted significant research interest in recent years due to their unique properties, such as metallic conductivity, hydrophilic surfaces, and good stability in

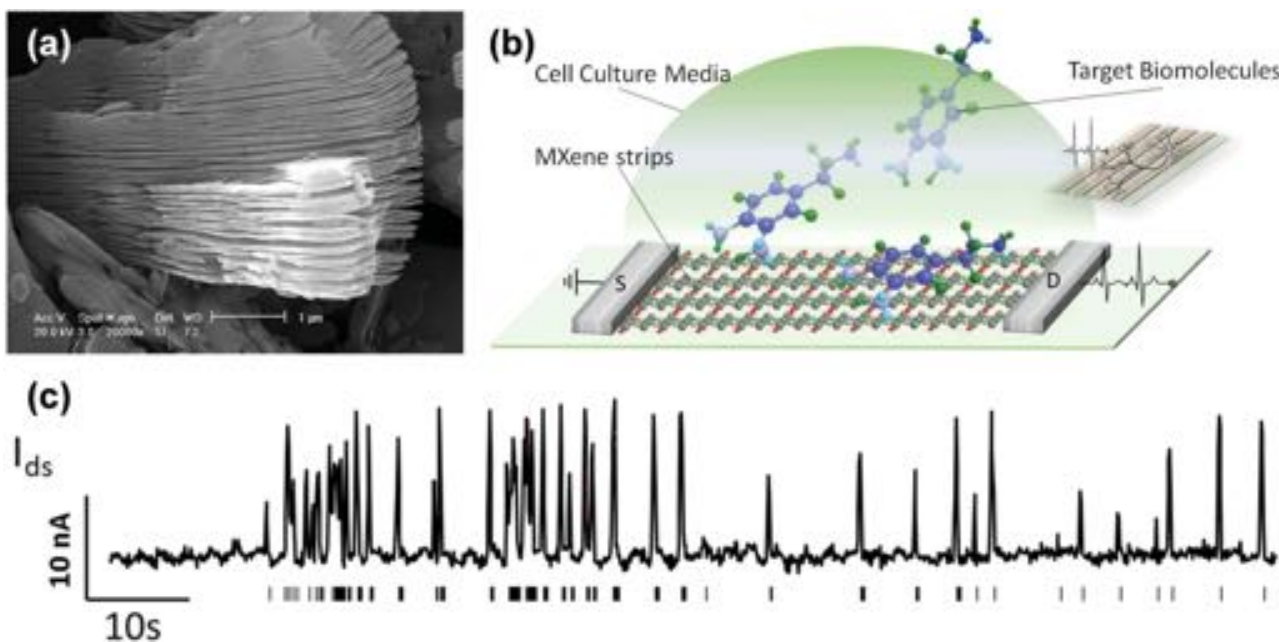


Figure 60. (a) SEM image of the multilayer-structured MXene. (b) Schematic of a biosensing device based on MXene field-effect transistors. (c) The derivation of neuronal spiking activities by using current measurements with the MXene–FET device.¹⁰⁴⁹ Reproduced with permission from ref 1049. Copyright 2016 John Wiley and Sons.

aqueous environments.¹²¹ This combination of properties makes them suitable candidates for various analytical applications.¹⁰⁴⁸ Xu et al. constructed an ultrathin conductive $\text{Ti}_3\text{C}_2\text{T}_x$ ($\text{T} = \text{O}$, $-\text{OH}$, and $-\text{F}$) based FET device and used it for the monitoring of cultured primary hippocampal neurons, as well as the detection of dopamine (Figure 60a–c).¹⁰⁴⁹ The ultrathin $\text{Ti}_3\text{C}_2\text{T}_x$ micropatterns were formed by microcontact printing (μCP) of $\text{Ti}_3\text{C}_2\text{T}_x$ aqueous dispersion directly onto the 3-aminopropyltriethoxysilane modified coverslips. The resulting devices could detect dopamine through the interaction between DA, and the electrons from the terminal groups (e.g., $-\text{OH}$ or $-\text{F}$) of the $\text{Ti}_3\text{C}_2\text{T}_x$ leading to an increase in the number of holes in the material and subsequently enhancement in the conductance of the FET device. In addition, the same device was used for real-time monitoring of activity of cultured primary hippocampal neurons with excellent biocompatibility even in long-term culturing. Wang et al. fabricated a mediator-free biosensor for the detection of H_2O_2 using MXene $\text{Ti}_3\text{C}_2\text{T}_x$ as scaffold for the immobilization of hemoglobin (Hb).¹⁰⁵⁰ $\text{Ti}_3\text{C}_2\text{T}_x\text{-Ti}_3\text{C}_2$ sensing layer was prepared by etching Al from Ti_3AlC_2 in HF and subsequently by mixing the synthesized MXene with Hb and Nafion to produce a stable nanocomposite. The resulting biosensors responded linearly to changing concentrations of H_2O_2 in the range of $0.1\text{--}260\text{ }\mu\text{M}$ with the LODs of 20 nM . The authors observed that the enzyme was adsorbed by surface functional groups of the nanolayers and then was funneled down toward the interior of the MXene nanolayers allowing the immobilization of enzyme on the inner surfaces of the organ-like structure. This effect led to an increased chance of effective collisions between substrate and redox proteins resulting in enhanced performance of the developed sensor. The same research group utilized the special organ-like structure of $\text{TiO}_2\text{-Ti}_3\text{C}_2$ nanohybrids to entrap Hb on the surface of the electrode and used it as a biosensor for analytical detection of H_2O_2 .¹⁰⁵¹ The resulting device exhibited wide linear range of response $0.1\text{--}380\text{ }\mu\text{M}$, and detection limits of 14 nM . In addition, the $\text{TiO}_2\text{-Ti}_3\text{C}_2$ based sensor retained up to 94.6% of the initial response to H_2O_2 after 60-day storage, demonstrating excellent robustness for bioanalytical applications. Lorencova et al. used $\text{Ti}_3\text{C}_2\text{T}_x$ layer drop-cast on GCE as electrocatalyst for reduction of H_2O_2 . The fabricated biosensor could detect H_2O_2 amperometrically at the concentrations as low as 0.7 nM with the response time shorter than 10 s . The same sensor also exhibited sensitivity to direct oxidation of NADH.¹⁰⁵² An amperometric biosensor platform constructed from $\text{Ti}_3\text{C}_2\text{T}_x/\text{Au}/\text{Nafion}/\text{GOD}$ deposited on GCE was recently applied for enzymatic sensing of glucose.¹⁰⁵³ The nanocomposite-based biosensor exhibited a linear amperometric response to glucose in the concentration range from 0.1 to 18 mM with a sensitivity of $4.2\text{ }\mu\text{AmM}^{-1}\text{ cm}^{-2}$ and a detection limit of $5.9\text{ }\mu\text{M}$. The superior sensing performance of this sensor was attributed to the presence of $\text{Au}/\text{Ti}_3\text{C}_2\text{T}_x$, which effectively facilitated electron transfer between the active redox centers of the enzyme and the electrode.

Zhu and co-workers also utilized MXene- Ti_3C_2 and Nafion composite layer as effective scaffold for the immobilization of Hb on the GCE to fabricate a mediator-free biosensor for nitrite determination.¹⁰⁵⁴ The resulting MXene-based sensing-platform displayed a low detection limit of $0.12\text{ }\mu\text{M}$, and a linear response range spanning from 0.5 to $11\text{ 800 }\mu\text{M}$, and was applied for the detection of nitrite in environmental water samples without any other pretreatment. GOD immobilized on

the surface of $\text{Ti}_3\text{C}_2\text{T}_x$ nanosheets decorated with Au nanoparticles and Nafion was used to construct an enzymatic glucose biosensor by Rakhi et al.¹⁰⁵⁵ The fabricated biosensor demonstrated electrocatalytic activity toward the detection of glucose within $0.1\text{--}18\text{ mM}$ concentration range with the LOD of $5.9\text{ }\mu\text{M}$ and good selectivity over biological interferents, including DA, UA, and AA.¹⁰⁵⁵ $\text{Ti}_3\text{C}_2\text{T}_x$ sheets doped with Pt nanoparticles have been adopted by Lorencova et al. to develop biosensor for the detection of AA, DA, UA, acetaminophen, and H_2O_2 .¹⁰⁵² The authors observed that the detection of H_2O_2 (LOD of 448 nM) was not compromised by the presence AA, DA, UA, and acetaminophen, since the applied potential for H_2O_2 catalysis was below the redox potential required to oxidize the interferents. Even though each individual biomolecule could be detected at the nM concentrations, the selectivity of the formed nanohybrid material was largely dictated by the presence of outer membrane, e.g., chitosan or Nafion, and in particular $\text{Ti}_3\text{C}_2\text{T}_x\text{-Pt}$ hybrids offer limited resolution between DA and AA, which may create difficulties in the practical application of these sensing devices.

The intriguing properties of 2D nanomaterials, such as tunable conductivity, large surface area, biocompatibility, or electronic anisotropy further suggest that future advances in the interdisciplinary research are likely to lead to a new generation of electrochemical biosensors. The most recent progress in this field relies on the synthesis of novel hybrid materials by combining the 2D nanostructures with other compounds such as metal nanoparticles, metal oxides, or conductive polymers leading to the fabrication of electrochemical sensors and biosensors with improved analytical performance due to the synergistic combination of their electroanalytical properties. Most of the biosensing experiments reported using 2D materials had to be performed under a controlled environment due to often limited stability to water and air that results in the degradation of the nanostructures. Therefore, novel ways to improve stability of these materials (e.g., through the application of protective coating or careful device engineering) need to be addressed for practical biosensing applications. The evaluation of the toxicity and biocompatibility of each 2D material is also critical for in vivo applications in sensing. The electrical properties of many 2D materials in the context of biosensing also vary significantly with the presence of lattice defects including corner atoms, uncoordinated open sites, kinks, nanoribbons, or edges, where the edge sites, in contrast to basal plane, typically exhibit high electrocatalytic transformations for material-analyte interactions. Hence, future work needs to concentrate on obtaining better understanding of the influence of structural and compositional defects on the sensing properties of 2D materials, as well as developing novel synthetic approaches that provide high degree of compositional control over the final structure. The lack of suitable technology for manufacturing of 2D nanostructures at the industrial scale, with uniform quality and large area presents another challenge. Despite these challenges, 2D materials possess numerous attractive properties for biosensor development, thus opening new realm of possibilities for analytical applications that are currently non-accessible using conventional 0D, 1D, or 3D materials. In particular, the field of flexible/wearable electronics could significantly benefit from the mechanical compatibility of these 2D nanomaterials with current device fabrication methods,

Table 6. Summary of Sensing Performances for Biomolecules by 2D Materials^a

specific analyte	material	architecture	readout/ method	LOD	experimental range	(R)-2-methylferro-cene carboxylic acids	notes	ref
(S)-2-methylferrocene carboxylic acids	TiO ₂	FET: Si/SiO ₂ /TiO ₂	I	0.6 mM	0.125–6.25 mM			1031
(S)-2-phenylbutanoic acid	TiO ₂	FET: Si/SiO ₂ /TiO ₂	I	0.5 mM	0.25–2.5 mM	(R)-2-phenylbutanoic acid		1031
(S)-2-propanoic acid	TiO ₂	FET: Si/SiO ₂ /TiO ₂ WS ₂ –Au NP–AP	I DPV Amp	0.45 mM 2 pM 6.45 μM	0.3–1.25 mM 1.0 × 10 ⁻¹¹ to 5.0 × 10 ⁻⁹ M	(R)-2-propanoic acid		1031
17β-estradiol	Gr	Gr/GCE	CV	0.12 mM	9.00–2314 μM	naphthalene, 1-aminoanthraquinone	DA, UA	996
AA	Gr	Gr/PPF		0.4–6.0 mM	0.4–6.0 mM	glucose		1056
AA	Gr–Fe ₃ O ₄ –NH ₂	Gr–Fe ₃ O ₄ –NH ₂ /GCE	Amp	0.074 μM	5.0–1600 μM	DA, UA		921
AA	Gr–Pt–Nafion	Gr–Pt–Nafion/GCE	DPV	0.15 μM	0.15–34.4 μM	DA, UA		1057
AA	h-BN	h-BN/GCE	DPV	3.77 μM	30–1000 μM	DA, UA		1058
AA	rGO	rGO/GCE	DPV	250 μM	0.5–2 mM	K ⁺ , Ca ²⁺ , Na ⁺ , Mg ²⁺ , Zn ²⁺ , NH ₄ ⁺ , Cl ⁻ , SO ₄ ²⁻ , NO ₃ ⁻ , HCO ₃ ⁻		1043
AA	rGO–Au	rGO–Au/GCE	DPV	5.1 × 10 ⁻⁵ M	2.4 × 10 ⁻⁴ to 1.5 × 10 ⁻³ M	NaCl, KCl, NaNO ₃ , CaCl ₂ , glucose, L-cysteine, CA		1059
AFP	Gr–anti–AFP–Thi	Gr–anti–AFP–Thi/GCE	CV	5.77 pg mL ⁻¹	0.05–2.00 ng mL ⁻¹	IgG, vitamin C, BSA, glucose		1060
AFP	Gr–Au–COOH–Thi–Nafion	Gr–Au–COOH–Nafion–Thi–anti–AFP/GCE	DPV	5.4 pg mL ⁻¹	0.016–50 ng mL ⁻¹	AFP, CEA, SS2		965
AFP	Gr–COOH–Au–Pd	Gr–COOH–Au–Pd/GCE	Amp	5 pg mL ⁻¹	0.05–30 ng mL ⁻¹	N/A		1061
AFP	Gr–CT–HRP–anti–AFP–Au–PTI/H/GCE	Gr–CT–HRP–anti–AFP–Au–PTI/H/GCE	CV	0.7 ng mL ⁻¹	1.0–10 ng mL ⁻¹	N/A		963
AFP	Gr–CT–HRP–anti–AFP–Au–PTI/H	Gr–CT–HRP–anti–AFP–Au–PTI/H/GCE	DPV	3.3 pg mL ⁻¹	0.01–50 ng mL ⁻¹	CEA, PSA, BSA, DA, AA, glucose		964
aliskiren	rGO–Au NP–PEDOT–PB	rGO–AuNP–PEDOT–PB/GCE	DPV	8.2 nM	0.045–0.45 μM	K ⁺ , Na ⁺ , Ca ²⁺ , Cl ⁻ , NO ₃ ⁻ , SO ₄ ²⁻		971
ATP	Gr–Pr–ATA	Gr–Pr–ATA/GCE	DPV	0.7 nM	2.2 nM to 1.3 μM	CTP, GTP, UTP		1063
ATP	MoS ₂ –Au NP–Apamer	MoS ₂ –AuNP–Apamer/GCE	SQWV	0.74 nM	1 nM to 10 mM	CTP, UTP, GTP		1021
biotin–streptavidin	MoS ₂	rGO–PtNP–Nafion/GCE	DPV	100 fM	N/A	IgG		184
bisphenol A	MoS ₂ –Au NP–CS	MoS ₂ –AuNP–CS/GCE	CV	5 nM	0.05–100 μM	Al ³⁺ , Fe ³⁺ , Ca ²⁺ , Mg ²⁺ , Cu ²⁺ , Zn ²⁺ , SO ₄ ²⁻ , Br ⁻ , Cl ⁻ , F ⁻ , NO ₃ ⁻		998
BNP	rGO–Pt NP–anti–BNP	FET: Si/SiO ₂ /rGO–Pt NP–anti–BNP/Au/Au	I	0.1 pM	100 fM to 1 nM	BSA, D–dimer, HAS		1064
BRCA1 5382	rGO–Au NP–ssDNA	rGO–Au NP–ssDNA/GCE	EIS	1.0 × 10 ⁻²⁰ M	3.0 × 10 ⁻²⁰ to 1.0 × 10 ⁻¹² M; 1.0 × 10 ⁻¹² to 1.0 × 10 ⁻⁷ M	CT–DNA, NC–DNA		961
BSA	MoO ₃	FET: Al ₂ O ₃ /MoO ₃ /Ag/Ag	R	15 μM	1–25 mg mL ⁻¹	N/A		1030
caffeine	rGO	rGO/GCE	DPV	N/A	50–300 μM	theophylline, methyl xanthine		943
carbofuran	Gr–COOH–NFO–Nafion	Gr–COOH–NFO–Nafion/GCE	Amp	5 × 10 ⁻¹³ M	1.0 × 10 ⁻¹² to 1 × 10 ⁻¹⁰ M;	Lucose, CA, OA, PO ₄ ³⁻ , SO ₄ ²⁻ , NO ₃ ⁻ , Cu ²⁺ , Pb ²⁺		1065
CEA	Gr–Anti–CEA	FET: Si/SiO ₂ /Gr–Anti–CEA/	I	100 pg L ⁻¹	1.0 × 10 ⁻¹ to 100 ng mL ⁻¹	NSE, CYFRE21–1		966
CEA	Gr–Au–COOH–Nafion	Gr–Au–COOH–Nafion/GCE	DPV	2.8 pg mL ⁻¹	0.010–50 ng mL ⁻¹	AFP, CEA, SS2		1061
CEA	Gr–IL–Nafion	Gr–IL–Nafion/GCE	DPV	0.34 fg mL ⁻¹	0.5 fg mL ⁻¹ to 0.5 ng mL ⁻¹	CEA, PSA, BSA, MUC1		1066
CEA	MoS ₂ –Au–Ab	MoS ₂ –Au–Ab/GCE	DPV	0.27 pg mL ⁻¹	1 pg mL ⁻¹ to 50 ng mL ⁻¹	HCG, CA125, PSA, AFP		999
CEA	MoS ₂ –PB	MoS ₂ –PB/GCE	DPV	0.54 pg mL ⁻¹	0.005–10 ng mL ⁻¹	AFP, NSE, BSA, IgG		1135
CEA	MoS ₂ –Thi–Au NP	MoS ₂ –Thi–Au NP/GCE	SWVQ	0.52 pg mL ⁻¹	1 pg mL ⁻¹ to 10 ng mL ⁻¹	NSE, IgG, AFP		1022
CEA	rGO–HRP–Ab ₂	rGO–HRP–Ab ₂ /GCE	EIS	0.64 pg mL ⁻¹	1.0 pg mL ⁻¹ to 80 ng mL ⁻¹	hIgG, AFP, PSA		967
cells	Gr–AP–Laminin	Gr–AP–Laminin/ITO	amperometric	0.1 × 10 ⁻⁶ M	0.1 × 10 ⁻⁶ to 100 × 10 ⁻⁶ M	N/A		978

Table 6. continued

specific analyte	material	architecture	readout/ method	LOD	experimental range	notes	ref
cells (Du-145)	Gr–Au NP–Ab–HRP	Gr–Au NP–Ab–HRP/Au	DPV	20 cells mL ⁻¹	10 ² –10 ⁶ cells mL ⁻¹	MCF–7, 293T, HepG2, L02 cells	979
cells (Hela)	Gr–PTCA–Aptamer	Gr–PTCA–Aptamer/GCE	EIS	794 cells mL ⁻¹	1.0 × 10 ³ to 1.0 × 10 ⁶ cells mL ⁻¹	HeLa cells, KS62 cells, MDA–231 cells, Normal cell line, NIH3T3 cells	975
cells (HL–60)	Gr–CMC–PEI–FA	Gr–CMC–PEI–FA/GCE	EIS	500 cells mL ⁻¹	5.0 × 10 ² to 5.0 × 10 ³ cells mL ⁻¹	A549 cells, HL–60 cells	976
cells (Leukemia)	Gr	Gr/GR	DPV	0.02 cell mL ⁻¹	1.0 × 10 ⁵ to 0.1 cell mL ⁻¹	CCRf–CEM, B–CLL	981
cells (Leukemia)	Gr–Au–Aptamer	Gr–Au–Aptamer/GCE	DPV	350 cells mL ⁻¹	5.0 × 10 ² to 1.0 × 10 ⁷ cells mL ⁻¹	HL–60, CEM, HeLa, KS62	982
cells (Leukemia)	Gr–N–Aptamer	Gr–N–Aptamer/SPE	DPV	10 cells mL ⁻¹	1.0 × 10 ¹ to 1.0 × 10 ⁶ cell mL ⁻¹	CCRf–CEM, Ramos cells	984
cells (Leukemia)	Gr–PLL	Gr–PLL/GCE	EIS	30 cells mL ⁻¹	1.0 × 10 ³ to 1.0 × 10 ⁷ cells mL ⁻¹	MDA–MB–435S, MDA–MB–231, MDA–MB–453, MCF–7, T–47D cell lines	126
cholesterol	Gr–ChOx	Gr–ChOx/GR	Amp	5 μM	50–350 μM	N/A	1067
cholesterol	Gr–CS–Pd–Pt	Gr–CS–Pd–Pt/GCE	Amp	0.75 μM	2.2 × 10 ^{–6} to 5.2 × 10 ^{–4} M	AA, UA, glucose	1068
cholesterol	Gr–Pt–ChE–ChO	Gr–Pt–ChE–ChO/GCE	Amp	0.2 μM	0.2–35 μM	N/A	926
cholesterol	Gr–PVP–PANI	Gr–PVP–PANI/SPE	Amp	1 μM	50 μM to 10 mM	AA, glucose	1069
cholesterol	Gr–TiO ₂ –PdPt–ChO	Gr–TiO ₂ –PdPt–ChOx/GCE	Amp	0.017 μM	5.0 × 10 ^{–8} to 5.9 × 10 ^{–4} M	AA, DA, UA, glucose	925
cholesterol	Gr–β–CD–MB	Gr–β–CD–MB/GCE	DPV	1 μM	1–100 μM	NaCl, KCl, MgCl ₂ , glycine, tyrosine, tryptophan, AA, SDS, lidocaine, chloropramine, quinine, quindine, piroxicam	924
cholesterol	ZnO–ChOx	ZnO–ChOx/ITO	CV	0.5 mg L ⁻¹	5–400 mg L ⁻¹	AA, UA, glucose, LA, urea, sodium pyruvate	1025
cocaine	rGO–Au–aptamer	rGO–Au–aptamer/SPE	DPV	1.5 × 10 ^{–3} pM	1–500 nM	egomine methyl ester, benzoyl eugenine	1070
cortisol	ZnO–Anti–C _{ab} –BSA	ZnO–Anti–C _{ab} –BSA/Au	CV/EIS	1 pM	1 pM to 100 nM	PSA, NSE, EGFR	1071
DNA	FET: Si/SiO ₂ /Gr/Au/Au	I	10 pM	N/A	N/A	SNS–DNA	1072
DNA	Gr	Gr/GCE	DPV	N/A	N/A	A, G, C, T	950
DNA	Gr	Gr/GCE	DPV	1 μg mL ⁻¹	N/A	A, G, C, T	951
DNA	Gr–Au	Gr–Au/GCE	Amp	3.4 fM	50–5000 fM	MM–DNA, NC–DNA	956
DNA	Gr–Au NP–DNA	Gr–Au NP–DNA/GCE	DPV	8.3 × 10 ^{–12} M	2.5 × 10 ^{–11} to 1.3 × 10 ^{–9} M	SBM–DNA, TBM–DNA, NC–DNA	957
DNA	Gr–MoS ₂ –CT–Au–ssDNA	Gr–MoS ₂ –CT–Au–ssDNA/GCE	DPV	0.0022 pM	5.0 × 10 ^{–14} to 5.0 × 10 ^{–9} M	SBM–O, C–O, TBM–O	1073
DNA	Gr–MoS ₂ –DNA	Gr–MoS ₂ –DNA/GCE	DPV	1.0 × 10 ^{–17} M	1.0 × 10 ^{–16} to 1.0 × 10 ^{–13} M	NC–DNA, SBM–DNA, DBM–DNA	953
DNA	Gr–ssDNA	FET: Si/SiO ₂ /Gr–ssDNA/Ct/Au	I	1 fM	100 pM to 100 nM	SBM–DNA, DBM–DNA, random sequence DNA	959
DNA	MoS ₂	MoS ₂ /DEP	DPV	0.03 nM	0.03–300 nM	C–DNA, SBM–DNA, NC–DNA	1010
DNA	MoS ₂	FET: Si/SiO ₂ /MoS ₂ /Cr–Au/	I	10 fM	1.0 × 10 ^{–14} to 1.0 × 10 ^{–8}	SS–DNA, C–DNA, NC–DNA, SBM–DNA	1014
DNA	MoS ₂ –Au	MoS ₂ –Au/GCE	DPV	11 fM	0.01–100 pM	BSA, IgE, thrombin, HAS	1074
DNA	MoS ₂ –PANI–DNA	MoS ₂ –PANI–DNA/GCE	EIS	2.0 × 10 ^{–16} M	1.0 × 10 ^{–15} to 1.0 × 10 ^{–6} M	NC–DNA, SBM–DNA	1016
DNA	MoS ₂ –ssDNA	MoS ₂ –ssDNA/CPE	DPV	1.9 × 10 ^{–17} M	1.0 × 10 ^{–16} to 1.0 × 10 ^{–10} M	NC–DNA, SBM–DNA, TBM–DNA	1018
DNA	MoS ₂ –Thi	MoS ₂ –Thi/GCE	SQWV	0.09 ng mL ⁻¹	0.09 ng mL ⁻¹ –1.9 ng mL ⁻¹	BSA	1013
DNA	MoS ₂ –ZnO–ssDNA	MoS ₂ –ZnO–ssDNA/GCE	DPV	6.6 × 10 ^{–16} M	1.0 × 10 ^{–15} to 1.0 × 10 ^{–6} M	N/A	1015
DNA	rGO	rGO/Gr	DPV	9.4 zM	0.1 fM to 10 nM	A, G, C, T	952
DNA	rGO	rGO/SPE	DPV	30 nM	N/A	wild-type, mutant, NC–DNA	958
DNA	rGO–Au	Gr–Au/GCE	DPV	2.0 × 10 ^{–7} M	2.0 × 10 ^{–7} to 1.0 × 10 ^{–6} M	synthetic DNA, SBM–DNA, DBM–DNA	948
DNA	rGO–Au NP–ssDNA	rGO–Au NP–ssDNA/GCE	DPV	5 aM	1 × 10 ^{–17} to 1 × 10 ^{–13} M	SBM–DNA, TBM–DNA	960
DNA	WS ₂ –Gr–CT–Au NP–ssDNA	WS ₂ –Gr–CT–Au NP–ssDNA/GCE	DPV	0.0023 pM	0.01–500 pM	NC–DNA, SBM–DNA, TBM–DNA	1017
adenine	Gr–COOH	Gr–COOH/GCE	DPV	2.5 × 10 ^{–8} M	0.5–200 μM	N/A	945

Table 6. continued

specific analyte	material	architecture	readout/ method	LOD	experimental range	notes	ref
adenine	Gr–PPy	Gr–PPy/GCE	LSV	0.02 μ M	0.06–100 μ M	AA, DA, glucose, K ⁺ , Na ⁺ , Ca ²⁺ , Mg ²⁺ , Fe ³⁺ , Al ³⁺ , Zn ²⁺ , NH ₄ ⁺ , Cl ⁻ , NO ₃ ⁻ , SO ₄ ²⁻ , CO ₃ ²⁻ , F ⁻ , Br ⁻	949
adenine	MoS ₂ –PXA	MoS ₂ –PXA/CPE	DPV	3.2 \times 10 ⁻⁸ M	0.5–10 μ M	N/A	1012
guanine	Gr–COOH	Gr–COOH/GCE	DPV	5.0 \times 10 ⁻⁸ M	0.5–200 μ M	N/A	945
guanine	Gr–PPy	Gr–PPy/GCE	LSV	0.01 μ M	0.04–100 μ M	AA, DA, Glucose, K ⁺ , Na ⁺ , Ca ²⁺ , Mg ²⁺ , Fe ³⁺ , Al ³⁺ , Zn ²⁺ , NH ₄ ⁺ , Cl ⁻ , NO ₃ ⁻ , SO ₄ ²⁻ , CO ₃ ²⁻ , F ⁻ , Br ⁻	949
guanine	MoS ₂ –PXA	MoS ₂ –PXA/CPE	DPV	2.7 \times 10 ⁻⁸ M	0.5–10 μ M	N/A	1012
DNA (HBV)	GO–DNA	GO–DNA/PGE	DPV	2.02 μ M	20–160 μ g mL ⁻¹	C–DNA, NC–DNA, MM–DNA	946
DA	GO–Au–polydA	GO–Au–polydA/Au	DPA	0.1 pg mL ⁻¹	1.0 \times 10 ⁵ cells mL ⁻¹	HL7702, HEK293, HeGp2, Hela, MCF–7	1075
DA	GO–Ferulic acid	GO–Ferulic acid/GCE	Amp	0.19 μ M	0.6–1000 μ M	5–HT, glucose, AA, H ₂ O ₂ , UA	1076
DA	Gr	Gr/Si	DPA	0.17 μ M	1–50 μ M; 50–100 μ M	AA, UA	908
DA	Gr	Gr/GCE	DPA	2.64 μ M	4–100 μ M	N/A	1077
DA	Gr	Gr/GCE	DPA	1 mM	N/A	AA, S–HT	1078
DA	Gr–CT	Gr–CT/GCE	DPA	5 μ M	5–200 μ M	AA, UA	909
DA	Gr–EDTA–Nafion	Gr–EDTA–Nafion/GCE	DPA	0.01 μ M	0.20–25 μ M	AA	910
DA	Gr–Fe ₃ O ₄ –NH ₂	Gr–Fe ₃ O ₄ –NH ₂ /GCE	Amp	0.13 μ M	0.2–38 μ M	AA, UA	1057
DA	Gr–LDH	Gr–LDH/GCE	SQWV	0.3 μ M	1.0–199 μ M	AA, UA	916
DA	Gr–PANI–DA–Aptamer	Gr–PANI–DA–Aptamer/GCE	CV	1.98 pM	0.007–90 nM	tyramine, AA, hydroxytyrosine, 3,4-dihydroxyphenylacetic acid, homovanillic acid	206
DA	Gr–Pt–Nafion	Gr–Pt–Nafion/GCE	DPA	0.03 μ M	0.03–8.13 μ M	AA, UA	1058
DA	Gr–PVP	Gr–PVP/GCE	Amp	0.2 nM	5.0 \times 10 ⁻¹⁰ to 1.1 \times 10 ⁻³	AA, UA	912
DA	Gr–SO ₃ ⁻	Gr–SO ₃ ⁻ /GCE	DPA	40 nM	0.20–20 μ M	AA, UA	913
DA	Gr– β -CD	Gr– β -CD/GCE	CV	5.0 nM	0.009–12.7 μ M	AA	911
DA	h–BN	h–BN/SPE	DPA	1.57 μ M	3–75 μ M	AA, UA	1042
DA	h–BN	h–BN/SPE	DPA	0.65 μ M	3–75 μ M	AA, UA	1041
DA	h–BN	h–BN/GCE	DPA	0.02 μ M	0.5–150 μ M	AA, UA	1043
DA	h–BN–PI	h–BN–PI/Pt	DPA	4 \times 10 ⁻⁸ M	4.0 \times 10 ⁻⁸ to 52.0 \times 10 ⁻⁸ M	AA, UA	1045
DA	MoS ₂ –APTES	MoS ₂ –APTES/GCE	DPA	1 μ M	1–50 μ M	AA, UA	1005
DA	rGO	rGO/GCE	DPA	0.5 μ M	0.5–60 μ M	K ⁺ , Ca ²⁺ , Na ⁺ , Mg ²⁺ , Zn ²⁺ , NO ₃ ⁻ , HCO ₃ ⁻	1059
DA	rGO–Au	rGO–Au/GCE	DPA	1.4 \times 10 ⁻⁶ M	6.8 \times 10 ⁻⁶ to 4.1 \times 10 ⁻⁵ M	NaCl, KCl, NaNO ₃ , CaCl ₂ , Glucose, L-cysteine, CA	1060
DA	rGO–Fe ₃ O ₄	rGO–Fe ₃ O ₄ /GCE	DPA	0.08 μ M	0.4–3.5 μ M	AA, UA	914
DA	rGO–milk blue–AuNP	rGO/milk blue/AuNP	SWV	1 nM	10 nM to 0.2 mM	AA, UA, epinephrine, norepinephrine, glucose	918
DA	rGO–Pd NP	rGO–Pd NP/GCE	DPA	0.233 μ M	1–150 μ M	AA, UA, glucose	915
DA	rGO–SnO ₂ –Au NP–PDA	rGO–SnO ₂ –Au NP–PDA/GCE	DPA	5 nM	0.008–20 μ M	AA, UA	917
DA	Ti ₃ C ₂ T _x	FET: Glass/Ti ₃ C ₂ T _x /Ag/Ag	I	100 \times 10 ⁻⁹ M	100 \times 10 ⁻⁹ to 50 \times 10 ⁻⁶ M	N/A	1049
DA	erythromycin	Gr–Lac–ABTS/GCE	Amp	10 μ M	0.05–0.4 mM	AA, UA	977
Escherichia coli	ZrO ₂ –ssDNA	ZrO ₂ –ssDNA/ITO	DPA	1.0 \times 10 ⁻⁶ pM	1.0 \times 10 ⁻⁶ to 1.0 \times 10 ⁶ pM	NC–DNA	1028
Escherichia coli O157:H7	rGO–Au NP–Ab	rGO–Au NP–Ab/rGO	EIS	1.5 \times 10 ² cfu mL ⁻¹	1.5 \times 10 ² to 1.5 \times 10 ⁷ cfu mL ⁻¹	<i>E. coli</i> DH 5 <i>a</i> , <i>S. aureus</i> , L. monocytogenes	983
glucose	CuO–Nafion	CuO–Nafion/GCE	Amp	50	0.1–4.0 mM	AA, UA, NaCl	1034
glucose	GO–Ag NP–SiO ₂ –GOD	GO–Ag NP–SiO ₂ –GOD/GCE	CV	0.31 mM	2–12 mM	N/A	892
glucose	GO–CT–Fe–GOD	GO–CT–Fe–GOD/GCE	Amp	7.6 μ M	0.02–6.78 mM	N/A	1079
glucose	GO–CuO	GO–CuO/GCE	Amp	0.69 μ M	2.79 μ M to 2.03 mM	AA, UA	1080

Table 6. continued

specific analyte	material	architecture	readout/ method	LOD	experimental range	notes	ref
glucose	GO–Pt NF	GO–Pt NE/GCE	Amp	2 μ M	2 μ M to 10.3 mM; 10.3–20.3 mM	N/A	902
glucose	Gr–Au–GOD–DNA	Gr–Au–GOD–DNA/GCE	CV	0.3 μ M	0.8–50 μ M	AA, UA, ACT	890
glucose	Gr–Co ₃ O ₄	Gr–Co ₃ O ₄ /GCE	Amp	2.5 nM	20–80 μ M	AA, UA	901
glucose	Gr–Cu	Gr–Cu/GCE	Amp	0.5 μ M	0.5 μ M to 4.5 mM	lactose, fructose, sucrose, AA, DA, UA	1081
glucose	Gr–CuO	Gr–CuO/GCE	Amp	0.23 μ M	0.5–5 μ M; 10–100 μ M	AA, UA, ethanol	897
glucose	Gr–GOD	FET: Au/PDMS/Gr–GOD/Gr–Ag NW/Gr–Ag NW	I	0.4 μ M	1 μ M to 10 mM	N/A	894
glucose	rGO–N–chitosan–GOD	rGO–N–chitosan–GOD/GCE	Amp	0.01 mM	0.1–1.1 mM	AA, UA	885
glucose	Gr–AuNP–GOD	Gr–AuNP–GOD/GCE	Amp/CV	8.9 μ M	43.6–261.6 mM	AA, UA	889
glucose	Gr–NiO	Gr–NiO/GCE	Amp	5 μ M	5 μ M to 4.2 mM	AA, DA, UA	1082
glucose	Gr–PDDA–CuO	Gr–PDDA–CuO/GCE	Amp	0.2 μ M	0.4–4000 μ M	fructose, lactose, sucrose, AA, UA, DA	896
glucose	Gr–Pd	FET: Au/PBS–NaOH/Gr–Pd/ Au/Au	I	1 nm	10 ^{−9} to 10 ^{−6} M	UA, AA	904
glucose	Gr–Pd NP–CT–GOD	Gr–Pd NP–CT–GOD/GCE	Amp	0.2 μ M	1.0 μ M to 1.0 mM	UA, AA	891
glucose	Gr–Pd NP–Naion	Gr–Pd NP–Naion/GCE	Amp	1 μ M	10 μ M to 5 mM	AA, UA, AP	903
glucose	Gr–Pt NP–CT–GOD	Gr–Pt NP–CT–GOD/GCE	Amp	0.6 μ M	0.15–5 μ M	N/A	893
glucose	h–BN–CuBTC–Naion	h–BN–CuBTC–Naion/GCE	Amp	5.5 μ M	10–900 μ M	AA, DA, UA, urea, NaCl, KNO ₃	1046
glucose	In ₂ O ₃	FET: Si/SiO ₂ /In ₂ O ₃ /Ti–Au/Ti–Au	I	7 fM	1.0 × 10 ^{−11} to 1.0 × 10 ^{−5} M	N/A	1083
MoS ₂	MoS ₂ /GCE	CV, Amp	2 mM	2.00–16.0 mM	N/A	250	
glucose	MoS ₂ –Au–GOD	MoS ₂ –Au–GOD	Amp	0.042 μ M	0.25–13.2 mM	N/A	1084
glucose	MoS ₂ –Au–GOD–Naion	MoS ₂ –Au–GOD–Naion/GCE	Amp	2.8 μ M	10–300 μ M	KCl, NaCl, DA, UA	1002
glucose	MoS ₂ –Cu–Naion	MoS ₂ –Cu–Naion/GCE	Amp	0.2 mM	0.2–4 mM	AA, DA, UA	1003
glucose	MXene–Au–Naion–GOD	MXene–Au–Naion–GOD/GCE	Amp	5.9 μ M	0.1–18 mM	DA, UA, AA	1055
NiO	NiO/FTO	Amp	1 μ M	0.1–1.1 mM	AA, FA, UA	1033	
glucose	rGO–CuS	rGO–CuS/GCE	Amp	0.19 μ M	1–2000 μ M	Na ⁺ , Ca ²⁺ , Al ³⁺ , NO ₃ [−] , Cl [−] , SO ₄ ^{2−} , FA, DA, OA, AA, UA, lactose	898
glucose	rGO–GOD–PPy	rGO–GOD–PPy/GCE	Amp	3 μ M	2–40 μ M	N/A	886
glucose	rGO–MWCNT	rGO–MWCNT/GCE	Amp	4.7 μ M	0.01–6.5 mM	N/A	1085
glucose	rGO–Pt–Ni NP	rGO–Pt–Ni NP/GCE	Amp	0.2 μ M	0.05–5.66 mM	AA, DA, UA, GA, LA, acetaminophen	1086
glucose	rGO–Pt–Ni NP	GO–Pt–Ni NP/GCE	Amp	0.01 mM	0.01–35 mM	AA, UA, urea, AAP, fructose	899
glucose	Ti ₃ C ₂ T _x –Au–Naion–GOD	Ti ₃ C ₂ T _x –Au–Naion–GOD/GCE	Amp	5.9 μ M	0.1–18 mM	N/A	1053
glucose	VS ₂ –Naion	VS ₂ –Naion/GCE	Amp	0.21 μ M	0.5 μ M to 3 mM	UA, AA, L-cysteine	1006
glucose	WS ₂ –GOD–GTA	WS ₂ –GOD–GTA/GCE	Amp	52.0 μ M	77–274 μ M; 0.77–22.3 mM	AA, DA, UA, glucose,	1001
guanosine	Gr–CT–Fe ₃ O ₄	Gr–CT–Fe ₃ O ₄ /GCE	DPV	7.5 × 10 ^{−7} M	2.0 × 10 ^{−6} to 3.5 × 10 ^{−4} M	A, G	947
H ₂ O ₂	BP	EIS	1.0 × 10 ^{−7} M	1.0 × 10 ^{−7} to 5.0 × 10 ^{−5} M	N/A	988	
H ₂ O ₂	BP–pLL	CV	10–700 μ M	10–700 μ M	AA, UA	989	
H ₂ O ₂	Co ₃ O ₄	Amp	2.8 μ M	0–5.35 mM	N/A	1036	
H ₂ O ₂	CuO	Amp	N/A	N/A	N/A	1038	
H ₂ O ₂	CuO–Naion	CuO–Naion/GCE	Amp	500 μ M	500 μ M–50 mM	N/A	1037
H ₂ O ₂	Gr–CT–Hb	Gr–CT–Hb/GCE	Amp	5.1 × 10 ^{−7} M	6.5–230 μ M	N/A	933
H ₂ O ₂	Gr–CT–MP11/Au	Gr–CT–MP11/Au	Amp	2.0 μ M	2.5–135 μ M	N/A	936
H ₂ O ₂	Gr–Pt	Gr–Pt/GCE	Amp	0.05 μ M	0.1 μ M–1.0 mM	N/A	1134

Table 6. continued

specific analyte	material	architecture	readout/ method	LOD	experimental range	notes	ref	
H ₂ O ₂	Gr-Pt	Gr-Pt/GCE	Amp	80 nM	1–500 μM	AA, UA	937	
H ₂ O ₂	Gr-SDBS-HRP	Gr-HRP/GCE	Amp	1.0 × 10 ⁻⁷ M	1.0 × 10 ⁻⁶ to 2.6 × 10 ⁻³ M	glucose, sucrose, ethanol, LA, AA, CA	935	
H ₂ O ₂	Gr-TBA-HRP	Gr-TPA-HRP/GCE	Amp	1.1 × 10 ⁻⁷ M	6.3 × 10 ⁻⁷ to 1.68 × 10 ⁻⁵ M	AA	934	
H ₂ O ₂	MoS ₂	MoS ₂ /GCE	Amp	2.5 nM	0.100–100 μM	AA, UA	250	
H ₂ O ₂	MoS ₂ –GO–myoglobin	MoS ₂ –GO–myoglobin/GCE	Amp	20 nM	N/A	AA, NaNO ₂ , NaHCO ₃	1009	
H ₂ O ₂	MoS ₂ –Gr-HRP	MoS ₂ –Gr-HRP/GCE	Amp	0.049 μM	0.2 μM–1.1 mM	AA, DA, cysteine, Lys	1008	
H ₂ O ₂	MoS ₂ –HRP	MoS ₂ –HRP/GCE	DPV	2.6 × 10 ⁻⁷ M	1.0 × 10 ⁻⁶ to 9.5 × 10 ⁻⁴ M	N/A	1007	
H ₂ O ₂	MXene	MXene/GCE	Amp	0.7 nM	0.1–380 μM	AA, DA, UA, Glucose	1052	
H ₂ O ₂	MXene–Nafion–Hb	MXene–Nafion–Hb/GCE	Amp	14 nM	0.1–260 μM	N/A	1051	
H ₂ O ₂	MXene–Nafion–Hb	MXene–Nafion–Hb/GCE	Amp	20 nM	0.35 μm	AA, DA, CA, U, AP, UA, NaCl, Glucose	1050	
H ₂ O ₂	rGO–MnFe ₂ O ₄ –Nafion	rGO–MnFe ₂ O ₄ –Nafion/GCE	Amp	45 nM	0.05–120 μM	N/A	940	
H ₂ O ₂	rGO–PB	rGO–PB/GCE	Amp	0.3 nM	1 nM–5.3 mM	Fructose, Glucose, AA, UA, Cl [−] , SO ₄ ^{2−}	938	
H ₂ O ₂	rGO–Pt–Ni	rGO–Pt–Ni/GCE	Amp	0.224 μM	0.5 μM–2.5 mM	UA, AA, L-cysteine	939	
H ₂ O ₂	VS ₂ –Nafion	VS ₂ –Nafion/GCE	Amp	9.0 × 10 ⁻⁶ M	1.5 × 10 ⁻⁵ to 1.1 × 10 ⁻³ M	N/A	1006	
H ₂ O ₂	ZnO–Au NP–Nafion–HRP	ZnO–Au NP–Nafion–HRP/GCE	FET: Au/SiO ₂ /Graphene/Au/Au	I	60 fM	0.0001–200 ng mL ^{−1}	N/A	1035
human growth factor 2	Gr						1087	
IAA	rGO–Hemin	rGO–Hemin/GCE	Amp	0.074 μM	0.1–43 μM, 43–183 μM	AA, SC, CPPU	1044	
IgE	Gr-Ag–Ab	Gr-Ag–SA/SPE	SWV	3.6 ng mL ^{−1}	10–1000 ng mL ^{−1}	N/A	1088	
IgE	WS ₂ –Gr–Au NP–Aptamer	WS ₂ –Gr–Au NP–Aptamer/GCE	DPV	1.2 × 10 ⁻¹³ M	1.0 × 10 ⁻¹² –1.0 × 10 ⁻⁸ M	thrombin, BSA	997	
IgG	BP	BP (label)	Amp	0.98 ng mL ^{−1}	2–100 ng mL ^{−1}	human Hb	362	
IgG	BP	Si/SiO ₂ /Br/Au/Au	I	2 ng mL ^{−1}	10–500 ng mL ^{−1}	avidin	363	
IgG	GO–protein	GO–Protein/GCE	EIS	0.67 nM	3.3–683 nM	myoglobin	883	
IgG	rGO–PDA–Au NP	rGO–PDA–Au NP/GCE	DPV	0.001 ng mL ^{−1}	0.1–100 ng mL ^{−1}	BSA, L-cysteine, TYR, PSA	962	
interleukin–6	Gr–HRP–Ab ₂ –Au NP–PDA–CNT	Gr–HRP–Ab ₂ –Au NP–PDA–CNT–ITTO	Amp	0.3 pg mL ^{−1}	1–40 pg mL ^{−1}	AFP, human chorionic gonadotropin, PSA	1089	
LDL	rGO–NiO–Ab	rGO–NiO–Ab/ITTO	EIS	0.07 mg L ^{−1}	0–130 mg L ^{−1}	cholesterol, cholesterol triglyceride	970	
<i>Listeria monocytogenes</i>	TiO ₂	TiO ₂ /Au	EIS	4.7 × 10 ² cfu mL ^{−1}	4.7 × 10 ³ –4.65 × 10 ⁷ cfu mL ^{−1}	N/A	1090	
microRNA–21	MoS ₂ –Thi–Au NP–DNA	MoS ₂ –Thi–Au NP–DNA/GCE	SQWV	0.26 pM	1.0 pM–10.0 nM	SBM–miRNA, NC–miRNA	1020	
miRNA	rGO–CP–DNA–miRNA	rGO–CP–DNA–miRNA/GCE	SQWV	8 fM	1 fM–1 nM	p–DNA29b–1, p–DNA–141, miR29b–, miR–141	955	
miRNA	rGO–MWCNT	rGO–MWCNT/GSPE	SQWV	30 fM	10 nM–30 fM	Ab1, HRP–Ab2, Ab1	954	
MMP–2	Gr–N–Au NP–Ab	Gr–N–Au NP–Ab/GCE	DPV	0.11 pg mL ^{−1}	0.0005–50 ng mL ^{−1}	MMP–7, IL–6, CEA, IgG	968	
<i>Mycobacterium tuberculosis</i>	ZnO ₂ –ssDNA	ZnO ₂ –ssDNA/Au	DPV	0.065 ng μL ^{−1}	640–665 ng μL ^{−1}	NC–O, SBM–O	1027	
myoglobin	BP–PLL–Aptamer	BP–PLL–Aptamer/SPE	CV	0.524 pg mL ^{−1}	1 pg mL ^{−1} –16 μg mL ^{−1}	Hb, BSA	361	
NADH	Gr–DNA–Au NP	Gr–DNA–Au NP/Au	DPV	1 fM	1 fM–10 pM	N/A	931	
NADH	rGO	rGO/GCE	Amp	0.6 μM	0–500 μM	AA	929	
NADH	rGO–Au	rGO–Au/GCE	Amp	1.13 nM	50 nM–300 μM	glutathione, glucose, AA, guanine	928	
nitrite	MXene–Hb–Nafion	MXene–Hb–Nafion/GCE	Amp	0.12 μM	0.5–1180 μM	N/A	1054	
ochratoxin–A	ZnO–BSA–r–IgG	ZnO–BSA–r–IgG/ITTO	EIS	0.006 nM	0.006–0.01 nM	N/A	1026	
octylphenol	Gr–CoNi NP–MIP	Gr–CoNi NP–MIP/CE	DPV	3.6 × 10 ^{−11} M	1.0 × 10 ^{−10} –1.0 × 10 ^{−7} M	OP, PL, NP, 4–AP, NTP, BPA	941	

Table 6. continued

specific analyte	material	architecture	readout/ method	LOD	experimental range	notes	ref
PDGF	GO-Pt-TBA-GOD-HRP-Au-SWCN	rGO-TB-FC-Pt-TBA-GOD-PDGF-HRP-Au-SWCN/GCE	DPV	8 pM	0.01–35 nM	thrombin	1091
PDGF	Gr-PDDA-Au	Gr-PDDA-Au/GCE	CV	1.7 pM	0.005–60 nM	PDGF-BSA, PDGF-Hb, PDGF-CEA, PDGF AMP	1092
PSA	GO-ssDNA-PLLA	GO-ssDNA-PLLA/Au	DPV	1 ng mL ⁻¹	1–100 ng mL ⁻¹	IgG, IgM, Glucose, AA, UA, PBS, human serum protein	1093
PSA	Gr-CT-MB	Gr-CT-MB/GCE	Amp	13 pg mL ⁻¹	0.05–5.00 ng mL ⁻¹	AFP, BSA, vitamin C, glucose	1094
PSA	Gr-HRP-Ab-Au	Gr-HRP-Ab-Au/SPE	LSV	0.46 pg mL ⁻¹	0.46 pg mL ⁻¹ –2.0 µg mL ⁻¹	cancer antigen 125 and 199, AFP, BSA	1095
PSA	Gr-NH ₂ -FCA-Ag-NH ₂ -MCM48	Gr-NH ₂ -FCA-Ag-NH ₂ -MCM48/GCE	Amp	2 pg mL ⁻¹	0.01–100 ng mL ⁻¹	PSA, IgG, lysozyme, AFP	1096
PSA	MoS ₂	FET: Si/SiO ₂ /MoS ₂ /Ti-Au/Ti-Au	I	1 pg mL ⁻¹	1 pg mL ⁻¹ –10 ng mL ⁻¹	IgG	992
PSA	MoS ₂ -Ab	FET: Si/SiO ₂ /MoS ₂ -Ab/Ti-Au/Ti-Au	I	375 fM	3.75 nM–375 fM	BSA	993
PTH	MoS ₂ -Au	MoS ₂ -Au/GCE	DPV	80 nM	0.1–200 µM	KCl, glucose, AA, UA	1097
PTH	MoS ₂ -Gr	MoS ₂ -Gr/Au	CV, EIS	1 pg mL ⁻¹	1–50 pg mL ⁻¹	N/A	1098
rutin	Gr	Gr/GCE	SDPV	2.1 × 10 ⁻⁸ M	1.0 × 10 ⁻⁷ –1.0 × 10 ⁻⁵ M	AA, glucose, Ca ²⁺ , Fe ²⁺ , Cu ²⁺ , Na ⁺ , K ⁺ , PO ₄ ³⁻ , CO ₃ ²⁻ , Cl ⁻	1099
serotonin	h-BN-Gr QDs	h-BN-Gr QDs/GCE	DPV	2.0 × 10 ⁻¹³ M	1.0 × 10 ⁻¹² –1.0 × 10 ⁻⁸ M	DA, tryptophan, and norepinephrine	1047
silodosin	Gr-Pt NP-Nafion	Gr-Pt NP-Nafion/GCE	DPV	0.55 nM	1.8–290 nM	K ⁺ , Na ⁺ , Ca ²⁺ , Cl ⁻ , NO ₃ ⁻ , SO ₄ ²⁻	972
thiodiglycerol	GO-Au	GO-Au/Au	DPV	0.2 µM	1.2 × 10 ⁻⁵ –0.82 × 10 ⁻³ M	N/A	1100
thrombin	Gr-aptaamer	FET: Si/SiO ₂ /Gr-aptaamer/Au/Au	I	30 nM	10–300 nM	N/A	974
thrombin	GO-aptaamer	GO-aptaamer/Carbon	DPV	3 pM	3 pM–0.3 µM	BSA, IgG, avidin	973
thrombin	GO-(Au-AlP)nLBL	GO-(Au-AlP)nLBL/GCE	LSV	2.7 fM	8 fM–15 nM	BSA, HRP, mouse IgG	1101
thrombin	Gr-CT-TBA	Gr-CT-TBA/GCE	CV, EIS	0.45 fM	0.45–100 fM	BSA, trypase	1102
thrombin	Gr-Nafion-NiHCF NP-Au	Gr-Nafion-NiHCF NP-Au/GCE	CV	0.3 pM	1 pM–1 nM; 1 nM–80 nM	Hb, L-cysteine, BSA	1103
thrombin	GO-TBA	GO-TBA/GCE	DPV	0.35 pM	1.0 × 10 ⁻¹² –4.0 × 10 ⁻¹⁰ M	BSA, HSA, IgG, trypsin, insulin, transferrin	1104
thrombin	Gr-PAMAM	Gr-PAMAM/GCE	DPV	0.05 pM	0.0001–80 nM	BSA, Hb, PDGF	1105
thrombin	Gr-PAMMA-Th-TBA-Hemin-BSA	Gr-PAMMA-Th-TBA-Hemin-BSA/GCE	DPV	0.1 pM	0.0002–30.0 nM	Lysozyme, IgG, BSA, L-cysteine	1106
thrombin	Gr-PANI-Au-MPTS-GOD-TBA	Gr-PANI-Au-MPTS-GOD-TBA/GCE	CV	0.56 pM	1.0 × 10 ⁻¹² –3.0 × 10 ⁻⁸ M	AFP, BSA, CEA	1107
thrombin	Gr-Pd-Tb-TBA-Hemin-BSA	Gr-Pd-Tb-TBA-Hemin-BSA/GCE	DPV	0.03 pM	0.1 pM–50 nM	BSA, HB, HAS, IgG, lysozyme	1108
thrombin	Gr-PTCA	Gr-PTCA/Au	CV	0.2 pM	0.001–40 nM	BSA, BHB, IgG	1109
thrombin	Gr-PTCDA-Au	Gr-PTCDA-Au/Au	Amp	6.5 × 10 ⁻¹⁶ M	1.0 × 10 ⁻¹⁵ –1.0 × 10 ⁻⁹ M	BSA, BHB, IgG, prothrombin, elastin	1110
thrombin	Gr-ssDNA	Gr-ssDNA/PGE	DPV	0.1 pM	100–500 nM	N/A	1111
thrombin	Gr-Tb-Au	Gr-Tb-Au/GCE	CV	0.33 pM	0.001–80 nM	Hb, BSA, L-cysteine	1112
thrombin	Gr-Tb-Pt-PBA-GOD-HRP	Gr-Tb-Pt-PBA-GOD-HRP/GCE	DPV	11.0 pM	0.02–45 nM	PDGF, thrombin	1091
thrombin	Gr-Th-Au	Gr-Th-Au/GCE	DPV	0.093 nM	0.5–40 nM	lysozyme, BSA	1113
thrombin	MoS ₂ -Au NP-Aptamer	MoS ₂ -Au NP-Aptamer/GCE	SQWV	0.0012 nM	0.01 nM–10 µM	Hb, L-lysine, BSA, L-histidine	1021
thrombin	MoS ₂ -Gr-PDDA-Pd NP-Aptamer	MoS ₂ -Gr-PDDA-Pd NP-Aptamer/GCE	DPV	0.062 pM	0.0001–40 nM	BSA, L-cysteine, IgG, Hb, CEA, AFP	1000
thrombin	rGO-TBA	GO-TBA/GCE	DPV	500 fM	0.001–50 nM	BSA, IgG, Hb	1114

Table 6. continued

specific analyte	material	architecture	readout/ method	LOD	experimental range	notes	ref
thrombin	rGO-TB-FC-Pt-TBA-GOD-PDGF-HRP-Au-SWCN	rGO-TB-FC-Pt-TBA-GOD-PDGF-HRP-Au-SWCN/GCE	DPV	11.0 pM	0.02–45 nM	platelet-derived growth factor	1091
TNF- α	MoS ₂ -Ab	FET: Si/SiO ₂ /MoS ₂ -Ab/Ti/Au	I	60 fM	60 fM–6 pM	interleukin-6 cytokine	995
TNF- α	MoS ₂ -Ab	FET: Si/SiO ₂ /MoS ₂ -Ab/Ti-Au/Ti-Au	I	60 fM	60 fM–6 pM	N/A	994
tridosan	Gr-PDDA-Pd	Gr-PDDA-Pd/GCE	DPV	3.5 nM	9.0 nM–20.0 μ M	AA, CA, Glucose, Na ⁺ , K ⁺ , Ca ²⁺ , Mg ²⁺ , Cl ⁻ , NO ₃ ⁻ , SO ₄ ²⁻	1115
tryptamine	Gr-PPy-HAMWCNTs-MIP	Gr-PPy-HAMWCNTs-MIP/GCE	Amp	7.4 \times 10 ⁻⁸ M	9.0 \times 10 ⁻⁸ –7.0 \times 10 ⁻⁵ M	tryptamine, tyramine, DA, tryptophan	1116
UA	Gr	Gr/GCE	Amp	4.82 μ M	6.00–1330 μ M	AA, DA	1056
UA	Gr-Fe ₃ O ₄ -NH ₂	Gr-Fe ₃ O ₄ -NH ₂ /GCE	Amp	0.056 μ M	1.0–850 μ M	AA, DA	1057
UA	Gr-PBA-Au NP	Gr-PBA-Au NP/GCE	Amp	2.0 \times 10 ⁻⁷ M	2.0 \times 10 ⁻⁶ –6.2 \times 10 ⁻⁵ M	N/A	922
UA	Gr-Pt-Nafion	Gr-Pt-Nafion/GCE	CV/DPV	0.05 μ M	0.05–11.85 μ M	AA, DA	1058
UA	<i>h</i> -BN	<i>h</i> -BN/GCE	DPV	0.15 μ M	1–300 μ M	AA, DA	1043
UA	rGO	rGO/GCE	DPV	0.5 μ M	0.5–60 μ M	K ⁺ , Ca ²⁺ , Na ⁺ , Mg ²⁺ , Zn ²⁺ , NH ₄ ⁺ , Cl ⁻ , SO ₄ ²⁻ , NO ₃ ⁻ , HCO ₃ ⁻	1059
UA	rGO-Au	rGO-Au/GCE	DPV	1.8 \times 10 ⁻⁶ M	8.8 \times 10 ⁻⁶ –5.3 \times 10 ⁻⁵ M	NaCl, KCl, NaNO ₃ , CaCl ₂ , Glucose, l-cysteine, CA	1060
VEGF	GO-ssDNA-PLLA	GO-ssDNA-PLLA/Au	DPV	0.05 ng mL ⁻¹	0.05–100 ng mL ⁻¹	IgG, IgM, Glucose, AA, UA, FBS, human serum protein	1093
vincristine	rGO-AuNP-MIP	rGO-AuNP-MIP/GCE	DPV	26 nM	5.0 \times 10 ⁻⁸ –5.0 \times 10 ⁻⁶ M	daunorubicin, vincristine, guanine, Ca ²⁺ , Mg ²⁺ , Zn ²⁺ , K ⁺	1117

^aNote: FET is described in a way of gate electrode/insulator/channel material/source electrode/drain electrode. N/A, not available.

giving rise to a new generation of multifunctional biosensing devices.

5. CONCLUSIONS AND PERSPECTIVES

In the past decade, advancements in the development of electrically-transduced sensors have been significantly propelled by the prediction, design, and synthesis of 2D materials, the exploration of their remarkable physical and chemical properties, as well as progress in the fabrication technology.⁷ The increasing number of experimental strategies for integrating these 2D nanostructures into functional devices, with desired strong interfacial interactions, further advanced the development of this unique group of materials. These materials have already found wide applications in areas where their unique physical and chemical properties, such as tunable band gap, large surface-to-volume ratio, or excellent mechanical stability can be harnessed.^{102,121}

In this review, we described recent advances in the development of electrically-transduced sensors based on the 2D nanomaterials to provide an overview of advances in areas ranging from unique structural features, device engineering, strategies for electrochemical signal amplification and transduction, and the development of novel electroanalytical techniques used in the miniaturization and integration of the sensors. We discussed necessary components, sensing mechanisms, and device architectures for the development of electrically-transduced sensing platforms, which highlighted the fundamental detection principles governing their response. We also demonstrated how structural and compositional features, as well as surface chemistry of 2D nanostructures dictate their electrical properties, ultimately allowing fascinating applications in the development of electrically-transduced sensors. Specific advances in the application of 2D materials in sensing were illustrated in the context of four major groups of analytes, including gases, volatile compounds, ions, and biomolecules, and discussed from both a historical and analytical perspective.

With recent advancements in the preparatory methods of 2D nanomaterials, an even greater degree of control over structural features, including size, thickness, crystallinity, engineered defects, doping, and functionalization, have been achieved,⁷³ leading to precise engineering of physicochemical properties. Further improvements in the integration and characterization methods of 2D nanostructures have allowed structural and compositional features to be effectively probed, thus enhancing the understanding of structure–property relationships within these materials.

The synergy of multifunctional properties in 2D nanostructures with electrochemical methods has already led to significant enhancements in the selectivity, stability, and reproducibility of sensing devices for a diverse range of analytes including small reactive gases,¹¹⁴ volatile organic compounds,¹¹³ ions,^{261,830} and biomolecules.²⁷² In particular, the inherent presence of a 2D basal plane in this class of materials ensures a large abundance of exposed active sites, as well as ultrashort diffusion paths, which together can effectively facilitate interactions with targeted analytes, and consequently enhance the charge transfer processes in electrically-transduced sensing.

Because 2D nanomaterials possess atomic thicknesses and are readily accessible by chemical synthetic methods,^{73,1118} their sensing properties such as selectivity or sensitivity can be further improved through surface functionalization with guest

molecules including nanoparticles, metal oxides or polymers.⁷² Generally, four major conceptual and experimental approaches have been demonstrated to obtain functional sensing devices. First, molecular engineering of 2D nanomaterials through edge and defect engineering has the potential to incorporate an increased number of active sites for material-analyte interactions.³⁸⁷ Second, the minimization of the thickness of the 2D layer can enhance the surface-to-volume ratio,⁷³ thus leading to substantial enhancements in sensitivity. Third, improvements in the kinetics of charge transfer through strain engineering, doping of heteroatoms, and designing synergistic composites with superior electrical properties (e.g., nanoparticles), which can effectively facilitate charge transfer, can significantly improve signal transduction.⁴⁷⁴ Fourth, the sensing properties of fabricated devices (e.g., selectivity and sensitivity) can also be tailored toward the detection of specific analytes through the incorporation of known recognition centers including enzymes, or ligands, onto the surface of 2D materials.^{80,282,575,1023} These unique properties, which arise from the ultrathin 2D structural characteristics of the nanomaterials, have been already extensively explored for a variety of sensing applications demonstrating excellent electroanalytical performance, as in the case of graphene, with the potential to complement the current commercial sensing systems/technologies [see refs 10, 80, 110, 126, 127, 146, 159, 264, 265, 272, 347, 412, 475, 575, 883, and 991].

Even though significant advances in many key areas related to the design and application of electrically-transduced sensors have been made, there is still an ongoing demand to implement these 2D materials in analytical applications.^{73,321} Synthetic routes toward high-quality, large area monolayers of most 2D materials are not yet readily accessible, although not all electroanalytical applications require this.⁴⁷³ Currently many available 2D materials exhibit a large degree of nonhomogeneity in their 2D size, which may lead to poor reproducibility in the sensing performance of electroanalytical devices including their sensitivity, stability, and reproducibility.^{70,72} The current manufacturing processes of 2D nanomaterials are often limited by low production rates and insufficient quality, and thus do not meet the industrial standards for their commercialization.¹¹¹⁸ The presence of structural defects, produced during synthesis, can have a large influence on the electronic properties of 2D materials and consequently on the electroanalytical performance of sensing technologies.^{123,353,821,1119} The mass production of ultrathin epitaxially oriented 2D nanomaterials with desired structural features in a highly controllable manner remains an unresolved challenge in this field, and requires further innovation, research, and development.

The ability to design 2D materials with targeted structure–property relationships remains an unresolved issue due to the limited understanding of growth mechanism and possible host–guest interactions within the material. To address these challenges, rigorous computational modeling together with analytical assessment of structure–property relationships through *in situ* transmission electron microscopy, spectroscopic techniques, such as X-ray photoelectron, Raman or infrared spectroscopy, and electron paramagnetic resonance in 2D materials is required. Hybrid 2D nanostructures can provide an efficient avenue for broadening and improvements in the performance in electrically-transduced sensing application. Furthermore, the ability to effectively incorporate receptor molecules for analyte-material interactions on the

surface of 2D materials, with control over their spatial distribution needs to be addressed due to its critical importance in enhancing the selectivity of fabricated electrochemical biosensors.

Many 2D nanostructures undergo oxidation in ambient conditions, resulting in structural alterations or even material decomposition, thus significantly limiting their application in functional devices.^{81,321} One critical challenge is finding new strategies to effectively stabilize the synthesized nanomaterials, not only during processing and storage, but also in practical applications. These challenges may be addressed with the development of novel 2D materials, as recently demonstrated through progress in the synthesis and application of 2D covalent organic frameworks, which exhibit excellent mechanical, thermal, and catalytic stability.^{90,91,1139,1140}

Due to large anisotropic structure, refined chemical control over nanoscale morphology of layered 2D structures is critical for further progress in the field.^{1120,1121} Development of methods for selective chemical functionalization of edge sites vs basal planes^{84,331} has the potential to enable improved approaches to creating dispersions of 2D materials that can interface with additive manufacturing technologies such as inkjet printing, roll-to-roll processing, and 3D printing.^{262,502,690,1122}

It is also important to consider whether 2D nanomaterials are more suited as components in the development of sensing devices than current available technologies, such as conductive polymers, in terms of their analytical performance, cost effectiveness, earth abundance, and toxicity. In particular, the biocompatibility of fabricated 2D materials and 2D material interfaces should be investigated to enable their practical implementation into bioanalysis.^{282,1123,1124}

Developing effective strategies of interfacing 2D materials with electrical contacts, within functional devices, remains an important consideration for producing high quality sensors that are capable of fully harnessing the unique and multifunctional nature of 2D nanostructures. Current integration methods, such as drop casting or microfabrication, often fail to harness the intrinsic properties of 2D materials.^{89,102,421} It is thus significant challenge to develop a facile, effective, and reliable strategies that improve the incorporation of 2D structures into functional devices. This challenge could be addressed by enhancing the current methods of fabrication to ideally couple the synthesis and device integration within one step.^{102,1125} The integration of multifunctional 2D materials with unique analyte recognition properties into soft and biocompatible substrates, miniaturized chips, and multiplex platforms for simultaneous detection of targeted analytes needs to be extensively explored to enable the development of portable, wearable, and interconnected devices and networks for addressing environmental monitoring, diagnosis of disease, and health care.^{103,104,124,324,334,1117,1118}

In addition to interfacing 2D materials with electrodes, van der Waals heterostructures resulting from interfaces of different 2D materials hold great promise for improving electrical contacts, material stability, and device performance.¹¹⁷ Creating new methods for fabricating such heterostructured interfaces in sensing devices has the potential to improve sensitivity, selectivity, and stability of sensors based on 2D materials.^{72,473}

Innovations in 2D material design are also critical to further progress in the field.^{70–73} Although the roadmap for 2D material discovery and development has progressed at a rapid

pace, many new 2D materials have not yet been explored as candidates for chemical sensing. Computational assessment combined with curiosity-driven research can offer many opportunities for fundamental discovery of stimuli-responsive 2D materials with promising utility in chemical sensing.¹¹²⁶

Finally, synergistic integration of multifunctionality in sensors based on 2D materials is critical for harnessing the multifaced features of these materials in electronic and electrochemical devices.^{94,113,321,474} For instance, design of porous conductive materials that enable synergistic coupling of high hydrophobicity, large surface area, high capacitance, and low charge transfer resistance can enhance the functional performance of potentiometric devices.^{88,89} Alternatively, coupling electronic and magnetic exchange interactions in 2D materials can enhance perturbations to charge transport caused by interactions with analytes.^{1127–1129}

The development of these sensing technologies may lead to significant advances in analytical technologies, in terms of simplicity, cost, and superior sensing performance. Although, the exploration of new 2D nanostructures is still in the early phases of research, the unprecedented diversity of these materials that arise from their unique physical and chemical structures is likely to further consolidate their position in the field of electrically-transduced sensors and nanoscience, and it is probable that the commercial and industrial technologies will incorporate them into widespread use in the coming years.

ASSOCIATED CONTENT

S Supporting Information

The Supporting Information is available free of charge on the ACS Publications website at DOI: [10.1021/acs.chemrev.8b00311](https://doi.org/10.1021/acs.chemrev.8b00311).

Table S1. Summary of Sensing Performances for Gases by 2D Materials ([XLXS](#))

Table S2. Summary of Sensing Performances for Volatile Compounds by 2D Materials ([XLXS](#))

Table S3. Summary of Sensing Performances for Ions by 2D Materials ([XLXS](#))

Table S4. Summary of Sensing Performances for Biomolecules by 2D Materials ([XLXS](#))

AUTHOR INFORMATION

Corresponding Author

*E-mail: katherine.a.mirica@dartmouth.edu.

ORCID ®

Zheng Meng: [0000-0002-6775-3213](https://orcid.org/0000-0002-6775-3213)

Katherine A. Mirica: [0000-0002-1779-7568](https://orcid.org/0000-0002-1779-7568)

Author Contributions

[†]Z.M., R.M.S., and L.M. contributed equally to this work.

Author Contributions

The manuscript was written through contributions of all authors. All authors have given approval to the final version of the manuscript.

Notes

The authors declare no competing financial interest.

Biographies

Zheng Meng obtained his B.S. at the University of Science and Technology Beijing in 2011. He received his Ph.D. at the Institute of Chemistry, Chinese Academy of Sciences under the supervision of

Prof. Chuan-Feng Chen in 2016. He then moved to Dartmouth College to work as a postdoctoral researcher with Prof. Mirica. His current interests focus on the developing of new two-dimensional conductive metal–organic frameworks and covalent organic frameworks and exploring their applications in sensing, catalysis, and electronics.

Robert M. Stoltz is a proud native of Cleveland, Ohio. His passion for chemistry and material science was inspired by undergraduate work in the laboratory of Professor Brian Northrop at Wesleyan University. After graduating with a B.A. in 2012 and an M.A. in 2013, Robert worked as a polymer chemist for Dow Chemical Company's Advanced Materials Division in Philadelphia. He joined the Mirica laboratory in the Spring of 2016 to pursue his doctorate in Chemistry.

Lukasz Mendecki obtained his M.Sc. in Forensic Science from King's College London. He then went on to earn his Ph.D. from Keele University under the supervision of Dr. Aleksandar Radu. His research explored the development of novel strategies for improvements in potentiometric ion selective electrodes. He then moved to Dartmouth College to work with Prof. Mirica on the application of two-dimensional conductive metal–organic frameworks in electrochemical sensors, catalysis, and energy storage.

Katherine A. Mirica received her B.S. degree in Chemistry (magna cum laude) in 2004 from Boston College, working in the laboratory of Prof. Lawrence T. Scott. In 2011, she earned her Ph.D. in Chemistry from Harvard University under the guidance of Prof. George M. Whitesides. She completed her postdoctoral training at the Massachusetts Institute of Technology with Prof. Timothy M. Swager during 2011–2015. Prof. Mirica began her independent scientific career as an Assistant Professor in the Department of Chemistry at Dartmouth College in July 2015. Her current research interests include multifunctional materials, electroanalysis, adhesion science, and self-assembly.

ACKNOWLEDGMENTS

The authors acknowledge support from start-up funds provided by Dartmouth College, from Walter and Constance Burke Research Initiation Award, the Army Research Office Young Investigator Program Grant No. W911NF-17-1-0398, National Science Foundation EPSCoR award (#1757371), Sloan Research Fellowship (FG-2018-10561), and 3M Non-Tenured Faculty Award.

ABBREVIATIONS

EDC	1-ethyl-3-(3-dimethylaminopropyl)carbodiimide
HA	1,6-hexanediamine
ABTS	2,2-azino-bis(3-ethylbenzothiazoline-6-sulfonic acid)
PTCA	3,4,9,10-perylene tetracarboxylic acid
APTES	3-aminopropyltriethoxysilane
MPTMOS	3-mercaptopropyltrimethoxysilane
4-AP	4-aminophenol
ACT	acetaminophen
AA	acetic acid
A, G, C, T	adenine, guanine, cytosine, and thymine
ATP	adenosine triphosphate
AFP	alpha-fetoprotein
AP	aptamer
ANI	aniline monomer
Anti-Cab	anti-cortisol antibody
APO	artificial peroxidase
AA	ascorbic acid
BTMAH	benzyltrimethylammonium hydroxide
BPA	bisphenol
BP	black phosphorus
BDD	boron-doped diamond
BSA	bovine serum albumin
BNP	brain natriuretic peptide
CA125	cancer antigen 125
C	capacitance
CE	carbon electrode
CN	carbon nitride
CNT	carbon nanotubes
CPE	carbon paste electrode
CNSP	carbon sphere
CMC	carboxymethyl chitosan
CEA	carcinoembryonic antigen
CTAB	cetyltrimethylammonium bromide
CNS	central nervous system
CS	chemical-sensitive
CVD	chemical vapor deposition
CT	chitosan
ChE	cholesterol esterase
ChO	cholesterol oxidase
K562	chronic leukemia cell line
ctDNA	circulating tumor DNA
CB	citrate buffer
CA	citric acid
CP	conductive polymer
σ	conductivity
COF	covalent organic framework
I	current
CV	cyclic voltammetry
CD	cyclodextrin
CsA	cysteic acid
CYFRA21	cytokeratin-19-fragment
DFT	density functional theory
DNA	deoxyribonucleic acid
DPCSV	differential pulse cathodic stripping voltammetry
DPV	differential pulse voltammetry
DPASV	differential pulse anodic stripping voltammetry
NADH	dihydronicotinamide adenine dinucleotide
DMA	dimethylacetamide
DMMP	dimethyl methylphosphonate
DNT	dinitrotoluene
DEP	disposable electrical printed carbon chips
DA	dopamine
DBM	double base mismatch
dsDNA	double stranded DNA
I_{DS}	drain current
V_{DS}	drain-source voltage
EIS	electrochemical impedance spectroscopy
ERGO	electrochemically reduced graphene oxide
EMF	electromotive force
EBL	electron beam lithography
EES	epidermal electronic system
EGFR	epidermal growth factor receptor
<i>E. coli</i>	<i>Escherichia coli</i>
EA	ethyl acetate
EDA	ethylenediamine
EDTA	ethylenediamine triacetic acid
FET	field-effect transistor
FISA	flexible integrated sensing array
FPCB	flexible printed circuit board
FA	folic acid

CPPU	forchlorfenuron	NMP	N-methyl-2-pyrrolidone
F	frequency	DMF	N,N-dimethylformamide
V _{GS}	gate voltage	NP	nonylphenol
GCE	glassy carbon electrode	ODA	octadecylamine
GOD	glucose oxidase	OP	octylphenol
GTA	glutaraldehyde	OA	oxalic acid
GA	glutaric acid	ORR	oxygen reduction reaction
GSPE	gold screen printed electrodes	PTH	parathyroid hormone
Gr	graphene	ppb	parts per billion
GO	graphene oxide	ppm	parts per million
GPO	graphite oxide	ppq	parts per quadrillion
GR	graphite rod	ppt	parts per trillion
Hb	hemoglobin	Pa	Pascal
HBV	hepatitis B virus	PGE	pencil graphite electrode
Hp	heparin	E	permittivity
<i>h</i> -BN	hexagonal boron nitride	Φ	phase
HHTP	hexahydroxytriphenylene	PL	phenol
HITP	hexaiminotriphenylene	PMA	phorbol-12-myristate-13-acetate
HOMO	highest occupied molecular orbital	PBS	phosphate buffered saline
HRP	horseradish peroxidase	PMO	phosphorodiamidate morpholino oligos
MCF-7	human breast cancer cell	PPF	photoresist film
HCG	human chorionic gonadotropin	PEDOT	poly(3,4-ethylenedioxythiophene)
NHDF	human dermal fibroblast cells	F8T2	poly(9,9'-dietyl-fluorene- <i>co</i> -bithiophene)
293T	human embryonic kidney cell	PAA	poly(acrylic acid)
IL-6	human interleukin-6	PDDA	poly(diallylimethylammonium chloride)
HepG2	human liver hepatocellular carcinoma	PEG	poly(ethylene glycol)
L02	human normal hepatocyte cell	PET	poly(ethylene terephthalate)
Du-145	human prostatic metastatic cancer cell	PEI	poly(ethylenimine)
Ig	immunoglobulin	PMMA	poly(methyl methacrylate)
IgE	immunoglobulin E	PSS	poly(sodium 4-styrenesulfonate)
IgG	immunoglobulin G	PXA	poly(xanthurenic acid)
ITO	indium tin oxide electrode	PANI	polyaniline
IAA	indole-3-acetic acid	PDA	polydopamine
L	inductance	PETP	polyehtylenetereph-thalate
IDE	interdigitated electrode	PEtN	Polyethylene naphthalate
ISE	ion-selective electrode	PFIL	Polyethylenimine-functionalized ionic liquid
ISFET	ion-selective field effect transistor	PF	polyfuran
ISM	ion-selective membranes	PI	polyimide
LACC	laccase	PLL	poly(<i>L</i> -lysine)
LACC-TYR	laccase-tyrosinase	PPr	polypyrene
LDHs	layered double hydroxides	Ppa	polypyrrole propylic acid
LMO	layered metal oxides	PPy	polypyrrole
CYS	L-cysteine	PTH	polythionine
LOD	limit of detection	PTHP	polythiophene
LDA	linear discriminant analysis	PVP	polyvinylpyrrolidone
LEU	L-leucine	Pr	porphyrin
LDL	low density lipoprotein	PCA	principle component analysis
LUMO	lowest unoccupied molecular orbital	PSA	prostate specific antigen
MMP-7	matrix metalloproteinases-7	PBA	pyrene butyric acid
MOF	metal–organic framework	PPF	pyrolyzed photoresist film
MB	methylene blue	PPBS	pyrrole phosphate buffer solution
μCP	microcontact printing	RNA	ribonucleic acid
MP-11	microperoxidase-11	rGO	reduced graphene oxide
MIP	molecularly imprinted polymer	R	resistance
MGNF	multilayer graphene nanoflake films	S	response
MWCNT	multiwall carbon nanotubes	RLS	restless legs syndrome
Mb	myoglobin	SPE	screen printed graphitic electrode
NF	nanoflower	5-HT	serotonin
NPs	nano particles	SBM-O	single base mismatched oligonucleotide
NW	nanowire	ssDNA	single stranded DNA
NSE	neuron specific enolase	SNS-DNA	single nucleotide substitution
NAD	nicotinamide adenine dinucleotide	SDBS	sodium dodecyl benzenesulfonate
NTP	nitrophenol	SWASV	square wave anodic stripping voltammetry

SS2	Streptococcus suis serotype 2
MM-DNA	target/mismatch (MM) mixtures
TPA	tetrasodium 1,3,6,8-pyrenetetrasulfonic acid
TGT	thiol group tagged
Thi	thionine
3D	three-dimensional
Tb	toluidine blue
TMDC	transient metal dichalcogenides
TEA	triethylamine
BTC	trimesic acid
ATA	triphasphate aptamer
TBM	triple base mismatch
TNF	tumor necrosis factor
2D	two-dimensional
TYR	tyrosinase
UV	ultraviolet
U	urea
UA	uric acid
VEGF	vascular endothelial growth factor
VOCs	volatile organic compounds
V	voltage
φ	work function
XA	xanthurenic acid
AFP	α -fetoprotein
β -CD	β -cyclodextrin

REFERENCES

- (1) Gellman, S. H. Introduction: Molecular Recognition. *Chem. Rev.* **1997**, *97*, 1231–1232.
- (2) De Marcellis, A.; Ferri, G. Physical and Chemical Sensors. In *Analog Circuits and Systems for Voltage-Mode and Current-Mode Sensor Interfacing Applications*; Springer Netherlands: Dordrecht, 2011; pp 1–35.
- (3) Janata, J.; Bezegh, A. Chemical Sensors. *Anal. Chem.* **1988**, *60*, 62–74.
- (4) Bănică, F. G. *Chemical Sensors and Biosensors: Fundamentals and Applications*; 2012.
- (5) Cammann, K.; Lemke, U.; Rohen, A.; Sander, J.; Wilken, H.; Winter, B. Chemical Sensors and Biosensors—Principles and Applications. *Angew. Chem., Int. Ed. Engl.* **1991**, *30*, 516–539.
- (6) Sekhar, P. K.; Brosha, E. L.; Mukundan, R.; Garzon, F. Chemical Sensors for Environmental Monitoring and Homeland Security. *Electrochem. Soc. Interface* **2010**, *19*, 35–40.
- (7) Chandran, G. T.; Li, X.; Ogata, A.; Penner, R. M. Electrically Transduced Sensors Based on Nanomaterials (2012–2016). *Anal. Chem.* **2017**, *89*, 249–275.
- (8) Windmiller, J. R.; Wang, J. Wearable Electrochemical Sensors and Biosensors: A Review. *Electroanalysis* **2013**, *25*, 29–46.
- (9) Bakker, E.; Telting-Diaz, M. Electrochemical Sensors. *Anal. Chem.* **2002**, *74*, 2781–2800.
- (10) Kimmel, D. W.; LeBlanc, G.; Meschievitz, M. E.; Cliffel, D. E. Electrochemical Sensors and Biosensors. *Anal. Chem.* **2012**, *84*, 685–707.
- (11) Bandodkar, A. J.; Wang, J. Non-Invasive Wearable Electrochemical Sensors: A Review. *Trends Biotechnol.* **2014**, *32*, 363–371.
- (12) Janata, J.; Josowicz, M. Conducting Polymers in Electronic Chemical Sensors. *Nat. Mater.* **2003**, *2*, 19–24.
- (13) Willner, I.; Zayats, M. Electronic Aptamer-Based Sensors. *Angew. Chem., Int. Ed.* **2007**, *46*, 6408–6418.
- (14) Drummond, T. G.; Hill, M. G.; Barton, J. K. Electrochemical DNA Sensors. *Nat. Biotechnol.* **2003**, *21*, 1192–1199.
- (15) Arshak, K.; Moore, E.; Lyons, G. M.; Harris, J.; Clifford, S. A Review of Gas Sensors Employed in Electronic Nose Applications. *Sens. Rev.* **2004**, *24*, 181–198.
- (16) Steinhubl, S. R.; Muse, E. D.; Topol, E. J. The Emerging Field of Mobile Health. *Sci. Transl. Med.* **2015**, *7*, 283rv3.
- (17) Diamond, D.; Coyle, S.; Scarmagnani, S.; Hayes, J. Wireless Sensor Networks and Chemo-/Biosensing. *Chem. Rev.* **2008**, *108*, 652–679.
- (18) Dieffenderfer, J.; Wilkins, M.; Hood, C.; Beppler, E.; Daniele, M. A.; Bozkurt, A. Towards a Sweat-Based Wireless and Wearable Electrochemical Sensor. *2016 IEEE Sensors* **2016**, 1–3.
- (19) Kim, D. H.; Lu, N.; Ma, R.; Kim, Y. S.; Kim, R. H.; Wang, S.; Wu, J.; Won, S. M.; Tao, H.; Islam, A.; Yu, K. J.; Kim, T. I.; Chowdhury, R.; Ying, M.; Xu, L.; Li, M.; Chung, H. J.; Keum, H.; McCormick, M.; Liu, P.; Zhang, Y. W.; Omenetto, F. G.; Huang, Y.; Coleman, T.; Rogers, J. A. Epidermal Electronics. *Science* **2011**, *333*, 838–843.
- (20) Kaltenbrunner, M.; Sekitani, T.; Reeder, J.; Yokota, T.; Kuribara, K.; Tokuhara, T.; Drack, M.; Schwodiauer, R.; Graz, I.; Bauer-Gogonea, S.; Bauer, S.; Someya, T. An Ultra-Lightweight Design for Imperceptible Plastic Electronics. *Nature* **2013**, *499*, 458–463.
- (21) Gao, W.; Emaminejad, S.; Nyein, H. Y. Y.; Challa, S.; Chen, K.; Peck, A.; Fahad, H. M.; Ota, H.; Shiraki, H.; Kiriya, D.; Lien, D. H.; Brooks, G. A.; Davis, R. W.; Javey, A. Fully Integrated Wearable Sensor Arrays for Multiplexed *In Situ* Perspiration Analysis. *Nature* **2016**, *529*, 509–514.
- (22) Kassal, P.; Kim, J.; Kumar, R.; de Araujo, W. R.; Steinberg, I. M.; Steinberg, M. D.; Wang, J. Smart Bandage with Wireless Connectivity for Uric Acid Biosensing as an Indicator of Wound Status. *Electrochim. Commun.* **2015**, *56*, 6–10.
- (23) Mannoor, M. S.; Tao, H.; Clayton, J. D.; Sengupta, A.; Kaplan, D. L.; Naik, R. R.; Verma, N.; Omenetto, F. G.; McAlpine, M. C. Graphene-Based Wireless Bacteria Detection on Tooth Enamel. *Nat. Commun.* **2012**, *3*, 763.
- (24) Kalantar-Zadeh, K.; Berean, K. J.; Ha, N.; Chrimes, A. F.; Xu, K.; Grando, D.; Ou, J. Z.; Pillai, N.; Campbell, J. L.; Brkljača, R.; Taylor, K. M.; Burgell, R. E.; Yao, C. K.; Ward, S. A.; McSweeney, C. S.; Muir, J. G.; Gibson, P. R. A. Human Pilot Trial of Ingestible Electronic Capsules Capable of Sensing Different Gases in the Gut. *Nat. Electron.* **2018**, *1*, 79–87.
- (25) Park, J.; Kim, J.; Kim, K.; Kim, S. Y.; Cheong, W. H.; Park, K.; Song, J. H.; Namgoong, G.; Kim, J. J.; Heo, J.; Bien, F.; Park, J. U. Wearable, Wireless Gas Sensors Using Highly Stretchable and Transparent Structures of Nanowires and Graphene. *Nanoscale* **2016**, *8*, 10591–10597.
- (26) Xu, L.; Gutbrod, S. R.; Bonifas, A. P.; Su, Y.; Sulkin, M. S.; Lu, N.; Chung, H. J.; Jang, K. I.; Liu, Z.; Ying, M.; Lu, C.; Webb, R. C.; Kim, J. S.; Laughner, J. I.; Cheng, H.; Liu, Y.; Ameen, A.; Jeong, J. W.; Kim, G. T.; Huang, Y.; Efimov, I. R.; Rogers, J. A. 3D Multifunctional Integumentary Membranes for Spatiotemporal Cardiac Measurements and Stimulation across the Entire Epicardium. *Nat. Commun.* **2014**, *5*, 3329.
- (27) Fahad, H. M.; Shiraki, H.; Amani, M.; Zhang, C.; Hebbar, V. S.; Gao, W.; Ota, H.; Hettick, M.; Kiriya, D.; Chen, Y. Z.; Chueh, Y. L.; Javey, A. Room Temperature Multiplexed Gas Sensing Using Chemical-Sensitive 3.5-nm-Thin Silicon Transistors. *Sci. Adv.* **2017**, *3*, No. e1602557.
- (28) McEvoy, M. A.; Correll, N. Materials Science. Materials That Couple Sensing, Actuation, Computation, and Communication. *Science* **2015**, *347*, 1261689.
- (29) Paolesse, R.; Nardis, S.; Monti, D.; Stefanelli, M.; Di Natale, C. Porphyrinoids for Chemical Sensor Applications. *Chem. Rev.* **2017**, *117*, 2517–2583.
- (30) Watson, J.; Ihokura, K. Gas-Sensing Materials. *MRS Bull.* **1999**, *24*, 14–17.
- (31) Poghossian, A.; Luth, H.; Schultze, J. W.; Schonning, M. J. (Bio-)Chemical and Physical Microsensor Arrays Using an Identical Transducer Principle. *Electrochim. Acta* **2001**, *47*, 243–249.
- (32) Schonning, M. J.; Poghossian, A.; Schultze, J. W.; Luth, H. Field-Effect Based Multifunctional Hybrid Sensor Module for the Determination of Both (Bio-)Chemical and Physical Parameters. *Proc. SPIE* **2001**, *4576*, 149–159.

- (33) Xu, S.; Zhang, Y.; Jia, L.; Mathewson, K. E.; Jang, K. I.; Kim, J.; Fu, H.; Huang, X.; Chava, P.; Wang, R.; Bhole, S.; Wang, L.; Na, Y. J.; Guan, Y.; Flavin, M.; Han, Z.; Huang, Y.; Rogers, J. A. Soft Microfluidic Assemblies of Sensors, Circuits, and Radios for the Skin. *Science* **2014**, *344*, 70–74.
- (34) Kenry; Yeo, J. C.; Lim, C. T. Emerging Flexible and Wearable Physical Sensing Platforms for Healthcare and Biomedical Applications. *Microsyst Nanoeng* **2016**, *2*, 16043.
- (35) Wang, P.; Liu, Q. Physical Sensors and Measurement. In *Biomedical Sensors and Measurement*; Springer: Berlin, 2011; pp 51–115.
- (36) Bhalla, M. R.; Bhalla, A. V. Comparative Study of Various Touchscreen Technologies. *International Journal of Computer Applications* **2010**, *6*, 12–18.
- (37) Yacobi, B. G. *Semiconductor Materials*; Springer: Boston, MA, 2003.
- (38) Pirondini, L.; Dalcanale, E. Molecular Recognition at the Gas-Solid Interface: A Powerful Tool for Chemical Sensing. *Chem. Soc. Rev.* **2007**, *36*, 695–706.
- (39) Ariga, K.; Hill, J. P.; Endo, H. Developments in Molecular Recognition and Sensing at Interfaces. *Int. J. Mol. Sci.* **2007**, *8*, 864–883.
- (40) Mu, B.; Zhang, J.; McNicholas, T. P.; Reuel, N. F.; Kruss, S.; Strano, M. S. Recent Advances in Molecular Recognition Based on Nanoengineered Platforms. *Acc. Chem. Res.* **2014**, *47*, 979–988.
- (41) Fortin, J., Transduction Principles. In *Functional Thin Films and Nanostructures for Sensors*; Springer: Boston, MA, 2009; pp 17–29.
- (42) Sinclair, I. *Passive Components for Circuit Design*; Elsevier Science: Amsterdam, 2000.
- (43) Wikipedia, S.; Books, L. *Diodes: Diode, Zener Diode, Pin Diode, Back-to-Back Connection, Resonant Tunneling Diode, Cat's-Whisker Detector, Schottky Diode, Impatt Diode*; General Books LLC: 2010.
- (44) Sevin, L. J. *Field-Effect Transistors*; McGraw-Hill: New York, 1965.
- (45) Deshpande, R. P. *Capacitors: Technology and Trends*; Tata McGraw Hill Education: New York, 2012.
- (46) Webster, J. G.; Eren, H. *Measurement, Instrumentation, and Sensors Handbook, Second ed.: Spatial, Mechanical, Thermal, and Radiation Measurement*; Taylor & Francis: London, 2014.
- (47) Wring, S. A.; Hart, J. P. Chemically Modified, Carbon-Based Electrodes and Their Application as Electrochemical Sensors for the Analysis of Biologically Important Compounds. A Review. *Analyst* **1992**, *117*, 1215–1229.
- (48) Jiang, L.; Nelson, G. W.; Abda, J.; Foord, J. S. Novel Modifications to Carbon-Based Electrodes to Improve the Electrochemical Detection of Dopamine. *ACS Appl. Mater. Interfaces* **2016**, *8*, 28338–28348.
- (49) Macpherson, J. V. A Practical Guide to Using Boron Doped Diamond in Electrochemical Research. *Phys. Chem. Chem. Phys.* **2015**, *17*, 2935–2949.
- (50) Bai, H.; Shi, G. Q. Gas Sensors Based on Conducting Polymers. *Sensors* **2007**, *7*, 267–307.
- (51) Synowczyk, A. W.; Heinze, J. Application of Fullerenes as Sensor Materials. In *Electronic Properties of Fullerenes*; Springer: Berlin, 1993; pp 73–77.
- (52) Pilehvar, S.; De Wael, K. Recent Advances in Electrochemical Biosensors Based on Fullerene-C₆₀ Nano-Structured Platforms. *Biosensors* **2015**, *5*, 712–735.
- (53) Fennell, J. F., Jr.; Liu, S. F.; Azzarelli, J. M.; Weis, J. G.; Rochat, S.; Mirica, K. A.; Ravnbaek, J. B.; Swager, T. M. Nanowire Chemical/Biological Sensors: Status and a Roadmap for the Future. *Angew. Chem., Int. Ed.* **2016**, *55*, 1266–1281.
- (54) Tang, R.; Shi, Y.; Hou, Z.; Wei, L. Carbon Nanotube-Based Chemiresistive Sensors. *Sensors* **2017**, *17*, 882.
- (55) Mirica, K. A.; Azzarelli, J. M.; Weis, J. G.; Schnorr, J. M.; Swager, T. M. Rapid Prototyping of Carbon-Based Chemiresistive Gas Sensors on Paper. *Proc. Natl. Acad. Sci. U. S. A.* **2013**, *110*, E3265–3270.
- (56) Kauffman, D. R.; Star, A. Carbon Nanotube Gas and Vapor Sensors. *Angew. Chem., Int. Ed.* **2008**, *47*, 6550–6570.
- (57) Howes, P. D.; Chandrawati, R.; Stevens, M. M. Bionanotechnology. Colloidal Nanoparticles as Advanced Biological Sensors. *Science* **2014**, *346*, 1247390.
- (58) El-Ansary, A.; Faddah, L. M. Nanoparticles as Biochemical Sensors. *Nanotechnol., Sci. Appl.* **2010**, *3*, 65–76.
- (59) Luo, X.; Morrin, A.; Killard, A. J.; Smyth, M. R. Application of Nanoparticles in Electrochemical Sensors and Biosensors. *Electroanalysis* **2006**, *18*, 319–326.
- (60) Lange, U.; Roznyatovskaya, N. V.; Mirsky, V. M. Conducting Polymers in Chemical Sensors and Arrays. *Anal. Chim. Acta* **2008**, *614*, 1–26.
- (61) Guo, L.; Jackman, J. A.; Yang, H.-H.; Chen, P.; Cho, N.-J.; Kim, D.-H. Strategies for Enhancing the Sensitivity of Plasmonic Nanosensors. *Nano Today* **2015**, *10*, 213–239.
- (62) Xia, F.; Wang, H.; Xiao, D.; Dubey, M.; Ramasubramanian, A. Two-Dimensional Material Nanophotonics. *Nat. Photonics* **2014**, *8*, 899–907.
- (63) Dean, C. R.; Young, A. F.; Meric, I.; Lee, C.; Wang, L.; Sorgenfrei, S.; Watanabe, K.; Taniguchi, T.; Kim, P.; Shepard, K. L.; Hone, J. Boron Nitride Substrates for High-Quality Graphene Electronics. *Nat. Nanotechnol.* **2010**, *5*, 722–726.
- (64) Huang, X.; Sheng, P.; Tu, Z.; Zhang, F.; Wang, J.; Geng, H.; Zou, Y.; Di, C. A.; Yi, Y.; Sun, Y.; Xu, W.; Zhu, D. A Two-Dimensional Pi-D Conjugated Coordination Polymer with Extremely High Electrical Conductivity and Ambipolar Transport Behaviour. *Nat. Commun.* **2015**, *6*, 7408.
- (65) Bao, W.; Cai, X.; Kim, D.; Sridhara, K.; Fuhrer, M. S. High Mobility Ambipolar MoS₂ Field-Effect Transistors: Substrate and Dielectric Effects. *Appl. Phys. Lett.* **2013**, *102*, 042104.
- (66) Perello, D. J.; Chae, S. H.; Song, S.; Lee, Y. H. High-Performance N-Type Black Phosphorus Transistors with Type Control via Thickness and Contact-Metal Engineering. *Nat. Commun.* **2015**, *6*, 7809.
- (67) Liu, H.; Neal, A. T.; Zhu, Z.; Luo, Z.; Xu, X.; Tomanek, D.; Ye, P. D. Phosphorene: An Unexplored 2D Semiconductor with a High Hole Mobility. *ACS Nano* **2014**, *8*, 4033–4041.
- (68) Bolotin, K. I.; Sikes, K. J.; Jiang, Z.; Klima, M.; Fudenberg, G.; Hone, J.; Kim, P.; Stormer, H. L. Ultrahigh Electron Mobility in Suspended Graphene. *Solid State Commun.* **2008**, *146*, 351–355.
- (69) Wang, Y.; Chen, Y.; Lacey, S. D.; Xu, L.; Xie, H.; Li, T.; Danner, V. A.; Hu, L. Reduced Graphene Oxide Film with Record-High Conductivity and Mobility. *Mater. Today* **2018**, *21*, 186–192.
- (70) Butler, S. Z.; Hollen, S. M.; Cao, L.; Cui, Y.; Gupta, J. A.; Gutierrez, H. R.; Heinz, T. F.; Hong, S. S.; Huang, J.; Ismach, A. F.; Johnston-Halperin, E.; Kuno, M.; Plashnitsa, V. V.; Robinson, R. D.; Ruoff, R. S.; Salahuddin, S.; Shan, J.; Shi, L.; Spencer, M. G.; Terrones, M.; Windl, W.; Goldberger, J. E. Progress, Challenges, and Opportunities in Two-Dimensional Materials Beyond Graphene. *ACS Nano* **2013**, *7*, 2898–2926.
- (71) Xu, M.; Liang, T.; Shi, M.; Chen, H. Graphene-Like Two-Dimensional Materials. *Chem. Rev.* **2013**, *113*, 3766–3798.
- (72) Novoselov, K. S.; Mishchenko, A.; Carvalho, A.; Castro Neto, A. H. 2D Materials and Van der Waals Heterostructures. *Science* **2016**, *353*, aac9439.
- (73) Tan, C.; Cao, X.; Wu, X. J.; He, Q.; Yang, J.; Zhang, X.; Chen, J.; Zhao, W.; Han, S.; Nam, G. H.; Sindoro, M.; Zhang, H. Recent Advances in Ultrathin Two-Dimensional Nanomaterials. *Chem. Rev.* **2017**, *117*, 6225–6331.
- (74) Li, J.; Wang, X.-Y.; Liu, X.-R.; Jin, Z.; Wang, D.; Wan, L.-J. Facile Growth of Centimeter-Sized Single-Crystal Graphene on Copper Foil at Atmospheric Pressure. *J. Mater. Chem. C* **2015**, *3*, 3530–3535.
- (75) Vlassiouk, I. V.; Stehle, Y.; Pudasaini, P. R.; Unocic, R. R.; Rack, P. D.; Baddorf, A. P.; Ivanov, I. N.; Lavrik, N. V.; List, F.; Gupta, N.; Bets, K. V.; Yakobson, B. I.; Smirnov, S. N. Evolutionary Selection Growth of Two-Dimensional Materials on Polycrystalline Substrates. *Nat. Mater.* **2018**, *17*, 318–322.

- (76) Novoselov, K. S.; Geim, A. K.; Morozov, S. V.; Jiang, D.; Zhang, Y.; Dubonos, S. V.; Grigorieva, I. V.; Firsov, A. A. Electric Field Effect in Atomically Thin Carbon Films. *Science* **2004**, *306*, 666–669.
- (77) Castro Neto, A. H.; Guinea, F.; Peres, N. M. R.; Novoselov, K. S.; Geim, A. K. The Electronic Properties of Graphene. *Rev. Mod. Phys.* **2009**, *81*, 109–162.
- (78) He, Q. Y.; Wu, S. X.; Yin, Z. Y.; Zhang, H. Graphene-Based Electronic Sensors. *Chem. Sci.* **2012**, *3*, 1764–1772.
- (79) Zhu, J.; Yang, D.; Yin, Z.; Yan, Q.; Zhang, H. Graphene and Graphene-Based Materials for Energy Storage Applications. *Small* **2014**, *10*, 3480–3498.
- (80) Pumera, M.; Ambrosi, A.; Bonanni, A.; Chng, E. L. K.; Poh, H. L. Graphene for Electrochemical Sensing and Biosensing. *TrAC, Trends Anal. Chem.* **2010**, *29*, 954–965.
- (81) Khandelwal, A.; Mani, K.; Karigerasi, M. H.; Lahiri, I. Phosphorene – the Two-Dimensional Black Phosphorous: Properties, Synthesis and Applications. *Mater. Sci. Eng., B* **2017**, *221*, 17–34.
- (82) Lin, Y.; Williams, T. V.; Connell, J. W. Soluble, Exfoliated Hexagonal Boron Nitride Nanosheets. *J. Phys. Chem. Lett.* **2010**, *1*, 277–283.
- (83) Li, L. H.; Chen, Y. Atomically Thin Boron Nitride: Unique Properties and Applications. *Adv. Funct. Mater.* **2016**, *26*, 2594–2608.
- (84) Chhowalla, M.; Shin, H. S.; Eda, G.; Li, L. J.; Loh, K. P.; Zhang, H. The Chemistry of Two-Dimensional Layered Transition Metal Dichalcogenide Nanosheets. *Nat. Chem.* **2013**, *5*, 263–275.
- (85) Tan, C.; Zhang, H. Two-Dimensional Transition Metal Dichalcogenide Nanosheet-Based Composites. *Chem. Soc. Rev.* **2015**, *44*, 2713–2731.
- (86) Kalantar-zadeh, K.; Ou, J. Z.; Daeneke, T.; Mitchell, A.; Sasaki, T.; Fuhrer, M. S. Two Dimensional and Layered Transition Metal Oxides. *Appl. Mater. Today* **2016**, *5*, 73–89.
- (87) Balendhran, S.; Walia, S.; Nili, H.; Ou, J. Z.; Zhuiykov, S.; Kaner, R. B.; Sriram, S.; Bhaskaran, M.; Kalantar-zadeh, K. Two-Dimensional Molybdenum Trioxide and Dichalcogenides. *Adv. Funct. Mater.* **2013**, *23*, 3952–3970.
- (88) Sun, L.; Campbell, M. G.; Dincă, M. Electrically Conductive Porous Metal–Organic Frameworks. *Angew. Chem., Int. Ed.* **2016**, *55*, 3566–3579.
- (89) Ko, M.; Mendecki, L.; Mirica, K. A. Conductive Two-Dimensional Metal–Organic Frameworks as Multifunctional Materials. *Chem. Commun.* **2018**, *54*, 7873–7891.
- (90) Jin, E.; Asada, M.; Xu, Q.; Dalapati, S.; Addicoat, M. A.; Brady, M. A.; Xu, H.; Nakamura, T.; Heine, T.; Chen, Q.; Jiang, D. Two-Dimensional sp^2 Carbon-Conjugated Covalent Organic Frameworks. *Science* **2017**, *357*, 673–676.
- (91) Yang, H.; Zhang, S.; Han, L.; Zhang, Z.; Xue, Z.; Gao, J.; Li, Y.; Huang, C.; Yi, Y.; Liu, H.; Li, Y. High Conductive Two-Dimensional Covalent Organic Framework for Lithium Storage with Large Capacity. *ACS Appl. Mater. Interfaces* **2016**, *8*, 5366–5375.
- (92) Rao, C. N.; Sood, A. K.; Subrahmanyam, K. S.; Govindaraj, A. Graphene: The New Two-Dimensional Nanomaterial. *Angew. Chem., Int. Ed.* **2009**, *48*, 7752–7777.
- (93) Sun, Y.; Lei, F.; Gao, S.; Pan, B.; Zhou, J.; Xie, Y. Atomically Thin Tin Dioxide Sheets for Efficient Catalytic Oxidation of Carbon Monoxide. *Angew. Chem., Int. Ed.* **2013**, *52*, 10569–10572.
- (94) Varghese, S.; Varghese, S.; Swaminathan, S.; Singh, K.; Mittal, V. Two-Dimensional Materials for Sensing: Graphene and Beyond. *Electronics* **2015**, *4*, 651–687.
- (95) Li, Z.; Wong, S. L. Functionalization of 2D Transition Metal Dichalcogenides for Biomedical Applications. *Mater. Sci. Eng., C* **2017**, *70*, 1095–1106.
- (96) Hirsch, A.; Hauke, F. Post-Graphene 2D Chemistry: The Emerging Field of Molybdenum Disulfide and Black Phosphorus Functionalization. *Angew. Chem., Int. Ed.* **2018**, *57*, 4338–4354.
- (97) Georgakilas, V.; Otyepka, M.; Bourlinos, A. B.; Chandra, V.; Kim, N.; Kemp, K. C.; Hobza, P.; Zboril, R.; Kim, K. S. Functionalization of Graphene: Covalent and Non-Covalent Approaches, Derivatives and Applications. *Chem. Rev.* **2012**, *112*, 6156–6214.
- (98) Kou, L.; Frauenheim, T.; Chen, C. Phosphorene as a Superior Gas Sensor: Selective Adsorption and Distinct I-V Response. *J. Phys. Chem. Lett.* **2014**, *5*, 2675–2681.
- (99) Lei, S. Y.; Luan, S.; Yu, H. Co-Doped Phosphorene: Enhanced Sensitivity of CO Gas Sensing. *Int. J. Mod. Phys. B* **2018**, *32*, 1850068.
- (100) Suvansinpan, N.; Hussain, F.; Zhang, G.; Chiu, C. H.; Cai, Y.; Zhang, Y. W. Substitutionally Doped Phosphorene: Electronic Properties and Gas Sensing. *Nanotechnology* **2016**, *27*, 065708.
- (101) Late, D. J.; Huang, Y. K.; Liu, B.; Acharya, J.; Shirodkar, S. N.; Luo, J.; Yan, A.; Charles, D.; Waghmare, U. V.; Dravid, V. P.; Rao, C. N. Sensing Behavior of Atomically Thin-Layered MoS₂ Transistors. *ACS Nano* **2013**, *7*, 4879–4891.
- (102) Zeng, M.; Xiao, Y.; Liu, J.; Yang, K.; Fu, L. Exploring Two-Dimensional Materials toward the Next-Generation Circuits: From Monomer Design to Assembly Control. *Chem. Rev.* **2018**, *118*, 6236–6296.
- (103) Gao, L. Flexible Device Applications of 2D Semiconductors. *Small* **2017**, *13*, 1603994.
- (104) Bandodkar, A. J.; Jeerapan, I.; Wang, J. Wearable Chemical Sensors: Present Challenges and Future Prospects. *ACS Sens* **2016**, *1*, 464–482.
- (105) Xiang, D.; Wang, X.; Jia, C.; Lee, T.; Guo, X. Molecular-Scale Electronics: From Concept to Function. *Chem. Rev.* **2016**, *116*, 4318–4440.
- (106) Chuang, C. H.; Brown, P. R.; Bulovic, V.; Bawendi, M. G. Improved Performance and Stability in Quantum Dot Solar Cells through Band Alignment Engineering. *Nat. Mater.* **2014**, *13*, 796–801.
- (107) Yue, Z.; Lisdat, F.; Parak, W. J.; Hickey, S. G.; Tu, L.; Sabir, N.; Dorfs, D.; Bigall, N. C. Quantum-Dot-Based Photoelectrochemical Sensors for Chemical and Biological Detection. *ACS Appl. Mater. Interfaces* **2013**, *5*, 2800–2814.
- (108) Pedireddy, S.; Lee, H. K.; Tju, W. W.; Phang, I. Y.; Tan, H. R.; Chua, S. Q.; Troadec, C.; Ling, X. Y. One-Step Synthesis of Zero-Dimensional Hollow Nanoporous Gold Nanoparticles with Enhanced Methanol Electrooxidation Performance. *Nat. Commun.* **2014**, *5*, 4947.
- (109) Yildirim, L.; Thanh, N. T.; Loizidou, M.; Seifalian, A. M. Toxicology and Clinical Potential of Nanoparticles. *Nano Today* **2011**, *6*, 585–607.
- (110) Comini, E.; Sberveglieri, G. Metal Oxide Nanowires as Chemical Sensors. *Mater. Today* **2010**, *13*, 36.
- (111) Zhao, X.; Cai, B.; Tang, Q.; Tong, Y.; Liu, Y. One-Dimensional Nanostructure Field-Effect Sensors for Gas Detection. *Sensors* **2014**, *14*, 13999–14020.
- (112) Choi, K. J.; Jang, H. W. One-Dimensional Oxide Nanostructures as Gas-Sensing Materials: Review and Issues. *Sensors* **2010**, *10*, 4083–4099.
- (113) Liu, X.; Ma, T.; Pinna, N.; Zhang, J. Two-Dimensional Nanostructured Materials for Gas Sensing. *Adv. Funct. Mater.* **2017**, *27*, 1702168.
- (114) Neri, G. Thin 2D: The New Dimensionality in Gas Sensing. *Chemosensors* **2017**, *5*, 21.
- (115) Kreno, L. E.; Leong, K.; Farha, O. K.; Allendorf, M.; Van Duyne, R. P.; Hupp, J. T. Metal–Organic Framework Materials as Chemical Sensors. *Chem. Rev.* **2012**, *112*, 1105–1125.
- (116) Xu, S.; Yan, Z.; Jang, K. I.; Huang, W.; Fu, H.; Kim, J.; Wei, Z.; Flavin, M.; McCracken, J.; Wang, R.; Badea, A.; Liu, Y.; Xiao, D.; Zhou, G.; Lee, J.; Chung, H. U.; Cheng, H.; Ren, W.; Banks, A.; Li, X.; Paik, U.; Nuzzo, R. G.; Huang, Y.; Zhang, Y.; Rogers, J. A. Materials Science. Assembly of Micro/Nanomaterials into Complex, Three-Dimensional Architectures by Compressive Buckling. *Science* **2015**, *347*, 154–159.
- (117) Cai, Z.; Liu, B.; Zou, X.; Cheng, H. M. Chemical Vapor Deposition Growth and Applications of Two-Dimensional Materials and Their Heterostructures. *Chem. Rev.* **2018**, *118*, 6091–6133.

- (118) Dong, R.; Zhang, T.; Feng, X. Interface-Assisted Synthesis of 2D Materials: Trend and Challenges. *Chem. Rev.* **2018**, *118*, 6189–6235.
- (119) Mannix, A. J.; Kiraly, B.; Hersam, M. C.; Guisinger, N. P. Synthesis and Chemistry of Elemental 2D Materials. *Nat. Rev. Chem.* **2017**, *1*, 0014.
- (120) Chen, Y.; Fan, Z.; Zhang, Z.; Niu, W.; Li, C.; Yang, N.; Chen, B.; Zhang, H. Two-Dimensional Metal Nanomaterials: Synthesis, Properties, and Applications. *Chem. Rev.* **2018**, *118*, 6409–6455.
- (121) Jin, H.; Guo, C.; Liu, X.; Liu, J.; Vasileff, A.; Jiao, Y.; Zheng, Y.; Qiao, S. Z. Emerging Two-Dimensional Nanomaterials for Electrocatalysis. *Chem. Rev.* **2018**, *118*, 6337–6408.
- (122) Holzinger, M.; Le Goff, A.; Cosnier, S. Nanomaterials for Biosensing Applications: A Review. *Front. Chem.* **2014**, *2*, 63.
- (123) Yuan, W.; Shi, G. Graphene-Based Gas Sensors. *J. Mater. Chem. A* **2013**, *1*, 10078.
- (124) Singh, E.; Meyyappan, M.; Nalwa, H. S. Flexible Graphene-Based Wearable Gas and Chemical Sensors. *ACS Appl. Mater. Interfaces* **2017**, *9*, 34544–34586.
- (125) Yavari, F.; Koratkar, N. Graphene-Based Chemical Sensors. *J. Phys. Chem. Lett.* **2012**, *3*, 1746–1753.
- (126) Wu, S.; He, Q.; Tan, C.; Wang, Y.; Zhang, H. Graphene-Based Electrochemical Sensors. *Small* **2013**, *9*, 1160–1172.
- (127) Sun, Y. F.; Liu, S. B.; Meng, F. L.; Liu, J. Y.; Jin, Z.; Kong, L. T.; Liu, J. H. Metal Oxide Nanostructures and Their Gas Sensing Properties: A Review. *Sensors* **2012**, *12*, 2610–2631.
- (128) Zhang, J.; Qin, Z.; Zeng, D.; Xie, C. Metal-Oxide-Semiconductor Based Gas Sensors: Screening, Preparation, and Integration. *Phys. Chem. Chem. Phys.* **2017**, *19*, 6313–6329.
- (129) Hahn, Y. B.; Ahmad, R.; Tripathy, N. Chemical and Biological Sensors Based on Metal Oxide Nanostructures. *Chem. Commun.* **2012**, *48*, 10369–10385.
- (130) Marco, S.; Gutierrez-Galvez, A. Signal and Data Processing for Machine Olfaction and Chemical Sensing: A Review. *IEEE Sens. J.* **2012**, *12*, 3189–3214.
- (131) Göpel, W. New Materials and Transducers for Chemical Sensors. *Sens. Actuators, B* **1994**, *18*, 1–21.
- (132) Lu, W.; Lieber, C. M. Nanoelectronics from the Bottom Up. *Nat. Mater.* **2007**, *6*, 841–850.
- (133) Shimomura, M.; Sawadaishi, T. Bottom-up Strategy of Materials Fabrication: A New Trend in Nanotechnology of Soft Materials. *Curr. Opin. Colloid Interface Sci.* **2001**, *6*, 11–16.
- (134) Cravotto, G.; Cintas, P. Sonication-Assisted Fabrication and Post-Synthetic Modifications of Graphene-Like Materials. *Chem. - Eur. J.* **2010**, *16*, 5246–5259.
- (135) Wang, Z.; Cohen, S. M. Postsynthetic Modification of Metal–Organic Frameworks. *Chem. Soc. Rev.* **2009**, *38*, 1315–1329.
- (136) Huang, X.; Qi, X.; Boey, F.; Zhang, H. Graphene-Based Composites. *Chem. Soc. Rev.* **2012**, *41*, 666–686.
- (137) Liu, Z.; Lau, S. P.; Yan, F. Functionalized Graphene and Other Two-Dimensional Materials for Photovoltaic Devices: Device Design and Processing. *Chem. Soc. Rev.* **2015**, *44*, 5638–5679.
- (138) Bhimanapati, G. R.; Lin, Z.; Meunier, V.; Jung, Y.; Cha, J.; Das, S.; Xiao, D.; Son, Y.; Strano, M. S.; Cooper, V. R.; Liang, L.; Louie, S. G.; Ringe, E.; Zhou, W.; Kim, S. S.; Naik, R. R.; Sumpter, B. G.; Terrones, H.; Xia, F.; Wang, Y.; Zhu, J.; Akinwande, D.; Alem, N.; Schuller, J. A.; Schaak, R. E.; Terrones, M.; Robinson, J. A. Recent Advances in Two-Dimensional Materials Beyond Graphene. *ACS Nano* **2015**, *9*, 11509–11539.
- (139) Gupta, A.; Sakthivel, T.; Seal, S. Recent Development in 2D Materials Beyond Graphene. *Prog. Mater. Sci.* **2015**, *73*, 44–126.
- (140) Zeghbrouck, V. *Principles of Semiconductor Devices and Heterojunctions*; Prentice Hall PTR: 2007.
- (141) Berger, L. I. *Semiconductor Materials*; Taylor & Francis: London, 1996.
- (142) Neamen, D. *An Introduction to Semiconductor Devices*; McGraw-Hill, Inc.: New York, 2006; p 720.
- (143) Kahn, A. Fermi Level, Work Function and Vacuum Level. *Mater. Horiz.* **2016**, *3*, 7–10.
- (144) Tung, R. T. The Physics and Chemistry of the Schottky Barrier Height. *Appl. Phys. Rev.* **2014**, *1*, 011304.
- (145) Griffiths, D. J. *Introduction to Electrodynamics*; Cambridge University Press: Cambridge, 2017.
- (146) Yang, S.; Jiang, C.; Wei, S.-h. Gas Sensing in 2D Materials. *Appl. Phys. Rev.* **2017**, *4*, 021304.
- (147) Wang, T.; Huang, D.; Yang, Z.; Xu, S.; He, G.; Li, X.; Hu, N.; Yin, G.; He, D.; Zhang, L. A Review on Graphene-Based Gas/Vapor Sensors with Unique Properties and Potential Applications. *Nano-Micro Lett.* **2016**, *8*, 95–119.
- (148) Ishihara, T.; Matsubara, S. Capacitive Type Gas Sensors. *J. Electroceram.* **1998**, *2*, 215–228.
- (149) Fonollosa, J.; Solorzano, A.; Marco, S. Chemical Sensor Systems and Associated Algorithms for Fire Detection: A Review. *Sensors* **2018**, *18*, 553
- (150) Potyrailo, R. A. Multivariable Sensors for Ubiquitous Monitoring of Gases in the Era of Internet of Things and Industrial Internet. *Chem. Rev.* **2016**, *116*, 11877–11923.
- (151) Shimizu, Y.; Egashira, M. Basic Aspects and Challenges of Semiconductor Gas Sensors. *MRS Bull.* **1999**, *24*, 18–24.
- (152) Barsan, N.; Weimar, U. Conduction Model of Metal Oxide Gas Sensors. *J. Electroceram.* **2001**, *7*, 143–167.
- (153) Lee, J. H.; Avsar, A.; Jung, J.; Tan, J. Y.; Watanabe, K.; Taniguchi, T.; Natarajan, S.; Eda, G.; Adam, S.; Castro Neto, A. H.; Ozilmez, B. Van der Waals Force: A Dominant Factor for Reactivity of Graphene. *Nano Lett.* **2015**, *15*, 319–325.
- (154) Collins, P. G. Extreme Oxygen Sensitivity of Electronic Properties of Carbon Nanotubes. *Science* **2000**, *287*, 1801–1804.
- (155) Yew, Y. T.; Ambrosi, A.; Pumera, M. Nitroaromatic Explosives Detection Using Electrochemically Exfoliated Graphene. *Sci. Rep.* **2016**, *6*, 33276.
- (156) Church, J.; Wang, X.; Calderon, J.; Lee, W. H.; Cho, H. J.; Zhai, L. A Graphene-Based Nanosensor for in Situ Monitoring of Polycyclic Aromatic Hydrocarbons (PAHs). *J. Nanosci. Nanotechnol.* **2016**, *16*, 1620–1623.
- (157) Schedin, F.; Geim, A. K.; Morozov, S. V.; Hill, E. W.; Blake, P.; Katsnelson, M. I.; Novoselov, K. S. Detection of Individual Gas Molecules Adsorbed on Graphene. *Nat. Mater.* **2007**, *6*, 652–655.
- (158) Cui, S.; Pu, H.; Wells, S. A.; Wen, Z.; Mao, S.; Chang, J.; Hersam, M. C.; Chen, J. Ultrahigh Sensitivity and Layer-Dependent Sensing Performance of Phosphorene-Based Gas Sensors. *Nat. Commun.* **2015**, *6*, 8632.
- (159) Abbas, A. N.; Liu, B.; Chen, L.; Ma, Y.; Cong, S.; Aroonyadet, N.; Kopf, M.; Nilges, T.; Zhou, C. Black Phosphorus Gas Sensors. *ACS Nano* **2015**, *9*, 5618–5624.
- (160) Donarelli, M.; Ottaviano, L.; Giancaterini, L.; Fioravanti, G.; Perrozzi, F.; Cantalini, C. Exfoliated Black Phosphorus Gas Sensing Properties at Room Temperature. *2D Mater.* **2016**, *3*, 025002.
- (161) Hussain, T.; Kaewmaraya, T.; Chakraborty, S.; Ahuja, R. Defect and Substitution-Induced Silicene Sensor to Probe Toxic Gases. *J. Phys. Chem. C* **2016**, *120*, 25256–25262.
- (162) Gupta, S. K.; Singh, D.; Rajput, K.; Sonvane, Y. Germanene: A New Electronic Gas Sensing. *RSC Adv.* **2016**, *6*, 102264–102271.
- (163) Prasongkit, J.; Amorim, R. G.; Chakraborty, S.; Ahuja, R.; Scheicher, R. H.; Amornkitbamrung, V. Highly Sensitive and Selective Gas Detection Based on Silicene. *J. Phys. Chem. C* **2015**, *119*, 16934–16940.
- (164) Thomas, R. C. Sensors for Detecting Molecular Hydrogen Based on Pd Metal Alloys. *J. Electrochem. Soc.* **1997**, *144*, 3245–3249.
- (165) Sen, S.; Muthe, K. P.; Joshi, N.; Gadkari, S. C.; Gupta, S. K.; Jagannath; Roy, M.; Deshpande, S. K.; Yakhmi, J. V. Room Temperature Operating Ammonia Sensor Based on Tellurium Thin Films. *Sens. Actuators, B* **2004**, *98*, 154–159.
- (166) Perkins, F. K.; Friedman, A. L.; Cobas, E.; Campbell, P. M.; Jernigan, G. G.; Jonker, B. T. Chemical Vapor Sensing with Monolayer MoS₂. *Nano Lett.* **2013**, *13*, 668–673.
- (167) Ovcharenko, R.; Dedkov, Y.; Voloshina, E. Adsorption of NO₂ on WSe₂: DFT and Photoelectron Spectroscopy Studies. *J. Phys.: Condens. Matter* **2016**, *28*, 364003.

- (168) Chen, B.; Sahin, H.; Suslu, A.; Ding, L.; Bertoni, M. I.; Peeters, F. M.; Tongay, S. Environmental Changes in MoTe₂ Excitonic Dynamics by Defects-Activated Molecular Interaction. *ACS Nano* **2015**, *9*, 5326–5332.
- (169) Enhanced Sensitivity of MoTe₂ Chemical Sensor through Light Illumination. *Micromachines* **2017**, *8*, 155.
- (170) Cho, B.; Hahm, M. G.; Choi, M.; Yoon, J.; Kim, A. R.; Lee, Y. J.; Park, S. G.; Kwon, J. D.; Kim, C. S.; Song, M.; Jeong, Y.; Nam, K. S.; Lee, S.; Yoo, T. J.; Kang, C. G.; Lee, B. H.; Ko, H. C.; Ajayan, P. M.; Kim, D. H. Charge-Transfer-Based Gas Sensing Using Atomic-Layer MoS₂. *Sci. Rep.* **2015**, *5*, 8052.
- (171) Shimizu, Y.; Egashira, M. Basic Aspects and Challenges of Semiconductor Gas Sensors. *MRS Bull.* **1999**, *24*, 18–24.
- (172) Zhang, J.; Liu, X.; Neri, G.; Pinna, N. Nanostructured Materials for Room-Temperature Gas Sensors. *Adv. Mater.* **2016**, *28*, 795–831.
- (173) Yao, M. S.; Lv, X. J.; Fu, Z. H.; Li, W. H.; Deng, W. H.; Wu, G. D.; Xu, G. Layer-by-Layer Assembled Conductive Metal–Organic Framework Nanofilms for Room-Temperature Chemiresistive Sensing. *Angew. Chem., Int. Ed.* **2017**, *56*, 16510–16514.
- (174) Campbell, M. G.; Liu, S. F.; Swager, T. M.; Dincă, M. Chemiresistive Sensor Arrays from Conductive 2D Metal–Organic Frameworks. *J. Am. Chem. Soc.* **2015**, *137*, 13780–13783.
- (175) Rubio-Gimenez, V.; Almora-Barrios, N.; Escoria-Ariza, G.; Galbiati, M.; Sessolo, M.; Tatay, S.; Martí-Gastaldo, C. Origin of the Chemiresistive Response of Ultrathin Films of Conductive Metal–Organic Frameworks. *Angew. Chem., Int. Ed.* **2018**, *57*, 15086.
- (176) Ko, M.; Aykanat, A.; Smith, M. K.; Mirica, K. A. Drawing Sensors with Ball-Milled Blends of Metal–Organic Frameworks and Graphite. *Sensors* **2017**, *17*, 2192.
- (177) Hong Ng, V. M.; Huang, H.; Zhou, K.; Lee, P. S.; Que, W.; Xu, J. Z.; Kong, L. B. Recent Progress in Layered Transition Metal Carbides and/or Nitrides (MXenes) and Their Composites: Synthesis and Applications. *J. Mater. Chem. A* **2017**, *5*, 3039–3068.
- (178) Naguib, M.; Kurtoglu, M.; Presser, V.; Lu, J.; Niu, J.; Heon, M.; Hultman, L.; Gogotsi, Y.; Barsoum, M. W. Two-Dimensional Nanocrystals Produced by Exfoliation of Ti₃AlC₂. *Adv. Mater.* **2011**, *23*, 4248–4253.
- (179) Zhu, J.; Ha, E.; Zhao, G.; Zhou, Y.; Huang, D.; Yue, G.; Hu, L.; Sun, N.; Wang, Y.; Lee, L. Y. S.; Xu, C.; Wong, K.-Y.; Astruc, D.; Zhao, P. Recent Advance in MXenes: A Promising 2D Material for Catalysis, Sensor and Chemical Adsorption. *Coord. Chem. Rev.* **2017**, *352*, 306–327.
- (180) Kamaraj, M.; Sundar, J. V.; Subramanian, V. Dioxin Sensing Properties of Graphene and Hexagonal Boron Nitride Based Van der Waals Solids: A First-Principles Study. *RSC Adv.* **2016**, *6*, 107114–107126.
- (181) Yamini, Y.; Moradi, M. Influence of Topological Defects on the Nitrogen Monoxide-Sensing Characteristics of Graphene-Analogue BN. *Sens. Actuators, B* **2014**, *197*, 274–279.
- (182) Safari, L.; Vessally, E.; Bekhradnia, A.; Hosseiniyan, A.; Edjlali, L. A Density Functional Theory Study of the Sensitivity of Two-Dimensional BN Nanosheet to Nerve Agents Cyclosarin and Tabun. *Thin Solid Films* **2017**, *623*, 157–163.
- (183) Ao, Z. M.; Yang, J.; Li, S.; Jiang, Q. Enhancement of CO Detection in Al Doped Graphene. *Chem. Phys. Lett.* **2008**, *461*, 276–279.
- (184) Sarkar, D.; Liu, W.; Xie, X.; Anselmo, A. C.; Mitragotri, S.; Banerjee, K. MoS₂ Field-Effect Transistor for Next-Generation Label-Free Biosensors. *ACS Nano* **2014**, *8*, 3992–4003.
- (185) Blackwood, D.; Josowicz, M. Work Function and Spectroscopic Studies of Interactions between Conducting Polymers and Organic Vapors. *J. Phys. Chem.* **1991**, *95*, 493–502.
- (186) Potje-Kamloth, K. Semiconductor Junction Gas Sensors. *Chem. Rev.* **2008**, *108*, 367–399.
- (187) Kong, J.; Javey, A. *Carbon Nanotube Electronics*; Springer US: Boston, MA, 2009.
- (188) Pinto, H.; Markevich, A. Electronic and Electrochemical Doping of Graphene by Surface Adsorbates. *Beilstein J. Nanotechnol.* **2014**, *5*, 1842–1848.
- (189) Rhoderick, E. H. The Physics of Schottky Barriers. *J. Phys. D: Appl. Phys.* **1970**, *3*, 1153–1167.
- (190) The Physics and Chemistry of the Schottky Barrier Height. *Appl. Phys. Rev.* **2014**, *1*, 011304.
- (191) Liu, B.; Chen, L.; Liu, G.; Abbas, A. N.; Fathi, M.; Zhou, C. High-Performance Chemical Sensing Using Schottky-Contacted Chemical Vapor Deposition Grown Monolayer MoS₂ Transistors. *ACS Nano* **2014**, *8*, 5304–5314.
- (192) Xu, Y.; Cheng, C.; Du, S. C.; Yang, J. Y.; Yu, B.; Luo, J.; Yin, W. Y.; Li, E. P.; Dong, S. R.; Ye, P. D.; Duan, X. F. Contacts between Two- and Three-Dimensional Materials: Ohmic, Schottky, and P-N Heterojunctions. *ACS Nano* **2016**, *10*, 4895–4919.
- (193) Ruths, P. F.; Ashok, S.; Fonash, S. J.; Ruths, J. M. A Study of Pd/Si MIS Schottky Barrier Diode Hydrogen Detector. *IEEE Trans. Electron Devices* **1981**, *28*, 1003–1009.
- (194) Ogawa, H.; Nishikawa, M.; Abe, A. Hall Measurement Studies and an Electrical Conduction Model of Tin Oxide Ultrafine Particle Films. *J. Appl. Phys.* **1982**, *53*, 4448–4455.
- (195) Xu, C.; Tamaki, J.; Miura, N.; Yamazoe, N. Grain Size Effects on Gas Sensitivity of Porous SnO₂-Based Elements. *Sens. Actuators, B* **1991**, *3*, 147–155.
- (196) Sharma, B. L. *Metal-Semiconductor Schottky Barrier Junctions and Their Applications*; Springer, Boston, MA, 1984.
- (197) Fonash, S. J.; Huston, H.; Ashok, S. Conducting MIS Diode Gas Detectors: The Pd/SiO_x/Si Hydrogen Sensor. *Sens. Actuators* **1981**, *2*, 363–369.
- (198) Li, P.; Zhang, D.; Jiang, C.; Zong, X.; Cao, Y. Ultra-Sensitive Suspended Atomically Thin-Layered Black Phosphorus Mercury Sensors. *Biosens. Bioelectron.* **2017**, *98*, 68–75.
- (199) Vig, J. R.; Walls, F. L. A Review of Sensor Sensitivity and Stability. *Proceedings of the 2000 IEEE/EIA International Frequency Control Symposium & Exhibition* **2000**, 30–33.
- (200) Loock, H.-P.; Wentzell, P. D. Detection Limits of Chemical Sensors: Applications and Misapplications. *Sens. Actuators, B* **2012**, *173*, 157–163.
- (201) Shrivastava, A.; Gupta, V. Methods for the Determination of Limit of Detection and Limit of Quantitation of the Analytical Methods. *Chronicles of Young Scientists* **2011**, *2*, 21–25.
- (202) Püntener, M.; Vigassy, T.; Baier, E.; Ceresa, A.; Pretsch, E. Improving the Lower Detection Limit of Potentiometric Sensors by Covalently Binding the Ionophore to a Polymer Backbone. *Anal. Chim. Acta* **2004**, *503*, 187–194.
- (203) Lee, E.; VahidMohammadi, A.; Prorok, B. C.; Yoon, Y. S.; Beidaghi, M.; Kim, D. J. Room Temperature Gas Sensing of Two-Dimensional Titanium Carbide (MXene). *ACS Appl. Mater. Interfaces* **2017**, *9*, 37184–37190.
- (204) Harris, D. C. *Quantitative Chemical Analysis*; W. H. Freeman: 2016.
- (205) Peveler, W. J.; Yazdani, M.; Rotello, V. M. Selectivity and Specificity: Pros and Cons in Sensing. *ACS Sens.* **2016**, *1*, 1282–1285.
- (206) Liu, S.; Xing, X.; Yu, J.; Lian, W.; Li, J.; Cui, M.; Huang, J. A Novel Label-Free Electrochemical Aptasensor Based on Graphene-Polyaniline Composite Film for Dopamine Determination. *Biosens. Bioelectron.* **2012**, *36*, 186–191.
- (207) Kalantar-zadeh, K. *Sensors*; Springer: Berlin, 2013.
- (208) Varghese, O. K.; Gong, D.; Paulose, M.; Ong, K. G.; Grimes, C. A. Hydrogen Sensing Using Titania Nanotubes. *Sens. Actuators, B* **2003**, *93*, 338–344.
- (209) Saaman, A. A.; Bergveld, P. A Note on the Use of the Word ‘Reversible’. *Sens. Actuators* **1985**, *7*, 69–71.
- (210) Valentini, L.; Cantalini, C.; Armentano, I.; Kenny, J. M.; Lozzi, L.; Santucci, S. Highly Sensitive and Selective Sensors Based on Carbon Nanotubes Thin Films for Molecular Detection. *Diamond Relat. Mater.* **2004**, *13*, 1301–1305.
- (211) Nah, J.; Kumar, S. B.; Fang, H.; Chen, Y.-Z.; Plis, E.; Chueh, Y.-L.; Krishna, S.; Guo, J.; Javey, A. Quantum Size Effects on the

- Chemical Sensing Performance of Two-Dimensional Semiconductors. *J. Phys. Chem. C* **2012**, *116*, 9750–9754.
- (212) Williams, D. E. Semiconducting Oxides as Gas-Sensitive Resistors. *Sens. Actuators, B* **1999**, *57*, 1–16.
- (213) Romain, A. C.; Nicolas, J. Long Term Stability of Metal Oxide-Based Gas Sensors for e-Nose Environmental Applications: An Overview. *Sens. Actuators, B* **2010**, *146*, 502–506.
- (214) Sisk, B. C.; Lewis, N. S. Comparison of Analytical Methods and Calibration Methods for Correction of Detector Response Drift in Arrays of Carbon Black-Polymer Composite Vapor Detectors. *Sens. Actuators, B* **2005**, *104*, 249–268.
- (215) Mao, S.; Lu, G.; Chen, J. Nanocarbon-Based Gas Sensors: Progress and Challenges. *J. Mater. Chem. A* **2014**, *2*, 5573–5579.
- (216) Tongay, S. Preface to a Special Topic: 2D Materials and Applications. *Appl. Phys. Rev.* **2018**, *5*, 010401.
- (217) Chiu, S. W.; Tang, K. T. Towards a Chemiresistive Sensor-Integrated Electronic Nose: A Review. *Sensors* **2013**, *13*, 14214–14247.
- (218) Neri, G. First Fifty Years of Chemoresistive Gas Sensors. *Chemosensors* **2015**, *3*, 1–20.
- (219) Salehi-Khojin, A.; Khalili-Araghi, F.; Kuroda, M. A.; Lin, K. Y.; Leburton, J. P.; Masel, R. I. On the Sensing Mechanism in Carbon Nanotube Chemiresistors. *ACS Nano* **2011**, *5*, 153–158.
- (220) Zhang, T.; Mubeen, S.; Myung, N. V.; Deshusses, M. A. Recent Progress in Carbon Nanotube-Based Gas Sensors. *Nanotechnology* **2008**, *19*, 332001.
- (221) Hangarter, C. M.; Chartuprayoon, N.; Hernández, S. C.; Choa, Y.; Myung, N. V. Hybridized Conducting Polymer Chemiresistive Nano-Sensors. *Nano Today* **2013**, *8*, 39–55.
- (222) Agladze, K.; Aliev, R. R.; Yamaguchi, T.; Yoshikawa, K. Chemical Diode. *J. Phys. Chem.* **1996**, *100*, 13895–13897.
- (223) Di Bartolomeo, A. Graphene Schottky Diodes: An Experimental Review of the Rectifying Graphene/Semiconductor Heterojunction. *Phys. Rep.* **2016**, *606*, 1–58.
- (224) Ross, J. S.; Klement, P.; Jones, A. M.; Ghimire, N. J.; Yan, J.; Mandrus, D. G.; Taniguchi, T.; Watanabe, K.; Kitamura, K.; Yao, W.; Cobden, D. H.; Xu, X. Electrically Tunable Excitonic Light-Emitting Diodes Based on Monolayer WSe₂ P-N Junctions. *Nat. Nanotechnol.* **2014**, *9*, 268–272.
- (225) Al Balushi, Z. Y.; Wang, K.; Ghosh, R. K.; Vila, R. A.; Eichfeld, S. M.; Caldwell, J. D.; Qin, X.; Lin, Y. C.; DeSario, P. A.; Stone, G.; Subramanian, S.; Paul, D. F.; Wallace, R. M.; Datta, S.; Redwing, J. M.; Robinson, J. A. Two-Dimensional Gallium Nitride Realized via Graphene Encapsulation. *Nat. Mater.* **2016**, *15*, 1166–1171.
- (226) Kim, H. Y.; Lee, K.; McEvoy, N.; Yim, C.; Duesberg, G. S. Chemically Modulated Graphene Diodes. *Nano Lett.* **2013**, *13*, 2182–2188.
- (227) Fonash, S. J.; Li, Z. Schottky-Barrier Diode and Metal-Oxide-Semiconductor Capacitor Gas Sensors. *ACS Symp. Ser.* **1986**, *309*, 177–202.
- (228) Yoshizumi, T.; Miyahara, Y. Field-Effect Transistors for Gas Sensing. *Different Types of Field-Effect Transistors - Theory and Applications*; IntechOpen: 2017.
- (229) Mao, S.; Chang, J.; Pu, H.; Lu, G.; He, Q.; Zhang, H.; Chen, J. Two-Dimensional Nanomaterial-Based Field-Effect Transistors for Chemical and Biological Sensing. *Chem. Soc. Rev.* **2017**, *46*, 6872–6904.
- (230) Cervenka, J.; Budi, A.; Dontschuk, N.; Stacey, A.; Tadich, A.; Rietwyk, K. J.; Schenk, A.; Edmonds, M. T.; Yin, Y. F.; Medhekar, N.; Kalbac, M.; Pakes, C. I. Graphene Field Effect Transistor as a Probe of Electronic Structure and Charge Transfer at Organic Molecule-Graphene Interfaces. *Nanoscale* **2015**, *7*, 1471–1478.
- (231) Torsi, L.; Maglìulo, M.; Manoli, K.; Palazzo, G. Organic Field-Effect Transistor Sensors: A Tutorial Review. *Chem. Soc. Rev.* **2013**, *42*, 8612–8628.
- (232) Stine, R.; Mulvaney, S. P.; Robinson, J. T.; Tamanaha, C. R.; Sheehan, P. E. Fabrication, Optimization, and Use of Graphene Field Effect Sensors. *Anal. Chem.* **2013**, *85*, 509–521.
- (233) Cramer, T.; Campana, A.; Leonardi, F.; Casalini, S.; Kyndiah, A.; Murgia, M.; Biscarini, F. Water-Gated Organic Field Effect Transistors – Opportunities for Biochemical Sensing and Extracellular Signal Transduction. *J. Mater. Chem. B* **2013**, *1*, 3728–3741.
- (234) Stern, E.; Wagner, R.; Sigworth, F. J.; Breaker, R.; Fahmy, T. M.; Reed, M. A. Importance of the Debye Screening Length on Nanowire Field Effect Transistor Sensors. *Nano Lett.* **2007**, *7*, 3405–3409.
- (235) Israelachvili, J. N. *Intermolecular and Surface Forces*; Elsevier Inc.: Amsterdam, 2011.
- (236) Forsyth, R.; Devadoss, A.; Guy, O. J. Graphene Field Effect Transistors for Biomedical Applications: Current Status and Future Prospects. *Diagnostics* **2017**, *7*, 45.
- (237) Stern, E.; Vacic, A.; Rajan, N. K.; Criscione, J. M.; Park, J.; Ilic, B. R.; Mooney, D. J.; Reed, M. A.; Fahmy, T. M. Label-Free Biomarker Detection from Whole Blood. *Nat. Nanotechnol.* **2010**, *5*, 138–142.
- (238) Elnathan, R.; Kwiat, M.; Pevzner, A.; Engel, Y.; Burstein, L.; Khatchtourints, A.; Lichtenstein, A.; Kantaev, R.; Patolsky, F. Biorecognition Layer Engineering: Overcoming Screening Limitations of Nanowire-Based FET Devices. *Nano Lett.* **2012**, *12*, 5245–5254.
- (239) Maehashi, K.; Tamiya, E. Label-Free Protein Biosensor Based on Aptamer-Modified Carbon Nanotube Field-Effect Transistors. *Anal. Chem.* **2007**, *79*, 782–787.
- (240) Gao, N.; Gao, T.; Yang, X.; Dai, X.; Zhou, W.; Zhang, A.; Lieber, C. M. Specific Detection of Biomolecules in Physiological Solutions Using Graphene Transistor Biosensors. *Proc. Natl. Acad. Sci. U. S. A.* **2016**, *113*, 14633–14638.
- (241) Terzic, E.; Terzic, J.; Nagarajah, R.; Alamgir, M. Capacitive Sensing Technology. In *A Neural Network Approach to Fluid Quantity Measurement in Dynamic Environments*; 2012; pp 11–37.
- (242) Kopp, T.; Mannhart, J. Calculation of the Capacitances of Conductors: Perspectives for the Optimization of Electronic Devices. *J. Appl. Phys.* **2009**, *106*, 15753–15757.
- (243) Zhang, Y.; Ma, R.; Zhen, X. V.; Kudva, Y. C.; Bühlmann, P.; Koester, S. J. Capacitive Sensing of Glucose in Electrolytes Using Graphene Quantum Capacitance Varactors. *ACS Appl. Mater. Interfaces* **2017**, *9*, 38863–38869.
- (244) Blue, R.; Uttamchandani, D. Chemicapacitors as a Versatile Platform for Miniature Gas and Vapor Sensors. *Meas. Sci. Technol.* **2017**, *28*, 022001.
- (245) Conductivity Sensors and Capacitive Sensors. In *Chemical Sensors*, 2007; pp 123–132.
- (246) Sze, S. M.; Ng, K. K. *Physics of Semiconductor Devices*; John Wiley & Sons, Inc.: New York, 2006.
- (247) Balkus, K. J.; Ball, L. J.; Gnade, B. E.; Anthony, J. M. A Capacitance Type Chemical Sensor Based on AlPO₄-S Molecular Sieves. *Chem. Mater.* **1997**, *9*, 380–386.
- (248) Bakker, E.; Bühlmann, P.; Pretsch, E. Carrier-Based Ion-Selective Electrodes and Bulk Optodes. 1. General Characteristics. *Chem. Rev.* **1997**, *97*, 3083–3132.
- (249) Bobacka, J.; Ivaska, A.; Lewenstam, A. Potentiometric Ion Sensors. *Chem. Rev.* **2008**, *108*, 329–351.
- (250) Wang, T.; Zhu, H.; Zhuo, J.; Zhu, Z.; Papakonstantinou, P.; Lubarsky, G.; Lin, J.; Li, M. Biosensor Based on Ultrasmall MoS₂ Nanoparticles for Electrochemical Detection of H₂O₂ Released by Cells at the Nanomolar Level. *Anal. Chem.* **2013**, *85*, 10289–10295.
- (251) Bakker, E. Determination of Unbiased Selectivity Coefficients of Neutral Carrier-Based Cation-Selective Electrodes. *Anal. Chem.* **1997**, *69*, 1061–1069.
- (252) Mikhelson, K. N. *Ion-Selective Electrodes*; Springer: Berlin, 2013.
- (253) Hu, J.; Stein, A.; Bühlmann, P. Rational Design of All-Solid-State Ion-Selective Electrodes and Reference Electrodes. *TrAC, Trends Anal. Chem.* **2016**, *76*, 102–114.
- (254) Nikolskii, B. P.; Materova, E. A. Solid Contact in Membrane Ion-Selective Electrodes. *Ion-Selective Electrode Rev.*; Elsevier Great Britain: 1985; Vol. 7, pp 3–39.

- (255) Bobacka, J. Conducting Polymer-Based Solid-State Ion-Selective Electrodes. *Electroanalysis* **2006**, *18*, 7–18.
- (256) Migdalski, J.; Blaz, T.; Lewenstam, A. Conducting Polymer-Based Ion-Selective Electrodes. *Anal. Chim. Acta* **1996**, *322*, 141–149.
- (257) Hu, J.; Zou, X. U.; Stein, A.; Buhlmann, P. Ion-Selective Electrodes with Colloid-Imprinted Mesoporous Carbon as Solid Contact. *Anal. Chem.* **2014**, *86*, 7111–7118.
- (258) Lai, C. Z.; Fierke, M. A.; Stein, A.; Buhlmann, P. Ion-Selective Electrodes with Three-Dimensionally Ordered Macroporous Carbon as the Solid Contact. *Anal. Chem.* **2007**, *79*, 4621–4626.
- (259) Crespo, G. A.; Macho, S.; Rius, F. X. Ion-Selective Electrodes Using Carbon Nanotubes as Ion-to-Electron Transducers. *Anal. Chem.* **2008**, *80*, 1316–1322.
- (260) Crespo, G. A.; Macho, S.; Bobacka, J.; Rius, F. X. Transduction Mechanism of Carbon Nanotubes in Solid-Contact Ion-Selective Electrodes. *Anal. Chem.* **2009**, *81*, 676–681.
- (261) Ping, J.; Wang, Y.; Wu, J.; Ying, Y. Development of an All-Solid-State Potassium Ion-Selective Electrode Using Graphene as the Solid-Contact Transducer. *Electrochim. Commun.* **2011**, *13*, 1529–1532.
- (262) He, Q.; Das, S. R.; Garland, N. T.; Jing, D.; Hondred, J. A.; Cargill, A. A.; Ding, S.; Karunakaran, C.; Claussen, J. C. Enabling Inkjet Printed Graphene for Ion Selective Electrodes with Postprint Thermal Annealing. *ACS Appl. Mater. Interfaces* **2017**, *9*, 12719–12727.
- (263) Hernández, R.; Riu, J.; Bobacka, J.; Vallés, C.; Jiménez, P.; Benito, A. M.; Maser, W. K.; Rius, F. X. Reduced Graphene Oxide Films as Solid Transducers in Potentiometric All-Solid-State Ion-Selective Electrodes. *J. Phys. Chem. C* **2012**, *116*, 22570–22578.
- (264) Liu, Y.; Dong, X.; Chen, P. Biological and Chemical Sensors Based on Graphene Materials. *Chem. Soc. Rev.* **2012**, *41*, 2283–2307.
- (265) Turner, A. P. Biosensors: Sense and Sensibility. *Chem. Soc. Rev.* **2013**, *42*, 3184–3196.
- (266) Zhang, X.; Ju, H.; Wang, J. *Electrochemical Sensors, Biosensors and Their Biomedical Applications*; Academic Press: New York, 2008.
- (267) Bard, A. J.; Faulkner, L. R. *Electrochemical Methods: Fundamentals and Applications*; Wiley: Weinheim, Germany, 2000.
- (268) Langhus, D. L. *Analytical Electrochemistry*, 2nd Edition (Wang, Joseph). *J. Chem. Educ.* **2001**, *78*, 457.
- (269) Thiagarajan, N.; Chang, J.-L.; Senthilkumar, K.; Zen, J.-M. Disposable Electrochemical Sensors: A Mini Review. *Electrochim. Commun.* **2014**, *38*, 86–90.
- (270) Privett, B. J.; Shin, J. H.; Schoenfisch, M. H. Electrochemical Sensors. *Anal. Chem.* **2010**, *82*, 4723–4741.
- (271) Silwana, B.; Van der Horst, C.; Iwuoha, E.; Somerset, V. A Brief Review on Recent Developments of Electrochemical Sensors in Environmental Application for Pgms. *J. Environ. Sci. Health, Part A: Toxic/Hazard. Subst. Environ. Eng.* **2016**, *S1*, 1233–1247.
- (272) Fang, Y.; Wang, E. Electrochemical Biosensors on Platforms of Graphene. *Chem. Commun.* **2013**, *49*, 9526–9539.
- (273) Wang, J. Electrochemical Glucose Biosensors. *Chem. Rev.* **2008**, *108*, 814–825.
- (274) Yugeswaran, U.; Chen, S. M. A Review on the Electrochemical Sensors and Biosensors Composed of Nanowires as Sensing. *Sensors* **2008**, *8*, 290–313.
- (275) Wei, D.; Ivaska, A. Applications of Ionic Liquids in Electrochemical Sensors. *Anal. Chim. Acta* **2008**, *607*, 126–135.
- (276) Rieger, P. H. *Electrochemistry*; Springer Netherlands: 1993.
- (277) Thirsk, H. R. *Electrochemistry*; The Chemical Society: 1978.
- (278) Stradiotto, N. R.; Yamanaka, H.; Zanoni, M. V. B. Electrochemical Sensors: A Powerful Tool in Analytical Chemistry. *J. Braz. Chem. Soc.* **2003**, *14*, 159–173.
- (279) Grieshaber, D.; MacKenzie, R.; Voros, J.; Reimhult, E. Electrochemical Biosensors - Sensor Principles and Architectures. *Sensors* **2008**, *8*, 1400–1458.
- (280) Hendry, S. P.; Higgins, I. J.; Bannister, J. V. Amperometric Biosensors. *J. Biotechnol.* **1990**, *15*, 229–238.
- (281) Zoski, C. G. *Handbook of Electrochemistry*; Elsevier: Amsterdam, 2007.
- (282) Suvarnaphaet, P.; Pechprasarn, S. Graphene-Based Materials for Biosensors: A Review. *Sensors* **2017**, *17*, 2161.
- (283) Shao, Y.; Wang, J.; Wu, H.; Liu, J.; Aksay, I. A.; Lin, Y. Graphene Based Electrochemical Sensors and Biosensors: A Review. *Electroanalysis* **2010**, *22*, 1027–1036.
- (284) Lvovich, V. F. *Impedance Spectroscopy: Applications to Electrochemical and Dielectric Phenomena*; Wiley: 2015.
- (285) Barsoukov, E.; Macdonald, J. R. *Impedance Spectroscopy: Theory, Experiment, and Applications*; Wiley: 2018.
- (286) Orazem, M. E.; Tribollet, B. *Electrochemical Impedance Spectroscopy*; Wiley: 2017.
- (287) Lasia, A. *Electrochemical Impedance Spectroscopy and Its Applications*; Springer: New York, 2014.
- (288) Park, S.-M.; Yoo, J.-S. Peer Reviewed: Electrochemical Impedance Spectroscopy for Better Electrochemical Measurements. *Anal. Chem.* **2003**, *75*, 455A–461A.
- (289) Randviir, E. P.; Banks, C. E. Electrochemical Impedance Spectroscopy: An Overview of Bioanalytical Applications. *Anal. Methods* **2013**, *5*, 1098.
- (290) Park, J. Y.; Park, S. M. DNA Hybridization Sensors Based on Electrochemical Impedance Spectroscopy as a Detection Tool. *Sensors* **2009**, *9*, 9513–9532.
- (291) Daniels, J. S.; Pourmand, N. Label-Free Impedance Biosensors: Opportunities and Challenges. *Electroanalysis* **2007**, *19*, 1239–1257.
- (292) Narakathu, B. B.; Wen, G.; Obare, S. O.; Atashbar, M. Z. Electrochemical Impedance Spectroscopy Sensing of Toxic Organophosphorus Compounds. **2010**; pp 1518–1521.
- (293) Zourab, M.; Elwary, S.; Turner, A. P. F. *Principles of Bacterial Detection: Biosensors, Recognition Receptors and Microsystems*; Springer: New York, 2008.
- (294) Lisdat, F.; Schafer, D. The Use of Electrochemical Impedance Spectroscopy for Biosensing. *Anal. Bioanal. Chem.* **2008**, *391*, 1555–1567.
- (295) Bogomolova, A.; Komarova, E.; Reber, K.; Gerasimov, T.; Yavuz, O.; Bhatt, S.; Aldissi, M. Challenges of Electrochemical Impedance Spectroscopy in Protein Biosensing. *Anal. Chem.* **2009**, *81*, 3944–3949.
- (296) Chao, Y.; Rairigh, D.; Mason, A. On-Chip Electrochemical Impedance Spectroscopy for Biosensor Arrays. **2006**, 93–96.
- (297) Bissett, M. A.; Worrall, S. D.; Kinloch, I. A.; Dryfe, R. A. W. Comparison of Two-Dimensional Transition Metal Dichalcogenides for Electrochemical Supercapacitors. *Electrochim. Acta* **2016**, *201*, 30–37.
- (298) Levi, M. D.; Aurbach, D. Diffusion Coefficients of Lithium Ions During Intercalation into Graphite Derived from the Simultaneous Measurements and Modeling of Electrochemical Impedance and Potentiostatic Intermittent Titration Characteristics of Thin Graphite Electrodes. *J. Phys. Chem. B* **1997**, *101*, 4641–4647.
- (299) Geim, A. K.; Novoselov, K. S. The Rise of Graphene. *Nat. Mater.* **2007**, *6*, 183–191.
- (300) Chen, J. H.; Jang, C.; Xiao, S.; Ishigami, M.; Fuhrer, M. S. Intrinsic and Extrinsic Performance Limits of Graphene Devices on SiO₂. *Nat. Nanotechnol.* **2008**, *3*, 206–209.
- (301) Akturk, A.; Goldsman, N. Electron Transport and Full-Band Electron-Phonon Interactions in Graphene. *J. Appl. Phys.* **2008**, *103*, 053702.
- (302) Grüneis, A.; Attaccalite, C.; Wirtz, L.; Shiozawa, H.; Saito, R.; Pichler, T.; Rubio, A. Tight-Binding Description of the Quasiparticle Dispersion of Graphite and Few-Layer Graphene. *Phys. Rev. B: Condens. Matter Mater. Phys.* **2008**, *78*, 205425.
- (303) Bonaccorso, F.; Colombo, L.; Yu, G.; Stoller, M.; Tozzini, V.; Ferrari, A. C.; Ruoff, R. S.; Pellegrini, V. 2D Materials. Graphene, Related Two-Dimensional Crystals, and Hybrid Systems for Energy Conversion and Storage. *Science* **2015**, *347*, 1246501.
- (304) Lee, C.; Wei, X.; Kysar, J. W.; Hone, J. Measurement of the Elastic Properties and Intrinsic Strength of Monolayer Graphene. *Science* **2008**, *321*, 385–388.

- (305) Lerf, A.; He, H.; Forster, M.; Klinowski, J. Structure of Graphite Oxide Revisited^{II}. *J. Phys. Chem. B* **1998**, *102*, 4477–4482.
- (306) Xiao, J.; Zhang, L.; Zhou, K.; Li, J.; Xie, X.; Li, Z. Anisotropic Friction Behaviour of Highly Oriented Pyrolytic Graphite. *Carbon* **2013**, *65*, 53–62.
- (307) Warner, J. H. The Influence of the Number of Graphene Layers on the Atomic Resolution Images Obtained from Aberration-Corrected High Resolution Transmission Electron Microscopy. *Nanotechnology* **2010**, *21*, 255707.
- (308) Dave, S. H.; Gong, C.; Robertson, A. W.; Warner, J. H.; Grossman, J. C. Chemistry and Structure of Graphene Oxide Via Direct Imaging. *ACS Nano* **2016**, *10*, 7515–7522.
- (309) Lotya, M.; Hernandez, Y.; King, P. J.; Smith, R. J.; Nicolosi, V.; Karlsson, L. S.; Blighe, F. M.; De, S.; Wang, Z.; McGovern, I. T.; Duesberg, G. S.; Coleman, J. N. Liquid Phase Production of Graphene by Exfoliation of Graphite in Surfactant/Water Solutions. *J. Am. Chem. Soc.* **2009**, *131*, 3611–3620.
- (310) Park, S.; Ruoff, R. S. Chemical Methods for the Production of Graphenes. *Nat. Nanotechnol.* **2009**, *4*, 217–224.
- (311) Kim, K. S.; Zhao, Y.; Jang, H.; Lee, S. Y.; Kim, J. M.; Kim, K. S.; Ahn, J. H.; Kim, P.; Choi, J. Y.; Hong, B. H. Large-Scale Pattern Growth of Graphene Films for Stretchable Transparent Electrodes. *Nature* **2009**, *457*, 706–710.
- (312) Li, X.; Cai, W.; An, J.; Kim, S.; Nah, J.; Yang, D.; Piner, R.; Velamakanni, A.; Jung, I.; Tutuc, E.; Banerjee, S. K.; Colombo, L.; Ruoff, R. S. Large-Area Synthesis of High-Quality and Uniform Graphene Films on Copper Foils. *Science* **2009**, *324*, 1312–1314.
- (313) Bae, S.; Kim, H.; Lee, Y.; Xu, X.; Park, J. S.; Zheng, Y.; Balakrishnan, J.; Lei, T.; Kim, H. R.; Song, Y. I.; Kim, Y. J.; Kim, K. S.; Ozyilmaz, B.; Ahn, J. H.; Hong, B. H.; Iijima, S. Roll-to-Roll Production of 30-Inch Graphene Films for Transparent Electrodes. *Nat. Nanotechnol.* **2010**, *5*, 574–578.
- (314) Sun, Z.; Yan, Z.; Yao, J.; Beitler, E.; Zhu, Y.; Tour, J. M. Growth of Graphene from Solid Carbon Sources. *Nature* **2010**, *468*, 549–552.
- (315) Tran-Van, A. F.; Wegner, H. A. Strategies in Organic Synthesis for Condensed Arenes, Coronene, and Graphene. *Top. Curr. Chem.* **2013**, *349*, 121–157.
- (316) Nguyen, G. D.; Tsai, H. Z.; Omrani, A. A.; Marangoni, T.; Wu, M.; Rizzo, D. J.; Rodgers, G. F.; Cloke, R. R.; Durr, R. A.; Sakai, Y.; Liou, F.; Aikawa, A. S.; Chelikowsky, J. R.; Louie, S. G.; Fischer, F. R.; Crommie, M. F. Atomically Precise Graphene Nanoribbon Heterojunctions from a Single Molecular Precursor. *Nat. Nanotechnol.* **2017**, *12*, 1077–1082.
- (317) Wu, J.; Pisula, W.; Müllen, K. Graphenes as Potential Material for Electronics. *Chem. Rev.* **2007**, *107*, 718–747.
- (318) Brodie, B. C. On the Atomic Weight of Graphite. *Philosophical Transactions of the Royal Society of London* **1859**, *149*, 249–259.
- (319) Staudenmaier, L. Verfahren Zur Darstellung Der Graphitsäure. *Ber. Dtsch. Chem. Ges.* **1898**, *31*, 1481–1487.
- (320) Hummers, W. S.; Offeman, R. E. Preparation of Graphitic Oxide. *J. Am. Chem. Soc.* **1958**, *80*, 1339–1339.
- (321) Zhang, H. Ultrathin Two-Dimensional Nanomaterials. *ACS Nano* **2015**, *9*, 9451–9469.
- (322) Allen, M. J.; Tung, V. C.; Kaner, R. B. Honeycomb Carbon: A Review of Graphene. *Chem. Rev.* **2010**, *110*, 132–145.
- (323) Zhang, Y.; Zhang, L.; Zhou, C. Review of Chemical Vapor Deposition of Graphene and Related Applications. *Acc. Chem. Res.* **2013**, *46*, 2329–2339.
- (324) Yu, X.; Cheng, H.; Zhang, M.; Zhao, Y.; Qu, L.; Shi, G. Graphene-Based Smart Materials. *Nat. Rev. Mater.* **2017**, *2*, 17046.
- (325) Guo, S.; Dong, S. Graphene and Its Derivative-Based Sensing Materials for Analytical Devices. *J. Mater. Chem.* **2011**, *21*, 18503.
- (326) Choi, W.; Lahiri, I.; Seelaboyina, R.; Kang, Y. S. Synthesis of Graphene and Its Applications: A Review. *Crit. Rev. Solid State Mater. Sci.* **2010**, *35*, 52–71.
- (327) Tang, S.; Cao, Z. Adsorption of Nitrogen Oxides on Graphene and Graphene Oxides: Insights from Density Functional Calculations. *J. Chem. Phys.* **2011**, *134*, 044710.
- (328) Ishii, A.; Yamamoto, M.; Asano, H.; Fujiwara, K. DFT Calculation for Adatom Adsorption on Graphene Sheet as a Prototype of Carbon Nanotube Functionalization. *J. Phys. Conf. Ser.* **2008**, *100*, 052087.
- (329) Qin, W.; Li, X.; Bian, W. W.; Fan, X. J.; Qi, J. Y. Density Functional Theory Calculations and Molecular Dynamics Simulations of the Adsorption of Biomolecules on Graphene Surfaces. *Biomaterials* **2010**, *31*, 1007–1016.
- (330) Zhang, H.-p.; Luo, X.-g.; Lin, X.-y.; Lu, X.; Leng, Y.; Song, H.-t. Density Functional Theory Calculations on the Adsorption of Formaldehyde and Other Harmful Gases on Pure, Ti-Doped, or N-Doped Graphene Sheets. *Appl. Surf. Sci.* **2013**, *283*, 559–565.
- (331) Zhou, M.; Zhai, Y.; Dong, S. Electrochemical Sensing and Biosensing Platform Based on Chemically Reduced Graphene Oxide. *Anal. Chem.* **2009**, *81*, 5603–5613.
- (332) Lin, Y. M.; Avouris, P. Strong Suppression of Electrical Noise in Bilayer Graphene Nanodevices. *Nano Lett.* **2008**, *8*, 2119–2125.
- (333) Qinghui, S.; Guanxiong, L.; Teweldebrhan, D.; Balandin, A. A.; Rumyantsev, S.; Shur, M. S.; Dong, Y. Flicker Noise in Bilayer Graphene Transistors. *IEEE Electron Device Lett.* **2009**, *30*, 288–290.
- (334) Jang, H.; Park, Y. J.; Chen, X.; Das, T.; Kim, M. S.; Ahn, J. H. Graphene-Based Flexible and Stretchable Electronics. *Adv. Mater.* **2016**, *28*, 4184–4202.
- (335) Liu, J. Q.; Liu, Z.; Barrow, C. J.; Yang, W. R. Molecularly Engineered Graphene Surfaces for Sensing Applications: A Review. *Anal. Chim. Acta* **2015**, *859*, 1–19.
- (336) Zhang, Y. H.; Chen, Y. B.; Zhou, K. G.; Liu, C. H.; Zeng, J.; Zhang, H. L.; Peng, Y. Improving Gas Sensing Properties of Graphene by Introducing Dopants and Defects: A First-Principles Study. *Nanotechnology* **2009**, *20*, 185504.
- (337) Wei, X. L.; Chen, Y. P.; Liu, W. L.; Zhong, J. X. Enhanced Gas Sensor Based on Nitrogen-Vacancy Graphene Nanoribbons. *Phys. Lett. A* **2012**, *376*, 559–562.
- (338) Hussain, T.; Panigrahi, P.; Ahuja, R. Enriching Physisorption of H₂S and NH₃ Gases on a Graphane Sheet by Doping with Li Adatoms. *Phys. Chem. Chem. Phys.* **2014**, *16*, 8100–8105.
- (339) Niu, F.; Liu, J.-M.; Tao, L.-M.; Wang, W.; Song, W.-G. Nitrogen and Silica Co-Doped Graphene Nanosheets for NO₂ Gas Sensing. *J. Mater. Chem. A* **2013**, *1*, 6130.
- (340) Sundaram, R. S.; Gómez-Navarro, C.; Balasubramanian, K.; Burghard, M.; Kern, K. Electrochemical Modification of Graphene. *Adv. Mater.* **2008**, *20*, 3050–3053.
- (341) Chu, B. H.; Lo, C. F.; Nicolosi, J.; Chang, C. Y.; Chen, V.; Strupinski, W.; Pearton, S. J.; Ren, F. Hydrogen Detection Using Platinum Coated Graphene Grown on SiC. *Sens. Actuators, B* **2011**, *157*, 500–503.
- (342) Yi, J.; Lee, J. M.; Park, W. I. Vertically Aligned ZnO Nanorods and Graphene Hybrid Architectures for High-Sensitive Flexible Gas Sensors. *Sens. Actuators, B* **2011**, *155*, 264–269.
- (343) Song, Z.; Wei, Z.; Wang, B.; Luo, Z.; Xu, S.; Zhang, W.; Yu, H.; Li, M.; Huang, Z.; Zang, J.; Yi, F.; Liu, H. Sensitive Room-Temperature H₂S Gas Sensors Employing SnO₂ Quantum Wire/Reduced Graphene Oxide Nanocomposites. *Chem. Mater.* **2016**, *28*, 1205–1212.
- (344) Choi, S. J.; Choi, C.; Kim, S. J.; Cho, H. J.; Hakim, M.; Jeon, S.; Kim, I. D. Highly Efficient Electronic Sensitization of Non-Oxidized Graphene Flakes on Controlled Pore-Loaded WO₃ Nanofibers for Selective Detection of H₂S Molecules. *Sci. Rep.* **2015**, *5*, 8067.
- (345) Konkena, B.; Vasudevan, S. Covalently Linked, Water-Dispersible, Cyclodextrin: Reduced-Graphene Oxide Sheets. *Langmuir* **2012**, *28*, 12432–12437.
- (346) Konwer, S.; Guha, A. K.; Dolui, S. K. Graphene Oxide-Filled Conducting Polyaniline Composites as Methanol-Sensing Materials. *J. Mater. Sci.* **2013**, *48*, 1729–1739.
- (347) Wu, J.; Tao, K.; Miao, J.; Norford, L. K. Graphene for Future High-Performance Gas Sensing. *Outlook and Challenges of Nano Devices, Sensors, and Mems*; 2017; pp 347–363.

- (348) Lei, W.; Si, W.; Xu, Y.; Gu, Z.; Hao, Q. Conducting Polymer Composites with Graphene for Use in Chemical Sensors and Biosensors. *Microchim. Acta* **2014**, *181*, 707–722.
- (349) Liu, Y.; Yu, D.; Zeng, C.; Miao, Z.; Dai, L. Biocompatible Graphene Oxide-Based Glucose Biosensors. *Langmuir* **2010**, *26*, 6158–6160.
- (350) Bridgman, P. W. Two New Modifications of Phosphorus. *J. Am. Chem. Soc.* **1914**, *36*, 1344–1363.
- (351) Li, L.; Yu, Y.; Ye, G. J.; Ge, Q.; Ou, X.; Wu, H.; Feng, D.; Chen, X. H.; Zhang, Y. Black Phosphorus Field-Effect Transistors. *Nat. Nanotechnol.* **2014**, *9*, 372–377.
- (352) Rodin, A. S.; Carvalho, A.; Castro Neto, A. H. Strain-Induced Gap Modification in Black Phosphorus. *Phys. Rev. Lett.* **2014**, *112*, 176801.
- (353) Gusmao, R.; Sofer, Z.; Pumera, M. Black Phosphorus Rediscovered: From Bulk Material to Monolayers. *Angew. Chem., Int. Ed.* **2017**, *56*, 8052–8072.
- (354) Cartz, L.; Srinivasa, S. R.; Riedner, R. J.; Jorgensen, J. D.; Worlton, T. G. Effect of Pressure on Bonding in Black Phosphorus. *J. Chem. Phys.* **1979**, *71*, 1718–1721.
- (355) Zhang, C. D.; Lian, J. C.; Yi, W.; Jiang, Y. H.; Liu, L. W.; Hu, H.; Xiao, W. D.; Du, S. X.; Sun, L. L.; Gao, H. J. Surface Structures of Black Phosphorus Investigated with Scanning Tunneling Microscopy. *J. Phys. Chem. C* **2009**, *113*, 18823–18826.
- (356) Tran, V.; Soklaski, R.; Liang, Y.; Yang, L. Layer-Controlled Band Gap and Anisotropic Excitons in Few-Layer Black Phosphorus. *Phys. Rev. B: Condens. Matter Mater. Phys.* **2014**, *89*, 235319.
- (357) Kim, J.; Baik, S. S.; Ryu, S. H.; Sohn, Y.; Park, S.; Park, B. G.; Denlinger, J.; Yi, Y.; Choi, H. J.; Kim, K. S. Observation of Tunable Band Gap and Anisotropic Dirac Semimetal State in Black Phosphorus. *Science* **2015**, *349*, 723–726.
- (358) Tran, V.; Yang, L. Scaling Laws for the Band Gap and Optical Response of Phosphorene Nanoribbons. *Phys. Rev. B: Condens. Matter Mater. Phys.* **2014**, *89*, 548–555.
- (359) Peng, X.; Copple, A.; Wei, Q. Edge Effects on the Electronic Properties of Phosphorene Nanoribbons. *J. Appl. Phys.* **2014**, *116*, 2994–2998.
- (360) Kistanov, A. A.; Cai, Y.; Zhou, K.; Dmitriev, S. V.; Zhang, Y.-W. Large Electronic Anisotropy and Enhanced Chemical Activity of Highly Rippled Phosphorene. *J. Phys. Chem. C* **2016**, *120*, 6876–6884.
- (361) Kumar, V.; Brent, J. R.; Shorie, M.; Kaur, H.; Chadha, G.; Thomas, A. G.; Lewis, E. A.; Rooney, A. P.; Nguyen, L.; Zhong, X. L.; Burke, M. G.; Haigh, S. J.; Walton, A.; McNaughton, P. D.; Tedstone, A. A.; Savjani, N.; Muryn, C. A.; O'Brien, P.; Ganguli, A. K.; Lewis, D. J.; Sabherwal, P. Nanostructured Aptamer-Functionalized Black Phosphorus Sensing Platform for Label-Free Detection of Myoglobin, a Cardiovascular Disease Biomarker. *ACS Appl. Mater. Interfaces* **2016**, *8*, 22860–22868.
- (362) Mayorga-Martinez, C. C.; Mohamad Latiff, N.; Eng, A. Y.; Sofer, Z.; Pumera, M. Black Phosphorus Nanoparticle Labels for Immunoassays via Hydrogen Evolution Reaction Mediation. *Anal. Chem.* **2016**, *88*, 10074–10079.
- (363) Chen, Y.; Ren, R.; Pu, H.; Chang, J.; Mao, S.; Chen, J. Field-Effect Transistor Biosensors with Two-Dimensional Black Phosphorus Nanosheets. *Biosens. Bioelectron.* **2017**, *89*, 505–510.
- (364) Ben Aziza, Z.; Zhang, K.; Baillargeat, D.; Zhang, Q. Enhancement of Humidity Sensitivity of Graphene through Functionalization with Polyethylenimine. *Appl. Phys. Lett.* **2015**, *107*, 134102.
- (365) Kuriakose, S.; Ahmed, T.; Balendhran, S.; Bansal, V.; Sriram, S.; Bhaskaran, M.; Walia, S. Black Phosphorus: Ambient Degradation and Strategies for Protection. *2D Mater.* **2018**, *5*, 032001.
- (366) Choi, J. R.; Yong, K. W.; Choi, J. Y.; Nilghaz, A.; Lin, Y.; Xu, J.; Lu, X. Black Phosphorus and its Biomedical Applications. *Theranostics* **2018**, *8*, 1005–1026.
- (367) Abellan, G.; Wild, S.; Lloret, V.; Scheuschner, N.; Gillen, R.; Mundloch, U.; Maultzsch, J.; Varela, M.; Hauke, F.; Hirsch, A. Fundamental Insights into the Degradation and Stabilization of Thin Layer Black Phosphorus. *J. Am. Chem. Soc.* **2017**, *139*, 10432–10440.
- (368) Wang, Q. H.; Kalantar-Zadeh, K.; Kis, A.; Coleman, J. N.; Strano, M. S. Electronics and Optoelectronics of Two-Dimensional Transition Metal Dichalcogenides. *Nat. Nanotechnol.* **2012**, *7*, 699–712.
- (369) Joensen, P.; Frindt, R. F.; Morrison, S. R. Single-Layer MoS₂. *Mater. Res. Bull.* **1986**, *21*, 457–461.
- (370) Mak, K. F.; Lee, C.; Hone, J.; Shan, J.; Heinz, T. F. Atomically Thin MoS₂: A New Direct-Gap Semiconductor. *Phys. Rev. Lett.* **2010**, *105*, 136805.
- (371) Kolobov, A. V.; Tominaga, J. Bulk Tmdcs: Review of Structure and Properties. *Two-Dimensional Transition-Metal Dichalcogenides*; Springer, Berlin, 2016; pp 29–77.
- (372) Yoshida, M.; Ye, J.; Zhang, Y.; Imai, Y.; Kimura, S.; Fujiwara, A.; Nishizaki, T.; Kobayashi, N.; Nakano, M.; Iwasa, Y. Extended Polymorphism of Two-Dimensional Material. *Nano Lett.* **2017**, *17*, 5567–5571.
- (373) Voiry, D.; Mohite, A.; Chhowalla, M. Phase Engineering of Transition Metal Dichalcogenides. *Chem. Soc. Rev.* **2015**, *44*, 2702–2712.
- (374) Wilson, J. A.; Yoffe, A. D. The Transition Metal Dichalcogenides Discussion and Interpretation of the Observed Optical, Electrical and Structural Properties. *Adv. Phys.* **1969**, *18*, 193–335.
- (375) Li, H.; Lu, G.; Yin, Z.; He, Q.; Li, H.; Zhang, Q.; Zhang, H. Optical Identification of Single- and Few-Layer MoS₂ Sheets. *Small* **2012**, *8*, 682–686.
- (376) Castellanos-Gomez, A.; Barkelid, M.; Goossens, A. M.; Calado, V. E.; van der Zant, H. S.; Steele, G. A. Laser-Thinning of MoS₂: On Demand Generation of a Single-Layer Semiconductor. *Nano Lett.* **2012**, *12*, 3187–3192.
- (377) Eda, G.; Yamaguchi, H.; Voiry, D.; Fujita, T.; Chen, M.; Chhowalla, M. Photoluminescence from Chemically Exfoliated MoS₂. *Nano Lett.* **2011**, *11*, 5111–5116.
- (378) Eda, G.; Fujita, T.; Yamaguchi, H.; Voiry, D.; Chen, M.; Chhowalla, M. Coherent Atomic and Electronic Heterostructures of Single-Layer MoS₂. *ACS Nano* **2012**, *6*, 7311–7317.
- (379) Coleman, J. N.; Lotya, M.; O'Neill, A.; Bergin, S. D.; King, P. J.; Khan, U.; Young, K.; Gaucher, A.; De, S.; Smith, R. J.; Shvets, I. V.; Arora, S. K.; Stanton, G.; Kim, H. Y.; Lee, K.; Kim, G. T.; Duesberg, G. S.; Hallam, T.; Boland, J. J.; Wang, J. J.; Donegan, J. F.; Grunlan, J. C.; Moriarty, G.; Shmeliov, A.; Nicholls, R. J.; Perkins, J. M.; Grieveson, E. M.; Theuwissen, K.; McComb, D. W.; Nellist, P. D.; Nicolosi, V. Two-Dimensional Nanosheets Produced by Liquid Exfoliation of Layered Materials. *Science* **2011**, *331*, 568–571.
- (380) Cunningham, G.; Lotya, M.; Cucinotta, C. S.; Sanvito, S.; Bergin, S. D.; Menzel, R.; Shaffer, M. S.; Coleman, J. N. Solvent Exfoliation of Transition Metal Dichalcogenides: Dispersibility of Exfoliated Nanosheets Varies Only Weakly between Compounds. *ACS Nano* **2012**, *6*, 3468–3480.
- (381) Liu, K. K.; Zhang, W.; Lee, Y. H.; Lin, Y. C.; Chang, M. T.; Su, C. Y.; Chang, C. S.; Li, H.; Shi, Y.; Zhang, H.; Lai, C. S.; Li, L. J. Growth of Large-Area and Highly Crystalline MoS₂ Thin Layers on Insulating Substrates. *Nano Lett.* **2012**, *12*, 1538–1544.
- (382) Lee, H. S.; Min, S. W.; Chang, Y. G.; Park, M. K.; Nam, T.; Kim, H.; Kim, J. H.; Ryu, S.; Im, S. MoS₂ Nanosheet Phototransistors with Thickness-Modulated Optical Energy Gap. *Nano Lett.* **2012**, *12*, 3695–3700.
- (383) Lee, Y. H.; Zhang, X. Q.; Zhang, W.; Chang, M. T.; Lin, C. T.; Chang, K. D.; Yu, Y. C.; Wang, J. T.; Chang, C. S.; Li, L. J.; Lin, T. W. Synthesis of Large-Area MoS₂ Atomic Layers with Chemical Vapor Deposition. *Adv. Mater.* **2012**, *24*, 2320–2325.
- (384) Vancso, P.; Magda, G. Z.; Peto, J.; Noh, J. Y.; Kim, Y. S.; Hwang, C.; Biro, L. P.; Tapaszto, L. The Intrinsic Defect Structure of Exfoliated MoS₂ Single Layers Revealed by Scanning Tunneling Microscopy. *Sci. Rep.* **2016**, *6*, 29726.
- (385) Hong, J.; Hu, Z.; Probert, M.; Li, K.; Lv, D.; Yang, X.; Gu, L.; Mao, N.; Feng, Q.; Xie, L.; Zhang, J.; Wu, D.; Zhang, Z.; Jin, C.; Ji,

- W.; Zhang, X.; Yuan, J.; Zhang, Z. Exploring Atomic Defects in Molybdenum Disulphide Monolayers. *Nat. Commun.* **2015**, *6*, 6293.
- (386) Manzeli, S.; Ovchinnikov, D.; Pasquier, D.; Yazyev, O. V.; Kis, A. 2D Transition Metal Dichalcogenides. *Nat. Rev. Mater.* **2017**, *2*, 17033.
- (387) Hu, Z.; Wu, Z.; Han, C.; He, J.; Ni, Z.; Chen, W. Two-Dimensional Transition Metal Dichalcogenides: Interface and Defect Engineering. *Chem. Soc. Rev.* **2018**, *47*, 3100–3128.
- (388) Li, X.; Zhu, H. Two-Dimensional MoS₂: Properties, Preparation, and Applications. *Journal of Materomics* **2015**, *1*, 33–44.
- (389) Lauritsen, J. V.; Kibsgaard, J.; Helveg, S.; Topsoe, H.; Clausen, B. S.; Laegsgaard, E.; Besenbacher, F. Size-Dependent Structure of MoS₂ Nanocrystals. *Nat. Nanotechnol.* **2007**, *2*, 53–58.
- (390) Tuxen, A.; Kibsgaard, J.; Gobel, H.; Laegsgaard, E.; Topsoe, H.; Lauritsen, J. V.; Besenbacher, F. Size Threshold in the Dibenzothiophene Adsorption on MoS₂ Nanoclusters. *ACS Nano* **2010**, *4*, 4677–4682.
- (391) Ou, J. Z.; Ge, W.; Carey, B.; Daeneke, T.; Rotbart, A.; Shan, W.; Wang, Y.; Fu, Z.; Chrimes, A. F.; Włodarski, W.; Russo, S. P.; Li, Y. X.; Kalantar-Zadeh, K. Physisorption-Based Charge Transfer in Two-Dimensional SnS₂ for Selective and Reversible NO₂ Gas Sensing. *ACS Nano* **2015**, *9*, 10313–10323.
- (392) Li, Y.; Leonardi, S. G.; Bonavita, A.; Neri, G.; Włodarski, W. Two-Dimensional (2D) SnS₂-Based Oxygen Sensor. *Procedia Eng.* **2016**, *168*, 1102–1105.
- (393) Bharatula, L. D.; Erande, M. B.; Mulla, I. S.; Rout, C. S.; Late, D. J. SnS₂ Nanoflakes for Efficient Humidity and Alcohol Sensing at Room Temperature. *RSC Adv.* **2016**, *6*, 105421–105427.
- (394) Hu, Y.; Huang, Y.; Tan, C.; Zhang, X.; Lu, Q.; Sindoro, M.; Huang, X.; Huang, W.; Wang, L.; Zhang, H. Two-Dimensional Transition Metal Dichalcogenide Nanomaterials for Biosensing Applications. *Mater. Chem. Front.* **2017**, *1*, 24–36.
- (395) Rao, C. N. R. Transition Metal Oxides. *Annu. Rev. Phys. Chem.* **1989**, *40*, 291–326.
- (396) Ray, C.; Pal, T. Recent Advances of Metal–Metal Oxide Nanocomposites and Their Tailored Nanostructures in Numerous Catalytic Applications. *J. Mater. Chem. A* **2017**, *5*, 9465–9487.
- (397) Kalantar-zadeh, K.; Tang, J.; Wang, M.; Wang, K. L.; Shailos, A.; Galatsis, K.; Kojima, R.; Strong, V.; Lech, A.; Włodarski, W.; Kaner, R. B. Synthesis of Nanometre-Thick MoO₃ Sheets. *Nanoscale* **2010**, *2*, 429–433.
- (398) Kalantar-zadeh, K.; Vijayaraghavan, A.; Ham, M.-H.; Zheng, H.; Breedon, M.; Strano, M. S. Synthesis of Atomically Thin WO₃ sheets from Hydrated Tungsten Trioxide. *Chem. Mater.* **2010**, *22*, S660–S666.
- (399) Sun, Z.; Liao, T.; Dou, Y.; Hwang, S. M.; Park, M. S.; Jiang, L.; Kim, J. H.; Dou, S. X. Generalized Self-Assembly of Scalable Two-Dimensional Transition Metal Oxide Nanosheets. *Nat. Commun.* **2014**, *5*, 3813.
- (400) Xiao, X.; Song, H.; Lin, S.; Zhou, Y.; Zhan, X.; Hu, Z.; Zhang, Q.; Sun, J.; Yang, B.; Li, T.; Jiao, L.; Zhou, J.; Tang, J.; Gogotsi, Y. Scalable Salt-Templated Synthesis of Two-Dimensional Transition Metal Oxides. *Nat. Commun.* **2016**, *7*, 11296.
- (401) ten Elshof, J. E.; Yuan, H.; Gonzalez Rodriguez, P. Two-Dimensional Metal Oxide and Metal Hydroxide Nanosheets: Synthesis, Controlled Assembly and Applications in Energy Conversion and Storage. *Adv. Energy Mater.* **2016**, *6*, 1600355.
- (402) Biener, M. M.; Biener, J.; Schalek, R.; Friend, C. M. Growth of Nanocrystalline MoO₃ on Au(111) Studied by in Situ Scanning Tunneling Microscopy. *J. Chem. Phys.* **2004**, *121*, 12010–12016.
- (403) Mannhart, J.; Schlom, D. G. Oxide Interfaces—an Opportunity for Electronics. *Science* **2010**, *327*, 1607–1611.
- (404) Campbell, C. T.; Sauer, J. Introduction: Surface Chemistry of Oxides. *Chem. Rev.* **2013**, *113*, 3859–3862.
- (405) Pacchioni, G.; Freund, H. Electron Transfer at Oxide Surfaces. The MgO Paradigm: From Defects to Ultrathin Films. *Chem. Rev.* **2013**, *113*, 4035–4072.
- (406) Kuhlenbeck, H.; Shaikhutdinov, S.; Freund, H. J. Well-Ordered Transition Metal Oxide Layers in Model Catalysis—a Series of Case Studies. *Chem. Rev.* **2013**, *113*, 3986–4034.
- (407) Helander, M. G.; Wang, Z. B.; Qiu, J.; Lu, Z. H. Band Alignment at Metal/Organic and Metal/Oxide/Organic Interfaces. *Appl. Phys. Lett.* **2008**, *93*, 193310.
- (408) Hwang, H. Y.; Iwasa, Y.; Kawasaki, M.; Keimer, B.; Nagaosa, N.; Tokura, Y. Emergent Phenomena at Oxide Interfaces. *Nat. Mater.* **2012**, *11*, 103–113.
- (409) Bielaski, A. Adsorption Species of Oxygen on the Surfaces of Transition Metal Oxides. *J. Catal.* **1972**, *25*, 398–406.
- (410) Kanan, S. M.; El-Kadri, O. M.; Abu-Yousef, I. A.; Kanan, M. C. Semiconducting Metal Oxide Based Sensors for Selective Gas Pollutant Detection. *Sensors* **2009**, *9*, 8158–8196.
- (411) Tomchenko, A. A.; Harmer, G. P.; Marquis, B. T.; Allen, J. W. Semiconducting Metal Oxide Sensor Array for the Selective Detection of Combustion Gases. *Sens. Actuators, B* **2003**, *93*, 126–134.
- (412) Wang, C.; Yin, L.; Zhang, L.; Xiang, D.; Gao, R. Metal Oxide Gas Sensors: Sensitivity and Influencing Factors. *Sensors* **2010**, *10*, 2088–2106.
- (413) Gardon, M.; Guilemany, J. M. A Review on Fabrication, Sensing Mechanisms and Performance of Metal Oxide Gas Sensors. *J. Mater. Sci.: Mater. Electron.* **2013**, *24*, 1410–1421.
- (414) Yaghi, O. M.; Li, H. L. Hydrothermal Synthesis of a Metal–Organic Framework Containing Large Rectangular Channels. *J. Am. Chem. Soc.* **1995**, *117*, 10401–10402.
- (415) Batten, S. R.; Champness, N. R.; Chen, X.-M.; Garcia-Martinez, J.; Kitagawa, S.; Öhrström, L.; O’Keeffe, M.; Paik Suh, M.; Reedijk, J. Terminology of Metal–Organic Frameworks and Coordination Polymers (IUPAC Recommendations 2013). *Pure Appl. Chem.* **2013**, *85*, 1715–1724.
- (416) Stassen, I.; Burtch, N.; Talin, A.; Falcaro, P.; Allendorf, M.; Ameloot, R. An Updated Roadmap for the Integration of Metal–Organic Frameworks with Electronic Devices and Chemical Sensors. *Chem. Soc. Rev.* **2017**, *46*, 3185–3241.
- (417) Morozan, A.; Jaouen, F. Metal Organic Frameworks for Electrochemical Applications. *Energy Environ. Sci.* **2012**, *5*, 9269.
- (418) Campbell, M. G.; Sheberla, D.; Liu, S. F.; Swager, T. M.; Dincă, M. Cu₃(Hexaiminotriphenylene)₂: An Electrically Conductive 2D Metal–Organic Framework for Chemiresistive Sensing. *Angew. Chem., Int. Ed.* **2015**, *54*, 4349–4352.
- (419) Hendon, C. H.; Rieth, A. J.; Korzynski, M. D.; Dincă, M. Grand Challenges and Future Opportunities for Metal–Organic Frameworks. *ACS Cent. Sci.* **2017**, *3*, 554–563.
- (420) Walsh, A.; Butler, K.; Hendon, C. Chemical Principles for Electroactive Metal–Organic Frameworks. *MRS Bull.* **2016**, *41*, 870–876.
- (421) Campbell, M. G.; Dincă, M. Metal–Organic Frameworks as Active Materials in Electronic Sensor Devices. *Sensors* **2017**, *17*, 1108.
- (422) Hmaded, M.; Lu, Z.; Liu, Z.; Gandara, F.; Furukawa, H.; Wan, S.; Augustyn, V.; Chang, R.; Liao, L.; Zhou, F.; Perre, E.; Ozolins, V.; Suenaga, K.; Duan, X. F.; Dunn, B.; Yamamoto, Y.; Terasaki, O.; Yaghi, O. M. New Porous Crystals of Extended Metal-Catecholates. *Chem. Mater.* **2012**, *24*, 3511–3513.
- (423) Hu, Z.; Zhao, D. Metal–Organic Frameworks with Lewis Acidity: Synthesis, Characterization, and Catalytic Applications. *CrystEngComm* **2017**, *19*, 4066–4081.
- (424) Liu, H.; Li, X.; Chen, L.; Wang, X.; Pan, H.; Zhang, X.; Zhao, M. Gas Adsorption Effects on the Electronic Properties of Two-Dimensional Nickel Bis(dithiolene) Complex. *J. Phys. Chem. C* **2016**, *120*, 3846–3852.
- (425) Miner, E. M.; Gul, S.; Ricke, N. D.; Pastor, E.; Yano, J.; Yachandra, V. K.; Van Voorhis, T.; Dincă, M. Mechanistic Evidence for Ligand-Centered Electrocatalytic Oxygen Reduction with the Conductive MOF Ni₃(Hexaiminotriphenylene)₂. *ACS Catal.* **2017**, *7*, 7726–7731.
- (426) Miner, E. M.; Fukushima, T.; Sheberla, D.; Sun, L.; Surendranath, Y.; Dincă, M. Electrochemical Oxygen Reduction

- Catalysed by Ni₃(Hexaiminotriphenylene)₂. *Nat. Commun.* **2016**, *7*, 10942.
- (427) Furukawa, H.; Cordova, K. E.; O'Keeffe, M.; Yaghi, O. M. The Chemistry and Applications of Metal–Organic Frameworks. *Science* **2013**, *341*, 1230444.
- (428) James, S. L. Metal–Organic Frameworks. *Chem. Soc. Rev.* **2003**, *32*, 276.
- (429) Sheberla, D.; Sun, L.; Blood-Forsythe, M. A.; Er, S.; Wade, C. R.; Brozek, C. K.; Aspuru-Guzik, A.; Dincă, M. High Electrical Conductivity in Ni₃(2,3,6,7,10,11-Hexamimotriphenylene)₂, a Semiconducting Metal–Organic Graphene Analogue. *J. Am. Chem. Soc.* **2014**, *136*, 8859–8862.
- (430) Zhao, J.; Liu, H.; Yu, Z.; Quhe, R.; Zhou, S.; Wang, Y.; Liu, C. C.; Zhong, H.; Han, N.; Lu, J.; Yao, Y.; Wu, K. Rise of Silicene: A Competitive 2D Material. *Prog. Mater. Sci.* **2016**, *83*, 24–151.
- (431) Molle, A.; Goldberger, J.; Houssa, M.; Xu, Y.; Zhang, S. C.; Akinwande, D. Buckled Two-Dimensional Xene Sheets. *Nat. Mater.* **2017**, *16*, 163–169.
- (432) Molle, A. Xenes: A New Emerging Two-Dimensional Materials Platform for Nanoelectronics. *ECS Trans.* **2016**, *75*, 163–173.
- (433) Chen, X. P.; Tan, C. J.; Yang, Q.; Meng, R. S.; Liang, Q. H.; Cai, M.; Zhang, S. L.; Jiang, J. K. Ab Initio Study of the Adsorption of Small Molecules on Stanene. *J. Phys. Chem. C* **2016**, *120*, 13987–13994.
- (434) Wang, T. X.; Zhao, R. M.; Zhao, M. Y.; Zhao, X.; An, Y. P.; Dai, X. Q.; Xia, C. X. Effects of Applied Strain and Electric Field on Small-Molecule Sensing by Stanene Monolayers. *J. Mater. Sci.* **2017**, *52*, 5083–5096.
- (435) Daniel, M. C.; Astruc, D. Gold Nanoparticles: Assembly, Supramolecular Chemistry, Quantum-Size-Related Properties, and Applications toward Biology, Catalysis, and Nanotechnology. *Chem. Rev.* **2004**, *104*, 293–346.
- (436) Fan, Z.; Huang, X.; Tan, C.; Zhang, H. Thin Metal Nanostructures: Synthesis, Properties and Applications. *Chem. Sci.* **2015**, *6*, 95–111.
- (437) Niu, J.; Wang, D.; Qin, H.; Xiong, X.; Tan, P.; Li, Y.; Liu, R.; Lu, X.; Wu, J.; Zhang, T.; Ni, W.; Jin, J. Novel Polymer-Free Iridescent Lamellar Hydrogel for Two-Dimensional Confined Growth of Ultrathin Gold Membranes. *Nat. Commun.* **2014**, *5*, 3313.
- (438) Huang, X.; Tang, S.; Mu, X.; Dai, Y.; Chen, G.; Zhou, Z.; Ruan, F.; Yang, Z.; Zheng, N. Freestanding Palladium Nanosheets with Plasmonic and Catalytic Properties. *Nat. Nanotechnol.* **2011**, *6*, 28–32.
- (439) Duan, H.; Yan, N.; Yu, R.; Chang, C. R.; Zhou, G.; Hu, H. S.; Rong, H.; Niu, Z.; Mao, J.; Asakura, H.; Tanaka, T.; Dyson, P. J.; Li, J.; Li, Y. Ultrathin Rhodium Nanosheets. *Nat. Commun.* **2014**, *5*, 3093.
- (440) Wang, L.; Zhu, Y.; Wang, J. Q.; Liu, F.; Huang, J.; Meng, X.; Bassett, J. M.; Han, Y.; Xiao, F. S. Two-Dimensional Gold Nanostructures with High Activity for Selective Oxidation of Carbon-Hydrogen Bonds. *Nat. Commun.* **2015**, *6*, 6957.
- (441) Puntes, V. F.; Krishnan, K. M.; Alivisatos, A. P. Colloidal Nanocrystal Shape and Size Control: The Case of Cobalt. *Science* **2001**, *291*, 2115–2117.
- (442) Favier, F.; Walter, E. C.; Zach, M. P.; Benter, T.; Penner, R. M. Hydrogen Sensors and Switches from Electrodeposited Palladium Mesowire Arrays. *Science* **2001**, *293*, 2227–2231.
- (443) Hakkinen, H. The Gold-Sulfur Interface at the Nanoscale. *Nat. Chem.* **2012**, *4*, 443–455.
- (444) Campbell, C. T. Ultrathin Metal Films and Particles on Oxide Surfaces: Structural, Electronic and Chemisorptive Properties. *Surf. Sci. Rep.* **1997**, *27*, 1–111.
- (445) Paggel, J. J. Quantum-Well States as Fabry-Pérot Modes in a Thin-Film Electron Interferometer. *Science* **1999**, *283*, 1709–1711.
- (446) Qin, S.; Kim, J.; Niu, Q.; Shih, C. K. Superconductivity at the Two-Dimensional Limit. *Science* **2009**, *324*, 1314–1317.
- (447) Zhang, K.; Feng, Y.; Wang, F.; Yang, Z.; Wang, J. Two Dimensional Hexagonal Boron Nitride (2D-hBN): Synthesis, Properties and Applications. *J. Mater. Chem. C* **2017**, *5*, 11992–12022.
- (448) Li, L. H.; Chen, Y. Atomically Thin Boron Nitride: Unique Properties and Applications. *Adv. Funct. Mater.* **2016**, *26*, 2594–2608.
- (449) Weng, Q.; Wang, X.; Wang, X.; Bando, Y.; Golberg, D. Functionalized Hexagonal Boron Nitride Nanomaterials: Emerging Properties and Applications. *Chem. Soc. Rev.* **2016**, *45*, 3989–4012.
- (450) Vogt, P.; De Padova, P.; Quaresima, C.; Avila, J.; Frantzeskakis, E.; Asensio, M. C.; Resta, A.; Ealet, B.; Le Lay, G. Silicene: Compelling Experimental Evidence for Graphenelike Two-Dimensional Silicon. *Phys. Rev. Lett.* **2012**, *108*, 155501.
- (451) Wang, J.; Ma, F.; Sun, M. Graphene, Hexagonal Boron Nitride, and Their Heterostructures: Properties and Applications. *RSC Adv.* **2017**, *7*, 16801–16822.
- (452) Ryu, G. H.; Park, H. J.; Ryou, J.; Park, J.; Lee, J.; Kim, G.; Shin, H. S.; Bielawski, C. W.; Ruoff, R. S.; Hong, S.; Lee, Z. Atomic-Scale Dynamics of Triangular Hole Growth in Monolayer Hexagonal Boron Nitride under Electron Irradiation. *Nanoscale* **2015**, *7*, 10600–10605.
- (453) Thomas, A.; Fischer, A.; Goettmann, F.; Antonietti, M.; Müller, J.-O.; Schlögl, R.; Carlsson, J. M. Graphitic Carbon Nitride Materials: Variation of Structure and Morphology and Their Use as Metal-Free Catalysts. *J. Mater. Chem.* **2008**, *18*, 4893.
- (454) Algara-Siller, G.; Severin, N.; Chong, S. Y.; Bjorkman, T.; Palgrave, R. G.; Laybourn, A.; Antonietti, M.; Khimyak, Y. Z.; Krasheninnikov, A. V.; Rabe, J. P.; Kaiser, U.; Cooper, A. I.; Thomas, A.; Bojdys, M. J. Triazine-Based Graphitic Carbon Nitride: A Two-Dimensional Semiconductor. *Angew. Chem., Int. Ed.* **2014**, *53*, 7450–7455.
- (455) Anasori, B.; Xie, Y.; Beidaghi, M.; Lu, J.; Hosler, B. C.; Hultman, L.; Kent, P. R.; Gogotsi, Y.; Barsoum, M. W. Two-Dimensional, Ordered, Double Transition Metals Carbides (MXenes). *ACS Nano* **2015**, *9*, 9507–9516.
- (456) Wang, C.; Yang, S.; Cai, H.; Ataca, C.; Chen, H.; Zhang, X.; Xu, J.; Chen, B.; Wu, K.; Zhang, H.; Liu, L.; Li, J.; Grossman, J. C.; Tongay, S.; Liu, Q. Enhancing Light Emission Efficiency without Color Change in Post-Transition Metal Chalcogenides. *Nanoscale* **2016**, *8*, 5820–5825.
- (457) Miller, T. S.; Jorge, A. B.; Suter, T. M.; Sella, A.; Cora, F.; McMillan, P. F. Carbon Nitrides: Synthesis and Characterization of a New Class of Functional Materials. *Phys. Chem. Chem. Phys.* **2017**, *19*, 15613–15638.
- (458) Kroke, E. Novel Group 14 Nitrides. *Coord. Chem. Rev.* **2004**, *248*, 493–532.
- (459) Zhu, J.; Xiao, P.; Li, H.; Carabineiro, S. A. Graphitic Carbon Nitride: Synthesis, Properties, and Applications in Catalysis. *ACS Appl. Mater. Interfaces* **2014**, *6*, 16449–16465.
- (460) Barsoum, M. W. *MAX Phases: Properties of Machinable Ternary Carbides and Nitrides*; Wiley: 2013.
- (461) Tang, Q.; Zhou, Z.; Shen, P. Are MXenes Promising Anode Materials for Li Ion Batteries? Computational Studies on Electronic Properties and Li Storage Capability of Ti₃C₂ and Ti₃C₂X₂ (X = F, OH) Monolayer. *J. Am. Chem. Soc.* **2012**, *134*, 16909–16916.
- (462) Xie, Y.; Kent, P. R. C. Hybrid Density Functional Study of Structural and Electronic Properties of Functionalized Ti_{n+1}X_n (X = C, N) Monolayers. *Phys. Rev. B: Condens. Matter Mater. Phys.* **2013**, *87*, 235441.
- (463) Yu, X. F.; Li, Y. C.; Cheng, J. B.; Liu, Z. B.; Li, Q. Z.; Li, W. Z.; Yang, X.; Xiao, B. Monolayer Ti₂Co₂: A Promising Candidate for NH₃ Sensor or Capturer with High Sensitivity and Selectivity. *ACS Appl. Mater. Interfaces* **2015**, *7*, 13707–13713.
- (464) Junkaew, A.; Arroyave, R. Enhancement of the Selectivity of MXenes (M₂C, M = Ti, V, Nb, Mo) via Oxygen-Functionalization: Promising Materials for Gas-Sensing and -Separation. *Phys. Chem. Chem. Phys.* **2018**, *20*, 6073–6082.
- (465) Afzaal, M.; O'Brien, P. Recent Developments in II–VI and III–VI Semiconductors and Their Applications in Solar Cells. *J. Mater. Chem.* **2006**, *16*, 1597–1602.

- (466) Gouskov, A.; Camassel, J.; Gouskov, L. Growth and Characterization of III–VI Layered Crystals Like GaSe, GaTe, InSe, Ga_{Se_{1-x}}Te_x and Ga_xIn_{1-x}Se. *Prog. Cryst. Growth Charact.* **1982**, *5*, 323–413.
- (467) Chen, Z.; Biscaras, J.; Shukla, A. A High Performance Graphene/Few-Layer InSe Photo-Detector. *Nanoscale* **2015**, *7*, 5981–5986.
- (468) Ma, D.; Li, T.; Yuan, D.; He, C.; Lu, Z.; Lu, Z.; Yang, Z.; Wang, Y. The Role of the Intrinsic Se and in Vacancies in the Interaction of O₂ and H₂O Molecules with the InSe Monolayer. *Appl. Surf. Sci.* **2018**, *434*, 215–227.
- (469) Politano, A.; Chiarello, G.; Samnakay, R.; Liu, G.; Gurbulak, B.; Duman, S.; Balandin, A. A.; Boukhvalov, D. W. The Influence of Chemical Reactivity of Surface Defects on Ambient-Stable InSe-Based Nanodevices. *Nanoscale* **2016**, *8*, 8474–8479.
- (470) Li, X.; Li, X.; Li, Z.; Wang, J.; Zhang, J. WS₂ Nanoflakes Based Selective Ammonia Sensors at Room Temperature. *Sens. Actuators, B* **2017**, *240*, 273–277.
- (471) Cai, Y.; Zhang, G.; Zhang, Y.-W. Charge Transfer and Functionalization of Monolayer InSe by Physisorption of Small Molecules for Gas Sensing. *J. Phys. Chem. C* **2017**, *121*, 10182–10193.
- (472) Bandurin, D. A.; Tyurnina, A. V.; Yu, G. L.; Mishchenko, A.; Zolyomi, V.; Morozov, S. V.; Kumar, R. K.; Gorbachev, R. V.; Kudrynskyi, Z. R.; Pezzini, S.; Kovalyuk, Z. D.; Zeitler, U.; Novoselov, K. S.; Patane, A.; Eaves, L.; Grigorieva, I. V.; Fal'ko, V. I.; Geim, A. K.; Cao, Y. High Electron Mobility, Quantum Hall Effect and Anomalous Optical Response in Atomically Thin InSe. *Nat. Nanotechnol.* **2017**, *12*, 223–227.
- (473) Lin, Z.; McCreary, A.; Briggs, N.; Subramanian, S.; Zhang, K.; Sun, Y.; Li, X.; Borys, N. J.; Yuan, H.; Fullerton-Shirey, S. K.; Chernikov, A.; Zhao, H.; McDonnell, S.; Lindenberg, A. M.; Xiao, K.; LeRoy, B. J.; Drndić, M.; Hwang, J. C. M.; Park, J.; Chhowalla, M.; Schaak, R. E.; Javey, A.; Hersam, M. C.; Robinson, J.; Terrones, M. 2D Materials Advances: From Large Scale Synthesis and Controlled Heterostructures to Improved Characterization Techniques, Defects and Applications. *2D Mater.* **2016**, *3*, 042001.
- (474) Fiori, G.; Bonaccorso, F.; Iannaccone, G.; Palacios, T.; Neumaier, D.; Seabaugh, A.; Banerjee, S. K.; Colombo, L. Electronics Based on Two-Dimensional Materials. *Nat. Nanotechnol.* **2014**, *9*, 768–779.
- (475) Varghese, S. S.; Lonkar, S.; Singh, K. K.; Swaminathan, S.; Abdala, A. Recent Advances in Graphene Based Gas Sensors. *Sens. Actuators, B* **2015**, *218*, 160–183.
- (476) Dos Santos-Alves, J. S. G.; Patier, R. F. The Environmental Control of Atmospheric Pollution. The Framework Directive and its Development. The New European Approach. *Sens. Actuators, B* **1999**, *59*, 69–74.
- (477) Xu, K.; Fu, C.; Gao, Z.; Wei, F.; Ying, Y.; Xu, C.; Fu, G. Nanomaterial-Based Gas Sensors: A Review. *Instrum. Sci. Technol.* **2018**, *46*, 115–145.
- (478) Sutariya, B. B.; Penney, D. G.; Nallamothu, B. G. Hypothermia Following Acute Carbon-Monoxide Poisoning Increases Mortality. *Toxicol. Lett.* **1990**, *52*, 201–208.
- (479) Atkinson, R. Atmospheric Chemistry of VOCs and NOx. *Atmos. Environ.* **2000**, *34*, 2063–2101.
- (480) Savel'ev, A. M.; Starik, A. M.; Titova, N. S. Formation Kinetics of Sulfur-Bearing Compounds in Combustion of Hydrocarbon Fuels in Air. *Combust., Explos. Shock Waves* **2002**, *38*, 609–621.
- (481) Timmer, B.; Olthuis, W.; Berg, A. v. d. Ammonia Sensors and Their Applications—a Review. *Sens. Actuators, B* **2005**, *107*, 666–677.
- (482) Mustafa, A. K.; Gadalla, M. M.; Snyder, S. H. Signaling by Gasotransmitters. *Sci. Signaling* **2009**, *2*, re2.
- (483) Takahashi, N.; Kozai, D.; Mori, Y. TRP Channels: Sensors and Transducers of Gasotransmitter Signals. *Front. Physiol.* **2012**, *3*, 324.
- (484) Zhou, X.; Lee, S.; Xu, Z.; Yoon, J. Recent Progress on the Development of Chemosensors for Gases. *Chem. Rev.* **2015**, *115*, 7944–8000.
- (485) Tricoli, A.; Righetto, M.; Teleki, A. Semiconductor Gas Sensors: Dry Synthesis and Application. *Angew. Chem., Int. Ed.* **2010**, *49*, 7632–7659.
- (486) Wehling, T. O.; Novoselov, K. S.; Morozov, S. V.; Vdovin, E. E.; Katsnelson, M. I.; Geim, A. K.; Lichtenstein, A. I. Molecular Doping of Graphene. *Nano Lett.* **2008**, *8*, 173–177.
- (487) Leenaerts, O.; Partoens, B.; Peeters, F. M. Adsorption of Small Molecules on Graphene. *Microelectron. J.* **2009**, *40*, 860–862.
- (488) Bunch, J. S.; van der Zande, A. M.; Verbridge, S. S.; Frank, I. W.; Tanenbaum, D. M.; Parpia, J. M.; Craighead, H. G.; McEuen, P. L. Electromechanical Resonators from Graphene Sheets. *Science* **2007**, *315*, 490–493.
- (489) Kong, J.; Franklin, N. R.; Zhou, C. W.; Chapline, M. G.; Peng, S.; Cho, K. J.; Dai, H. J. Nanotube Molecular Wires as Chemical Sensors. *Science* **2000**, *287*, 622–625.
- (490) Chen, G.; Paronyan, T. M.; Harutyunyan, A. R. Sub-ppt Gas Detection with Pristine Graphene. *Appl. Phys. Lett.* **2012**, *101*, 053119.
- (491) Lin, J.; Zhong, J.; Kyle, J. R.; Penchev, M.; Ozkan, M.; Ozkan, C. S. Molecular Absorption and Photodesorption in Pristine and Functionalized Large-Area Graphene Layers. *Nanotechnology* **2011**, *22*, 355701.
- (492) Singh, A.; Uddin, A.; Sudarshan, T.; Koley, G. Tunable Reverse-Biased Graphene/Silicon Heterojunction Schottky Diode Sensor. *Small* **2014**, *10*, 1555–1565.
- (493) Dan, Y.; Lu, Y.; Kybert, N. J.; Luo, Z.; Johnson, A. T. Intrinsic Response of Graphene Vapor Sensors. *Nano Lett.* **2009**, *9*, 1472–1475.
- (494) Li, D.; Muller, M. B.; Gilje, S.; Kaner, R. B.; Wallace, G. G. Processable Aqueous Dispersions of Graphene Nanosheets. *Nat. Nanotechnol.* **2008**, *3*, 101–105.
- (495) Gilje, S.; Han, S.; Wang, M.; Wang, K. L.; Kaner, R. B. A Chemical Route to Graphene for Device Applications. *Nano Lett.* **2007**, *7*, 3394–3398.
- (496) Stankovich, S.; Dikin, D. A.; Piner, R. D.; Kohlhaas, K. A.; Kleinhammes, A.; Jia, Y.; Wu, Y.; Nguyen, S. T.; Ruoff, R. S. Synthesis of Graphene-Based Nanosheets via Chemical Reduction of Exfoliated Graphite Oxide. *Carbon* **2007**, *45*, 1558–1565.
- (497) Tung, V. C.; Allen, M. J.; Yang, Y.; Kaner, R. B. High-Throughput Solution Processing of Large-Scale Graphene. *Nat. Nanotechnol.* **2009**, *4*, 25–29.
- (498) Fowler, J. D.; Allen, M. J.; Tung, V. C.; Yang, Y.; Kaner, R. B.; Weiller, B. H. Practical Chemical Sensors from Chemically Derived Graphene. *ACS Nano* **2009**, *3*, 301–306.
- (499) Lu, G.; Ocola, L. E.; Chen, J. Gas Detection Using Low-Temperature Reduced Graphene Oxide Sheets. *Appl. Phys. Lett.* **2009**, *94*, 083111.
- (500) Lu, G.; Ocola, L. E.; Chen, J. Reduced Graphene Oxide for Room-Temperature Gas Sensors. *Nanotechnology* **2009**, *20*, 445502.
- (501) Ghosh, R.; Midya, A.; Santra, S.; Ray, S. K.; Guha, P. K. Chemically Reduced Graphene Oxide for Ammonia Detection at Room Temperature. *ACS Appl. Mater. Interfaces* **2013**, *5*, 7599–7603.
- (502) Dua, V.; Surwade, S. P.; Ammu, S.; Agnihotra, S. R.; Jain, S.; Roberts, K. E.; Park, S.; Ruoff, R. S.; Manohar, S. K. All-Organic Vapor Sensor Using Inkjet-Printed Reduced Graphene Oxide. *Angew. Chem., Int. Ed.* **2010**, *49*, 2154–2157.
- (503) Wang, D. H.; Hu, Y.; Zhao, J. J.; Zeng, L. L.; Tao, X. M.; Chen, W. Holey Reduced Graphene Oxide Nanosheets for High Performance Room Temperature Gas Sensing. *J. Mater. Chem. A* **2014**, *2*, 17415–17420.
- (504) Zhang, Y.; Guo, L.; Wei, S.; He, Y.; Xia, H.; Chen, Q.; Sun, H.-B.; Xiao, F.-S. Direct Imprinting of Microcircuits on Graphene Oxides Film by Femtosecond Laser Reduction. *Nano Today* **2010**, *5*, 15–20.
- (505) Lin, J.; Peng, Z.; Liu, Y.; Ruiz-Zepeda, F.; Ye, R.; Samuel, E. L.; Yacaman, M. J.; Yakobson, B. I.; Tour, J. M. Laser-Induced Porous Graphene Films from Commercial Polymers. *Nat. Commun.* **2014**, *5*, 5714.

- (506) Strong, V.; Dubin, S.; El-Kady, M. F.; Lech, A.; Wang, Y.; Weiller, B. H.; Kaner, R. B. Patterning and Electronic Tuning of Laser Scribed Graphene for Flexible All-Carbon Devices. *ACS Nano* **2012**, *6*, 1395–1403.
- (507) Yuan, W.; Liu, A.; Huang, L.; Li, C.; Shi, G. High-Performance NO₂ Sensors Based on Chemically Modified Graphene. *Adv. Mater.* **2013**, *25*, 766–771.
- (508) Yin, P. T.; Shah, S.; Chhowalla, M.; Lee, K. B. Design, Synthesis, and Characterization of Graphene-Nanoparticle Hybrid Materials for Bioapplications. *Chem. Rev.* **2015**, *115*, 2483–2531.
- (509) Li, W.; Geng, X.; Guo, Y.; Rong, J.; Gong, Y.; Wu, L.; Zhang, X.; Li, P.; Xu, J.; Cheng, G.; Sun, M.; Liu, L. Reduced Graphene Oxide Electrically Contacted Graphene Sensor for Highly Sensitive Nitric Oxide Detection. *ACS Nano* **2011**, *5*, 6955–6961.
- (510) Huang, L.; Wang, Z.; Zhang, J.; Pu, J.; Lin, Y.; Xu, S.; Shen, L.; Chen, Q.; Shi, W. Fully Printed, Rapid-Response Sensors Based on Chemically Modified Graphene for Detecting NO₂ at Room Temperature. *ACS Appl. Mater. Interfaces* **2014**, *6*, 7426–7433.
- (511) Deng, S.; Tjoa, V.; Fan, H. M.; Tan, H. R.; Sayle, D. C.; Olivo, M.; Mhaisalkar, S.; Wei, J.; Sow, C. H. Reduced Graphene Oxide Conjugated Cu₂O Nanowire Mesocrystals for High-Performance NO₂ Gas Sensor. *J. Am. Chem. Soc.* **2012**, *134*, 4905–4917.
- (512) Yang, W.; Wan, P.; Zhou, X.; Hu, J.; Guan, Y.; Feng, L. Additive-Free Synthesis of In₂O₃ Cubes Embedded into Graphene Sheets and Their Enhanced NO₂ Sensing Performance at Room Temperature. *ACS Appl. Mater. Interfaces* **2014**, *6*, 21093–21100.
- (513) An, X.; Yu, J. C.; Wang, Y.; Hu, Y.; Yu, X.; Zhang, G. WO₃ Nanorods/Graphene Nanocomposites for High-Efficiency Visible-Light-Driven Photocatalysis and NO₂ Gas Sensing. *J. Mater. Chem.* **2012**, *22*, 8525.
- (514) Yang, S.; Song, X.; Zhang, P.; Sun, J.; Gao, L. Self-Assembled α-Fe₂O₃ Mesocrystals/Graphene Nanohybrid for Enhanced Electrochemical Capacitors. *Small* **2014**, *10*, 2270–2279.
- (515) Kang, I.-S.; So, H.-M.; Bang, G.-S.; Kwak, J.-H.; Lee, J.-O.; Won Ahn, C. Recovery Improvement of Graphene-Based Gas Sensors Functionalized with Nanoscale Heterojunctions. *Appl. Phys. Lett.* **2012**, *101*, 123504.
- (516) Lin, Q.; Li, Y.; Yang, M. Tin Oxide/Graphene Composite Fabricated via a Hydrothermal Method for Gas Sensors Working at Room Temperature. *Sens. Actuators, B* **2012**, *173*, 139–147.
- (517) Lu, G.; Ocola, L. E.; Chen, J. Room-Temperature Gas Sensing Based on Electron Transfer between Discrete Tin Oxide Nanocrystals and Multiwalled Carbon Nanotubes. *Adv. Mater.* **2009**, *21*, 2487–2491.
- (518) Mao, S.; Cui, S.; Yu, K.; Wen, Z.; Lu, G.; Chen, J. Ultrafast Hydrogen Sensing through Hybrids of Semiconducting Single-Walled Carbon Nanotubes and Tin Oxide Nanocrystals. *Nanoscale* **2012**, *4*, 1275–1279.
- (519) Liu, S.; Yu, B.; Zhang, H.; Fei, T.; Zhang, T. Enhancing NO₂ Gas Sensing Performances at Room Temperature Based on Reduced Graphene Oxide-ZnO Nanoparticles Hybrids. *Sens. Actuators, B* **2014**, *202*, 272–278.
- (520) Huang, X.; Hu, N.; Gao, R.; Yu, Y.; Wang, Y.; Yang, Z.; Siu-Wai Kong, E.; Wei, H.; Zhang, Y. Reduced Graphene Oxide–Polyaniline Hybrid: Preparation, Characterization and Its Applications for Ammonia Gas Sensing. *J. Mater. Chem.* **2012**, *22*, 22488.
- (521) Seekaew, Y.; Lokavee, S.; Phokharatkul, D.; Wisitsoraat, A.; Kerdcharoen, T.; Wongchoosuk, C. Low-Cost and Flexible Printed Graphene–PEDOT:PSS Gas Sensor for Ammonia Detection. *Org. Electron.* **2014**, *15*, 2971–2981.
- (522) Yang, Y.; Li, S.; Yang, W.; Yuan, W.; Xu, J.; Jiang, Y. In Situ Polymerization Deposition of Porous Conducting Polymer on Reduced Graphene Oxide for Gas Sensor. *ACS Appl. Mater. Interfaces* **2014**, *6*, 13807–13814.
- (523) Wu, Z.; Chen, X.; Zhu, S.; Zhou, Z.; Yao, Y.; Quan, W.; Liu, B. Enhanced Sensitivity of Ammonia Sensor Using Graphene/Polyaniline Nanocomposite. *Sens. Actuators, B* **2013**, *178*, 485–493.
- (524) Bai, H.; Sheng, K.; Zhang, P.; Li, C.; Shi, G. Graphene Oxide/Conducting Polymer Composite Hydrogels. *J. Mater. Chem.* **2011**, *21*, 18653.
- (525) Yuan, W.; Huang, L.; Zhou, Q.; Shi, G. Ultrasensitive and Selective Nitrogen Dioxide Sensor Based on Self-Assembled Graphene/Polymer Composite Nanofibers. *ACS Appl. Mater. Interfaces* **2014**, *6*, 17003–17008.
- (526) Huang, J.; Virji, S.; Weiller, B. H.; Kaner, R. B. Polyaniline Nanofibers: Facile Synthesis and Chemical Sensors. *J. Am. Chem. Soc.* **2003**, *125*, 314–315.
- (527) Zhang, T.; Nix, M. B.; Yoo, B.-Y.; Deshusses, M. A.; Myung, N. V. Electrochemically Functionalized Single-Walled Carbon Nanotube Gas Sensor. *Electroanalysis* **2006**, *18*, 1153–1158.
- (528) Ding, M.; Tang, Y.; Gou, P.; Reber, M. J.; Star, A. Chemical Sensing with Polyaniline Coated Single-Walled Carbon Nanotubes. *Adv. Mater.* **2011**, *23*, 536–540.
- (529) Hübert, T.; Boon-Brett, L.; Black, G.; Banach, U. Hydrogen Sensors – a Review. *Sens. Actuators, B* **2011**, *157*, 329–352.
- (530) Ma, J.; Michaelides, A.; Alfe, D. Binding of Hydrogen on Benzene, Coronene, and Graphene from Quantum Monte Carlo Calculations. *J. Chem. Phys.* **2011**, *134*, 134701.
- (531) Johnson, J. L.; Behnam, A.; Pearson, S. J.; Ural, A. Hydrogen Sensing Using Pd-Functionalized Multi-Layer Graphene Nanoribbon Networks. *Adv. Mater.* **2010**, *22*, 4877–4880.
- (532) Shin, D. H.; Lee, J. S.; Jun, J.; An, J. H.; Kim, S. G.; Cho, K. H.; Jang, J. Flower-Like Palladium Nanoclusters Decorated Graphene Electrodes for Ultrasensitive and Flexible Hydrogen Gas Sensing. *Sci. Rep.* **2015**, *5*, 12294.
- (533) Hong, J.; Lee, S.; Seo, J.; Pyo, S.; Kim, J.; Lee, T. A Highly Sensitive Hydrogen Sensor with Gas Selectivity Using a PMMA Membrane-Coated Pd Nanoparticle/Single-Layer Graphene Hybrid. *ACS Appl. Mater. Interfaces* **2015**, *7*, 3554–3561.
- (534) Lee, J. S.; Oh, J.; Jun, J.; Jang, J. Wireless Hydrogen Smart Sensor Based on Pt/Graphene-Immobilized Radio-Frequency Identification Tag. *ACS Nano* **2015**, *9*, 7783–7790.
- (535) Vedala, H.; Sorescu, D. C.; Kotchey, G. P.; Star, A. Chemical Sensitivity of Graphene Edges Decorated with Metal Nanoparticles. *Nano Lett.* **2011**, *11*, 2342–2347.
- (536) Mishra, R. K.; Upadhyay, S. B.; Kushwaha, A.; Kim, T. H.; Murali, G.; Verma, R.; Srivastava, M.; Singh, J.; Sahay, P. P.; Lee, S. H. SnO₂ Quantum Dots Decorated on rGO: A Superior Sensitive, Selective and Reproducible Performance for a H₂ and LPG Sensor. *Nanoscale* **2015**, *7*, 11971–11979.
- (537) Anand, K.; Singh, O.; Singh, M. P.; Kaur, J.; Singh, R. C. Hydrogen Sensor Based on Graphene/ZnO Nanocomposite. *Sens. Actuators, B* **2014**, *195*, 409–415.
- (538) Al-Mashat, L.; Shin, K.; Kalantar-zadeh, K.; Plessis, J. D.; Han, S. H.; Kojima, R. W.; Kaner, R. B.; Li, D.; Gou, X.; Ippolito, S. J.; Włodarski, W. Graphene/Polyaniline Nanocomposite for Hydrogen Sensing. *J. Phys. Chem. C* **2010**, *114*, 16168–16173.
- (539) Zheng, Y.; Lee, D.; Koo, H. Y.; Maeng, S. Chemically Modified Graphene/PEDOT:PSS Nanocomposite Films for Hydrogen Gas Sensing. *Carbon* **2015**, *81*, 54–62.
- (540) Panda, D.; Nandi, A.; Datta, S. K.; Saha, H.; Majumdar, S. Selective Detection of Carbon Monoxide (CO) Gas by Reduced Graphene Oxide (rGO) at Room Temperature. *RSC Adv.* **2016**, *6*, 47337–47348.
- (541) Kim, J. H.; Katoch, A.; Kim, H. W.; Kim, S. S. Realization of ppm-Level CO Detection with Exceptionally High Sensitivity Using Reduced Graphene Oxide-Loaded SnO₂ Nanofibers with Simultaneous Au Functionalization. *Chem. Commun.* **2016**, *52*, 3832–3835.
- (542) Zhang, D.; Jiang, C.; Liu, J.; Cao, Y. Carbon Monoxide Gas Sensing at Room Temperature Using Copper Oxide-Decorated Graphene Hybrid Nanocomposite Prepared by Layer-by-Layer Self-Assembly. *Sens. Actuators, B* **2017**, *247*, 875–882.
- (543) Yoon, H. J.; Jun, D. H.; Yang, J. H.; Zhou, Z.; Yang, S. S.; Cheng, M. M.-C. Carbon Dioxide Gas Sensor Using a Graphene Sheet. *Sens. Actuators, B* **2011**, *157*, 310–313.

- (544) Nemade, K. R.; Waghuley, S. A. Chemiresistive Gas Sensing by Few-Layered Graphene. *J. Electron. Mater.* **2013**, *42*, 2857–2866.
- (545) Nemade, K. R.; Waghuley, S. A. Carbon Dioxide Gas Sensing Application of Graphene/Y₂O₃ Quantum Dots Composite. *Int. J. Mod. Phys.: Conf. Ser.* **2013**, *22*, 380–384.
- (546) Nemade, K. R.; Waghuley, S. A. Role of Defects Concentration on Optical and Carbon Dioxide Gas Sensing Properties of Sb₂O₃/Graphene Composites. *Opt. Mater.* **2014**, *36*, 712–716.
- (547) Nemade, K. R.; Waghuley, S. A. Highly Responsive Carbon Dioxide Sensing by Graphene/Al₂O₃ Quantum Dots Composites at Low Operable Temperature. *Indian J. Phys.* **2014**, *88*, 577–583.
- (548) Zhang, Y.-H.; Han, L.-F.; Xiao, Y.-H.; Jia, D.-Z.; Guo, Z.-H.; Li, F. Understanding Dopant and Defect Effect on H₂S Sensing Performances of Graphene: A First-Principles Study. *Comput. Mater. Sci.* **2013**, *69*, 222–228.
- (549) Liu, X.-Y.; Zhang, J.-M.; Xu, K.-W.; Ji, V. Improving SO₂ Gas Sensing Properties of Graphene by Introducing Dopant and Defect: A First-Principles Study. *Appl. Surf. Sci.* **2014**, *313*, 405–410.
- (550) Shao, L.; Chen, G.; Ye, H.; Niu, H.; Wu, Y.; Zhu, Y.; Ding, B. Sulfur Dioxide Molecule Sensors Based on Zigzag Graphene Nanoribbons with and without Cr Dopant. *Phys. Lett. A* **2014**, *378*, 667–671.
- (551) Qin, X.; Meng, Q.; Feng, Y. P. Strain Effects on Enhanced Hydrogen Sulphide Detection Capability of Ag-Decorated Defective Graphene: A First-Principles Investigation. *Mod. Phys. Lett. B* **2012**, *26*, 1250166.
- (552) Berahman, M.; Sheikhi, M. H. Hydrogen Sulfide Gas Sensor Based on Decorated Zigzag Graphene Nanoribbon with Copper. *Sens. Actuators, B* **2015**, *219*, 338–345.
- (553) Abdulkader Tawfik, S.; Cui, X. Y.; Carter, D. J.; Ringer, S. P.; Stampfl, C. Sensing Sulfur-Containing Gases Using Titanium and Tin Decorated Zigzag Graphene Nanoribbons from First-Principles. *Phys. Chem. Chem. Phys.* **2015**, *17*, 6925–6932.
- (554) Shen, F.; Wang, D.; Liu, R.; Pei, X.; Zhang, T.; Jin, J. Edge-Tailored Graphene Oxide Nanosheet-Based Field Effect Transistors for Fast and Reversible Electronic Detection of Sulfur Dioxide. *Nanoscale* **2013**, *5*, 537–540.
- (555) Ren, Y. J.; Zhu, C. F.; Cai, W. W.; Li, H. F.; Ji, H. X.; Kholmanov, I.; Wu, Y. P.; Piner, R. D.; Ruoff, R. S. Detection of Sulfur Dioxide Gas with Graphene Field Effect Transistor. *Appl. Phys. Lett.* **2012**, *100*, 163114.
- (556) Zhou, L.; Shen, F.; Tian, X.; Wang, D.; Zhang, T.; Chen, W. Stable Cu₂O Nanocrystals Grown on Functionalized Graphene Sheets and Room Temperature H₂S Gas Sensing with Ultrahigh Sensitivity. *Nanoscale* **2013**, *5*, 1564–1569.
- (557) Cuong, T. V.; Pham, V. H.; Chung, J. S.; Shin, E. W.; Yoo, D. H.; Hahn, S. H.; Huh, J. S.; Rue, G. H.; Kim, E. J.; Hur, S. H.; Kohl, P. A. Solution-Processed ZnO-Chemically Converted Graphene Gas Sensor. *Mater. Lett.* **2010**, *64*, 2479–2482.
- (558) Zhang, Z.; Zou, R.; Song, G.; Yu, L.; Chen, Z.; Hu, J. Highly Aligned SnO₂ Nanorods on Graphene Sheets for Gas Sensors. *J. Mater. Chem.* **2011**, *21*, 17360.
- (559) Jiang, Z.; Li, J.; Aslan, H.; Li, Q.; Li, Y.; Chen, M.; Huang, Y.; Froning, J. P.; Otyepka, M.; Zboril, R.; Besenbacher, F.; Dong, M. A High Efficiency H₂S Gas Sensor Material: Paper Like Fe₂O₃/Graphene Nanosheets and Structural Alignment Dependency of Device Efficiency. *J. Mater. Chem. A* **2014**, *2*, 6714–6717.
- (560) Choi, S. J.; Jang, B. H.; Lee, S. J.; Min, B. K.; Rothschild, A.; Kim, I. D. Selective Detection of Acetone and Hydrogen Sulfide for the Diagnosis of Diabetes and Halitosis Using SnO₂ Nanofibers Functionalized with Reduced Graphene Oxide Nanosheets. *ACS Appl. Mater. Interfaces* **2014**, *6*, 2588–2597.
- (561) Cho, S.; Lee, J. S.; Jun, J.; Kim, S. G.; Jang, J. Fabrication of Water-Dispersible and Highly Conductive PSS-Doped PANI/Graphene Nanocomposites Using a High-Molecular Weight PSS Dopant and Their Application in H₂S Detection. *Nanoscale* **2014**, *6*, 15181–15195.
- (562) Choi, S.-J.; Kim, S.-J.; Kim, I.-D. Ultrafast Optical Reduction of Graphene Oxide Sheets on Colorless Polyimide Film for Wearable Chemical Sensors. *NPG Asia Mater.* **2016**, *8*, e315–e315.
- (563) Rodriguez, J. A.; Chaturvedi, S.; Kuhn, M.; Hrbek, J. Reaction of H₂S and S₂ with Metal/Oxide Surfaces: Band-Gap Size and Chemical Reactivity. *J. Phys. Chem. B* **1998**, *102*, 5511–5519.
- (564) Rodriguez, J. A.; Maiti, A. Adsorption and Decomposition of H₂S on MgO(100), NiMgO(100), and ZnO(0001) Surfaces: A First-Principles Density Functional Study. *J. Phys. Chem. B* **2000**, *104*, 3630–3638.
- (565) Fattah, A.; Khatami, S. Selective H₂S Gas Sensing with a Graphene/N-Si Schottky Diode. *IEEE Sens. J.* **2014**, *14*, 4104–4108.
- (566) Ramamoorthy, R.; Dutta, P. K.; Akbar, S. A. Oxygen Sensors: Materials, Methods, Designs and Applications. *J. Mater. Sci.* **2003**, *38*, 4271–4282.
- (567) Chen, C. W.; Hung, S. C.; Yang, M. D.; Yeh, C. W.; Wu, C. H.; Chi, G. C.; Ren, F.; Pearton, S. J. Oxygen Sensors Made by Monolayer Graphene under Room Temperature. *Appl. Phys. Lett.* **2011**, *99*, 243502.
- (568) Zhang, J.; Zhao, C.; Hu, P. A.; Fu, Y. Q.; Wang, Z.; Cao, W.; Yang, B.; Placido, F. A UV Light Enhanced TiO₂/Graphene Device for Oxygen Sensing at Room Temperature. *RSC Adv.* **2013**, *3*, 22185–22190.
- (569) Wang, Q.; Guo, X.; Cai, L.; Cao, Y.; Gan, L.; Liu, S.; Wang, Z.; Zhang, H.; Li, L. TiO₂-Decorated Graphenes as Efficient Photoswitches with High Oxygen Sensitivity. *Chem. Sci.* **2011**, *2*, 1860–1864.
- (570) Ellis, J. E.; Sorescu, D. C.; Burkert, S. C.; White, D. L.; Star, A. Uncondensed Graphitic Carbon Nitride on Reduced Graphene Oxide for Oxygen Sensing via a Photoredox Mechanism. *ACS Appl. Mater. Interfaces* **2017**, *9*, 27142–27151.
- (571) Cho, S.-Y.; Koh, H.-J.; Yoo, H.-W.; Jung, H.-T. Tunable Chemical Sensing Performance of Black Phosphorus by Controlled Functionalization with Noble Metals. *Chem. Mater.* **2017**, *29*, 7197–7205.
- (572) Lei, S. Y.; Yu, Z. Y.; Shen, H. Y.; Sun, X. L.; Wan, N.; Yu, H. CO Adsorption on Metal-Decorated Phosphorene. *ACS Omega* **2018**, *3*, 3957–3965.
- (573) Island, J. O.; Steele, G. A.; Zant, H. S. J. v. d.; Castellanos-Gomez, A. Environmental Instability of Few-Layer Black Phosphorus. *2D Mater.* **2015**, *2*, 011002.
- (574) Irshad, R.; Tahir, K.; Li, B.; Sher, Z.; Ali, J.; Nazir, S. A Revival of 2D Materials, Phosphorene: Its Application as Sensors. *J. Ind. Eng. Chem.* **2018**, *64*, 60–69.
- (575) Pumera, M. Phosphorene and Black Phosphorus for Sensing and Biosensing. *TrAC, Trends Anal. Chem.* **2017**, *93*, 1–6.
- (576) Carvalho, A.; Wang, M.; Zhu, X.; Rodin, A. S.; Su, H.; Castro Neto, A. H. Phosphorene: From Theory to Applications. *Nat. Rev. Mater.* **2016**, *1*, 16061.
- (577) Kang, M.; Kim, B.; Ryu, S. H.; Jung, S. W.; Kim, J.; Moreschini, L.; Jozwiak, C.; Rotenberg, E.; Bostwick, A.; Kim, K. S. Universal Mechanism of Band-Gap Engineering in Transition-Metal Dichalcogenides. *Nano Lett.* **2017**, *17*, 1610–1615.
- (578) Lin, Z.; Carvalho, B. R.; Kahn, E.; Lv, R.; Rao, R.; Terrones, H.; Pimenta, M. A.; Terrones, M. Defect Engineering of Two-Dimensional Transition Metal Dichalcogenides. *2D Mater.* **2016**, *3*, 022002.
- (579) Huang, X.; Zeng, Z.; Zhang, H. Metal Dichalcogenide Nanosheets: Preparation, Properties and Applications. *Chem. Soc. Rev.* **2013**, *42*, 1934–1946.
- (580) Li, H.; Yin, Z.; He, Q.; Li, H.; Huang, X.; Lu, G.; Fam, D. W.; Tok, A. I.; Zhang, Q.; Zhang, H. Fabrication of Single- and Multilayer MoS₂ Film-Based Field-Effect Transistors for Sensing NO at Room Temperature. *Small* **2012**, *8*, 63–67.
- (581) Kim, Y. H.; Kim, K. Y.; Choi, Y. R.; Shim, Y.-S.; Jeon, J.-M.; Lee, J.-H.; Kim, S. Y.; Han, S.; Jang, H. W. Ultrasensitive Reversible Oxygen Sensing by Using Liquid-Exfoliated MoS₂ Nanoparticles. *J. Mater. Chem. A* **2016**, *4*, 6070–6076.

- (582) Late, D. J.; Doneux, T.; Bougouma, M. Single-Layer MoSe₂ Based NH₃ Gas Sensor. *Appl. Phys. Lett.* **2014**, *105*, 233103.
- (583) Sarkar, D.; Xie, X.; Kang, J.; Zhang, H.; Liu, W.; Navarrete, J.; Moskovits, M.; Banerjee, K. Functionalization of Transition Metal Dichalcogenides with Metallic Nanoparticles: Implications for Doping and Gas-Sensing. *Nano Lett.* **2015**, *15*, 2852–2862.
- (584) Choi, S. Y.; Kim, Y.; Chung, H. S.; Kim, A. R.; Kwon, J. D.; Park, J.; Kim, Y. L.; Kwon, S. H.; Hahm, M. G.; Cho, B. Effect of Nb Doping on Chemical Sensing Performance of Two-Dimensional Layered MoSe₂. *ACS Appl. Mater. Interfaces* **2017**, *9*, 3817–3823.
- (585) Ruiz, A.; Calleja, A.; Espiell, F.; Cornet, A.; Morante, J. R. Nanosized Nb-TiO₂ Gas Sensors Derived from Alkoxides Hydrolyzation. *IEEE Sens. J.* **2003**, *3*, 189–194.
- (586) Cho, B.; Kim, A. R.; Kim, D. J.; Chung, H. S.; Choi, S. Y.; Kwon, J. D.; Park, S. W.; Kim, Y.; Lee, B. H.; Lee, K. H.; Kim, D. H.; Nam, J.; Hahm, M. G. Two-Dimensional Atomic-Layered Alloy Junctions for High-Performance Wearable Chemical Sensor. *ACS Appl. Mater. Interfaces* **2016**, *8*, 19635–19642.
- (587) Feng, Z.; Xie, Y.; Chen, J.; Yu, Y.; Zheng, S.; Zhang, R.; Li, Q.; Chen, X.; Sun, C.; Zhang, H.; Pang, W.; Liu, J.; Zhang, D. Highly Sensitive MoTe₂ Chemical Sensor with Fast Recovery Rate through Gate Biasing. *2D Mater.* **2017**, *4*, 025018.
- (588) O'Brien, M.; Lee, K.; Morrish, R.; Berner, N. C.; McEvoy, N.; Wolden, C. A.; Duesberg, G. S. Plasma Assisted Synthesis of WS₂ for Gas Sensing Applications. *Chem. Phys. Lett.* **2014**, *615*, 6–10.
- (589) Ko, K. Y.; Song, J. G.; Kim, Y.; Choi, T.; Shin, S.; Lee, C. W.; Lee, K.; Koo, J.; Lee, H.; Kim, J.; Lee, T.; Park, J.; Kim, H. Improvement of Gas-Sensing Performance of Large-Area Tungsten Disulfide Nanosheets by Surface Functionalization. *ACS Nano* **2016**, *10*, 9287–9296.
- (590) Xu, Y.; Schoonen, M. A. A. The Absolute Energy Positions of Conduction and Valence Bands of Selected Semiconducting Minerals. *Am. Mineral.* **2000**, *85*, 543–556.
- (591) Patil, S. G.; Tredgold, R. H. Electrical and Photoconductive Properties of SnS₂ Crystals. *J. Phys. D: Appl. Phys.* **1971**, *4*, 718–722.
- (592) Zappa, D. Molybdenum Dichalcogenides for Environmental Chemical Sensing. *Materials* **2017**, *10*, 1418.
- (593) Hsu, L. C.; Newman, J.; Ativanichayaphong, T.; Cao, H.; Sin, J.; Graff, M.; Stephanou, H. E.; Chiao, J. C. Evaluation of Commercial Metal-Oxide Based NO₂ Sensors. *Sens. Rev.* **2007**, *27*, 121–131.
- (594) Leonardi, S. Two-Dimensional Zinc Oxide Nanostructures for Gas Sensor Applications. *Chemosensors* **2017**, *5*, 17.
- (595) Chen, M.; Wang, Z.; Han, D.; Gu, F.; Guo, G. Porous ZnO Polygonal Nanoflakes: Synthesis, Use in High-Sensitivity NO₂ Gas Sensor, and Proposed Mechanism of Gas Sensing. *J. Phys. Chem. C* **2011**, *115*, 12763–12773.
- (596) Yu, L.; Wei, J.; Luo, Y.; Tao, Y.; Lei, M.; Fan, X.; Yan, W.; Peng, P. Dependence of Al³⁺ on the Growth Mechanism of Vertical Standing ZnO Nanowalls and Their NO₂ Gas Sensing Properties. *Sens. Actuators, B* **2014**, *204*, 96–101.
- (597) Yu, L.; Guo, F.; Liu, S.; Yang, B.; Jiang, Y.; Qi, L.; Fan, X. Both Oxygen Vacancies Defects and Porosity Facilitated NO₂ Gas Sensing Response in 2D ZnO Nanowalls at Room Temperature. *J. Alloys Compd.* **2016**, *682*, 352–356.
- (598) Xiao, C.; Yang, T.; Chuai, M.; Xiao, B.; Zhang, M. Synthesis of ZnO Nanosheet Arrays with Exposed (100) Facets for Gas Sensing Applications. *Phys. Chem. Chem. Phys.* **2016**, *18*, 325–330.
- (599) Mun, Y.; Park, S.; An, S.; Lee, C.; Kim, H. W. NO₂ Gas Sensing Properties of Au-Functionalized Porous ZnO Nanosheets Enhanced by UV Irradiation. *Ceram. Int.* **2013**, *39*, 8615–8622.
- (600) Wang, J.; Li, X.; Xia, Y.; Komarneni, S.; Chen, H.; Xu, J.; Xiang, L.; Xie, D. Hierarchical ZnO Nanosheet-Nanorod Architectures for Fabrication of Poly(3-Hexylthiophene)/ZnO Hybrid NO₂ Sensor. *ACS Appl. Mater. Interfaces* **2016**, *8*, 8600–8607.
- (601) Song, X.; Gao, L. Facile Synthesis and Hierarchical Assembly of Hollow Nickel Oxide Architectures Bearing Enhanced Photocatalytic Properties. *J. Phys. Chem. C* **2008**, *112*, 15299–15305.
- (602) Hoa, N. D.; El-Safty, S. A. Synthesis of Mesoporous NiO Nanosheets for the Detection of Toxic NO₂ Gas. *Chem. - Eur. J.* **2011**, *17*, 12896–12901.
- (603) Bao, M.; Chen, Y.; Li, F.; Ma, J.; Lv, T.; Tang, Y.; Chen, L.; Xu, Z.; Wang, T. Plate-Like P-N Heterogeneous NiO/WO₃ Nanocomposites for High Performance Room Temperature NO₂ Sensors. *Nanoscale* **2014**, *6*, 4063–4066.
- (604) Liu, J.; Guo, Z.; Meng, F.; Luo, T.; Li, M.; Liu, J. Novel Porous Single-Crystalline ZnO Nanosheets Fabricated by Annealing ZnS(en)_{0.5} (en = ethylenediamine) Precursor. Application in a Gas Sensor for Indoor Air Contaminant Detection. *Nanotechnology* **2009**, *20*, 125501.
- (605) Nguyen, D. D.; Do, D. T.; Vu, X. H.; Dang, D. V.; Nguyen, D. C. ZnO Nanoplates Surfaced-Decorated by WO₃ Nanorods for NH₃ Gas Sensing Application. *Adv. Nat. Sci.: Nanosci. Nanotechnol.* **2016**, *7*, 015004.
- (606) Li, Y.; Jiao, M.; Yang, M. In-Situ Grown Nanostructured ZnO via a Green Approach and Gas Sensing Properties of Polypyrrole/ZnO Nanohybrids. *Sens. Actuators, B* **2017**, *238*, 596–604.
- (607) Wang, J.; Yang, P.; Wei, X.; Zhou, Z. Preparation of NiO Two-Dimensional Grainy Films and Their High-Performance Gas Sensors for Ammonia Detection. *Nanoscale Res. Lett.* **2015**, *10*, 119.
- (608) Li, X.; Chen, N.; Lin, S.; Wang, J.; Zhang, J. NiO-Wrapped Mesoporous TiO₂ Microspheres Based Selective Ammonia Sensor at Room Temperature. *Sens. Actuators, B* **2015**, *209*, 729–734.
- (609) Zhang, F.; Zhu, A.; Luo, Y.; Tian, Y.; Yang, J.; Qin, Y. CuO Nanosheets for Sensitive and Selective Determination of H₂S with High Recovery Ability. *J. Phys. Chem. C* **2010**, *114*, 19214–19219.
- (610) Li, Z.; Wang, N.; Lin, Z.; Wang, J.; Liu, W.; Sun, K.; Fu, Y. Q.; Wang, Z. Room-Temperature High-Performance H₂S Sensor Based on Porous CuO Nanosheets Prepared by Hydrothermal Method. *ACS Appl. Mater. Interfaces* **2016**, *8*, 20962–20968.
- (611) Yu, T.; Cheng, X.; Zhang, X.; Sui, L.; Xu, Y.; Gao, S.; Zhao, H.; Huo, L. Highly Sensitive H₂S Detection Sensors at Low Temperature Based on Hierarchically Structured NiO Porous Nanowall Arrays. *J. Mater. Chem. A* **2015**, *3*, 11991–11999.
- (612) Urasinska-Wojcik, B.; Vincent, T. A.; Gardner, J. W. H₂S Sensing Properties of WO₃ Based Gas Sensor. *Procedia Eng.* **2016**, *168*, 255–258.
- (613) Li, H.-Y.; Huang, L.; Wang, X.-X.; Lee, C.-S.; Yoon, J.-W.; Zhou, J.; Guo, X.; Lee, J.-H. Molybdenum Trioxide Nanopaper as a Dual Gas Sensor for Detecting Trimethylamine and Hydrogen Sulfide. *RSC Adv.* **2017**, *7*, 3680–3685.
- (614) Hu, J.; Sun, Y.; Wang, X.; Chen, L.; Zhang, W.; Chen, Y. Synthesis and Gas Sensing Properties of Molybdenum Oxide Modified Tungsten Oxide Microstructures for ppb-Level Hydrogen Sulphide Detection. *RSC Adv.* **2017**, *7*, 28542–28547.
- (615) Moon, C. S.; Kim, H.-R.; Auchterlonie, G.; Drennan, J.; Lee, J.-H. Highly Sensitive and Fast Responding CO Sensor Using SnO₂ Nanosheets. *Sens. Actuators, B* **2008**, *131*, 556–564.
- (616) Jones, D. R.; Maffei, T. G. G. Analysis of the Kinetics of Surface Reactions on a Zinc Oxide Nanosheet-Based Carbon Monoxide Sensor Using an Eley–Rideal Model. *Sens. Actuators, B* **2015**, *218*, 16–24.
- (617) Zeng, Y.; Qiao, L.; Bing, Y.; Wen, M.; Zou, B.; Zheng, W.; Zhang, T.; Zou, G. Development of Microstructure CO Sensor Based on Hierarchically Porous ZnO Nanosheet Thin Films. *Sens. Actuators, B* **2012**, *173*, 897–902.
- (618) Chang, S.-P.; Wen, C.-H.; Chang, S.-J. Two-Dimensional ZnO Nanowalls for Gas Sensor and Photoelectrochemical Applications. *Electron. Mater. Lett.* **2014**, *10*, 693–697.
- (619) Chen, T. P.; Chang, S. P.; Chang, S. J. Fabrication of ZnO Nanowall-Based Hydrogen Gas Nanosensor. *Adv. Mater. Res.* **2013**, *684*, 21–25.
- (620) Chen, T. P.; Chang, S. P.; Hung, F. Y.; Chang, S. J.; Hu, Z. S.; Chen, K. J. Simple Fabrication Process for 2D ZnO Nanowalls and Their Potential Application as a Methane Sensor. *Sensors* **2013**, *13*, 3941–3950.

- (621) Alsaif, M. M. Y. A.; Balendhran, S.; Field, M. R.; Latham, K.; Włodarski, W.; Ou, J. Z.; Kalantar-zadeh, K. Two Dimensional A-MoO_3 Nanoflakes Obtained Using Solvent-Assisted Grinding and Sonication Method: Application for H_2 Gas Sensing. *Sens. Actuators, B* **2014**, *192*, 196–204.
- (622) Yang, S.; Wang, Z.; Hu, Y.; Luo, X.; Lei, J.; Zhou, D.; Fei, L.; Wang, Y.; Gu, H. Highly Responsive Room-Temperature Hydrogen Sensing of $\alpha\text{-MoO}_3$ Nanoribbon Membranes. *ACS Appl. Mater. Interfaces* **2015**, *7*, 9247–9253.
- (623) Smith, M. K.; Jensen, K. E.; Pivak, P. A.; Mirica, K. A. Direct Self-Assembly of Conductive Nanorods of Metal–Organic Frameworks into Chemiresistive Devices on Shrinkable Polymer Films. *Chem. Mater.* **2016**, *28*, 5264–5268.
- (624) Smith, M. K.; Mirica, K. A. Self-Organized Frameworks on Textiles (SOFT): Conductive Fabrics for Simultaneous Sensing, Capture, and Filtration of Gases. *J. Am. Chem. Soc.* **2017**, *139*, 16759–16767.
- (625) Kim, S. J.; Koh, H. J.; Ren, C. E.; Kwon, O.; Maleski, K.; Cho, S. Y.; Anasori, B.; Kim, C. K.; Choi, Y. K.; Kim, J.; Gogotsi, Y.; Jung, H. T. Metallic $\text{Ti}_3\text{C}_2\text{T}_x$ MXene Gas Sensors with Ultrahigh Signal-to-Noise Ratio. *ACS Nano* **2018**, *12*, 986–993.
- (626) Shukla, V.; Wärnå, J.; Jena, N. K.; Grigoriev, A.; Ahuja, R. Toward the Realization of 2D Borophene Based Gas Sensor. *J. Phys. Chem. C* **2017**, *121*, 26869–26876.
- (627) Yong, Y.; Su, X.; Cui, H.; Zhou, Q.; Kuang, Y.; Li, X. Two-Dimensional Tetragonal Gan as Potential Molecule Sensors for No and NO_2 Detection: A First-Principle Study. *ACS Omega* **2017**, *2*, 8888–8895.
- (628) Bhattacharyya, K.; Pratik, S. M.; Datta, A. Controlled Pore Sizes in Monolayer C_{2n} Act as Ultrasensitive Probes for Detection of Gaseous Pollutants (HF , HCN , and H_2S). *J. Phys. Chem. C* **2018**, *122*, 2248–2258.
- (629) Wang, D.; Gu, W.; Zhang, Y.; Hu, Y.; Zhang, T.; Tao, X.; Chen, W. Novel C-Rich Carbon Nitride for Room Temperature NO_2 Gas Sensors. *RSC Adv.* **2014**, *4*, 18003–18006.
- (630) Li, S.; Wang, Z.; Wang, X.; Sun, F.; Gao, K.; Hao, N.; Zhang, Z.; Ma, Z.; Li, H.; Huang, X.; Huang, W. Orientation Controlled Preparation of Nanoporous Carbon Nitride Fibers and Related Composite for Gas Sensing under Ambient Conditions. *Nano Res.* **2017**, *10*, 1710–1719.
- (631) Zhang, S.; Hang, N. T.; Zhang, Z.; Yue, H.; Yang, W. Preparation of $\text{G-C}_3\text{N}_4$ /Graphene Composite for Detecting NO_2 at Room Temperature. *Nanomaterials* **2017**, *7*, 12.
- (632) Tian, H.; Fan, H.; Ma, J.; Liu, Z.; Ma, L.; Lei, S.; Fang, J.; Long, C. Pt-Decorated Zinc Oxide Nanorod Arrays with Graphitic Carbon Nitride Nanosheets for Highly Efficient Dual-Functional Gas Sensing. *J. Hazard. Mater.* **2018**, *341*, 102–111.
- (633) Raghu, S.; Santhosh, P. N.; Ramaprabhu, S. Nanostructured Palladium Modified Graphitic Carbon Nitride – High Performance Room Temperature Hydrogen Sensor. *Int. J. Hydrogen Energy* **2016**, *41*, 20779–20786.
- (634) Sajjad, M.; Feng, P. Study the Gas Sensing Properties of Boron Nitride Nanosheets. *Mater. Res. Bull.* **2014**, *49*, 35–38.
- (635) Lin, L.; Liu, T.; Zhang, Y.; Sun, R.; Zeng, W.; Wang, Z. Synthesis of Boron Nitride Nanosheets with a Few Atomic Layers and Their Gas-Sensing Performance. *Ceram. Int.* **2016**, *42*, 971–975.
- (636) Ayari, T.; Bishop, C.; Jordan, M. B.; Sundaram, S.; Li, X.; Alam, S.; ElGmili, Y.; Patriarche, G.; Voss, P. L.; Salvestrini, J. P.; Ougazzaden, A. Gas Sensors Boosted by Two-Dimensional $h\text{-BN}$ Enabled Transfer on Thin Substrate Foils: Towards Wearable and Portable Applications. *Sci. Rep.* **2017**, *7*, 15212.
- (637) Fang, H.; Battaglia, C.; Carraro, C.; Nemsak, S.; Ozdol, B.; Kang, J. S.; Bechtel, H. A.; Desai, S. B.; Kronast, F.; Unal, A. A.; Conti, G.; Conlon, C.; Palsson, G. K.; Martin, M. C.; Minor, A. M.; Felley, C. S.; Yablonovitch, E.; Maboudian, R.; Javey, A. Strong Interlayer Coupling in Van der Waals Heterostructures Built from Single-Layer Chalcogenides. *Proc. Natl. Acad. Sci. U. S. A.* **2014**, *111*, 6198–6202.
- (638) Jariwala, D.; Sangwan, V. K.; Lauhon, L. J.; Marks, T. J.; Hersam, M. C. Emerging Device Applications for Semiconducting Two-Dimensional Transition Metal Dichalcogenides. *ACS Nano* **2014**, *8*, 1102–1120.
- (639) Niu, Y.; Wang, R.; Jiao, W.; Ding, G.; Hao, L.; Yang, F.; He, X. MoS_2 Graphene Fiber Based Gas Sensing Devices. *Carbon* **2015**, *95*, 34–41.
- (640) Xu, Z.; Liu, Z.; Sun, H.; Gao, C. Highly Electrically Conductive Ag-Doped Graphene Fibers as Stretchable Conductors. *Adv. Mater.* **2013**, *25*, 3249–3253.
- (641) Zhou, Y.; Liu, G.; Zhu, X.; Guo, Y. Ultrasensitive NO_2 Gas Sensing Based on rGO/ MoS_2 Nanocomposite Film at Low Temperature. *Sens. Actuators, B* **2017**, *251*, 280–290.
- (642) Feng, Z. H.; Chen, B. Y.; Qian, S. B.; Xu, L. Y.; Feng, L. F.; Yu, Y. Y.; Zhang, R.; Chen, J. C.; Li, Q. Q.; Li, Q. N.; Sun, C. L.; Zhang, H.; Liu, J.; Pang, W.; Zhang, D. H. Chemical Sensing by Band Modulation of a Black Phosphorus/Molybdenum Diselenide Van der Waals Hetero-Structure. *2D Mater.* **2016**, *3*, 035021.
- (643) Chung, M. G.; Kim, D.-H.; Seo, D. K.; Kim, T.; Im, H. U.; Lee, H. M.; Yoo, J.-B.; Hong, S.-H.; Kang, T. J.; Kim, Y. H. Flexible Hydrogen Sensors Using Graphene with Palladium Nanoparticle Decoration. *Sens. Actuators, B* **2012**, *169*, 387–392.
- (644) Phan, D.-T.; Chung, G.-S. Effects of Pd Nanocube Size of Pd Nanocube-Graphene Hybrid on Hydrogen Sensing Properties. *Sens. Actuators, B* **2014**, *204*, 437–444.
- (645) Chen, X.; Yasin, F. M.; Eggers, P. K.; Boulos, R. A.; Duan, X.; Lamb, R. N.; Iyer, K. S.; Raston, C. L. Non-Covalently Modified Graphene Supported Ultrafine Nanoparticles of Palladium for Hydrogen Gas Sensing. *RSC Adv.* **2013**, *3*, 3213.
- (646) Kaniyoor, A.; Imran Jafri, R.; Arockiadoss, T.; Ramaprabhu, S. Nanostructured Pt Decorated Graphene and Multi Walled Carbon Nanotube Based Room Temperature Hydrogen Gas Sensor. *Nanoscale* **2009**, *1*, 382–386.
- (647) Chu, B. H.; Nicolosi, J.; Lo, C. F.; Strupinski, W.; Pearton, S. J.; Ren, F. Effect of Coated Platinum Thickness on Hydrogen Detection Sensitivity of Graphene-Based Sensors. *Electrochim. Solid-State Lett.* **2011**, *14*, K43.
- (648) Zhang, Z.; Zou, X.; Xu, L.; Liao, L.; Liu, W.; Ho, J.; Xiao, X.; Jiang, C.; Li, J. Hydrogen Gas Sensor Based on Metal Oxide Nanoparticles Decorated Graphene Transistor. *Nanoscale* **2015**, *7*, 10078–10084.
- (649) Paul, R. K.; Badhulika, S.; Saucedo, N. M.; Mulchandani, A. Graphene Nanomesh as Highly Sensitive Chemiresistor Gas Sensor. *Anal. Chem.* **2012**, *84*, 8171–8178.
- (650) Ben Aziza, Z.; Baillargeat, D. Graphene/Mica Based Ammonia Gas Sensors. *Appl. Phys. Lett.* **2014**, *105*, 254102.
- (651) Cho, B.; Yoon, J.; Lim, S. K.; Kim, A. R.; Kim, D. H.; Park, S. G.; Kwon, J. D.; Lee, Y. J.; Lee, K. H.; Lee, B. H.; Ko, H. C.; Hahn, M. G. Chemical Sensing of 2D Graphene/ MoS_2 Heterostructure Device. *ACS Appl. Mater. Interfaces* **2015**, *7*, 16775–16780.
- (652) Lee, K.; Gatensby, R.; McEvoy, N.; Hallam, T.; Duesberg, G. S. High-Performance Sensors Based on Molybdenum Disulfide Thin Films. *Adv. Mater.* **2013**, *25*, 6699–6702.
- (653) Huang, X.; Hu, N.; Zhang, L.; Wei, L.; Wei, H.; Zhang, Y. The NH_3 Sensing Properties of Gas Sensors Based on Aniline Reduced Graphene Oxide. *Synth. Met.* **2013**, *185–186*, 25–30.
- (654) Hu, N.; Yang, Z.; Wang, Y.; Zhang, L.; Wang, Y.; Huang, X.; Wei, H.; Wei, L.; Zhang, Y. Ultrafast and Sensitive Room Temperature NH_3 Gas Sensors Based on Chemically Reduced Graphene Oxide. *Nanotechnology* **2014**, *25*, 025502.
- (655) Meng, H.; Yang, W.; Ding, K.; Feng, L.; Guan, Y. Cu_2O Nanorods Modified by Reduced Graphene Oxide for NH_3 Sensing at Room Temperature. *J. Mater. Chem. A* **2015**, *3*, 1174–1181.
- (656) Ye, Z.; Jiang, Y.; Tai, H.; Yuan, Z. The Investigation of Reduced Graphene Oxide/P3HT Composite Films for Ammonia Detection. *Integr. Ferroelectr.* **2014**, *154*, 73–81.
- (657) Wang, Y.; Zhang, L.; Hu, N.; Wang, Y.; Zhang, Y.; Zhou, Z.; Liu, Y.; Shen, S.; Peng, C. Ammonia Gas Sensors Based on Chemically Reduced Graphene Oxide Sheets Self-Assembled on Au Electrodes. *Nanoscale Res. Lett.* **2014**, *9*, 251.

- (658) Xu, K.; Li, N.; Zeng, D.; Tian, S.; Zhang, S.; Hu, D.; Xie, C. Interface Bonds Determined Gas-Sensing of $\text{SnO}_2\text{-SnS}_2$ Hybrids to Ammonia at Room Temperature. *ACS Appl. Mater. Interfaces* **2015**, *7*, 11359–11368.
- (659) Chung, M. G.; Kim, D. H.; Lee, H. M.; Kim, T.; Choi, J. H.; Seo, D. k.; Yoo, J.-B.; Hong, S.-H.; Kang, T. J.; Kim, Y. H. Highly Sensitive NO_2 Gas Sensor Based on Ozone Treated Graphene. *Sens. Actuators, B* **2012**, *166–167*, 172–176.
- (660) Hoa, L. T.; Tien, H. N.; Luan, V. H.; Chung, J. S.; Hur, S. H. Fabrication of a Novel 2D-Graphene/2D-NiO Nanosheet-Based Hybrid Nanostructure and Its Use in Highly Sensitive NO_2 Sensors. *Sens. Actuators, B* **2013**, *185*, 701–705.
- (661) Lee, C.; Ahn, J.; Lee, K. B.; Kim, D.; Kim, J. Graphene-Based Flexible NO_2 Chemical Sensors. *Thin Solid Films* **2012**, *520*, 5459–5462.
- (662) Srivastava, S.; Jain, K.; Singh, V. N.; Singh, S.; Vijayan, N.; Dilawar, N.; Gupta, G.; Senguttuvan, T. D. Faster Response of NO_2 Sensing in Graphene-WO₃ Nanocomposites. *Nanotechnology* **2012**, *23*, 205501.
- (663) He, Q.; Zeng, Z.; Yin, Z.; Li, H.; Wu, S.; Huang, X.; Zhang, H. Fabrication of Flexible MoS₂ Thin-Film Transistor Arrays for Practical Gas-Sensing Applications. *Small* **2012**, *8*, 2994–2999.
- (664) Cui, S.; Wen, Z.; Huang, X.; Chang, J.; Chen, J. Stabilizing MoS₂ Nanosheets through SnO₂ Nanocrystal Decoration for High-Performance Gas Sensing in Air. *Small* **2015**, *11*, 2305–2313.
- (665) Su, P.-G.; Shieh, H.-C. Flexible NO_2 Sensors Fabricated by Layer-by-Layer Covalent Anchoring and in Situ Reduction of Graphene Oxide. *Sens. Actuators, B* **2014**, *190*, 865–872.
- (666) Dong, Y.-l.; Zhang, X.-f.; Cheng, X.-l.; Xu, Y.-m.; Gao, S.; Zhao, H.; Huo, L.-h. Highly Selective NO_2 Sensor at Room Temperature Based on Nanocomposites of Hierarchical Nanosphere-Like $\alpha\text{-Fe}_2\text{O}_3$ and Reduced Graphene Oxide. *RSC Adv.* **2014**, *4*, 57493–57500.
- (667) Chen, Z.; Umar, A.; Wang, S.; Wang, Y.; Tian, T.; Shang, Y.; Fan, Y.; Qi, Q.; Xu, D.; Jiang, L. Supramolecular Fabrication of Multilevel Graphene-Based Gas Sensors with High NO_2 Sensibility. *Nanoscale* **2015**, *7*, 10259–10266.
- (668) Farahani, H.; Wagiran, R.; Hamidon, M. N. Humidity Sensors Principle, Mechanism, and Fabrication Technologies: A Comprehensive Review. *Sensors* **2014**, *14*, 7881–7939.
- (669) Mirzaei, A.; Leonardi, S. G.; Neri, G. Detection of Hazardous Volatile Organic Compounds (VOCs) by Metal Oxide Nanostructures-Based Gas Sensors: A Review. *Ceram. Int.* **2016**, *42*, 15119–15141.
- (670) Li, B.; Sauve, G.; Iovu, M. C.; Jeffries-El, M.; Zhang, R.; Cooper, J.; Santhanam, S.; Schultz, L.; Revelli, J. C.; Kusne, A. G.; Kowalewski, T.; Snyder, J. L.; Weiss, L. E.; Fedder, G. K.; McCullough, R. D.; Lambeth, D. N. Volatile Organic Compound Detection Using Nanostructured Copolymers. *Nano Lett.* **2006**, *6*, 1598–1602.
- (671) WHO Regional Office for Europe. *WHO Guidelines for Indoor Air Quality: Selected Pollutants*; Copenhagen, 2010.
- (672) Chung, P. R.; Tzeng, C. T.; Ke, M. T.; Lee, C. Y. Formaldehyde Gas Sensors: A Review. *Sensors* **2013**, *13*, 4468–4484.
- (673) Yavari, F.; Kritzinger, C.; Gaire, C.; Song, L.; Gulapalli, H.; Borca-Tasciuc, T.; Ajayan, P. M.; Koratkar, N. Tunable Bandgap in Graphene by the Controlled Adsorption of Water Molecules. *Small* **2010**, *6*, 2535–2538.
- (674) Dimiev, A. M.; Alemany, L. B.; Tour, J. M. Graphene Oxide. Origin of Acidity, Its Instability in Water, and a New Dynamic Structural Model. *ACS Nano* **2013**, *7*, 576–588.
- (675) Yao, Y.; Chen, X.; Zhu, J.; Zeng, B.; Wu, Z.; Li, X. The Effect of Ambient Humidity on the Electrical Properties of Graphene Oxide Films. *Nanoscale Res. Lett.* **2012**, *7*, 363.
- (676) Zhao, F.; Cheng, H.; Zhang, Z.; Jiang, L.; Qu, L. Direct Power Generation from a Graphene Oxide Film under Moisture. *Adv. Mater.* **2015**, *27*, 4351–4357.
- (677) Nair, R. R.; Wu, H. A.; Jayaram, P. N.; Grigorieva, I. V.; Geim, A. K. Unimpeded Permeation of Water through Helium-Leak-Tight Graphene-Based Membranes. *Science* **2012**, *335*, 442–444.
- (678) Borini, S.; White, R.; Wei, D.; Astley, M.; Haque, S.; Spigone, E.; Harris, N.; Kivioja, J.; Ryhanen, T. Ultrafast Graphene Oxide Humidity Sensors. *ACS Nano* **2013**, *7*, 11166–11173.
- (679) Bi, H.; Yin, K.; Xie, X.; Ji, J.; Wan, S.; Sun, L.; Terrones, M.; Dresselhaus, M. S. Ultrahigh Humidity Sensitivity of Graphene Oxide. *Sci. Rep.* **2013**, *3*, 2714.
- (680) Chen, W. P.; Zhao, Z. G.; Liu, X. W.; Zhang, Z. X.; Suo, C. G. A Capacitive Humidity Sensor Based on Multi-Wall Carbon Nanotubes (MWCTNs). *Sensors* **2009**, *9*, 7431–7444.
- (681) Chen, X.; Zhang, J.; Wang, Z.; Yan, Q.; Hui, S. Humidity Sensing Behavior of Silicon Nanowires with Hexamethyldisilazane Modification. *Sens. Actuators, B* **2011**, *156*, 631–636.
- (682) Wang, Y.; Park, S.; Yeow, J. T. W.; Langner, A.; Müller, F. A Capacitive Humidity Sensor Based on Ordered Macroporous Silicon with Thin Film Surface Coating. *Sens. Actuators, B* **2010**, *149*, 136–142.
- (683) Wang, Z.; Shi, L.; Wu, F.; Yuan, S.; Zhao, Y.; Zhang, M. The Sol-Gel Template Synthesis of Porous TiO₂ for a High Performance Humidity Sensor. *Nanotechnology* **2011**, *22*, 275502.
- (684) Kim, Y.; Jung, B.; Lee, H.; Kim, H.; Lee, K.; Park, H. Capacitive Humidity Sensor Design Based on Anodic Aluminum Oxide. *Sens. Actuators, B* **2009**, *141*, 441–446.
- (685) Su, P.-G.; Chiou, C.-F. Electrical and Humidity-Sensing Properties of Reduced Graphene Oxide Thin Film Fabricated by Layer-by-Layer with Covalent Anchoring on Flexible Substrate. *Sens. Actuators, B* **2014**, *200*, 9–18.
- (686) Zhang, D.; Tong, J.; Xia, B. Humidity-Sensing Properties of Chemically Reduced Graphene Oxide/Polymer Nanocomposite Film Sensor Based on Layer-by-Layer Nano Self-Assembly. *Sens. Actuators, B* **2014**, *197*, 66–72.
- (687) Guo, L.; Jiang, H.-B.; Shao, R.-Q.; Zhang, Y.-L.; Xie, S.-Y.; Wang, J.-N.; Li, X.-B.; Jiang, F.; Chen, Q.-D.; Zhang, T.; Sun, H.-B. Two-Beam-Laser Interference Mediated Reduction, Patterning and Nanostructuring of Graphene Oxide for the Production of a Flexible Humidity Sensing Device. *Carbon* **2012**, *50*, 1667–1673.
- (688) Ma, R.; Tsukruk, V. V. Serigraphy-Guided Reduction of Graphene Oxide Biopapers for Wearable Sensory Electronics. *Adv. Funct. Mater.* **2017**, *27*, 1604802.
- (689) Sinar, D.; Knopf, G. K. Printed Graphene Interdigitated Capacitive Sensors on Flexible Polyimide Substrates. *2014 IEEE 14th International Conference on Nanotechnology (IEEE-Nano)* **2014**; pp 538–542.
- (690) Yuan, Y.; Peng, B.; Chi, H.; Li, C.; Liu, R.; Liu, X. Layer-by-Layer Inkjet Printing SPS:PEDOT NP/rGO Composite Film for Flexible Humidity Sensors. *RSC Adv.* **2016**, *6*, 113298–113306.
- (691) Deen, D. A.; Olson, E. J.; Ebrish, M. A.; Koester, S. J. Graphene-Based Quantum Capacitance Wireless Vapor Sensors. *IEEE Sens. J.* **2014**, *14*, 1459–1466.
- (692) Kumar, B.; Min, K.; Bashirzadeh, M.; Farimani, A. B.; Bae, M. H.; Estrada, D.; Kim, Y. D.; Yasaeei, P.; Park, Y. D.; Pop, E.; Aluru, N. R.; Salehi-Khojin, A. The Role of External Defects in Chemical Sensing of Graphene Field-Effect Transistors. *Nano Lett.* **2013**, *13*, 1962–1968.
- (693) Xu, K.; Cao, P.; Heath, J. R. Graphene Visualizes the First Water Adlayers on Mica at Ambient Conditions. *Science* **2010**, *329*, 1188–1191.
- (694) Temmen, M.; Ochedowski, O.; Schleberger, M.; Reichling, M.; Bollmann, T. R. J. Hydration Layers Trapped between Graphene and a Hydrophilic Substrate. *New J. Phys.* **2014**, *16*, 053039.
- (695) Olson, E. J.; Ma, R.; Sun, T.; Ebrish, M. A.; Haratipour, N.; Min, K.; Aluru, N. R.; Koester, S. J. Capacitive Sensing of Intercalated H₂O Molecules Using Graphene. *ACS Appl. Mater. Interfaces* **2015**, *7*, 25804–25812.
- (696) Shehzad, K.; Shi, T.; Qadir, A.; Wan, X.; Guo, H.; Ali, A.; Xuan, W.; Xu, H.; Gu, Z.; Peng, X.; Xie, J.; Sun, L.; He, Q.; Xu, Z.; Gao, C.; Rim, Y.-S.; Dan, Y.; Hasan, T.; Tan, P.; Li, E.; Yin, W.;

- Cheng, Z.; Yu, B.; Xu, Y.; Luo, J.; Duan, X. Designing an Efficient Multimode Environmental Sensor Based on Graphene-Silicon Heterojunction. *Adv. Mater. Technol.* **2017**, *2*, 1600262.
- (697) Smith, A. D.; Elgammal, K.; Niklaus, F.; Delin, A.; Fischer, A. C.; Vaziri, S.; Forsberg, F.; Rasander, M.; Hugosson, H.; Bergqvist, L.; Schroder, S.; Kataria, S.; Ostling, M.; Lemme, M. C. Resistive Graphene Humidity Sensors with Rapid and Direct Electrical Readout. *Nanoscale* **2015**, *7*, 19099–19109.
- (698) Yu, H. W.; Kim, H. K.; Kim, T.; Bae, K. M.; Seo, S. M.; Kim, J. M.; Kang, T. J.; Kim, Y. H. Self-Powered Humidity Sensor Based on Graphene Oxide Composite Film Intercalated by Poly(Sodium 4-Styrenesulfonate). *ACS Appl. Mater. Interfaces* **2014**, *6*, 8320–8326.
- (699) Lin, W.-D.; Chang, H.-M.; Wu, R.-J. Applied Novel Sensing Material Graphene/Polyppyrrole for Humidity Sensor. *Sens. Actuators, B* **2013**, *181*, 326–331.
- (700) Su, P.-G.; Lu, Z.-M. Flexibility and Electrical and Humidity-Sensing Properties of Diamine-Functionalized Graphene Oxide Films. *Sens. Actuators, B* **2015**, *211*, 157–163.
- (701) Porter, T. L.; Vail, T. L.; Eastman, M. P.; Stewart, R.; Reed, J.; Venedam, R.; Delinger, W. A Solid-State Sensor Platform for the Detection of Hydrogen Cyanide Gas. *Sens. Actuators, B* **2007**, *123*, 313–317.
- (702) Robinson, J. T.; Perkins, F. K.; Snow, E. S.; Wei, Z.; Sheehan, P. E. Reduced Graphene Oxide Molecular Sensors. *Nano Lett.* **2008**, *8*, 3137–3140.
- (703) Zhou, S.; Xu, H.; Gan, W.; Yuan, Q. Graphene Quantum Dots: Recent Progress in Preparation and Fluorescence Sensing Applications. *RSC Adv.* **2016**, *6*, 110775–110788.
- (704) Sreeprasad, T. S.; Rodriguez, A. A.; Colston, J.; Graham, A.; Shishkin, E.; Pallem, V.; Berry, V. Electron-Tunneling Modulation in Percolating Network of Graphene Quantum Dots: Fabrication, Phenomenological Understanding, and Humidity/Pressure Sensing Applications. *Nano Lett.* **2013**, *13*, 1757–1763.
- (705) Alizadeh, T.; Shokri, M.; Hanifehpour, Y.; Joo, S. W. A New Hydrogen Cyanide Chemiresistor Gas Sensor Based on Graphene Quantum Dots. *Int. J. Environ. Anal. Chem.* **2016**, *96*, 763–775.
- (706) Yang, M.; He, J.; Hu, X.; Yan, C.; Cheng, Z. CuO Nanostructures as Quartz Crystal Microbalance Sensing Layers for Detection of Trace Hydrogen Cyanide Gas. *Environ. Sci. Technol.* **2011**, *45*, 6088–6094.
- (707) Dong, Y.; Shao, J.; Chen, C.; Li, H.; Wang, R.; Chi, Y.; Lin, X.; Chen, G. Blue Luminescent Graphene Quantum Dots and Graphene Oxide Prepared by Tuning the Carbonization Degree of Citric Acid. *Carbon* **2012**, *50*, 4738–4743.
- (708) Mlsna, T. E.; Cemalovic, S.; Warburton, M.; Hobson, S. T.; Mlsna, D. A.; Patel, S. V. Chemicapacitive Microsensors for Chemical Warfare Agent and Toxic Industrial Chemical Detection. *Sens. Actuators, B* **2006**, *116*, 192–201.
- (709) Legako, J. A.; White, B. J.; Harmon, H. J. Detection of Cyanide Using Immobilized Porphyrin and Myoglobin Surfaces. *Sens. Actuators, B* **2003**, *91*, 128–132.
- (710) Roerecke, M.; Rehm, J. Alcohol Use Disorders and Mortality: A Systematic Review and Meta-Analysis. *Addiction* **2013**, *108*, 1562–1578.
- (711) Selvam, A. P.; Muthukumar, S.; Kamakoti, V.; Prasad, S. A Wearable Biochemical Sensor for Monitoring Alcohol Consumption Lifestyle through Ethyl Glucuronide (EtG) Detection in Human Sweat. *Sci. Rep.* **2016**, *6*, 23111.
- (712) McPherson, S.; Lucey, M. R.; Moriarty, K. J. Decompensated Alcohol Related Liver Disease: Acute Management. *BMJ* **2016**, *352*, i124.
- (713) Chen, B. D.; Liu, H. Z.; Li, X.; Lu, C. X.; Ding, Y. C.; Lu, B. H. Fabrication of a Graphene Field Effect Transistor Array on Microchannels for Ethanol Sensing. *Appl. Surf. Sci.* **2012**, *258*, 1971–1975.
- (714) Kim, Y.; An, T. K.; Kim, J.; Hwang, J.; Park, S.; Nam, S.; Cha, H.; Park, W. J.; Baik, J. M.; Park, C. E. A Composite of a Graphene Oxide Derivative as a Novel Sensing Layer in an Organic Field-Effect Transistor. *J. Mater. Chem. C* **2014**, *2*, 4539–4544.
- (715) Liang, S. M.; Zhu, J. W.; Wang, C.; Yu, S. T.; Bi, H. P.; Liu, X. H.; Wang, X. Fabrication of α -Fe₂O₃@Graphene Nanostructures for Enhanced Gas-Sensing Property to Ethanol. *Appl. Surf. Sci.* **2014**, *292*, 278–284.
- (716) Liu, Y.; Lin, S.; Lin, L. A Versatile Gas Sensor with Selectivity Using a Single Graphene Transistor. *2015 Transducers - 2015 18th International Conference on Solid-State Sensors, Actuators and Microsystems (Transducers)* **2015**, 961–964.
- (717) Korpan, Y. I.; Gonchar, M. V.; Sibirny, A. A.; Martelet, C.; El'skaya, A. V.; Gibson, T. D.; Soldatkin, A. P. Development of Highly Selective and Stable Potentiometric Sensors for Formaldehyde Determination. *Biosens. Bioelectron.* **2000**, *15*, 77–83.
- (718) Alizadeh, T.; Soltani, L. H. Graphene/Poly(Methyl Methacrylate) Chemiresistor Sensor for Formaldehyde Odor Sensing. *J. Hazard. Mater.* **2013**, *248*, 401–406.
- (719) Minh Triet, N.; Thai Duy, L.; Hwang, B. U.; Hanif, A.; Siddiqui, S.; Park, K. H.; Cho, C. Y.; Lee, N. E. High-Performance Schottky Diode Gas Sensor Based on the Heterojunction of Three-Dimensional Nanohybrids of Reduced Graphene Oxide-Vertical ZnO Nanorods on an AlGaN/GaN Layer. *ACS Appl. Mater. Interfaces* **2017**, *9*, 30722–30732.
- (720) Dong, L.; Shen, X.; Deng, C. Development of Gas Chromatography–Mass Spectrometry Following Headspace Single-Drop Microextraction and Simultaneous Derivatization for Fast Determination of the Diabetes Biomarker, Acetone in Human Blood Samples. *Anal. Chim. Acta* **2006**, *569*, 91–96.
- (721) Li, X.; Xu, Z.; Lu, X.; Yang, X.; Yin, P.; Kong, H.; Yu, Y.; Xu, G. Comprehensive Two-Dimensional Gas Chromatography/Time-of-Flight Mass Spectrometry for Metabonomics: Biomarker Discovery for Diabetes Mellitus. *Anal. Chim. Acta* **2009**, *633*, 257–262.
- (722) Shin, J.; Choi, S.-J.; Lee, I.; Youn, D.-Y.; Park, C. O.; Lee, J.-H.; Tuller, H. L.; Kim, I.-D. Thin-Wall Assembled SnO₂ fibers Functionalized by Catalytic Pt Nanoparticles and Their Superior Exhaled-Breath-Sensing Properties for the Diagnosis of Diabetes. *Adv. Funct. Mater.* **2013**, *23*, 2357–2367.
- (723) Choi, S.-J.; Ryu, W.-H.; Kim, S.-J.; Cho, H.-J.; Kim, I.-D. Bi-Functional Co-Sensitization of Graphene Oxide Sheets and Ir Nanoparticles on P-Type Co₃O₄ Nanofibers for Selective Acetone Detection. *J. Mater. Chem. B* **2014**, *2*, 7160–7167.
- (724) Liu, F.; Chu, X.; Dong, Y.; Zhang, W.; Sun, W.; Shen, L. Acetone Gas Sensors Based on Graphene-ZnFe₂O₄ Composite Prepared by Solvothermal Method. *Sens. Actuators, B* **2013**, *188*, 469–474.
- (725) Kehayias, C. E.; MacNaughton, S.; Sonkusale, S.; Staici, C. Kelvin Probe Microscopy and Electronic Transport Measurements in Reduced Graphene Oxide Chemical Sensors. *Nanotechnology* **2013**, *24*, 245502.
- (726) Myers, M.; Cooper, J.; Pejcic, B.; Baker, M.; Raguse, B.; Wieczorek, L. Functionalized Graphene as an Aqueous Phase Chemiresistor Sensing Material. *Sens. Actuators, B* **2011**, *155*, 154–158.
- (727) Duesberg, G. S.; Kim, H. Y.; Lee, K.; McEvoy, N.; Winters, S.; Yim, C. Investigation of Carbon-Silicon Schottky Diodes and Their Use as Chemical Sensors. *Proceedings of the European Solid-State Device Research Conference (Esdrc)* **2013**; pp 85–90.
- (728) Zheng, Q.; Fu, Y.-c.; Xu, J.-q. Advances in the Chemical Sensors for the Detection of DMMP — a Simulant for Nerve Agent Sarin. *Procedia Eng.* **2010**, *7*, 179–184.
- (729) Alizadeh, T.; Soltani, L. H. Reduced Graphene Oxide-Based Gas Sensor Array for Pattern Recognition of DMMP Vapor. *Sens. Actuators, B* **2016**, *234*, 361–370.
- (730) Hu, N.; Wang, Y.; Chai, J.; Gao, R.; Yang, Z.; Kong, E. S.-W.; Zhang, Y. Gas Sensor Based on p-Phenylenediamine Reduced Graphene Oxide. *Sens. Actuators, B* **2012**, *163*, 107–114.
- (731) Na, K.; Ma, H.; Park, J.; Yeo, J.; Park, J. U.; Bien, F. Graphene-Based Wireless Environmental Gas Sensor on PET Substrate. *IEEE Sens. J.* **2016**, *16*, 5003–5009.

- (732) Salehi-Khojin, A.; Estrada, D.; Lin, K. Y.; Bae, M. H.; Xiong, F.; Pop, E.; Masel, R. I. Polycrystalline Graphene Ribbons as Chemiresistors. *Adv. Mater.* **2012**, *24*, 53–57.
- (733) Nagareddy, V. K.; Goss, J. P.; Wright, N. G.; Horsfall, A. B.; Hernandez, S. C.; Wheeler, V. D.; Nyakiti, L. O.; Myers-Ward, R. L.; Eddy, C. R., Jr.; Walton, S. G.; Gaskill, D. K. Oxygen Functionalised Epitaxial Graphene Sensors for Enhanced Polar Organic Chemical Vapour Detection. *2012 IEEE Sensors Proceedings*, 2012; pp 2126–2129.
- (734) Pan, B.; Xing, B. Adsorption Mechanisms of Organic Chemicals on Carbon Nanotubes. *Environ. Sci. Technol.* **2008**, *42*, 9005–9013.
- (735) Hutchison, G. R.; Ratner, M. A.; Marks, T. J.; Naaman, R. Adsorption of Polar Molecules on a Molecular Surface. *J. Phys. Chem. B* **2001**, *105*, 2881–2884.
- (736) Nallon, E. C.; Schnee, V. P.; Bright, C.; Polcha, M. P.; Li, Q. Chemical Discrimination with an Unmodified Graphene Chemical Sensor. *ACS Sens.* **2016**, *1*, 26–31.
- (737) Fattah, A.; Khatami, S.; Mayorga-Martinez, C. C.; Medina-Sanchez, M.; Baptista-Pires, L.; Merkoci, A. Graphene/Silicon Heterojunction Schottky Diode for Vapors Sensing Using Impedance Spectroscopy. *Small* **2014**, *10*, 4193–4199.
- (738) Hasani, A.; Dehsari, H. S.; Gavgani, J. N.; Shalamzari, E. K.; Salehi, A.; Taromi, F. A.; Mahyari, M. Sensor for Volatile Organic Compounds Using an Interdigitated Gold Electrode Modified with a Nanocomposite Made from Poly(3,4-Ethylenedioxythiophene)-Poly(Styrenesulfonate) and Ultra-Large Graphene Oxide. *Microchim. Acta* **2015**, *182*, 1551–1559.
- (739) Teradal, N. L.; Marx, S.; Morag, A.; Jelinek, R. Porous Graphene Oxide Chemi-Capacitor Vapor Sensor Array. *J. Mater. Chem. C* **2017**, *5*, 1128–1135.
- (740) Kulkarni, G. S.; Reddy, K.; Zhong, Z. H.; Fan, X. D. Graphene Nanoelectronic Heterodyne Sensor for Rapid and Sensitive Vapour Detection. *Nat. Commun.* **2014**, *5*, 4376.
- (741) Kybert, N. J.; Han, G. H.; Lerner, M. B.; Dattoli, E. N.; Esfandiar, A.; Johnson, A. T. C. Scalable Arrays of Chemical Vapor Sensors Based on DNA-Decorated Graphene. *Nano Res.* **2014**, *7*, 95–103.
- (742) Gautam, M.; Jayatissa, A. H. Detection of Organic Vapors by Graphene Films Functionalized with Metallic Nanoparticles. *J. Appl. Phys.* **2012**, *112*, 114326.
- (743) Nemade, K. R.; Waghuley, S. A. LPG Sensing Application of Graphene/CeO₂ Quantum Dots Composite. *AIP Conf. Proc.* **2013**, *1536*, 1258–1259.
- (744) Majumder, D.; Roy, S. Development of Low-ppm CO Sensors Using Pristine CeO₂ Nanospheres with High Surface Area. *ACS Omega* **2018**, *3*, 4433–4440.
- (745) Ranola, R. A. G.; Kalaw, J. M.; Sevilla, F. B., III Surface Adsorbed Reduced Graphene Oxide on Nylon-6 via Vacuum-Assisted Self-Assembly for Chemiresistor Sensing of Trimethylamine. *IEEE Sens. J.* **2016**, *16*, 1880–1886.
- (746) Ranola, R. A. G.; Kalaw, J. M.; Sevilla, F. B., III Graphene/Nylon-6 Chemiresistor Sensor for Trimethylamine Gas Sensing. In *Power and Energy Systems III*; Leeprechanon, N., Ed.; 2014; Vol. 492, pp 321–325.
- (747) Wood, J. D.; Wells, S. A.; Jariwala, D.; Chen, K. S.; Cho, E.; Sangwan, V. K.; Liu, X.; Lauhon, L. J.; Marks, T. J.; Hersam, M. C. Effective Passivation of Exfoliated Black Phosphorus Transistors against Ambient Degradation. *Nano Lett.* **2014**, *14*, 6964–6970.
- (748) Hanlon, D.; Backes, C.; Doherty, E.; Cucinotta, C. S.; Berner, N. C.; Boland, C.; Lee, K.; Harvey, A.; Lynch, P.; Gholamvand, Z.; Zhang, S.; Wang, K.; Moynihan, G.; Pokle, A.; Ramasse, Q. M.; McEvoy, N.; Blau, W. J.; Wang, J.; Abellan, G.; Hauke, F.; Hirsch, A.; Sanvito, S.; O'Regan, D. D.; Duesberg, G. S.; Nicolosi, V.; Coleman, J. N. Liquid Exfoliation of Solvent-Stabilized Few-Layer Black Phosphorus for Applications Beyond Electronics. *Nat. Commun.* **2015**, *6*, 8563.
- (749) Yasaei, P.; Behranginia, A.; Foroozan, T.; Asadi, M.; Kim, K.; Khalili-Araghi, F.; Salehi-Khojin, A. Stable and Selective Humidity Sensing Using Stacked Black Phosphorus Flakes. *ACS Nano* **2015**, *9*, 9898–9905.
- (750) Erande, M. B.; Pawar, M. S.; Late, D. J. Humidity Sensing and Photodetection Behavior of Electrochemically Exfoliated Atomically Thin-Layered Black Phosphorus Nanosheets. *ACS Appl. Mater. Interfaces* **2016**, *8*, 11548–11556.
- (751) Late, D. J. Liquid Exfoliation of Black Phosphorus Nanosheets and its Application as Humidity Sensor. *Microporous Mesoporous Mater.* **2016**, *225*, 494–503.
- (752) Miao, J.; Cai, L.; Zhang, S.; Nah, J.; Yeom, J.; Wang, C. Air-Stable Humidity Sensor Using Few-Layer Black Phosphorus. *ACS Appl. Mater. Interfaces* **2017**, *9*, 10019–10026.
- (753) Walia, S.; Sabri, Y.; Ahmed, T.; Field, M. R.; Ramanathan, R.; Arash, A.; Bhargava, S. K.; Sriram, S.; Bhaskaran, M.; Bansal, V.; Balendhran, S. Defining the Role of Humidity in the Ambient Degradation of Few-Layer Black Phosphorus. *2D Mater.* **2017**, *4*, 015025.
- (754) Kruse, J. A. Methanol Poisoning. *Intensive Care Med.* **1992**, *18*, 391–397.
- (755) Mayorga-Martinez, C. C.; Sofer, Z.; Pumera, M. Layered Black Phosphorus as a Selective Vapor Sensor. *Angew. Chem., Int. Ed.* **2015**, *54*, 14317–14320.
- (756) Feng, J.; Peng, L.; Wu, C.; Sun, X.; Hu, S.; Lin, C.; Dai, J.; Yang, J.; Xie, Y. Giant Moisture Responsiveness of VS₂ Ultrathin Nanosheets for Novel Touchless Positioning Interface. *Adv. Mater.* **2012**, *24*, 1969–1974.
- (757) Zhang, S.-L.; Choi, H.-H.; Yue, H.-Y.; Yang, W.-C. Controlled Exfoliation of Molybdenum Disulfide for Developing Thin Film Humidity Sensor. *Curr. Appl. Phys.* **2014**, *14*, 264–268.
- (758) Tahir, M. N.; Zink, N.; Eberhardt, M.; Therese, H. A.; Kolb, U.; Theato, P.; Tremel, W. Overcoming the Insolubility of Molybdenum Disulfide Nanoparticles through a High Degree of Sidewall Functionalization Using Polymeric Chelating Ligands. *Angew. Chem., Int. Ed.* **2006**, *45*, 4809–4815.
- (759) Pawbake, A. S.; Waykar, R. G.; Late, D. J.; Jadkar, S. R. Highly Transparent Wafer-Scale Synthesis of Crystalline WS₂ Nanoparticle Thin Film for Photodetector and Humidity-Sensing Applications. *ACS Appl. Mater. Interfaces* **2016**, *8*, 3359–3365.
- (760) Guo, H. Y.; Lan, C. Y.; Zhou, Z. F.; Sun, P. H.; Wei, D. P.; Li, C. Transparent, Flexible, and Stretchable WS₂ Based Humidity Sensors for Electronic Skin. *Nanoscale* **2017**, *9*, 6246–6253.
- (761) Selin, N. E. Global Biogeochemical Cycling of Mercury: A Review. *Annual Review of Environment and Resources* **2009**, *34*, 43–63.
- (762) <https://www.osha.gov/SLTC/etools/hospital/hazards/mercury/mercury.html>.
- (763) Wang, D.; Zhou, K.; Sun, M.; Fang, Z.; Liu, X.; Sun, X. Room Temperature Elemental Mercury Sensor Using MoS₂-PANI Nano-Sheet-Flowers Composite. *Anal. Methods* **2013**, *5*, 6576.
- (764) Friedman, A. L.; Keith Perkins, F.; Cobas, E.; Jernigan, G. G.; Campbell, P. M.; Hanbicki, A. T.; Jonker, B. T. Chemical Vapor Sensing of Two-Dimensional MoS₂ Field Effect Transistor Devices. *Solid-State Electron.* **2014**, *101*, 2–7.
- (765) Zonneville, M. C.; Hoffmann, R.; Harris, S. Thiophene Hydrodesulfurization on MoS₂; Theoretical Aspects. *Surf. Sci.* **1988**, *199*, 320–360.
- (766) Galvan, D. H.; Antúnez-García, J.; Moyado, S. F. Electronic Properties of NbSe₂ over Graphene: A Meticulous Theoretical Analysis. *OALib* **2017**, *04*, 1–9.
- (767) Yan, H.; Song, P.; Zhang, S.; Yang, Z.; Wang, Q. Dispersed SnO₂ Nanoparticles on MoS₂ Nanosheets for Superior Gas-Sensing Performances to Ethanol. *RSC Adv.* **2015**, *5*, 79593–79599.
- (768) Huo, N.; Yang, S.; Wei, Z.; Li, S. S.; Xia, J. B.; Li, J. Photoresponsive and Gas Sensing Field-Effect Transistors Based on Multilayer WS₂ Nanoflakes. *Sci. Rep.* **2015**, *4*, 5209.
- (769) Dwivedi, P.; Das, S.; Dhanekar, S. Wafer-Scale Synthesized MoS₂/Porous Silicon Nanostructures for Efficient and Selective Ethanol Sensing at Room Temperature. *ACS Appl. Mater. Interfaces* **2017**, *9*, 21017–21024.

- (770) Shur, M.; Rumyantsev, S.; Jiang, C.; Samnakay, R.; Renteria, J.; Balandin, A. A. Selective Gas Sensing with MoS₂ Thin Film Transistors. *2014 IEEE Sensors* **2014**, 55–57.
- (771) Samnakay, R.; Jiang, C.; Rumyantsev, S. L.; Shur, M. S.; Balandin, A. A. Selective Chemical Vapor Sensing with Few-Layer MoS₂ Thin-Film Transistors: Comparison with Graphene Devices. *Appl. Phys. Lett.* **2015**, 106, 023115.
- (772) Kim, J. S.; Yoo, H. W.; Choi, H. O.; Jung, H. T. Tunable Volatile Organic Compounds Sensor by Using Thiolated Ligand Conjugation on MoS₂. *Nano Lett.* **2014**, 14, 5941–5947.
- (773) Sreeprasad, T. S.; Nguyen, P.; Kim, N.; Berry, V. Controlled, Defect-Guided, Metal-Nanoparticle Incorporation onto MoS₂ via Chemical and Microwave Routes: Electrical, Thermal, and Structural Properties. *Nano Lett.* **2013**, 13, 4434–4441.
- (774) Cho, S. Y.; Koh, H. J.; Yoo, H. W.; Kim, J. S.; Jung, H. T. Tunable Volatile-Organic-Compound Sensor by Using Au Nanoparticle Incorporation on MoS₂. *ACS Sens.* **2017**, 2, 183–189.
- (775) Hong, X.; Liu, J.; Zheng, B.; Huang, X.; Zhang, X.; Tan, C.; Chen, J.; Fan, Z.; Zhang, H. A Universal Method for Preparation of Noble Metal Nanoparticle-Decorated Transition Metal Dichalcogenide Nanobelts. *Adv. Mater.* **2014**, 26, 6250–6254.
- (776) Umar, A.; Akhtar, M. S.; Dar, G. N.; Abaker, M.; Al-Hajry, A.; Baskoutas, S. Visible-Light-Driven Photocatalytic and Chemical Sensing Properties of SnS₂ Nanoflakes. *Talanta* **2013**, 114, 183–190.
- (777) Jing, Z.; Zhan, J. Fabrication and Gas-Sensing Properties of Porous ZnO Nanoplates. *Adv. Mater.* **2008**, 20, 4547–4551.
- (778) Zhang, J.; Liu, X.; Wu, S.; Cao, B.; Zheng, S. One-Pot Synthesis of Au-Supported ZnO Nanoplates with Enhanced Gas Sensor Performance. *Sens. Actuators, B* **2012**, 169, 61–66.
- (779) Zhang, L.; Zhao, J.; Lu, H.; Li, L.; Zheng, J.; Li, H.; Zhu, Z. Facile Synthesis and Ultrahigh Ethanol Response of Hierarchically Porous ZnO Nanosheets. *Sens. Actuators, B* **2012**, 161, 209–215.
- (780) Meng, F.; Hou, N.; Ge, S.; Sun, B.; Jin, Z.; Shen, W.; Kong, L.; Guo, Z.; Sun, Y.; Wu, H.; Wang, C.; Li, M. Flower-Like Hierarchical Structures Consisting of Porous Single-Crystalline ZnO Nanosheets and Their Gas Sensing Properties to Volatile Organic Compounds (VOCs). *J. Alloys Compd.* **2015**, 626, 124–130.
- (781) Li, K.-M.; Li, Y.-J.; Lu, M.-Y.; Kuo, C.-I.; Chen, L.-J. Direct Conversion of Single-Layer SnO₂ Nanoplates to Multi-Layer SnO₂ nanoplates with Enhanced Ethanol Sensing Properties. *Adv. Funct. Mater.* **2009**, 19, 2453–2456.
- (782) Sun, P.; Cao, Y.; Liu, J.; Sun, Y.; Ma, J.; Lu, G. Dispersive SnO₂ Nanosheets: Hydrothermal Synthesis and Gas-Sensing Properties. *Sens. Actuators, B* **2011**, 156, 779–783.
- (783) Zhang, L.; Yin, Y. Hierarchically Mesoporous SnO₂ Nanosheets: Hydrothermal Synthesis and Highly Ethanol-Sensitive Properties Operated at Low Temperature. *Sens. Actuators, B* **2013**, 185, 594–601.
- (784) Sun, P.; Zhao, W.; Cao, Y.; Guan, Y.; Sun, Y.; Lu, G. Porous SnO₂ Hierarchical Nanosheets: Hydrothermal Preparation, Growth Mechanism, and Gas Sensing Properties. *CrystEngComm* **2011**, 13, 3718.
- (785) Lou, Z.; Wang, L.; Wang, R.; Fei, T.; Zhang, T. Synthesis and Ethanol Sensing Properties of SnO₂ Nanosheets via a Simple Hydrothermal Route. *Solid-State Electron.* **2012**, 76, 91–94.
- (786) Guo, J.; Zhang, J.; Ju, D.; Xu, H.; Cao, B. Three-Dimensional SnO₂ Microstructures Assembled by Porous Nanosheets and Their Superior Performance for Gas Sensing. *Powder Technol.* **2013**, 250, 40–45.
- (787) Zhou, Q.; Chen, W.; Li, J.; Tang, C.; Zhang, H. Nanosheet-Assembled Flower-Like SnO₂ Hierarchical Structures with Enhanced Gas-Sensing Performance. *Mater. Lett.* **2015**, 161, 499–502.
- (788) Li, T.; Zeng, W.; Long, H.; Wang, Z. Nanosheet-Assembled Hierarchical SnO₂ Nanostructures for Efficient Gas-Sensing Applications. *Sens. Actuators, B* **2016**, 231, 120–128.
- (789) Liu, Y.; Jiao, Y.; Zhang, Z.; Qu, F.; Umar, A.; Wu, X. Hierarchical SnO₂ Nanostructures Made of Intermingled Ultrathin Nanosheets for Environmental Remediation, Smart Gas Sensor, and Supercapacitor Applications. *ACS Appl. Mater. Interfaces* **2014**, 6, 2174–2184.
- (790) Zhao, C.; Fu, J.; Zhang, Z.; Xie, E. Enhanced Ethanol Sensing Performance of Porous Ultrathin NiO Nanosheets with Neck-Connected Networks. *RSC Adv.* **2013**, 3, 4018.
- (791) Wang, J.; Zeng, W.; Wang, Z. Assembly of 2D Nanosheets into 3D Flower-Like NiO: Synthesis and the Influence of Petal Thickness on Gas-Sensing Properties. *Ceram. Int.* **2016**, 42, 4567–4573.
- (792) Jia, X.; Fan, H.; Yang, W. Hydrothermal Synthesis and Primary Gas Sensing Properties of CuO Nanosheets. *J. Dispersion Sci. Technol.* **2010**, 31, 866–869.
- (793) Che, H.; Liu, A.; Zhang, X.; Hou, J.; Mu, J.; He, H. Two-Dimensional Nanosheets-Assembled Flower-Like Co₃O₄ Microspheres and their Gas Sensing Performance. *Nano* **2014**, 09, 1450071.
- (794) Chen, D.; Hou, X.; Wen, H.; Wang, Y.; Wang, H.; Li, X.; Zhang, R.; Lu, H.; Xu, H.; Guan, S.; Sun, J.; Gao, L. The Enhanced Alcohol-Sensing Response of Ultrathin WO₃ Nanoplates. *Nanotechnology* **2010**, 21, 035501.
- (795) Ji, F.; Ren, X.; Zheng, X.; Liu, Y.; Pang, L.; Jiang, J.; Liu, S. F. 2D -MoO₃ Nanosheets for Superior Gas Sensors. *Nanoscale* **2016**, 8, 8696–8703.
- (796) Liu, C.; Lu, H.; Zhang, J.; Yang, Z.; Zhu, G.; Yin, F.; Gao, J.; Chen, C.; Xin, X. Abnormal P-Type Sensing Response of TiO₂ Nanosheets with Exposed {001} Facets. *J. Alloys Compd.* **2017**, 705, 112–117.
- (797) Guo, W.; Fu, M.; Zhai, C.; Wang, Z. Hydrothermal Synthesis and Gas-Sensing Properties of Ultrathin Hexagonal ZnO Nanosheets. *Ceram. Int.* **2014**, 40, 2295–2298.
- (798) Li, G.; Wang, X.; Ding, H.; Zhang, T. A Facile Synthesis Method for Ni(OH)₂ Ultrathin Nanosheets and Their Conversion to Porous NiO Nanosheets Used for Formaldehyde Sensing. *RSC Adv.* **2012**, 2, 13018.
- (799) Zhang, Z.; Wen, Z.; Ye, Z.; Zhu, L. Gas Sensors Based on Ultrathin Porous Co₃O₄ Nanosheets to Detect Acetone at Low Temperature. *RSC Adv.* **2015**, 5, 59976–59982.
- (800) Yang, C.; Xiao, F.; Wang, J.; Su, X. 3D Flower- and 2D Sheet-Like CuO Nanostructures: Microwave-Assisted Synthesis and Application in Gas Sensors. *Sens. Actuators, B* **2015**, 207, 177–185.
- (801) Wan, W.; Li, Y.; Ren, X.; Zhao, Y.; Gao, F.; Zhao, H. 2D SnO₂ Nanosheets: Synthesis, Characterization, Structures, and Excellent Sensing Performance to Ethylene Glycol. *Nanomaterials* **2018**, 8, 112.
- (802) Xu, J. Q.; Xue, Z. G.; Qin, N.; Cheng, Z. X.; Xiang, Q. The Crystal Facet-Dependent Gas Sensing Properties of ZnO Nanosheets: Experimental and Computational Study. *Sens. Actuators, B* **2017**, 242, 148–157.
- (803) Stassen, I.; Bueken, B.; Reinsch, H.; Oudenhoven, J. F. M.; Wouters, D.; Hajek, J.; Van Speybroeck, V.; Stock, N.; Vereecken, P. M.; Van Schaijk, R.; De Vos, D.; Ameloot, R. Towards Metal–Organic Framework Based Field Effect Chemical Sensors: Uio-66-Nh2 for Nerve Agent Detection. *Chem. Sci.* **2016**, 7, 5827–5832.
- (804) Hoppe, B.; Hindricks, K. D. J.; Warwas, D. P.; Schulze, H. A.; Mohmeyer, A.; Pinkvos, T. J.; Zailskas, S.; Krey, M. R.; Belke, C.; König, S.; Fröba, M.; Haug, R. J.; Behrens, P. Graphene-Like Metal–Organic Frameworks: Morphology Control, Optimization of Thin Film Electrical Conductivity and Fast Sensing Applications. *CrystEngComm* **2018**, 20, 6458.
- (805) Tomer, V. K.; Thangaraj, N.; Gahlot, S.; Kailasam, K. Cubic Mesoporous Ag@CN: A High Performance Humidity Sensor. *Nanoscale* **2016**, 8, 19794–19803.
- (806) Tomer, V. K.; Duhan, S.; Sharma, A. K.; Malik, R.; Nehra, S. P.; Devi, S. One Pot Synthesis of Mesoporous ZnO–SiO₂ Nanocomposite as High Performance Humidity Sensor. *Colloids Surf., A* **2015**, 483, 121–128.
- (807) Zhang, Z.; Huang, J.; Yuan, Q.; Dong, B. Intercalated Graphitic Carbon Nitride: A Fascinating Two-Dimensional Nanomaterial for an Ultra-Sensitive Humidity Nanosensor. *Nanoscale* **2014**, 6, 9250–9256.

- (808) Sajid, M.; Kim, H. B.; Lim, J. H.; Choi, K. H. Liquid-Assisted Exfoliation of 2D *h*-BN Flakes and Their Dispersion in PEO to Fabricate Highly Specific and Stable Linear Humidity Sensors. *J. Mater. Chem. C* **2018**, *6*, 1421–1432.
- (809) Chung, Y.; Park, H.; Lee, E.; Kim, S.-H.; Kim, D.-J. Communication—Gas Sensing Behaviors of Electrophoretically Deposited Nickel Oxide Films from Morphologically Tailored Particles. *J. Electrochem. Soc.* **2016**, *163*, B624–B626.
- (810) Kim, H.-J.; Lee, J.-H. Highly Sensitive and Selective Gas Sensors Using P-Type Oxide Semiconductors: Overview. *Sens. Actuators, B* **2014**, *192*, 607–627.
- (811) Shahzad, F.; Alhabeb, M.; Hatter, C. B.; Anasori, B.; Man Hong, S.; Koo, C. M.; Gogotsi, Y. Electromagnetic Interference Shielding with 2D Transition Metal Carbides (MXenes). *Science* **2016**, *353*, 1137–1140.
- (812) Zhang, H.; Kulkarni, A.; Kim, H.; Woo, D.; Kim, Y.-J.; Hong, B. H.; Choi, J.-B.; Kim, T. Detection of Acetone Vapor Using Graphene on Polymer Optical Fiber. *J. Nanosci. Nanotechnol.* **2011**, *11*, 5939–5943.
- (813) Kim, N.-H.; Choi, S.-J.; Kim, S.-J.; Cho, H.-J.; Jang, J.-S.; Koo, W.-T.; Kim, M.; Kim, I.-D. Highly Sensitive and Selective Acetone Sensing Performance of WO_3 Nanofibers Functionalized by Rh_2O_3 Nanoparticles. *Sens. Actuators, B* **2016**, *224*, 185–192.
- (814) Koo, W. T.; Yu, S.; Choi, S. J.; Jang, J. S.; Cheong, J. Y.; Kim, I. D. Nanoscale Pdo Catalyst Functionalized Co_3O_4 Hollow Nanocages Using MOF Templates for Selective Detection of Acetone Molecules in Exhaled Breath. *ACS Appl. Mater. Interfaces* **2017**, *9*, 8201–8210.
- (815) Chen, W.; Qin, Z.; Liu, Y.; Zhang, Y.; Li, Y.; Shen, S.; Wang, Z. M.; Song, H. Z. Promotion on Acetone Sensing of Single SnO_2 Nanobelt by Eu Doping. *Nanoscale Res. Lett.* **2017**, *12*, 405.
- (816) Zhang, L.; Li, C.; Liu, A. R.; Shi, G. Q. Electrosynthesis of Graphene Oxide/Polypprylene Composite Films and Their Applications for Sensing Organic Vapors. *J. Mater. Chem.* **2012**, *22*, 8438–8443.
- (817) Zhu, C.; Xu, F.; Zhang, L.; Li, M.; Chen, J.; Xu, S.; Huang, G.; Chen, W.; Sun, L. Ultrafast Preparation of Black Phosphorus Quantum Dots for Efficient Humidity Sensing. *Chem. - Eur. J.* **2016**, *22*, 7357–7362.
- (818) Su, P.-G.; Shiu, W.-L.; Tsai, M.-S. Flexible Humidity Sensor Based on Au Nanoparticles/Graphene Oxide/Thiolated Silica Sol-Gel Film. *Sens. Actuators, B* **2015**, *216*, 467–475.
- (819) Mauter, M. S.; Elimelech, M. Environmental Applications of Carbon-Based Nanomaterials. *Environ. Sci. Technol.* **2008**, *42*, 5843–5859.
- (820) Perreault, F.; Fonseca de Faria, A.; Elimelech, M. Environmental Applications of Graphene-Based Nanomaterials. *Chem. Soc. Rev.* **2015**, *44*, 5861–5896.
- (821) Ambrosi, A.; Chua, C. K.; Bonanni, A.; Pumera, M. Electrochemistry of Graphene and Related Materials. *Chem. Rev.* **2014**, *114*, 7150–7188.
- (822) Blake, P.; Brimicombe, P. D.; Nair, R. R.; Booth, T. J.; Jiang, D.; Schedin, F.; Ponomarenko, L. A.; Morozov, S. V.; Gleeson, H. F.; Hill, E. W.; Geim, A. K.; Novoselov, K. S. Graphene-Based Liquid Crystal Device. *Nano Lett.* **2008**, *8*, 1704–1708.
- (823) Aragay, G.; Merkoçi, A. Nanomaterials Application in Electrochemical Detection of Heavy Metals. *Electrochim. Acta* **2012**, *84*, 49–61.
- (824) Gong, X.; Liu, G.; Li, Y.; Yu, D. Y. W.; Teoh, W. Y. Functionalized-Graphene Composites: Fabrication and Applications in Sustainable Energy and Environment. *Chem. Mater.* **2016**, *28*, 8082–8118.
- (825) Gumpu, M. B.; Sethuraman, S.; Krishnan, U. M.; Rayappan, J. B. B. A Review on Detection of Heavy Metal Ions in Water – an Electrochemical Approach. *Sens. Actuators, B* **2015**, *213*, 515–533.
- (826) Zhu, L.; Xu, L.; Huang, B.; Jia, N.; Tan, L.; Yao, S. Simultaneous Determination of Cd(II) and Pb(II) Using Square Wave Anodic Stripping Voltammetry at a Gold Nanoparticle-Graphene-Cysteine Composite Modified Bismuth Film Electrode. *Electrochim. Acta* **2014**, *115*, 471–477.
- (827) Wen, Y.; Li, F. Y.; Dong, X.; Zhang, J.; Xiong, Q.; Chen, P. The Electrical Detection of Lead Ions Using Gold-Nanoparticle- and DNAzyme-Functionalized Graphene Device. *Adv. Healthcare Mater.* **2013**, *2*, 271–274.
- (828) Xuan, X.; Hossain, M. F.; Park, J. Y. A Fully Integrated and Miniaturized Heavy-Metal-Detection Sensor Based on Micro-Patterned Reduced Graphene Oxide. *Sci. Rep.* **2016**, *6*, 33125.
- (829) Li, J.; Guo, S.; Zhai, Y.; Wang, E. High-Sensitivity Determination of Lead and Cadmium Based on the Nafion-Graphene Composite Film. *Anal. Chim. Acta* **2009**, *649*, 196–201.
- (830) Willemse, C. M.; Tilhomelang, K.; Jahed, N.; Baker, P. G.; Iwuoha, E. I. Metallo-Graphene Nanocomposite Electrocatalytic Platform for the Determination of Toxic Metal Ions. *Sensors* **2011**, *11*, 3970–3987.
- (831) Kong, N.; Liu, J.; Kong, Q.; Wang, R.; Barrow, C. J.; Yang, W. Graphene Modified Gold Electrode via $\pi-\pi$ Stacking Interaction for Analysis of Cu^{2+} and Pb^{2+} . *Sens. Actuators, B* **2013**, *178*, 426–433.
- (832) Gong, X.; Bi, Y.; Zhao, Y.; Liu, G.; Teoh, W. Y. Graphene Oxide-Based Electrochemical Sensor: A Platform for Ultrasensitive Detection of Heavy Metal Ions. *RSC Adv.* **2014**, *4*, 24653–24657.
- (833) Zhang, Y.; Qi, M.; Liu, G. C–C Bonding of Graphene Oxide on 4-Aminophenyl Modified Gold Electrodes Towards Simultaneous Detection of Heavy Metal Ions. *Electroanalysis* **2015**, *27*, 1110–1118.
- (834) Liu, J.; Fu, S.; Yuan, B.; Li, Y.; Deng, Z. Toward a Universal "Adhesive Nanosheet" for the Assembly of Multiple Nanoparticles Based on a Protein-Induced Reduction/Decoration of Graphene Oxide. *J. Am. Chem. Soc.* **2010**, *132*, 7279–7281.
- (835) Williams, G.; Seger, B.; Kamat, P. V. TiO_2 -Graphene Nanocomposites. UV-Assisted Photocatalytic Reduction of Graphene Oxide. *ACS Nano* **2008**, *2*, 1487–1491.
- (836) Gong, J.; Zhou, T.; Song, D.; Zhang, L. Monodispersed Au Nanoparticles Decorated Graphene as an Enhanced Sensing Platform for Ultrasensitive Stripping Voltammetric Detection of Mercury(II). *Sens. Actuators, B* **2010**, *150*, 491–497.
- (837) Wei, Y.; Gao, C.; Meng, F.-L.; Li, H.-H.; Wang, L.; Liu, J.-H.; Huang, X.-J. SnO_2 /Reduced Graphene Oxide Nanocomposite for the Simultaneous Electrochemical Detection of Cadmium(II), Lead(II), Copper(II), and Mercury(II): An Interesting Favorable Mutual Interference. *J. Phys. Chem. C* **2012**, *116*, 1034–1041.
- (838) Park, J. W.; Park, S. J.; Kwon, O. S.; Lee, C.; Jang, J. High-Performance Hg^{2+} FET -Type Sensors Based on Reduced Graphene Oxide-Polyfuran Nanohybrids. *Analyst* **2014**, *139*, 3852–3855.
- (839) Zhang, Y.; Xie, J.; Liu, Y.; Pang, P.; Feng, L.; Wang, H.; Wu, Z.; Yang, W. Simple and Signal-Off Electrochemical Biosensor for Mercury(II) Based on Thymine-Mercury-Thymine Hybridization Directly on Graphene. *Electrochim. Acta* **2015**, *170*, 210–217.
- (840) Yu, C.; Guo, Y.; Liu, H.; Yan, N.; Xu, Z.; Yu, G.; Fang, Y.; Liu, Y. Ultrasensitive and Selective Sensing of Heavy Metal Ions with Modified Graphene. *Chem. Commun.* **2013**, *49*, 6492–6494.
- (841) Tan, F.; Cong, L.; Saucedo, N. M.; Gao, J.; Li, X.; Mulchandani, A. An Electrochemically Reduced Graphene Oxide Chemiresistive Sensor for Sensitive Detection of Hg^{2+} Ion in Water Samples. *J. Hazard. Mater.* **2016**, *320*, 226–233.
- (842) Zhang, T.; Cheng, Z.; Wang, Y.; Li, Z.; Wang, C.; Li, Y.; Fang, Y. Self-Assembled 1-Octadecanethiol Monolayers on Graphene for Mercury Detection. *Nano Lett.* **2010**, *10*, 4738–4741.
- (843) Afsharmani, N.; Ulutuklu, B.; Saygin, V.; Baykara, M. Z. Self-Assembled Molecular Films of Alkanethiols on Graphene for Heavy Metal Sensing. *J. Phys. Chem. C* **2018**, *122*, 474–480.
- (844) Liu, L.; Wang, C.; Wang, G. Novel Cysteic Acid/Reduced Graphene Oxide Composite Film Modified Electrode for the Selective Detection of Trace Silver Ions in Natural Waters. *Anal. Methods* **2013**, *5*, 5812.
- (845) Wonsawat, W.; Chuanuwatanakul, S.; Dungchai, W.; Punrat, E.; Motomizu, S.; Chailapakul, O. Graphene-Carbon Paste Electrode for Cadmium and Lead Ion Monitoring in a Flow-Based System. *Talanta* **2012**, *100*, 282–289.

- (846) Zhao, Z.-Q.; Chen, X.; Yang, Q.; Liu, J.-H.; Huang, X.-J. Beyond the Selective Adsorption of Polypyrrole-Reduced Graphene Oxide Nanocomposite toward Hg^{2+} : Ultra-Sensitive and -Selective Sensing Pb^{2+} by Stripping Voltammetry. *Electrochem. Commun.* **2012**, *23*, 21–24.
- (847) Gao, C.; Yu, X. Y.; Xu, R. X.; Liu, J. H.; Huang, X. J. AlOOH-Reduced Graphene Oxide Nanocomposites: One-Pot Hydrothermal Synthesis and Their Enhanced Electrochemical Activity for Heavy Metal Ions. *ACS Appl. Mater. Interfaces* **2012**, *4*, 4672–4682.
- (848) Silwana, B.; van der Horst, C.; Iwuoha, E.; Somerset, V. Reduced Graphene Oxide Impregnated Antimony Nanoparticle Sensor for Electroanalysis of Platinum Group Metals. *Electroanalysis* **2016**, *28*, 1597–1607.
- (849) Ziolkowski, R.; Górska, Ł.; Malinowska, E. Carboxylated Graphene as a Sensing Material for Electrochemical Uranyl Ion Detection. *Sens. Actuators, B* **2017**, *238*, 540–547.
- (850) Wu, Q. Y.; Lan, J. H.; Wang, C. Z.; Xiao, C. L.; Zhao, Y. L.; Wei, Y. Z.; Chai, Z. F.; Shi, W. Q. Understanding the Bonding Nature of Uranyl Ion and Functionalized Graphene: A Theoretical Study. *J. Phys. Chem. A* **2014**, *118*, 2149–2158.
- (851) Kumar, S.; Bhanjana, G.; Dilbaghi, N.; Kumar, R.; Umar, A. Fabrication and Characterization of Highly Sensitive and Selective Arsenic Sensor Based on Ultra-Thin Graphene Oxide Nanosheets. *Sens. Actuators, B* **2016**, *227*, 29–34.
- (852) Li, F.; Ye, J.; Zhou, M.; Gan, S.; Zhang, Q.; Han, D.; Niu, L. All-Solid-State Potassium-Selective Electrode Using Graphene as the Solid Contact. *Analyst* **2012**, *137*, 618–623.
- (853) Dutta, J. C. In *Ion Sensitive Field Effect Transistor for Applications in Bioelectronic Sensors: A Research Review*, 2012 2nd National Conference on Computational Intelligence and Signal Processing (CISP), 2012; pp 185–191.
- (854) Patil, A. V.; Fernandes, F. B.; Bueno, P. R.; Davis, J. J. Graphene-Based Protein Biomarker Detection. *Bioanalysis* **2015**, *7*, 725–742.
- (855) Fu, W.; Jiang, L.; van Geest, E. P.; Lima, L. M.; Schneider, G. F. Sensing at the Surface of Graphene Field-Effect Transistors. *Adv. Mater.* **2017**, *29*, 1603610.
- (856) Fu, W.; Nef, C.; Tarasov, A.; Wipf, M.; Stoop, R.; Knopfmacher, O.; Weiss, M.; Calame, M.; Schonenberger, C. High Mobility Graphene Ion-Sensitive Field-Effect Transistors by Non-covalent Functionalization. *Nanoscale* **2013**, *5*, 12104–12110.
- (857) Dankerl, M.; Hauf, M. V.; Lippert, A.; Hess, L. H.; Birner, S.; Sharp, I. D.; Mahmood, A.; Mallet, P.; Veullien, J.-Y.; Stutzmann, M.; Garrido, J. A. Graphene Solution-Gated Field-Effect Transistor Array for Sensing Applications. *Adv. Funct. Mater.* **2010**, *20*, 3117–3124.
- (858) Zhan, B.; Li, C.; Yang, J.; Jenkins, G.; Huang, W.; Dong, X. Graphene Field-Effect Transistor and Its Application for Electronic Sensing. *Small* **2014**, *10*, 4042–4065.
- (859) Li, H.; Zhu, Y.; Islam, M. S.; Rahman, M. A.; Walsh, K. B.; Koley, G. Graphene Field Effect Transistors for Highly Sensitive and Selective Detection of K^+ Ions. *Sens. Actuators, B* **2017**, *253*, 759–765.
- (860) Mao, S.; Pu, H.; Chang, J.; Sui, X.; Zhou, G.; Ren, R.; Chen, Y.; Chen, J. Ultrasensitive Detection of Orthophosphate Ions with Reduced Graphene Oxide/Ferritin Field-Effect Transistor Sensors. *Environ. Sci.: Nano* **2017**, *4*, 856–863.
- (861) Sudibya, H. G.; He, Q.; Zhang, H.; Chen, P. Electrical Detection of Metal Ions Using Field-Effect Transistors Based on Micropatterned Reduced Graphene Oxide Films. *ACS Nano* **2011**, *5*, 1990–1994.
- (862) Sofue, Y.; Ohno, Y.; Maehashi, K.; Inoue, K.; Matsumoto, K. Highly Sensitive Electrical Detection of Sodium Ions Based on Graphene Field-Effect Transistors. *Jpn. J. Appl. Phys.* **2011**, *50*, 06GE07.
- (863) Liu, X.; Ye, C.; Li, X.; Cui, N.; Wu, T.; Du, S.; Wei, Q.; Fu, L.; Yin, J.; Lin, C. T. Highly Sensitive and Selective Potassium Ion Detection Based on Graphene Hall Effect Biosensors. *Materials* **2018**, *11*, 399.
- (864) Du, Y.; Liu, H.; Deng, Y.; Ye, P. D. Device Perspective for Black Phosphorus Field-Effect Transistors: Contact Resistance, Ambipolar Behavior, and Scaling. *ACS Nano* **2014**, *8*, 10035–10042.
- (865) Xia, F.; Wang, H.; Jia, Y. Rediscovering Black Phosphorus as an Anisotropic Layered Material for Optoelectronics and Electronics. *Nat. Commun.* **2014**, *5*, 4458.
- (866) Saito, Y.; Iwasa, Y. Ambipolar Insulator-to-Metal Transition in Black Phosphorus by Ionic-Liquid Gating. *ACS Nano* **2015**, *9*, 3192–3198.
- (867) Koenig, S. P.; Doganov, R. A.; Schmidt, H.; Castro Neto, A. H.; Özyilmaz, B. Electric Field Effect in Ultrathin Black Phosphorus. *Appl. Phys. Lett.* **2014**, *104*, 103106.
- (868) Li, P.; Zhang, D.; Liu, J.; Chang, H.; Sun, Y.; Yin, N. Air-Stable Black Phosphorus Devices for Ion Sensing. *ACS Appl. Mater. Interfaces* **2015**, *7*, 24396–24402.
- (869) Kou, L.; Fu, M.; Liang, R. Solid-Contact Ca^{2+} -Selective Electrodes Based on Two-Dimensional Black Phosphorus as Ion-to-Electron Transducers. *RSC Adv.* **2017**, *7*, 43905–43908.
- (870) Li, P.; Zhang, D.; Wu, J.; Cao, Y.; Wu, Z. Flexible Integrated Black Phosphorus Sensor Arrays for High Performance Ion Sensing. *Sens. Actuators, B* **2018**, *273*, 358–364.
- (871) Ping, J.; Fan, Z.; Sindoro, M.; Ying, Y.; Zhang, H. Recent Advances in Sensing Applications of Two-Dimensional Transition Metal Dichalcogenide Nanosheets and Their Composites. *Adv. Funct. Mater.* **2017**, *27*, 1605817.
- (872) Zhou, G.; Chang, J.; Pu, H.; Shi, K.; Mao, S.; Sui, X.; Ren, R.; Cui, S.; Chen, J. Ultrasensitive Mercury Ion Detection Using DNA-Functionalized Molybdenum Disulfide Nanosheet/Gold Nanoparticle Hybrid Field-Effect Transistor Device. *ACS Sens.* **2016**, *1*, 295–302.
- (873) Jiang, S.; Cheng, R.; Ng, R.; Huang, Y.; Duan, X. Highly Sensitive Detection of Mercury(II) Ions with Few-Layer Molybdenum Disulfide. *Nano Res.* **2015**, *8*, 257–262.
- (874) Ghanei-Motlagh, M.; Taher, M. A. A Novel Electrochemical Sensor Based on Silver/Halloysite Nanotube/Molybdenum Disulfide Nanocomposite for Efficient Nitrite Sensing. *Biosens. Bioelectron.* **2018**, *109*, 279–285.
- (875) Waheed, A.; Mansha, M.; Ullah, N. Nanomaterials-Based Electrochemical Detection of Heavy Metals in Water: Current Status, Challenges and Future Direction. *TrAC, Trends Anal. Chem.* **2018**, *105*, 37–51.
- (876) Liu, Z.-G.; Chen, X.; Liu, J.-H.; Huang, X.-J. Well-Arranged Porous Co_3O_4 Microsheets for Electrochemistry of $Pb(II)$ Revealed by Stripping Voltammetry. *Electrochem. Commun.* **2013**, *30*, 59–62.
- (877) Yu, L.; Zhang, P.; Dai, H.; Chen, L.; Ma, H.; Lin, M.; Shen, D. An Electrochemical Sensor Based on Co_3O_4 Nanosheets for Lead Ions Determination. *RSC Adv.* **2017**, *7*, 39611–39616.
- (878) Zhang, J.; Liao, J.; Yang, F.; Xu, M.; Lin, S. Regulation of the Electroanalytical Performance of Ultrathin Titanium Dioxide Nanosheets toward Lead Ions by Non-Metal Doping. *Nanomaterials* **2017**, *7*, 327.
- (879) Mendecki, L.; Mirica, K. A. Conductive Metal–Organic Frameworks as Ion-to-Electron Transducers in Potentiometric Sensors. *ACS Appl. Mater. Interfaces* **2018**, *10*, 19248–19257.
- (880) Chen, Y.; Tan, C.; Zhang, H.; Wang, L. Two-Dimensional Graphene Analogues for Biomedical Applications. *Chem. Soc. Rev.* **2015**, *44*, 2681–2701.
- (881) Chimene, D.; Alge, D. L.; Gaharwar, A. K. Two-Dimensional Nanomaterials for Biomedical Applications: Emerging Trends and Future Prospects. *Adv. Mater.* **2015**, *27*, 7261–7284.
- (882) Khin, M. M.; Nair, A. S.; Babu, V. J.; Murugan, R.; Ramakrishna, S. A Review on Nanomaterials for Environmental Remediation. *Energy Environ. Sci.* **2012**, *5*, 8075–8109.
- (883) Roy, S.; Soin, N.; Bajpai, R.; Misra, D. S.; McLaughlin, J. A.; Roy, S. S. Graphene Oxide for Electrochemical Sensing Applications. *J. Mater. Chem.* **2011**, *21*, 14725.
- (884) Kang, X.; Wang, J.; Wu, H.; Aksay, I. A.; Liu, J.; Lin, Y. Glucose Oxidase-Graphene-Chitosan Modified Electrode for Direct Electrochemistry and Glucose Sensing. *Biosens. Bioelectron.* **2009**, *25*, 901–905.

- (885) Wang, Y.; Shao, Y.; Matson, D. W.; Li, J.; Lin, Y. Nitrogen-Doped Graphene and Its Application in Electrochemical Biosensing. *ACS Nano* **2010**, *4*, 1790–1798.
- (886) Alwarappan, S.; Liu, C.; Kumar, A.; Li, C.-Z. Enzyme-Doped Graphene Nanosheets for Enhanced Glucose Biosensing. *J. Phys. Chem. C* **2010**, *114*, 12920–12924.
- (887) Zeng, G.; Xing, Y.; Gao, J.; Wang, Z.; Zhang, X. Unconventional Layer-by-Layer Assembly of Graphene Multilayer Films for Enzyme-Based Glucose and Maltose Biosensing. *Langmuir* **2010**, *26*, 15022–15026.
- (888) Shan, C.; Yang, H.; Song, J.; Han, D.; Ivaska, A.; Niu, L. Direct Electrochemistry of Glucose Oxidase and Biosensing for Glucose Based on Graphene. *Anal. Chem.* **2009**, *81*, 2378–2382.
- (889) Chen, Y.; Li, Y.; Sun, D.; Tian, D.; Zhang, J.; Zhu, J.-J. Fabrication of Gold Nanoparticles on Bilayer Graphene for Glucose Electrochemical Biosensing. *J. Mater. Chem.* **2011**, *21*, 7604.
- (890) Zheng, J.; He, Y.; Sheng, Q.; Zhang, H. DNA as a Linker for Biocatalytic Deposition of Au Nanoparticles on Graphene and Its Application in Glucose Detection. *J. Mater. Chem.* **2011**, *21*, 12873.
- (891) Zeng, Q.; Cheng, J. S.; Liu, X. F.; Bai, H. T.; Jiang, J. H. Palladium Nanoparticle/Chitosan-Grafted Graphene Nanocomposites for Construction of a Glucose Biosensor. *Biosens. Bioelectron.* **2011**, *26*, 3456–3463.
- (892) Lu, W.; Luo, Y.; Chang, G.; Sun, X. Synthesis of Functional SiO₂-Coated Graphene Oxide Nanosheets Decorated with Ag Nanoparticles for H₂O₂ and Glucose Detection. *Biosens. Bioelectron.* **2011**, *26*, 4791–4797.
- (893) Wu, H.; Wang, J.; Kang, X.; Wang, C.; Wang, D.; Liu, J.; Aksay, I. A.; Lin, Y. Glucose Biosensor Based on Immobilization of Glucose Oxidase in Platinum Nanoparticles/Graphene/Chitosan Nanocomposite Film. *Talanta* **2009**, *80*, 403–406.
- (894) Kim, J.; Kim, M.; Lee, M. S.; Kim, K.; Ji, S.; Kim, Y. T.; Park, J.; Na, K.; Bae, K. H.; Kyun Kim, H.; Bien, F.; Young Lee, C.; Park, J. U. Wearable Smart Sensor Systems Integrated on Soft Contact Lenses for Wireless Ocular Diagnostics. *Nat. Commun.* **2017**, *8*, 14997.
- (895) Bohunicky, B.; Mousa, S. A. Biosensors: The New Wave in Cancer Diagnosis. *Nanotechnol., Sci. Appl.* **2010**, *4*, 1–10.
- (896) Yang, J.; Lin, Q.; Yin, W.; Jiang, T.; Zhao, D.; Jiang, L. A Novel Nonenzymatic Glucose Sensor Based on Functionalized PDDA-Graphene/CuO Nanocomposites. *Sens. Actuators, B* **2017**, *253*, 1087–1095.
- (897) Liu, S.; Wang, Z.; Wang, F.; Yu, B.; Zhang, T. High Surface Area Mesoporous CuO: A High-Performance Electrocatalyst for Non-Enzymatic Glucose Biosensing. *RSC Adv.* **2014**, *4*, 33327–33331.
- (898) Yan, X.; Gu, Y.; Li, C.; Zheng, B.; Li, Y.; Zhang, T.; Zhang, Z.; Yang, M. A Non-Enzymatic Glucose Sensor Based on the CuS Nanoflakes–Reduced Graphene Oxide Nanocomposite. *Anal. Methods* **2018**, *10*, 381–388.
- (899) Gao, H.; Xiao, F.; Ching, C. B.; Duan, H. One-Step Electrochemical Synthesis of PtNi Nanoparticle-Graphene Nanocomposites for Nonenzymatic Amperometric Glucose Detection. *ACS Appl. Mater. Interfaces* **2011**, *3*, 3049–3057.
- (900) Zhu, X.; Jiao, Q.; Zhang, C.; Zuo, X.; Xiao, X.; Liang, Y.; Nan, J. Amperometric Nonenzymatic Determination of Glucose Based on a Glassy Carbon Electrode Modified with Nickel(II) Oxides and Graphene. *Microchim. Acta* **2013**, *180*, 477–483.
- (901) Dong, X. C.; Xu, H.; Wang, X. W.; Huang, Y. X.; Chan-Park, M. B.; Zhang, H.; Wang, L. H.; Huang, W.; Chen, P. 3D Graphene-Cobalt Oxide Electrode for High-Performance Supercapacitor and Enzymeless Glucose Detection. *ACS Nano* **2012**, *6*, 3206–3213.
- (902) Wu, G. H.; Song, X. H.; Wu, Y. F.; Chen, X. M.; Luo, F.; Chen, X. Non-Enzymatic Electrochemical Glucose Sensor Based on Platinum Nanoflowers Supported on Graphene Oxide. *Talanta* **2013**, *105*, 379–385.
- (903) Lu, L. M.; Li, H. B.; Qu, F.; Zhang, X. B.; Shen, G. L.; Yu, R. Q. In Situ Synthesis of Palladium Nanoparticle-Graphene Nano-hybrids and Their Application in Nonenzymatic Glucose Biosensors. *Biosens. Bioelectron.* **2011**, *26*, 3500–3504.
- (904) Shin, D. H.; Kim, W.; Jun, J.; Lee, J. S.; Kim, J. H.; Jang, J. Highly Selective FET-Type Glucose Sensor Based on Shape-Controlled Palladium Nanoflower-Decorated Graphene. *Sens. Actuators, B* **2018**, *264*, 216–223.
- (905) Beaulieu, J. M.; Gainetdinov, R. R. The Physiology, Signaling, and Pharmacology of Dopamine Receptors. *Pharmacol. Rev.* **2011**, *63*, 182–217.
- (906) Jackowska, K.; Krysinski, P. New Trends in the Electrochemical Sensing of Dopamine. *Anal. Bioanal. Chem.* **2013**, *405*, 3753–3771.
- (907) McCreery, R. L. Advanced Carbon Electrode Materials for Molecular Electrochemistry. *Chem. Rev.* **2008**, *108*, 2646–2687.
- (908) Shang, N. G.; Papakonstantinou, P.; McMullan, M.; Chu, M.; Stamboulis, A.; Potenza, A.; Dhesi, S. S.; Marchetto, H. Catalyst-Free Efficient Growth, Orientation and Biosensing Properties of Multilayer Graphene Nanoflake Films with Sharp Edge Planes. *Adv. Funct. Mater.* **2008**, *18*, 3506–3514.
- (909) Wang, Y.; Li, Y.; Tang, L.; Lu, J.; Li, J. Application of Graphene-Modified Electrode for Selective Detection of Dopamine. *Electrochem. Commun.* **2009**, *11*, 889–892.
- (910) Hou, S.; Kasner, M. L.; Su, S.; Patel, K.; Cuellari, R. Highly Sensitive and Selective Dopamine Biosensor Fabricated with Silanized Graphene. *J. Phys. Chem. C* **2010**, *114*, 14915–14921.
- (911) Tan, L.; Zhou, K.-G.; Zhang, Y.-H.; Wang, H.-X.; Wang, X.-D.; Guo, Y.-F.; Zhang, H.-L. Nanomolar Detection of Dopamine in the Presence of Ascorbic Acid at β -Cyclodextrin/Graphene Nanocomposite Platform. *Electrochem. Commun.* **2010**, *12*, 557–560.
- (912) Liu, Q.; Zhu, X.; Huo, Z.; He, X.; Liang, Y.; Xu, M. Electrochemical Detection of Dopamine in the Presence of Ascorbic Acid Using PVP/Graphene Modified Electrodes. *Talanta* **2012**, *97*, 557–562.
- (913) Li, S.-J.; He, J.-Z.; Zhang, M.-J.; Zhang, R.-X.; Lv, X.-L.; Li, S.-H.; Pang, H. Electrochemical Detection of Dopamine Using Water-Soluble Sulfonated Graphene. *Electrochim. Acta* **2013**, *102*, 58–65.
- (914) Teymourian, H.; Salimi, A.; Khezrian, S. Fe₃O₄ Magnetic Nanoparticles/Reduced Graphene Oxide Nanosheets as a Novel Electrochemical and Bioelectrochemical Sensing Platform. *Biosens. Bioelectron.* **2013**, *49*, 1–8.
- (915) Palanisamy, S.; Ku, S.; Chen, S.-M. Dopamine Sensor Based on a Glassy Carbon Electrode Modified with a Reduced Graphene Oxide and Palladium Nanoparticles Composite. *Microchim. Acta* **2013**, *180*, 1037–1042.
- (916) Wang, Y.; Peng, W.; Liu, L.; Tang, M.; Gao, F.; Li, M. Enhanced Conductivity of a Glassy Carbon Electrode Modified with a Graphene-Doped Film of Layered Double Hydroxides for Selectively Sensing of Dopamine. *Microchim. Acta* **2011**, *174*, 41–46.
- (917) Cui, X.; Fang, X.; Zhao, H.; Li, Z.; Ren, H. An Electrochemical Sensor for Dopamine Based on Polydopamine Modified Reduced Graphene Oxide Anchored with Tin Dioxide and Gold Nanoparticles. *Anal. Methods* **2017**, *9*, 5322–5332.
- (918) Jin, H.; Zhao, C.; Gui, R.; Gao, X.; Wang, Z. Reduced Graphene Oxide/Nile Blue/Gold Nanoparticles Complex-Modified Glassy Carbon Electrode Used as a Sensitive and Label-Free Aptasensor for Ratiometric Electrochemical Sensing of Dopamine. *Anal. Chim. Acta* **2018**, *1025*, 154–162.
- (919) Duarte, T. L.; Lunec, J. Review: When Is an Antioxidant Not an Antioxidant? A Review of Novel Actions and Reactions of Vitamin C. *Free Radical Res.* **2005**, *39*, 671–686.
- (920) Brownson, D. A. C.; Munro, L. J.; Kampouris, D. K.; Banks, C. E. Electrochemistry of Graphene: Not Such a Beneficial Electrode Material? *RSC Adv.* **2011**, *1*, 978.
- (921) Keeley, G. P.; O'Neill, A.; McEvoy, N.; Peltekis, N.; Coleman, J. N.; Duesberg, G. S. Electrochemical Ascorbic Acid Sensor Based on DMF-Exfoliated Graphene. *J. Mater. Chem.* **2010**, *20*, 7864.
- (922) Hong, W.; Bai, H.; Xu, Y.; Yao, Z.; Gu, Z.; Shi, G. Preparation of Gold Nanoparticle/Graphene Composites with Controlled Weight Contents and Their Application in Biosensors. *J. Phys. Chem. C* **2010**, *114*, 1822–1826.

- (923) Dietschy, J. M.; Turley, S. D. Thematic Review Series: Brain Lipids. Cholesterol Metabolism in the Central Nervous System During Early Development and in the Mature Animal. *J. Lipid Res.* **2004**, *45*, 1375–1397.
- (924) Agnihotri, N.; Chowdhury, A. D.; De, A. Non-Enzymatic Electrochemical Detection of Cholesterol Using β -Cyclodextrin Functionalized Graphene. *Biosens. Bioelectron.* **2015**, *63*, 212–217.
- (925) Cao, S.; Zhang, L.; Chai, Y.; Yuan, R. An Integrated Sensing System for Detection of Cholesterol Based on TiO₂-Graphene-Pt-Pd Hybrid Nanocomposites. *Biosens. Bioelectron.* **2013**, *42*, 532–538.
- (926) Dey, R. S.; Raj, C. R. Development of an Amperometric Cholesterol Biosensor Based on Graphene–Pt Nanoparticle Hybrid Material. *J. Phys. Chem. C* **2010**, *114*, 21427–21433.
- (927) Radoi, A.; Compagnone, D. Recent Advances in NADH Electrochemical Sensing Design. *Bioelectrochemistry* **2009**, *76*, 126–134.
- (928) Govindhan, M.; Amiri, M.; Chen, A. Au Nanoparticle/Graphene Nanocomposite as a Platform for the Sensitive Detection of NADH in Human Urine. *Biosens. Bioelectron.* **2015**, *66*, 474–480.
- (929) Tabrizi, M. A.; Zand, Z. A Facile One-Step Method for the Synthesis of Reduced Graphene Oxide Nanocomposites by NADH as Reducing Agent and Its Application in NADH Sensing. *Electroanalysis* **2014**, *26*, 171–177.
- (930) Li, Z.; Huang, Y.; Chen, L.; Qin, X.; Huang, Z.; Zhou, Y.; Meng, Y.; Li, J.; Huang, S.; Liu, Y.; Wang, W.; Xie, Q.; Yao, S. Amperometric Biosensor for NADH and Ethanol Based on Electroreduced Graphene Oxide–Polythionine Nanocomposite Film. *Sens. Actuators, B* **2013**, *181*, 280–287.
- (931) Li, Z.; Su, W.; Liu, S.; Ding, X. An Electrochemical Biosensor Based on DNA Tetrahedron/Graphene Composite Film for Highly Sensitive Detection of NADH. *Biosens. Bioelectron.* **2015**, *69*, 287–293.
- (932) Jones, C. W. *Applications of Hydrogen Peroxide and Derivatives*; 1999; Vol. 122, pp 6339–6340.
- (933) Xu, H.; Dai, H.; Chen, G. Direct Electrochemistry and Electrocatalysis of Hemoglobin Protein Entrapped in Graphene and Chitosan Composite Film. *Talanta* **2010**, *81*, 334–338.
- (934) Lu, Q.; Dong, X.; Li, L. J.; Hu, X. Direct Electrochemistry-Based Hydrogen Peroxide Biosensor Formed from Single-Layer Graphene Nanoplatelet-Enzyme Composite Film. *Talanta* **2010**, *82*, 1344–1348.
- (935) Zeng, Q.; Cheng, J.; Tang, L.; Liu, X.; Liu, Y.; Li, J.; Jiang, J. Self-Assembled Graphene-Enzyme Hierarchical Nanostructures for Electrochemical Biosensing. *Adv. Funct. Mater.* **2010**, *20*, 3366–3372.
- (936) Zhou, Y.; Liu, S.; Jiang, H.-J.; Yang, H.; Chen, H.-Y. Direct Electrochemistry and Bioelectrocatalysis of Microperoxidase-11 Immobilized on Chitosan-Graphene Nanocomposite. *Electroanalysis* **2010**, *22*, 1323–1328.
- (937) Guo, S.; Wen, D.; Zhai, Y.; Dong, S.; Wang, E. Platinum Nanoparticle Ensemble-on-Graphene Hybrid Nanosheet: One-Pot, Rapid Synthesis, and Used as New Electrode Material for Electrochemical Sensing. *ACS Nano* **2010**, *4*, 3959–3968.
- (938) Cao, L.; Liu, Y.; Zhang, B.; Lu, L. In Situ Controllable Growth of Prussian Blue Nanocubes on Reduced Graphene Oxide: Facile Synthesis and Their Application as Enhanced Nanoelectrocatalyst for H₂O₂ Reduction. *ACS Appl. Mater. Interfaces* **2010**, *2*, 2339–2346.
- (939) Sun, Y.; Luo, M.; Qin, Y.; Zhu, S.; Li, Y.; Xu, N.; Meng, X.; Ren, Q.; Wang, L.; Guo, S. Atomic-Thick PtNi Nanowires Assembled on Graphene for High-Sensitivity Extracellular Hydrogen Peroxide Sensors. *ACS Appl. Mater. Interfaces* **2017**, *9*, 34715–34721.
- (940) Rani, G. P. J.; Saravanan, J.; Sheet, S.; Rajan, M. A. J.; Lee, Y. S.; Balasubramani, A.; Kumar, G. G. The Sensitive and Selective Enzyme-Free Electrochemical H₂O₂ Sensor Based on rGO/MnFe₂O₄ Nanocomposite. *Electrocatalysis* **2018**, *9*, 102–112.
- (941) Long, F.; Zhang, Z.; Wang, J.; Yan, L.; Zhou, B. Cobalt-Nickel Bimetallic Nanoparticles Decorated Graphene Sensitized Imprinted Electrochemical Sensor for Determination of Octylphenol. *Electrochim. Acta* **2015**, *168*, 337–345.
- (942) Oliveira, T. M.; Barroso, M. F.; Morais, S.; Araujo, M.; Freire, C.; de Lima-Neto, P.; Correia, A. N.; Oliveira, M. B.; Delerue-Matos, C. Sensitive Bi-Enzymatic Biosensor Based on Polyphenoloxidases-Gold Nanoparticles-Chitosan Hybrid Film-Graphene Doped Carbon Paste Electrode for Carbamates Detection. *Bioelectrochemistry* **2014**, *98*, 20–29.
- (943) Khoo, W. Y.; Pumera, M.; Bonanni, A. Graphene Platforms for the Detection of Caffeine in Real Samples. *Anal. Chim. Acta* **2013**, *804*, 92–97.
- (944) Liu, J.; Cao, Z.; Lu, Y. Functional Nucleic Acid Sensors. *Chem. Rev.* **2009**, *109*, 1948–1998.
- (945) Huang, K. J.; Niu, D. J.; Sun, J. Y.; Han, C. H.; Wu, Z. W.; Li, Y. L.; Xiong, X. Q. Novel Electrochemical Sensor Based on Functionalized Graphene for Simultaneous Determination of Adenine and Guanine in DNA. *Colloids Surf., B* **2011**, *82*, 543–549.
- (946) Muti, M.; Sharma, S.; Erdem, A.; Papakonstantinou, P. Electrochemical Monitoring of Nucleic Acid Hybridization by Single-Use Graphene Oxide-Based Sensor. *Electroanalysis* **2011**, *23*, 272–279.
- (947) Yin, H.; Zhou, Y.; Ma, Q.; Ai, S.; Chen, Q.; Zhu, L. Electrocatalytic Oxidation Behavior of Guanosine at Graphene, Chitosan and Fe₃O₄ Nanoparticles Modified Glassy Carbon Electrode and its Determination. *Talanta* **2010**, *82*, 1193–1199.
- (948) Du, M.; Yang, T.; Jiao, K. Immobilization-Free Direct Electrochemical Detection for DNA Specific Sequences Based on Electrochemically Converted Gold Nanoparticles/Graphene Composite Film. *J. Mater. Chem.* **2010**, *20*, 9253.
- (949) Gao, Y. S.; Xu, J. K.; Lu, L. M.; Wu, L. P.; Zhang, K. X.; Nie, T.; Zhu, X. F.; Wu, Y. Overoxidized Polypyrrole/Graphene Nanocomposite with Good Electrochemical Performance as Novel Electrode Material for the Detection of Adenine and Guanine. *Biosens. Bioelectron.* **2014**, *62*, 261–267.
- (950) Ambrosi, A.; Pumera, M. Stacked Graphene Nanofibers for Electrochemical Oxidation of DNA Bases. *Phys. Chem. Chem. Phys.* **2010**, *12*, 8943–8947.
- (951) Lim, C. X.; Hoh, H. Y.; Ang, P. K.; Loh, K. P. Direct Voltammetric Detection of DNA and pH Sensing on Epitaxial Graphene: An Insight into the Role of Oxygenated Defects. *Anal. Chem.* **2010**, *82*, 7387–7393.
- (952) Akhavan, O.; Ghaderi, E.; Rahighi, R. Toward Single-DNA Electrochemical Biosensing by Graphene Nanowalls. *ACS Nano* **2012**, *6*, 2904–2916.
- (953) Chu, Y.; Cai, B.; Ma, Y.; Zhao, M.; Ye, Z.; Huang, J. Highly Sensitive Electrochemical Detection of Circulating Tumor DNA Based on Thin-Layer MoS₂/Graphene Composites. *RSC Adv.* **2016**, *6*, 22673–22678.
- (954) Tran, H. V.; Piro, B.; Reisberg, S.; Huy Nguyen, L.; Dung Nguyen, T.; Duc, H. T.; Pham, M. C. An Electrochemical Elisa-Like Immunosensor for Mirnas Detection Based on Screen-Printed Gold Electrodes Modified with Reduced Graphene Oxide and Carbon Nanotubes. *Biosens. Bioelectron.* **2014**, *62*, 25–30.
- (955) Tran, H. V.; Piro, B.; Reisberg, S.; Duc, H. T.; Pham, M. C. Antibodies Directed to RNA/DNA Hybrids: An Electrochemical Immunosensor for Micrornas Detection Using Graphene-Composite Electrodes. *Anal. Chem.* **2013**, *85*, 8469–8474.
- (956) Liu, A. L.; Zhong, G. X.; Chen, J. Y.; Weng, S. H.; Huang, H. N.; Chen, W.; Lin, L. Q.; Lei, Y.; Fu, F. H.; Sun, Z. L.; Lin, X. H.; Lin, J. H.; Yang, S. Y. A Sandwich-Type DNA Biosensor Based on Electrochemical Co-Reduction Synthesis of Graphene-Three Dimensional Nanostructure Gold Nanocomposite Films. *Anal. Chim. Acta* **2013**, *767*, 50–58.
- (957) Niu, S.; Sun, J.; Nan, C.; Lin, J. Sensitive DNA Biosensor Improved by 1,10-Phenanthroline Cobalt Complex as Indicator Based on the Electrode Modified by Gold Nanoparticles and Graphene. *Sens. Actuators, B* **2013**, *176*, 58–63.
- (958) Bonanni, A.; Chua, C. K.; Zhao, G.; Sofer, Z.; Pumera, M. Inherently Electroactive Graphene Oxide Nanoplatelets as Labels for Single Nucleotide Polymorphism Detection. *ACS Nano* **2012**, *6*, 8546–8551.

- (959) Ping, J.; Vishnubhotla, R.; Vrudhula, A.; Johnson, A. T. Scalable Production of High-Sensitivity, Label-Free DNA Biosensors Based on Back-Gated Graphene Field Effect Transistors. *ACS Nano* **2016**, *10*, 8700–8704.
- (960) Dong, H.; Zhu, Z.; Ju, H.; Yan, F. Triplex Signal Amplification for Electrochemical DNA Biosensing by Coupling Probe-Gold Nanoparticles-Graphene Modified Electrode with Enzyme Functionalized Carbon Sphere as Tracer. *Biosens. Bioelectron.* **2012**, *33*, 228–232.
- (961) Benvidi, A.; Firouzabadi, A. D.; Moshtaghiun, S. M.; Mazloum-Ardakani, M.; Tezerjani, M. D. Ultrasensitive DNA Sensor Based on Gold Nanoparticles/Reduced Graphene Oxide/Glassy Carbon Electrode. *Anal. Biochem.* **2015**, *484*, 24–30.
- (962) Zhang, S.; Huang, N.; Lu, Q.; Liu, M.; Li, H.; Zhang, Y.; Yao, S. A Double Signal Electrochemical Human Immunoglobulin G Immunosensor Based on Gold Nanoparticles-Polydopamine Functionalized Reduced Graphene Oxide as a Sensor Platform and AgNPs/Carbon Nanocomposite as Signal Probe and Catalytic Substrate. *Biosens. Bioelectron.* **2016**, *77*, 1078–1085.
- (963) Su, B.; Tang, J.; Huang, J.; Yang, H.; Qiu, B.; Chen, G.; Tang, D. Graphene and Nanogold-Functionalized Immunosensing Interface with Enhanced Sensitivity for One-Step Electrochemical Immunoassay of α -Fetoprotein in Human Serum. *Electroanalysis* **2010**, *22*, 2720–2728.
- (964) Yang, T. T.; Jia, H. Y.; Liu, Z.; Qiu, X. L.; Gao, Y. S.; Xu, J. K.; Lu, L. M.; Yu, Y. F. Label-Free Electrochemical Immunoassay for α -Fetoprotein Based on a Redox Matrix of Prussian Blue-Reduced Graphene Oxide/Gold Nanoparticles-Poly(3, 4-Ethylenedioxythiophene) Composite. *J. Electroanal. Chem.* **2017**, *799*, 625–633.
- (965) Wei, Q.; Mao, K.; Wu, D.; Dai, Y.; Yang, J.; Du, B.; Yang, M.; Li, H. A Novel Label-Free Electrochemical Immunosensor Based on Graphene and Thionine Nanocomposite. *Sens. Actuators, B* **2010**, *149*, 314–318.
- (966) Zhou, L.; Mao, H.; Wu, C.; Tang, L.; Wu, Z.; Sun, H.; Zhang, H.; Zhou, H.; Jia, C.; Jin, Q.; Chen, X.; Zhao, J. Label-Free Graphene Biosensor Targeting Cancer Molecules Based on Non-Covalent Modification. *Biosens. Bioelectron.* **2017**, *87*, 701–707.
- (967) Hou, L.; Cui, Y.; Xu, M.; Gao, Z.; Huang, J.; Tang, D. Graphene Oxide-Labeled Sandwich-Type Impedimetric Immunoassay with Sensitive Enhancement Based on Enzymatic 4-Chloro-1-Naphthol Oxidation. *Biosens. Bioelectron.* **2013**, *47*, 149–156.
- (968) Yang, G.; Li, L.; Rana, R. K.; Zhu, J.-J. Assembled Gold Nanoparticles on Nitrogen-Doped Graphene for Ultrasensitive Electrochemical Detection of Matrix Metalloproteinase-2. *Carbon* **2013**, *61*, 357–366.
- (969) Chen, H.; Zhang, J.; Gao, Y.; Liu, S.; Koh, K.; Zhu, X.; Yin, Y. Sensitive Cell Apoptosis Assay Based on Caspase-3 Activity Detection with Graphene Oxide-Assisted Electrochemical Signal Amplification. *Biosens. Bioelectron.* **2015**, *68*, 777–782.
- (970) Ali, M. A.; Singh, C.; Mondal, K.; Srivastava, S.; Sharma, A.; Malhotra, B. D. Mesoporous Few-Layer Graphene Platform for Affinity Biosensing Application. *ACS Appl. Mater. Interfaces* **2016**, *8*, 7646–7656.
- (971) Ateş, A. K.; Er, E.; Çelikkan, H.; Erk, N. Reduced Graphene Oxide/Platinum Nanoparticles/Nafion Nanocomposite as a Novel 2D Electrochemical Sensor for Voltammetric Determination of Aliskiren. *New J. Chem.* **2017**, *41*, 15320–15326.
- (972) Er, E.; Çelikkan, H.; Erk, N. An Ultra-Sensitive 2D Electrochemical Sensor Based on a PtNPs@Graphene/Nafion Nanocomposite for Determination of A1-Ar Antagonist Silodosin in Human Plasma. *Anal. Methods* **2017**, *9*, 3782–3789.
- (973) Loo, A. H.; Bonanni, A.; Pumera, M. Thrombin Aptasensing with Inherently Electroactive Graphene Oxide Nanoplatelets as Labels. *Nanoscale* **2013**, *5*, 4758–4762.
- (974) Saltzgaber, G.; Wojcik, P.; Sharf, T.; Leyden, M. R.; Wardini, J. L.; Heist, C. A.; Adenuga, A. A.; Remcho, V. T.; Minot, E. D. Scalable Graphene Field-Effect Sensors for Specific Protein Detection. *Nanotechnology* **2013**, *24*, 355502.
- (975) Feng, L.; Chen, Y.; Ren, J.; Qu, X. A Graphene Functionalized Electrochemical Aptasensor for Selective Label-Free Detection of Cancer Cells. *Biomaterials* **2011**, *32*, 2930–2937.
- (976) Yang, G.; Cao, J.; Li, L.; Rana, R. K.; Zhu, J.-J. Carboxymethyl Chitosan-Functionalized Graphene for Label-Free Electrochemical CytoSensing. *Carbon* **2013**, *51*, 124–133.
- (977) Wu, X.; Hu, Y.; Jin, J.; Zhou, N.; Wu, P.; Zhang, H.; Cai, C. Electrochemical Approach for Detection of Extracellular Oxygen Released from Erythrocytes Based on Graphene Film Integrated with Laccase and 2,2-Azino-Bis(3-Ethylbenzothiazoline-6-Sulfonic Acid). *Anal. Chem.* **2010**, *82*, 3588–3596.
- (978) Guo, C. X.; Zheng, X. T.; Lu, Z. S.; Lou, X. W.; Li, C. M. BioInterface by Cell Growth on Layered Graphene-Artificial Peroxidase-Protein Nanostructure for in Situ Quantitative Molecular Detection. *Adv. Mater.* **2010**, *22*, 5164–5167.
- (979) Yadegari, A.; Omidi, M.; Yazdian, F.; Zali, H.; Tayebi, L. An Electrochemical CytoSensor for Ultrasensitive Detection of Cancer Cells Using Modified Graphene–Gold Nanostructures. *RSC Adv.* **2017**, *7*, 2365–2372.
- (980) Zhang, D.; Zhang, Y.; Zheng, L.; Zhan, Y.; He, L. Graphene Oxide/Poly-L-Lysine Assembled Layer for Adhesion and Electrochemical Impedance Detection of Leukemia K562 Cancer Cells. *Biosens. Bioelectron.* **2013**, *42*, 112–118.
- (981) Akhavan, O.; Ghaderi, E.; Rahighi, R.; Abdolahad, M. Spongy Graphene Electrode in Electrochemical Detection of Leukemia at Single-Cell Levels. *Carbon* **2014**, *79*, 654–663.
- (982) Zheng, T.; Tan, T.; Zhang, Q.; Fu, J. J.; Wu, J. J.; Zhang, K.; Zhu, J. J.; Wang, H. Multiplex Acute Leukemia CytoSensing Using Multifunctional Hybrid Electrochemical Nanoprobes at a Hierarchically Nanoarchitected Electrode Interface. *Nanoscale* **2013**, *5*, 10360–10368.
- (983) Wang, Y.; Ping, J.; Ye, Z.; Wu, J.; Ying, Y. Impedimetric Immunosensor Based on Gold Nanoparticles Modified Graphene Paper for Label-Free Detection of Escherichia Coli O157:H7. *Biosens. Bioelectron.* **2013**, *49*, 492–498.
- (984) Khoshfetrat, S. M.; Mehrgard, M. A. Amplified Detection of Leukemia Cancer Cells Using an Aptamer-Conjugated Gold-Coated Magnetic Nanoparticles on a Nitrogen-Doped Graphene Modified Electrode. *Bioelectrochemistry* **2017**, *114*, 24–32.
- (985) Wang, L.; Sofer, Z.; Pumera, M. Voltammetry of Layered Black Phosphorus: Electrochemistry of Multilayer Phosphorene. *ChemElectroChem* **2015**, *2*, 324–327.
- (986) Latiff, N. M.; Teo, W. Z.; Sofer, Z.; Fisher, A. C.; Pumera, M. The Cytotoxicity of Layered Black Phosphorus. *Chem. - Eur. J.* **2015**, *21*, 13991–13995.
- (987) Sofer, Z.; Sedmidubsky, D.; Huber, S.; Luxa, J.; Bousa, D.; Boothroyd, C.; Pumera, M. Layered Black Phosphorus: Strongly Anisotropic Magnetic, Electronic, and Electron-Transfer Properties. *Angew. Chem., Int. Ed.* **2016**, *55*, 3382–3386.
- (988) Yan, S.; Wang, B.; Wang, Z.; Hu, D.; Xu, X.; Wang, J.; Shi, Y. Supercritical Carbon Dioxide-Assisted Rapid Synthesis of Few-Layer Black Phosphorus for Hydrogen Peroxide Sensing. *Biosens. Bioelectron.* **2016**, *80*, 34–38.
- (989) Zhao, Y.; Zhang, Y. H.; Zhuge, Z.; Tang, Y. H.; Tao, J. W.; Chen, Y. Synthesis of a Poly-L-Lysine/Black Phosphorus Hybrid for Biosensors. *Anal. Chem.* **2018**, *90*, 3149–3155.
- (990) Huang, Y.; Guo, J.; Kang, Y.; Ai, Y.; Li, C. M. Two Dimensional Atomically Thin MoS₂ Nanosheets and Their Sensing Applications. *Nanoscale* **2015**, *7*, 19358–19376.
- (991) Kalantar-zadeh, K.; Ou, J. Z. Biosensors Based on Two-Dimensional MoS₂. *ACS Sens.* **2016**, *1*, 5–16.
- (992) Lee, J.; Dak, P.; Lee, Y.; Park, H.; Choi, W.; Alam, M. A.; Kim, S. Two-Dimensional Layered MoS₂ Biosensors Enable Highly Sensitive Detection of Biomolecules. *Sci. Rep.* **2015**, *4*, 7352.
- (993) Wang, L.; Wang, Y.; Wong, J. I.; Palacios, T.; Kong, J.; Yang, H. Y. Functionalized MoS₂ Nanosheet-Based Field-Effect Biosensor for Label-Free Sensitive Detection of Cancer Marker Proteins in Solution. *Small* **2014**, *10*, 1101–1105.

- (994) Nam, H.; Oh, B.-R.; Chen, P.; Yoon, J. S.; Wi, S.; Chen, M.; Kurabayashi, K.; Liang, X. Two Different Device Physics Principles for Operating MoS₂ Transistor Biosensors with Femtomolar-Level Detection Limits. *Appl. Phys. Lett.* **2015**, *107*, 012105.
- (995) Nam, H.; Oh, B. R.; Chen, P.; Chen, M.; Wi, S.; Wan, W.; Kurabayashi, K.; Liang, X. Multiple MoS₂ Transistors for Sensing Molecule Interaction Kinetics. *Sci. Rep.* **2015**, *5*, 10546.
- (996) Huang, K.-J.; Liu, Y.-J.; Zhang, J.-Z.; Liu, Y.-M. A Novel Aptamer Sensor Based on Layered Tungsten Disulfide Nanosheets and Au Nanoparticles Amplification for 17 β -Estradiol Detection. *Anal. Methods* **2014**, *6*, 8011–8017.
- (997) Huang, K.-J.; Liu, Y.-J.; Cao, J.-T.; Wang, H.-B. An Aptamer Electrochemical Assay for Sensitive Detection of Immunoglobulin E Based on Tungsten Disulfide–Graphene Composites and Gold Nanoparticles. *RSC Adv.* **2014**, *4*, 36742.
- (998) Huang, K. J.; Liu, Y. J.; Liu, Y. M.; Wang, L. L. Molybdenum Disulfide Nanoflower–Chitosan–Au Nanoparticles Composites Based Electrochemical Sensing Platform for Bisphenol A Determination. *J. Hazard. Mater.* **2014**, *276*, 207–215.
- (999) Wang, X.; Chu, C.; Shen, L.; Deng, W.; Yan, M.; Ge, S.; Yu, J.; Song, X. An Ultrasensitive Electrochemical Immunosensor Based on the Catalytical Activity of MoS₂–Au Composite Using Ag Nanospheres as Labels. *Sens. Actuators, B* **2015**, *206*, 30–36.
- (1000) Jing, P.; Yi, H.; Xue, S.; Chai, Y.; Yuan, R.; Xu, W. A Sensitive Electrochemical Aptasensor Based on Palladium Nanoparticles Decorated Graphene–Molybdenum Disulfide Flower-Like Nanocomposites and Enzymatic Signal Amplification. *Anal. Chim. Acta* **2015**, *853*, 234–241.
- (1001) Rohaizad, N.; Mayorga-Martinez, C. C.; Sofer, Z.; Pumera, M. 1T-Phase Transition Metal Dichalcogenides (MoS₂, MoSe₂, WS₂, and WSe₂) with Fast Heterogeneous Electron Transfer: Application on Second-Generation Enzyme-Based Biosensor. *ACS Appl. Mater. Interfaces* **2017**, *9*, 40697–40706.
- (1002) Su, S.; Sun, H.; Xu, F.; Yuwen, L.; Fan, C.; Wang, L. Direct Electrochemistry of Glucose Oxidase and a Biosensor for Glucose Based on a Glass Carbon Electrode Modified with MoS₂ Nanosheets Decorated with Gold Nanoparticles. *Microchim. Acta* **2014**, *181*, 1497–1503.
- (1003) Huang, J.; Dong, Z.; Li, Y.; Li, J.; Tang, W.; Yang, H.; Wang, J.; Bao, Y.; Jin, J.; Li, R. MoS₂ Nanosheet Functionalized with Cu Nanoparticles and Its Application for Glucose Detection. *Mater. Res. Bull.* **2013**, *48*, 4544–4547.
- (1004) Narayanan, T. N.; Vusa, C. S.; Alwarappan, S. Selective and Efficient Electrochemical Biosensing of Ultrathin Molybdenum Disulfide Sheets. *Nanotechnology* **2014**, *25*, 335702.
- (1005) Wu, S.; Zeng, Z.; He, Q.; Wang, Z.; Wang, S. J.; Du, Y.; Yin, Z.; Sun, X.; Chen, W.; Zhang, H. Electrochemically Reduced Single-Layer MoS₂ Nanosheets: Characterization, Properties, and Sensing Applications. *Small* **2012**, *8*, 2264–2270.
- (1006) Sarkar, A.; Ghosh, A. B.; Saha, N.; Bhadu, G. R.; Adhikary, B. Newly Designed Amperometric Biosensor for Hydrogen Peroxide and Glucose Based on Vanadium Sulfide Nanoparticles. *ACS Appl. Nano Mater.* **2018**, *1*, 1339–1347.
- (1007) Wang, G.-X.; Bao, W.-J.; Wang, J.; Lu, Q.-Q.; Xia, X.-H. Immobilization and Catalytic Activity of Horseradish Peroxidase on Molybdenum Disulfide Nanosheets Modified Electrode. *Electrochem. Commun.* **2013**, *35*, 146–148.
- (1008) Song, H.; Ni, Y.; Kokot, S. Investigations of an Electrochemical Platform Based on the Layered MoS₂–Graphene and Horseradish Peroxidase Nanocomposite for Direct Electrochemistry and Electrocatalysis. *Biosens. Bioelectron.* **2014**, *56*, 137–143.
- (1009) Yoon, J.; Lee, T.; Bapurao, G. B.; Jo, J.; Oh, B. K.; Choi, J. W. Electrochemical H₂O₂ Biosensor Composed of Myoglobin on MoS₂ Nanoparticle–Graphene Oxide Hybrid Structure. *Biosens. Bioelectron.* **2017**, *93*, 14–20.
- (1010) Loo, A. H.; Bonanni, A.; Ambrosi, A.; Pumera, M. Molybdenum Disulfide (MoS₂) Nanoflakes as Inherently Electroactive Labels for DNA Hybridization Detection. *Nanoscale* **2014**, *6*, 11971–11975.
- (1011) Loo, A. H.; Bonanni, A.; Sofer, Z.; Pumera, M. Transitional Metal/Chalcogen Dependant Interactions of Hairpin DNA with Transition Metal Dichalcogenides, MX₂. *ChemPhysChem* **2015**, *16*, 2304–2306.
- (1012) Yang, T.; Chen, M.; Nan, F.; Chen, L.; Luo, X.; Jiao, K. Enhanced Electropolymerization of Poly(Xanthurenic Acid)–MoS₂ Film for Specific Electrocatalytic Detection of Guanine and Adenine. *J. Mater. Chem. B* **2015**, *3*, 4884–4891.
- (1013) Wang, T.; Zhu, R.; Zhuo, J.; Zhu, Z.; Shao, Y.; Li, M. Direct Detection of DNA Below ppb Level Based on Thionin-Functionalized Layered MoS₂ Electrochemical Sensors. *Anal. Chem.* **2014**, *86*, 12064–12069.
- (1014) Lee, D.-W.; Lee, J.; Sohn, I. Y.; Kim, B.-Y.; Son, Y. M.; Bark, H.; Jung, J.; Choi, M.; Kim, T. H.; Lee, C.; Lee, N.-E. Field-Effect Transistor with a Chemically Synthesized MoS₂ Sensing Channel for Label-Free and Highly Sensitive Electrical Detection of DNA Hybridization. *Nano Res.* **2015**, *8*, 2340–2350.
- (1015) Yang, T.; Chen, M.; Kong, Q.; Luo, X.; Jiao, K. Toward DNA Electrochemical Sensing by Free-Standing ZnO Nanosheets Grown on 2D Thin-Layered MoS₂. *Biosens. Bioelectron.* **2017**, *89*, 538–544.
- (1016) Yang, T.; Meng, L.; Chen, H.; Luo, S.; Li, W.; Jiao, K. Synthesis of Thin-Layered Molybdenum Disulfide-Based Polyaniline Nanointerfaces for Enhanced Direct Electrochemical DNA Detection. *Adv. Mater. Interfaces* **2016**, *3*, 1500700.
- (1017) Huang, K.-J.; Liu, Y.-J.; Wang, H.-B.; Gan, T.; Liu, Y.-M.; Wang, L.-L. Signal Amplification for Electrochemical DNA Biosensor Based on Two-Dimensional Graphene Analogue Tungsten Sulfide–Graphene Composites and Gold Nanoparticles. *Sens. Actuators, B* **2014**, *191*, 828–836.
- (1018) Wang, X.; Nan, F.; Zhao, J.; Yang, T.; Ge, T.; Jiao, K. A Label-Free Ultrasensitive Electrochemical DNA Sensor Based on Thin-Layer MoS₂ Nanosheets with High Electrochemical Activity. *Biosens. Bioelectron.* **2015**, *64*, 386–391.
- (1019) Mei, J.; Li, Y. T.; Zhang, H.; Xiao, M. M.; Ning, Y.; Zhang, Z. Y.; Zhang, G. J. Molybdenum Disulfide Field-Effect Transistor Biosensor for Ultrasensitive Detection of DNA by Employing Morpholino as Probe. *Biosens. Bioelectron.* **2018**, *110*, 71–77.
- (1020) Zhu, D.; Liu, W.; Zhao, D.; Hao, Q.; Li, J.; Huang, J.; Shi, J.; Chao, J.; Su, S.; Wang, L. Label-Free Electrochemical Sensing Platform for Microrna-21 Detection Using Thionine and Gold Nanoparticles Co-Functionalized MoS₂ Nanosheet. *ACS Appl. Mater. Interfaces* **2017**, *9*, 35597–35603.
- (1021) Su, S.; Sun, H.; Cao, W.; Chao, J.; Peng, H.; Zuo, X.; Yuwen, L.; Fan, C.; Wang, L. Dual-Target Electrochemical Biosensing Based on DNA Structural Switching on Gold Nanoparticle-Decorated MoS₂ Nanosheets. *ACS Appl. Mater. Interfaces* **2016**, *8*, 6826–6833.
- (1022) Su, S.; Zou, M.; Zhao, H.; Yuan, C.; Xu, Y.; Zhang, C.; Wang, L.; Fan, C.; Wang, L. Shape-Controlled Gold Nanoparticles Supported on MoS₂ Nanosheets: Synergistic Effect of Thionine and MoS₂ and Their Application for Electrochemical Label-Free Immunosensing. *Nanoscale* **2015**, *7*, 19129–19135.
- (1023) Wang, Y. H.; Huang, K. J.; Wu, X. Recent Advances in Transition-Metal Dichalcogenides Based Electrochemical Biosensors: A Review. *Biosens. Bioelectron.* **2017**, *97*, 305–316.
- (1024) Sticker, D.; Rothbauer, M.; Charwat, V.; Steinkühler, J.; Bethge, O.; Bertagnolli, E.; Wanzenboeck, H. D.; Ertl, P. Zirconium Dioxide Nanolayer Passivated Impedimetric Sensors for Cell-Based Assays. *Sens. Actuators, B* **2015**, *213*, 35–44.
- (1025) Solanki, P. R.; Kaushik, A.; Ansari, A. A.; Malhotra, B. D. Nanostructured Zinc Oxide Platform for Cholesterol Sensor. *Appl. Phys. Lett.* **2009**, *94*, 143901 MoS₂.
- (1026) Ansari, A. A.; Kaushik, A.; Solanki, P. R.; Malhotra, B. D. Nanostructured Zinc Oxide Platform for Mycotoxin Detection. *Bioelectrochemistry* **2010**, *77*, 75–81.
- (1027) Das, M.; Sumana, G.; Nagarajan, R.; Malhotra, B. D. Zirconia Based Nucleic Acid Sensor for Mycobacterium Tuberculosis Detection. *Appl. Phys. Lett.* **2010**, *96*, 133703.

- (1028) Solanki, P. R.; Kaushik, A.; Chavhan, P. M.; Maheshwari, S. N.; Malhotra, B. D. Nanostructured Zirconium Oxide Based Genosensor for Escherichia Coli Detection. *Electrochim. Commun.* **2009**, *11*, 2272–2277.
- (1029) Kaisti, M. Detection Principles of Biological and Chemical FET Sensors. *Biosens. Bioelectron.* **2017**, *98*, 437–448.
- (1030) Balendhran, S.; Walia, S.; Alsaif, M.; Nguyen, E. P.; Ou, J. Z.; Zhuiykov, S.; Sriram, S.; Bhaskaran, M.; Kalantar-Zadeh, K. Field Effect Biosensing Platform Based on 2D α -MoO₃. *ACS Nano* **2013**, *7*, 9753–9760.
- (1031) Lahav, M.; Kharitonov, A. B.; Willner, I. Imprinting of Chiral Molecular Recognition Sites in Thin TiO₂ Films Associated with Field-Effect Transistors: Novel Functionalized Devices for Chiroselective and Chirospecific Analyses. *Chem. - Eur. J.* **2001**, *7*, 3992–3997.
- (1032) Pogorelova, S. P.; Kharitonov, A. B.; Willner, I.; Sukenik, C. N.; Pizem, H.; Bayer, T. Development of Ion-Sensitive Field-Effect Transistor-Based Sensors for Benzylphosphonic Acids and Thiophenols Using Molecularly Imprinted TiO₂ Films. *Anal. Chim. Acta* **2004**, *504*, 113–122.
- (1033) Mishra, S.; Yogi, P.; Sagdeo, P. R.; Kumar, R. Mesoporous Nickel Oxide (NiO) Nanopetals for Ultrasensitive Glucose Sensing. *Nanoscale Res. Lett.* **2018**, *13*, 16.
- (1034) Sun, S.; Sun, Y.; Chen, A.; Zhang, X.; Yang, Z. Nanoporous Copper Oxide Ribbon Assembly of Free-Standing Nanoneedles as Biosensors for Glucose. *Analyst* **2015**, *140*, 5205–5215.
- (1035) Xiang, C.; Zou, Y.; Sun, L.-X.; Xu, F. Direct Electrochemistry and Enhanced Electrocatalysis of Horseradish Peroxidase Based on Flowerlike ZnO–Gold Nanoparticle–Nafion Nanocomposite. *Sens. Actuators, B* **2009**, *136*, 158–162.
- (1036) Jia, W.; Guo, M.; Zheng, Z.; Yu, T.; Rodriguez, E. G.; Wang, Y.; Lei, Y. Electrocatalytic Oxidation and Reduction of H₂O₂ on Vertically Aligned Co₃O₄ Nanowalls Electrode: Toward H₂O₂ Detection. *J. Electroanal. Chem.* **2009**, *625*, 27–32.
- (1037) Li, R.; Du, J.; Luan, Y.; Xue, Y.; Zou, H.; Zhuang, G.; Li, Z. Ionic Liquid Precursor-Based Synthesis of CuO Nanoplates for Gas Sensing and Amperometric Sensing Applications. *Sens. Actuators, B* **2012**, *168*, 156–164.
- (1038) Li, Y.; Cao, D.; Liu, Y.; Liu, R.; Yang, F.; Yin, J.; Wang, G. CuO Nanosheets Grown on Copper Foil as the Catalyst for H₂O₂ Electrocatalysis in Alkaline Medium. *Int. J. Hydrogen Energy* **2012**, *37*, 13611–13615.
- (1039) Khan, A. F.; Randviir, E. P.; Brownson, D. A. C.; Ji, X.; Smith, G. C.; Banks, C. E. 2D Hexagonal Boron Nitride (2D - hBN) Explored as a Potential Electrocatalyst for the Oxygen Reduction Reaction. *Electroanalysis* **2017**, *29*, 622–634.
- (1040) Huang, C.; Chen, C.; Zhang, M.; Lin, L.; Ye, X.; Lin, S.; Antonietti, M.; Wang, X. Carbon-Doped BN Nanosheets for Metal-Free Photoredox Catalysis. *Nat. Commun.* **2015**, *6*, 7698.
- (1041) Khan, A. F.; Brownson, D. A. C.; Randviir, E. P.; Smith, G. C.; Banks, C. E. 2D Hexagonal Boron Nitride (2D - hBN) Explored for the Electrochemical Sensing of Dopamine. *Anal. Chem.* **2016**, *88*, 9729–9737.
- (1042) Khan, A. F.; Brownson, D. A. C.; Foster, C. W.; Smith, G. C.; Banks, C. E. Surfactant Exfoliated 2D Hexagonal Boron Nitride (2D - h-BN) Explored as a Potential Electrochemical Sensor for Dopamine: Surfactants Significantly Influence Sensor Capabilities. *Analyst* **2017**, *142*, 1756–1764.
- (1043) Li, Q.; Huo, C.; Yi, K.; Zhou, L.; Su, L.; Hou, X. Preparation of Flake Hexagonal BN and Its Application in Electrochemical Detection of Ascorbic Acid, Dopamine and Uric Acid. *Sens. Actuators, B* **2018**, *260*, 346–356.
- (1044) Liu, F.; Tang, J.; Xu, J.; Shu, Y.; Xu, Q.; Wang, H.; Hu, X. Low Potential Detection of Indole-3-Acetic Acid Based on the Peroxidase-Like Activity of Hemin/Reduced Graphene Oxide Nanocomposite. *Biosens. Bioelectron.* **2016**, *86*, 871–878.
- (1045) Aksoy, B.; Paşahan, A.; Güngör, Ö.; Köytepe, S.; Seçkin, T. A Novel Electrochemical Biosensor Based on Polyimide-Boron Nitride Composite Membranes. *Int. J. Polym. Mater.* **2017**, *66*, 203–212.
- (1046) Ranganathan, S.; Lee, S.-M.; Lee, J.; Chang, S.-C. Electrochemical Non-Enzymatic Glucose Sensor Based on Hexagonal Boron Nitride with Metal–Organic Framework Composite. *J. Sensor Sci. Technol.* **2017**, *26*, 379–385.
- (1047) Yola, M. L.; Atar, N. A Novel Detection Approach for Serotonin by Graphene Quantum Dots/Two-Dimensional (2D) Hexagonal Boron Nitride Nanosheets with Molecularly Imprinted Polymer. *Appl. Surf. Sci.* **2018**, *458*, 648–655.
- (1048) Naguib, M.; Mashtalir, O.; Carle, J.; Presser, V.; Lu, J.; Hultman, L.; Gogotsi, Y.; Barsoum, M. W. Two-Dimensional Transition Metal Carbides. *ACS Nano* **2012**, *6*, 1322–1331.
- (1049) Xu, B.; Zhu, M.; Zhang, W.; Zhen, X.; Pei, Z.; Xue, Q.; Zhi, C.; Shi, P. Ultrathin MXene-Micropattern-Based Field-Effect Transistor for Probing Neural Activity. *Adv. Mater.* **2016**, *28*, 3333–3339.
- (1050) Wang, F.; Yang, C.; Duan, C.; Xiao, D.; Tang, Y.; Zhu, J. An Organ-Like Titanium Carbide Material (MXene) with Multilayer Structure Encapsulating Hemoglobin for a Mediator-Free Biosensor. *J. Electrochem. Soc.* **2015**, *162*, B16–B21.
- (1051) Wang, F.; Yang, C.; Duan, M.; Tang, Y.; Zhu, J. TiO₂ Nanoparticle Modified Organ-Like Ti₃C₂ MXene Nanocomposite Encapsulating Hemoglobin for a Mediator-Free Biosensor with Excellent Performances. *Biosens. Bioelectron.* **2015**, *74*, 1022–1028.
- (1052) Lorencova, L.; Bertok, T.; Dosekova, E.; Holazova, A.; Paprckova, D.; Vikartovska, A.; Sasinkova, V.; Filip, J.; Kasak, P.; Jerigova, M.; Velic, D.; Mahmoud, K. A.; Tkac, J. Electrochemical Performance of Ti₃C₂T_x MXene in Aqueous Media: Towards Ultrasensitive H₂O₂ Sensing. *Electrochim. Acta* **2017**, *235*, 471–479.
- (1053) Rakhi, R. B.; Nayak, P.; Xia, C.; Alshareef, H. N. Novel Amperometric Glucose Biosensor Based on MXene Nanocomposite. *Sci. Rep.* **2016**, *6*, 36422.
- (1054) Liu, H.; Duan, C.; Yang, C.; Shen, W.; Wang, F.; Zhu, Z. A Novel Nitrite Biosensor Based on the Direct Electrochemistry of Hemoglobin Immobilized on MXene-Ti₃C₂. *Sens. Actuators, B* **2015**, *218*, 60–66.
- (1055) Rakhi, R. B.; Nayak, P.; Xia, C.; Alshareef, H. N. Novel Amperometric Glucose Biosensor Based on MXene Nanocomposite. *Sci. Rep.* **2016**, *6*, 36422.
- (1056) Qi, S.; Zhao, B.; Tang, H.; Jiang, X. Determination of Ascorbic Acid, Dopamine, and Uric Acid by a Novel Electrochemical Sensor Based on Pristine Graphene. *Electrochim. Acta* **2015**, *161*, 395–402.
- (1057) Wu, D.; Li, Y.; Zhang, Y.; Wang, P.; Wei, Q.; Du, B. Sensitive Electrochemical Sensor for Simultaneous Determination of Dopamine, Ascorbic Acid, and Uric Acid Enhanced by Amino-Group Functionalized Mesoporous Fe₃O₄@Graphene Sheets. *Electrochim. Acta* **2014**, *116*, 244–249.
- (1058) Sun, C. L.; Lee, H. H.; Yang, J. M.; Wu, C. C. The Simultaneous Electrochemical Detection of Ascorbic Acid, Dopamine, and Uric Acid Using Graphene/Size-Selected Pt Nanocomposites. *Biosens. Bioelectron.* **2011**, *26*, 3450–3455.
- (1059) Yang, L.; Liu, D.; Huang, J.; You, T. Simultaneous Determination of Dopamine, Ascorbic Acid and Uric Acid at Electrochemically Reduced Graphene Oxide Modified Electrode. *Sens. Actuators, B* **2014**, *193*, 166–172.
- (1060) Wang, C.; Du, J.; Wang, H.; Zou, C. e.; Jiang, F.; Yang, P.; Du, Y. A Facile Electrochemical Sensor Based on Reduced Graphene Oxide and Au Nanoplates Modified Glassy Carbon Electrode for Simultaneous Detection of Ascorbic Acid, Dopamine and Uric Acid. *Sens. Actuators, B* **2014**, *204*, 302–309.
- (1061) Zhu, Q.; Chai, Y.; Yuan, R.; Zhuo, Y.; Han, J.; Li, Y.; Liao, N. Amperometric Immunosensor for Simultaneous Detection of Three Analytes in One Interface Using Dual Functionalized Graphene Sheets Integrated with Redox-Probes as Tracer Matrixes. *Biosens. Bioelectron.* **2013**, *43*, 440–445.
- (1062) Zhao, L.; Li, S.; He, J.; Tian, G.; Wei, Q.; Li, H. Enzyme-Free Electrochemical Immunosensor Configured with Au-Pd Nanocrystals and N-Doped Graphene Sheets for Sensitive Detection of AFP. *Biosens. Bioelectron.* **2013**, *49*, 222–225.

- (1063) Zhang, H.; Han, Y.; Guo, Y.; Dong, C. Porphyrin Functionalized Graphene Nanosheets-Based Electrochemical Aptasensor for Label-Free ATP Detection. *J. Mater. Chem.* **2012**, *22*, 23900.
- (1064) Lei, Y. M.; Xiao, M. M.; Li, Y. T.; Xu, L.; Zhang, H.; Zhang, Z. Y.; Zhang, G. J. Detection of Heart Failure-Related Biomarker in Whole Blood with Graphene Field Effect Transistor Biosensor. *Biosens. Bioelectron.* **2017**, *91*, 1–7.
- (1065) Yang, L.; Wang, G.; Liu, Y.; Wang, M. Development of a Biosensor Based on Immobilization of Acetylcholinesterase on NiO Nanoparticles-Carboxylic Graphene-Nafion Modified Electrode for Detection of Pesticides. *Talanta* **2013**, *113*, 135–141.
- (1066) Huang, J. Y.; Zhao, L.; Lei, W.; Wen, W.; Wang, Y. J.; Bao, T.; Xiong, H. Y.; Zhang, X. H.; Wang, S. F. A High-Sensitivity Electrochemical Aptasensor of Carcinoembryonic Antigen Based on Graphene Quantum Dots-Ionic Liquid-Nafion Nanomatrix and Dnazyme-Assisted Signal Amplification Strategy. *Biosens. Bioelectron.* **2018**, *99*, 28–33.
- (1067) Manjunatha, R.; Shivappa Suresh, G.; Melo, J. S.; D'Souza, S. F.; Venkatesha, T. V. An Amperometric Bierenzymatic Cholesterol Biosensor Based on Functionalized Graphene Modified Electrode and Its Electrocatalytic Activity Towards Total Cholesterol Determination. *Talanta* **2012**, *99*, 302–309.
- (1068) Cao, S.; Zhang, L.; Chai, Y.; Yuan, R. Electrochemistry of Cholesterol Biosensor Based on a Novel Pt-Pd Bimetallic Nanoparticle Decorated Graphene Catalyst. *Talanta* **2013**, *109*, 167–172.
- (1069) Ruecha, N.; Rangkupan, R.; Rodthongkum, N.; Chailapakul, O. Novel Paper-Based Cholesterol Biosensor Using Graphene/Polyvinylpyrrolidone/Polyaniline Nanocomposite. *Biosens. Bioelectron.* **2014**, *52*, 13–19.
- (1070) Jiang, B.; Wang, M.; Chen, Y.; Xie, J.; Xiang, Y. Highly Sensitive Electrochemical Detection of Cocaine on Graphene/AuNP Modified Electrode via Catalytic Redox-Recycling Amplification. *Biosens. Bioelectron.* **2012**, *32*, 305–308.
- (1071) Vabbina, P. K.; Kaushik, A.; Pokhrel, N.; Bhansali, S.; Pala, N. Electrochemical Cortisol Immunosensors Based on Sonochemically Synthesized Zinc Oxide 1D Nanorods and 2D Nanoflakes. *Biosens. Bioelectron.* **2015**, *63*, 124–130.
- (1072) Xu, S.; Zhan, J.; Man, B.; Jiang, S.; Yue, W.; Gao, S.; Guo, C.; Liu, H.; Li, Z.; Wang, J.; Zhou, Y. Real-Time Reliable Determination of Binding Kinetics of DNA Hybridization Using a Multi-Channel Graphene Biosensor. *Nat. Commun.* **2017**, *8*, 14902.
- (1073) Cao, X. Ultra-Sensitive Electrochemical DNA Biosensor Based on Signal Amplification Using Gold Nanoparticles Modified with Molybdenum Disulfide, Graphene and Horseradish Peroxidase. *Microchim. Acta* **2014**, *181*, 1133–1141.
- (1074) Liu, Y.-M.; Zhou, M.; Liu, Y.-Y.; Shi, G.-F.; Zhang, J.-J.; Cao, J.-T.; Huang, K.-J.; Chen, Y.-H. Fabrication of Electrochemiluminescence Aptasensor Based on In Situ Growth of Gold Nanoparticles on Layered Molybdenum Disulfide for Sensitive Detection of Platelet-Derived Growth Factor-BB. *RSC Adv.* **2014**, *4*, 22888.
- (1075) Wang, K.; He, M. Q.; Zhai, F. H.; He, R. H.; Yu, Y. L. A Novel Electrochemical Biosensor Based on Polyadenine Modified Aptamer for Label-Free and Ultrasensitive Detection of Human Breast Cancer Cells. *Talanta* **2017**, *166*, 87–92.
- (1076) Han, H. S.; Seol, H.; Kang, D. H.; Ahmed, M. S.; You, J.-M.; Jeon, S. Electrochemical Oxidation and Determination of Dopamine in the Presence of AA Using Ferulic Acid Functionalized Electrochemically Reduced Graphene. *Sens. Actuators, B* **2014**, *204*, 289–296.
- (1077) Kim, Y. R.; Bong, S.; Kang, Y. J.; Yang, Y.; Mahajan, R. K.; Kim, J. S.; Kim, H. Electrochemical Detection of Dopamine in the Presence of Ascorbic Acid Using Graphene Modified Electrodes. *Biosens. Bioelectron.* **2010**, *25*, 2366–2369.
- (1078) Alwarappan, S.; Erdem, A.; Liu, C.; Li, C.-Z. Probing the Electrochemical Properties of Graphene Nanosheets for Biosensing Applications. *J. Phys. Chem. C* **2009**, *113*, 8853–8857.
- (1079) Qiu, J.-D.; Huang, J.; Liang, R.-P. Nanocomposite Film Based on Graphene Oxide for High Performance Flexible Glucose Biosensor. *Sens. Actuators, B* **2011**, *160*, 287–294.
- (1080) Song, J.; Xu, L.; Zhou, C.; Xing, R.; Dai, Q.; Liu, D.; Song, H. Synthesis of Graphene Oxide Based CuO Nanoparticles Composite Electrode for Highly Enhanced Nonenzymatic Glucose Detection. *ACS Appl. Mater. Interfaces* **2013**, *5*, 12928–12934.
- (1081) Luo, J.; Jiang, S.; Zhang, H.; Jiang, J.; Liu, X. A Novel Non-Enzymatic Glucose Sensor Based on Cu Nanoparticle Modified Graphene Sheets Electrode. *Anal. Chim. Acta* **2012**, *709*, 47–53.
- (1082) Zeng, G.; Li, W.; Ci, S.; Jia, J.; Wen, Z. Highly Dispersed NiO Nanoparticles Decorating Graphene Nanosheets for Non-Enzymatic Glucose Sensor and Biofuel Cell. *Sci. Rep.* **2016**, *6*, 36454.
- (1083) Chen, H.; Rim, Y. S.; Wang, I. C.; Li, C.; Zhu, B.; Sun, M.; Goorsky, M. S.; He, X.; Yang, Y. Quasi-Two-Dimensional Metal Oxide Semiconductors Based Ultrasensitive Potentiometric Biosensors. *ACS Nano* **2017**, *11*, 4710–4718.
- (1084) Parlak, O.; Incel, A.; Uzun, L.; Turner, A. P. F.; Tiwari, A. Structuring Au Nanoparticles on Two-Dimensional MoS₂ Nanosheets for Electrochemical Glucose Biosensors. *Biosens. Bioelectron.* **2017**, *89*, 545–550.
- (1085) Mani, V.; Devadas, B.; Chen, S. M. Direct Electrochemistry of Glucose Oxidase at Electrochemically Reduced Graphene Oxide-Multiwalled Carbon Nanotubes Hybrid Material Modified Electrode for Glucose Biosensor. *Biosens. Bioelectron.* **2013**, *41*, 309–315.
- (1086) Li, M.; Bo, X.; Mu, Z.; Zhang, Y.; Guo, L. Electrodeposition of Nickel Oxide and Platinum Nanoparticles on Electrochemically Reduced Graphene Oxide Film as a Nonenzymatic Glucose. *Sens. Actuators, B* **2014**, *192*, 261–268.
- (1087) Yang, Y.; Yang, X.; Zou, X.; Wu, S.; Wan, D.; Cao, A.; Liao, L.; Yuan, Q.; Duan, X. Ultrafine Graphene Nanomesh with Large on/off Ratio for High-Performance Flexible Biosensors. *Adv. Funct. Mater.* **2017**, *27*, 1604096.
- (1088) Song, W.; Li, H.; Liu, H.; Wu, Z.; Qiang, W.; Xu, D. Fabrication of Streptavidin Functionalized Silver Nanoparticle Decorated Graphene and Its Application in Disposable Electrochemical Sensor for Immunoglobulin. *Electrochim. Commun.* **2013**, *31*, 16–19.
- (1089) Wang, G.; He, X.; Chen, L.; Zhu, Y.; Zhang, X. Ultrasensitive IL-6 Electrochemical Immunosensor Based on Au Nanoparticles-Graphene-Silica Biointerface. *Colloids Surf., B* **2014**, *116*, 714–719.
- (1090) Wang, R.; Ruan, C.; Kanayeva, D.; Lassiter, K.; Li, Y. TiO₂ Nanowire Bundle Microelectrode Based Impedance Immunosensor for Rapid and Sensitive Detection of Listeria Monocytogenes. *Nano Lett.* **2008**, *8*, 2625–2631.
- (1091) Bai, L.; Yuan, R.; Chai, Y.; Zhuo, Y.; Yuan, Y.; Wang, Y. Simultaneous Electrochemical Detection of Multiple Analytes Based on Dual Signal Amplification of Single-Walled Carbon Nanotubes and Multi-Labeled Graphene Sheets. *Biomaterials* **2012**, *33*, 1090–1096.
- (1092) Deng, K.; Xiang, Y.; Zhang, L.; Chen, Q.; Fu, W. An Aptamer-Based Biosensing Platform for Highly Sensitive Detection of Platelet-Derived Growth Factor via Enzyme-Mediated Direct Electrochemistry. *Anal. Chim. Acta* **2013**, *759*, 61–65.
- (1093) Pan, L. H.; Kuo, S. H.; Lin, T. Y.; Lin, C. W.; Fang, P. Y.; Yang, H. W. An Electrochemical Biosensor to Simultaneously Detect VEGF and PSA for Early Prostate Cancer Diagnosis Based on Graphene Oxide/ssDNA/PLLA Nanoparticles. *Biosens. Bioelectron.* **2017**, *89*, 598–605.
- (1094) Mao, K.; Wu, D.; Li, Y.; Ma, H.; Ni, Z.; Yu, H.; Luo, C.; Wei, Q.; Du, B. Label-Free Electrochemical Immunosensor Based on Graphene/Methylene Blue Nanocomposite. *Anal. Biochem.* **2012**, *422*, 22–27.
- (1095) Yan, M.; Zang, D.; Ge, S.; Ge, L.; Yu, J. A Disposable Electrochemical Immunosensor Based on Carbon Screen-Printed Electrodes for the Detection of Prostate Specific Antigen. *Biosens. Bioelectron.* **2012**, *38*, 355–361.
- (1096) Li, Y.; Han, J.; Chen, R.; Ren, X.; Wei, Q. Label Electrochemical Immunosensor for Prostate-Specific Antigen Based

- on Graphene and Silver Hybridized Mesoporous Silica. *Anal. Biochem.* **2015**, *469*, 76–82.
- (1097) Su, S.; Sun, H.; Xu, F.; Yuwen, L.; Wang, L. Highly Sensitive and Selective Determination of Dopamine in the Presence of Ascorbic Acid Using Gold Nanoparticles-Decorated MoS₂nanosheets Modified Electrode. *Electroanalysis* **2013**, *25*, 2523–2529.
- (1098) Kim, H. U.; Kim, H. Y.; Kulkarni, A.; Ahn, C.; Jin, Y.; Kim, Y.; Lee, K. N.; Lee, M. H.; Kim, T. A Sensitive Electrochemical Sensor for in Vitro Detection of Parathyroid Hormone Based on a MoS₂-Graphene Composite. *Sci. Rep.* **2016**, *6*, 34587.
- (1099) Du, H.; Ye, J.; Zhang, J.; Huang, X.; Yu, C. Graphene Nanosheets Modified Glassy Carbon Electrode as a Highly Sensitive and Selective Voltammetric Sensor for Rutin. *Electroanalysis* **2010**, *22*, 2399–2406.
- (1100) Singh, V. V.; Nigam, A. K.; Yadav, S. S.; Tripathi, B. K.; Srivastava, A.; Boopathi, M.; Singh, B. Graphene Oxide as Carboelectrocatalyst for in Situ Electrochemical Oxidation and Sensing of Chemical Warfare Agent Simulant. *Sens. Actuators, B* **2013**, *188*, 1218–1224.
- (1101) Wang, Y.; Yuan, R.; Chai, Y.; Yuan, Y.; Bai, L. In Situ Enzymatic Silver Enhancement Based on Functionalized Graphene Oxide and Layer-by-Layer Assembled Gold Nanoparticles for Ultrasensitive Detection of Thrombin. *Biosens. Bioelectron.* **2012**, *38*, 50–54.
- (1102) Wang, Y.; Xiao, Y.; Ma, X.; Li, N.; Yang, X. Label-Free and Sensitive Thrombin Sensing on a Molecularly Grafted Aptamer on Graphene. *Chem. Commun.* **2012**, *48*, 738–740.
- (1103) Jiang, L.; Yuan, R.; Chai, Y.; Yuan, Y.; Bai, L.; Wang, Y. Aptamer-Based Highly Sensitive Electrochemical Detection of Thrombin via the Amplification of Graphene. *Analyst* **2012**, *137*, 2415–2420.
- (1104) Guo, Y.; Han, Y.; Guo, Y.; Dong, C. Graphene-Orange II Composite Nanosheets with Electroactive Functions as Label-Free Aptasensing Platform for "Signal-on" Detection of Protein. *Biosens. Bioelectron.* **2013**, *45*, 95–101.
- (1105) Zhang, J.; Chai, Y.; Yuan, R.; Yuan, Y.; Bai, L.; Xie, S. A Highly Sensitive Electrochemical Aptasensor for Thrombin Detection Using Functionalized Mesoporous Silica@Multiwalled Carbon Nanotubes as Signal Tags and DNAzyme Signal Amplification. *Analyst* **2013**, *138*, 6938–6945.
- (1106) Yuan, Y.; Liu, G.; Yuan, R.; Chai, Y.; Gan, X.; Bai, L. Dendrimer Functionalized Reduced Graphene Oxide as Nanocarrier for Sensitive Pseudobienzyme Electrochemical Aptasensor. *Biosens. Bioelectron.* **2013**, *42*, 474–480.
- (1107) Bai, L.; Yan, B.; Chai, Y.; Yuan, R.; Yuan, Y.; Xie, S.; Jiang, L.; He, Y. An Electrochemical Aptasensor for Thrombin Detection Based on Direct Electrochemistry of Glucose Oxidase Using a Functionalized Graphene Hybrid for Amplification. *Analyst* **2013**, *138*, 6595–6599.
- (1108) Xie, S.; Chai, Y.; Yuan, R.; Bai, L.; Yuan, Y.; Wang, Y. A Dual-Amplification Aptasensor for Highly Sensitive Detection of Thrombin Based on the Functionalized Graphene-Pd Nanoparticles Composites and the Hemin/G-Quadruplex. *Anal. Chim. Acta* **2012**, *755*, 46–53.
- (1109) Yuan, Y.; Gou, X.; Yuan, R.; Chai, Y.; Zhuo, Y.; Ye, X.; Gan, X. Graphene-Promoted 3,4,9,10-Perylenetetracarboxylic Acid Nanocomposite as Redox Probe in Label-Free Electrochemical Aptasensor. *Biosens. Bioelectron.* **2011**, *30*, 123–127.
- (1110) Peng, K.; Zhao, H.; Wu, X.; Yuan, Y.; Yuan, R. Ultrasensitive Aptasensor Based on Graphene-3,4,9,10-Perylenetetracarboxylic Dianhydride as Platform and Functionalized Hollow PtCo Nano-chains as Enhancers. *Sens. Actuators, B* **2012**, *169*, 88–95.
- (1111) Zhao, J.; Chen, G.; Zhu, L.; Li, G. Graphene Quantum Dots-Based Platform for the Fabrication of Electrochemical Biosensors. *Electrochim. Commun.* **2011**, *13*, 31–33.
- (1112) Xie, S.; Yuan, R.; Chai, Y.; Bai, L.; Yuan, Y.; Wang, Y. Label-Free Electrochemical Aptasensor for Sensitive Thrombin Detection Using Layer-by-Layer Self-Assembled Multilayers with Toluidine Blue-Graphene Composites and Gold Nanoparticles. *Talanta* **2012**, *98*, 7–13.
- (1113) Zhang, Z.; Luo, L.; Zhu, L.; Ding, Y.; Deng, D.; Wang, Z. Aptamer-Linked Biosensor for Thrombin Based on AuNPs/Thionine-Graphene Nanocomposite. *Analyst* **2013**, *138*, 5365–5370.
- (1114) Xu, Z.; He, C.; Sun, T.; Wang, L. Sensitive Electrochemical Aptasensor for Thrombin Detection with Platinum Nanoparticles, Blocking Reagent-Horseradish Peroxidase and Graphene Oxide as Enhancers. *Electroanalysis* **2013**, 2339–2344.
- (1115) Wu, T.; Li, T.; Liu, Z.; Guo, Y.; Dong, C. Electrochemical Sensor for Sensitive Detection of Triclosan Based on Graphene/Palladium Nanoparticles Hybrids. *Talanta* **2017**, *164*, 556–562.
- (1116) Xing, X.; Liu, S.; Yu, J.; Lian, W.; Huang, J. Electrochemical Sensor Based on Molecularly Imprinted Film at Polypyrrole-Sulfonated Graphene/Hyaluronic Acid-Multiwalled Carbon Nanotubes Modified Electrode for Determination of Tryptamine. *Biosens. Bioelectron.* **2012**, *31*, 277–283.
- (1117) Zhang, Y.; Zheng, J.; Guo, M. Preparation of Molecularly Imprinted Electrochemical Sensor for Detection of Vincristine Based on Reduced Graphene Oxide/Gold Nanoparticle Composite Film. *Chin. J. Chem.* **2016**, *34*, 1268–1276.
- (1118) Duong, D. L.; Yun, S. J.; Lee, Y. H. Van der Waals Layered Materials: Opportunities and Challenges. *ACS Nano* **2017**, *11*, 11803–11830.
- (1119) Chia, X.; Eng, A. Y.; Ambrosi, A.; Tan, S. M.; Pumera, M. Electrochemistry of Nanostructured Layered Transition-Metal Dichalcogenides. *Chem. Rev.* **2015**, *115*, 11941–11966.
- (1120) Eredia, M.; Bertolazzi, S.; Leydecker, T.; El Garah, M.; Janica, I.; Melinte, G.; Ersen, O.; Ciesielski, A.; Samori, P. Morphology and Electronic Properties of Electrochemically Exfoliated Graphene. *J. Phys. Chem. Lett.* **2017**, *8*, 3347–3355.
- (1121) Choi, W.; Choudhary, N.; Han, G. H.; Park, J.; Akinwande, D.; Lee, Y. H. Recent Development of Two-Dimensional Transition Metal Dichalcogenides and Their Applications. *Mater. Today* **2017**, *20*, 116–130.
- (1122) McManus, D.; Vranic, S.; Withers, F.; Sanchez-Romaguera, V.; Macucci, M.; Yang, H.; Sorrentino, R.; Parvez, K.; Son, S. K.; Iannaccone, G.; Kostarelos, K.; Fiori, G.; Casiraghi, C. Water-Based and Biocompatible 2D Crystal Inks for All-Inkjet-Printed Heterostructures. *Nat. Nanotechnol.* **2017**, *12*, 343–350.
- (1123) Shavanova, K.; Bakakina, Y.; Burkova, I.; Shtepliuk, I.; Viter, R.; Ubelis, A.; Beni, V.; Starodub, N.; Yakimova, R.; Khranovskyy, V. Application of 2D Non-Graphene Materials and 2D Oxide Nanostructures for Biosensing Technology. *Sensors* **2016**, *16*, 223.
- (1124) Kenry; Lim, C. T. Biocompatibility and Nanotoxicity of Layered Two-Dimensional Nanomaterials. *ChemNanoMat* **2017**, *3*, 5–16.
- (1125) Seo, H.-K.; Kim, K.; Min, S.-Y.; Lee, Y.; Park, C. E.; Raj, R.; Lee, T.-W. Direct Growth of Graphene-Dielectric Bi-Layer Structure on Device Substrates from Si-Based Polymer. *2D Mater.* **2017**, *4*, 024001.
- (1126) Hastrup, S.; Strange, M.; Pandey, M.; Deilmann, T.; Schmidt, P. S.; Hinsche, N. F.; Gjerding, M. N.; Torelli, D.; Larsen, P. M.; Riis-Jensen, A. C.; Gath, J.; Jacobsen, K. W.; Jørgen Mortensen, J.; Olsen, T.; Thygesen, K. S. The Computational 2D Materials Database: High-Throughput Modeling and Discovery of Atomically Thin Crystals. *2D Mater.* **2018**, *5*, 042002.
- (1127) Burch, K. S. Electric Switching of Magnetism in 2D. *Nat. Nanotechnol.* **2018**, *13*, 532.
- (1128) Hellman, F.; Hoffmann, A.; Tserkovnyak, Y.; Beach, G. S. D.; Fullerton, E. E.; Leighton, C.; MacDonald, A. H.; Ralph, D. C.; Arena, D. A.; Durr, H. A.; Fischer, P.; Grollier, J.; Heremans, J. P.; Jungwirth, T.; Kimel, A. V.; Koopmans, B.; Krivorotov, I. N.; May, S. J.; Petford-Long, A. K.; Rondinelli, J. M.; Samarth, N.; Schuller, I. K.; Slavin, A. N.; Stiles, M. D.; Tchernyshov, O.; Thiaville, A.; Zink, B. L. Interface-Induced Phenomena in Magnetism. *Rev. Mod. Phys.* **2017**, *89*, 025006.
- (1129) Bartual-Murgui, C.; Akou, A.; Thibault, C.; Molnár, G.; Vieu, C.; Salmon, L.; Bousseksou, A. Spin-Crossover Metal–Organic

Frameworks: Promising Materials for Designing Gas Sensors. *J. Mater. Chem. C* **2015**, *3*, 1277–1285.

(1130) Nakatsuka, N.; Yang, K. A.; Abendroth, J. M.; Cheung, K. M.; Xu, X.; Yang, H.; Zhao, C.; Zhu, B.; Rim, Y. S.; Yang, Y.; Weiss, P. S.; Stojanovic, M. N.; Andrews, A. M. Aptamer-Field-Effect Transistors Overcome Debye Length Limitations for Small-Molecule Sensing. *Science* **2018**, *362*, 319–324.

(1131) Hoskins, B. F.; Robson, R. Design and Construction of a New Class of Scaffolding-Like Materials Comprising Infinite Polymeric Frameworks of 3D-Linked Molecular Rods. *J. Am. Chem. Soc.* **1990**, *112*, 1546–1554.

(1132) Fujita, M.; Kwon, Y. J.; Washizu, S.; Ogura, K. Preparation, Clathration Ability, and Catalysis of a Two-Dimensional Square Network Material Composed of Cadmium(II) and 4,4'-Bipyridine. *J. Am. Chem. Soc.* **1994**, *116*, 1151–1152.

(1133) Yaghi, O. M.; Li, H. L. Hydrothermal Synthesis of a Metal–Organic Framework Containing Large Rectangular Channels. *J. Am. Chem. Soc.* **1995**, *117*, 10401–10402.

(1134) Chen, X.-M.; Cai, Z.-X.; Huang, Z.-Y.; Oyama, M.; Jiang, Y.-Q.; Chen, X. Ultrafine Palladium Nanoparticles Grown on Graphene Nanosheets for Enhanced Electrochemical Sensing of Hydrogen Peroxide. *Electrochim. Acta* **2013**, *97*, 398–403.

(1135) Su, S.; Han, X.; Lu, Z.; Liu, W.; Zhu, D.; Chao, J.; Fan, C.; Wang, L.; Song, S.; Weng, L.; Wang, L. Facile Synthesis of a MoS₂-Prussian Blue Nanocube Nanohybrid-Based Electrochemical Sensing Platform for Hydrogen Peroxide and Carcinoembryonic Antigen Detection. *ACS Appl. Mater. Interfaces* **2017**, *9*, 12773–12781.

(1136) Zhang, D.; Liu, J.; Jiang, C.; Li, P.; Sun, Y. e. High-Performance Sulfur Dioxide Sensing Properties of Layer-by-Layer Self-Assembled Titania-Modified Graphene Hybrid Nanocomposite. *Sens. Actuators, B* **2017**, *245*, 560–567.

(1137) Wu, P.; Shao, Q.; Hu, Y.; Jin, J.; Yin, Y.; Zhang, H.; Cai, C. Direct Electrochemistry of Glucose Oxidase Assembled on Graphene and Application to Glucose Detection. *Electrochim. Acta* **2010**, *55*, 8606–8614.

(1138) Galdino, N. M.; Brehm, G. S.; Bussamara, R.; Gonçalves, W. D. G.; Abarca, G.; Scholten, J. D. Sputtering Deposition of Gold Nanoparticles onto Graphene Oxide Functionalized with Ionic Liquids: Biosensor Materials for Cholesterol Detection. *J. Mater. Chem. B* **2017**, *5*, 9482–9486.

(1139) Ding, S. Y.; Wang, W. Covalent Organic Frameworks (COFs): From Design to Applications. *Chem. Soc. Rev.* **2013**, *42*, 548–568.

(1140) Huang, N.; Wang, P.; Jiang, D. Covalent Organic Frameworks: A Materials Platform for Structural and Functional Designs. *Nat. Rev. Mater.* **2016**, *1*, 16068.